X International Workshop

MICROWAVE DISCHARGES: FUNDAMENTALS AND APPLICATIONS

3-7 September, 2018, Zvenigorod, Russia

Proceedings

Edited by Yu. A. Lebedev

Yanus-K
Moscow
2018

PASC 52.25, 52.70, 52.77, 52.80

Microwave Discharges: Fundamentals and Applications. Proceedings of the X International Workshop on Microwave Discharges: Fundamentals and Applications (MD-10). Zvenigorod, September 3-7, 2018.

Moscow: Yanus-K, 2018. – 268 p.

ISBN 978-5-8037-0746-2

ISBN 978-5-9903264-9-1

Edited by Yu. A. Lebedev

This book includes the papers presented on the MD-10 by scientists from different countries on the methods of microwave plasma generations, physics of high and low pressure microwave discharges, microwave discharge modeling and diagnostics and application.

Workshop is held under financial support of RFBR grant # 18-02-20099

ISBN 978-5-8037-0746-2

ISBN 978-5-9903264-9-1

X International Workshop "Microwave Discharges: Fundamentals and Applications"

Workshop Chairman: Yu. Lebedev (Russia)

International Scientific Committee

J. Asmussen (USA)
P. Awakowicz (Germany)
E. Benova (Bulgaria)
F. Dias (Portugal)
A. Gamero (Spain)
E. Jerby (Israel)
Yu. Lebedev (Russia, Chairman)
A. Lacoste (France)
M. Moisan (Canada)
M. Nagatsu (Japan)
J.J.A.M. van der Mullen (Belgium)

Honorary Members:

M. Kando (Japan)
J. Marec (France)

Local Organizing Committee (LOC)

Yu. A. Lebedev (Chairman)
V. A. Ivanov (Vice-chairman)
T. I. Kamolova
T.E. Krivonosova
S. N. Satunin (Web-page)
D.G.Vasil'kov
E.V.Voronova

Organizers

- Russian Foundation for Basic Research
- Russian Academy of Sciences
- European Physical Society
- The United Physical Society of the Russia
- Scientific Council of RAS on Physics of Low temperature plasma
- Scientific Council of RAS on Plasma Physics
- Topchiev Institute of Petrochemical Synthesis of the Russian Academy of Sciences
- Prokhorov General Physics Institute of the Russian Academy of Sciences
- Science and Technology Center PLASMAIOFAN

Information support:

- Association for Microwave Power in Europe for Research and Education (AMPERE)
- Scientific and Technical Journal "Prikladnaya Fizika" (Applied Physics)

PREFACE

This book is a result of the X International Workshop on "Microwave Discharges: Fundamentals and Applications" which was held in September 3-7, 2018 in Zvenigorod, Russia.

Physics of microwave discharges is the intensively developed area of plasma physics. This interest is caused by two main reasons. From one side it is initiated by principal fundamental problems that are integrated in one object: the problems of electrodynamics of microwaves in the plasma with strongly coupled physical and chemical phenomena in gas phase and heterogeneous systems. From other side it is initiated by promising applications, part of which have already realized but main part are still waiting for their technical solution

The main purposes of the Workshop were discussing of recent achievements in the study and application of microwave plasma, searching the directions for future investigations, and promotion of close relationship between scientists from different countries. Topics of the Workshop cover wide range of problems in theory, experiments, and applications of microwave discharges and yield the state-of-the-art and trends in discharge theory, modeling, and diagnostics, methods of microwave plasma generation, high and low pressure microwave discharges, continuous wave and pulsed microwave discharges, interaction of microwaves with a plasma, applications of microwave plasma. All these topics are contained in many of papers and therefore they are difficult to attribute unambiguously to one of the sections. Therefore, in this book they are grouped by presentation status: plenary, invited, topical papers, and posters.

We hope that this book will be useful for scientists and engineers involved in the study of low temperature plasma physics and plasma application.

CALENDAR

of the International Workshops "Microwave Discharges: Fundamentals and Applications"

- 1992, May 11-15, NATO ARW Workshop, Vimeiro, Portugal. Director Prof. C.M. Ferreira
- 1994, September 5-8, Zvenigorod, Russia. Chairman Prof. A.A. Rukhadze
- 1997, April 20-25, Fontenvraud, France. Chairman Prof. J. Marec
- 2000, September 18-22, Zvenigorod, Russia. Chairman Prof. Yu.A. Lebedev
- 2003, July 08-12, Greifswald, Germany. Chairman Dr. A. Ohl
- 2006, September 11-16, Zvenigorod, Russia. Chairman Prof. Yu.A. Lebedev
- 2009, September 22-27, Hamamatsu, Japan. Chairman Prof. M.Kando
- 2012, September 10-14, Zvenigorod, Russia. Chairman Prof. Yu.A. Lebedev
- 2015, September 7-11, Cordoba, Spain. Chairman Prof. A. Gamero
- 2018, September 3-7, Zvenigorod, Russia. Chairman Prof. Yu.A. Lebedev

The Local Organizing Committee wishes to thank the following for their contribution for success of this Workshop:

- The Russian Academy of Sciences
- The Russian Foundation for Basic Research
- Plasmaiofan Co.Ltd. Science&Technology Center

We would like to acknowledge all people who helped to organize the Workshop. Special thanks are given to Dr. V.A. Ivanov, S.N. Satunin, Ms. T.I.Kamolova, T.E. Krivonosova and E.V. Voronova for their invaluable contribution to preparing and holding of the Workshop. We would like also to acknowledge all participants for interesting presentations and discussions that made our scientific meeting successful.

Yuri A. Lebedev

CONTENTS

I. PLENARY TALKS

2. INVITED TALKS

3. TOPICAL TALKS

IV. POSTERS

1. Plenary papers

SELF-ORGANIZATION IN MICROWAVE FILAMENTARY DISCHARGES

V. Kudrle, M. Snirer, J. Toman, O. Jašek, J. Jurmanová, L. Potočňáková, J. Hnilica

Masaryk University, Kotlarska 267/2, CZ-61137 Brno, Czech Republic

Abstract. In this work we present an overview of common instabilities in medium and atmospheric pressure microwave discharges and their influence on applications of such plasma sources. To demonstrate a general validity of the results, three different types of plasma excitation were chosen – surfatron, surfaguide and microwave plasma torch.

1. INTRODUCTION

Microwave (MW) discharges can operate under wide-range of experimental conditions leading to variety of applications from plasma surface modification, thin film deposition to production of various nanomaterials [1]. Generally, stable and repeatable functioning is required and so the understanding of processes, which can lead to sudden changes in important plasma parameters, is needed.

In this work we investigated various aspects of self-organisation in microwave discharges at medium and atmospheric pressure, which were excited by travelling electromagnetic wave. To demonstrate a general validity of the results, three common types of microwave discharges were used – surfatron and surfaguide launchers [2] and microwave plasma torch [3]. Atmospheric pressure plasma columns are often radially constricted [2, 4], forming one or multiple bright filaments depending on the external conditions, such as input power, flow rates or reactor dimensions. These filaments have often a random spatial and temporal locations. However, in specific cases there are collective regimes in which the filaments are spatially and temporary self-organized at large scales [5], usually axially oriented and wall-stabilized.

The filaments can be stationary or transient (revolving), helically twisted, creating different operational modes [6]. Similarity with different types of discharges was shown for example for RF plasma jet [7, 8]. Some conditions can lead to stratification of the filaments. There were observed striations and spherical nonuniformities in atmospheric argon micro discharges [9], stationary striations in SW produced plasma columns of Ar [10] or as a droplet striations formed in MW Ar atmospheric pressure jets [11].

Instabilities in form of filaments or striations are usually considered as a demonstration of the self-organization in the system. It is caused by combination of many factors as e.g. electromagnetic forces, thermal gradients or gas flows.

2. EXPERIMENTAL

In this paper three different experimental set-ups for the microwave discharge excitation were used (Fig. 1). All of them are of quite standard arrangement. The microwave power was generated by 2450 MHz magnetron, which was protected by ferrite circulator, both of them water-cooled. Directional coupler with calibrated diode detectors and impedance matching unit were used to minimise the reflected power. The microwave line used standard WR340 waveguide. Typical operating power was in the range of several hundred Watts.

The gas line was also standard – argon (99.998% purity) from pressure bottle went through pressure reducing valve and mass flow controller (Bronkhorst). While most of the gas line is made of stainless steel, the last meter or two are of polyethylene tubing, which greatly simplifies manipulation.

2.1. Experimental set-up: Surfatron. Microwave plasma was excited in commercial surfatron launcher Sairem 80 with integrated matching, inside vertically oriented fused silica discharge tube (6 mm inner/8 mm outer diameter). The microwave power was supplied from the waveguide line to the surfatron by a high power coaxial cable. This limited the maximum power to 300 W. The argon flow was in 200-500 sccm (standard cubic centimetre per minute) range.

2.2. Experimental set-up: Surfaguide. In this set-up the waveguide line was connected to commercial Sairem surfaguide [1] and terminated by movable short. Plasma was sustained in fused silica discharge tube (20 mm external and 16 mm internal diameter) placed vertically in the surfaguide. Typical operating microwave power was in 350–550 range.

Argon was used as a main working gas with flow rates varying in range 1000–1400 sccm. For intended application – plasma synthesis of graphene – an ethanol precursor [12] was added, too. It was done using auxiliary argon flow (28–84 sccm) passing through ethanol filled bubbler. The main gas line and ethanol vapours carrying auxiliary line were mixed before entering the discharge tube from below. For reduced pressure experiments, the system was continuously pumped by rotary vane oil pump ($p<10$ kPa) or dry diaphragm pump (10 kPa$<p<$40 kPa). The experiments were carried out also at the atmospheric pressure, i.e. without any pumping.

2.3. Experimental set-up: MW torch. The common microwave line (see above) ended with a waveguide-to-rigid coaxial transition, able to operate at substantially higher power levels than flexible coaxial cable. Its central conductor (diameter 6 mm) was hollow which enabled passing of the gas lines and ended in exchangeable carbon or stainless steel nozzle. The central (axial) channel (0.8 mm diameter) was used for argon (360−920 sccm). For graphene synthesis, a secondary channel (annulus with outer radius 8.4 mm and inner radius 7.7 mm) was used for introduction of ethanol containing gas mixture. Ethanol was vaporised in bubbler by the carrying gas (argon, 500−1400 sccm). The flow of the carrying gas controlled the amount of ethanol in 2−25 sccm range. Plasma reactor consists of fused silica tube (80 mm diameter, 200 mm long) terminated by duralumin flange.

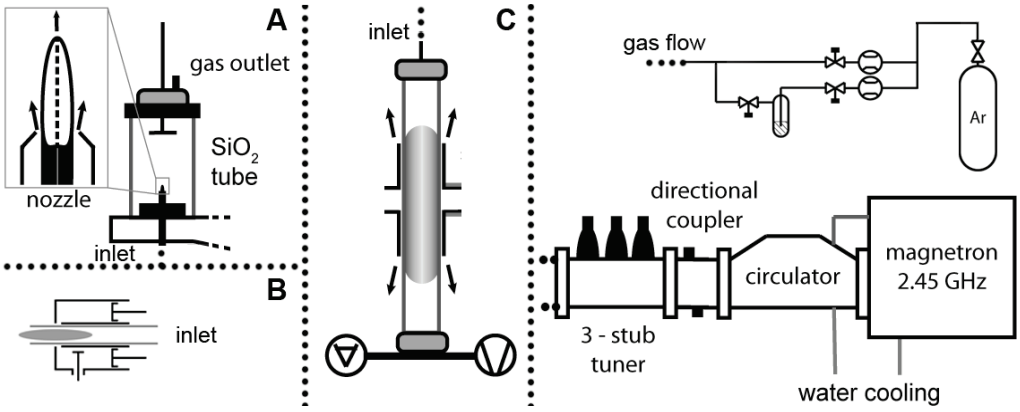

Figure 1. Experimental set-up: A − MW torch, B − surfatron, C − surfaguide.

2.4. Plasma diagnostics. Optical emission spectroscopy and colour imaging was carried out. Digital camera Nikon D5200 was used with Sigma 105 mm macro lens.

2.5. Sample analysis. Synthesized carbon nanopowder was collected from the reactor wall, on the Si/SiO_2 (92 nm) substrates fixed in the holder, or from microfibre filter in the gas flow downstream from the plasma reactor.

Raman spectroscopy was carried out using HORIBA LabRAM HR Evolution system with 532 nm laser, using 100x objective and 25% ND filter in the range from 1000 to 3200 cm^{-1}. Samples were imaged with TESCAN MIRA3 scanning electron microscope (SEM) with Schottky field emission electron gun

equipped with secondary electron (SE) and back-scattered electron (BSE) detectors as well as characteristic X-ray detector Oxford Instruments EDX analyser.

3. RESULTS AND DISCUSSION

Generally, a system at equilibrium may be disturbed by small perturbative forces acting on it. The instability or stability of the system then describes whether the perturbations will grow or be damped. In context of plasma physics, the most easily observable instabilities are those with changes in spatial homogeneity of the plasma. Probably the most famous instabilities are those in the fusion plasma research, where various types of plasma instabilities effectively limit [13] the lifetime of plasma and so negatively affect the Lawson criterion. Low temperature plasmas exhibit various types of instabilities, too.

Atmospheric pressure discharges in general exhibit a tendency to strong radial contraction, i.e. not filling entire cross-section available to them but forming a relatively thin and dense plasma channel. The main underlying cause is a localised heating of the neutral gas in the filament which increases the common plasma scaling parameter E/N and by consequence, the ionisation rate. The effect is easily observed in many types of atmospheric discharges – DC, RF, DBD, MW, lightning, etc. The diffusion (which is pressure dependent) counteracts this and thus at low pressure the discharges are mostly diffusive but high pressure discharges are filamentary.

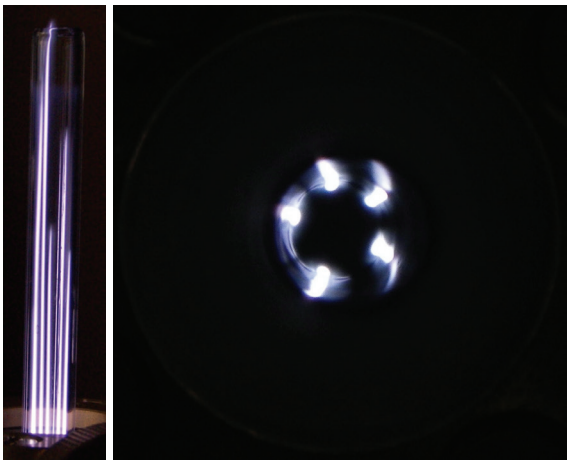

Figure 2. Sideview and top view (in different scales) of atmospheric pressure plasma excited by surfatron.

The length and diameter of the filament depends on the experimental conditions, i.e. pressure, working gas composition and flow, and most of all, the input power. When the input power is sufficiently high, multiple filaments can be formed (Fig. 2). The number of filaments and their spatial distribution are the result of quite complex interplay between electromagnetic, thermal, chemical, flow and plasma phenomena. While multiple filament theories certainly do exist, e.g. [14, 15], they consider only a part of the whole problem. As they mostly deal with steady state solutions, they cannot answer the detailed questions about switching between various filament numbers or spatial patterns.

It is interesting to note, that self-organised patterns can be not only fully stable, but also dynamically stable, e.g. the whole patterns rotate. This was observed in [5] for both RF (Fig. 3a, b) and microwave atmospheric pressure jets (Fig. 3c, d) and explained in [5, 7]. It was found [6] that main controlling parameters are the gas flow and the input power. Figure 4 shows regular alternating stripes of stationary modes (SM) and locked (i.e. rotating) modes LM with number indicating number of filaments.

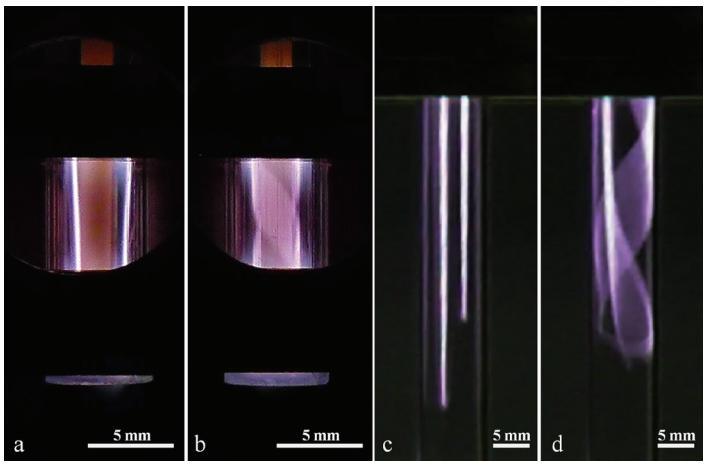

Figure 3. Stationary and rotating modes in RF and microwave atmospheric pressure plasma jets. Published in [5].

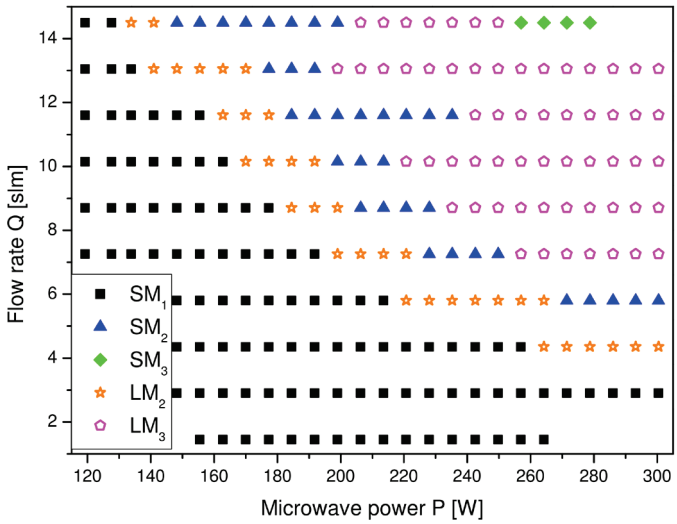

Figure 4. Mode diagram for argon plasma in surfatron, for varying power and flow rate. Published in [6].

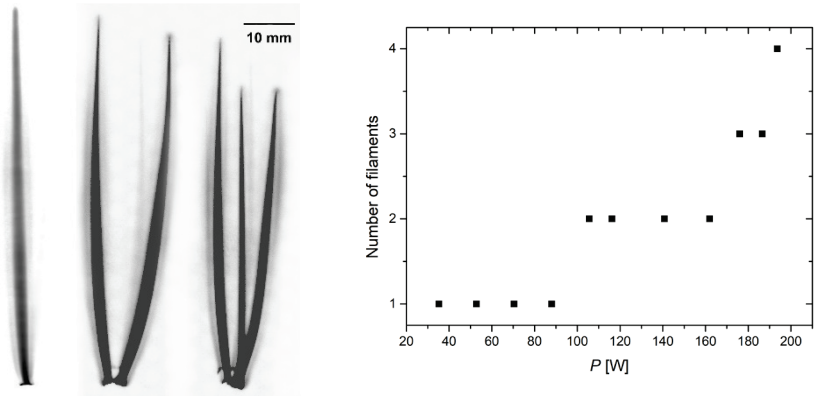

Figure 5. Typical influence of the MW power on filamentation in MW torch (left) and derived data - number of filaments as a function of input power (right).

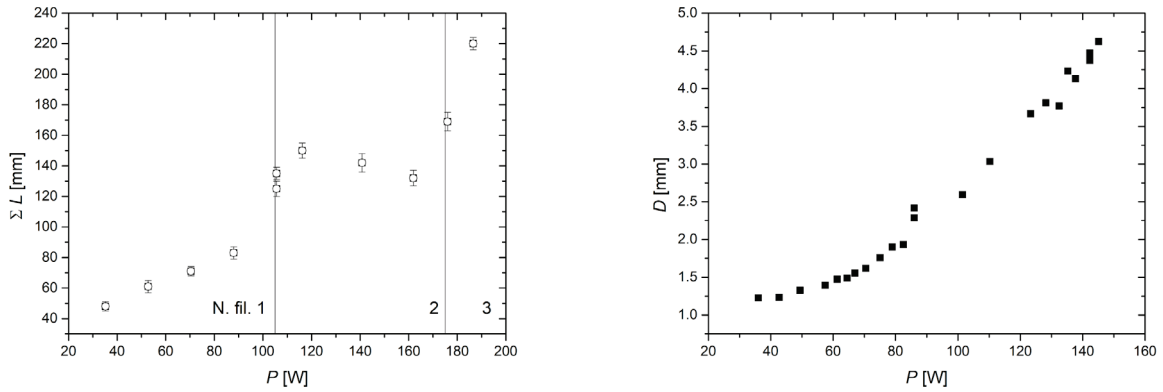

Figure 6. Total length of the filaments (left) and total diameter (right) dependence on input MW power.

Filamentation was observed in atmospheric MW plasma torch, too. Typically, one bright filament was formed with fast oscillating tip. Use of graphite nozzle electrode offered a new operational mode forming one or multiple stationary filaments growing from the surface of the nozzle. The influence of the electrode material can be explained by (i) bulk properties − relatively high resistivity of carbon in comparison with iron, leading to current limitation in one filament and natural division to multiple filaments, (ii) difference in surface chemical properties – formation or non-formation of thin oxide layer or (iii) difference in surface electric properties, mainly different work function. The number of filaments was power dependent as is shown in Fig. 5. Gas flow had to be in range 200−600 sccm to remain in stationary regime. Second filament is created by slow separation from the first one, growing in size with input power to match with the original. According to [16] each of these filaments is probably sustained by surface wave propagating along. Digital imaging with computer post-processing makes an investigation of the length and the diameter of filaments quite straightforward. In the case of one filament, length was growing linearly with power but after the second filament appearance, the total filament length (the sum of individual filament lengths) decreased while the total diameter (a sum of individual diameters) was still growing as is shown in Fig. 6.

Figure 7. Longitudinal striation of plasma filament in surfaguide.

Besides the interaction between the filaments there are also perturbative effects which exerts the filament on itself. This is direct analogy to plasma stratification known from low pressure DC discharges. Recent works [5] studied this effect in atmospheric pressure RF jets both experimentally and by modelling. We observed this phenomenon in MW discharge, see Fig. 7. Striated filament appears as pearls on string. The phenomenon is rather unstable due to high sensitivity to any perturbation, so the spatially resolved diagnostics was not carried out yet.

3.1. Plasma synthesis of graphene nanosheets. Unique properties of graphene prompted rapid development of many methods of its preparation. Plasma synthesis in microwave plasma using ethanol as a precursor was reported in [12, 17]. In the present paper the influence of experimental conditions on plasma synthesis of graphene was investigated, using microwave plasma torch. The varied parameters were input microwave power (P = 140−350 W), argon flow rate in central channel (Q_C = 60−780 sccm) and argon flow rate through the bubbler and the secondary channel (Q_S = 300−1400 sccm). During the deposition, visual observation and digital imaging of the plasma were carried out, while after the deposition, the nanopowder samples were collected and analysed by SEM and Raman spectroscopy.

It was found that both flow rates had significant influence on discharge stability, where a gradual transition from laminar to turbulent mode with increasing flow rates was well observable (see Fig. 8-1A and 8-2A). However, the quality of synthesized nanosheets was mainly influenced by the microwave power.

The SEM analysis of nanopowders by secondary electrons (SE) showed, in dependence on deposition conditions, presence of amorphous carbon nanostructures and well graphitized graphene nanosheets. Prepared nanosheets had rectangular shape with lateral dimensions of several hundred of nanometres. The thickness of the individual sheets was below 2 nm.

Raman spectroscopy was carried out as a key analysis [18, 19] and evaluated by changes in shape (full width at half maximum value (FWHM) of Lorentzian profile) and integrated intensity of D (~ 1300 cm^{-1}) and 2D (~2690 cm^{-1}) peaks normalized to the G (~ 1580 cm^{-1}) peak, in the same manner as was done in our paper [20].

Figure 8 combines digital plasma imaging with material analyses (SEM and Raman) for two different central channel flow rates Q_C = 500 and 780 sccm, auxiliary channel flow rate being constant at 700 sccm. For lower Q_C, the plasma appears to be laminar. Plasma is excited mainly in the central pure argon and the energy is gradually transferred from the excited Ar to surrounding Ar+ethanol mixture. The main interaction (e.g. dissociation of ethanol and excitation of its fragments) takes place at the laminar boundary layer between the two flows. Immediately, carbon clusters/nanoparticles are formed, as evidenced by orange glow of Planck blackbody radiation.

Increasing the central gas flow rate, the shear between two flows (flow speeds 25.9 and 0.32 m/s) becomes too high and whole plasma becomes turbulent. Mixing of gases is greatly enhanced. Higher velocity also affects the residence time of the dissociated hydrocarbon precursor in discharge region. Consequently, the typical orange glow region (nanoparticle formation zone) is smaller and less intensive which results in reduction of the amount of synthesized nanomaterial.

The quality of graphene nanosheets is slightly changed, too. This can be described in terms of Raman spectra. Figure 8-1B represents Raman measurements of a sample deposited under laminar flow conditions. Relatively high 2D/G peak intensity ratio indicates growth of few-layer graphene nanosheets. As the D peak corresponds to defectivity or disorder, its low intensity and FWHM suggests good graphitisation and low amount of defects. With higher central channel flows turbulent regime develops, affecting the graphene nanosheet growth. Figure 8-2B shows lower 2D/G ratio and much broader and higher D peak meaning much disordered graphene [18] with higher number of atomic layers. SEM imaging in Fig. 8-1C and 8-2C corresponds well with the Raman spectra analysis.

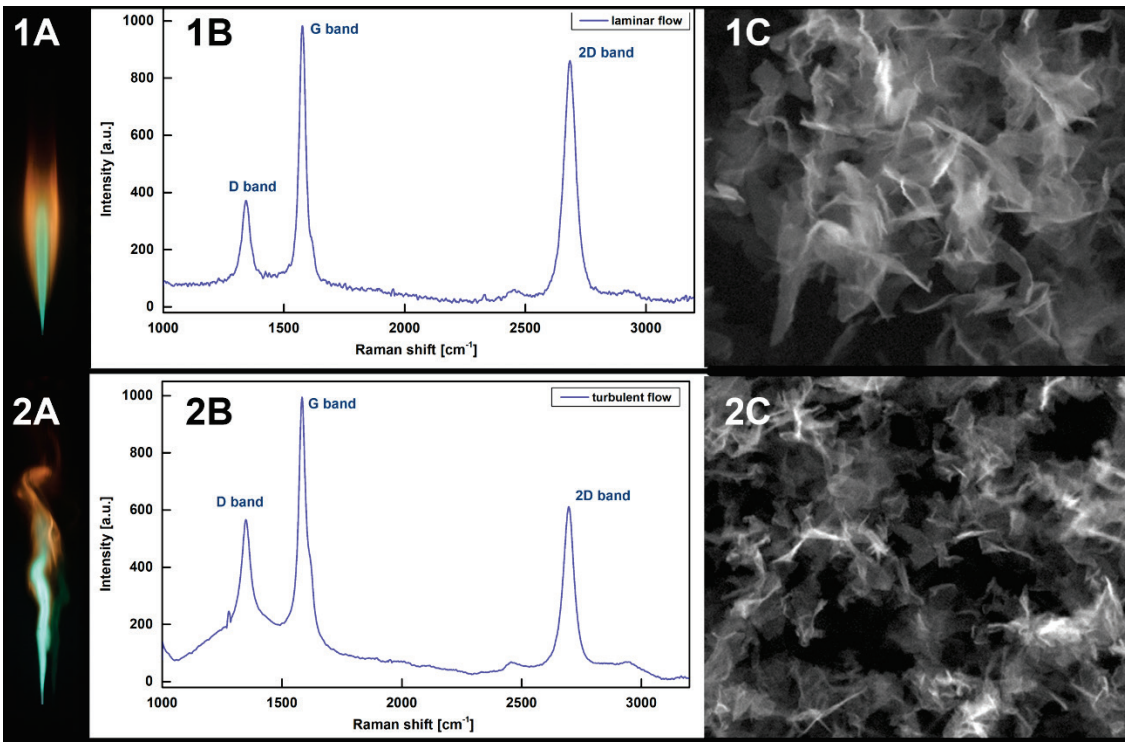

Figure 8. Comparison of stationary and turbulent regime. A − photography of plasma flame, B − Raman spectrum, C − SEM image of graphene.

4. CONCLUSIONS

The instabilities and self-organization in microwave discharges at medium and atmospheric pressure can profoundly influence spatial distribution of ionisation and excitation rates, and by consequence also the plasmachemical reactions. The most common instabilities in microwave filamentary plasma were demonstrated. Effects of microwave power and fluid dynamics on the quality of plasma synthesised graphene nanosheets were discussed, too.

Acknowledgements

This work was supported by the Czech Science Foundation under project 18-08520S and in part by the project LO1411 (NPU I) funded by Ministry of Education, Youth and Sports of Czech Republic.

References

1. Moisan M. et al., Elsevier Science Serials, 1992.
2. Moisan M. et al., J. Phys. E, 1987, **20**, 1356.
3. Zajíčková L. et al, Plasma Phys. Controlled Fusion, 2005, **47**, B655.
4. Moisan M. et al., Springer Science & Business Media, 2012.
5. Schafer J. et al., IEEE Trans. Plasma Sci. IEEE Nucl. Plasma Sci. Soc., 2011, **39**, 2350.
6. Hnilica J. et al., J. Phys. D Appl. Phys., 2012, **45**, 055201.
7. Schäfer J. et al., Plasma Phys. Controlled Fusion, 2017, **60**, 014038.
8. Schäfer J. et al., Plasma Phys. Controlled Fusion, 2009, **51**, 124045.
9. Iza F. et al., IEEE Trans. Plasma Sci. IEEE Nucl. Plasma Sci. Soc., 2005, **33**, 306.
10. Kumar R. et al., Phys. Plasmas, 2007, **14**, 122101.
11. Kang S.K. et al., IEEE Trans. Plasma Sci. IEEE Nucl. Plasma Sci. Soc., 2011, **39**, 2318.
12. Tatarova E. et al., Appl. Phys. Lett., 2013, **103**, 134101.
13. Mikhailovskii A.B., CRC Press, 1998.
14. Maximov A.V. et al., Phys. Scr., 1999, **60**, 556.
15. Maximov A.V. et al., Phys. Scr., 2002, **65**, 263.
16. Nowakowska H. et al., J. Phys. D Appl. Phys., 2001, **34**, 1474.
17. Dato A. et al., Nano Lett., 2008, **8**, 2012.
18. Ferrari A.C. et al., Phys. Rev. Lett., 2006, **97**, 187401.
19. Malard L.M. et al., Phys. Rep., 2009, **473**, 51.
20. Toman J. et al., 8th Nanocon, TANGER Ltd, n.d., 2006, 122.

PLASMA POWER-INTERUPTION; THE ROLE OF POST-HEATING

Joost van der Mullen, Nikolay Britun[1], Maryam Khaji, Gérard Degrez

Université libre de Bruxelles, 50 av. F.D. Roosevelt, 1050 Brussels, Belgium
[1]University of Mons, Place du Parc 23, B-7000, Mons, Belgium

Abstract. The power interruption (PI) technique is based on a sudden disturbance of the Steady State (SS) by dropping the plasma driving power (PI) to zero, after which the plasma is re-ignited (RI). The sequence of PI and RI generates various equilibrium disturbing and restoring mechanisms and insight in phenomena can be obtained by following the responses to PI and RI. Of special importance is the response of the electron gas, which can be studied via optical emission spectrometry OES or, better, Thomson scattering (TS). In the past, the method was applied using OES to plasmas with high electron densities, n_e. These experiments were mainly devoted to find the decay rate of n_e just after PI and to determine the inequality of the temperatures of the electrons T_e and the heavy particles T_g. However, by comparing the PI results with other methods it was found that T_e^*, the electron temperature during the power-off period, is substantially higher than the gas temperature; $T_e^* > T_g$. Thus, T_g cannot be determined with this method. And since the electric field is absent, there must be a certain mechanism post-heating the electrons! TS during PI has the advantage that it can also be applied to low-n_e plasmas. Performed on microwave discharges it was found that the post-heating present in high pressure is absent in low pressure pure Ar plasmas. However, if small percentages of N_2 or CO_2 are added to low-pressure Ar plasmas it pops up again! This points to the relation between post-heating and the dissociation of molecules of CO_2 and N_2 in power pulsed plasmas.

1. INTRODUCTION

The power interruption (PI) technique is a 'powerful' experimental method that gives insight in plasma phenomena and time-scales. It is a global intervention technique that changes the main plasma parameters such as the electron density n_e and temperature T_e. These changes of the electron gas {e} are manifest in the behavior of plasma light. So by applying Optical Emission Spectroscopy (OES) insight can be obtained in the gas of free electrons {e}. However, in order to get a proper understanding it is better to apply Thomson scattering (TS) during PI.

The PI technique was often applied to get insight in transport phenomena and the related departures from equilibrium [1−6]. The first one can be obtained by the study of the decay of the electron density just after power switch-off as given by $\tau^{off}(n_e)$, while the departure of equilibrium is among others reflected in the inequality of the electron and heavy particle temperature ($T_e \neq T_g$). To determine these temperatures PI was often chosen as an adequate technique. Moreover, the method of the OES observation of PI plasmas seems easy and elegant, as there is no need for intensity calibration, nor optical transition probabilities. However, by comparing the PI results with those of other methods it was found that, T_e^*, the electron temperature during the power-off period, is substantially higher than the gas temperature T_g. Thus, after PI the electrons remain hot and since the electric field is absent there must be a certain post-heating mechanism! The first PI experiments on plasmas were done on plasmas generated in high power DC arcs and Inductively Coupled Plasmas (ICPs). However, more insight is gained by applying PI experiments to microwave discharges as generated in surface-wave induced plasmas (SIP). The operational conditions of these plasmas can be determined more precisely and the plasmas are better assessable for Thomson scattering.

The plasma PI technique has many aspects and we cannot give a complete review here. So, a selection was made that leads to the following organization of the paper:

In Section 2 we will study power interrupted (PI) plasmas using OES; briefly denoted by OES@PI. Two types of plasmas will be considered: namely the 'spectroscopical' Inductively Coupled Plasmas (ICP) and the surface-wave induced plasma (SIP), both operated in argon under atmospheric conditions.

The n_e-value of these plasmas is rather high so that the densities of the excited Ar levels are (mainly) determined by Saha balances. This implies that OES can be used, not only to obtain the decay time of the electron density, but also to get the temperature of the electrons before (T_e) and just after (T_e^*) the PI. Section 3 will be devoted to PI of plasmas studied with TS; briefly TS@PI, Here we start again with the atmospheric ICP. Apart from T_e, T_e^* and $\tau^{off}(n_e)$ we can also determine n_e in absolute value. Moreover with TS we can measure T_e, T_e^* and n_e (and thus $\tau^{off}(n_e)$) time and spatially resolved. It is found that in the plasma skin, the region of energy coupling, the n_e -decay is extra large while T_e^*, the electron temperature just after power switch-off, is substantially higher than the gas temperature T_g. An important post heating mechanism must be in action! After that, we will deal in 3.2 with PI applied to low pressure SIP operated in pure Ar and in 3.3 in Ar with small additions of molecules. It is suggested that the role of molecules and especially the vibrational excitation is very important. This is the topic of Section 4 where we address the role of anharmonicity. We conclude with Section 5.

2. OES@PI

The PI experiments performed on DC arc plasmas [1, 2] in the 1960s were followed in the 1980s by PI studies on inductively coupled plasmas (ICPs) [3−5]. All these plasmas [1−5] have relatively high n_e-values so that the excited states are mainly oriented to the continuum, the reservoir of free electron {e}, and thus ruled by the Saha balance of ionization and two electron (2e-) recombination. This implies that the time evolution of line emission gives insight in the evolution of {e} during PI. Using OES makes it possible to determine the value of T_e at SS and T_e^*, the value just after PI, together with the decay time of the electron density $\tau^{off}(n_e)$. In short: OES@PI gives T_e, T_e^* and $\tau^{off}(n_e)$. The first two (could) give the departure from thermal equilibrium, the latter, gives insight in plasma transport phenomena.

2.1. OES@PI for the ICP. The ICP used for spectro-chemical analysis is an atmospheric plasma created in a argon flow in open air. The supplied power of typically 1.2 kW and a flow rate of 12 slm lead to electron densities and temperatures in the order of $n_e = 10^{21}$ m^{-3} and $T_e = 8$ kK (~0.7 eV); the radial size of the plasma is around 9 mm. Figure 1 (cf. Fig. 2.5 in [5]) gives the behavior of the Ar lines in response to the PI for a power-off time of $\tau^{off}(P) = 100\mu$s. The intensities in Fig. 1 are scaled to their corresponding maximum values.

The time-behavior shows four features; labeled by F1−F4 (cf. Fig.1):

F1) at switch-off (PI) all these lines jump-up in intensity within a few μs,

F2) after that all the lines decay, with the same time-constant of about 80 μs,

F3) the re-ignition (RI) at about 100μs, is accompanied by a sharp decrease in intensities,

F4) after which there is a slow increase towards the value of the intensity before the PI.

Anticipating on next pages and referring to [1−6] we find the following underlying plasma changes:

P1) Cooling $T_e \downarrow T_e^*$; the T_e rapidly decreases to a lower value denoted by T_e^*.

P2) Plasma decay; the n_e decreases due to recombination and/or transport (diffusion).

P3) Heating $T_e^* \uparrow T_e^{**}$; the opposite of cooling, demanding for a higher electron temperature.

P4) Ionization; the electron density increases and approaches the steady state (SS) value.

The changes in T_e are sudden while n_e changes much more slowly. The precise values of the time scales depend on the plasma settings and plasma zone under investigation. The values corresponding to RI of $\tau^{on}(n_e)$ and $\tau^{on}(T_e)$ depend on the power-off time $\tau^{off}(P)$. Note that $\tau^{off}(T_e)$ and $\tau^{on}(T_e)$ are in most cases so small that they cannot be distinguished from the switching-time of the power supply.

The following notes can be made:

N1) It is assumed that after the drop $T_e \downarrow T_e^*$ the T_e^* remains (more or less) constant while n_e decreases. It was often postulated that T_e^* equals the heavy particle temperature; thus $T_e^* \approx T_g$, but this assumption is (in general) not valid, as we will see below.

N2) As said, the line intensities in Fig. 1 are scaled to their maximum values that are achieved just after switch-off; this shows that the decays found in the lines have the same time-behavior; they reflect the

decrease in $n_e{}^2$ (assuming $n_e = n_+$, cf. Eq. 2). Thus, as the intensities of the Ar lines (in Fig. 1) decrease roughly with a time constant of $\tau^{off}(Ar^*) = 80$ μs we find for the {e} a value of $\tau^{off}(n_e) \approx 160$ μs.

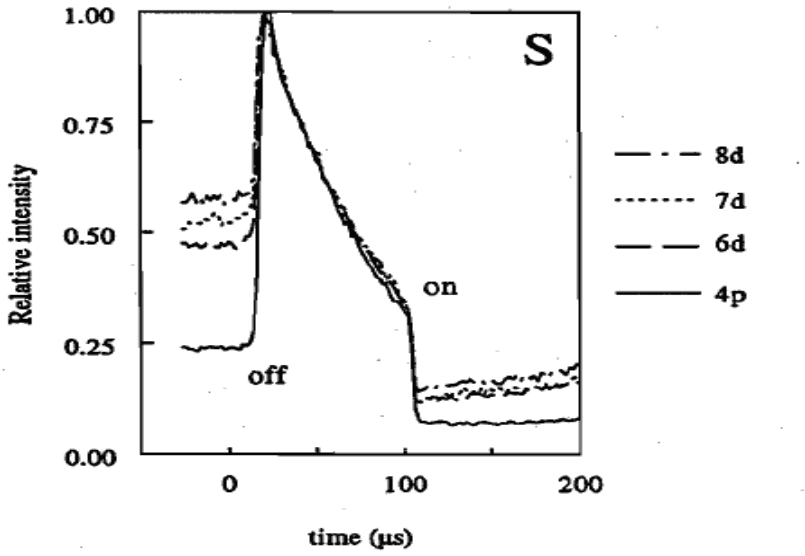

Figure 1. Responses of 4 different Ar lines to PI and RI. They are scaled to their maximum intensities that are obtained just after switch-off, showing that all lines decay with the same time constant of about 80 μs; cf. Fig. 2.5 in [5].

N3) Heating; it is expected that T_e^{**}, the electron temperature just after RI, is larger than T_e, the electron temperature in steady state (SS). The electron production rate (i.e. ionization rate) at RI must be extra high to rebuild the plasma. Thus $T_e^{**} > T_e > T_e^*$. This extra high T_e^{**}-value can be realized after PI since the electric field can penetrate more easily and deeper into the plasma than in the SS case; the decrease in n_e achieved in the power-off time implies less shielding. It is indeed found in [5] and [11] that longer power switch-off times lead to higher T_e^{**}-values.
N4) The time-constant $\tau^{on}(n_e)$ is larger than $\tau^{off}(n_e)$. The plasma needs, apart from an enhanced electron production, also to reshape flow-patterns. The $\tau^{on}(n_e)$ -value depends on the SS power-value and off-time.

Saha-like responses. The features of cooling, decay, heating and re-ionization, (F1−F4), can be explained by the assumption that the occupations of line-emitting argon levels (Ar*) are ruled by the Saha balance of ionization and 2-electron recombination. For the level Ar(p) this balance schematically reads

$$e\ (\varepsilon_{fast}) + Ar(p) \ \leftrightarrow\ e\ (\varepsilon_{slow}) + Ar^+ + e(\varepsilon_{slow}) \qquad (1)$$

If this balance equilibrates we find for the density of the states in excited atomic level p the Saha density.

$$\eta^s\ (p, T_e) = \eta_e\ \eta_+\ h^3/(2\pi m_e\ kT_e)^{3/2}\ exp\ (I_p/\ kT_e). \qquad (2)$$

Here I_p is the ionization potential of the atom in state p, and $\eta^s(p) = n^s(p)/g(p)$ is the density of the states in level p according to Saha as indicated by the *'s'* as upper index; while $\eta_e = n_e/2$ and $\eta_+ = n_+/g_+$, where n_e and n_+ are the density of the electrons and ions.

Feature 1, the intensity jump at cooling, can be understood qualitatively by the electron-energy indications given in Eq. 1 showing that the ionization (process to the right) needs electrons with high energy (ε_{fast}) whereas the inverse process of two electron (2e) recombination is mainly ruled by low energy electrons (ε_{slow}). At switch-off (cooling) the number of electrons with ε_{fast} will go down, therewith obstructing ionization, whereas the recombination keeps on-going as the density of electrons with ε_{slow} electrons is not changed (much). Thus the depopulation of Ar* by means of ionization is reduced while recombination (population of Ar*) continues. This causes the rapid upward cooling jump and explains the counter-intuitive behavior of Ar emission: the lines *go-up* while the power *goes-down*.

Quantitatively we can determine the magnitude of the jumps via Eq. 2. Just after PI the Saha density reads $\eta^s\ (p, T_e^*)$, thus Eq. 2 in which T_e is replaced by T_e^*. Dividing $\eta^s\ (p, T_e^*)$ by $\eta^s\ (p, T_e)$, introducing $\gamma = T_e/T_e^*$ and assuming that n_e and n_+ remain constant we get

$$ln\ \{J(p)\} = 3/2\ ln\ \gamma\ + I_p/kT_e\ (\gamma - 1), \qquad (3)$$

where $J(p) = \eta^s(p,T_e^*)/\eta^s(p,T_e) = I(p,T_e^*)/I(p,T_e)$ is the intensity-jump at cooling. In the last part we added the ratio of the intensities and assume that these are directly proportional to the density of the emitting levels. This is justified if the plasma is optically thin for the transitions under study.

This is illustrated in Fig 2a, where (part of) the Atomic State Distribution Functions (ASDFs) are shown obeying the Saha distribution for two different T_e-values, together with the jumps at cooling for 4 levels. It is seen that the lower levels, having high ionization potential I_p-values, undergo higher intensity jumps.

Figure 2b gives an expectation of what happens in a (strongly) ionizing plasma. The cooling jump of lower levels, will be reduced with respect to the Saha jump. We will come back to this in Section 2.2.

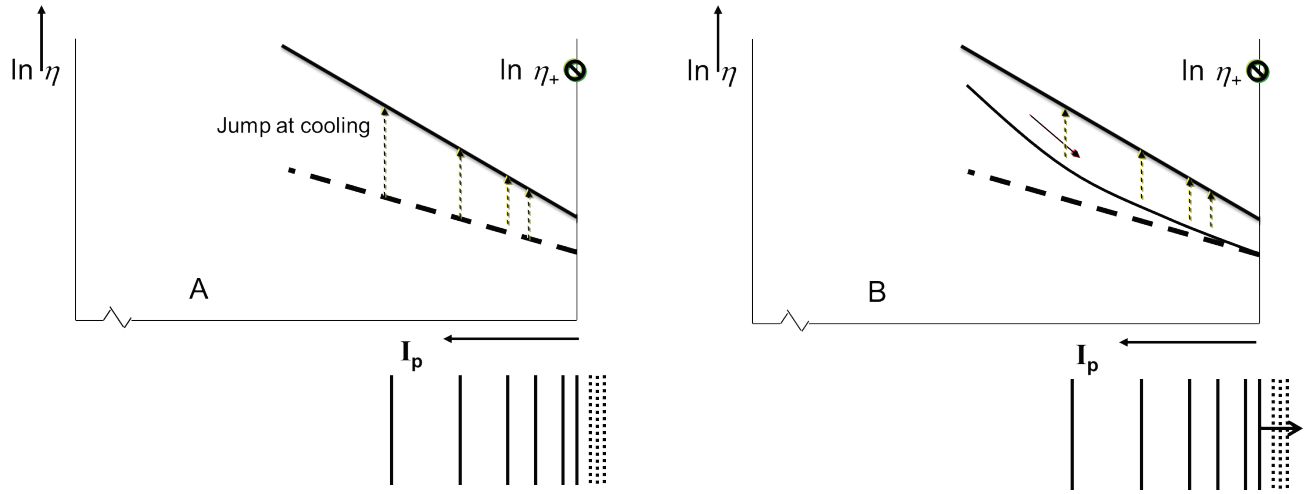

Figure 2. A) Part of the energy diagram (bottom) with the ASDF (upper) for two points in time, the dashed line gives the ASDF ruled by the Saha equation for T_e (SS; just before PI) for the solid line it is T_e^* (just after PI). The n_e-value is the same in both cases. The vertical arrows depict the jumps at cooling for 4 different levels; the lower the level the larger the jump. Note that I_p, the ionization potential, is large for low lying levels. The set of dotted lines depict the free electron states {e}. B) A plasma that in SS is (strongly) ionizing has an ASDF with overpopulated lower levels; the cooling jump is then relatively small for these lower levels; the arrows along the ASDF and in {e} depict the transport in space and excitation space.

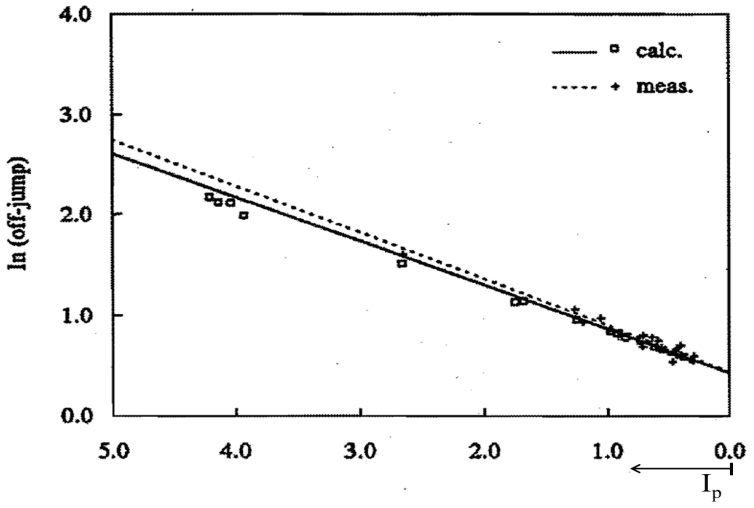

Figure 3. Measured and calculated cooling jumps as a function of I_p as reported in [5] for an Ar ICP; cf. Fig.6.17 in [5].

By plotting *ln J(p)* versus I_p we find from the intersection with the $I_p=0$ line the value of γ, while γ together with the slope gives T_e. This provides an elegant way to get T_e and T_e^*. There is no need for intensity calibration; even the knowledge of A-values is redundant. The result of applying this procedure to the PI of an ICP is given in Fig. 3 where it is compared to theoretical results, cf. Fig .6.17 in [5]. A fair agreement between experiment and modeling is found and leads to the values T_e = 10 kK and T_e^* = 7 kK.

Another aspect of the Saha equation (Eq. 2) is that charge neutrality, $n_e = n_+$, implies that $\eta^s(p, T_e)$ scales with n_e^2. This explains why all the intensities in Fig. 1, decay with the same time-constant $\tau^{off}(Ar^*)$ giving the decay time of n_e via $\tau^{off}(n_e) = 2\,\tau^{off}(Ar^*)$.

Notes. 1) By comparing T_e^*, determined above, with that of the gas temperature T_g as found by Rayleigh scattering (cf. p. 89 in [6]) we must conclude that T_e^* is substantially higher than T_g. The difference can (cf. 3.1) even amount $T_e^* - T_g = 4\ kK$! This stands in strong contrast with the assumption that $T_e^* \approx T_g$ as postulated in several old studies. As the electrons during PI remain cooled due to elastic collisions, and as the power is switched off, there must be an important post-heating mechanism keeping $T_e^* > T_g$.

2) For plasmas with lower n_e-values for which the Saha balance is not fully settled we can expect deviations from the behavior sketched above (cf. Fig 2b and Section 2.2). But as long as there is an upward cooling jump we talk about Saha-*like* responses (cf. [5, 11]); this in contrast to the Boltzmann-like responses for which the line-intensities jump-down at PI.

3) As OES results are based on line-of-sight measurements, the method does not give direct insight in spatial dependencies.

2.2. OES@PI of an atmospheric SIP. The typical response to PI of an Ar-line as emitted by an atmospheric SIP is given in Fig. 4 where it is compared to that found for the ICP. It is seen that the decay time $\tau^{off}(Ar^*)$ is much smaller than that found for the ICP. The insets of these figures present pictures of the corresponding plasmas showing that the radius of the SIP is much smaller than that of the ICP. So, in first instance one tends to attribute the much faster decay of the SIP to its smaller size and thus higher diffusion losses. However, one should also realize that the atom density in the SIP is larger since the (atmospheric) gas temperature is lower and that this implies an obstruction for diffusion. In Section 3.2 we will address the competition between diffusion and recombination more in depth.

In analogy with Fig. 3 we could make a plot of *ln J(p)* versus *I(p)* for the SIP. Such a graph is published in [7], where it is found that the lower levels cannot follow the Saha response (cf. Fig. 2b). Apparently the SS plasma is strongly ionizing which also follows from the fact that at PI the decay is fast (thus $\tau^{off}(Ar^*)$ small). Nevertheless, extrapolating *ln J(p)* towards $I_p = 0$ gives $\gamma = 1.4$. Together with $T_e \approx$ 12 kK we get $T_e^* \approx 8.5$ kK. This is much higher than the gas temperature that was found to be $T_g \approx$ 1.5 kK. Thus especially in this type of plasmas where $\tau^{off}(Ar^*)$ is small, post-heating is very significant!!

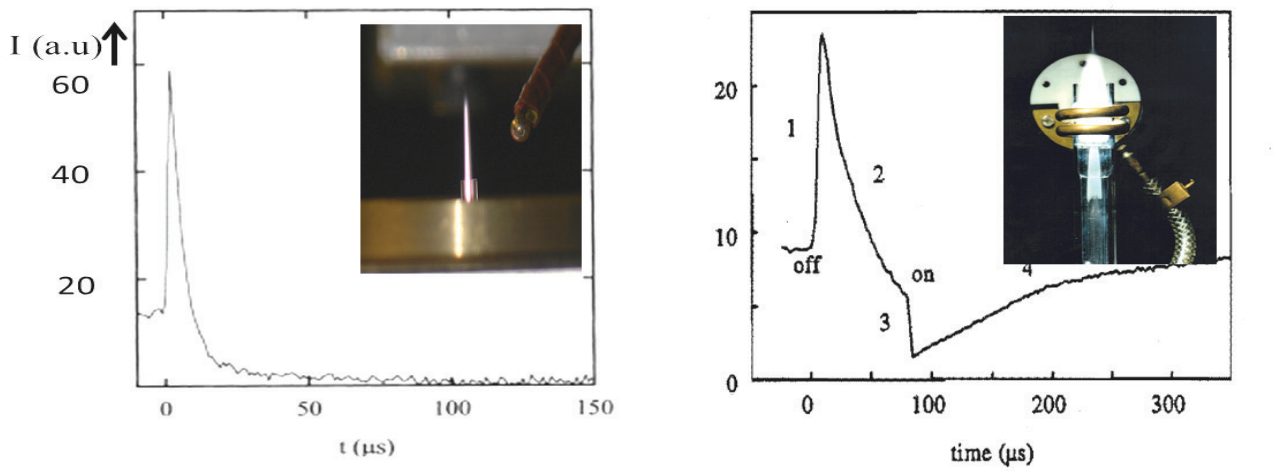

Figure 4. The Saha-like response of an Ar line for an atmospheric SIP compared to that of an ICP; for the SIP we have τ(Ar*) ≈ 5μs for the ICP: τ(Ar*) ≈ 50μs. Note the different time-scales. The photos show the smaller radial size of the SIP.

3. TS@PI

Although the radiation emitted by plasmas mainly results from electron excitation kinetics this does not imply that the properties of {e} can easily be determined with OES. In general, quite sophisticated models

are needed to derive n_e and T_e out of plasma emission, especially if transport plays an important role. In that case large deviations from Saha (Eq. 2) can be expected.

To get direct information on the behavior of {e} during PI we can apply laser TS. Thomson Scattering is the scattering of laser light on {e}. It provides time- and space resolved values for n_e and T_e in a rather straightforward manner that does not depend on the degree of equilibrium departure. The perfect space-resolution stands in contrast to OES being a pure line-of-sight method so that local plasma information can only be obtained via error-prone inversion methods (like Abel inversion). We first deal with the results of TS@PI of the ICP; this gives the possibility to inter-compare the results of OES and TS. Later in Section 3.2, attention will be paid to PI of low pressure SIPs.

3.1. TS@PI of the ICP. In [6 and 8] studies can be found of TS during the PI of an ICP. In general, one can state that the TS approach supports the global results as found by means of OES (Section 2.1). However, TS gives more precise insight as can be seen in Fig. 5. (Fig. 5.5 in [8]). The following observations can be made:

1) In the center of the plasma we find values of $\gamma = T_e/T_e^*$ of about 1.1 but at the plasma edge, in the plasma skin, the γ-value increases towards $\gamma = 1.5$. Moreover, if we compare T_e^* with the T_g- values that can be found on p. 89 in [6] we find that in the outer region where $\gamma = 1.4$ and $T_e^* = 6$ kK the gas temperature is as low as 2 kK. Thus, the difference between the temperature of the electrons and heavy particle at switch-off can amount $T_e^* - T_g = 4$ kK! Post-heating is clearly and dominantly present!

2) In [6 and 8] models were made to understand the temporal behavior of the radial n_e profile and to determine the radial profile of the electron decay frequency $\nu_{ne} = 1/\tau^{off}(n_e)$. These models, based on the combined action of diffusion and 2e-recombination, give good agreement with the experimental found ν_{ne} for r < 5 mm. However, for r > 5 mm, in the skin region where the energy coupling takes place, these models fail. The observed ν_{ne}-values are much larger than what the combination of diffusion and 2e recombination can deliver. In search for extra recombination the mechanism of Molecular Assisted Recombination (MAR) was proposed.

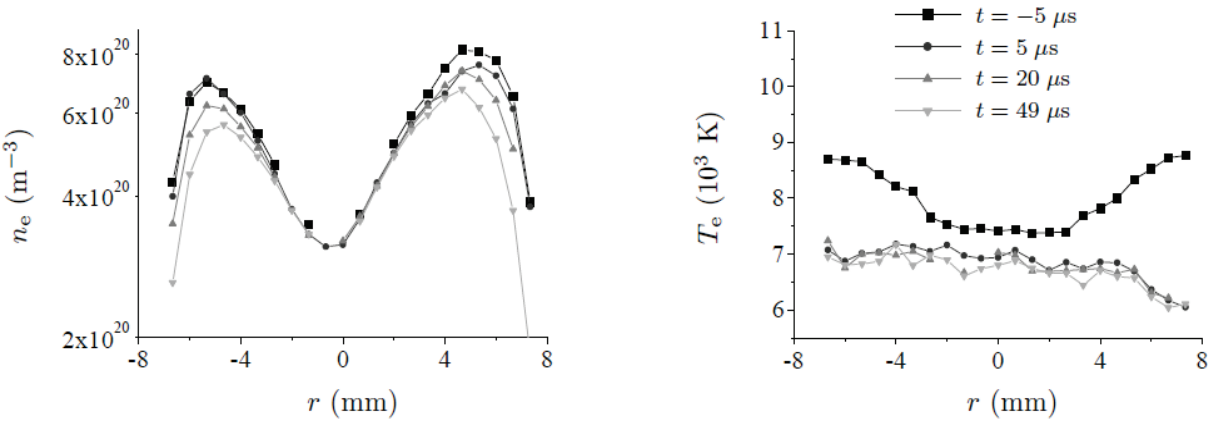

Figure 5. Radial profiles of n_e and T_e of an ICP at 7 mm above the load coil during a PI of 50 μs (starting t = 0). The data for t=-5 μs represent the SS situation whereas the profiles for t= 5 μs give the situation just after PI; cf. Fig 5.5 in [8].

MAR is a combination of molecular ion (MI) formation and dissociative recombination and consists of two subsequent reactions namely.

$$Ar^+ + 2Ar \rightarrow Ar_2^+ + Ar \ \text{(IC)} \quad \text{followed by} \quad Ar_2^+ + e \rightarrow Ar^* + Ar \ \text{(DR)} \qquad (4)$$

The first one is the ion conversion (IC) of atomic into molecular ions, whereas the second is dissociative recombination DR of the molecular ion. The latter is very fast so that the IC is the reaction limiting step.

It is remarkable that post-heating is strong in those region where ν_{ne} is fast ($\tau^{off}(n_e)$ small). Apparently the presence of molecules or MI that facilitate the decay also generate post-heating (cf. Section 4).

3.2. TS@PI for low pressure SIPs in pure Ar. The low pressure surface-wave induced plasmas (SIPs) for which the results are treated in this section are created in cylindrical quartz tubes. The pressure can

thus be varied and controlled while gas mixtures can be composed without the uncertain influence of atmospheric air entrainment. We start with the pure Ar case; in Section 3.3 the effect of small additions of molecular gases will be discussed.

Here we discuss the results published in [9] for pressures in the range 8−70 mbar and powers of about 70 W. The inner radius of the tube is 3 mm and the plasma driving frequency is 2.45 GHz. For this type of plasmas we find that the behavior of Ar line emission at PI is completely different from that as predicted by the Saha response. The main reason is that at low pressures the n_e- values is small. Thus, the OES method presented above to determine the $\tau^{off}(n_e)$, T_e and T_e^* will not work. We need another technique such as Thomson scattering (TS). With TS@PI large γ-values, in the order of γ=10, were found in [9] meaning that the T_e^* drops down to values close to the gas temperature T_g.

The decay of n_e is expected to result from the combination of diffusion and recombination. However, the role of 2e-recombination could be ruled out as the decay does not depend on SS-value of n_e.

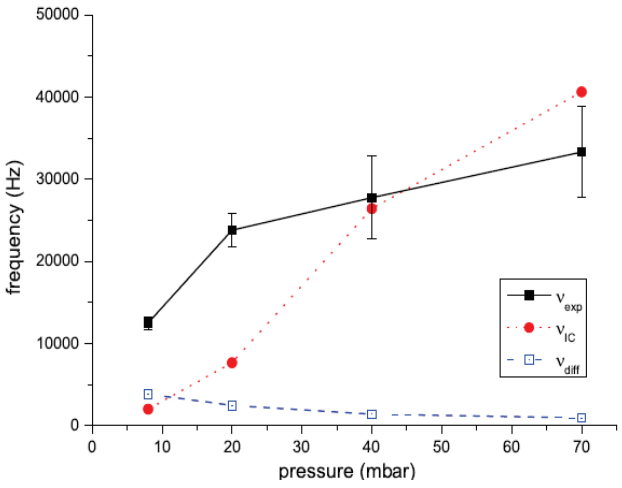

Figure 6. The measured decay frequency ν_{ne} (full curve) compared with the calculated frequency for diffusion ν_{diff} and ion conversion ν_{IC} as a function of the gas pressure; cf. [SH] Fig. 6.5. Increasing the pressure favors the creation of molecular ions.

The diffusion strength can be controlled by varying the pressure. It was expected that increasing the pressure would reduce the decay frequency ν_{ne}; collision with atoms will obstruct diffusion. However the opposite was found. As shown in Fig. 6 (Fig 6.5 in [9]) we find that increasing the pressure leads to larger values of ν_{ne} (thus smaller $\tau^{off}(n_e) = 1/\nu_{ne}$). This figure also gives ν_{diff}, the expected ν_{ne} related to diffusion, and ν_{IC}, the frequency of the conversion of atomic to molecular ions (cf. Eq. 4). As stated before this process is the rate-limiting link in the MAR chain. Once a molecular ion (Ar_2^+) is formed, it will immediately be destroyed by DR. Thus we must conclude that MAR is the most important mechanism for the plasma decay at higher pressure. This is in line with the findings in Section 2.2 for the atmospheric SIP and in 3.1 for the edge of the ICP. The presence of post-heating (i.e. difference between T_e^* and T_g) could not be verified as TS is difficult for low T_e-values.

3.3 TS@PI on a low pressure Ar-SIP with molecular admixtures. The method described in 3.2 was also applied to low pressure SIPs in argon with small molecular admixtures. Huge differences were found in the PI responses. Adding H_2 or O_2 does not lead to noticeable changes in the T_e and n_e decay behavior but an addition of small amounts of N_2 or CO_2 to the Ar-SIP leads to prominent post-heating [9]. Figure 7 shows that the addition of 1% of N_2 or CO_2 gives a T_e/T_e^* value of $\gamma \approx 1.4$. In other words the electron temperature during PI will stay as high as 70% of the value attained under steady state (SS) conditions, whereas for pure Ar we found in 3.2 that γ = 10!! So again we have to conclude that there must a post-heating mechanism; a mechanism that cannot be electromagnetic in nature and must be related to the presence of molecules.

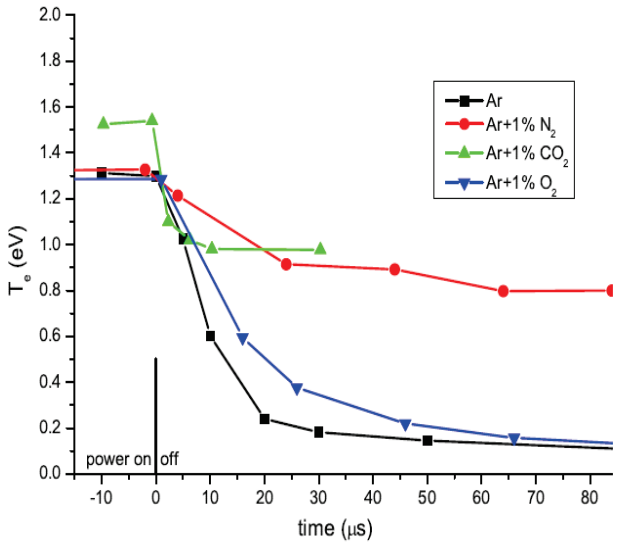

Figure7. The response of T_e to PI for an Ar-SIP of 11 mbar for different admixtures (1%). Post-heating is in action for admixtures of N_2 and CO_2 whereas adding O_2 has a minor influence; cf. Fig. 7.2 in [9].

4. THE ROLE OF MOLECULES; ANHARMONICITY

In Section 3.2 we found that increasing the atom density in a SIP leads to enhanced plasma decay which can only be explained by MAR. This supports the findings given in Fig. 5: in the outer part of the ICP where the atom density is high (since the T_g is low) we find large n_e-decay rates. Moreover, in that ICP region we also found that post heating is strong. So apparently the creation of molecular ions (MI) will not only speed up the plasma decay but also leads to post-heating. By adding molecules to an Ar plasma we also see that in several cases post-heating is present. So the most likely candidate for post-heating is the vibrational system of molecules (or MI). The energy distribution of vibrational levels is an-harmonic; they are separated by energy gaps that decrease for increasing vibrational energy, E_{vib}. This implies that in mutual collisions, molecules with high E_{vib}, will increase further while those with low E_{vib} will decrease.

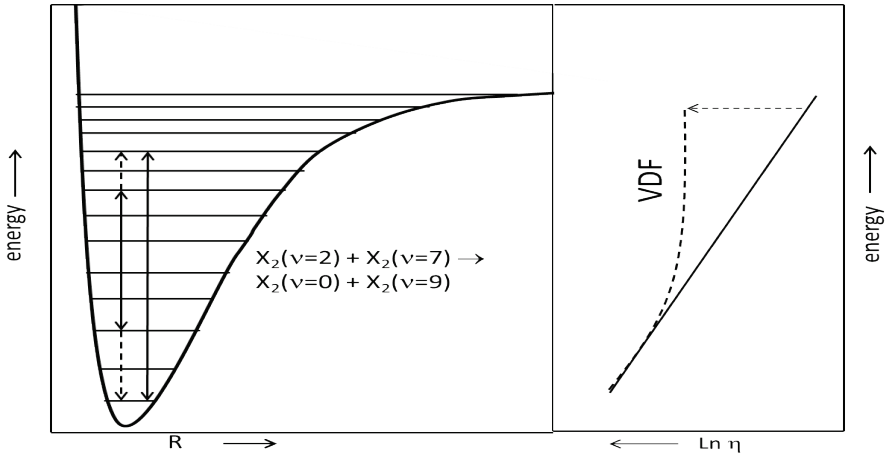

Figure 8. Left: a sketch of the energy diagram of an anharmonic vibration system of a fictitious molecule X_2; the vibration energy as a function of inter-nuclear distance R. The VV reaction X_2 (ν=2) + X_2 (ν=7) → X_2 (ν=0) + X_2 (ν =9) + (ΔE>0) given as example, shows how VV reactions favor the occupation of higher vibrational states.

Right: the consequences of this pooling on the VDF (occupation versus vibrational energy) given by the dashed curve, being a deflection of the solid curve that depicts the vibrational distribution function (VDF) in case of (Boltzmann) equilibrium.

This is illustrated in Fig. 8 giving as an example the VV-process of the fictitious molecules X_2 given by

$$X_2 (\nu=2) + X_2 (\nu=7) \rightarrow X_2 (\nu=0) + X_2 (\nu =9) + (\Delta E>0). \quad (5)$$

Since the energy gain by the vibrational transition $2\rightarrow0$ is larger than the cost for $7\rightarrow9$ we find that such reactions are exothermic ($\Delta E>0$) and favor the occupation of higher vibrational states. This so-called upward-pooling via VV collisions leads to the following scenario:

1) In SS the {e} equipped with a large n_e-value will, via electron-molecule collisions, impose their temperature, T_e, on the vibrational distribution function, VDF.

2) When during PI, the n_e goes down; the VV collisions between molecules become more important and tend to change the VDF such that for high ν-values the slope temperature increases (cf. Fig. 8, right pane).

3) This high T_{vib}-value will, in the power-off period, $\tau^{off}(P)$, energize the {e}, thereby increasing T_e^*.

A subsequent stage in the scenario is that:

4) The VV collisions will, during $\tau^{off}(P)$, support dissociation of molecules.

In [10] it was found that power interruption applied to microwave plasmas in pure CO_2 indeed leads to more dissociation ($CO_2 \rightarrow CO+O$). The final dissociation efficiency depends on the SS power, the gas pressure and temperature, the repetition rate of PI and the duty cycle. As mentioned above, a longer $\tau^{off}(P)$ leads to higher T_e^{**} values at RI [11]. Due to the n_e-decay realized in $\tau^{off}(P)$ the E-field can penetrate much better and deeper into the plasma than in the SS case. This extra high E-field will support the {e} in imposing a higher temperature on the VDF. For a proper understanding of this frequency-effect we need more insight in phenomena and time-scales [10]. The effect of convection should also be taken into account as the gas flow will affect the residence time and the shielding of the plasma.

5. CONCLUSIONS

Different plasma conditions were studies using the PI technique. Two methods were applied to monitor the changes of the electron gas, during PI and RI; Optical Emission Spectrometry (OES) and Thomson scattering. OES has the advantage that it is experimentally easy, but one of the disadvantage is that is limited to plasmas for which the densities of the line-emitting states are ruled by the Saha balance of ionization and 2e-recombination. TS is much more expensive and experimentally demanding, but has several advantages. It gives spatial resolved values of n_e and T_e and clearly shows how different plasma zones respond differently. Another advantage is that TS can also be used for low n_e conditions, thus for plasmas for which the levels are not ruled by the Saha balance of ionization and 2e-recombination.

For the conditions for which both methods can be applied we found that TS supports the OES findings in global terms, but also, that TS gives more detailed insights with values of better precision.

At the edge of the ICP we find a fast n_e-decay that cannot be attributed to a combination of diffusion and 2e-recombination. This points to the importance of Molecular Assisted Recombination (MAR); a mechanism that is confirmed by applying TS@PI to Surface-wave induced plasmas (SIPs) of variable pressure. Increasing the pressure, favoring molecular ion formation, leads to faster plasma decay rates. Remarkable is that in the ICP edge where the decay is so fast, the electrons do not cool down to the gas temperature T_g during PI. This points towards a post-heating mechanism that cannot be electromagnetic in nature, since the power is switched off. Apparently the electrons are heated in the formation process of molecular ions during the MAR mechanism. Most likely the energy comes from the release of internal molecular energy, for instance from the vibrational systems. This idea of the role of molecules is supported by the behavior of low pressure Ar plasmas mixed with small amounts of N_2 or CO_2. It is found that T_e does not change much after PI, electrons remain heated. That this post-heating phenomenon was not found in Ar plasmas with small admixtures of O_2 or H_2, can be attributed to the small cross sections related to the energy exchange between {e} and the corresponding vibrational states (cf. Fig. 7.4 in [9]).

The role of post-heating on CO_2 dissociation deserves further studies as it might lead to a better understanding of mechanisms that are essential in the many experimental efforts that are nowadays on-going in the field of CO_2 valorization. Thus PI is not only an interesting experimental method; it might also become an essential ingredient of new plasma applications.

References

1. Gurevich D.B., Podmoshenskii I.V., Opt. Spectrosc., 1963, **15**, 319.
2. Kafrouni H., Bagneux J.M., Gleizes A., Vacquie S., *JQSRT,* 1979, **21**, 457.
3. Farnsworth P.B., Rodham D.A., Ririe D.W., Spectrochim. Acta, 1987, **42B**, 393.
4. Bydder E.I., Miller G.P., Spectrochim. Acta, 1988, **43B**, 819.
5. Fey F.H.A.G., Thesis, http://dx.doi.org/10.6100/IR391169, 1993.
6. De Regt J.M., Thesis, DOI: 10.6100/IR455254, 1996.
7. Garcia M.C., Rodero A., Gamero A., Sola A., Spectrochim. Acta, 2000, **55**, 1611.
8. Van de Sande M., Thesis, alexandria.tue.nl/extra2/200210414.pdf, 2002.
9. Hübner S., Thesis, http://alexandria.tue.nl/extra2/759549.pdf, 2013.
10. Britun N. et al., J. Phys. D: Appl. Phys., 2018, **51,** 144002.
11. Kuzmanović M.M., Pavlović M.S., Savović J.J., Marinković M., Spectrochim. Acta, 2003, **58B**, 239.

METER-SCALE ATMOSPHERIC PRESSURE MICROWAVE LINE PLASMA AND ITS APPLICATION

H. Toyoda

Furo-cho, Chikusa-ku, Nagoya 464-8603, Japan

Abstract. Large-scale atmospheric pressure (AP) plasmas have been given much attention because of its high cost benefit and a variety of possibilities for industrial applications. Microwave discharge plasma using slot is attractive due to its ability of high-density and stable plasma production, and we have developed a long-scale AP microwave plasma (AP microwave line plasma: AP-MLP) source up to ~1 m in length using a loop-structured waveguide and travelling wave. The plasma source is composed of a looped waveguide with a circulator and an EH tuner. The circulator realizes circular microwave power flow in the looped waveguide and the EH tuner enables us to confine the microwave power in the looped waveguide as a travelling wave. By a long slot along the waveguide, uniform Ar and He AP-MLP of ~50 cm is produced using a 2.45 GHz microwave power of 1 kW. From optical measurement of N_2 emission profile and H_β Stark broadening with small N_2 or H_2 addition, very low gas temperature of 400~600 K and rather high electron density of ~10^{20} m^{-3} are confirmed. It is notable that the AP-MLP utilizes CW microwave power, although conventional APPs use pulsed power to suppress the gas heating and resulting arc discharge. To realize the AP-MLP application to industries, use of molecular gases is preferable. To aim at this, the cross-sectional configuration of the waveguide is modified. By changing the cross-section configuration of the waveguide from symmetric one to asymmetric one, enhancement of the electric field in the slot is realized. By this modification, plasma production becomes much easier and uniform Ar plasma with a length of 1m is realized with only 500 W CW microwave power. Furthermore, 50 cm-length N_2 plasma is realized at a CW microwave power of 5kW. Very fast wettability control is demonstrated.

1. INTRODUCTION

Recently, various kinds of large area electronics devices such as flat panel displays or solar cells are commonly used. Furthermore, surface treatment of polymer films is also given attention [1] bacause such films are frequently used for heat shielding film on glass window or new functional polymer-based electronics devices. So far, fabrication of electronics devices on glass plates are realized by low-pressure large-area plasma sources (2m × 3m) using capacitively coupled plasmas. For the polymer film processing, roll of polymer film with film widths of more than one meter is installed in a huge vacumm chamber (a few m in height, 3m × 10m in foot print) and metal films or dielectric films are deposited in the chamber by moving the film by a winding roll at film speeds of a few m/min. However, due to the use of low-pressure plasmas for the processing, all the process equipment requires huge vacuum system in which all the processing materials are introduced. Accordingly, the processing cost becomes very high not only because of the plasma source cost but also because of low cycle time of the materials.

As an alternative of low-pressure large-area plasma sources, atmospheric pressure plasmas (APP) have received much attention because of its cost benefit and a variety of possibilities for industrial applications. For example, dielectric barrier discharge (DBD) plasma sources [2−4] have been proposed. RF power is also utilized for the production of APP [5−9].

Among various APPs, microwave discharge plasma is attractive because of its capability of high-density plasma production [10−19]. Benefit of the high density plasma is its high process throughput. For example, the DBD discharge is well known as one of intermettent discharge plasmas because the discharge duration is limited to a few microseconds due to the limination of the surface charge on the dielectric materials. Furthermore, the plasma density is rather low and time-averaged plasma density becomes very low. If temporally constant and spatially uniform microwave APP is realized, priority of the microwave APP is fully utilized and conventional APP sources can be replaced even by one-dimentionally long microwave APP.

In this paper, verious kinds of line-shaped atmospheric pressure microwave plasma source, *i.e.*, atmospheric pressure microwave line plasma (AP-MLP) is demonstrated [20−23].

2. SLOT-EXCITED AP MICROWAVE PLASMA

In various ways of AP microwave plasma production, plasma production using slotted waveguide is one of easy way. Figure 1 shows concept of slot-excited AP microwave plasma. Placing a slot on a waveguide as the slot interrupts the surface current flow, strong electric field is induced in the slot and, when the field intensity becomes higher than the breakdown field, plasma is produced in the slot and plasma is sustained by the power deposition due to the current flowing through the plasma.

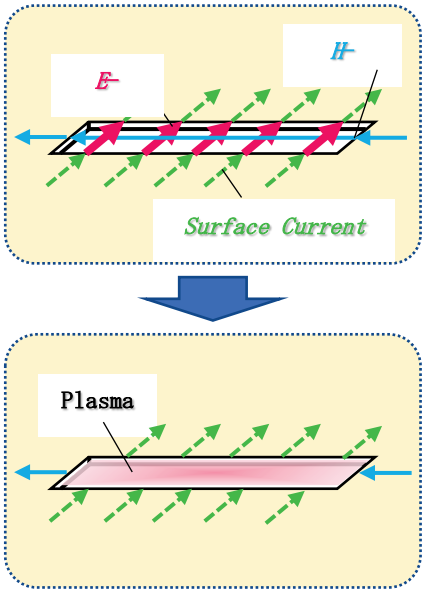

Figure 1. Plasma production by the slotted waveguide.

The most simple way to produce one dimensionally long AP microwave plasma is to use arrayed slot along the waveguide [20]. In this case, a long rectangular waveguide is utilized. By a short-end that is placed at the end of the waveguide, TE_{10}-mode microwave power in the waveguide produces standing wave along the waveguide. When the slot is placed as the slot direction is in parallel to the waveguide direction, the electric field in the slot becomes maximum when the slot is placed at a position of $(2n+1)\lambda_g/4$, where n and λ_g are integer and waveguide wavelength, respectively. The electric field also becomes larger when the slot is placed close to the edge of the E-face. Based on this concept, we have developed a 10 GHz microwave plasma source of two waveguides with an array of 41 slot antennas as a discharge line and succeeded in long-scale plasma production as shown in Fig. 2. However, size of the each plasma has been limited up to a few centimeters in length and production of continuous long-scale plasmas is difficult because slots are installed in accordance with antinodes of standing waves inside a waveguide which are discontinuous with fixed interval.

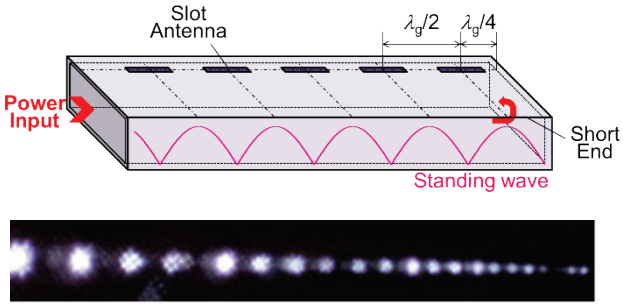

Figure 2. Atmospheric pressure microwave plasma with arrayed slots.

3. CONCEPT OF SPATIALLY UNIFORM LINE-SHAPED PLASMA

The AP microwave plasma using the arrayed slots is, of course, spatially not uniform and only discrete plasmas are aligned along the waveguide. This plasma structure is not suitable for real applications because the surface treatment process is realized by moving the materials perpendicular to the waveguide direction,

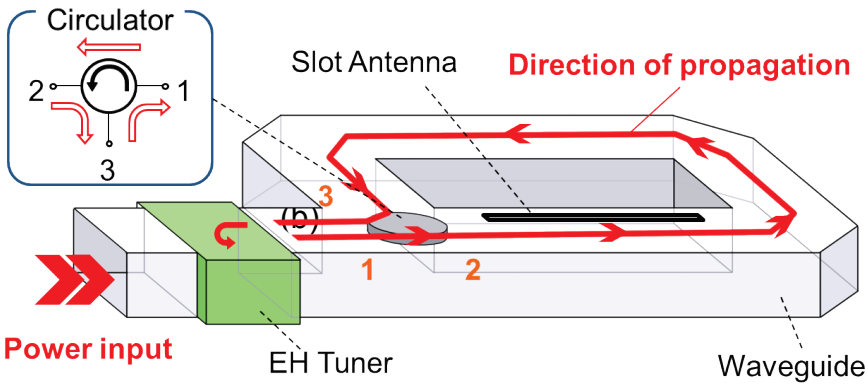

Figure 3. Waveguide structures for the line plasma production. A loop waveguide with a circulator and a long slot antenna is used.

i.e., by sweeping the plasma on the surface of two-dimensionally large materials. The reason why only discrete plasma array was produced in the above concept is simply because the spatial profile of the microwave energy along the waveguide is NOT uniform due to the existence of the standing wave. In other words, one-dimensionally uniform slot-excited microwave plasma is realized only when the microwave energy along the waveguide is uniform.

To solve this issue, we utilize one-dimensionally-long slot and standing-wave-free microwave power along the waveguide. The standing-wave-free microwave propagation is realized just only by placing a microwave power absorber at the end of the waveguide. In this configuration, however, fairly amount of microwave power is lost by the power absorber without contributing to the plasma sustainment. To effectively use the input microwave power, a waveguide configuration as shown in Fig. 3 is introduced [21]. The plasma source consists of a loop-structured waveguide with a line slot and a microwave circulator, as shown in the figure. The circulator is a non-reciprocal device with three ports and permits energy flow in only one direction, *e.g.*, port 1 to 2, 2 to 3 and 3 to 1. When a 2.45 GHz microwave power supply is connected to port 1 through an EH tuner, microwave power applied to the port 1 flows from port 2 into port 3 in a loop waveguide and exits from port 1. Supposing no power loss in the waveguide and the EH tuner, characteristic of the EH tuner can be expressed using *S* parameters as follows,

$$S_{mn} = |S_{mn}|e^{j\theta_{mn}}. \tag{1}$$

Here, m and n are port number. In the case of the EH tuner, *S* matrix can be considered as symmetric Unitari matrix and relation between *S* parameters becomes as follows.

$$S_{22} = S_{11} \tag{2}$$

$$S_{12} = S_{21} \tag{3}$$

$$|S_{22}|^2 + |S_{12}|^2 = 1 \tag{4}$$

Using the above Unitari matrix, square-root of the microwave power that flows through the loop waveguide can be expressed as follows.

$$\begin{aligned} I_L = S_{21}I_0 \sum_{k=0} S_{22}^k e^{jk\theta} &= \frac{S_{21}}{1 - |S_{22}|e^{j\theta'}} I_0 \\ &= \frac{|S_{21}|e^{j(\theta_{21}+\theta'')}}{\sqrt{1 - 2|S_{22}|\cos\theta' + |S_{22}|^2}} I_0, \end{aligned} \tag{5}$$

$$\theta' = \theta + \theta_{22}, \qquad \theta'' = \tan^{-1}\left(\frac{|S_{22}|\sin\theta'}{1-|S_{22}|\cos\theta'}\right)$$

Here, I_0 is input microwave power from the microwave power source to the EH tuner, and θ is phase difference when the microwave travel through the loop. When the EH tuner is adjusted as the phase difference between the microwave from the microwave power source and the microwave reflected by the EH tuner to be zero, *i.e.*, θ '=0, the microwave power flowing through the loop waveguide ($|I_L|^2$) is expressed to be

$$|I_L|^2 = \frac{|S_{21}|^2}{(1-|S_{22}|)^2}|I_0|^2 = \frac{1-|S_{22}|^2}{(1-|S_{22}|)^2}|I_0|^2 = \frac{1+|S_{22}|}{1-|S_{22}|}|I_0|^2. \tag{6}$$

When the S_{22} approaches unity, power gain ($|I_L|^2$ / $|I_0|^2$) monotonically increases. This means that the EH tuner reflects the power back into the loop again by the impedance matching and confines the microwave power in the looped waveguide. Thus, the power flow of only traveling wave is superimposed

in the loop without the energy loss and the microwave power inside the waveguide is enhanced. This result strongly supports the possibility of the microwave plasma production along a long slot even under atmospheric pressure conditions.

4. PRODUCTION OF ATMOSPHRIC PRESSURE MICROWAVE LINE PLASMA

To realize the concept of the one dimensionally long atmospheric pressure microwave plasma (hereafter, atmospheric pressure microwave line plasma: AP-MLP), a plasma source based on the above-mentioned concept is constructed and plasma characteristics are investigated [22]. In the experiment, a long slot of 600 mm in length and 0.5 mm in width with a displacement of 40 mm with respect to the waveguide centerline is placed on a rectangular waveguide (inside dimensions: 96 mm × 27 mm, length: 700 mm) along the direction of the microwave propagation, as is illustrated. Discharge gas (He: 2.0 slm) that is introduced into the waveguide through small holes on the center of the waveguide flows out through the slot. Pulsed-microwave (pulse-frequency: 20 kHz, duty ratio: 20-100, peak power: <2 kW) generates line plasmas over a half meter scale under the atmospheric pressure. The spatiotemporal development of the discharges is observed by a digital still camera and a high-speed camera (frame rate: 2000 frame/s, exposure time: $2.5\text{x}10^{-5}$ s).

Figure 4a shows is an image of the plasma emission with exposure time fixed at 1.0 s. Continuous plasma of over a half meter in length is generated. To investigate spatial variation of the emission intensity along the slot, the still camera is installed in front of the slot antenna and photo-image is analyzed by a software as shown in Fig. 4b. Although minute fluctuations and slight decrease in the intensity along the slot is observed, rather uniform plasma is produced along the slot antenna. The spatiotemporal development of the discharges is observed by a high-speed camera with a frame rate of 2000 frame/s and an exposure time of 2.5×10^{-5} s. Figure 5 shows the high-speed photographs of the plasmas in the center of the slot of 100 mm length in a certain time. It is shown that a number of small plasmas move in the direction of the microwave propagation.

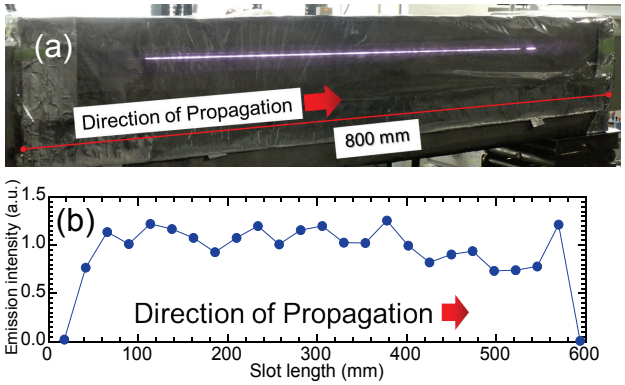

Figure 4. (a) An image of the plasma emission and (b) its distribution of the emission intensity along the slot.

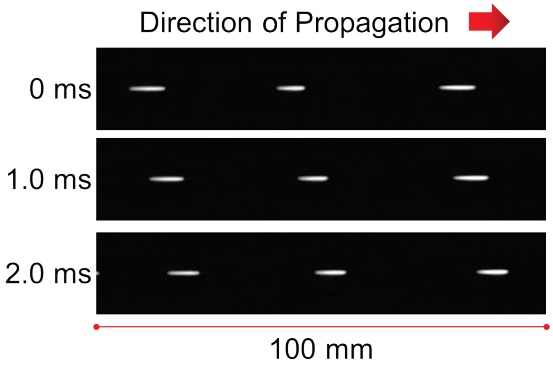

Figure 5. Single-shot images of the plasmas travelling according to the microwave power.

In the above experiment, the plasma looks uniform along the long slot. However, the plasma looks uniform only as time averaged one and is not real uniform plasma. We next investigate the behavior of the plasma by changing the slot width and the microwave pulse duty ratio. Figure 6a shows duty ratio dependence of the plasma size at slot widths from 0.1 to 0.7 mm. The length of the moving plasma increases with increasing the duty ratio and with reducing the slot width. It is notable that in the case of the slot width of 0.1 mm, the plasma size becomes drastically long at duty ratios above 90%. When the microwave power becomes CW power (duty ratio: 100%), each plasma connects each other and one very long plasma at a length comparable to the slot length is confirmed even with the high speed camera. Figure 6b shows a photograph example obtained by the high-speed camera at a pulsed microwave power of 2 kW and a duty ratio of 92%. Even by the high-speed camera, no plasma movement is observed and

production of temporally stable plasma is confirmed. Figure 7 shows example of the emission profile along the slot in the case of the He AP-MLP. Although some fluctuation due to the edge of the slot is observed in both ends of the slot, uniform emission intensity is observed in the middle of the plasma (10~50 cm in the figure). This means that the spatially uniform and temporally stable plasma can be produced by CW microwave power.

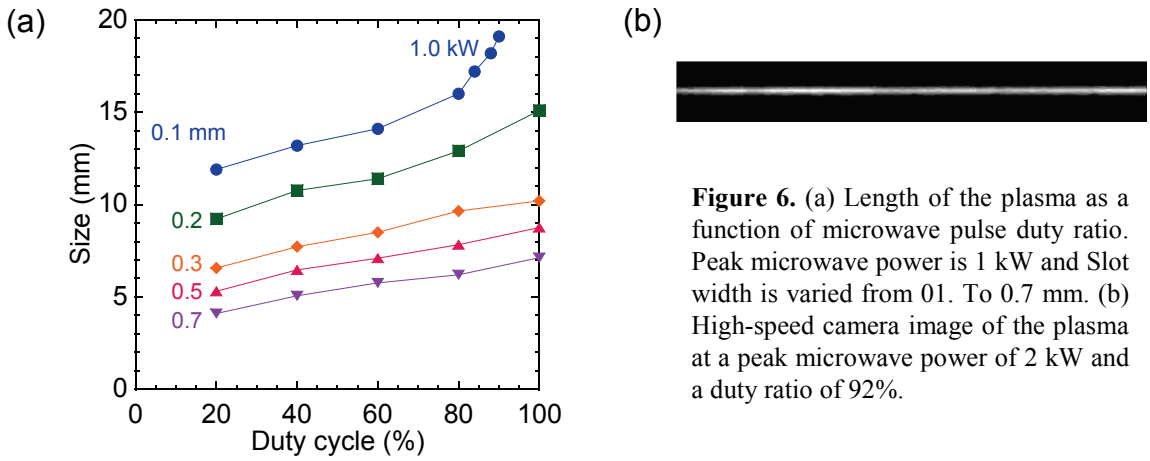

Figure 6. (a) Length of the plasma as a function of microwave pulse duty ratio. Peak microwave power is 1 kW and Slot width is varied from 01. To 0.7 mm. (b) High-speed camera image of the plasma at a peak microwave power of 2 kW and a duty ratio of 92%.

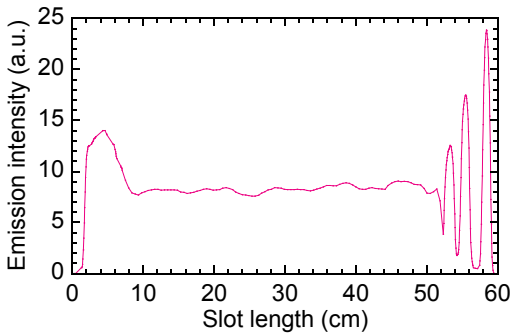

Figure 7. Spatial profile of emission intensity by the AP-MLP with He gas.

5. BASIC CHARACTERISTICS OF THE AP-MLP

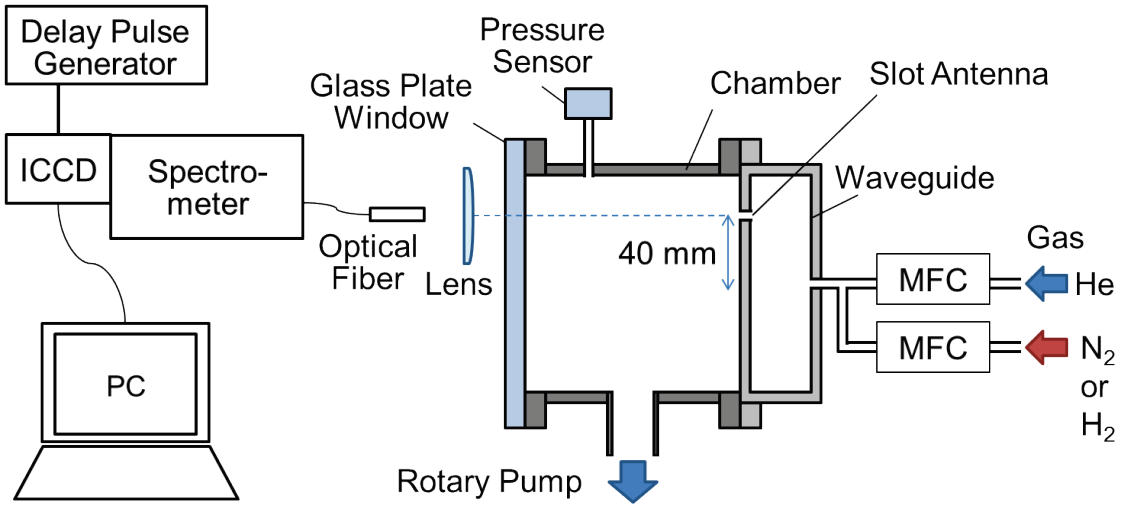

Figure 8. Experimental setup for the plasma diagnostics.

Electron density is one of essential plasma parameters to determine the plasma characteristics. Gas temperature in the plasma is also important key parameter to determine characteristics of processing, especially for processing of non-heat-resistant materials such as polymer films. From this viewpoint, the electron density is measured by the Stark measurement and the gas temperature of the discharges is estimated from the rotational temperature of $N_2(C\text{-}B)$ by optical emission spectroscopy [22].

Figure 8 shows schematic of the experimental apparatus. A 2.45 GHz microwave power (CW power, 1.0 kW) is introduced to the circulator through an EH tuner. A long slot (600 mm in length, 0.1 mm in width) is vacuum-sealed by two airtight windows and is connected to a vacuum chamber evacuated by a rotary pump. After the evacuation, discharge gas (He: 5 slm, N_2: 10 sccm) is introduced into the vacuum-sealed waveguide through small holes on the waveguide till the chamber is filled with the gas at the atmospheric pressure. The emission spectra of the second positive system of nitrogen are obtained around the slot center by a monochromator with an ICCD camera at a gating time of 100 ns after 5 μs from the plasma ignition. Figure 9 shows experimentally observed and simulated spectra of $N_2(C\text{-}B)$ shown as a solid curve and a broken curve between 377 and 381 nm. The rotational temperature (T_r) of 450 K is obtained. Similar experiment is carried out using Ar and the gas temperature of ~600 K is observed. It should be noted that the gas temperature is very low even the CW microwave power is used under the atmospheric pressure condition. These results suggest that this plasma source can be utilized for the treatment of non-heat-resistant materials.

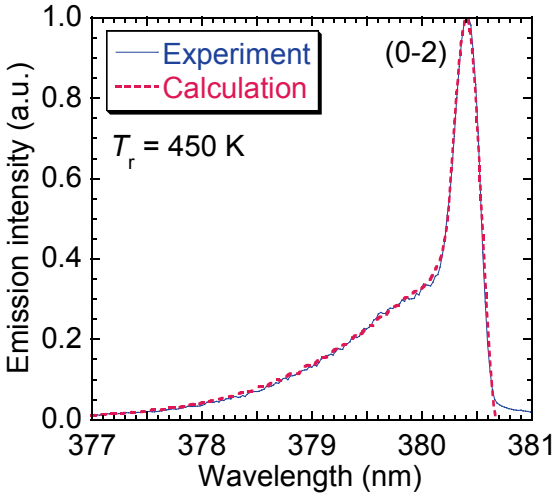

Figure 9. Emission spectrum of N_2. Solid curve is measured spectrum. Broken curve is simulated and best-fitted specturum varying the gas temperature.

Plasma density of the AP-MLP is also investigated by Stark measurement of H_β line. In the measurement, a 0.5 m focal length spectrometer with a grating of 3600 groove/mm is used. An ICCD camera is used for the spectrum measurement. The experimental conditions are almost the same as those of Fig. 9, except for the addition gas (H_2 instead of N_2). Figure 10 shows an example of H_β spectrum measured by the ICCD optical multichannel analyzer. Measured line width is ~86 pm. The line width, however, includes broadening factors not only from Stark effect but also other broadening effect (natural broadening, Doppler broadening, Van der Waals broadening) as well as the spectral resolution of the spectrometer. These factors are carefully removed taking the broadening profiles (Lorenzian, Gaussian) into account, and the broadening factor from the Stark broadening is obtained and the electron density is calculated to be $1.2\text{x}10^{14}$ cm^{-3} at a slot width of 0.1 mm. From the Stark measurement, high plasma density of the AP-MLP is confirmed.

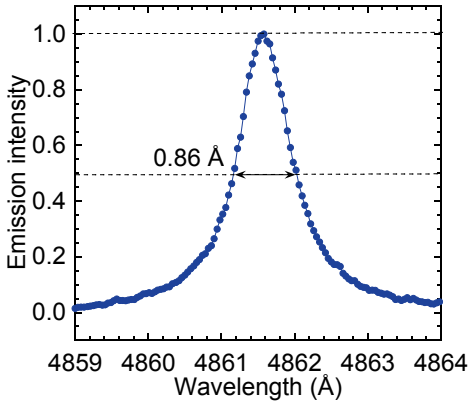

Figure 10. An example of Hβ spectrum measured by the ICCD optical multichannel analyzer.

6. FURTHER IMPROVEMENT OF THE AP-MLP

In the above chapters, the AP-MLP is produced only by rare gases such as helium or argon. In the industrial applications, however, not only rare gases but also molecular gases must be considered not only because of cost benefit but also because of usefulness of chemically reactive species produced by molecular gases. In the case of the molecular gas discharge, however, it is well known that the discharge power that sustains the plasma becomes much higher than that of rare gas discharges because the discharge power absorbed by the plasma is used not only by the ionization or the electronic excitation but also by dissociative, vibrational or rotational excitations. In the case of the slot-type microwave atmospheric pressure plasma, the plasma is sustained by the current that flows through the plasma and the power is absorbed by the plasma through ohmic heating, due to very high collisionality. This implies that the power absorption becomes more effective when the current becomes much larger, resulting in the

effective plasma sustainment in the molecular gas discharge. In the conventional rectangular waveguides, typical mode of the electromagnetic wave in the waveguide is TE_{10}. This mode is symmetric with respect to the center plane of the waveguide and the surface current is also symmetric with respect to the center plane of the waveguide. In this slot-type AP-MLP, the slot is positioned close to the edge of the H-plane and this means that only one side of the surface current is utilized for the discharge. However, if the spatial profile of the surface current is controlled by the structure of the waveguide and the surface current is concentrated at a certain position in the waveguide, the microwave power is effectively utilized for the plasma production and even the molecular gas discharge becomes rather easy. Based on this concept, cross sectional structure of the rectangular waveguide is modified and the cross sectional profile of the electromagnetic wave is investigated through a simulation of the finite element method.

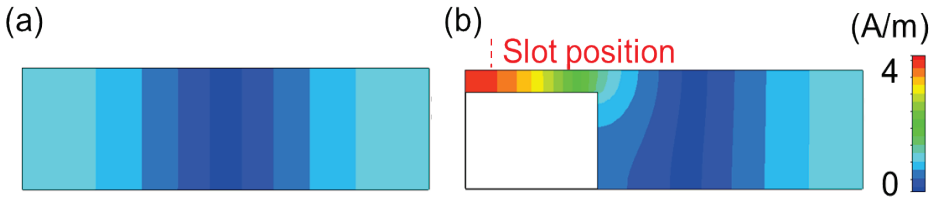

Figure 11. Cross-sectional view of magnetic field distribution of (a) the standard waveguide and (b) the modified waveguide.

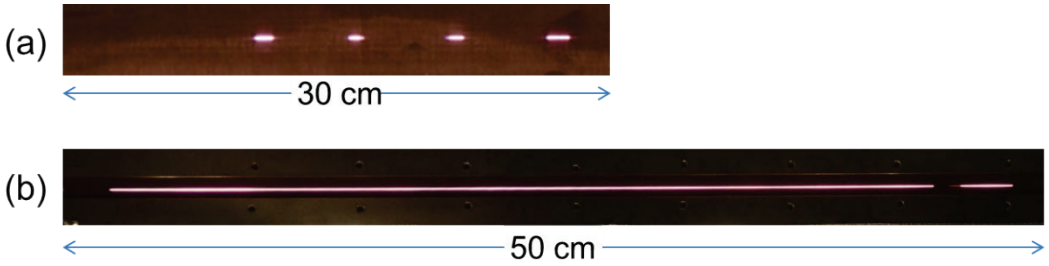

Figure 12. Pure N_2 line plasma emissions inside slots in the cases of (a) the standard waveguide and (b) the modified waveguide.

In the simulation, commercially available MW-Studio is used, where the spatial profile of the electromagnetic wave is calculated by the finite integration method. Figure 11 shows one example of the cross-sectional profiles of the magnetic field both in the cases of the conventional rectangular waveguide and a cross-section modified waveguide. In the case of the conventional rectangular waveguide, the magnetic field profile is completely symmetric with respect to the center plane of the waveguide. In the case of the modified waveguide, however, the magnetic field becomes localized in the vicinity of the short-spacing waveguide part and strong magnetic field is realized near the edge of the waveguide. This result strongly suggests easy production of the plasma using the modified waveguide structure.

Based on the simulation, a new AP-MLP is constructed using the modified waveguide. In the experiment, pure N_2 gas is used at a N_2 gas flow rate of 10 slm per 1m slot-length. Figure 12 shows photo images of the N_2 emission in the cases of the standard-size waveguide and the modified waveguide. In the case of the standard waveguide (Fig. 12a), the discharge becomes discrete and line plasma is not produced even using a slot of 30 cm length. In the case of the modified waveguide (Fig. 12b), however, a line plasma with pure N_2 gas is successfully produced at a plasma length of ~40 cm. This result clearly indicates the effectiveness of the waveguide structure modification to enhance the plasma production with molecular gases.

7. APPLICATION EXAMPLE OF THE AP-MLP

The AP-MLP can be applied to various applications. One of typical applications of the AP-MLP is surface wettability control. Figure 13 shows the experimental apparatus with additional information of the film treatment setup. As is shown in Fig. 13a, a loop-waveguide antenna consists of a loop-structured waveguide and a microwave circulator. A pulse-modulated 2.45 GHz microwave source (pulse-frequency: 20-80 kHz, duty cycle: 60%, peak power: 2.0 kW) is connected to the circulator through an EH tuner. A section of the loop waveguide with a long slot (60 cm or 90 cm in length, 0.1 mm in width, 1.0 mm in thickness) is vacuum-sealed by two airtight windows and is connected to a vacuum chamber evacuated by a rotary pump to confirm gas purity during the experiment. Figure 13b shows the cross-sectional view of the vacuum-sealed chamber and film-treatment setup. After the evacuation, mixture gas of helium and nitrogen (1%) is introduced to the gap of the slot antenna through small holes on the waveguide wall facing the slot at total flow rates of 5.0 slm and 7.0 slm for 60 cm and 90 cm slot respectively, filling the chamber and the waveguide with the mixture gas at a pressure of 100 kPa (atmospheric pressure) monitored by a pressure sensor. AP microwave line plasma is produced inside the slot gap by applying the microwave power. PET film is set at the front of the antenna and the distance between the antenna and the substrate is 2 mm.

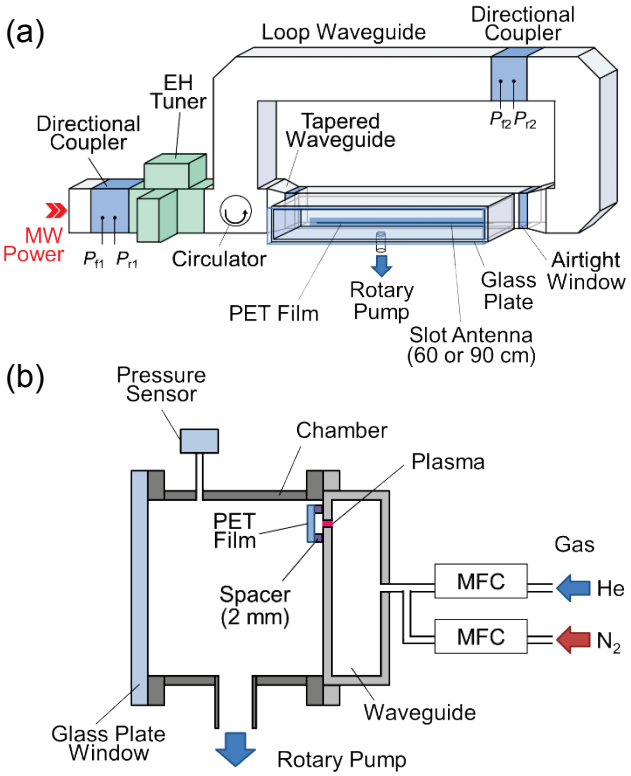

Figure 13. Schematic of (a) experimental apparatus and (b) its cross sectional view and film-treatment.

Figure 14 shows the water contact angles at the center of the slot as a function of the treatment time under various pulse-frequency conditions with a fixed duty cycle of 60%. The contact angle rapidly decreases within 5 s of the treatment time and the processing speed increases with increasing pulse frequencies from 20 to 60 kHz.

To evaluate treatment-uniformity of a meter-scale substrate, PET films were treated by 90 cm slot-antenna plasma at pulse frequency of 80 kHz and a duty cycle of 25%. Figure 15 shows the spatial profile of the treatment performance. The water contact angle decreased down to ~25 degree within 5 s. Furthermore, the distribution of the contact angle was almost uniform along the slot. It should be also mentioned that there was no thermal damage on the substrate, suggesting that this plasma source can be easily applied to non-heat-resistant materials and long area processing.

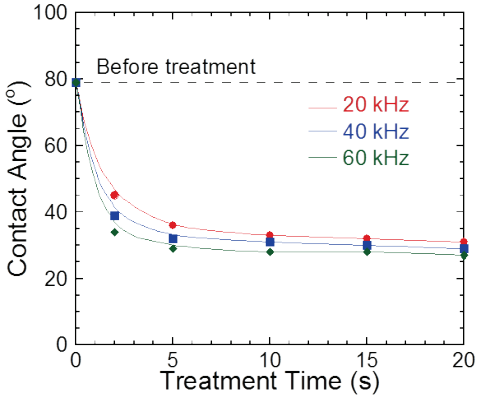

Figure 14. The water contact angle as a function of the treatment time with a fixed duty cycle of 60%.

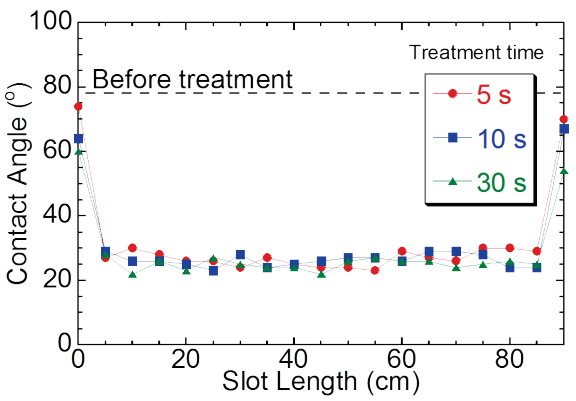

Figure 15. The water contact angle as a function of the treatment time with a fixed duty cycle of 60%.

8. CONCLUSIONS

A long-scale AP microwave plasma (AP microwave line plasma: AP-MLP) source up to ~1 m in length using a loop-structured waveguide and travelling wave was developed for large area surface treatment. The plasma source was composed of a looped waveguide with a circulator and an EH tuner. The circulator realized circular microwave power flow in the looped waveguide and the EH tuner enabled us to confine the microwave power in the looped waveguide as a travelling wave. By a long slot along the waveguide, uniform Ar or He AP-MLP of ~50 cm was produced using a 2.45 GHz microwave power of 1 kW. From optical measurement of N_2 emission profile and H_β Stark broadening with small H_2 addition, very low gas temperature of 400~600 K and rather high electron density of ~10^{20} m^{-3} were confirmed using CW microwave power. To realize the AP-MLP application to industries, cross-sectional configuration of the waveguide was modified aimng at molecular gas discharge. By changing the cross-section configuration from symmetric one to asymmetric one, enhancement of the electric field in the slot was realized. By this modification, plasma production became much easier and uniform Ar plasma with a length of 1 m was realized with only 500 W CW microwave power. Furthermore, 50 cm-length N_2 plasma was realized at a CW microwave power of 5 kW. Very fast wettability control was demonstrated.

Acknowledgments

This work is supported by JSPS KAKENHI Grant Number 25286079 and 16H03893.

References

1. Borcia G., Anderson C.A., Brown N.M.D., Plasma Sources Sci. Technol., 2003, **12**, 335.
2. Kogelschatz U., Eliason B., Egli W., IUPAC Pure Appl. Chem., 1999, **71**, 1819.
3. Miclea M., Kunze K., Musa G., Franzke J., Niemax K., Spectrochim. Acta Part B, 2001, **56**, 37.
4. Kunze K., Miclea M., Franzke J., Niemax K., Spectrochim. Acta Part B, 2003, **58**, 1435.
5. Babayan S.E., Jeong J.Y., Tu V.J., Park J., Selwyn G.S., Hicks R.F., Plasma Sources Sci. Technol., 1998, **7**, 286.
6. Park J., Henins I., Herrmann H.W., Selwyn G.S., Hicks R.F., J. Appl. Phys., 2001, **89**, 20.
7. Yoshiki H., Horiike Y., Jpn. J. Appl. Phys., 2001, **40**, L360.
8. Ichiki T., Koidesawa T., Horiike Y., Plasma Sources Sci. Technol., 2003, **12**, S16.
9. Bass A., Chevalier C., Blades M.W., J. Anal. At. Spectrom., 2001, **16**, 919.
10. Moisan M., Zakrzewski Z., Etemadi R., Rostaing J. C., J. Appl. Phys., 1998, **83**, 5691.
11. Mizojiri T., Morimoto Y., Kando M., Jpn. J. Appl. Phys., 2007, **46**, 3573.
12. Takamura S., Kando M., Ohno N., J. Plasma Fusion Res., 2009, **8**, 910.
13. Al-Shamma'a A.I., Wylie S.R., Lucas J., Pau C.F., J. Phys., 2001, **D 34**, 2734.
14. Iza F., Hopwood J.A., IEEE Trans. Plasma Sci., 2003, **31**, 782.
15. Hoskinson A.R., Gregorio J., Parsons S., Hopwood J., J. Appl. Phys., 2015, **117**, 163301.
16. Kim J.H., Terashima K., Appl. Phys. Lett., 2005, **86**, 191504.
17. Schermer S., Bings N.H., Bilgic A.M., Stonies R., Voges E., Broekaert J.A.C., Spectrochim. Acta Part B, 2003, **58**, 1585.
18. Kono A., Sugiyama T., Goto T., Furuhashi H., Uchida Y., Jpn. J. Appl. Phys., 2001, **40**, L238.
19. Kono A., Wang J., Aramaki M., Thin Solid Films, 2006, **506–507**, 444.
20. Itoh H., Kubota Y., Kashiwagi Y., Takeda K., Ishikawa K., Kondo H., Sekine M., Toyoda H., M. Hori, J. Phys.: Conf. Ser., 2013, **441**, 012019.
21. Suzuki H., Nakano S., Itoh H., Sekine M., Hori M., Toyoda H., Appl. Phys. Express, 2015, **8**, 036001.
22. Suzuki H., Nakano S., Itoh H., Sekine M., Hori M., Toyoda H., Jpn. J. Appl. Phys., 2016, **55**, 01AH09.
23. Suzuki H., Toyoda H., Jpn. J. Appl. Phys., 2017, **56**, 116001.

HIGH CURRENT PULSED ECR ION SOURCES

V. A. Skalyga, S. V. Golubev, I. V. Izotov, R. L. Lapin, S. V. Razin, R. A. Shaposhnikov, A. V. Sidorov, A. V. Vodopyanov, A. F. Bokhanov, M. Yu. Kazakov

Federal Research Center “Institute of Applied Physics of the Russian Academy of Sciences", Ul`yanova Str., 46, Nizhny Novgorod, 603950, Russian Federation

Abstract. In present time some ECR ion sources use a high frequency powerful microwave radiation of modern gyrotrons for plasma heating. Due to high radiation power such systems mainly operate in a pulsed mode. This type of ECR ion sources was developed at the Institute of Applied Physics of Russian Academy of Sciences and the most part of experimental research was performed at SMIS 37 facility. At SMIS 37 gyrotrons with 37.5 and 75 GHz frequencies and 100 and 200 kW maximum power respectively are used for plasma production. Such heating microwaves allow creating plasma with unique parameters: electron density > 10^{13} cm^{-3}, electron temperature 50−300 eV, ion temperature about 1 eV. The principal difference between these systems from the conventional ECR sources is a so-called quasi-gasdynamic regime of plasma confinement. In accordance with the confinement regime such sources have been called "gas-dynamic ECR sources". Typically, plasma lifetime in such systems is about 10 microseconds, which in combination with the high plasma density leads to formation of the plasma fluxes from a trap with density up to 1−10 A/cm^2. The confinement parameter (the product of plasma density and lifetime) reaches a value (> 10^8 $cm^{-3}s$) sufficient to generate multiply charged ions. The possibility of multiply charged ion beams (nitrogen, argon) production with currents up to 200 mA was demonstrated. Particularly the gas-dynamic ECR ion sources are effective for generation of high current proton beams with low emittance (high brightness). Recently a possibility of proton and deuteron beams formation with currents up to 500 mA and rms normalized emittance 0.07 pi • mm • mrad was demonstrated.
The next step in the research is a transition to continuous wave (CW) operation. For this purpose, a new experimental facility is under construction at the IAP RAS. Future source will utilize 28 and 37.5 GHz gyrotron radiation for plasma heating. Overview of the obtained results and the status of the new source development will be presented.

1. INTRODUCTION

Production of high intensity ion beams from an ECR discharge could be realized in a pulsed mode when microwave power level coupled into a plasma is much higher than it is used in continuous wave (CW) operation. Basic principal is rather simple: a high current density ion beam could be produced in case of dense plasma flux from a magnetic trap coursed by fast losses; fast losses mean high heating power required for electron temperature sustaining at the level necessary for efficient ionization. Investigations of pulsed ECR discharge in an open magnetic trap under conditions of powerful ECR heating with gyrotron mm-waveband radiation were carried out over the last 20 years at the Institute of Applied Physics (IAP RAS, Nizhniy Novgorod, Russia) [1−5] and continued at Laboratoire de Physique Subatomique & Cosmologie (LPSC, Grenoble France) [6, 7]. In the beginning the work was devoted to development of a high frequency ECR source of multi-charged ions with outstanding parameters of plasma heating (37.5 GHz, 100 kW). According to Geller’s scaling laws [8] such increase in frequency and power in comparison to conventional ECRIS was expected to boost the ion source performance and provide a significant progress in ECRIS development. However, due to short pulse operation mode and low repetition rate of the used gyrotrons (pulse duration < 1 ms, 0.1 Hz) breakdown and discharge conditions similar to a conventional ECRIS were unreachable. The minimum neutral gas pressure was two orders higher (10^{-4} mbar) and the plasma parameters differed significantly from conventional ECRIS. After years this work resulted in development of a new type of ion source – high current gasdynamic ion source.

2. QUASI-GASDYNAMIC PLASMA CONFINEMENT

The use of powerful mm-band radiation allows to increase the plasma density in the discharge significantly (proportional to the square of the radiation frequency [4−9]) in comparison to conventional ECRISs, which utilize microwave radiation with frequencies on the order of 10 GHz [8]. In experiments with gyrotrons frequency range 37.5 – 75 GHz the plasma density reaches values of 10^{13}−10^{14} cm^{-3}[10, 11]. Significant increase of the plasma density leads to a change of the confinement mode. A so-called quasi-gasdynamic confinement [4, 5] was realized in the presented experiments instead of the collision-less confinement [12], which is typical for modern ECRISs. The transition from collision-less to quasi-gasdynamic confinement occurs when the plasma density is high enough for the scattering rate of electrons into the loss-cone to be higher than the maximum possible electron loss rate caused by the ion-sound flux through the magnetic mirrors [13]. In such situation the loss-cone in the velocity space is populated, and the plasma lifetime does not depend on the collisional electron scattering rate into the loss-cone i.e. on the plasma density, but is determined by the trap size, magnetic field structure and ion sound velocity [13]. The plasma lifetime, which is much shorter than in conventional classical ECRISs, can be expressed as $\tau=(L\cdot R)/(2Vis)$, where L is the magnetic trap length, R the trap mirror ratio (ratio between magnetic field in the magnetic mirror and in the trap center) and Vis the ion sound velocity. Short plasma lifetime provides high plasma flux density from the trap. The flux is proportional to the plasma density and ion lifetime i.e. $I \sim N / \tau$, where N is the plasma density. Due to the high plasma density, the confinement parameter $Ne\cdot\tau$, which determines the ionization degree and average ion charge, can be as high as 10^{8}–10^{9} $s\cdot cm^{-3}$, which is enough for efficient ionization. The main advantages of quasi-gasdynamic confinement are the following. The plasma lifetime does not depend on its density and, therefore increase of the density would lead to rising of confinement parameter and average ion charge. In addition, the plasma lifetime is proportional to the magnetic trap length and the source performance could be improved by adjusting the trap length. In case of extremely high frequency heating and accordingly higher plasma density multiple ionization is possible even in a small plasma volumes. ECR sources running under conditions of such plasma confinement are called gasdynamic ECRISs.

Possibilities and prospects of the gasdynamic confinement were demonstrated at SMIS 37 facility [4, 5] and at SEISM Prototype [6, 7]. It was shown that the described peculiarities of quasi-gasdynamic ECR discharge sustained by mm-waveband radiation, namely, short lifetime and high density, provide unprecedented ion current densities up to 800 emA/cm^2.

3. SMIS 37 EXPERIMENTAL FACILITY

The main part of the experiments devoted to the topic was conducted at SMIS 37 facility. During the years its configuration has been changing slightly, the latest one being schematically depicted in Fig. 1. The plasma is created and sustained inside a d=4 cm vacuum chamber (placed in a magnetic trap) by pulsed (1 ms) 37.5 GHz or 75 GHz linearly polarized gyrotron radiation with power up to 100 kW. The simple mirror magnetic field (or a cups trap for some experiments) is created by means of pulsed solenoids positioned at a distance of 15 cm from each other, providing a mirror ratio of 5. The magnetic field strength could be varied in a range of 1−4 T at mirror plugs, whereas the resonant field strength is 1.34 T for 37.5 GHz and 2.7 T for 75 GHz. The microwave radiation is coupled to the chamber quasi-optically through a quartz window and a special coupling system, which protects the window from the plasma flux. Quasi-optical coupling appears to be the best choice for high power microwave radiation transport into an ion source especially because air gaps additionally could be used as a DC-break between high voltage plasma chamber and microwave source. At SMIS 37 the pulsed gas feeding is used and gas line is incorporated into the coupling system i.e. the neutral gas is injected axially.

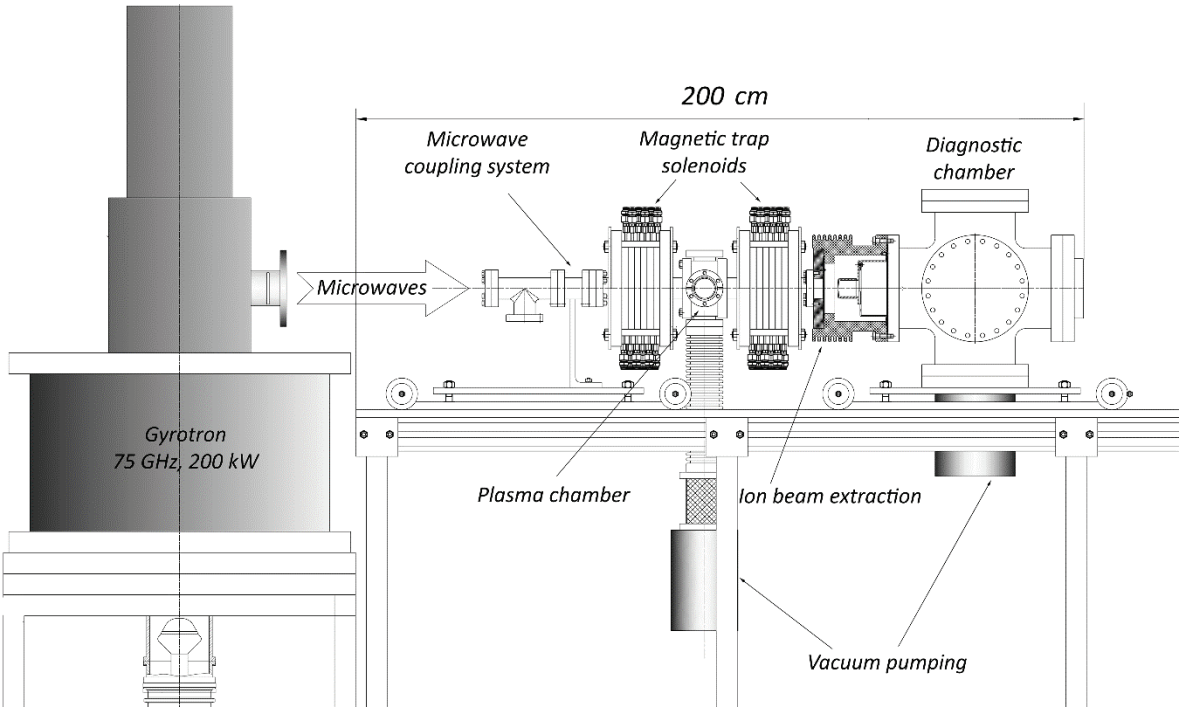

Figure 1. Schematic view of SMIS 37 experimental facility.

The ion extraction and beam formation is realized by a two-electrode (diode) system consisting of a plasma electrode and a puller. The diameter of the extraction aperture is varied from 1 to 10 mm. The distance between the extraction system and the magnetic plug at the center of the solenoid magnet was designed to be variable, which allows tuning the plasma flux density at the plasma electrode. The maximum applied extraction voltage is up to 100 kV. A Faraday cup with an aperture of 85 mm is placed right behind the puller (grounded hollow electrode) to capture the whole beam. The cup is equipped with an electrostatic secondary electron suppression. A 42^{o} bending magnet is installed downstream in the beam line for measuring extracted beam spectrum.

4. MULTICHARGED IONS PRODUCTION

A number of papers were devoted to multi-charged beam production at SMIS 37 [1−5]. In this paper the main results obtained some years ago are shown to demonstrate the typical source performance. In Fig. 2 two ion spectra with nitrogen and argon are presented in the case of 37.5 GHz, 100 kW plasma heating.

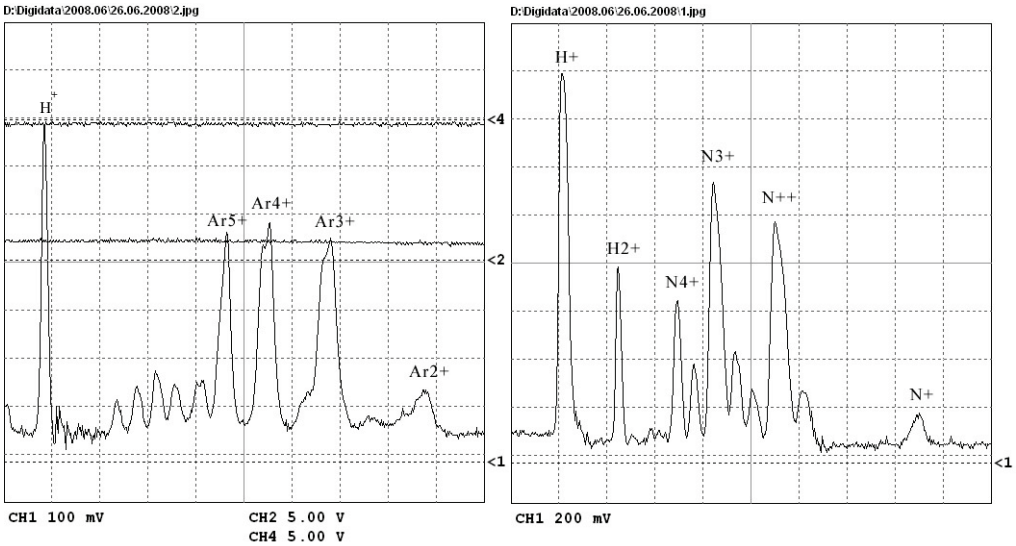

Figure 2. Argon and Nitrogen spectra. ECR plasma heating with 37.5 GHz, 100 kW gyrotron radiation in a simple mirror trap.

The effect of plasma density increase within gasdynamic confinement with increase of microwave frequency is shown in Fig. 3. Helium ion spectra for 37.5 and 75 GHz, 100 kW and 200 kW heating correspondingly demonstrate a great improvement in average ion charge.

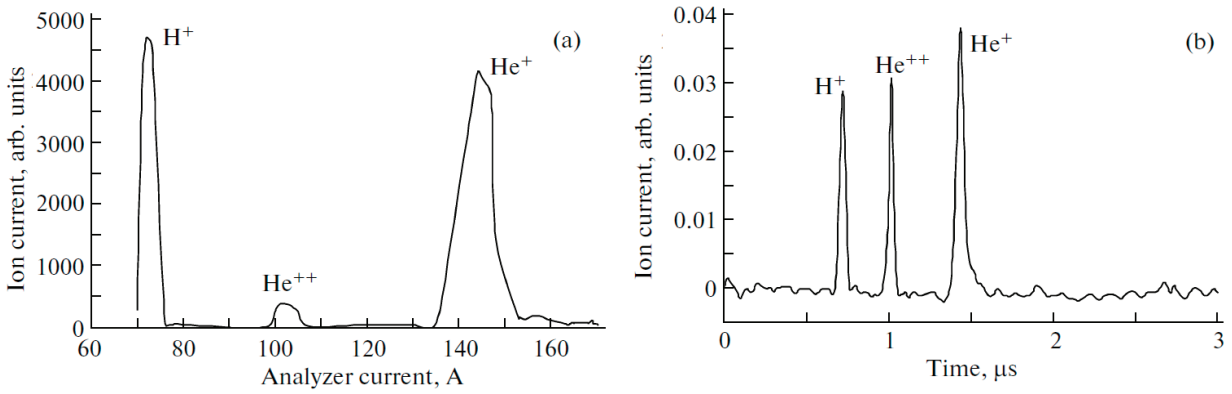

Figure 3. Helium spectra. 37.5, 100 kW ECR heating (left) and 75 GHz, 200 kW ECR heating (right). Plasma is confined in a cusp trap with an effective length of 28 cm, the gas pressure is 10^{-4} Torr.

In these experiments a single aperture two electrode extraction system with 1 mm hole was used for beam formation providing total ion current up to 10 mA [2]. Normalized beam emittance measured with pepper-pot method was of the order of 0.01 π·mm·mrad. The experiments were repeated later with multi-aperture extraction systems. Extracted ion current dependence on the accelerating voltage in case of 13-hole (each 3 mm in diameter) plasma electrode is shown in Fig. 4.

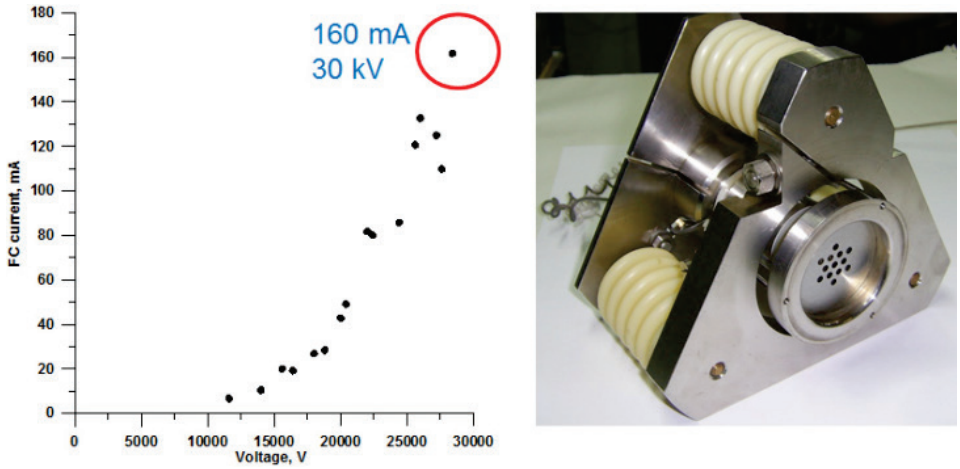

Figure 4. Faraday cup current dependence on extraction voltage (left) obtained with multi-aperture extraction system (right).

Presented results demonstrate that gasdynamic ion source is able to produce hundreds of emA of moderately charged (Q up to 6+) beams. Low emittance and high current of such beams may allow using them together with charge-breeding or stripping techniques. Further increase of the microwave frequency is promising for the production of high current heavy ion beams with the average charge about +10 and their injection into accelerators with strippers after first acceleration stage.

The state of the art ion source of this type called SEISM Prototype have been built recently in Grenoble in frames of international collaboration between LPSC, IAP RAS and LNCMI (CNRS). It is the first ECRIS with a topologically closed 60 GHz ECR resonance zone, using radially cooled polyhelices. Unique ion beam intensities have been extracted from this prototype, like 1.1 mA of O^{3+} through a 1 mm hole representing a current density of 140 mA/cm^2 [7]. In first experiments a significant currents of highly charged ions like O^{5+} were also observed. Further investigation at this experimental facility should demonstrate the ultimate performance of gasdynamic ECR ion sources.

5. SHORT PULSE ION BEAMS

Many of the modern technologies and basic research facilities require the creation of an ion source capable of generating short-pulse (20–100 μs), high current (tens or hundreds of milliamps) heavy gases ion beams with a fairly high average charge and low emittance. Gasdynamic ECR sources of multicharged ions seem to be the most promising in this respect. In this case, the plasma confinement in a magnetic trap is quasigasdynamic and has a typical lifetime of 10 to 20 μs. Under these conditions, there are two modes of generating high-current ion pulses of short duration, namely, quasi-stationary and non-stationary. The possibility of quasi-stationary generation of short-pulse multicharged ion beams is related to a short plasma lifetime in the trap of a gas-dynamic ECR source, which ensures that the plasma density can reach a steady-state level within a short time. To obtain short pulses in the non-stationary generation mode, one can use the well-known preglow effect [14−17], in which a peak current of extracted multiply charged ion beam with amplitude exceeding several steady-state values is observed at the initial stage of a discharge. In addition, it was found in [18] that in the case the gyrotron pulse duration is less than or of the order of the typical time of the preglow peak formation the beam current occurs predominantly after the end of the microwave pumping in the form of an intense short burst. Apparently a similar effect was observed earlier in [19] and was named “the micropulsed mode”. In experiments conducted at SMIS 37 it was demonstrated that gasdynamic ECR ion source running in such “micropulsed mode” is able to produce multicharged ion beams with duration less than 100 μs. Waveforms of the full beam current and for Ar^{4+} and Ar^{5+} currents are shown in Fig. 5.

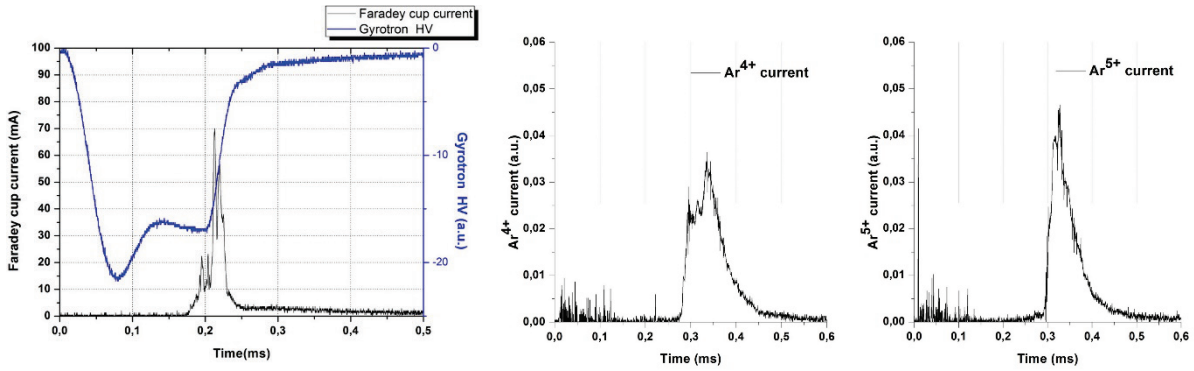

Figure 5. Oscillogram of the argon ion beam current (Faraday cup current) for an extraction voltage of 23 kV is on the left. High-voltage pulse of the gyrotron cathode (which duration is close to the one of microwave power pulse) is shown. Corresponding currents of separate beam species (Ar^{4+} and Ar^{5+}) are on the right.

The total beam current extracted with multiaperture extraction system described above was at the level of 100 mA.

Later some theoretical work showing a possibility of high ionization efficiency in case of short-living radioactive isotopes beams production was reported in [20]. For the needs of Beta Beam project [21] it was shown that gasdynamic ECR source in the short pulse mode could provide up to 50% utilization of ^{6}He in fully striped ions.

6. PROTON AND DEUTERON BEAMS FORMATION

Operation of modern high power accelerators often requires production of intense proton and deuterium beams. H+ beams are utilized or envisioned for use in linear accelerators e.g. the future European Spallation Source under design [22, 23]; some special applications such as neutron generators or the IFMIF project, require D+ (deuteron) ion beams. Requirements for the brightness of such beams grow together with the demand of accelerator development and arising experimental needs. New facilities aiming at outperforming the previous generation accelerators are usually designed for higher beam currents. Enhancing the beam intensity and maintaining low transverse emittance at the same time is, however, quite a challenging task. The most modern accelerators require H+/D+ ion beams with currents up to hundreds of emA (pulsed or CW), and normalized emittance less than 0.2 π·mm·mrad [22, 24] to

keep the beam losses at high energy sections of the linacs below commonly imposed 1 W/m limit. Previous experiments on heavy multi-charged ion production demonstrated that gasdynamic ion source is able to produce ion beams with record beam current density and moderate ion charge. The average electron energy in plasma of ECR discharge with quasi-gasdynamic confinement sustained by gyrotron radiation varies from 50 to 300 eV and it is optimal for efficient hydrogen ionization. Due to this coincidence it was decided to test the gasdynamic ECR source performance for proton and deuteron beams formation. In previous papers [25, 26] it was demonstrated that proton beams with current of hundreds of mA could be produced. The latest results are presented below.

A single-aperture extraction system was used for beam formation in the presented experiments. As only two fixed puller holes were available (i.e. 10 and 22 mm in diameter), the optimization of extraction electrode configuration was done varying the gap between the electrodes The biggest hole diameter in plasma electrode was 10 mm. In this case the optimal gap between electrodes for 10 mm plasma electrode aperture appeared to be 6 mm, while the puller hole diameter was 22 mm. The Faraday cup and puller currents are shown in Fig. 6(a). The total beam current remains relatively stable at the level of 450 mA through 70% of the microwave pulse. Accelerating voltage of 41.5 kV was used. Transversal emittance diagram is presented in Fig. 6(b), showing an RMS value of 0.07 π•mm•mrad.

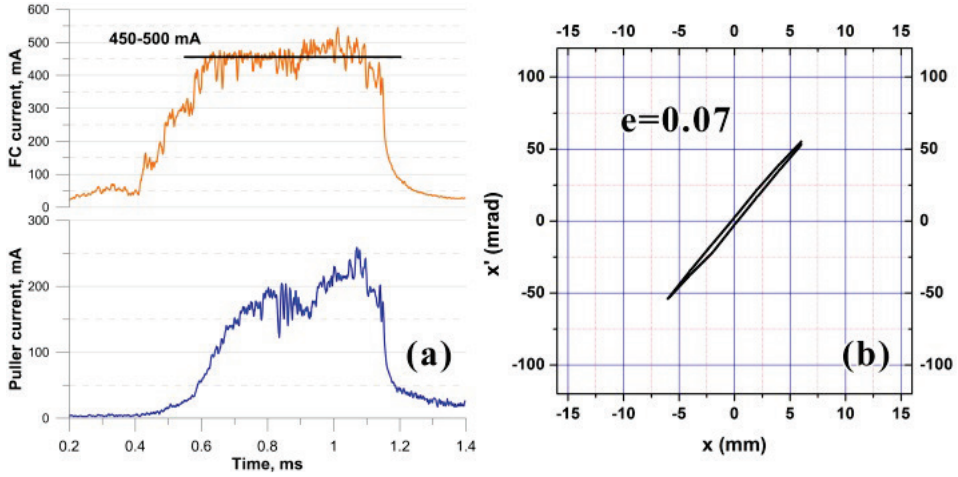

Figure 6. Hydrogen, 10 mm plasma electrode hole (a) Faraday cup and puller currents, (b) RMS emittance diagram.

The experiments with deuterium were performed under similar conditions. Source settings were adjusted slightly from the optimal ones for proton beam to maximize the total current. It was observed that the total beam current rapidly reached a value of 400 mA, then slowly increased to 500 mA and remain there till the end of the microwave pulse. Accelerating voltage of 42 kV was used. Transversal emittance had the same RMS value of 0.07 π·mm·mrad.

The presented results demonstrate the prospects of the high current gasdynamic ECR source for light ion beams production. The maximum RMS brightness of extracted beam reached 100 A/(π·mm·mrad)^2. The proton (deuteron) fraction in extracted beams was about 94 % as it was shown in [25].

The extracted beam current could be further enhanced by moving the plasma electrode closer to the magnetic mirror and scaling the extraction voltage and geometry appropriately. According to simulations, the extracted current may eventually exceed 1 A while maintaining the low emittance. Such result would outperform the conventional ECRISs by a great margin.

7. CONTINUOUS WAVE OPERATIONAL "GISMO" EXPERIMENTAL FACILITY

The main part of previous experiments was carried out in a pulsed operation mode. Preliminary studies of plasma parameters were performed using a CW source with 24 GHz/5 kW gyrotron heating [27]. Obtained experimental results have demonstrated that all gasdynamic source advantages could be realized in CW operation. To continue development of a CW gasdynamic ion source a new experimental facility named GISMO (Gasdynamic Ion Source for Multipurpose Operation) is under construction at the IAP RAS. Future facility has been named GISMO (Gasdynamic Ion Source for Multipurpose Operation). This

facility is aimed to produce continuous high-current (>200 mA) ion beams with low emittance (<0.2 π·mm·mrad). The scheme of the future experimental facility is show in Fig. 7. The key elements of the setup are 28 GHz/10 kW and 37.5 GHz/20 kW CW gyrotrons manufactured by Gycom [28]. These microwave generators are equipped with power supplies suitable for CW or pulsed operation. A fully permanent magnet magnetic trap is to be used for plasma confinement. Magnetic field configuration was designed to be similar to a simple mirror trap close to the system axis with field strength at magnetic mirrors of 1.5 T and mirror ratio close to 6. Distance between magnetic mirrors is about 12 cm. For ion beam extraction it is planned to use 3 or 4-electrode system with maximum acceleration voltage up to 100 kV. Such extraction requires development of an appropriate high-voltage insulation of the discharge chamber from other parts. In this regard, one of the key elements of the installation is the DC-break of the microwave transmission line. It was proposed to implement a quasioptical system shown in Fig. 7. Plasma chamber is 30 cm in length and 4 cm in diameter. It is equipped with water cooling along whole surface from the coupling system to the flange.

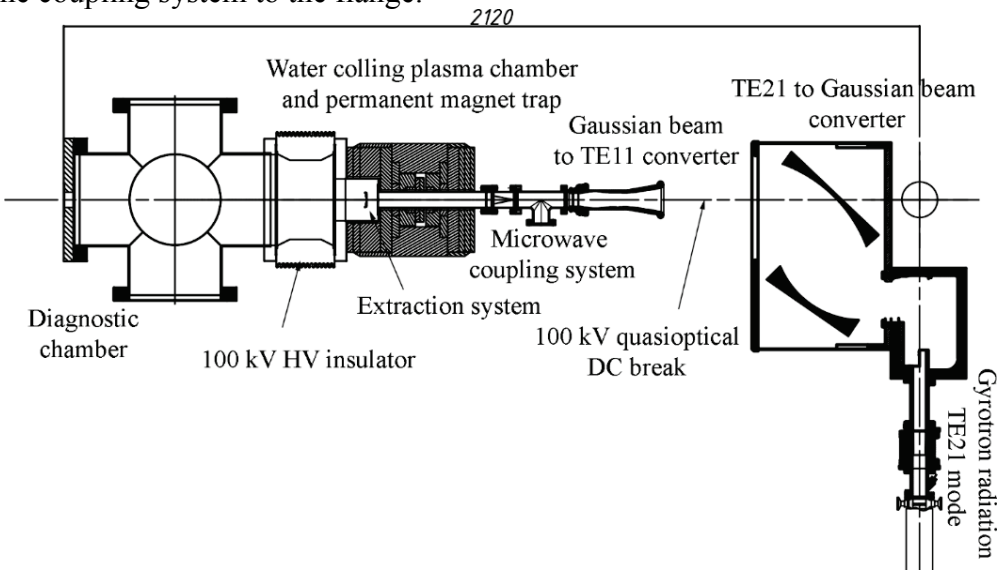

Figure 7. Scheme of the GISMO 28/37 CW high current ion source.

First results at GISMO facility would be published at the end of the year 2018.

8. CONCLUSIONS

The presented results demonstrate the main prospects of the gasdynamic ECRIS. This type of ECRIS has already demonstrated its benefits for light ion beam production. Further studies could significantly increase its performance in multi-charged beam formation. One of the most promising new ion sources which may demonstrate all capabilities of gasdynamic confinement is the SEISM, 60 GHz ECRIS at LPSC, Grenoble. The Grenoble facility has a number of advantages in comparison with SMIS 37. The first is a high repetition rate (up to 2 Hz) which allows better control of plasma parameters due to satisfactory wall conditioning. The second is the cusp magnetic field of high intensity (up to 7 T) with closed ECR surface. It is the first ion source which can operate effectively in gasdynamic mode having a closed-ECR field, which is of great importance for trapping of energetic electrons. Therefore, interesting results are foreseen from SEISM source, as it may be the first ECRIS able to operate in-between of gasdynamic and traditional collision-less confinement, thus producing high currents and charges.

Acknowledgments

The work is being realized in frames of realization of Federal targeted program R&D in Priority Fields of the S&T Complex of Russia (2014-2020) contract #14.604.21.0195 (unique identification number RFMEFI60417X0195).

References

1. Golubev S.V., Razin S.V., Sidorov A.V., Skalyga V.A., Vodopyanov A.V., Zorin V.G., Rev. Sci. Instrum., 2004, **75**, N 5, 1675.
2. Golubev S.V., Izotov I.V., Razin S.V., Skalyga V.A., Vodopyanov A.V., Zorin V.G., Fusion Sci. Technol., 2005, **47,** N 1T, 345.
3. Sidorov A., Izotov I., Razin S., Skalyga V., Zorin V., Balabaev A., Kondrashev S., Bokhanov A., Rev. Sci. Instrum., 2006, **77**, N 3, 03A341-1.
4. Skalyga V., Zorin V., Izotov I., Razin S., Sidorov A., Bohanov A., Plasma Sources Sci. Technol., 2006, **15**, 727.
5. Golubev S., Izotov I., Razin S., Sidorov A., Skalyga V., Vodopyanov A., Zorin V., Bokhanov A., Nuclear Instruments and Methods in Physics Research Section B, 2007, **256**, 537.
6. Marie-Jeanne M. et al., "Status of the SEISM experiment", Proc. 20th Int. Workshop on Electron Cyclotron Resonance Ion Sources ECRIS, 2012, Sydney, Australia, 111.
7. Lamy T. et al., Proc. 13th Int. Conf. on Heavy Ion Accelerator Technology. P. THM2I01.
8. Geller R. Electron cyclotron resonance ion sources and ECR plasmas. Institute of Physics. Bristol. 1996.
9. Dorf M.A., Zorin V.G., Sidorov A.V., Bokhanov A.F., Izotov I.V., Razin S.V., Skalyga V.A., Nuclear Instruments and Methods in Physics Research Section A, 2014, **733**, 107.
10. Golubev S.V. et al., Rev. Sci. Instrum., 2000, **71**, N 2, 669.
11. Vodopyanov A.V. et al., High Energy Phys. and Nucl. Phys., 2007, **31** (S1), 152.
12. Pastukhov V., Voprosy teorii plasma, 1984, **13**, 160.
13. Mirnov V.V., Ryutov D.D., Pisma v Zhurnal Theknicheskoi Fiziki, 1979, **5**, 678.
14. Zorin V.G., Skalyga V.A., Izotov I.V., Razin S.V., Sidorov A.V., Lamy T., Thuillier T., Trans. Fusion Sci. Technol., 2011, **59**, 140.
15. Thuillier T., Lamy T., Latrasse L., Izotov I.V., Sidorov A.V., Skalyga V.A., Zorin V.G., Marie-Jeanne M., Rev. Sci. Instrum., 2008, **79**, 02A314.
16. Izotov I.V., Sidorov A.V., Skalyga V.A., Zorin V.G., Lamy T., Latrasse L., Thuillier T., IEEE Trans. Plasma Sci., 2008, **36**, 1494.
17. Skalyga V., Izotov I., Zorin V., Sidorov A., Physics of Plasmas, 2012, **19**, 023509.
18. Skalyga V., Izotov I., Razin S., Sidorov A., Zorin V. Proc. 8th Int. Workshop «Strong microwaves and terahertz waves: sources and applications». Nizhny Novgorod − St. Petersburg, Russia, July 9-16, 2011, p. 200.
19. Maunoury L., Adoui L., Grandin J.P., Noury F., Huber B.A., Lamour E., Prigent C., Rozet J.P., Vernhet D., Leherissier P., Pacquet J.Y., Rev. Sci. Instrum., 2008, **79**, 02A313.
20. Izotov I.V., Skalyga V.A., Zorin V. G., Rev. Sci. Instrum., 2012, **83**, 02A342.
21. beta-beam.web.cern.ch
22. Gammino S. et al., LINAC2010, Tsukuba, Japan, THP116, (2010). http://www.JACoW.org
23. Lindroos M. et al., Nucl. Instrum. Methods B, 2011, **269**, 3258.
24. Gobin R. et al., Rev. Sci. Instrum., 2012, **83**, 02A345.
25. Skalyga V., Izotov I., Razin S., Sidorov A., Golubev S., Kalvas T., Koivisto H., Tarvainen O., Rev. Sci. Instrum., 2014, **85**, N 2, 02A702-1.
26. Skalyga V., Izotov I., Sidorov A., Razin S., Zorin V., Tarvainen O., Koivisto H., Kalvas T., JINST, 2012, **7**, P10010.
27. Skalyga V., Izotov I., Golubev S., Vodopyanov A., Tarvainen O., Rev. Sci. Instrum., 2016, **87**, N 2, 02A715.
28. www.gycom.ru

CONTROLLABLE LARGE-SCALE *N*-GRAPHENE SYNTHESIS: *IN-SITU* PLASMA-BASED METHOD

F. M. Dias, N. Bundaleska, J. Henriques, M. Abrashev[1], A. M. Botelho do Rego[2], A. M. Ferraria[2], A. Almeida[3], E. Valcheva[1], B. Arnaudov[1], K. K. Upadhyay[4], M. F. Montemor[4], E. Tatarova

Instituto de Plasmas e Fusão Nuclear, Instituto Superior Técnico, Universidade de Lisboa, Lisboa-1049, Portugal
[1]Faculty of Physics, Sofia University, 1164 Sofia, Bulgaria
[2]CQFM-Centro de Química-Física Molecular and IN and IBB-Institute for Bioengineering and Biosciences, Instituto Superior Técnico, Universidade de Lisboa, 1049-001 Lisboa, Portugal
[3]Faculty Centre of Physics and Engineering of Advanced Materiais, Instituto Superior Técnico, Universidade de Lisboa, 1049-001 Lisboa, Portugal
[4]Centro de Química Estrutural (CQE), Departamento de Engenharia Química, Instituto Superior Técnico, Universidade de Lisboa, 1049-001 Lisboa, Portugal

Abstract. A direct synthesis of N-graphene, *i.e.*, nitrogen doped graphene, was achieved in a controllable manner using a microwave discharge at atmospheric pressure conditions. Synthesis was obtained in a single-step procedure using ethanol and ammonia, respectively as carbon and nitrogen precursors. N-graphene having a ~0.4% doping level of nitrogen was achieved by adjusting the pertinent external parameters that control plasma characteristics, namely, precursors and background gas fluxes, plasma reactor design, and microwave power. In addition, infrared and ultraviolet irradiation of free-standing sheets in the post-plasma zone proved to be an effective tool to tailor the sp^2 %, the N-doping type, and oxygen functionalities. X-ray photoelectron spectroscopy revealed the relative extension of the graphene sheets π-system and the type of nitrogen chemical functions present in the lattice structure. Scanning electron microscopy, transmission electron microscopy, and Raman Spectroscopy were applied to determine morphological and structural characteristics of the sheets. Optical emission and FT-IR spectroscopy were applied for the characterization of the high-energy density plasma environment and of the outlet gas stream. Electrical conductivity and electrochemical measurements were also performed for material characterization keeping in mind its application in supercapacitors.

1. INTRODUCTION

The unique properties of graphene, such as high thermal conductivity and electron mobility, extremely high surface area, mechanical stability, *etc.*, are now well-understood and recognized through extensive research in the past years. Its promising applicability includes areas such as electronics, medicine, light processing, environmental remediation, energy production and storage technologies [1−3]. However, practical applications of pristine graphene in semiconductor and energy storage technologies are limited to some extent due to the lack of band gap in its electronic structure. In order to practically implement graphene, it must be functionalized and electrochemically modified. Further theoretical and experimental research demonstrated that graphene properties can be drastical and permanently altered by molecular and atomic doping, leading to new application opportunities [4−8]. It is known that chemical doping with foreign atoms is an effective way to modify and enhance the intrinsic properties of host materials. Among various doping agents, nitrogen is a promising candidate because it has an atomic radius comparable to that of carbon and it contains five valence electrons available to form strong covalent bonds. Depending on the bonding configuration of the nitrogen in the lattice, graphene hybridization state can be changed from sp^2 to sp^3 [8].

Numerous methods for the synthesis of graphene and for N-doping graphene, such as chemical vapour deposition (CVD), bottom-up syntheses, wet chemical methods, plasma methods, etc., have already been

developed [7−9]. The reported techniques can be categorized into *in-situ* and post-treatment approaches. *In-situ* approaches are distinguished by simultaneous graphene synthesis and N-doping, include CVD, ball milling, and bottom-up syntheses. The post-treatment is characterized by modification of previously fabricated graphene through nitrogen doping. Post-treatment methods involve wet chemical methods, thermal annealing of graphene oxides (GO) with heteroatom precursors and plasma based approaches [7].

Despite great progresses made so far, it still remains a challenge to precisely control the doping process and to provide sustainability at high processing temperature. In this respect, the strategy to synthesize N-doped graphene (N-G) through plasma treatment presents significant advantages. To this end, plasma techniques are applied for both the initial synthesis of graphene and for its post-processing [8, 9]. The reactive plasma medium can provide fixation of different chemical species to the graphene structure, thus making the plasma an effective doping tool. Additionally, atmospheric, non-thermal plasmas favor low-temperature material processing and do not require sophisticated and expensive vacuum equipment. Moreover, plasmas are associated with selectivity in terms of creating definite structural defects and to control doping. A direct plasma-based approach for N-G synthesis may involve arc discharge between carbon electrodes in the presence of a nitrogen-containing precursor. Successful synthesis of N-doped multi-layered graphene by the DC arc-discharge method in an atmosphere of ammonia was reported in [10]. In this single step method a 1% N-doping was achieved. However, the majority of the plasma induced N-doping relies on post-treatment approaches, commonly treating graphene by N_2 or ammonia plasma [11−17]. Doping levels in the 5−15 % range at the surface of graphene and Highly Oriented Pyrolytic Graphite (HOPG) was achieved by low pressure nitrogen RF plasma treatment in [11]. Similarly, a microwave N_2-Ar plasma reactor was used for N-doping of free-standing graphene, with maximum level of 5.6% [12]. Also nitrogen plasmas were applied for doping nanoplatelets and then used as a catalyst support for platinum nanoparticles for oxygen reduction reactions in proton exchange membrane fuel cells [13]. In addition, N-G based supercapacitors with high capacitance (~280 F/g), excellent life number of cycles (> 200,000), high power capability, and compatible with flexible substrates were developed in [14]. The N-G was produced by nitrogen plasma treatment and had a nitrogen content of 1.68–2.51%. Applications of N-G in direct electrochemistry of glucose oxidase and glucose biosensing were studied in [15]. Gas-phase controllable doping of graphene by ammonia plasma exposure, with a maximum doping level of 1.5×10^{13} cm^{-2}, was reported in [16]. Having in mind the carbon atom concentration in graphene layers of about 3.8×10^{15} cm^{-2} (graphene has hexagonal structure with the lattice parameter of 142 pm), the relative concentration of N reported in [16] is actually 0.4 %.

Generally, plasma based post-treatment seems to provide higher level of N-doping as compared to direct methods. However, they have some major drawbacks. Firstly, the fact of being a two-step process implies it is slower, more complex and expensive, and commonly it is performed at low pressure. Secondly, plasma post-treatment affects only the surface of the sample which significantly reduces its effectiveness. So, the sample needs to be extremely thin in order to provide uniform distribution of dopants. Therefore, the amount of treated material per one charge is very small. The advantage of an *in-situ* method for N-G production is that it involves a single-step fabrication of uniformly doped material. Consequently, it has a potential to significantly increase the production yield with respect to the post-treatment methods.

In the present work, *in-situ* direct synthesis of free-standing N-G flakes was achieved in a single step process in a microwave plasma working at atmospheric pressure conditions. To improve the sp^2/sp^3 carbon ratio and to decrease the oxygen impurities of the produced N-G, flakes were irradiated by infrared (IR) and ultraviolet (UV) radiation. The so obtained material was characterized using Raman spectroscopy, scanning electron microscopy (SEM), transmission electron microscopy (TEM), and X-ray photoelectron spectroscopy (XPS). Keeping in mind the application of N-graphene in supercapacitors, electrical and electrochemical characterizations were also performed. The plasma medium was analyzed by optical emission spectroscopy (OES) and exhaust gases were detected by Fourier-Transform Infrared spectroscopy (FT-IR).

2. EXPERIMENTAL SETUP AND SYNTHESIS METHOD

The discharge is sustained at atmospheric pressure conditions by a 2.45 GHz surface wave, whose microwave typical components are shown in the sketch depicted in Fig. 1: a 2 kW-generator, a circulator with water-load, a 3-stub tuner, a waveguide-surfatron (launcher) [17], and a short-circuit. The discharge takes place inside a tapered diameter, fused silica tube (internal/external diameters: *id/od* = 15−43/18−46 mm), inserted vertically and perpendicularly to the waveguide wider wall. A thinner fused silica tube (*id/od* = 4/6 mm) is used to introduce precursors in vapor phase, currently a 4*wt.* % solution of ammonia in ethanol, into the discharge zone. Vaporization is achieved by bubbling argon, at a flow rate $Q_{Ar+Et/Am}$ = 50–120 sccm, through ammonia/ethanol inside a thermostatically controlled tank. Argon, at a flow rate Q_{Ar} = 1200 sccm, is additionally injected between the two tubes mentioned above. Argon flow rates are controlled by mass flow controllers.

For an increased control over the synthesis process, namely to improve the structural quality of the assembled flowing nanostructures, the gas-phase zone was irradiated by IR radiation. IR lamps, located immediately after the end of the plasma zone (15−30 cm downstream from the launcher), were powered by an adjustable supply, and the wall temperature of the discharge vessel was monitored by a thermal imaging camera (FLIR E60). The N-G flakes, before being collected mainly inside a glass container by a cyclone system, have been irradiated by UV lamps (4 W; 300–400 nm) to further modify their structural properties.

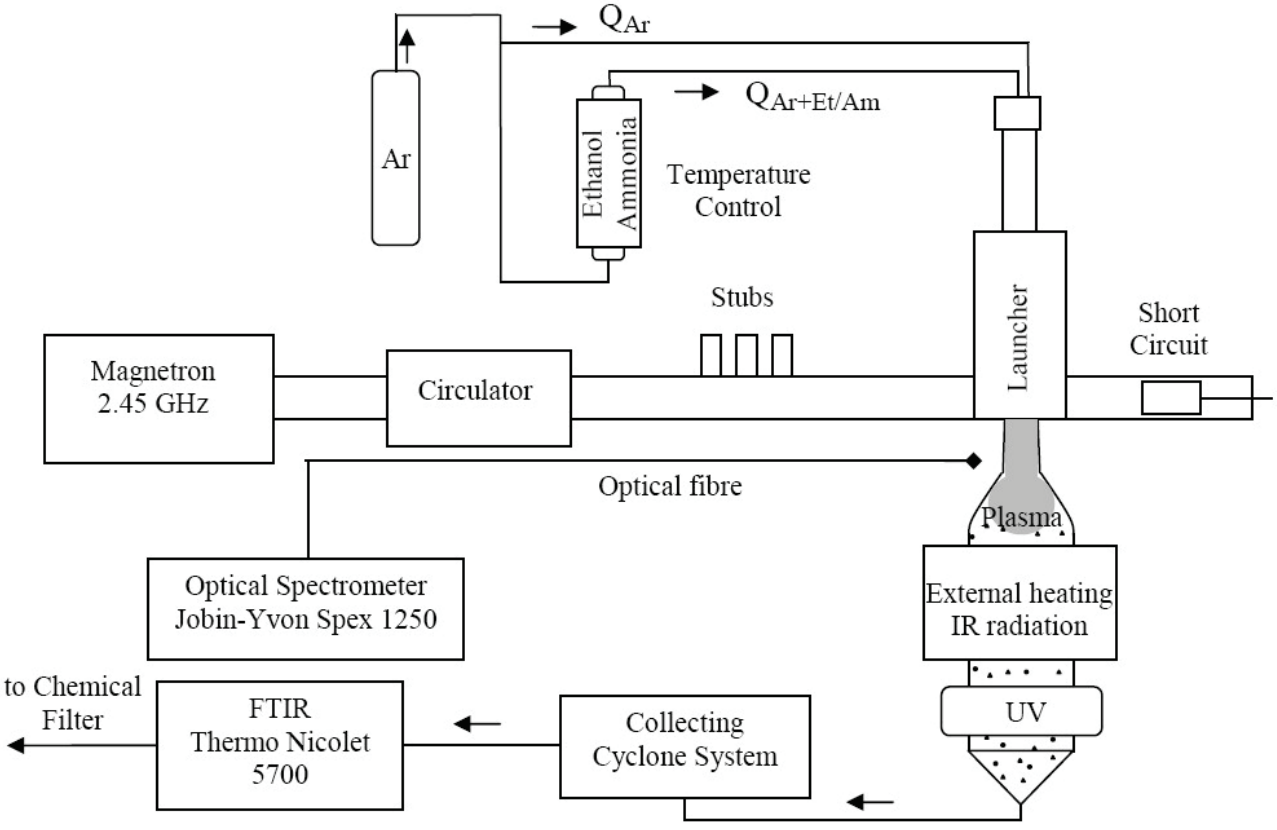

Figure 1. Sketch of the experimental setup.

The experimental setup comprised two main *in-situ* diagnostics: i) the output gas stream was directed to a FT-IR spectrometer (Thermo Nicolet 5700) and absorption spectra were analyzed in the 1000–4000 cm^{-1} range, which enabled the identification of exhaust gases; ii) the plasma emission spectra in the 200–900 nm range were analyzed by OES (Jobin-Yvon Spex 1250 spectrometer with 1200/2400 mm^{-1} gratings and a CCD camera) to monitor in real time the main "building units", *i.e.*, carbon and nitrogen species.

Before being launched into the atmosphere, exhaust gases had to pass by a water-trap and a NaOH bath intended to capture, respectively, remaining N-G flakes and HCN.

3. RESULTS

3.1. Plasma and output gas stream. The emission spectrum of Ar/ethanol/ammonia plasma was recorded in the 200–900 nm range. As a result of the decomposition of the ethanol/ammonia, new molecular and atomic species could be detected, such as CN, by the violet system ($B^2\Sigma^+ \rightarrow X^2\Sigma^+$) between 350–420 nm, C_2, by the Swan system ($A^3\Pi_g \rightarrow X'^3\Pi_u$) between 450–570 nm, hydrogen, *e.g.* the Balmer-alpha line Hα (6563 Å), and several Ar lines.

The plasma presents a typical blue-green color due to C_2 emission generated by the radiative decay of the $C_2^*(A^3\Pi_g)$ state. Due to the low energy threshold (E_{ext} = 2.4 eV), ground state C_2 molecules can easily be excited to this level either by electron impact [18]:

$$C_2(X) + e \rightarrow C_2^*(A^3\Pi_g) + e, \quad (1)$$

or by three body recombination processes involving carbon (C) and argon (Ar) atoms:

$$C + C + Ar \rightarrow C_2^*(A^3\Pi_g) + Ar. \quad (2)$$

CN species are formed in a three-body recombination reaction:

$$C + N + Ar \rightarrow CN^*(B^2\Sigma) + Ar. \quad (3)$$

Intensities of the Q_1 branch of the OH band were used to estimate the rotational temperature, which at atmospheric pressure conditions is usually assumed to be equal to the gas temperature. The rotational temperature at an axial position z = 2.5 cm from the launcher, estimated using the classical Boltzmann plot method (spectrum in the 307.5–315 nm range; Q_{Ar} = 1200 sccm, $Q_{Ar+Et/Am}$ = 100 sccm, P = 2 kW) was T ≈ 3790 K. It should be noted that the fused silica tubes of the discharge vessel became readily devitrified but without a clear indication of softening, meaning that maximum wall temperatures are in the 1400–1940 K range, which we think corroborates the gas temperature value presented above. Thermographic results suggest temperatures slightly below 1000 K close to the exit of the inner fused silica tube, but we consider such values unreliable because radiation had to cross the cooler, semi-transparent outer tube.

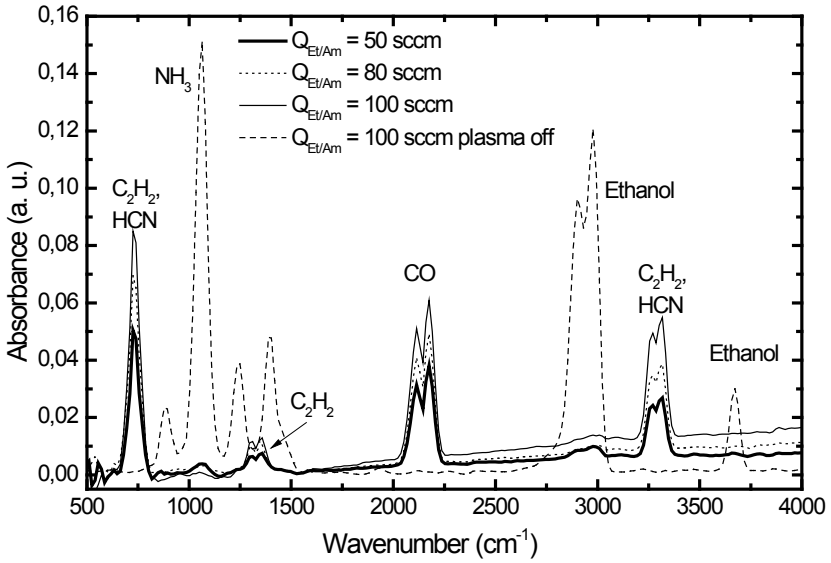

Figure 2. FT-IR analysis of the argon/ethanol/ammonia outlet gas stream with the plasma turned off and on for different flow rate of argon bubbling through the ethanol/ammonia mixture.

FT-IR analysis of the argon/ethanol/ammonia outlet gas stream has been performed when the plasma was turned off and on (see Fig. 2). The absorption spectra detected without plasma showed spectral lines at around 2900 and 3700 cm^{-1}, which correspond to ethanol molecules and lines around 1000 cm^{-1}, which are characteristic for ammonia. When the plasma is ignited, these lines are no longer present in the spectrum, which demonstrates that the ethanol and ammonia molecules were decomposed in the argon plasma environment. Instead, the absorption peak of CO at around 2170 cm^{-1} and of C_2H_2 at around 720, 1350 and 3300 cm^{-1} are detected. Note that HCN may also contribute for absorptions at around 720 and

3300 cm^{-1} (a precise calibration is required). As can be seen in Fig. 2, an increased flow of precursors leads to an increase of the CO and C_2H_2/HCN concentrations in the exhaust plasma gas.

3.2. Material characterization. The results shown in the continuation were obtained under the following discharge conditions: Q_{Ar} = 1200 sccm, $Q_{Ar+Et/Am}$ = 120 sccm, and P = 2 kW, which lead to a N-G yield of 1.3 $mg.min^{-1}$.

SEM characterization of samples, deposited on a double-sided carbon tape mounted on an aluminum stub, has been performed using a JEOL, JSM-7001F field emission gun scanning electron microscope operating in secondary electron imaging mode (SEI) using a 15kV accelerating voltage. For TEM characterization, a Hitachi H8100 TEM, operating at a 200 kV accelerating voltage, was used. N-G flakes were placed directly onto the TEM copper grid. SEM images of the samples presented the usual curved, tiny structure with the paper-like look characteristic of graphene. SEM and TEM images did not show a noticeable change of the morphology of samples after irradiation by IR and IR + UV.

Following recent theoretical and experimental findings [19−24], we used Raman spectroscopy to analyze structural parameters of N-G samples. Samples were freely standing over a glass substrate and the Raman spectra from different regions on the substrate were obtained using a LabRAM HR Visible (Horiba Jobin-Yvon) Raman spectrometer with 1 cm^{-1} spectral resolution and a 633 nm He-Ne laser excitation with laser spot size of 2 μm. Measurements were performed at a laser power of P_l = 0.054 mW to avoid overheating. The resulting spectra are presented in Fig. 3 (A−C).

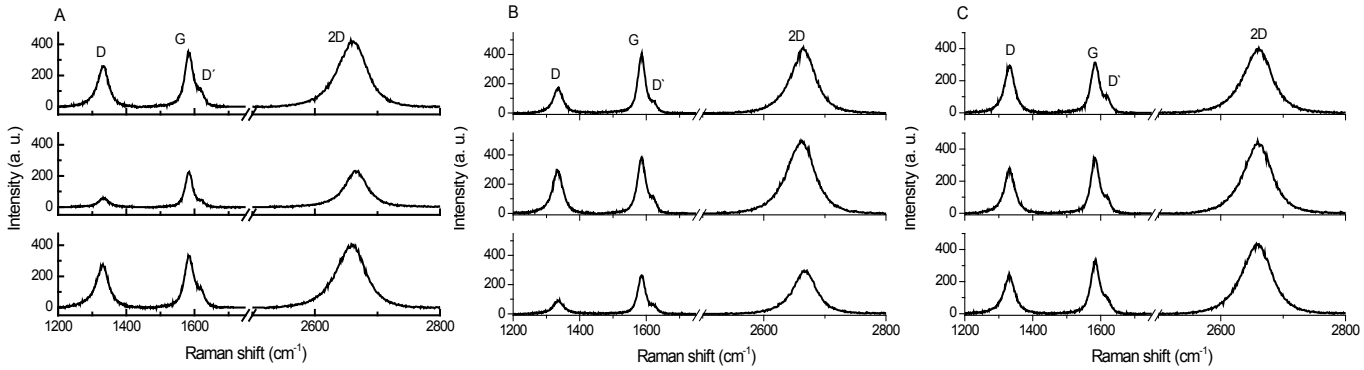

Figure 3. Raman spectra of N-G from three randomly chosen positions in the samples: (A) unirradiated sample; (B) submitted to IR irradiation; (C) submitted to IR and UV irradiation.

As can be seen in the above figures, spectra present three main peaks, assigned to D, G, and 2D bands, respectively at about ~1332, 1583, and 2658 cm^{-1}. In the case of the unirradiated sample (Fig. 3A), the D/G peak intensity ratio for three positions varies from 0.26 to 0.83, while 2D/G ratio varies from 1 to 1.2, which suggests that the sample was not homogeneously doped. A similar result is observed in Fig. 3B for samples IR-irradiated. Conversely, in the case of simultaneous IR and UV irradiation (Fig. 3C), the D/G ratio increased (~ 0.9) and remained almost constant along the sample.

N-G flakes were characterized by X-ray photoelectron spectroscopy using a KRATOS XSAM800 spectrometer with incident X-radiation from a Mg Kα source (1253.6 eV). Operating conditions and spectra acquisition parameters are detailed elsewhere [25]. Samples were mounted on the XPS holder with a double face tape. No silicon was detected discarding any interference of the tape spectrum. No charge correction was needed, since the C 1s main peak, detected at 284.4 ± 0.1 eV, is typical of aromatic C-C or C-H in graphene [26]. The sensitivity factors (from Vision 2 library) used for quantification purposes were 0.318 for C 1s, 0.736 for O 1s and 0.505 for N 1s.

Ex-situ XPS analysis was used to determine the elemental composition of synthesized samples, and to identify the chemical bonds and the relative extension of the delocalized system. The survey XPS spectrum presented in Fig. 4 exhibits peaks at about 284.5, 400, and 533 eV, which can be assigned to the C1s, N1s and O1s lines, respectively. The C KLL Auger region is also present.

Nitrogen is present in all the samples. N 1s peaks were analyzed in detail by fitting three contributions centered at 398.7 ± 0.3 eV, 400.2 ± 0.3 and 402.3 ± 0.1 eV attributed, respectively, to pyridinic, pyrrolic and graphitic nitrogen [26]. Results are shown in Table 1, where we can see that IR + UV irradiation increases the relative amount of pyridinic and pyrrolic N-bonding, and, conversely, decreases graphitic one.

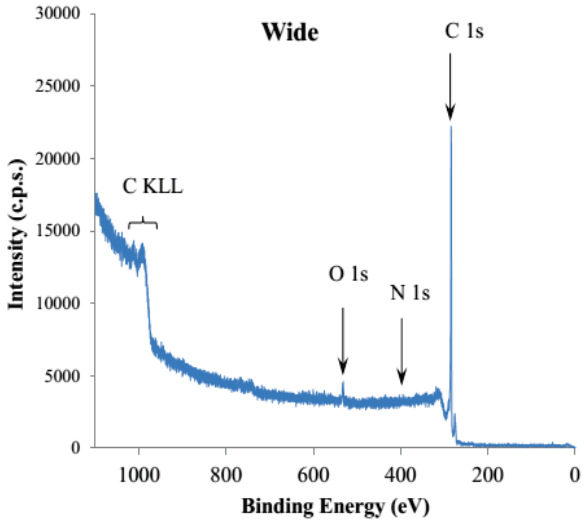

Figure 4. Survey XPS spectrum.

Similar deconvolution processes were applied to C 1s peaks, namely to quantify the relative amount of sp^2 carbon atoms (main peak at 284.4 ± 0.1 eV in highly delocalized C-C bonds) and energy losses associated to π-π* excitations (287–295 eV, overlapping much less intense peaks assigned to carbon-oxygen bonds, *e.g.* epoxide, carbonyl, carboxylate). Overall results of the composition of the analyzed samples are presented in Table 2, where we can see that simultaneous IR and UV irradiation leads to an increased doping level (N/C = 0.39%), a decreased level of oxidation (O/C = 1.5%), and an increased percentage of sp^2 carbon (70.9%). We believe that the observed decrease in the amount of oxygen is due to UV irradiation at 300–400 nm.

Table 1. Atomic concentrations (%)

		Unirradiated	IR	IR+UV
C		98.0	97.7	98.1
O		1.8	2.1	1.5
N	Pyridinic	0.10	0.11	0.14
	Pyrrolic	0.10	0.07	0.21
	Graphitic	0.13	0.04	0.04

Table 2. Atomic ratios

	Unirradiated	IR	IR+UV
N/C	0.0033	0.0023	**0.0039**
O/C	0.018	0.021	**0.015**
N/O	0.19	0.11	**0.25**
sp^2 (%)	69.9	70.4	**70.9**

The electrical conductivity of N-G was measured applying the Van der Pauw method [27] at room temperature to disc-shaped pellets of 8 mm in diameter. Although the same maximum pressure (27 MPa) has been applied to all discs, the resulting thicknesses were not the same (1.2–3.2 mm) due to differences in the amount of flakes. Results are presented in Table 3, where we can see that there is a strong correlation between conductivity and density values. Nevertheless, differences in conductivity also arise from the different composition of pellets, namely the percentage of pyridinic and pyrrolic nitrogen as well as the oxygen content, which lead to a decrease of conductivity. We would like to emphasize that electrical conductivity values obtained in the current work are much higher than the one obtained for graphene produced by chemical methods, which demonstrates the advantages of the plasma synthesis method [28].

Table 3. Longitudinal, electrical characteristics

Samples	Density (g/cm^3)	ρ (Ω.cm)	Conductivity (S.m^{-1})
Unirradiated	1.25	0.032	3125
IR	1.14	0.06	1666
IR+UV	1.2	0.04	2500

N-G samples submitted to IR and UV irradiation were tested as electrodes in actual supercapacitor applications by performing cyclic voltammetry (CV), galvanostatic charge-discharge (GCD) and Electrochemical Impedance Spectroscopy (EIS) in 1 M H_2SO_4 electrolyte. Measurements were performed in a three-electrode electrochemical cell using Pt and Standard Calomel Electrode (SCE) as counter and reference electrodes, respectively.

The CV curves, obtained in the potential window of 0–0.8 V *vs.* SCE at varying scan rates, evidence an almost perfect rectangular behavior, as expected for a material storing charge thanks to an electric double layer (EDLC) mechanism. The nearly rectangular voltammogram also indicates the absence of resistive features, meaning that N-G possesses very high electronic conductivity. Anodic and cathodic currents increase as the scan rate was increased, which accounts for the occurrence of highly reversible electrochemical processes at the electrode/electrolyte interface, a behavior that was perfectly retained even at the highest scan rate (400 mVs^{-1}). Such rectangular features and high reversibility can be attributed to the high and easily accessible active surface area of the N-G.

GCD measurements were also performed by applying current densities in the 0.1–1 Ag^{-1} range. A linear charge and discharge behavior at all current densities confirms the EDLC mechanism of charge storage. It is worth to mention that curves evidence a coulombic efficiency of 100% and do not show any internal resistance drop, which confirms that N-G possesses very good electronic conducting properties. The specific (gravimetric) capacitance, C_s, was calculated as:

$$C_s = (I\,\Delta t)/\Delta V \tag{4}$$

where I is the current density (Ag^{-1}), Δt is discharge time (s), and ΔV is working potential window. A specific capacitance of 8.87 Fg^{-1} was obtained at current density of 0.1 Ag^{-1}, and capacitance was ~100% retained while the applied current was increased up to 1 Ag^{-1}. Despite the fact of having low specific capacitance, such materials can be used to formulate composites to enhance the electronic conductivity of redox based metal compounds, which generally possess high resistive nature and require improvement in the overall performance for supercapacitor/energy storage devices [29]. The specific capacitance of this material can be further increased by optimizing pore size distribution and by increasing the nitrogen doping level, which is an ongoing work.

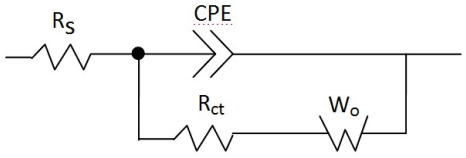

Figure 5. Equivalent circuit diagram: series resistance, R_s, charge transfer resistance, R_{ct}, constant phase element, *CPE*, Warburg element, W_o.

EIS was performed at open circuit potential to study the resistive nature of the synthesized N-G. From the obtained spectra, the parameters of the suggested equivalent circuit (see Fig. 5) could be fitted: R_s = 1.49 Ω cm^2; R_{ct} = 0.045 Ω cm^2; *CPE* = 0.98 n; W_o = 0.386 Ω cm^2 @ n = 0.51. We wish to emphasize the very low values of the charge transfer and Warbug resistances, as well as the high value of the constant phase element, which indicates an almost ideal supercapacitor response.

4. CONCLUSIONS

The microwave plasma-based method was applied for direct synthesis of free-standing N-graphene sheets at atmospheric pressure conditions. A nitrogen doping level of 0.4% has been obtained in a single step procedure using ethanol and ammonia, respectively as carbon and nitrogen precursors. The method is fast, highly cost-efficient, and does not depend on catalysts, vacuum systems and multistep, cumbersome procedures. Results show that applying infrared and ultraviolet irradiation to the flow of free-standing sheets in the post-plasma zone leads to changes in the percentage of sp^2 %, N-doping type, and oxygen functionalities. A detailed study on the nature of these changes is under way. The main advantage of the approach presented here is the control over the energy and material fluxes towards growing nanostructures via proper reactor design and tailoring of the plasma environment in a synergistic way.

Electrodes assembled with the produced N-graphene showed good electrochemical response with negligible interfacial resistance, even considering that the percentage of N-doping was low, which is a very interesting result for supercapacitor applications.

By optimizing the microwave plasma reactor performance, along with a detailed modelling of the plasma environment, a well controlled synthesis of carbon/nitrogen atom lattices can be generated. Further investigations are underway in these directions, including the use of other carbon/nitrogen precursors such as methane, air, pyridine, *etc*., to achieve further advancements in this technique and to increase the yield along with a reduction of the production cost, namely by scaling-up the plasma reactor. Focus will be kept on achieving an optimum balance between yield and level of doping *vs*. bond configuration.

The method is highly scalable and versatile: i) precursors can be used in liquid, gas, and solid state; ii) different graphene derivatives can be synthesized using the same plasma reactor.

Acknowledgments

This work was performed under the framework of the Plasma Enabled and Graphene Allowed Synthesis of Unique nano-Structures, funded by the European Union's Horizon research and innovation programme under grant agreement No 766894, and was partially supported by Fundação para a Ciência e a Tecnologia (FCT) under Project UID/FIS/50010/2013. A. M. Ferraria acknowledges FCT for the fellowship SFRH/BPD/108338/2015 and the project UID/NAN/50024/2013. N. Bundaleska acknowledges FCT for the fellowship under Project UID/FIS/50010/2013.

References

1. Novoselov K.S., Geim A.K., Morozov S.V., Jiang D., Zhang Y., Dubonos S.V., Grigorieva I.V., Firsov A.A., Science 2004, **306**, 666.
2. Ostrikov K., Cvelbar U., Murphy A.B., J. Phys. D: Appl. Phys., 2011, **44**, 174001.
3. Tatarova E., Bundaleska N., Sarrette J.Ph. and Ferreira C.M., Plasma Sources Sci. Technol., 2014, **23**, 063002.
4. Cervantes-Sodi F., Csányi G., Piscanec S., Ferrari A.C., Phys. Rev. B, 2008, **77**, 165427.
5. Calandra M., Mauri F., Phys. Rev. B, 2007, **76**, 205411.
6. Tsetseris L., Wang B., and Pantelides S.T. Phys. Rev. B, 2014, **89**, 035411.
7. Wang X., Sun G., Routh P., Kim D.-H., Huangb W. and Chen P. Chem. Soc. Rev., 2014, **43**,7067.
8. Dey A., Chroneos A., Braithwaite N.St.J., Gandhiraman R.P., and Krishnamurthy S., Appl. Phys. Rev., 2016, **3**, 021301.
9. Lu, Y., Huang, Y., Zhang, M., Chen, Y., J. Nanosci. Nanotec., 2014, **14**, 1134–1144.
10. Li, N., Wang, Z., Zhao, K., Shi, Z., Gu, Z., Xu, S., Carbon, 2010, **48**, 255–259.
11. Bertoti, I., Mohai, M., Laszlo, K., Carbon, 2015, **84**, 185–196.
12. Dias, A. *et al.*, J. Phys. D: Appl. Phys., 2016, **49**, 055307.
13. Jafri, R.I., Rajalakshmi, N., Ramaprabhu, S., J. Mater. Chem., 2010, **20**, 7114–7117.
14. Jeong, H. M. *et al.*, Nano Lett., 2011, **11**, 2472–2477.

15. Wang, Y., Shao, Y., Matson, D.W., Li, J., Lin, Y., ACS Nano, 2010, **4,** 1790–1798.
16. Lin, Y-C, Lin, C-Y, Chiu, P.-W., Appl. Phys. Let., 2010, **96**, 133110.
17. Moisan, M., Zakrzewski, Z. J Phys D: Appl. Phys., 1991, **24**, 1025.
18. Tsyganov, D. *et al.* Plasma Sources Sci. Technol., 2016, **25**, 015013.
19. Ferrari, A.C. *et al*., Phys. Rev. Lett., 2006, **97**, 187401.
20. Cancado, L. *et al.*, Appl. Phys. Lett., 2006, **88**, 163106.
21. Hao, Y. *et al.*, Small., 2010, **6**, 195–200.
22. Robinson, J. A., Nano Lett., 2009, **9**, 2873–2876.
23. Cancado, L.G. *et al*., Nano Lett., 2011, **11**, 3190–3196.
24. Zhao, L. *et al*., Science, 2011, **333**, 999–1003.
25. Carapeto, A. P., Ferraria, A. M., Botelho do Rego, A. M., Carbohydrate Polymers, 2017, **174,** 601–609.
26. Tatarova, E., *et al.*, Scientific Reports, 2017, **7**, 10175.
27. Sze, S. M., Lee, M.-K., Semiconductor Devices: Physics and Technology. New York: Wiley, 2016.
28. Choucair, M., Thordarson, P., Stride, J. A., Nature Nanotech., 2009, **4**, 30–33.
29. Li, X., Zhi, L., Chem. Soc. Rev., 2018, **47***,* 3189–216.

SURFACE-WAVE-SUSTAINED PLASMA SOURCE FOR BIOMEDICAL APPLICATIONS

T. Bogdanov, I. Tsonev[1], M. Atanasova[2], P. Marinova[3], Y. Topalova[4], Y. Todorova[4], I. Yotinov[4], E. Benova[5]

Medical Faculty, Medical University – Sofia, 1 Georgi Sofiiski Blvd., 1431 Sofia, Bulgaria
[1] Faculty of Physics, Sofia University, 5 James Bourchier Blvd., 1164 Sofia, Bulgaria
[2] Faculty of Mathematics and Informatics, Sofia University, 5 James Bourchier Blvd., 1164 Sofia, Bulgaria
[3] Faculty of Forest Industry, University of Forestry, 10 Kliment Ohridski Blvd., 1797 Sofia, Bulgaria
[4] Faculty of Biology, Sofia University, 8 Dragan Tsankov Blvd., 1164 Sofia, Bulgaria
[5] DLTIS, Sofia University, 27 Kosta Loulchev Street, 1111 Sofia, Bulgaria

Abstract. Argon plasma torch sustained by travelling electromagnetic wave excited by surfatron type wave launcher at 2.45 GHz is studied in terms of its potential use for biomedical applications. These plasma sources allows varying of the: geometrical parameters (length, diameter, cross section of the discharge tube), main plasma parameters (wave power, electron and gas temperatures, concentration of charged particles and reactive species, UV and microwave radiation), gas and gas mixture parameters (flow velocity, gas mixture ratio). The fact that we are able to vary these parameters allows us to sustain low temperature plasma torch (with gas temperature up to 30–37^{o}C) applicable for treatment of temperature sensitive materials and even leaving tissue. Investigation is focused on the dependence of the plasma torch length and gas temperature on the discharge conditions; the treated surface heating by the plasma; the reactive species in the torch. Some examples of the MW plasma torch biomedical applications are also included.

1. INTRODUCTION

Cold plasma has proven to be an innovative approach for tackling important medical and biological problems. Plasma medicine is a promising field that combines plasma physics and life sciences. Plasma medicine is defined as the application of physical plasma for medical purposes. This multidisciplinary field of science inspires researchers to develop suitable for the given medical need plasma sources [1–3]. For this purpose two main concepts of plasma devices that can vary configuration and design are most investigated: the Dielectric Barrier Discharge (DBD) and the Atmospheric Pressure Plasma Jet's (APPJ) [4–6]. They are both considered as Cold Atmospheric pressure Plasmas (CAP) sources. By applying electrical energy to a noble gas (He, Ar, N_2 or their mixtures) hot electrons are produced but the ions and molecules remain with low kinetic energy. Both concepts have a variety of designs, which follow two simple principles: are cold (< 40^{o}C) at sample contact point and are stable under atmospheric conditions. The precise mechanism of plasma interaction with different biological objects is not completely clear. It is well known that CAP produce Reactive Oxygen Species (ROS), and Reactive Nitrogen Species (RNS), which are then transferred to the cell through liquid phase reactions [7]. Other plasma components that can influence biological responses are UV radiation, electric field/current, electrons and ions. This unique combination of plasma active components provides a broad spectrum of application in life sciences. A large variety of effects is discovered, of which a few are well established [8]: 1) decontamination of a large number of microorganisms; 2) acceleration of wound healing; 3) plasma induced cancer cells apoptosis. Clear evidences, such as bacteria decontamination of microflora on skin and sterilization of live rat model wound have been reported. Cold plasma treatments seem to be very effective for

disinfection purposes eradicating even fungal pathogens. Wound healing is another area of interest, in which a lot of progress has been done. It is believed that plasma treatment influences the genetic pathways of cells thus accelerating blood vessel formation and wound healing. Studies prove the elevation of tissue generation factors after plasma treatment of wounds and show signs of reduced inflammatory processes.

Both the DBD and APPJ are well-investigated plasma sources. Various methods of investigation are proposed for plasma diagnostics. Mass spectrometry, TALIF spectroscopy, UV-VIS emission and absorption spectroscopy are part of the techniques used for diagnostics. Few atoms and molecules are of the highest interest: OH radicals and hydrogen peroxide molecules H_2O_2 because of their key role in biological processes; NO, which also plays a crucial role in a large number of cellular pathways, especially regarding wound regeneration; atomic oxygen because of the high oxidative potential. Discharges operating in pure gases (Ar, He, N_2) or mixtures react with the air to form the given molecules. Some devices operate directly in air as a working gas. Unfortunately, for both configurations contact with the treated object is in the region of the effluent after the active zone of the discharge.

In this work we are investigating a well know microwave surface-wave-sustained discharge (SWD) for potential biomedical applications. The plasma is sustained by 2.45 GHz electromagnetic wave excited by a wave launcher surfatron type in Argon at atmospheric pressure. The discharge conditions have been optimized in order to obtain a steady-state Argon plasma torch with gas temperature less than 40°C. High resolution optical emission spectroscopy is used for diagnostics of reactive molecules that can activate biological responses. Determination of the gas temperature at the treated surfaces was done by using an IR camera. Some examples of surface-wave plasma torch bio-medical applications as decontamination of microorganisms and enhancing wound healing in live mice models are shown.

2. EXPERIMENTAL

The experimental set-up is schematically presented in Fig. 1. Solid-state microwave generator at 2.45 GHz (Sairem, GMS 200 W) was connected by coaxial cable to the commercial electromagnetic surface wave resonator (Sairem, SURFATRON 80). Argon discharge was created inside a quartz tube (with real dielectric permittivity $\varepsilon_r = 3.2541$ and imaginary $\varepsilon_i = 0.0062$) with dimensions 8 mm outer diameter to 3 mm inner diameter. Working gas was argon 5.0 (purity of 99.999%) at constant mass flow 2 l/min controlled by Omega FMA-A2408 mass flow controller. The system axis was installed vertically with the gas flow from top to down (see Fig. 1).

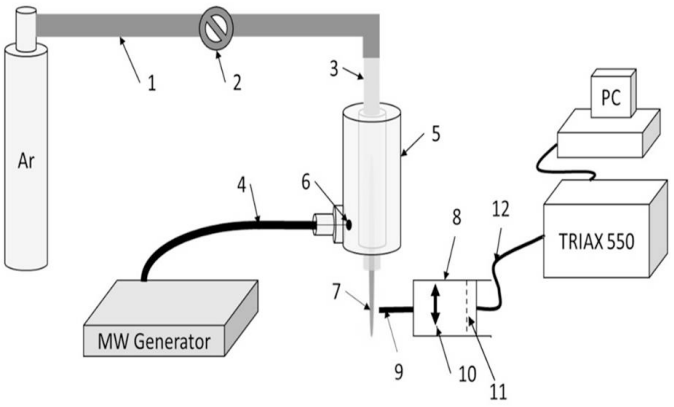

Figure 1. Scheme of the experimental set-up. 1 – gas tube; 2 – mass flow controller; 3 – quartz tube; 4 – coaxial cable; 5 – surfatron; 6 – antenna; 7 – plasma torch; 8 – xyz movable optical line (composed from parts 9–11); 9 – black rectangular light guide; 10 – quartz lens; 11 – yellow optical filter (optional); 12 – multimode quartz optical fiber.

Optical emission spectroscopy (OES) was used for diagnostics of the plasma torch. A quartz lens (diameter – 25 mm, focal length – 35 mm) focused light emitted from the discharge to a multimode optical cable connected to a spectrometer (TRIAX 550). A 3600 gr/mm grating (holographic blazed for 150–450 nm) was used for measurement of OH (A→X) 0-0 band (306.0–310.8 nm) intensity from which the rotational temperature was calculated using Boltzmann plot technique. The 1200 gr/mm grating (ruled, blazed at 550 nm) was used for registering of the Ar* spectra. From the integral intensity of several argon lines: 603.21, 667.73, 675.28, 687.13, and 714.70 nm with constants given by NIST the excitation temperature of Argon atoms is calculated. Experiments were conducted for series of applied microwave power of 15, 20 and 25 W.

3. RESULTS

3.1. Analysis of plasma torch temperature and length as function of the gas flow and applied power.

The Argon gas flow was fixed to 5 l/min and three discharge tubes with outer diameter of 8 mm and varying inner diameter as 2, 3 and 4 mm were used in this experiments.

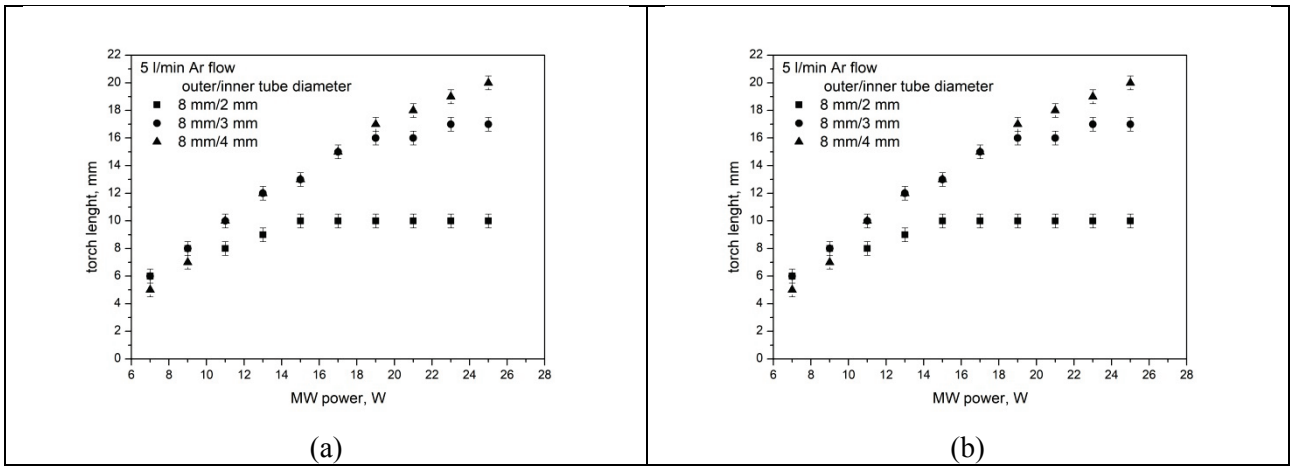

Figure 2. Plasma torch temperature (a) and length (b) as function of power for fixed gas flow and different discharge tubes.

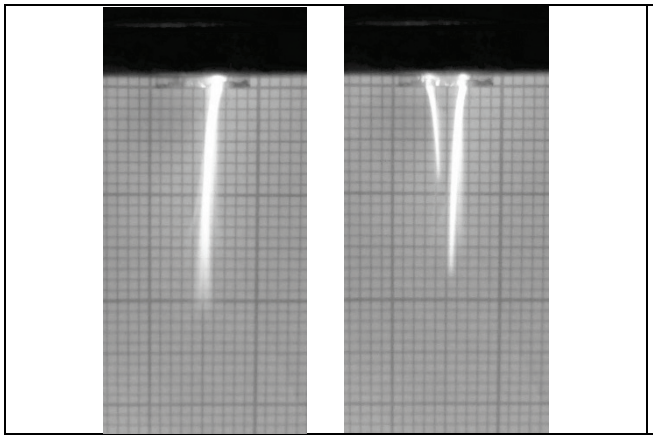

Figure 2(c). Plasma torch at lower power (left) and formation of second filament at higher power (right).

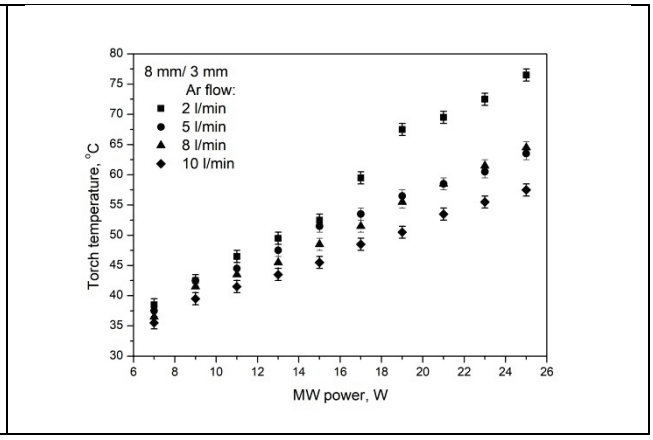

Figure 3. Gas flow effect on the torch temperature.

The dependence between the plasma torch temperature at a fixed axial position and the applied microwave power is presented in Fig. 2a. It is well visible that for tubes with higher inner diameter the temperature is significantly lower at the same wave power. The well-known almost linear increase of the plasma length with increasing the MW power is obtained at low powers (Fig. 2b). Appling higher microwave power results in deviation from the linear increase and formation of a plateau or decreasing

region. This is due to appearance of a second filament with wave power increasing (Fig. 2c). At low inner diameter (2 mm) we observed appearance of the second filament at wave power higher than 16 W; at 3 mm inner diameter of the discharge tube, the second filament is formed at powers higher than 20 W. Configuration with the biggest inner diameter investigated here extends linearly the length of the torch and does not forming second filament up to wave power of 28 W. From Fig. 2 we conclude that at low power around 6–8 W the temperature of the plasma torch is lower than 40^{o}C and the torch has significant length which allows treatment of various thermo-sensitive materials. The variation of the gas temperature of the plasma torch with the wave power at different gas flow rates is further investigated for 8/3 mm tube. The results presented in Fig. 3 show clearly decreasing of the gas temperature with increasing the gas flow. We assume that the higher gas flow results in creation of turbulence, which cools the plasma torch.

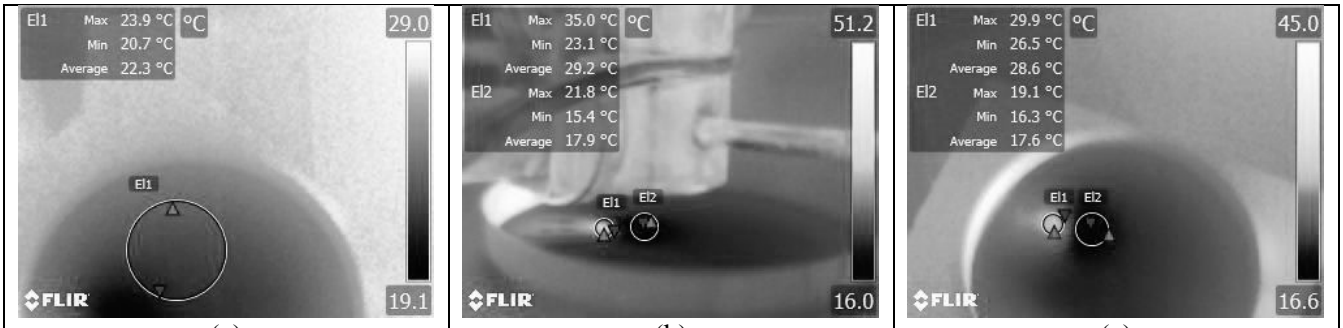

(a) (b) (c)

Figure 4. Petri dish with agar: (a) before treatment; (b) during treatment; (c) after treatment.

Phantom model of human skin, pigskin, and agar plates were used for further temperature investigation. IR images of the different objects during plasma treatment further confirm the idea that higher gas flows cool the plasma torch.

The plasma torch is sustained with applied power of 9 W and gas flow of 6 l/min in 8/4 mm discharge tube. The thermal camera images of agar plate are presented in Fig. 4. Figure 4a shows the temperature of the agar before plasma treatment and its maximum is about 24°C. The IR images during 30 s plasma treatment (Fig. 4b) and immediately (up to 15 s) after treatment stopping (Fig. 4c) show that two spots are formed under the torch: a hot spot denoted as EI1 and a cold one EI2. The cold spot is formed at the region of the treated surface, which is touched by the plasma torch. Its maximum temperature is even lower than the agar temperature before treatment being about 22°C during the treatment and decreasing very fast to about 19°C after stopping it. One not yet understood problem is the appearance of the hot spot by hot Argon flow on the side where the plasma torch touches the dielectric wall. Its temperature is much higher than the plasma torch temperature at the same conditions reaching about 35°C and 30°C after stopping it.

The results are consistent with obtained during treatments of pigskin. Patches of pigskin 5×5 cm^2 were treated for 10 s with 10 W of applied power for different gas flows. Increasing the Argon flow rate from 2 l/min to 4 l/min and then to 6 l/min we obtain decrease of the maximum temperature of pigskin from 68.9 to 41.2°C and then to 32.6°C at the highest flow rate.

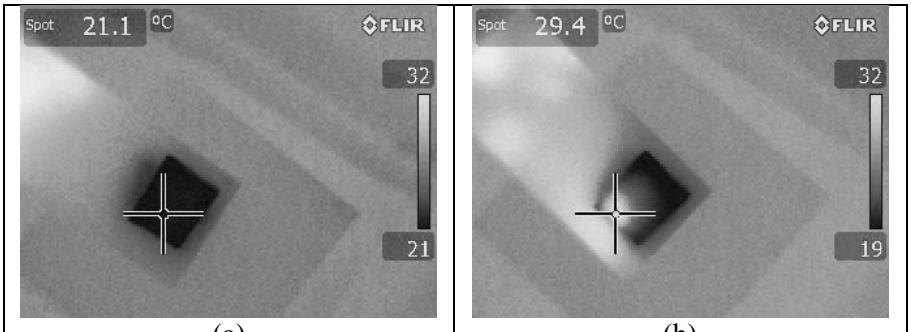

(a) (b)

Figure 5. Phantom temperature: (a) before and (b) after plasma treatment.

A phantom model with the same properties as the human skin was treated by the plasma torch produced in 8/3 mm discharge tube with applied power of 9 W and Argon gas flow 8 l/min. The phantom has a cubic form and the discharge was positioned to treat the center area of the cube. Five

minutes treatment time was enough to obtain a well distinguished hot spot with temperature 29.4°C (Fig. 5b) while the initial temperature is 21.1°C (Fig. 5a). The position of the spot is at the cube edge suggesting that the plasma column itself is cold but the Ar gas, which flows between the plasma and the dielectric tube is hot. Increasing the gas flow leads to lower heat transfer because of the turbulence. In that case the plasma column is moving inside the tube and is in contact with different parts of the tube and Argon gas thus cannot heat only a small part of the tube and the Argon to very high temperatures.

3.2. Spectroscopic investigation of the active species in the plasma torch, electron excitation and rotational temperatures. The dissipation of the electromagnetic wave sustaining the torch leads to its axial inhomogeneity. The axial distribution of the electron excitation temperature as function of the applied wave power for given gas flow is presented in Fig. 6.

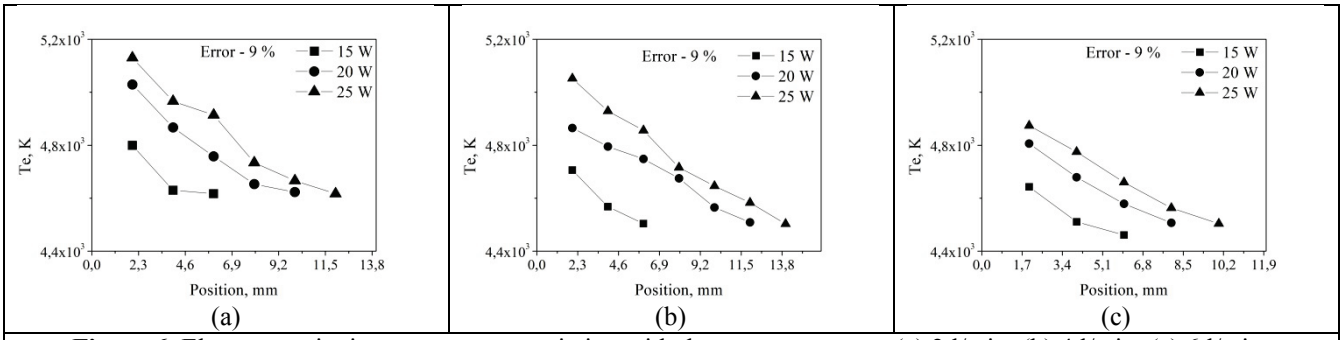

Figure 6. Electron excitation temperature variation with the wave power at: (a) 2 l/min; (b) 4 l/min; (c) 6 l/min.

Nearly liner decrease in the electron excitation temperature along the plasma torch was observed in all of the experimental conditions. Increasing the applied MW power also increases the electron excitation temperature.

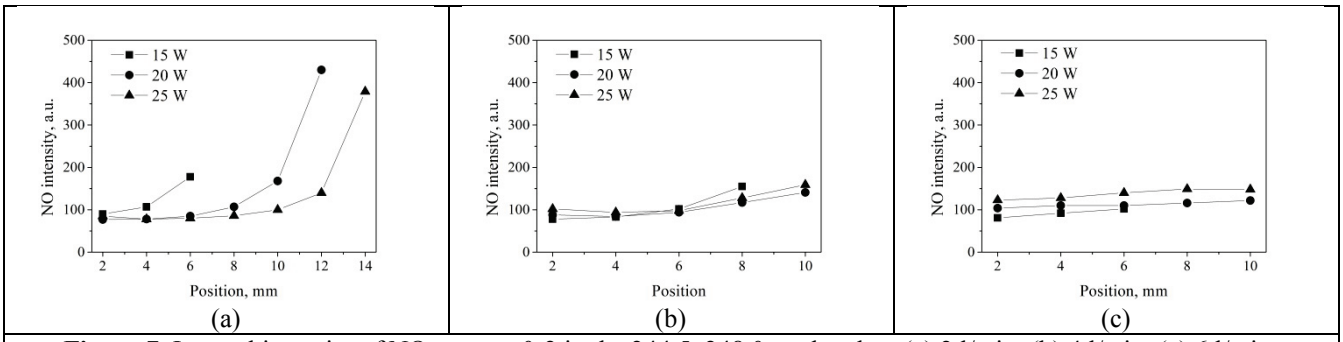

Figure 7. Integral intensity of NO-gamma 0-2 in the 244.5–248.0 nm band at: (a) 2 l/min; (b) 4 l/min; (c) 6 l/min.

The dependence of the integral intensity of NO-gamma 0-2 as function of power for given gas flow is presented in Fig. 7. One can see that at the lowest gas flow of 2 l/min the intensity increases at the tip of the plasma torch while at higher flow rates (Fig. 7b, c) it remains almost constant. At flow of 2 l/min the plasma torch looks to be a relatively homogenous needle and because of that the interactions with nitrogen from the air are with higher probability at low flows. Increasing the flow creates turbulences and the plasma no longer had needle-like structure, which leads to less nitrogen reactions at the tip of the torch.

Atomic Oxygen intensity variation with wave power for given gas flow is presented in Fig. 8. Increase in the intensity at higher wave power is observed at all gas flow rates. Generally, the atomic Oxygen intensity is higher at lower Argon flow and the reason can be the same as in the case of NO, keeping in mind that it is produced by reactions of the Argon plasma torch with the Oxygen in the ambient air.

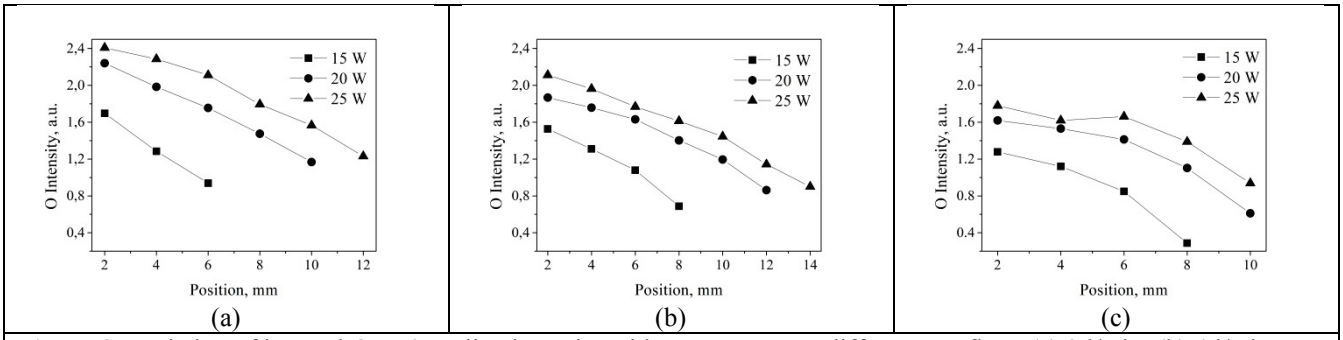

Figure 8. Variation of integral O 776 nm line intensity with wave power at different gas flow: (a) 2 l/min; (b) 4 l/min; (c) 6 l/min.

OH integral intensity presented in Fig. 9 shows strong dependence on the applied power for higher gas flows (Fig. 9b, c). At low gas flow increasing the applied microwave power does not change the intensity of the band emission (Fig. 9a).

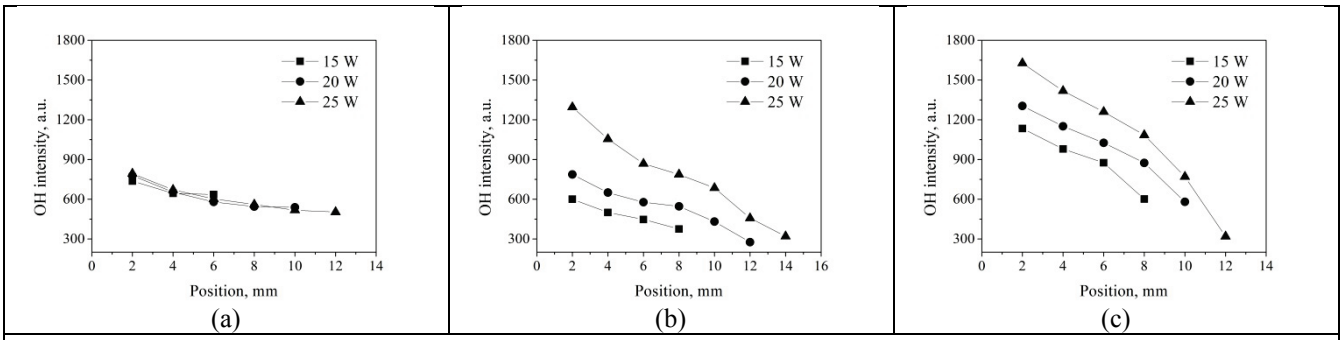

Figure 9. Integral intensity of OH(A→X) 0-0 in the 306.0–310.8 nm band variation with the wave power at Argon gas flow: (a) 2 l/min; (b) 4 l/min; (c) 6 l/min.

Above results show that because of Argon microwave plasma torch interaction with ambient air we can detect the same molecules that are controlling basic biological processes inside the human body and nature. Higher gas flow reduces the temperature of the treated object at the contact point between the plasma and the samples.

We have also investigated the variation of the same species intensities with the gas flow rates at fixed microwave power of 15 W. The results at 2, 4 and 6 l/min Argon flow are presented in Fig. 10. We have observed increasing of the OH band intensity at gas flow of 6 l/min (Fig. 10a) while the intensity at 4 l/min is even lower than at 2 l/min. Further investigations are needed for understanding the mechanism of OH radical creation by the MW torch. Atomic oxygen intensity is not significantly influenced by the gas flow change (Fig. 10b). The same is observed also for the electron excitation temperature shown in Fig. 10c. The intensity of NO-gamma band intensity increases around the tip of the discharge at lower gas flows, and remains almost constant at 6 l/min, which can be explained by the plasma interaction with the atmosphere.

The axial distribution of the rotational temperature obtained from the OH (A→X) 0-0 band (306.0–310.8 nm) intensity is presented in Fig. 11. One can see that with increasing the gas flow the rotational temperature decreases. Even so the temperature is far from being close to the electron temperature or the gas temperature measured by the IR camera. This means that the microwave plasma torch is strongly non-equilibrium. Conventional method of using the OH rotational temperature to determine the gas temperature of CAP cannot be applied to our discharge. For precise determination of the gas temperature using optical emission spectroscopy a self-consistent model is needed taking into account all of the processes in the discharge kinetics and the electrodynamics of electromagnetic wave propagation and sustaining the plasma torch.

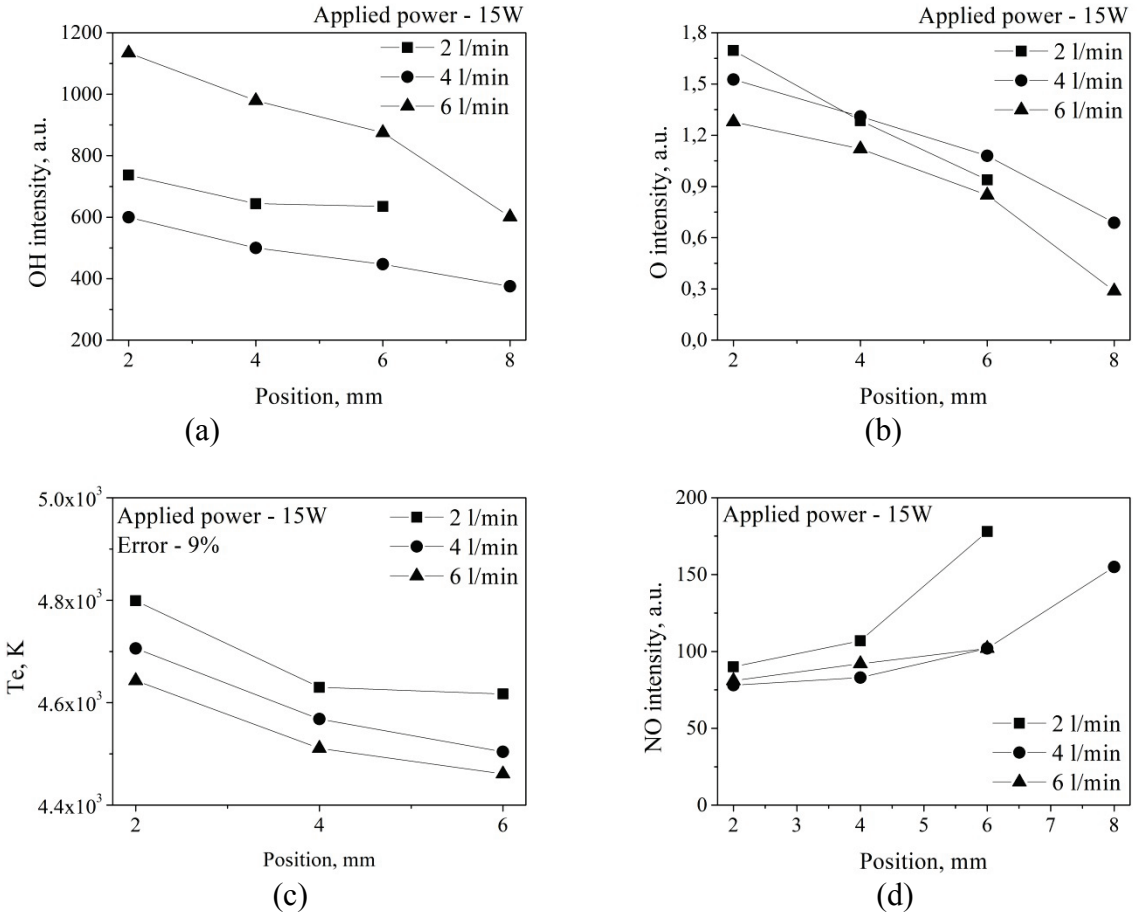

Figure 10. Variation of: (a) OH (A-X) 0-0 band integral intensity; (b) atomic oxygen O integral intensity; (c) electron excitation energy of Ar; (d) integral intensity of NO-gamma band with Argon gas flow at applied power of 15 W.

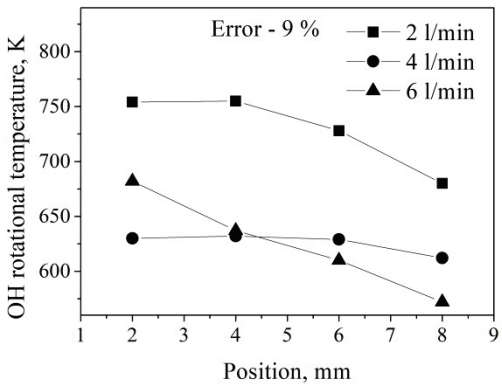

Figure 11. OH rotational temperature variation with gas flow.

The axial distribution of the rotational temperature obtained from the OH (A→X) 0-0 band (306.0–310.8 nm) intensity is presented in Fig. 11. One can see that with increasing the gas flow the rotational temperature decreases. Even so the temperature is far from being close to the electron temperature or the gas temperature measured by the IR camera. This means that the microwave plasma torch is strongly non-equilibrium. Conventional method of using the OH rotational temperature to determine the gas temperature of CAP cannot be applied to our discharge. For precise determination of the gas temperature using optical emission spectroscopy a self-consistent model is needed taking into account all of the processes in the discharge kinetics and the electrodynamics of electromagnetic wave propagation and sustaining the plasma torch.

3.3. Effects of microwave plasma torch treatment on selected examples of biological systems. The plasma torch is applied for direct treatment of (i) bacteria for investigation of its bactericidal effect; (ii) mouse wound for the possible effect in wound healing.

(i) A bacterial strain *Pseudomonas sp. AP-9* was used as a suitable model of pathogenic Gram negative bacteria. Thick layers of *Pseudomonas* with density from 2×10^7 to 6×10^9 cells/ml in agar plate were treated directly by the plasma torch. The sterilization effect dependence on the discharge conditions was studied by varying the wave power from 14 to 22 W and the treatment time from 3 to 20 s. In Fig. 12 well-presented completely sterilized zones can be seen (dark zones on the right). For comparison the non-treated control without such zones is presented on the left photo. The sterilized zones diameter depends on the wave power and treatment time which is shown in Fig. 13. The diameter of the plasma torch is about 2 mm and that of sterilized zones can be more than 1 cm with no movement in radial direction during the treatment. The sterilized zones diameter increases with increasing the treatment time but does not depend significantly on the wave power and is bigger at lower bacteria concentration (compare Fig. 13a and b). The sterilization was complete, without any survived colonies and stable (confirmed by more than 168 h monitoring).

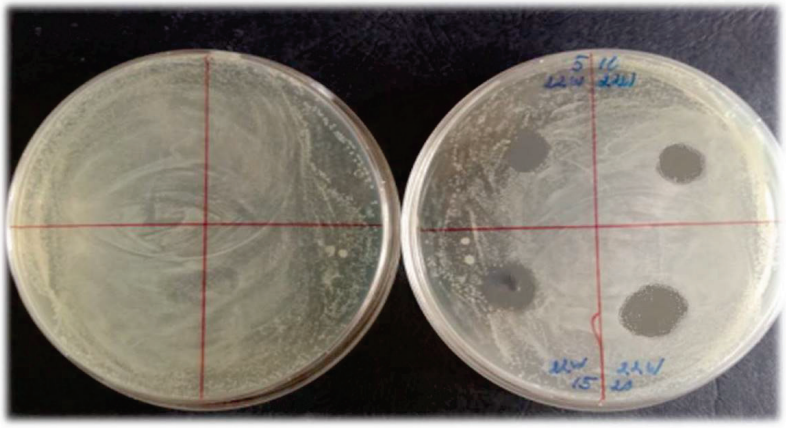

Figure 12. Control (left) and plasma treated agar plates (right) inoculated with *Pseudomonas sp. AP-9*.

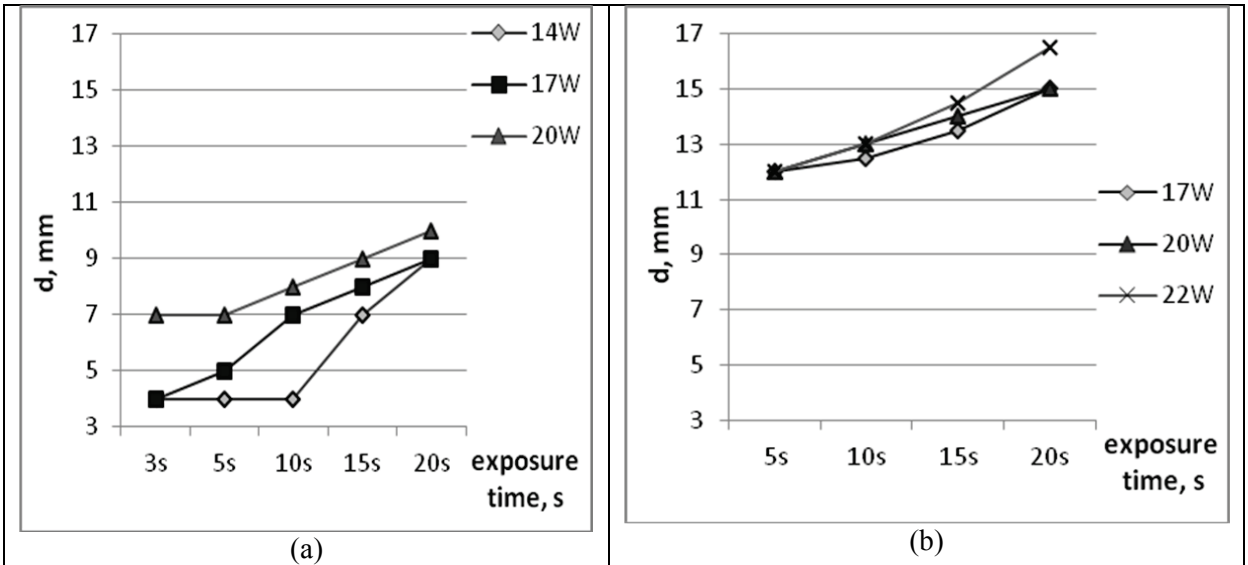

Figure 13. Diameter of sterilization area at various wave power and treatment time at *Pseudomonas* concentration: (a) 6×10^9 cells/ml and (b) 2×10^7 cells/ml.

(ii) Some preliminary results of mice wound healing by MW plasma torch treatment are obtained. The wave power was fixed to 9 W and Argon flow was 7 l/min. The treatment was organized in series: first day 45 s, next three days 15 s each with 24 h interval between treatments. In Fig. 14 the effect on wound closure is presented. The left wound is treated by the plasma torch and the right one is untreated control. The time necessary for wound closure is normally about 3 weeks. As one can see, after a week the treated wound is almost closed. Wound treatment in series with short treatment time accelerates wound closing with days. This effect needs further investigation with various different schemes of the series but the very positive results show the applicability of the microwave plasma torch for such applications.

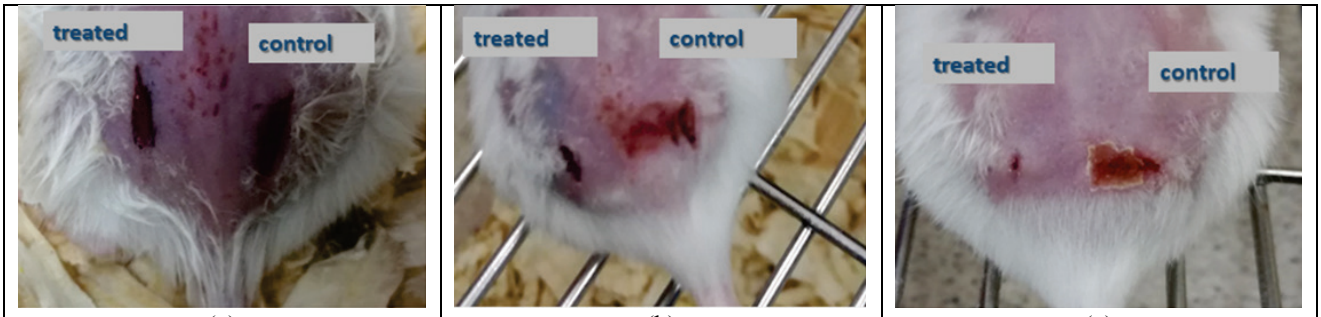

(a) (b) (c)

Figure 14. Effect of mouse wound treatment by MW plasma torch: (a) Day 1; (b) Day 4; (c) Day 7.

Acknowledgments

This work was supported by Bulgarian National Science Fund under Grant No. DN08/8, 2016.

References

1. Samukawa S., Hori M., Rauf S., Tachibana K., Bruggeman P., Kroesen G., Whitehead J. C., Murphy A.B., Gutsol A.F., Starikovskaia S., Kortshagen U., Boeuf J.-P., Sommerer T.J., Kushner M.J., Czarnetzki U., Mason N., J. Phys. D: Appl. Phys., 2012, **45**, 253001.
2. Graves D.B., Phys. Plasmas, 2014, **21**, 080901.
3. Weltmann K.-D., von Woedtke T., Plasma Phys. Control Fusion, 2017, **59**, 014031.
4. Romero-Mangado J., Dey A., Diaz-Cartagena D.C., Solis-Marcano N.E., Lopez-Nieves M., Santiago-Garcia V., Nordlund D., Krishnamurthy S., Meyyappan M., Koehne J.E., Gandhiraman R.P., J. Vac. Sci. Technol., 2017, **A35**, 041101.
5. Kuzminova A., Kretková T., Kylián O., Hanuš J., Khalakhan I., Prukner V., Doležalová E., Šimek M., Biederman H., J. Phys. D: Appl. Phys., 2017, **50**, 135201.
6. Babaeva N.Y., Kushner M.J., IEEE Trans. Plasma Sci., 2011, **39**, 2964.
7. Lu X., Naidis G.V., Laroussi M., Reuter S., Graves D.B., Ostrikov K., Phys. Rep., 2016, **630**, 1.
8. Vandamme M., Robert E., Dozias S. Sobilo J., Lerondel S., Le Pape A., Pouvesle J.-M., Plasma Med., 2011, **1**, 27.

DECISIVE ROLE OF NON-EQUILIBRIUM MICROWAVE PLASMAS IN GREENHOUSE GAS CONVERSION

N. Britun[1], T. Godfroid[2], R. Snyders[1,2]

[1] Chimie des Interactions Plasma-Surface (ChIPS), University of Mons, Place du Parc 23, B-7000, Mons, Belgium
[2] 'Materia Nova' Research Center, av. Copernic 1, B-7000, Mons, Belgium

Abstract. For optimization of CO_2 conversion in microwave plasma for industrial applications as well as for in-depth understanding of the key processes in plasma and its main parameters, such as the electron temperature, gas temperature, vibrational excitation, etc. the energy delivery in a particular plasma system is of a great importance. In this work the recent results obtained in our group and related to the various spectroscopic diagnostic techniques applied for optimization of the microwave plasma parameters aiming at the increase of CO_2 conversion and its energy efficiency are presented. The in-situ diagnostic methods including optical spectroscopy and laser-induced fluorescence have been implemented in a microwave plasma discharge and post-discharge regions for non-intrusive time-resolved characterization of the mechanisms responsible for efficient gas decomposition. A decisive role of the plasma power modulation, gas heating, and gas residence time for optimization of the CO_2 conversion is demonstrated. The combination of the obtained plasma diagnostic results with the plasma catalysis approach should further increase the area of applicability of non-equilibrium microwave discharges for CO_2 conversion bringing them on a highly competitive level, including future industry-grade greenhouse gas conversion systems.

1. INTRODUCTION

The basic green energy activities include reduction of greenhouse gas emission, in particular the emission of CO_2, development and implementation of the green energy sources, as well as local conversion, reforming and utilization of the greenhouse gases. The last activities are represented by the well-known carbon capture and storage (CCS) and carbon capture and utilization (CCU) paradigms being under intensive development during the last decades [1, 2]. Among the approaches suitable for local greenhouse gas conversion, in particular for conversion of CO_2, the plasma-assisted conversion based on the decomposition of the molecules of interest in low-temperature discharges is of a special interest. The efficiency of such a conversion depends on various factors, such as proper choice of the plasma source, as well as its further optimization. The plasma optimization in this case implies first of all tuning the fundamental physical parameters, such as electron density and temperature, vibrational excitation of the involved molecules, discharge pressure, residence time of the particles in the active discharge zone, etc. For a successful optimization the plasma source has to be characterized in details, preferably using non-intrusive in-situ plasma diagnostics methods often combined with modeling [3].

Since 1970s the utilization of low-temperature discharges is considered as a promising approach for molecular gases decomposition [4, 5], which can be applied in particular for CO_2 reforming. It is well-known that the low-temperature discharges are the unique media where selectivity towards various plasma chemical processes can be realized [5, 6]. This is the result of a strong non-equilibrium between the main degrees of excitation in plasma, namely the electronic, translational, rotational, and vibrational ones. At the same time, as also shown previously, the vibrational excitation is particularly crucial for molecular dissociation in many cases, including the CO_2 case [6, 7]. A decisive role belongs here to the low-temperature microwave (MW) discharges where up to 90% of the applied electro-magnetic field energy is absorbed by plasma electrons further transmitting their energy to the vibrationally-excited molecular states, while the gas temperature remains relatively low, typically about a thousand degree Kelvin or lower [5, 8].

The importance of the asymmetric vibrational mode of CO_2 (see below) for its efficient plasma-based decomposition has been also deduced from the past research. The mentioned efficiency is defined, however, by several mechanisms working along with the mentioned vibrational excitation, such as: (i) fast excitation of the CO_2 asymmetric mode by plasma electrons as a result of the electron-vibrational (e-V) energy transfer, (ii) several orders of magnitude faster vibrational-vibrational (V-V) energy transfer, providing fast vibrational excitation of the CO_2 molecules up to the dissociative level (≈ 5.5 eV), and (iii) rather slow vibrational-translational (V-T) transfer rates which would result in the gas heating, rather than molecular decomposition. The fast V-V process facilitates so-called vibrational 'ladder climbing', i.e. fast excitation of the highly-excited vibrational states of CO_2 finally resulting in its dissociation [5]. The low gas temperature in the discharge, on the other hand, is important for keeping the V-T energy transfer at the relatively low level, thus preserving a certain level of vibrational excitation for a longer time. The V-T exchange time may vary from few μs to tens of ms, depending on the discharge parameters. As a result, the energy efficiency (see the definition below) up to 0.8 in a subsonic [9] and about 0.9 in a supersonic [10] gas flow has been achieved in the microwave plasmas. The non-equilibrium discharge conditions can also be effectively realized in the other discharges, for example in gliding arc plasma (GAP) as a result of a thermal – non-thermal plasma transition caused by plasma length extension and gas cooling, as proposed in [11].

Nowadays scientific interest to the greenhouse gas decomposition in the low-temperature discharges is growing again. This is related to both low-pressure and high-pressure (atmospheric) cases. Talking about MW plasma sources we should note that, along with their general effectiveness for molecular decomposition, the power modulation effect is known to be an additional alternative for enhancing the CO_2 conversion in these discharges [12]. To realize this effect, an electromagnetic wave with a filling frequency in the GHz range (typically 2.45 GHz) is modulated by nearly squared pulses typically in the kHz range. Such modulation might be very important when the vibrational excitation is involved in molecular decomposition process, as in the CO_2 case [5]. Since in the pulsed MW discharges the characteristic time of V-T energy transfer may be comparable to the typical plasma pulse repetition period (μs − ms range) resonance-like effects between the power delivery and the energy transfer processes may happen. Thus, the periodic power delivery in these discharges represents an additional way for improving the efficiency of CO_2 conversion, at the same time requiring additional understanding of the corresponding physical processes.

In spite of the numerous works devoted to the plasma-based greenhouse gas conversion in the MW discharges [10, 13, 14], dielectric barrier discharges (DBDs) [15–20], GAPs [21–23], radiofrequency (RF) discharges [24], as well as in different discharges using plasma catalysis [13, 25–27], the effects of CO_2 conversion and power modulation, are still far from being fully understood. The number of the research works in this domain is also very limited, mainly by the theoretical speculations of the usability of pulsed plasma regime in MW and DBD cases [28], as well as by few experimental evidences of the pulsed discharge benefits so far only shown for DBD case [16–18]. At the same time the domain of the power modulation in MW low-temperature plasmas, representing one of the most promising non-equilibrium media for selective plasma chemistry remains mainly unexplored. The present work summarizes the recent achievements in the domain of optimization of the CO_2 conversion made in our Lab. using modulated microwave power delivery, as well as optical spectroscopy techniques for plasma characterization.

2. THEORETICAL BACKGROUND

2.1. Structure of CO_2 molecule. The structure of CO_2 molecule is schematically shown in Fig. 1. Being a triatomic molecule CO_2 possesses three vibrational modes, namely the *symmetric stretch* mode (with the main vibrational energy gap of about 0.17 eV), the double-degenerated *bending* mode (0.083 eV), and the *asymmetric* mode (0.291 eV). The different energy gaps for these modes define the differences in the energy transfer rates between them and the translational particle motion (V-T transfer). The vibrational excitation states for CO_2 are normally denoted through three vibrational quantum numbers corresponding to symmetric (v_1), bending (v_2), and asymmetric (v_3) vibrational modes.

One of the possible pathways for CO_2 decomposition is the electron impact dissociation:

$$CO_2 + e \rightarrow CO + O + e \text{ (the energy required is } \approx 5.5 \text{ eV)}. \quad (1)$$

However, as a result of recombination of atomic O with vibrationally excited CO_2 (denoted as CO_2^{vibr}) another CO molecule may be produced [6], giving the energy per one produced CO molecule equal to ≈ 2.9 eV:

$$O + CO_2^{vibr} \rightarrow CO + O_2 \text{ (the energy required is } \approx 0.3 \text{ eV)}. \quad (2)$$

As mentioned earlier, the actual CO_2 dissociation strongly relies of the e-V energy transfer resulting in the excitation of the lowest vibrational states of CO_2 molecule, e.g.:

$$e + CO_2 \rightarrow CO_2(0,0,1) + e\,, \quad (3)$$

where the parenthesized numbers stand for the vibrational quantum numbers mentioned above. The excitation of the higher vibrational states is happening at the same time as a result of the fast energy transfer between the different vibrational states within the same vibrational mode (i.e. V-V transfer), e.g.:

$$CO_2(0,0,1) + CO_2(0,0,1) \rightarrow CO_2(0,0,2) + CO_2(0,0,0). \quad (4)$$

The energy transfer between different vibrational modes (so called 'non-resonant' transfer, or V-V') is less efficient, with typical transfer rates several times lower, according to [29].

In addition to the abovementioned reactions, various two- or three- body collisional processes leading to O atom recombination (some of them are exothermic) may also be important for the total energy balance in the O-containing discharges. These processes may involve both ground state (^3P) as well as the first excited (^1D) state of atomic oxygen, as well as the other states [30]. Among the typical examples are:

$$O(^1D) + O_2 \rightarrow O(^3P) + O_2, \quad (5a)$$

$$O(^3P) + O(^1D) \rightarrow O(^3P) + O(^3P)\,, \quad (5b)$$

$$O(^3P) + O(^3P) + O_2 \rightarrow O_2 + O_2(X,0), \text{ etc.} \quad (5c)$$

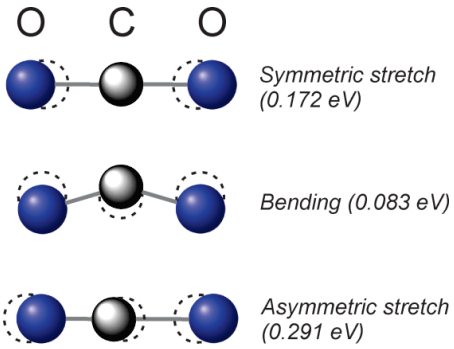

Figure 1. Structure of CO_2 molecule showing its three vibrational modes with the corresponding energy gaps.

2.2. The CO_2 conversion efficiency. The CO_2 conversion efficiency is usually determined as a ratio between the densities of the decomposed CO_2 molecules to their initial density:

$$\chi = \frac{[CO_2]_{dec.}}{[CO_2]_{init.}}\,, \quad (6)$$

where $[CO_2]_{dec.}$ and $[CO_2]_{init.}$ refer to the decomposed and initial CO_2 molecular density, respectively. Let us note that in the pure CO_2 case χ can be defined simply as $[CO]/[CO_2]_{init.}$, where [CO] stands for the density of CO molecules produced.

At the same time, the energy efficiency η is normally defined via the enthalpy of CO_2 dissociation ($\Delta H_{CO_2} = 2.9$ eV) and the energy spent for production of one CO molecule (E_{CO}) [5]:

$$\eta = \frac{\Delta H_{CO_2}}{E_{CO}}\,. \quad (7)$$

In general case both χ and η quantities are defined locally, as the supplied energy might be different depending on the point of interest in the discharge. Combining last two expressions and defining *specific energy input* (E_S or SEI) as the energy delivered per a single CO_2 molecule in a certain discharge volume (usually expressed in eV or eV/molec), the energy efficiency yields:

$$\eta = \chi \frac{\Delta H_{CO_2}}{E_S}\,. \quad (8)$$

The specific energy E_S can be determined via the power P applied to the discharge and the flux of the gas F in the discharge tube: $E_S = \frac{P}{F}$, or using more convenient units (where P is expressed in Watts, and slm stands for standard liter per minute):

$$E_S(\text{eV/molec}) = 0.014\ \frac{P(W)}{F(\text{slm})}\ . \quad (9)$$

3. EXPERIMENTAL

3.1. The plasma sources used. *2.45 GHz plasma source -1*. The scheme of this MW surfaguide discharge is shown in Fig. 2. The discharge operates at 2.45 GHz having an auto-tuning 3-stab system for minimization of the reflected power. The reflected power does not exceed 5% of the total applied power. The mean power of 0.4 kW has been used in this work (MUEGGE pulsed power generator). The discharge was sustained in a quarts tube, with 14 mm of the inner diameter, 31 cm long, surrounded by a 32 mm diameter polycarbonate tube of nearly the same length. The 8−10°C Si oil flowing between the tubes was used for cooling of the quartz tube. The microwave power has been modulated by nearly the square pulses with the 50% duty ratio. The repetition rate of the pulses was in the range from 0.5 kHz to about 30 kHz. More details on the described MW system is available in [14, 31]. Pure CO_2 or CO_2 with 5% N_2 admixture (for optical actinometry needs) with an electronically controlled total gas flow rate ranging from 0.08 to 2.7 slm has been used as a feeding gas. The pumping speed of the gas was constant during the measurements (unless stated otherwise). In spite of the pulsed discharge nature the optical measurements performed in this plasma source were not synchronized with the discharge pulses in order to obtain a time-averaged information on the CO_2 conversion. Due to the same reason, both E_S and η values were determined based on the time- and space- averaged applied power, which distribution is assumed to be uniform across the discharge volume.

2.45 GHz plasma source -2. For verification of the OES results two photon absorption laser-induced fluorescence (TALIF) technique has been used, as described below. In this case another pulsed flowing gas MW plasma source with a horizontally placed discharge tube and similar plasma parameters has been used. The optimized plasma source geometry supports direct introduction of the laser beam into the discharge and post-discharge regions. The gas flow and the resulting gas pressure values used in this case were comparable to those used in the first 2.45 GHz source. The mean power was equal to 0.8 kW, while the reflected power was kept at the level of 5% from this level or below (no auto tuning was available). In this case the TALIF measurements were synchronized with the discharge pulses using a TTL (transistor-transistor logic) signal. The TTL signal was generated using an external waveform generator synchronized with a pulsed laser, TALIF detector, and the SAIREM 6 kW power supply used for plasma generation.

In addition, some data presented in this work are related to yet another MW plasma source working at *0.915 GHz* and used mainly for plasma catalysis studies, as described elsewhere [32, 33].

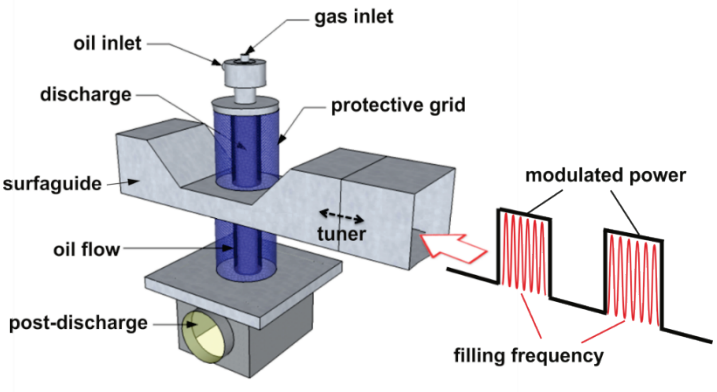

Figure 2. The concept of a pulsed surfaguide-type microwave discharge system used in the work. See [31,34] for the details. Power modulation by square pulses filled by 2.45 GHz sin-waveform is shown schematically.

3.2. The diagnostic methods used. Optical emission spectroscopy (OES), including emission actinometry and ro-vibrational analysis has been applied for characterization of the CO_2 conversion efficiency as well as the gas temperature in the discharge zone. Gas temperature has been also monitored by a thermocouple at the beginning of the post-discharge (i.e. about 17 cm below the excitation point in the case of the source -1). The rotational band from the CO Angstrom system corresponding to the $B\ ^1\Sigma^+ (v'=0) – A\ ^1\Pi (v''=1)$ optical transition with the bandhead located at about 482 nm has been used for the rotational temperature determination in the discharge. Gas temperature has been assumed equal to rotational temperature of the CO molecules [14, 35].

In order to determine the CO_2 conversion efficiency in the discharge area, optical actinometry based on the addition of a small amount of molecular nitrogen (5% in our case) to the CO_2 gas, has been used. This method is based on the measurement of emission lines ratio between the unknown species in the discharge (CO) and the known admixture (N_2). As a result, assuming corona excitation in the discharge volume, the absolute density of species of interest can be determined [14]. The relative error of this method is < 10%.

An Andor Shamrock-750 monochromator having 0.75 m of focal length and equipped with an Andor iStar-740 series intensified charge coupled device (ICCD) camera has been used for spectral acquisition in this work. The spectral resolution during the measurements was equal to about 0.05 nm (at 500 nm). The accumulative ICCD mode of the spectral acquisition has been used during all the measurements. The typical emission spectra acquired in the MW plasma zone are shown in Fig. 3a, b along with the rovibrational bands used for characteristic temperature determination (see Fig. 3c, d).

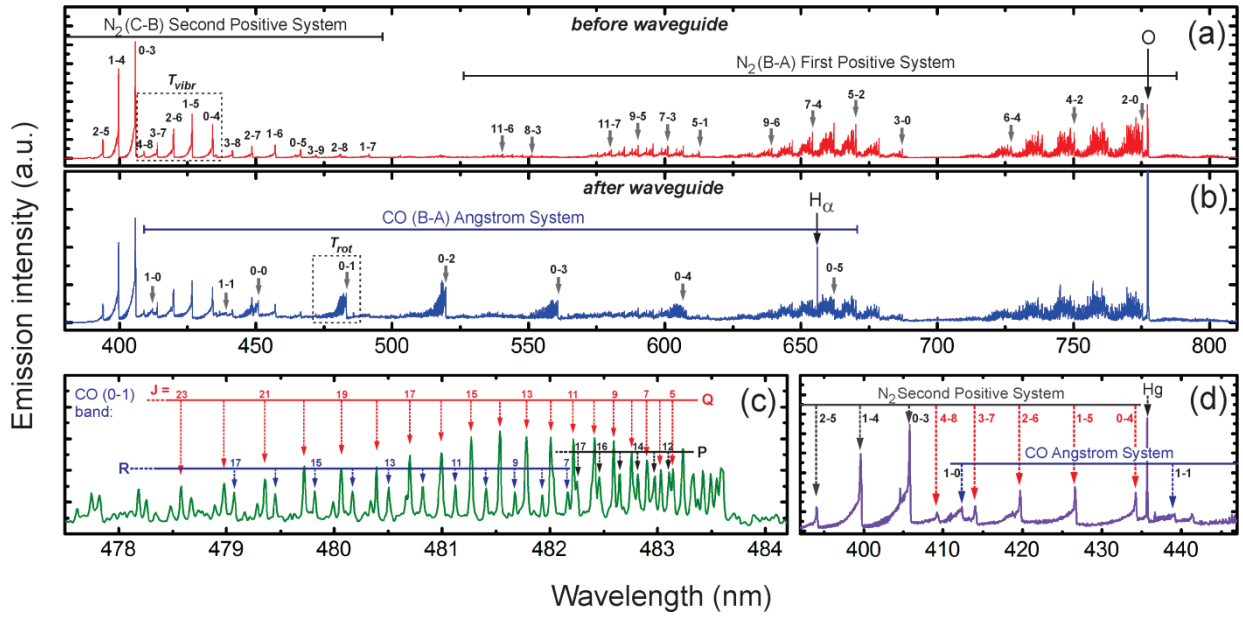

Figure 3. Typical emission spectra obtained in the described *2.45 GHz -2* microwave discharge. The spectra were obtained in the CO_2-N_2 gas mixture upstream (a) and downstream (b) of the waveguide. The illustration of determination of the T_{gas}(c) and T_{vibr} (d) temperatures is given as magnified views.

In the case of *2.45 GHz -2* plasma source TALIF technique has been used for detection of the products of CO_2 dissociation (such as CO ground state molecules and O ground state atoms) [36]. This technique is based on the laser excitation of the molecular or atomic species in the discharge or post-discharge by a simultaneous absorption of two laser photons, following by a fluorescence corresponding to an optical transition between the upper (excited) state and the intermediate state. The spectral schemes using laser excitation at 225.6 nm (for O atom) or 230.07 nm (for CO molecule) following by the fluorescence at 844.7 nm (O) or 483.5 nm (CO) have been applied in this work, based on [37, 38]. A Sirah dye laser working at 10 Hz of repetition rate and having 5 ns of the pulse duration pumped by a SpectraPhysics YAG:Nd laser has been utilized for TALIF diagnostics. A Coumarin 450 dye solution has been used. During the measurements laser pulses were not synchronized with the plasma pulses (except for some special cases), thus giving the time-averaged values of the corresponding ground state densities in the post-discharge.

Another type of diagnostics applied to the 0.915 GHz MW discharge was gas chromatography (GC) technique. This technique is based on the different gas elution time on the analyzer walls, representing ex-situ time-averaged gas analysis which has been used for characterization of various gas mixtures, including the products of the CO_2 decomposition [10]. In spite of being an ex-situ technique, GC provides the results which can be compared with the laser-based (in-situ) techniques for the stable dissociation products, which is valid for CO ground state molecules. In our case a Bruker 450-GC gas chromatograph equipped with a sampling system has been used for the post-discharge characterization in the 0.915 GHz MW source as well as for TALIF signal calibration in the 2.45 GHz -2 MW source. In the described GC system a low-pressure gas sample is diluted with carrier gas (argon) before its injection into the gas chromatograph.

4. RESULTS

4.1. Plasma characterization results. Since the characteristic plasma temperatures such as the gas temperature (T_{gas}), vibrational temperature of the gas molecules (T_{vibr}), and electron temperature (T_e) play a very important role in the plasma kinetics and molecular decomposition, this work is partially focused on determination of these parameters by the available optical spectroscopy methods, namely the rotational and vibrational spectral analysis, as mentioned above.

The general emission spectra obtained in the CO_2−N_2 microwave discharge are shown in Fig 3 (a, b). These spectra illustrate the CO_2 conversion before (upstream) and after (downstream) the waveguide. Due to the much higher dissociation threshold for N_2 (about 9.8 eV, according to [39]), the dissociation of this molecule in nearly negligible in the plasma source and the electron and vibrational energy is mainly channelized for CO_2 decomposition. Due to this reason the N_2 dissociation in the optical actinometry method has also been neglected. The appearance of the intensive CO emission lines in the 450−600 nm spectral region (corresponding to the so-called Angstrom emission band of CO) downstream the waveguide is evident from Fig. 3(b). These bands are very weak before the waveguide, underlining the importance of the so-called discharge ‘active zone’ where the majority of the injected CO_2 molecules get decomposed [14]. At the same time the molecular emission bands corresponding to the First Positive System of N_2 hold their intensity at almost the same level before and after the waveguide, confirming rather weak dissociation of N_2 in this plasma source.

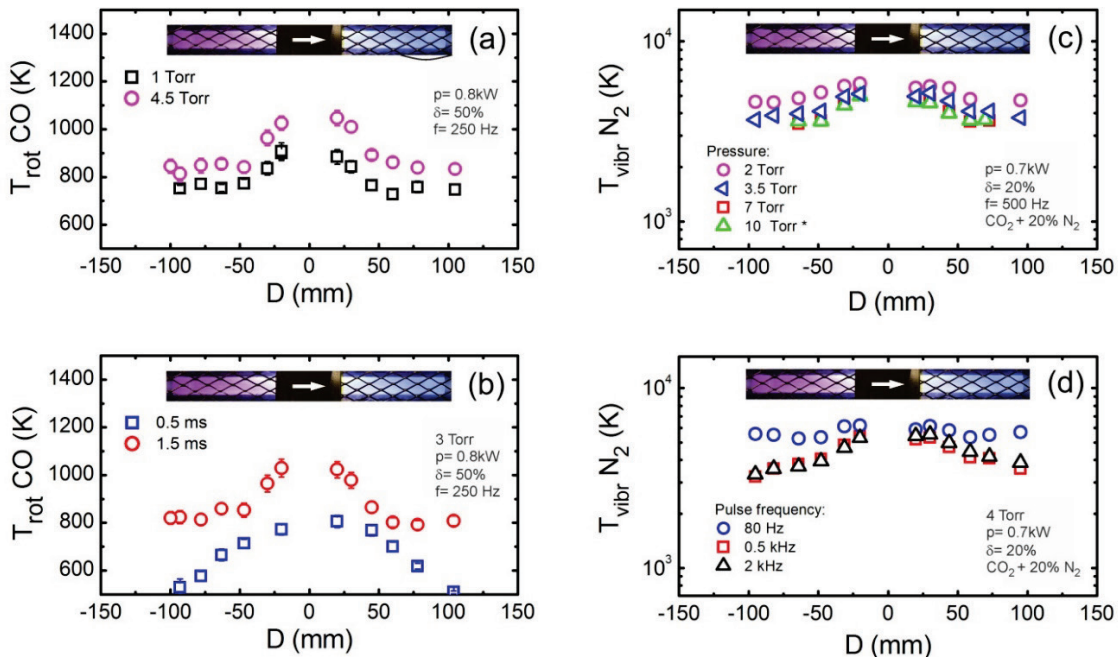

Figure 4. The CO rotational temperature T_{rot} (a, b) as well as the N_2(C) vibrational temperature T_{vibr} (c, d) measured along the MW discharge tube under various discharge conditions. Gas pressure is shown in the legends. p and δ symbols denote mean applied power and pulse duty ratio, respectively. D denotes the distance along the discharge tube. The discharge pictures and the gas flow direction are shown for reference. See [40] for the details.

The typical temperature profiles along the discharge tube (visible area of ~ 200 mm long) are given in Fig. 4. A clear increase in the gas temperature (i.e. T_{rot} of CO) can be observed in the middle of the discharge tube at any plasma condition. This increase is likely related to the e-T energy transfer in the waveguide vicinity (when gas is being efficiently heating by electrons), as well as to the V-T energy transfer in this area. Fig. 4a clearly shows that the higher gas pressure corresponds to higher gas temperature in the discharge area. This is most likely related to the higher e-T and T-T transfer rates at high gas pressure. Moreover, the effect of the gas heating is highly dynamic, as shown in Fig 4b, where we can see the evolution of the temperature profile during the MW plasma pulse (in this case pulse duration is 2 ms, with 50% duty ratio). At the beginning of the pulse (at 0.5 ms) the gas temperature is clearly lower, than the one measured at the end of the pulse (at 1.5 ms) showing especially low values at the tube edges. This partially confirms the efficient gas heating by electrons in the active zone.

The vibrational temperature, on the other hand, demonstrates rather similar spatial distributions at various plasma conditions, as shown in Fig. 4c, d. As we can see, T_{vibr}, although to a lesser extent, shows a maximum in the tube center, i.e. in the waveguide vicinity. This maximum points out on the efficient e-V (electron-vibrational) energy transfer in the discharge, which promotes excitation of N_2 molecules. The efficient vibrational excitation of the CO_2 molecules have not been confirmed by a direct measurement, however, the final width of the active discharge zone (~ 5−6 cm, according to [14]), where most of the CO_2 decomposition takes place, is well-correlated with observed the T_{vibr} behavior. At 80 Hz of the plasma pulse repetition rate (see Fig. 4d, blue circles) the T_{vibr} profile is somewhat more flat than the other measured profiles, shown in Fig. 4c, d, which remains unclear at the moment. The electron temperature in our system has been found equal to about 1−2 eV for most of the studied conditions (except for the higher pressure cases, at p>10 Torr, where T_e drops below 1 eV, as a result of more efficient electron cooling).

4.2. Gas conversion results. Needless to say that the actual gas conversion results in the described MW plasma sources represent real practical significance. In this work the CO_2 conversion has been experimentally determined either by optical emission spectroscopy (namely by optical actinometry) or LIF (calibrated with gas chromatography) methods. The example of the CO_2 conversion and energy efficiency data measured by actinometry is shown in Fig. 5. For the detailed description of the experimental approaches, reader may refer to our recently published work [34], where the *2.45 GHz -1* plasma source has been used. As we can see from Fig. 5, the typical conversion/energy efficiency values of about 0.25/0.25 can be achieved without applying the plasma catalyst. In this case the intermediate gas pressure (about 7 Torr) in the 2.45 GHz MW plasma source has been achieved (see [34]). A pre-activated by Ar MW discharge Ni-based plasma catalyst further promotes CO_2 decomposition, as demonstrated recently by Chen et al. in a 0.915 GHz MW plasma source case [13, 27]. The estimated MW system performance using this type of catalyst is marked in Fig. 5 by a red star symbol, showing roughly twice higher conversion values. The estimated value is a subject of verification by the future measurements, though.

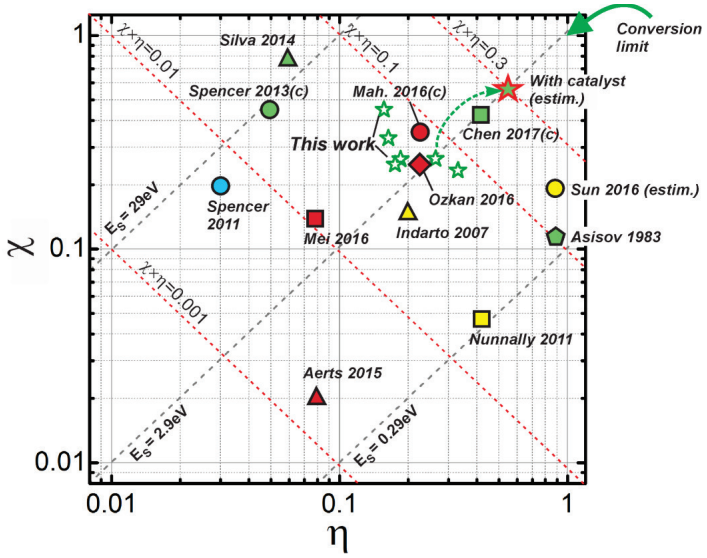

Figure 5. Selected CO_2 conversion efficiency (χ) and energy efficiency (η) values obtained in the *2.45 GHz -1* MW discharge compared to the literature data. The values obtained in this work (green stars) are measured by optical actinometry [14]. The literature data are related to the microwave (green symbols), gliding arc (yellow), radiofrequency (blue), and dielectric barrier (red) discharges. The χ×η product represents overall conversion efficiency. Usage of plasma catalyst is marked by '(c)'. The estimated values are marked by '(estim.)'.

The conversion data from the most competitive literature sources are also given in Fig. 5. As we can see, the catalyst-based processes have clear advantage over those based on plasma only. The low-pressure MW plasma sources are clearly superior in terms of the CO_2 conversion, presumably due to their suitable range of electron temperature (about 1−2 eV), and better channeling of the electron energy toward the vibrational energy, as studied in the past [5]. On the other hand, the gliding arc discharges have clear advantage due to the transition from thermal to non-thermal mode achievable at the atmospheric pressure [21]. Indeed, the non-equilibrium regime achievable in these discharges boosts namely the energy efficiency of CO_2 conversion, as shown in Fig. 5, at the same time leaving the conversion values at a rather low level. On the other hand, the conversion results achieved in the dielectric barrier discharges are comparable to those obtained in the MW plasma sources. Two best performing DBD cases achieved so far are either achieved in a DBD with catalyst [26] or using a pulsed DBD plasma source [17]. The last work confirms the importance of power interruption during the greenhouse gas conversion in low-temperature plasmas, since the resonance between the energy dissipation channels (such as the V-T channel) as well as with the gas residence time in the system can be achieved in this case, further optimizing the system performance towards CO_2 conversion.

5. CONCLUSIONS

The works represent recent progress in the domain of CO_2 conversion by the non-equilibrium low-temperature microwave discharges, achieved in our Lab. Overall it is confirmed that, the key (and rather well-known) properties of the microwave discharges, namely the low electron temperature range (1−2 eV), rather high degree of non-equilibrium, along with high vibrational excitation are beneficial for the efficient CO_2 gas conversion showing rather high conversion efficiency as well as high energy efficiency of the process. High values for both conversion and energy efficiency of CO_2 conversion (~ 25%) have been achieved as a result of optimization of the microwave discharge, first of all in terms of power interruption (in the pulsed mode).

In addition, the optical diagnostics of microwave plasmas along with the power pulsed delivery to the discharge active zone may open new possibilities for the detailed studies of gas conversion, including further optimization of the discharge geometry and power application schemes, both in space and time. The concept of modulated power delivery in a form of square pulses has already proven its efficiency, showing significantly higher gas conversion efficiency. The role of optical emission spectroscopy as well as the laser-based plasma characterization methods in this case is crucial. The further studies of the CO_2 vibrational kinetics (as well as that of the other gases) involving infrared absorption spectroscopy should significantly increase our understanding of the CO_2 vibrational kinetics, both in time and space, which is crucial for efficient CO_2 conversion and future industrial applications related to the greenhouse gas reforming.

References

1. Cuéllar-Franca R.M., Azapagic A., J. CO_2 Util., 2015, **9**, 82.
2. Goede A.P.H., EPJ Web Conf., 2015, **98**, 7002.
3. Bogaerts A., De Bie C., Snoeckx R., Kozák T., Plasma Process. Polym., 2016, DOI: 10.1002/ppap.201600070.
4. Fridman A.A., Kennedy L.A., Plasma Physics and Engineering. New York: Taylor and Francis, 2011.
5. Fridman A.A., Plasma Chemistry. New York: Cambridge University Press, 2005.
6. Rusanov V.D., Fridman A.A., Sholin G.V., Sov. Phys. Usp., 1981, **24**, 447.
7. Ochkin V.N., Spectroscopy of Low Temperature Plasma. Weinheim: Wiley-VCH, 2009.
8. Lebedev Yu.A., J. Phys. Conf. Ser., 2010, **257**, 12016.
9. Legasov V.A., Nuclear – Hydrogen Energy and Technology. Vol 1. Moscow: Atom-Izdat, 1978.
10. Asisov R.I., Vakar A.K., Jivotov V.K., et al., Proc. USSR Acad. Sci. 1983, **271**, 94.
11. Fridman A., Nester S., Kennedy L.A., Saveliev A., Mutaf-Yardimci O., Prog. Energy Combust. Sci., 1999, **25**, 211.

12. Godfroid T., Dauchot J.P., Hecq M., Surf. Coatings Technol., 2005, **200**, 649.
13. Chen G., Britun N., Godfroid T., Georgieva V., Snyders R., Delplancke M.-P., J. Phys. D Appl. Phys., 2017, **50**, 84001.
14. Silva T., Britun N., Godfroid T., Snyders R., Plasma Sources Sci. Technol., 2014, **23**, 25009.
15. Aerts R., Somers W., Bogaerts A., ChemSusChem., 2015, **8**, 702.
16. Paulussen S., Verheyde B., Tu X., De Bie C., Martens T., Petrovic D., Bogaerts A., Sels B., Plasma Sources Sci. Technol., 2010, **19**, 034015.
17. Ozkan A., Dufour T., Silva T., Britun N., Snyders R., Reniers F., Bogaerts A., Plasma Sources Sci. Technol., 2016, **25**, 55005.
18. Ozkan A., Dufour T., Silva T., Britun N., Snyders R., Bogaerts A., Reniers F., Plasma Sources Sci. Technol., 2016, **25**, 25013.
19. Mei D., He Y.-L., Liu S., Yan J., Tu X., Plasma Process. Polym., 2016, **13**, 544.
20. Duan X., Li Y., Ge W., Wang B., Greenh. Gases Sci. Technol., 2015, **5**, 131.
21. Nunnally T., Gutsol K., Rabinovich A., Fridman A., Gutsol A., Kemoun A., J. Phys. D. Appl. Phys., 2011, **44**, 274009.
22. Indarto A., Yang D.R., Choi J.-W., Lee H., Song H.K., J. Hazard. Mater., 2007, **146**, 309.
23. Sun S.R., Wang H.X., Mei D.H., Tu X., Bogaerts A., J. CO_2 Util., 2017, **17**, 220.
24. Spencer L.F., Gallimore A.D., Plasma Chem. Plasma Process., 2011, **31**, 79.
25. Spencer L.F., Gallimore A.D., Plasma Sources Sci. Technol., 2013, **22**, 15019.
26. Mahammadunnisa S., Reddy E.L., Ray D., Subrahmanyam C., Whitehead J.C., Int. J. Greenhouse Gas Control, 2013, **16**, 361.
27. Chen G., Godfroid T., Britun N., Georgieva V., Delplancke M.-P., Snyders R., Appl. Catal. B. Environ., 2017, **214**, 114.
28. Kozák T., Bogaerts A., Plasma Sources Sci. Technol., 2014, **23**, 45004.
29. Blauer J.A., Nickerson G.R., Rep. Ultrasystems Inc., 1973.
30. Kutasi K., Guerra V., Sá P., J. Phys. D. Appl. Phys., 2010, **43**, 175201.
31. Silva T., Britun N., Godfroid T., Snyders R., Plasma Process. Polym., DOI: 10.1002/ppap.201600103 (2016).
32. Chen G., Silva T., Georgieva V., Godfroid T., Britun N., Snyders R., Delplancke-Ogletree M.P., Int. J. Hydrogen Energy, 2015, **40**, 3789.
33. Chen G., Georgieva V., Godfroid T., Snyders R., Delplancke-Ogletree M. P., Appl. Catal. B Environ., 2016, **190**, 115.
34. Britun N., Silva T., Chen G., Godfroid T., van der Mullen J., Snyders R., J. Phys. D. Appl. Phys., 2018, **51**, 144002.
35. Silva T., Britun N., Godfroid T., Snyders R., Opt. Lett., 2014, **39**, 6146.
36. Kirkbright G.F., Sargent M., Atomic Absorption and Fluorescence Spectroscopy. London: Academic Press, 1974.
37. Niemi K., der Gathen V.S., Döbele H.F., J. Phys. D. Appl. Phys., 2001, **34**, 2330.
38. Rosell J., Sjöholm J., Richter M., Aldén M., Appl. Spectrosc., 2013, **67**, 314.
39. Darwent D., Natl. Stand. Ref. Data Ser. Natl. Bur. Stand., 1970, **31**, 9.
40. Britun N., Godfroid T., Snyders R., Plasma Sources Sci. Technol., *In Preparation* (2018).

METAL OXIDE NANOTUBES PREPARED BY MICROWAVE-PLASMA ENHANCED CHEMICAL VAPOUR DEPOSITION FOR ADVANCED APPLICATIONS

J. R. Sanchez-Valencia,[1,2]* A. N. Filippin,[1] M. Macias-Montero,[1] F. J. Aparicio,[1] M. Alcaire,[1] M. C. Lopez-Santos,[1] V. Lopez-Flores,[1] Z. Saghi,[3] J. P. Espinos,[1] A. Barranco,[1] A. Borras[1]

[1] *Nanotechnology on Surfaces Laboratory*. Materials Science Institute of Seville (CSIC-US), C/ Americo Vespucio 49, 41092, Seville, Spain
[2] Departamento de Física Atómica, Molecular y Nuclear, University of Seville, Avda. Reina Mercedes, 41012, Seville, Spain
[3] University of Grenoble Alpes, Grenoble F-38000, France; CEA, LETI, MINATEC Campus, Grenoble, F- 38054, France

Abstract. In this work we present a step forward to the synthesis of heterostructured 1D materials such as core@shell and core@multishell nanowires and nanotubes with controlled shells composition, microstructure and porosity prepared by Microwave-Plasma Enhanced Chemical Vapour Deposition. Our approach provides a direct route for the fabrication of multi-functional nanostructures that opens the way towards the realization of single-wire devices and optimization of high-density arrays devices. Several examples will be shown for the fabrication of semiconducting organic and inorganic nanotubes and core@shell/multishell nanowires on processable substrates with advanced performances.

1. INTRODUCTION

"Nanomaterial" is a term used for those materials whose size is in the range of molecular dimensions. It is widely spread that at least one of their dimensions should be below 100 nm. Nanomaterials can be classified according to their dimensionality [1] , that can be catalogued as 0D (zero dimensional, all dimensions below 100 nm), i.e. nanodots, nanoparticles or nanoclusters; 1D (one dimensional) such as nanowires, nanorods or nanotubes; 2D (two dimensional), for example, thin films, monolayers or nanocoatings and 3D (three dimensional), where the dimensions are not in the nanoscale but the material itself is formed by lower dimensional materials such as frameworks, nanotrees or nanonetworks. Particularly, one dimensional (1D) nanomaterials have received an increasing attention during the last decades due to their wide range of applications in microelectronics, photonics, energy storage, or biomedicine, among many others [2–6]. Despite the efforts of the research community, the implementation of 1D nanomaterials in real devices still requires the study of these nanostructures from the fundamental point of view and, above all, for the research on low cost (economical and environmental) methodologies for their production in high rates with a strict control on composition, structure and microstructure [2–6].

Different types of 1D nanostructures and nanosystems are presented in Fig. 1. Starting from 1D nanomaterials composed by just one compound or element: they can present different nanostructures such as round and squared nanowires (a, b), nanobelts (c) and nanotubes (d). When the system comprised several types of materials, their arrangement in the nanostructure is crucial for the applications. One possible modulation of the material can be arranged either axially (g) or radially (h), giving rise to very different properties. These latter 1D nanosystems are referred as core@shell (or core@multishell if more than two materials are present), and are the scope of the present work. Some other examples of multicomponent 1D systems can be found in nanowires decorated with nanoparticles (e) or in branched or hierarchical nanowires (f).

This work is focused in the fabrication of 1D nanotubes (NTs) (Fig. 1d) and core@shell (core@multishell) nanostructures (Fig. 1h) by Microwave Plasma Enhanced Chemical Vapour Deposition

(PECVD). In particular, Core@shell 1D nanomaterials has been utilized for a diversity of fields, including catalysis [7, 8], solar cells [9, 10] or electronics [11], among others. The core@shell nanostructures consist of an internal 1D nanomaterial, the core, such as nanowires or nanobelts, which is surrounded by a second nanomaterial (nanoparticles, secondary nanowires, layers, etc.), known as the shell. The interest in 1D core@shell (including for extension NTs and @multishells NTs) nanostructures is twofold. On one hand, these nanostructures are foreseen to open the path to novel applications based on their inherent multi-functional character. On the other hand, it is also presumable the improving of the performance in an ample range of applications in comparison to the standard thin film approach. The advantages and unique properties of the proposed systems are Remarkably high surface area, highly interconnected networks of nanowires and compatibility with delicate substrates and flexible ones.

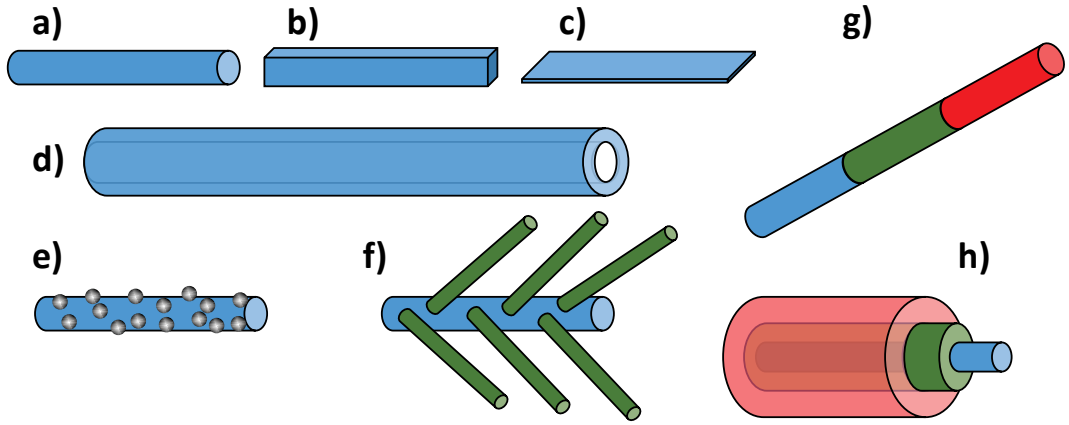

Figure 1. Some examples of 1D nanostructures. Composed by one simple material: a) cylindrical and b) square nanowire, c) nanobelt, d) nanotube. Composed by two or more nanomaterials: e) nanowire decorated with nanoparticles and f) branched / hierarchical nanowire, g) axial and h) radial junction (core@shell).

The core@shell structures used in the present work have been fabricated by a methodology that employ Organic Nanowires (ONWs) produced by Organic Physical Vapour Deposition (OPVD). These ONWs are used as templates for the fabrication of Metal Oxides fabricated by Plasma Enhanced Chemical Vapour Deposition to produce hybrid 1D core@shell (core@multishell) nanostructures. The methodology has originated an enormous field of exciting possibilities and new challenges, with promising potential in the fields of wettability, solar cells, waveguides and sensors, among others [12–17].

2. EXPERIMENTAL

2.1. Methodology. Fabrication steps

2.1.1. Organic Nanowires by OPVD. The organic precursor 2,9-dimethyl-anthra(2,1,9-def:6,5,10-d'e'f') diisoquinoline-1,3,8,10-tetraone (MePTCDI) was acquired from Sensient Imaging Technologies, and Phthalocyanine (H_2Pc) were supplied from Aldrich and used as received without further purification. The OPVD procedure for the formation of single crystal ONWs has been fully described in previous references [18, 19]. It consists of the sublimation within a high vacuum system of the organic molecules from a Knudsen cell at a pressure of 0.02 mbar of Ar using a growth rate of about 0.3 Å/s and controlled substrate temperature. The substrates temperatures were settled at ~175ºC for the Me-PTCDI and ~230ºC for the H_2Pc. The thickness of the NWs (as measured by a Quartz Crystal Monitor, providing density of 0.5 g cm^{-3}) was set to 0.65 kÅ which corresponds to NWs 2−3 μm long.

MePTCDI have been used for the growth of NWs used as templates for multishell nanostructures, while H_2Pc has been employed for the formation of anatase NTs because it withstands higher temperatures.

ONWs aimed to work as templates for the fabrication of 1D core@shell nanostructures were grown on a thin film of ZnO or TiO_2 (anatase) previously deposited by PECVD on the different substrates, providing the needed roughness for the ONWs growth (see Section 3.1).

2.1.2. ZnO and TiO_2 layers by PECVD. Both semiconducting oxides, ZnO and TiO_2, were fabricated by PECVD in a microwave (2.45 GHz) ECR reactor with a down-stream configuration. The plasma source, SLAN (Slot Antenna) was provided by the company Plasma Consult GmbH. The plasma is feed with several gases which are introduced into the chamber using the appropriate mass flow controller and the pressure of the system is varied employing a mechanical pressure control valve.

The precursors are finely dispersed just over the substrates by means of a homemade diffusor, allowing the homogeneous distribution of the metal oxide in relatively large areas (10 x 10 cm^2).

Diethylzinc ($ZnEt_2$) and titanium tetraisopropoxide (TTIP) were utilized as precursors (Sigma Aldrich). Crystalline ZnO was grown at RT with oxygen as plasma gas. Total pressure in the chamber was settled at 1.5 x 10^{-2} mbar and plasma power at 400 W. Amorphous TiO_2 layers were grown at the same conditions with a slightly lower pressure (8.6 x 10^{-3} mbar) using either pure oxygen or mixtures Ar/O_2 (90−10%). TiO_2 anatase layers were prepared as the amorphous TiO_2 (100%O_2) but heating the substrates at 250ºC using halogen lamps during the fabrication process.

2.1.3. Emptying of the 1D nanostructures. Under standard conditions a heating treatment at ca. 200 and 300ºC for MePTCDI and H_2Pc, respectively, and 10^{-6} mbar of pressure was applied to these samples for 1−3 hours to achieve a complete emptying of the inner organic core. No alteration of the vacuum was detected during the process. After the annealing process is performed, the samples were allowed to cool down in high vacuum avoiding water condensation in the highly porous nanotube walls.

2.1.4. Fabrication of the anatase stack. The stack of anatase nanotubes was produced by a consecutive deposition process. A first layer of NTs was produced growing 0.65 kÅ (QCM) of H_2Pc using an anatase thin film as seed followed by the deposition of 860 nm of anatase. This process was repeated two more times but increasing the thickness of the deposited anatase in third layer to 1.03 μm.

2.2. Characterization. Scanning Electron Microscopy (SEM) images were acquired in a Hitachi S4800 working at 2 kV. HAADF-STEM and HRTEM were carried out with both Osiris and FEI Tecnai G2F30 S-Twin STEM microscope working at 200 kV. The samples were dispersed onto Holey carbon films deposited on Cu or Ni grids obtained from Agar scientific.

EDX maps were acquired with a FEI Tecnai Osiris TEM/STEM 80-200 working at 200 kV. EDX raw data was post-processed to obtain more accurate compositional maps of the core@multishell system.

3. RESULTS

3.1. Fabrication of supported Organic Nanowires. Owing to their relevance in this work, a brief description of the growth mechanism of Organic Nanowires is summarized here. ONWs are formed by repeated small-molecules (in this work MePTCDI and H_2Pc) which are stacked along the long axis of the nanowire. This axis possesses lengths generally in the micron range, while the other two dimensions stay below 100 nm.

The growth mechanism of ONWs from this type of planar aromatic molecules is triggered by the π-stacking. This molecular interaction directs the crystallization process responsible for the growth of these 1D nanostructures. The growth mechanism of the ONWs is depicted in Fig. 2 and comprises several stages [18]: i) Presence of nucleation sites on the substrates: rough surfaces, nanoparticles, defects, etc.; ii) Flux of molecules reaching the surface in an appropriate concentration (to achieve supersaturation) and sufficient surficial molecular diffusion to reach the nucleation sites; iii) Formation of the crystal by self-assembly of the molecules directed by the π-stacking; iv) Development of the nanowire.

The role played by small-molecules in this work is critical. The molecules like perylenes, free- or metal- porphyrins and phthalocyanines has served as building blocks for the growth of ONWs that will either work as core in the hybrid core@shell nanowires or as 1D template for the formation of nanotubes.

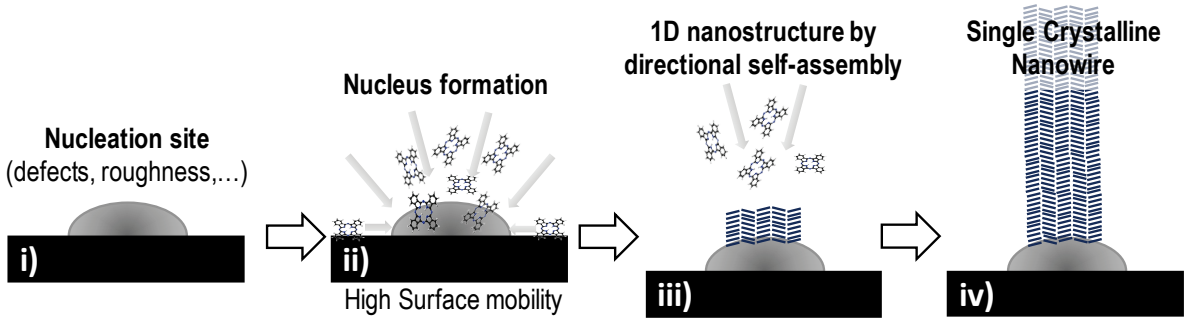

Figure 2. Stages of ONWs formation and growth [18].

3.2. 1D Core@Shell nanostructures. The methodology for the fabrication of inorganic nanotubes and more generally core@multishell 1D nanostructures involve basically 4 steps, which are shown in Fig. 3.

a) Formation of nucleation centers. As it has been detailed above, the ONWs growth is induced by the presence of nucleation sites (Fig. 2i)). In fact, the critical requirement for the substrate is to present a minimum roughness. Among the strategies followed to induce a certain roughness to the substrates are: growth of no-percolated metal layers or metal nanoparticles; plasma treatment of polymeric or organic surfaces; ablation by laser to ceramic or metallic substrates or deposition of microstructured metal oxide thin film (usually columnar). This latter strategy is the one followed in the present work.

b) Growth of supported ONWs. The formation of ONWs (Figs. 2 and 3a) is a temperature controlled physical vacuum deposition (hereafter referred as OPVD) process that allows the growth of a highly dense forest of organic nanowires, as shown in the inset of Fig. 3a [12, 20–22].

c) Formation of a metal oxide (MO_x) shell. Once the ONWs have been grown onto the substrates, the third step represents the conformal deposition by PECVD of the metal oxide (MO_x) shell (Fig. 3b)) in order to form a hybrid ONW@MO_x (core@shell). Different metal oxides have been grown by this technique, but in this work we will focus in the fabrication of TiO_2 and ZnO nanostructures. It is important to remark that the MO_x deposition by PECVD induces the vertical alignment of the nanostructures otherwise randomly oriented. This aspect will be shown below with microscopy images.

d) Evacuation of the 1D hybrid core@shell nanostructures (if required). A simple additional step can be performed to remove the organic core and obtain vertical aligned inorganic nanotubes (see Fig. 3). This step consists of the annealing under vacuum or air at a temperature of ca. 200 and 300ºC for MePTCDI and H_2Pc, respectively. One important aspect of this step is that final nanotube microstructure strongly depends on the heating ramp. The MO_x shells possess open pores connecting the inner channel of the nanotubes with the exterior. For slow heating ramps, the increased pressure induced by the sublimation of the organic core is released by diffusion of the organic molecules through the pores in a continuous and homogeneous way, producing no changes to the shell microstructure (Fig. 3, c−e). For faster heating ramps, the overpressure drives to the detachment of the tips (Fig. 3, f−h). In general, temperature ramps below than 10ºC min^{-1} lead to closed nanotubes meanwhile higher temperature ramps result in open nanotubes as it is shown in Fig. 3, e and h, respectively.

One of the main advantages of the approach developed in this work relies in the microstructural control that can be obtained for the MO_x shell deposited by PECVD. Figure 4 shows two different amorphous TiO_2 shells, that have been deposited under different PECVD conditions, particularly under pure oxygen plasma (Fig. 4, a−d) and Ar-O_2 mixture plasma (Fig. 4, e−i). It is worth to mention that the organic core has been emptied by annealing the samples in vacuum with a small heating ramp (5ºC min^{-1}). It can be observed the different characteristic porosity, columnar and mesoporous in the first case (Fig. 4, a−d) and continuous and microporous in the second one (Fig. 4, e−i). Another critical advantage of using PECVD for the formation of such hybrid nanowires and nanotubes is the vertical alignment of the final nanostructures, in which the MO_x shell is conformally covering the ONWs down to the bottom of the substrate. This effect can be observed in the overview image shown in Fig. 4i, that gives an impression about the verticality and homogeneity of the nanotubes supported on substrates. In both cases, the NTs synthesis was carried out in dowstream deposition conditions at low temperature and, therefore,

is compatible with delicate substrates. The length of the NTs can be tuned simply varying the deposition time of the ONWs, ranging between 500 nm to tens of micrometers.

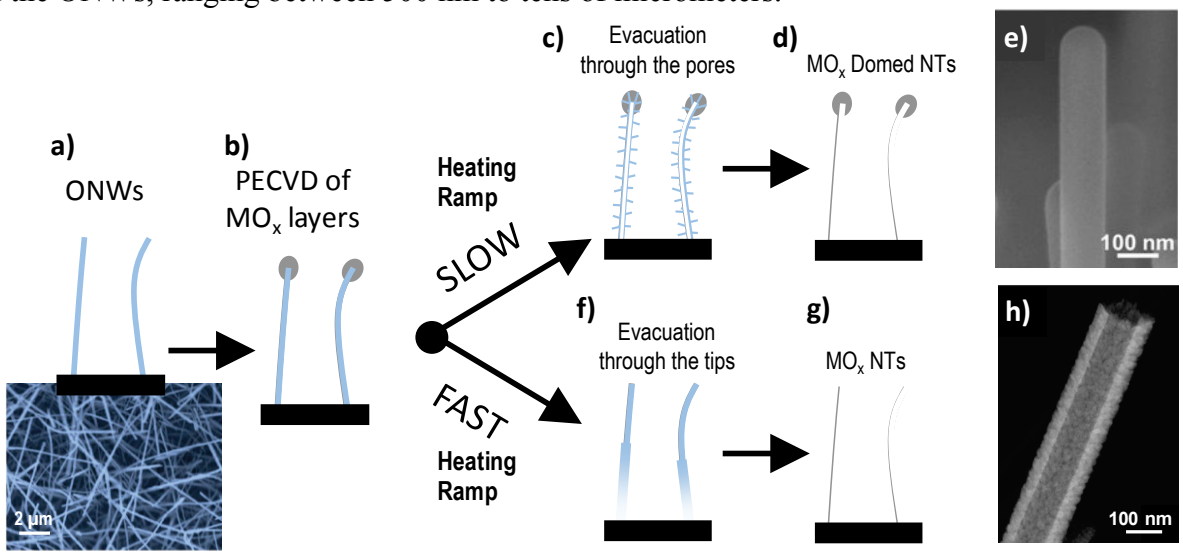

Figure 3. Schematic representation of the steps involved in the formation of the oxide nanotubes for slow (c−d) and fast (f−g) heating ramps. Microscopy images for both cases are shown at the right (e and h).

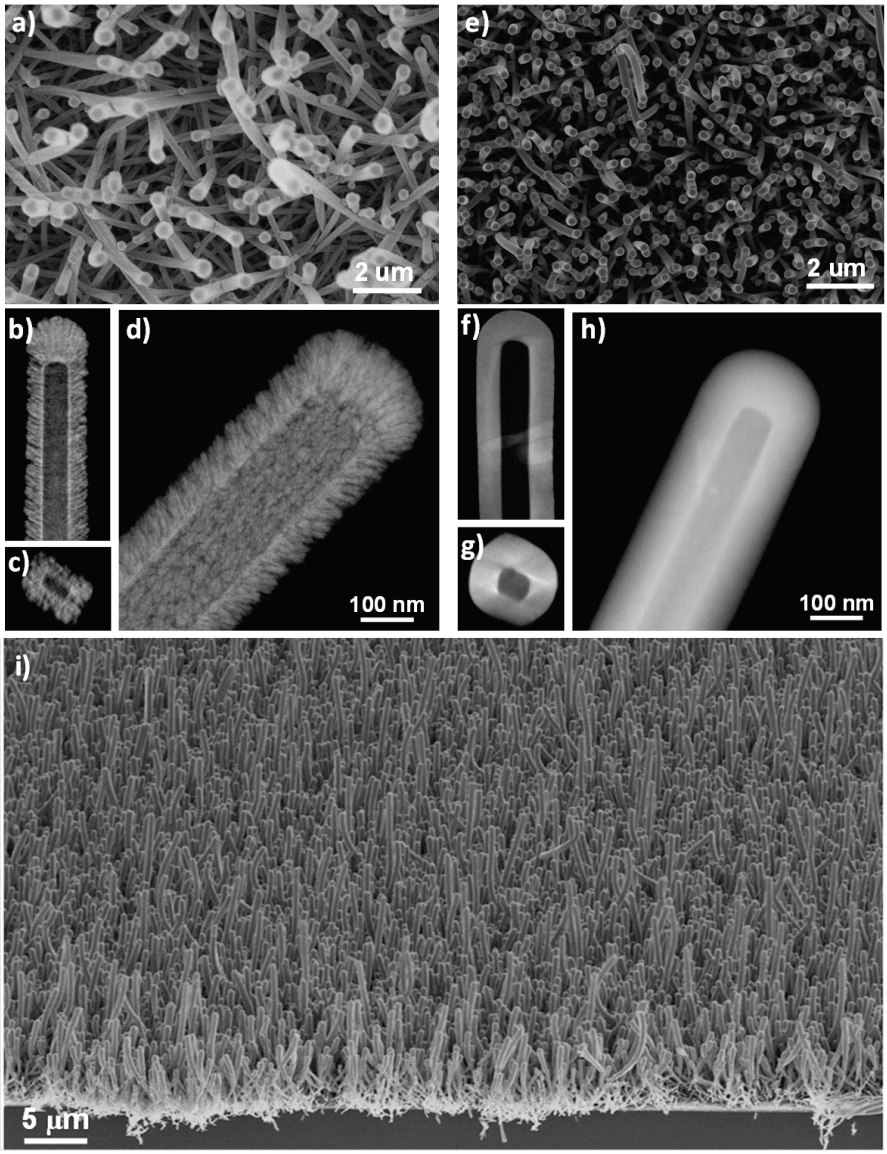

Figure 4. Columnar (a−d) and continuous (e−i) TiO_2 nanotubes. SEM (a, e, i) and HAADF-STEM (b−d and f−h) characterization of the TiO_2 nanotubes. Micrograph in b, c and f, g gather snapshots of the HAADF-STEM 3D reconstruction were the rectangular cross section of the tube is clearly appreciable.

It is also worth noting the flatness of the inner face of the nanotube (e.g. Fig. 4, b and f). The interface between the empty core and the shell kept memory of the smooth surface of the single-crystal wire template. Meanwhile, the outer surface of the NT presented the typical surface roughness of the TiO_2 layers. It is also worth mentioning that the good mechanical stability of the samples is provided by the formation of a continuous layer between the columns and the empty core (around 10 nm). This interface can be easily observed in the HAADF-STEM reconstruction in Fig. 4, b−c and f−g. These TiO_2 shells were amorphous since the fabrication process has been carried out at room temperature. As it will be shown below, the formation of the anatase crystalline films can be synthesized just by increasing the substrate temperature up to 250ºC as described in the experimental section.

It is interesting to remark several additional features of this methodology. On one hand, the thickness of the nanotubes is easily controlled by adjusting certain deposition parameters such as deposition time, chamber pressure, reagent flux, etc. Our plasma assisted deposition methodology induces a vertical alignment of the nanostructures that arises from the alignment of the hybrid nanowires along the plasma sheath electric field (see Fig. 4i). Our results are of special relevance since they open the way for a straightforward growth of these 1D nanostructures on electrodes, processable substrates and devices.

3.3. 1D Core@multishell nanostructures. The reported methodology allows the formation of coaxial multilayer systems (nanotubes with multiple walls formed by layers of different metal oxides) within the same reactor without exposing the interfaces to air. The oxides layers can be fabricated by simply alternating the different metalorganic precursors introduced in the PECVD reactor. Unlike from the previous example, our protocol can be also applied to the fabrication of coaxial crystalline shells. As an example, Fig. 5, a−b show the formation a wurtzite ZnO nanotube (the organic core has been emptied) covered by TiO_2 anatase layer. It is noticeable in the EDX maps (Fig. 5a) that even for such a low thickness (20 nm), the anatase shell is covering the whole ZnO tube, that conformally follows the roughness of the ZnO surface.

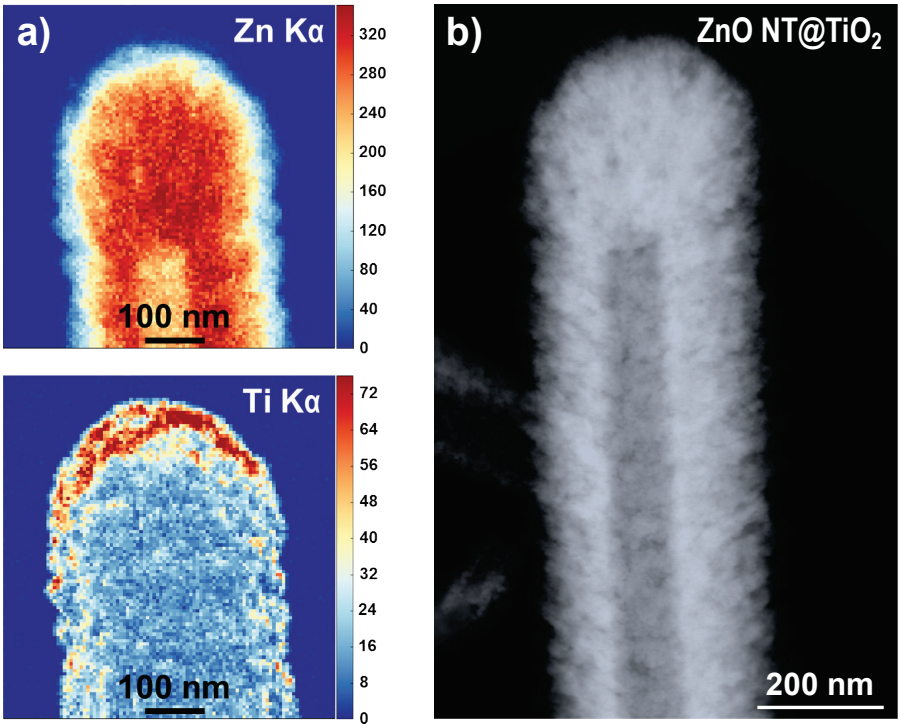

Figure 5. a) Distribution of Zn (up) and Ti (down) in the EDX maps obtained from the ZnO@TiO_2 crystalline nanotube (b).

It is worth to remark, that the example presented here represents a proof of concept about the feasibility of the reported approach to fabricate coaxial shells of different functional layers. Our methodology is straightforwardly applicable to other oxides deposited by PECVD such as Al_2O_3, SiO_2, $SiO_xC_yH_z$, Ta_2O_5, oxynitrides, etc. and even to metal layers deposited by sputtering. The universality of

our methodology and the large variety of possible synthesized materials represent a new route to the fabrication of coaxial multishell 1D nanostructures for a large number of applications, as well as their implementation in single-wire devices.

3.4. Multistack of hierarchical nanotubes. Figure 6 gathers the steps involved in the formation of a new achitecture based on a multistack of hierarchical nanotubes. The first step a) in the Fig. 6 begins from TiO_2 NTs (the previous steps for the fabrication of MO_x nanotubes are detailed in the Fig. 3), which are used as seeds for the formation of ONWs (Fig. 6b). Then, this second layer of ONWs are covered by a TiO_2 shell fabricated by PECVD (Fig. 6c). For the growth of crystalline TiO_2 by PECVD it was necessary to use previous reported conditions for the formation of anatase layers [23], which required a temperature of 250ºC. This value is close to the sublimation temperature of the H_2PC molecules located in the core and would eventually lead to the sublimation and evacuation of the organic molecules. To overcome this drawback, an initial TiO_2 shell of about 50 nm was deposited at 150ºC to preserve the 1D organic scaffold and then gradually increase the temperature to 250ºC during the deposition. In this way, the growth of the anatase shell occurs at the same time that the organic core evacuation, producing domed-nanotubes (Fig. 3, c−f). The SEM images of the Anatase NTs synthesized are shown in Fig. 7, a−c. It can be observed the numerous sub-crystals emerging from each NT that resembles a feather, thus giving rise to a hierarchical nanotube. Unlike the previous examples, the diameter of the NTs was not uniform, appearing thicker at the top and gradually thinner towards the interface with the substrate (Fig. 7a). Such characteristic is due to a shadowing effect occurring during the growth of the shell and it is more prominent here owing to the bigger diameter of the NTs [24].

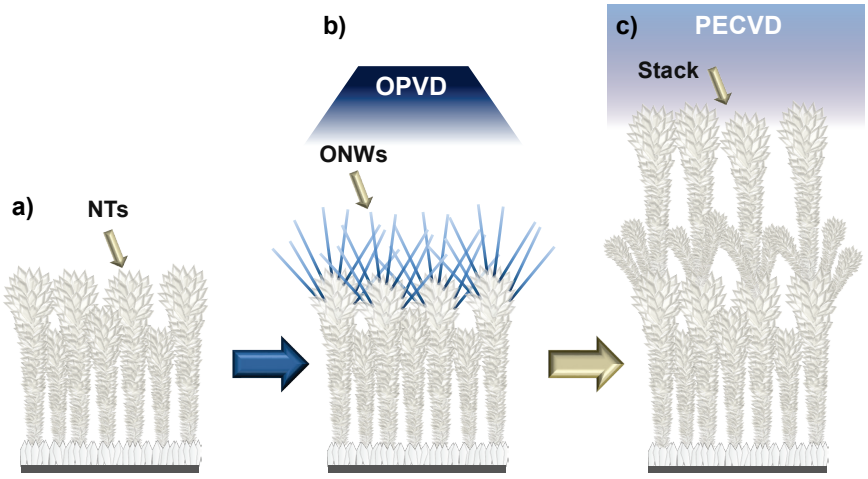

Figure 6. Schematic representation of the different steps in the multistacked nanotubes fabrication, starting from a) TiO_2 nanotubes, then b) secondary growth of ONWs on the NTs and c) reiterative reproduction to form a multistack.

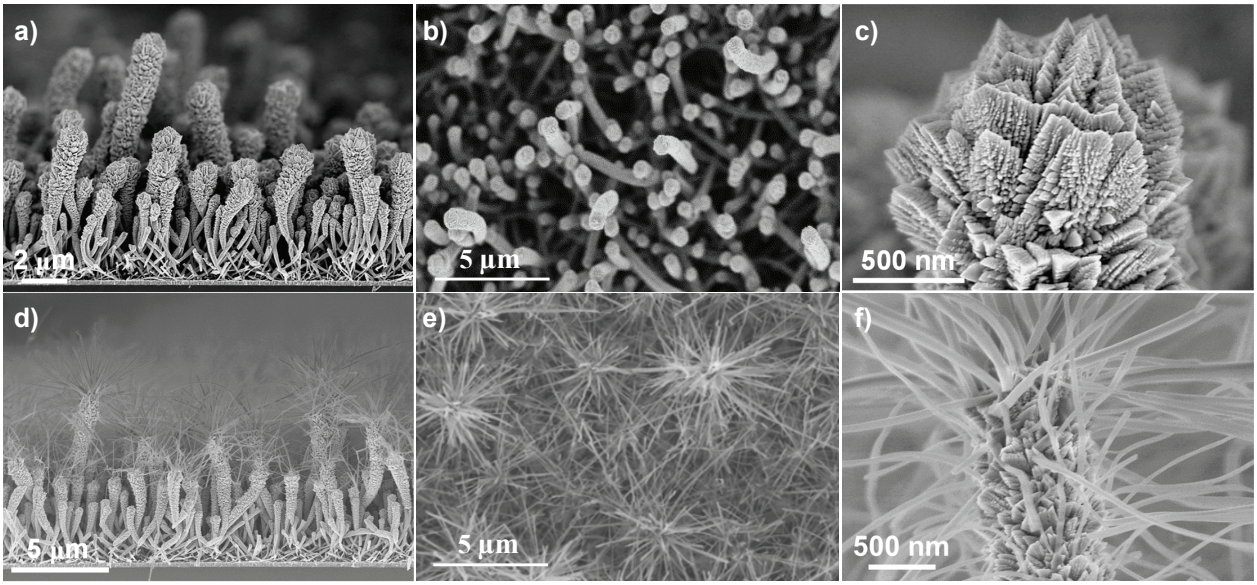

Figure 7. a) Characteristic cross-section (a, c, d, f) and top view (b, e) SEM images of the hierarchical TiO_2 NTs (a−c) and the formation of H_2Pc ONWs using the previous NTs as seed layer (d−f).

As mentioned before, the formation of 3D nanoarchitectures represent an important advance in the development of multifunctional nanomaterials for many different applications, for example in energy harvesting [25–27]. To show the potentiality of the reported approach, we propose here a new type of 3D architecture. As it can be observed in the Fig. 8a it consists on the stack of anatase hierarchical NTs layers synthesized as detailed in the Fig. 6, b and c. The idea is simple and consists in the use of the as-grown NTs as nucleation sites for the formation of secondary organic nanowires (see Fig. 6b). Due to geometrical restrictions, the secondary ONWs grow preferentially at the tips of the hierarchical NTs forming nanotrees, as can be observed in the Fig. 7, d−f. The next step (Fig. 6c) consists of the formation of an anatase layer that covers conformally these secondary ONWs. By the repetition of the steps b−c in Fig. 6, we have fabricated a three-layers multistack sample as it can be seen in Fig. 8a. The equivalent thin film synthesized without using ONWs templates is shown in the inset of Fig. 8a and present a total equivalent thickness of 2.75 um. It is worth to stress the huge surface area of the multi-stacked architecture presented (in comparison with the equivalent thin film with 2.75 um, the multistack possesses a thickness of 16 um), provided by the open gaps between the NTs and the internal porosity of the hierarchical NTs.

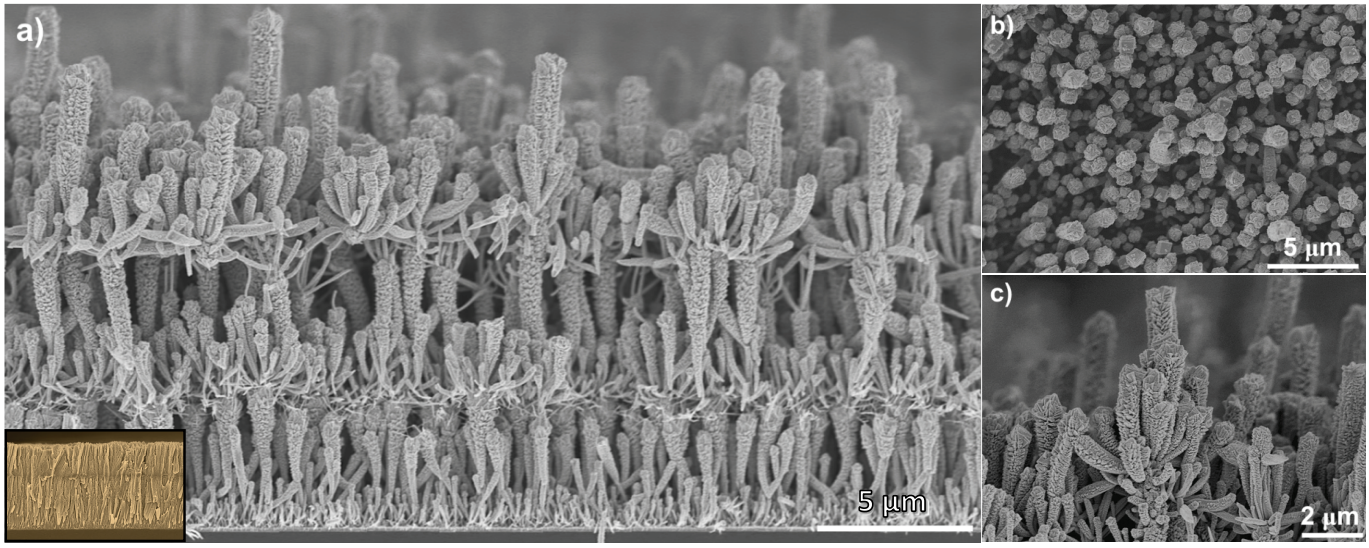

Figure 8. SEM cross sections of the complete stack of anatase hierarchical NTs (a) and a bundle of HNTs in the third layer (c). Normal view of the stack (b). The inset in a) is a SEM cross section of the equivalent thin film (without ONW template) of the complete stack, with the same scale bar than the stack shown in a).

The straightforward extension of our methodology to the growth of plasma assisted deposited functional shells with tailored nanostructures and properties will certainly lead to the development of a new generation of 3D nanoarchitectures with important applications in energy harvesting and storage, catalysis or sensing, among many others.

4. CONCLUSIONS

A reliable full vacuum and plasma methodology based on the use of supported ONWs as templates for the fabrication of metal oxide nanotubes with single and multishell configurations has been presented. The versatility of the plasma techniques such as PECVD for the growth of metal oxide thin films has been exploited here for the formation of nanostructured nanotubes with tailored shells in terms of microstructure, porosity, structure and thickness.

The procedure provides hollow's cross sections, keeping memory of the flat surface of the organic single crystal used as templates. Either closed or open nanotubes can be fabricated by selecting the evacuation conditions of the organic core. A completely new architecture based on a stack of hierarchical anatase nanotubes with extremely high surface-area has been developed.

It has been demonstrated that the method provides a straightforward way for the growth of supported nanotubes on an ample variety of substrates. Contrary to other template protocols, the ONWs used herein as 1D scaffolds are easily removed by annealing at mild temperature, avoiding the use of etching processes or solvents. It is also important to stress that the nanotubes remained attached to the substrates after the evacuation process and were mechanically stable.

The results provided here pave the way toward the implementation of our core@multishells and multistack systems in real devices for applications such as energy harvesting, conversion and storage, photonics, catalysis and sensing, among many others.

References

1. Sajanlal P.R., Sreeprasad T.S., Samal A.K., Pradeep T., Nano Rev., 2011, **2**, 5883.
2. Weber J., Singhal R., Zekri S., Kumar A., Int. Mater. Rev., 2008, **53**, 235.
3. Han N., Ho J.C., Nanocrystalline Materials (Second Edition). Oxford: Elsevier, 2014, p. 75.
4. Tian J., Zhao Z., Kumar A., Boughton R.I., Liu H., Chem. Soc. Rev., 2014, **43**, 6920.
5. Wei Q., Xiong F., Tan S., Huang L., Lan E.H., Dunn B., Mai L., Adv. Mater., 2017, **29**, 1602300.
6. Barth S., Hernandez-Ramirez F., Holmes J.D., Romano-Rodriguez A., Prog. Mater. Sci., 2010, **55**, 563.
7. Wei H., Wang L., Li Z., Ni S., Zhao Q., Nano-Micro Lett., 2011, **3**, 6.
8. Hasan M., Newcomb S.B., Razeeb K.M., J. Electrochem. Soc., 2012, **159**, F203.
9. Adachi M.M., Anantram M.P., Karim, K.S. Sci. Rep. 2013, 3, 1546.
10. Tamang, A., Pathirane, M., Parsons R., Schwarz M.M., Iheanacho B., Jovanov V., Wagner V., Wong W.S., Knipp D., Opt. Express, 2014, **22**, A622.
11. Dong Y., Yu G., McAlpine M.C., Lu W., Lieber C.M., Nano Lett., 2008, **8**, 386.
12. Macias-Montero M., Filippin A.N., Saghi Z., Aparicio F.J., Barranco A., Espinos J.P., Frutos F., Gonzalez-Elipe A.R., Borras A., Adv. Funct. Mater., 2013, **23**, 5981.
13. Filippin A.N., Sanchez-Valencia J.R., Idígoras J., Macias -Monter Espinos J.P., Lopez-Santos C., Frutos F., Barranco A., Anta J.A., Borras A., Adv. Mater. Interfaces, 2017, **4**, 1601233.
14. Filippin A.N., Macias-Montero M., Saghi Z., Idígoras J., Burdet P., Barranco A., Midgley P., Anta J.A., Borras A., Sci. Rep., 2016, **6**, 20637.
15. Filippin A.N., Sanchez-Valencia J.R., Idígoras J., Rojas T.C., Barranco A., Anta J.A., Borras A., Nanoscale, 2017, **9**, 8133.
16. Burdet P., Saghi Z., Filippin A.N., Borrás A., Midgley P.A., Ultramicroscopy, 2016, **160**, 118.
17. Filippin A.N., Macias-Montero M., Saghi Z., Idígoras J., Burdet P., Sanchez-Valencia J.R., Barranco A., Migdley P.A., Anta J.A., Borras A., Sci. Rep., 2017, **7**, 9621.
18. Borras A., Gröning O., Aguirre M., Gramm F., Gröning P., Langmuir, 2010, **26**, 5763.
19. Mbenkum B.N., Barrena E., Zhang X., Kelsch M., Dosch H., Nano Lett., 2006, **6**, 2852.
20. Borras A., Gröning O., Köble J., Gröning P., Adv. Mater., 2009, **21**, 4816.
21. Oulad-Zian Y., Sanchez-Valencia J.R., Parra-Barranco J., Hamad S., Espinos J.P., Barranco A., Ferrer J., Coll M., Borras A., Langmuir, 2015, **31**, 8294.
22. Borras A., Gröning P., Sanchez-Valencia J.R., Barranco A., Espinos J.P., Gonzalez-Elipe A.R., Langmuir, 2010, **26**, 1487.
23. Borras A., Sanchez-Valencia J.R., Widmer R., Rico V.J., Justo A., Gonzalez-Elipe A.R., Cryst. Growth Des., 2009, **9**, 2868.
24. Moore K., Clemons C.B., Kreider K.L., Young G.W., J. Appl. Phys., 2007, **101**, 064305.
25. Zhang Z., Li A., Cao S.-W., Bosman M., Li S., Xue C., Nanoscale, 2014, **6**, 5217.
26. Zou X., Wang J., Liu X., Wang C., Jiang Y., Wang Y., Xiao X., Ho J.C., Li J., Jiang C., Fang Y., Liu W., Liao L., Nano Lett., 2013, **13**, 3287.
27. Cheng C., Fan H.J., Nano Today, 2012, **7**, 327.

H^- NEGATIVE ION PRODUCTION IN MICROWAVE-DRIVEN DISCHARGES: PRINCIPLES AND DIAGNOSTICS

P. Svarnas[1], S. Béchu[2], A. Lacoste[2], S. Aleiferis[1,2,3]

[1]University of Patras, Electrical and Computer Engineering Department, High Voltage Laboratory, 26504 Rion – Patras, Greece
[2]LPSC, Université Grenoble-Alpes, CNRS/IN2P3, 53, Avenue des Martyrs, F-38026, France
[3]Current address: a) EUROfusion Consortium, JET, Culham Science Centre, Abington, OX14 3DB,UK, b) Fusion Technology Group, National Centre for Scientific Research "Demokritos", 15310 Aghia Paraskevi, Athens, Greece

Abstract. Next generation fusion reactor operation is based on neutral beam injection systems for the heating and current drive of fusion plasmas. These systems should produce hydrogen or deuterium beams with particle energies in the excess of 1 MeV. In this energy range, the gas cell neutralization efficiency remains acceptable only for negative ion neutralization, whereas it becomes negligible for positive ions. Furthermore, hydrogen negative ions may be employed in linacs, cyclotrons, synchrotrons, medical fields, material characterization or other applications. Accordingly, in the present work, H^- negative ions are produced in ECR-driven sources (2.45 GHz) developed by our group. The concept refers to Cs-free sources where negative ions are formed through the dissociative attachment reaction. In this case, the reactants are low-energy electrons and highly (ro)vibrationally excited molecules. The production of these excited molecules is considered, taking into account collisions with high-energy electrons and surface reactions like recombinative desorption. In view of the above concept, microwave plasmas in these ECR sources are appropriately characterized by conventional Langmuir probes, vacuum ultra-violet and visible emission spectroscopy, while more sophisticated diagnostics are also introduced. The latter include laser photo-detachment technique for measuring the absolute densities of H^- ions and synchrotron-radiation absorption for detecting highly excited molecular states. Results obtained by our group are presented and discussed.

1. INTRODUCTION

Hydrogen negative ions H^- are important in astrophysics, particle accelerators, medicine, material characterization, and particularly nowadays in fusion science where they are being accelerated and then neutralized to form high energy atom beams for heating fusion plasmas. Presently, efficient negative ion formation relies on the so-called surface production process, i.e. the surface ionization of hydrogen atoms and positive ions [1]. This process requires evaporation of cesium in order to reduce the work function of the production surface [1]. Even though the use of cesium allows negative ion sources to reach fusion-oriented specifications [2], it is related with a variety of problems including difficulties in maintenance and unstable operation [3]. Thus, avoiding cesium usage would be highly beneficial.

Another efficient process for producing negative ions in hydrogen discharges is related to the bulk of the plasma, where the so-called volume production mechanism takes place. The operation of volume production negative ion sources is based on the consideration of both formation and destruction mechanisms. While different processes might be responsible for the volume production of negative ions [4], the main negative hydrogen ion formation path in pure hydrogen plasma is the electron dissociative attachment (DA) to highly (ro)vibrationally excited molecules [1], i.e.

$$H_2(v'') + e \text{ (low energy)} \rightarrow H^- + H \quad (1)$$

Dissociative attachment to vibrationally excited cold molecules $H_2(v''=0)$ is known to have very small cross section (10^{-21} cm^2), while it increases by five orders of magnitude when the hydrogen molecules are vibrationally excited from v''=0 to v''=5 and stay constant at higher v''. An important feature discovered [5] is that the dissociative attachment cross sections peak at an energy threshold and this threshold goes

down when v" goes up. This implies that low-energy (cold) electrons can be very effective in generating H^- ions by DA.

Obviously, it is essential to generate sufficient density of highly vibrationally excited molecules, which are the precursors of H^- (Reaction 1), and for this generation high-energy (hot) electrons are needed according to the following statement (see Reaction 3). Vibrational excitation of molecules in collisions with cold electrons through the H_2^- resonance [6, 7]

$$H_2(v") + e(\text{low energy}) \rightarrow H_2^- \rightarrow H_2(v"+\Delta v") + e \quad (2)$$

is very effective in changing the vibrational state, but the most probable change in v" is $\Delta v" = \pm 1$, so a high collision rate would be required to significantly populate the $H_2(v")$ spectrum. An effective way for highly vibrationally excited molecule formation refers to radiative decay from singlet states excited by collisions of ground state molecules with hot primary electrons [7, 8]

$$e + H_2(X, v"=0) \rightarrow e + H_2^*(B, C, ...) \text{ followed by } H_2^*(B, C, ...) \rightarrow H_2(X, v") + hf \quad (3)$$

The electron excitation cross sections leading from v"=0 of the ground state, through the B and C singlet states, to higher v" levels of the ground state, show that the last reaction is efficient when the electron energy exceeds approximately the 20 eV [8].

According to the aforementioned processes, favorable conditions for DA may be obtained in negative hydrogen ion sources by spatially separating the plasma chamber into driving region and magnetic field-free H^- formation region. This is achieved by means of magnetic or electrostatic filters, with the first one being the preferred choice. Hot electrons are trapped in the magnetic field lines of the driving region and sustain the molecular excitations, while cold electrons being diffused in the magnetic field-free region are attached to the highly vibrationally excited molecules and, hence, form H^- through DA.

Two other vibrational excitation processes for $H_2(v")$ formation, related to plasma particle interaction with surfaces have also been identified: (i) production of vibrationally excited molecules due to the recombination and dissociation of molecular hydrogen ions on walls [9] and (ii) production of a wide spectrum of vibrationally excited molecules in the recombinative desorption process of atomic hydrogen on some metal surfaces [10]

$$H^o + H^o + \text{Wall} \rightarrow H_2(v") + \text{Wall} \quad (4)$$

This reaction can be of three generic types: (i) Langmuir-Hinshelwood which involves mutual reactions between already absorbed atoms onto a surface, (ii) Eley-Rideal during which a gas-phase particle incident on a substrate combines with a particle adsorbed onto that substrate [11] and (iii) hot-atom reactions induced by the fact that many of the incident atoms are trapped onto the surface without reacting, forming hot atoms which then diffuse across the surface, possibly reacting at a later time [11].

Contrary to surface production-based sources, volume production sources operate with pure hydrogen, having the practical advantage of inherently cesium-free operation, which makes them an attractive choice. However, as it becomes obvious from the above discussion, DA is very sensitive to both electron energy and molecule vibrational distributions, which in turn may be affected by a variety of parameters. Thus, appropriate diagnostic techniques for probing H^- ions, electron energy distributions and molecule vibrational distributions are imperative and the corresponding ones applied by our group are discussed below.

At the same time, H^- ions have low electron affinity (0.75 eV) and thus collisions in the bulk of the plasma with a variety of particles may destroy them. There are, however, three processes of primary importance: a) mutual neutralization (MN) during collisions with positive ions (Reaction 5), b) collisions with neutral particles from which the associative detachment (AD) (Reaction 6) is the most prominent for cold plasmas and c) electron detachment (ED) (Reaction 7) during collisions with energetic electrons.

$$H^- + H^+, H_2^+, H_3^+ \rightarrow H\ldots \quad (5)$$

$$H^- + H \rightarrow H_2 + e \quad (6)$$

$$H^- + e \rightarrow H + e + e \quad (7)$$

Reaction (5) has a total rate coefficient which is about $1.3x10^{-7}$ $(300/T_g)^{1/2}$ for the H^+ positive ion, $1.0x10^{-6}$ $(300/T_g)^{1/2}$ for the H_2^+ positive ion and $1.0x10^{-6}$ $(300/T_g)^{1/2}$ for the H_3^+ positive ion [12, 13]. The rate coefficient of Reaction (6) is approximately $1.3x10^{-9}cm^3s^{-1}$ [13] and finally the loss rate due to Reaction (7) needs to be calculated using the available cross section [14] and the estimated or measured electron temperature. In the above references T_g stands for the gas temperature. Gas temperature refers here to the translational temperature of the species that participate in each reaction. Furthermore, it is reminded that the reaction rates depend as well on the species densities.

In the present work, and in agreement with the above fundamental principles, results from Electron Cyclotron Resonance (ECR) driven different reactors are presented and commented. The study employs a combination of diagnostics including electrostatic probes, laser photo-detachment, visible and vacuum ultra-violet (VUV) emission spectroscopy, VUV irradiance, and synchrotron-radiation absorption measurements.

2. ECR MODULES AND DRIVEN REACTORS

2.1. ECR modules. For the experimental setups considered in this work, the electrical power is delivered into the plasma by elementary ECR modules [15]. This type of power delivery was firstly proposed for negative ion sources by our group [16−20], instead of traditional filament-based sources [21−24]. The drawbacks of the filament limited lifetime due to heating and the undesirable material deposition on the source walls due to filament evaporation are thus overcome. Furthermore, the microwave (MW) power is generated either by a conventional magnetron following power division to the modules or by a solid state generator (2.45 GHz; 0−200 W per generator) for each module. By the latter way, a higher flexibility is achieved since each generator is digitally controlled independently.

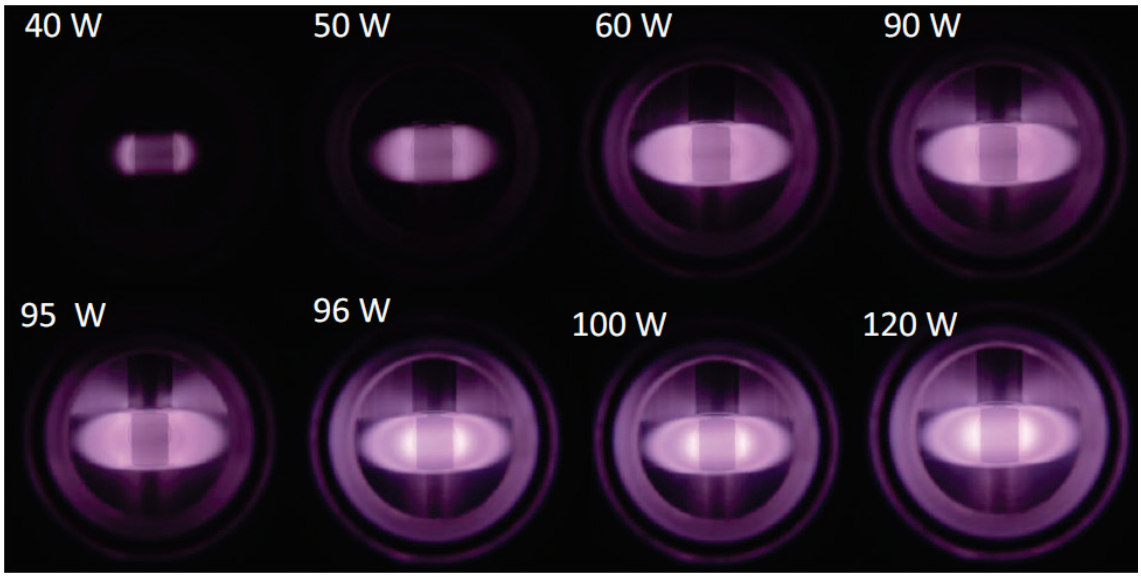

Figure 1. Representative images of a single ECR module driven at different MW power levels. The hydrogen pressure is maintained constant at 4 mTorr. The images are captured during the operation of the "Prometheus I" reactor [4, 26, 27] which houses five identical ECR modules (in the above images only the central one is activated).

The design for each ECR module is based on multi-dipolar plasma principles [15]. Each module is made up of two main parts: (i) a permanent magnet (875 G to fulfill the ECR condition) with an azimuthal symmetry around its magnetization axis and (ii) a microwave applicator constituted by a coaxial line parallel to the magnetization vector and opened on the rear pole of the magnet (ECR coupling zone). In the design proposed, the inner conductor of the coaxial line penetrates inside the cylindrical magnet through a hole drilled on its axis. Numerous modules may be combined to form 2D networks of magnetic dipoles and they are practically a first magnetic filter for the high energy electrons mentioned above [20]. Thus, hot electrons are trapped in the ECR zones sustaining the vibrational

excitations, whereas cold electrons escape downstream of the ECR zones and are attached to the highly vibrationally excited molecules which diffuse away from the magnetic filters, producing, eventually, H^- ions by DA. A tuner embedded on the main body of each module, is used for impedance matching which maximizes the microwave power absorbed by the plasma [25]. The impedance matching is manually optimized in order to reduce microwave power reflection (maximum acceptable value <3%). The ECR modules and their power supplies are cooled by water which is circulated by a water-cooling system. Figure 1 provides indicative aspects of the visible ECR zones formed in pure hydrogen around a module for various MW power levels (see caption for details).

2.2. ECR-driven reactors. In the present work, key results from three different reactors are presented and discussed with respect to H^- ion production in ECR discharges.

The first one is "Prometheus I" which is presented in detail in Refs. [4, 26, 27]. Briefly, it consists of a cubic (24 cm inner edge) stainless steel chamber with the necessary viewports for plasma diagnostics. The plasma is sustained by a 2D network of five ECR elementary modules, with four of them installed at the vertices and one at the center of an imaginary square on the top flange of the high vacuum cubic chamber (see Fig. 1 of Ref. [26]). The power supply for each ECR module is of solid state type. A turbo-molecular pump adapted under the bottom flange evacuates the chamber down to about 10^{-6} Torr. Pure H_2 (N50) is introduced by a digital mass flow controller at a flow rate between 2.1 and 23.2 sccm. The working pressure varies respectively between 1 and 20 mTorr (filling gas pressure), and it is accurately monitored with an absolute pressure transducer. The discharge is operated with flowing neutral gas with a typical duration for a complete gas renewal being approximately 0.5−1 s, typically exceeding the characteristic equilibration times in the plasma. Therefore, the only effect that the continuous gas flow has on the stationary plasma equilibrium is to prevent impurities from building-up [28].

The second one is the "Camembert III" reactor [24], where historically the ECR modules were tested for the first time to yield H^- ions [16].The inner wall of the cylindrical stainless-steel chamber is 44 cm in diameter and 45 cm high. This wall has twelve openings for windows, probe holders etc. Sixteen columns of samarium-cobalt magnets (with a surface magnetic field of 3500 G) are installed on the wall with the north and the south poles alternatively facing the plasma, forming a multi-cusp configuration. These magnets are contained in water cooled stainless-steel tubes (2.6 cm diameter) welded to the internal surface of the reactor to allow steady-state high-power discharge operation. The plasma diameter is therefore about 38.8 cm. The end plates are not magnetized. One end of the chamber is bounded, in part, by the stainless-steel plasma electrode of the extractor [29]. On the top flange a two-dimensional network of seven elementary independent ECR modules is installed (six of them on the periphery and one at the center of an imaginary cycle of 16.2 cm in diameter; see Fig. 1 of Ref. [16]). A conventional magnetron is used (max 1 kW) and the MW power is equally distributed among the seven modules. The plasma is produced under continuous pumping and gas flow conditions. The pumping of the negative ion source should ensure a high gradient between the source and the extractor where the pressure should be as low as possible. For this, a turbo-molecular pump (1000 l s^{-1}) connected to the source through the extractor and the extraction aperture is employed. To improve the residual pressure in the source, a small turbo-molecular pump (50 l s^{-1}) is installed directly on a wall opening.

Finally, "ROSAE III" [30] is a new chamber for fundamental studies on H^- negative ion volume production assisted by surface mechanisms. It has been designed to overcome a difficulty which arises in the above chamber Camembert III when plasma-surface interactions have to be investigated. The large volume of Camembert III is optimized for H^- ion production via DA. However, in studying surface mechanisms, a large surface of the investigated material compared to the other plasma facing surfaces is mandatory. Hence, the volume of ROSAE III has been chosen to be 0.02 m^3 (versus 0.3 m^3 of Camembert III) to allow the possibility of studying the contribution of small sample surfaces to H^- volume production. There are no magnets installed around the wall surface. A network of four ECR modules is installed on the top flange on an imaginary circle of 7.6 cm in diameter (or alternatively just one at the center of the top flange).The network is driven from a central magnetron of 1.2 kW (2.45 GHz) by dividing its power into four equal parts. The axial distance, on the chamber symmetry axis, between the mid-plane of the ECR modules and the studied plasma is similar to that of Camembert III.

3. DIAGNOSTICS RELATED TO H^- NEGATIVE ION PRODUCTION

3.1. Electrostatic probes. Conventional Langmuir-type probes are used, under certain assumptions, for evaluating fundamental parameters in the low-pressure hydrogen ECR discharges.

As regards results in Prometheus I, a cylindrical electrostatic probe is immersed in the plasma [27]. The probe is made from a 0.025 cm in diameter tungsten wire and the tip (exposed to the plasma) is L-bent in order to be aligned with the laser beam for the photo-detachment measurements (see below). The tip is 1.5 cm in total length with the bent part being 1.1 cm. The rest of the wire is housed in a telescopic configuration of dielectrics (alumina tube inside a wider quartz tube) that insulates and protects it from the plasma. The quartz tube is supported inside a stainless steel tube that ends in a standard BNC vacuum feed-through. A CF flange-to-quick connect coupling adapter makes a vacuum joint with the steel tube and at the same time allows the linear translation of the probe. The acquisition of electrostatic probe current-voltage (I-V) curves is accomplished with a custom-made system [31]. Each measurement procedure includes 10 s of probe cleaning by electron current-induced incandescence followed by another 10 s of cooling-down. The acquisition is realized point-by-point in steps of approximately 100 mV. For each point 2^{12}–2^{13} voltage-current samples are averaged in order to reduce plasma-induced noise. At the probe position, the magnetic field of the ECR modules has vertical downward direction and a magnitude of 51 Gauss, while the probe tip itself is oriented horizontally (i.e. perpendicular to the magnetic field). The lowest electron temperature observed during the present experiments is about 0.5 eV which corresponds to an electron Larmor radius of about 0.034 cm. Thus, even in the worst case, the probe radius (0.0125 cm) is sufficiently smaller than the electron Larmor radius, validating the use of the "classical" non-magnetized probe theory. Typical plasma parameters, i.e. floating and plasma potential, electron densities and temperatures, are obtained from numerical treatment and fitting procedures on the I-V curve data [31]. More specifically, plasma potential is estimated at the maximum of the I-V curve first derivative and positive ion current is linearly extrapolated from high retarding potentials and subtracted from the I-V curve. The remaining current (electron current) is fitted as the sum of two exponentials, which corresponds to a bi-Maxwellian Electron Energy Distribution Function (EEDF). The experimental EEDF is derived from the second derivative of the probe total current (Druyvesteyn method).

Similarly, in Camembert III an electrostatic probe made from tungsten wire of 0.05 cm in diameter is mounted on a three-axis manipulator installed on a wall opening [16, 20]. A 1.5 cm L-bent tip is exposed to the plasma, with the rest shielded by a ceramic cylinder. The tip is cleaned by regularly applying a sufficiently high positive voltage so as to cause tungsten incandescence. Current samples are averaged to reduce the effect of random noise, through a custom computer-based system. The present results are obtained in the central magnetic field-free region of the chamber.

In ROSAE III [30], measurements of plasma parameters are carried out with two L-bent Langmuir probes of similar dimensions (0.034 cm in diameter/1.77 cm long & 0.037 cm in diameter/0.98 cm long). The first one is used for photo-detachment measurements (see below) and the second one just for probe measurements. Three dimensional calculation of the magnetic field provide the **B** field components in the mid plane (xOy) of the ECR modules on the chamber axis (Oz): $B_x = B_y = 0.0035$ T and $B_z = 0.001$ T. Therefore, the probe tip has been oriented on the source axis (Oz) for being perpendicular to the main components of **B** (B_x and B_y). Measurements do not suffer from magnetic field perturbations or Bohm's criterion modification [30].

3.2. Laser photo-detachment. The photo-detachment diagnostic technique with one laser beam is used for the determination of the negative ion absolute density. Details on this technique may be found in Ref. [32].

In Prometheus I, a short (~5 ns) Nd:YAG 1064 nm laser pulse, generated from a 330 mJ (max) per pulse unit, is concentrically aligned with the bent part of the probe tip and detaches the extra electron of negative ions inside the irradiated cylindrical volume. The excess (i.e. photo-detached) electrons, in the section of the irradiated volume that contains the bent part of the probe tip, sharply increase the electron current collected by the positively biased probe. A photo-detachment current pulse is thus produced. The

density of negative ions can then be calculated from the amplitude of the current pulse as explained in Ref. [32]. A wideband current transformer (400 Hz - 250 MHz), connected directly to a digital oscilloscope (1 GHz; 5 GSamples s^{-1}), is used to measure the transient current pulse due to the photo-detached electrons. Various parameters of the photo-detachment diagnostic technique are properly set for its valid application. Firstly, the laser radius is chosen to be 0.3 cm which sufficiently exceeds the probe collection radius (~0.01 cm which is the typical Debye length for the present experimental conditions). Secondly, the probe bias has been set to +15 V (i.e. 7−8 V above plasma potential) which is sufficient for collecting all the detached electrons without causing the incandescence of the probe tip due to electron current. To establish this, a series of measurements was realized which demonstrated that a +15 V bias leads to the saturation of the photo-detached electron current. Lastly, the energy density of the laser beam is chosen to be around 70 mJ cm^{-2} which is high enough to destroy all the negative ions in the irradiated volume. This is ensured by the saturation of the photo-detachment signal while the latter is being recorded versus the increasing laser power density.

In the same context, in Camembert III, a Nd:YAG laser (repetition rate 10 Hz; photon energy 1.2 eV) is used to illuminate the plasma through a 0.6 cm diaphragm, and the photo-detached electrons from the H^- ions are collected by the aforementioned probe oriented coaxially to the laser beam. The probe is positively biased at +30 V with respect to the chamber wall. The probe transient current, which is generated by the collected photo-detached electrons, is recorded on a digital oscilloscope (500 MHz; 2 GSamples s^{-1}), operating in averaging mode, via capacitive decoupling.

Similarly in ROSAE III, a 1064 nm Nd:YAG laser (150 mJ per pulse; pulse width ~6 ns; repetition rate 50 Hz) is employed. The probe is positively biased at +25 V and the diameter of the illuminated volume is 0.4 cm. The photo-detached electron current is monitored by the L-bent probe described above, through capacitive decoupling, on a digital oscilloscope (400 MHz; 2.5 GSamples s^{-1}).

3.3. Visible emission spectroscopy. Optical emission spectroscopy is employed for the evaluation of the atomic and molecular absolute densities under various operating conditions. The process demands the estimation of the atomic temperature, the molecular temperature and the degree of dissociation. Details on the process during its application in Prometheus I may be found in Ref. [27]. The emissions of interest, in the visible range, are the Balmer series (H_α: transition n = 3 → n = 2 and H_β: transition n = 4 → n = 2) of atomic hydrogen and the molecular Fulcher-α band (triplet transition $d^3\Pi_u \rightarrow a^3\Sigma_g^+$). Accordingly, a motorized monochromator having focal length of 100 cm is used. It is equipped with a holographic grating (170−750 nm; 2400 grooves mm^{-1}). Absolute wavelength calibration is realized with an Hg(Ar) pencil-style lamp. The light is efficiently guided into the monochromator with an optical fiber adapted on an optical matcher and detected by an electron photo-multiplier tube (185−900 nm). In order to collect the light mainly from the bulk plasma, a bi-convex lens is used to focus the light from the center of the chamber into the entrance of the optical fiber. The lens is adapted inside a telescopic tube. The measured spectra are calibrated in terms of relative intensity. This is achieved by employing a quartz-tungsten-halogen lamp (3300 K color temperature). Similarly, visible emission spectroscopy is employed in ROSAE III (details in [33]).

3.4. VUV emission spectroscopy and VUV irradiance measurements. Discussion on the H^- ion production mechanisms requires information on the vibrational distribution function (VDF). The measurement of VDF would require absorption spectroscopy techniques which were not available in Prometheus I. Alternatively, VUV emission measurements may lead indirectly to reliable data for supporting such a discussion. Towards this direction, a VUV spectrometer and the irradiance meter described in detail by Komppula et al. [34], were both used in Prometheus I. The latter device is based on a photodiode with a responsivity of about 0.02 AW^{-1} in the VUV range. The photodiode current is measured with a digital pico-ammeter. Due to an iris adapted in front of the photodiode, the light is collected from a conic line of sight with an included angle of 4.6°. Using a filter wheel, band-pass filters centered at characteristic emissions of hydrogen plasma, are placed in front of the photodiode. For the present study, a filter centered on the intense part of the Lyman-band emission at 161 nm with a full

width at half maximum of 20 nm is used. The VUV irradiance meter is chosen instead of the VUV spectrometer due to its higher signal-to-noise ratio, especially for low power conditions.

The measurement of the Lyman-band is very important because of its relation with the vibrational excitation of the gas. Lyman-band is emitted during the decay of the $B^1\Sigma_u^+$ singlet, which together with the decay of the $C^1\Sigma_u^+$ singlet, is the main source of vibrationally excited molecules of a hydrogen discharge as discussed above. The transitions from the $B^1\Sigma_u^+$ singlet back to the ground state are optically allowed and, thus, its lifetime is in the order of ns [35]. At the same time, the measured irradiance includes the most intense part of Lyman-band which accounts for the majority of irradiance. Furthermore, the contribution of cascade effects from upper singlet states on the measured emission can be considered small in comparison to the effect of direct excitation to the $B^1\Sigma_u^+$ state. Thus, it may be argued that the irradiance is proportional to the excitation rate to the $B^1\Sigma_u^+$ singlet.

VUV emission spectroscopy is similarly applied in ROSAE III (see details in [33]) for accessing the Werner (90−132 nm) and Lyman (90−170 nm) bands, corresponding to transitions from the first two excited singlets to the ground state of the hydrogen molecule.

3.5. Synchrotron radiation. With the VUV absorption on the DESIRS beam line [36], it is possible to probe selectively the (ro)vibrational levels of excited H_2(v", J) molecules in the plasma. Results from ROSAE III are here reported with respect to surface-enhanced (ro)vibrational molecular excitations for increased DA. The monochromatized synchrotron radiation enters into the chamber through an MgF_2 window (to isolate the chamber from the synchrotron side which is at about $7.5\text{x}10^{-8}$ Torr) where it is selectively absorbed by these molecules. The remaining light directly hits a solar blind VUV photo-multiplier. In addition, to avoid stray light from the plasma itself, the synchrotron radiation is chopped by a tuning fork, oscillating at a constant frequency, for phase-sensitive detection, allowing a large improvement of the signal-to-noise ratio. More details may be found in Ref. [37].

4. REPRESENTATIVE RESULTS AND DICSUSSION

Figure 2 and its caption provide indicative electron densities and energies downstream of the ECR coupling zones of the three reactors. Independently of the ECR network, the concept of producing two different (cold and hot) electron populations is met, and their density and energy may be tuned as a function of the operating conditions (see e.g. Fig. 2c).

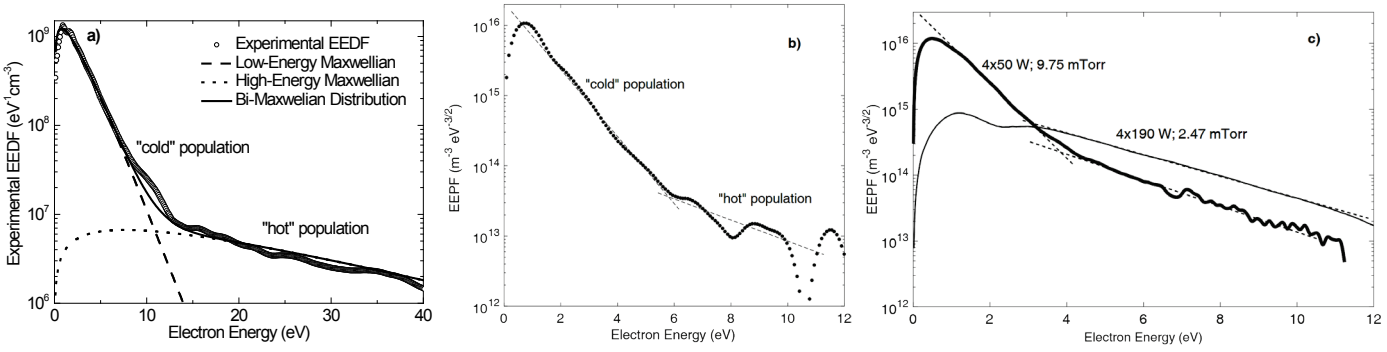

Figure 2. Representative electron energy distribution and probability functions downstream of the ECR networks in different sources. a) Prometheus I (5x180 W; 4 mTorr; $T_{e/cold}$ = 1.54 eV; $n_{e/cold} = 3.9\text{x}10^9$ cm^{-3}; $T_{e/hot}$= 15.2 eV; $n_{e/hot} = 2.1\text{x}10^8$cm^{-3}) [27], b) Camembert III (7x140 W; 3 mTorr; $T_{e/cold}$ = 1 eV; $n_{e/cold} = 1.4\text{x}10^{16}$ m^{-3}; $T_{e/hot}$= 3 eV; $n_{e/hot} = 0.34\text{x}10^{16}$ m^{-3}) [30] and c) ROSAE III (4x50 W; 9.75 mTorr; $T_{e/cold}$ = 1.4 eV; $n_{e/cold} = 1.4\text{x}10^{16}$ m^{-3}; $T_{e/hot}$= 2.7 eV; $n_{e/hot} = 0.3\text{x}10^{16}$ m^{-3}) & (4x190 W; 2.47 mTorr; $T_{e/cold}$ = 0.7 eV; $n_{e/cold} = 0.13\text{x}10^{16}$ m^{-3}; $T_{e/hot}$= 2 eV; $n_{e/hot} = 0.46\text{x}10^{16}$ m^{-3}) [30]. Part a) is reproduced (minor editing modifications) with permission of IOP Publishing in the format Other Published Product via Copyright Clearance Center (Order Detail ID: 71552559). Parts b) and c) are reproduced from Phys. Plasmas, 2013, 20, 101601, with the permission of AIP Publishing.

Figure 3 correlates the absolute density of the produced H^- ions with the Lyman-band irradiance, under various operating conditions, in Prometheus I. Although the power is efficiently deposited on excitation processes (almost linear increase; Fig. 3b), the H^- ion density increases moderately whereas it decreases at the lower pressure (Fig. 3a). It has been shown [27] that this fact is due to limited deposition of the power to ionization processes, preventing thus DA. Figure 3c clarifies this point by comparing the H^- ion density (measured) with the cold electron temperature (measured) and the $B^1\Sigma_u^+$ singlet excitation rate coefficient (calculated [27]).

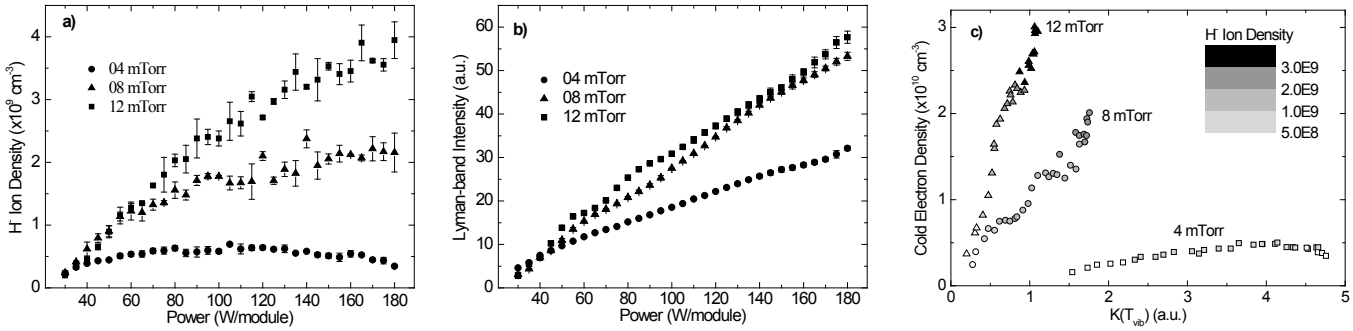

Figure 3. a) H^- ion density and **b)** Lyman-band intensity versus the MW power per ECR module (5 in total), at different filling gas pressures. **c)** Correlation between the measured H^- ion density, the measured cold electron density and the calculated $B^1\Sigma_u^+$ singlet excitation rate coefficient. The results are obtained in Prometheus I [4, 27]. Figures are reproduced (minor editing modifications) with permission of IOP Publishing in the format Other Published Product via Copyright Clearance Center (Order Detail ID: 71552559).

As regards the surface-enhanced production of vibrationally excited molecules, Fig. 4 indirectly supports its significance by presenting H^- ion densities versus the MW power when the quartz internal surface of ROSAE III is partially covered with materials of different recombination coefficients [33]. The latter is approximately equal to 0.004 at 290 K for quartz and 0.5 at 240−300 K for Ta/W.

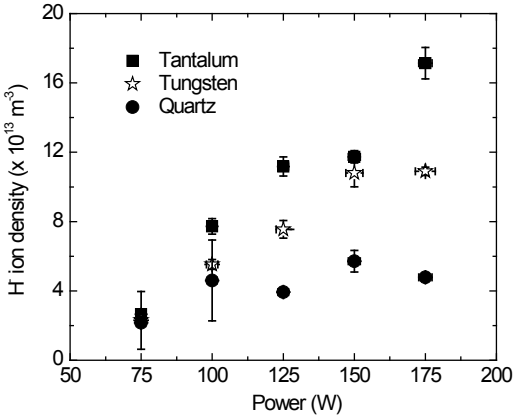

Figure 4. H^- negative ion density variation as a function of the applied MW power on a single ECR module installed in ROSAE III (single ECR module; 12 mTorr), for partial coverage of the inner surface with different materials ("quartz" corresponds to uncovered surface; see [33] for details). Reproduced (minor editing modifications) with permission of IOP Publishing in the format Other Published Product via Copyright Clearance Center (Order Detail ID: 71552575).

Finally, under similar conditions with those of Fig. 4 in ROSAE III, (ro)vibrationally excited species are directly probed by means of synchrotron radiation absorption measurements. Figure 5 demonstrates the variation of the peak absorption for rotational transitions (R0, R1, R2, R3, P1, P2) in the B(v' = 0) ← X(v'' = 3) (BX03) and B(v' = 0) ← X(v'' = 4) (BX04) vibrational levels.

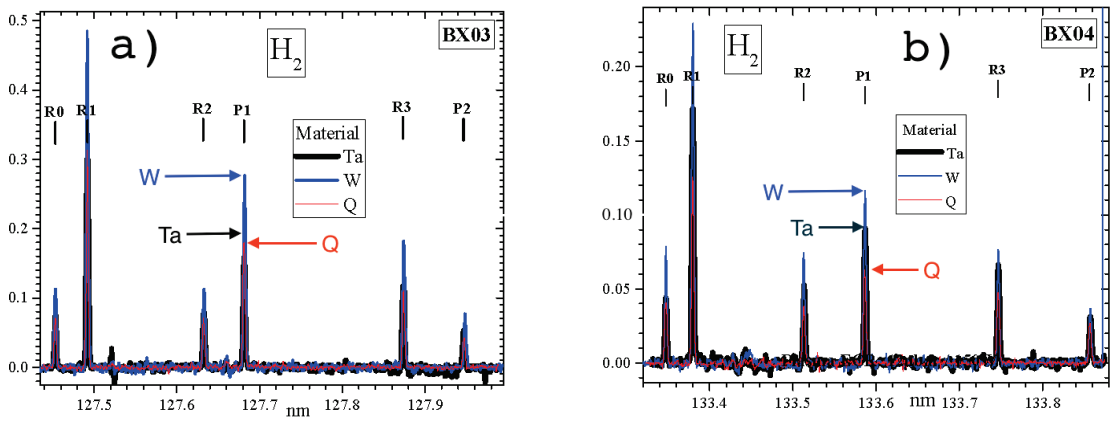

Figure 5. Synchrotron radiation absorption of (ro)vibrationally excited H_2 molecules in ROSAE III when its quartz (Q) internal surface is partially covered with tantalum (Ta) and tungsten (W) (single ECR module at 175 W; 12 mTorr) [33]. Vibrational transition: **a)** BX03 and **b)** BX04. Reproduced with permission of IOP Publishing in the format Other Published Product via Copyright Clearance Center (Order Detail ID: 71552575).

5. CONCLUSIONS

This paper comprises a brief review of representative results from different ECR plasmas (driven at 2.45 GHz) with respect to hydrogen negative ion production. The concept relies on the use of electron cyclotron resonance modules for achieving dissociative attachment of low-energy electrons to highly vibrationally excited molecules. This volume production process may be enhanced by surface mechanisms leading to rich spectra of (ro)vibrationally excited molecules. Appropriately adapted diagnostic techniques for probing both charged species and excited neutrals have been considered, and the results validate the efficiency of this kind of microwave discharges for yielding H^- ions. However, it is unveiled that this efficiency could potentially be increased if higher density of low-energy electrons were achieved with supplementary media.

References

1. Bacal M., Wada M., Appl. Phys. Rev., 2015, **2**, 021305.
2. Franzen P., Fantz U., Fusion Eng. Des., 2014, **89**, 2594.
3. Santoso J., Manoharan R., O'Byrne S., Corr C. S., Phys. Plasmas, 2015, **22**, 093513.
4. Aleiferis S., Tarvainen O., Svarnas P., Bacal M., Béchu S., J. Phys. D: Appl. Phys., 2016, **49**, 095203.
5. Wadehra J.M., Bardsley J.N., Phys. Rev. Lett., 1978, **41**, 1795.
6. Bardsley J.N., Wadehra J.M., Phys. Rev. A, 1979, **20**, 1398.
7. Capitelli M., Cacciatore M., Celiberto R., De Pascale O., Diomede P., Esposito F., Gicquel A., Gorse C., Hassouni K., Laricchiuta A., Longo S., Pagano D., Rutigliano M., Nucl. Fusion, 2006, **46**, S260.
8. Hiskes J.R., J. Appl. Phys., 1980, **51**, 4592.
9. Hiskes J.R., Karo A.M., J. Appl. Phys., 1990, **67**, 6621.
10. Hall R.I., Čadež I., Landau M., Pichou F., Schermann C., Phys. Rev. Lett., 1988, **60**, 337.
11. Jackson B., Lemoine D., J. Chem. Phys., 2001, **114**, 474.
12. Hjartarson A.T., Thorsteinsson E.G., Gudmundsson J.T., Plasma Sources Sci. Technol., 2010, **19**, 065008.
13. Matveyev A.A., Silakov V.P., Plasma Sources Sci. Technol., 1995, **4**, 606.
14. Janev R.K., Reiter D., Samm U., Collision Processes in Low-Temperature Hydrogen Plasmas, 2003, Report Forschungszentrum Jülich JUEL 4105.
15. Lacoste A., Lagarde T., Béchu S., Arnal Y., Pelletier J., Plasma Sources Sci. Technol., 2002, **11**, 407.
16. Ivanov A.A. Jr., Rouillé C., Bacal M., Arnal Y., Béchu S., Pelletier J., Rev. Sci. Instrum., 2004, **75**, 1750.
17. Svarnas P., Annaratone B.M., Béchu S., Pelletier J., Bacal M., Plasma Sources Sci. Technol., 2009, **18**, 045010.

18. Svarnas P., Breton J., Bacal M., Mosbach T., Rev. Sci. Instrum., 2006, **77**, 03A532.
19. Gobin R., Auvray P., Bacal M., Breton J., Delferrière O., Harrault F., Ivanov A.A. Jr., Svarnas P., Tuske O., Nucl. Fusion, 2006, **46**, S281.
20. Svarnas P., Breton J., Bacal M., Faulkner R., IEEE Trans. Plasma Sci., 2007, **35**, 1156.
21. Simonin A., Garibaldi P., Rev. Sci. Instrum., 2006, **77**, 03A525.
22. Hopkins M.B., Bacal M., Graham W.G., J. Appl. Phys., 1991, **70**, 2009.
23. Eenshuistra P.J., Gochitashvilli M., Becker R., Kleyn A.W., Hopman H.J., J. Appl. Phys., 1990, **67**, 85.
24. Courteille C., Bruneteau A.M., Bacal M., Rev. Sci. Instrum., 1995, **66**, 2533.
25. Baële P., Béchu S., Bès A., Pelletier J., Lacoste A., Plasma Sources Sci. Technol., 2014, **23**, 064006.
26. Aleiferis S., Svarnas P., Tsiroudis I., Béchu S., Bacal M., Lacoste A., IEEE Trans. Plasma Sci., 2014, **42**, 2828.
27. Aleiferis S., Svarnas P., Béchu S., Tarvainen O., Bacal M., Plasma Sources Sci. Technol., 2018, **27**, 075015.
28. Mosbach T., Plasma Sources Sci. Technol., 2005, **14**, 610.
29. Bacal M., Bruneteau J., Devynck P., Rev. Sci. Instrum., 1988, **59**, 2152.
30. Béchu S., Soum-Glaude A., Bès A., Lacoste A., Svarnas P., Aleiferis S., Ivanov A.A. Jr., Bacal M., Phys. Plasmas, 2013, **20**, 101601.
31. Aleiferis S., Svarnas P., Rev. Sci. Instrum., 2014, **85**, 123504.
32. Bacal M., Rev. Sci. Instrum., 2000, **71**, 3981.
33. Bentounes J., Béchu S., Biggins F., Michau A., Gavilan L., Menu J., Bonny L., Fombaron D., Bès A., Lebedev Yu.A., Shakhatov V.A., Svarnas P., Hassaine T., Lemaire J.L., Lacoste A., Plasma Sources Sci. Technol., 2018, **27**, 055015.
34. Komppula J., Tarvainen O., Kalvas T., Koivisto H., Kronholm R., Laulainen J., Myllyperkiö P., J. Phys. Appl. Phys., 2015, **48**, 365201.
35. Astashkevich S.A., Lavrov B.P., Opt. Spectrosc., 2002, **92**, 818.
36. Nahon L., de Oliveira N., Garcia G.A., Gil J.–F., Pilette B., Marcouille O., Lagarde B., Polack F, J. Synchrotron Radiat., 2012, **19**, 508.
37. Béchu S., Aleiferis S., Bentounes J., Gavilan L., Shakhatov V.A., Bès A., Svarnas P., Mazouffre S., de Oliviera N., Engeln R., Lemaire J.L., Appl. Phys. Lett., 2017, **111**, 074103.

2. Invited papers

UNREVEALED FEATURE OF SURFACE-WAVE SUSTAINED TUBULAR DISCHARGES (SWDs): SPACE-WAVE RADIATION REGION IN THE IMMEDIATE VICINITY OF THE WAVE LAUNCHING INTERSTICE BEFORE THE SWD DEVELOPS

M. Moisan, P. Levif, H. Nowakowska[1]

Groupe de physique des plasmas, Université de Montréal, Montréal, Québec
[1] Institute of Fluid Flow Machinery, Polish Academy of Sciences, 80-952 Gdansk, Poland

Abstract. As shown recently [1], whenever an electromagnetic (EM) surface wave (SW) sustains a plasma column, it is preceded over a short axial segment of the plasma column situated in the immediate vicinity of the wave launching interstice by a non-guided wave. This wave can be regarded as a space wave since it spreads out, into the free space, part of the power flow that could have supplied the subsequent SW discharge (SWD). In that respect, coaxially surrounding the SWD with a circular waveguide (termed a Faraday cage (FC)) under cut-off conditions eliminates, to some extent (depending on its length), the corresponding space-wave power loss. Such an outcome is first suggested by the fact that the plasma column length is observed to be longer when enclosed within a FC at cut-off, as opposed to calculations that predict, when ignoring the space-wave phenomenon, an increase in the electron density of the SWD as the diameter of the conducting enclosure around it is decreased, leading the plasma column length to decrease for a given power. In fact, experimentally the axial distribution of electron density in the plasma column enclosed in a FC at cut-off does not appear significantly different in shape from that in free space. However, integrating the axial distribution of electrons along the plasma column leads to a greater number of electrons when enclosed in a FC at cut-off, demonstrating that more SW power is made available as a consequence of the contribution of the space-wave power flow. The power loss due to space-wave radiation is calculated as a function of the length of the FC enclosing the plasma column. Even though the current work is centered on an SWD operated in argon at atmospheric pressure and at a field frequency of 915 MHz, some features are reported under different operating conditions (frequency, discharge tube diameter and gas pressure). It is observed that, for given operating conditions, the characteristic length of the space-wave radiation segment is constant and that its length decreases when increasing frequency; as a result, at 2450 MHz depending on the wave launcher used, it extends from 0.3 to 2.8 cm only, possibly explaining that it has escaped the attention of researchers. In conclusion, a space-wave region always stands in the immediate vicinity of the interstice of the ***E***-field applicator before a SWD develops, be it a tubular discharge or a TIA-TIAGO plasma torch [1]. Enclosing the plasma column in a FC at cut-off leads to an energy saving, approximately 30%, on achieving SWDs at both 915 and 2450 MHz.

1. PROPERTIES OF THE SPACE-WAVE RADIATION REGION PRECEDING THE DEVELOPMENT OF A SWD

1.1. Location and extent of the space-wave radiation region. Consider first Fig. 1 that schematically displays the ***E***-field applicator used to generate a tubular surface-wave discharge (SWD). The circular launching interstice (a 2–3 mm wide gap in the case of a surfatron) is the essential part of the various field applicators worked out for achieving efficiently tubular SWDs. The electromagnetic (EM) field emerging from this interstice allows generating a plasma column sustained by an EM surface wave in both directions from the gap. However, as illustrated in Fig. 1, the front column of the SWD begins at the power flow marked $P(z_0)$, i.e. past the space-wave radiation region.

In Fig. 2a, which plots the axial distribution of electron density, the SWD starts developing down the plasma column from the point designated with an arrow based on the fact that the linear decrease of electron density that ensues is an essential attribute of SWDs (as reported in the literature). Concerning the plasma column region preceding the SWD, its main features, according to Fig. 2a, are: i) its axial extent and shape remain the same when the microwave power is increased whereas its electron density increases accordingly; ii) the electron density and the intensity of the ***E***-field at the end of this plasma segment reach a relative maximum value that delineate the beginning of the SWD. In this region

preceding the SWD, microwave power is radiated through a non-guided wave, designated as a *space wave*, whereas the SWD results form a SW guided along the plasma column axis. Similar observations (i and ii)) can be made with Fig. 2b, this time at a much higher frequency and at a higher gas pressure (atmospheric pressure), all measurements provided in this paper being made in argon discharges.

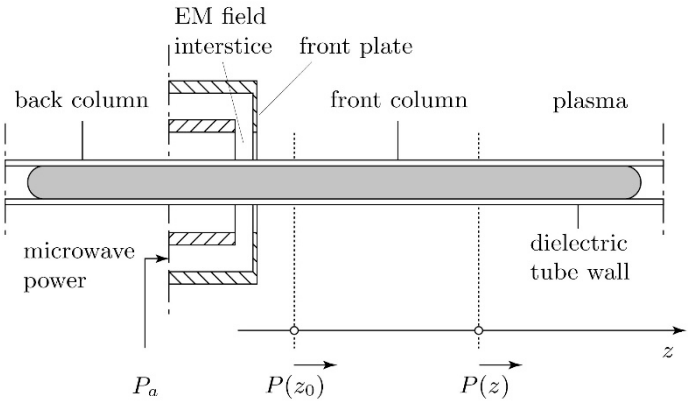

Figure 1. Schematic representation of an EM field applicator with a circular aperture such as used for achieving tubular SW discharges, highlighting its essential part, namely the EM field interstice, typically forming in the case of a surfatron a 2–3 mm wide gap with a front plate 0.5 mm thick and edgy. As a result of the EM field emerging from the interstice in connection with microwave (absorbed) power P_a, a SW is launched in both directions (specifically past the $P(z_0)$ point for the front wave[1]), sustaining a plasma column inserted in a dielectric tube. The impedance matching system of the feed line with the power generator is not represented.

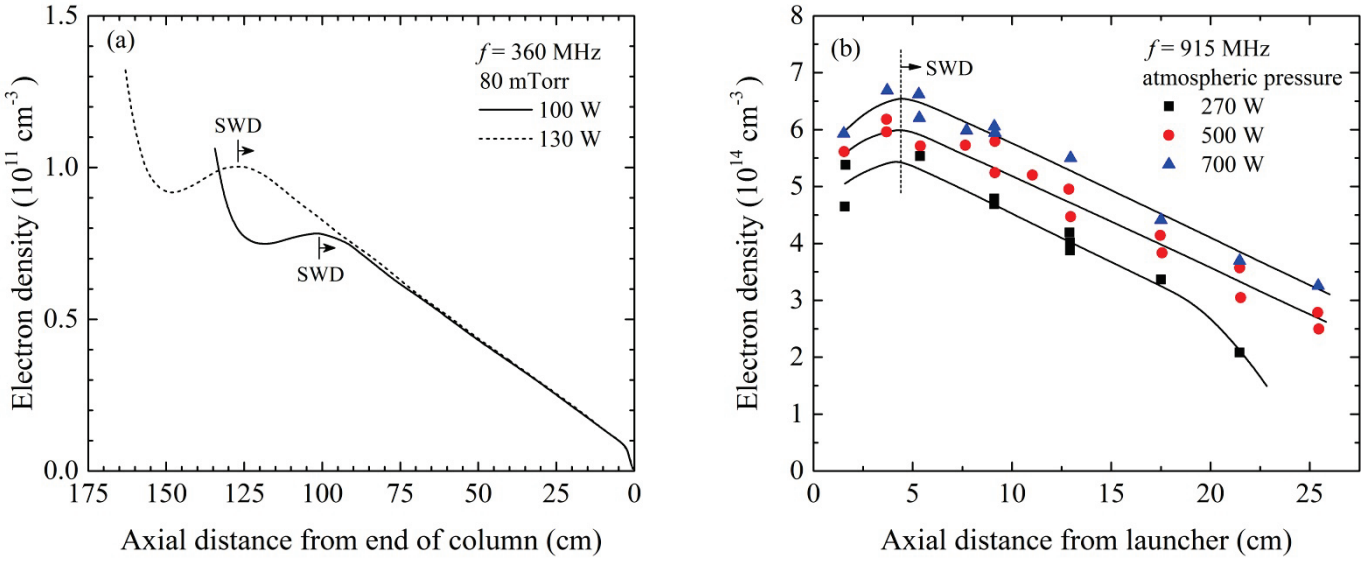

Figure 2. Radially averaged electron density measured along an argon SW plasma column sustained with a surfatron as a function of axial distance plotted: in (a) from the end of the plasma column of diameter 25 mm, at 80 mTorr (10.7 Pa) and at 360 MHz; the leftmost data point in the figure is situated at approximately 1–2 mm from the launcher interstice [2]; in (b) from the launcher aperture along a plasma column in a tube of 1.94 mm inner diameter, at atmospheric pressure and 915 MHz [3]. The SWD is open to free space in Fig. 2a while in Fig. 2b it is inserted coaxially in a Faraday cage of radius R_{Fc} = 67.5 mm, much smaller than the minimum radius for wave cut-off in a cylindrical waveguide at 915 MHz[2], which is $R_{Fc(co)}$ = 96.1 mm. (a) Reprinted from [2], with permission of AIP publishing. (b) [3] John Wiley & Sons. Copyright © 1990 WILEY-VCH Verlag GmbH Co. KGaA.

[1] A space-wave region that precedes the back column from the EM field interstice is also expected. However, the corresponding space-wave losses are minimized by the fact that the back plasma column is surrounded by the surfatron body acting as a FC (generally under cut-off conditions).

[2] A circular waveguide enclosing (coaxially) at cut-off (on its fundamental mode) the plasma tube prevents waves to propagate within this conducting cage (but not the SW, which uses the discharge tube and the plasma as its propagating medium). The fundamental mode of a circular waveguide (i.e. the lowest frequency at which a wave can propagate within it) is the H_{11} (TE_{11}) mode. The corresponding wavelength is given by $\lambda_c = 2\pi R_{Fc(co)}/1.841$. At 915 MHz, a circular waveguide (Faraday cage) with a radius smaller than $R_{Fc(co)}$ = 96.1 mm is at cut-off, i.e., no wave can propagate within it. At 2450 MHz, $R_{Fc(co)}$ is 35.9 mm [4].

1.2. Properties of the radiation region observed near the opening made for the passageway of the discharge tube in a TM_{010} Beenakker cavity used to achieve a tubular SWD. A TM_{010} Beenakker cavity can be utilized as a SW field applicator [5]. Figure 3 shows the axial variation, this time, of the intensity of the ***E***-field radial component of the microwave field detected with an electric-antenna radially oriented and situated at 2 mm away from the discharge tube outer wall [6]. An EM wave does propagate from the cavity aperture, reaching a maximum intensity value at approximately 17 mm from it, after which it decreases almost linearly. The fact that the SWD really starts developing at 17 mm, specifically at the maximum of electric field intensity in Fig. 3, was established by noticing that the ***E***-field intensity decreased radially in an exponential way at that position (not shown), which is an attribute of SWDs; such an exponential radial decay of the ***E***-field intensity is observed, according to Lebedev [6], up to aproximately 90 mm, marking the end of the SWD. The first part of the curve up to its maximum value in Fig. 3 is ascribed by Lebedev to a radiation wave: as a matter of fact, when the the antenna is axially set at 8 mm from the launcher or farther away, namely at 90 and 110 mm, the ***E***-field intensity radially decreases slowly away from the tube in contrast to the exponential radial decay observed in the SWD segment (corresponding figure not shown).

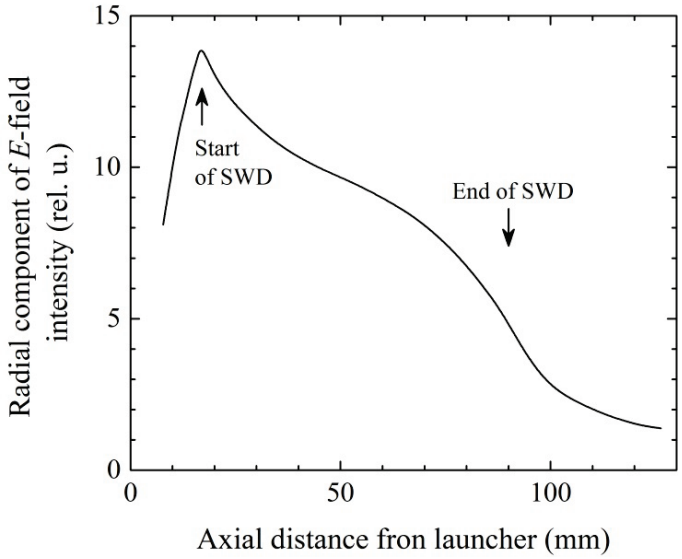

Figure 3. Radial component of the ***E***-field intensity detected with an electric antenna radially oriented with respect to the discharge tube as a function of axial distance from the launcher. The tip of the antenna is set at 2 mm from the discharge tube outer wall. The discharge is sustained in argon at atmospheric pressure from a Beenakker cavity supposedly operated on the TM_{010} mode (after [6]).

The total length of the plasma column is 90 mm for 175 W in argon at atmospheric pressure and at a field frequency of 2450 MHz in a 2/5 i.d./o.d. mm tube. We believe that the plasma column length should be longer under these operating conditions, the Beenakker cavity being of a lower efficiency than a surfatron as a SW launcher[3]; moreover, claiming the operation of this device at atmospheric pressure to be under a "resonant cavity TM_{010} mode" condition seems greatly improbable, the high number of electron-neutral collisions at such a pressure preventing to achieve a high enough *Q-factor* in the cavity.

1.3. Properties of the radiation region when sustaining a SWD with a surfaguide. In the case of a surfatron, the interstice plane is perpendicular to the end of a coaxial (internal) transmission line terminated on its other end by a conducting reflecting wall, an arrangement that should provide at the launching interstice an azimuthally symmetric power flow around the discharge tube. In contrast, the

[3] The surfatron used in the current series of experiments is an optimized SW launcher [7], which in particular requires that the front plate forming the outer plane of the interstice be thin (typically 0.5 mm) with a sharp edge. For a given microwave power input, a 0.5 mm front plate yields 23% more electron density than a 2 mm one [7]. In [6], the cavity circular plate was 2 mm thick.

surfaguide wave-launcher[4] (Fig. 4a) does not structurally ensure a similar azimuthally symmetric power flow at its exit around the discharge tube. This is because the movable plunger of the surfaguide system is tuned, for maximum power transfer (minimum reflected power) to the plasma column, leading to a maximum of intensity of the standing wave (within the waveguide) that takes place essentially on the portion of the discharge tube wall facing the plunger: microwave irradiation of the cylindrical discharge tube is thus asymmetric, as clearly shown from numerical calculations (for instance [9]) and, for example, in Fig. 4b at 210 μs.

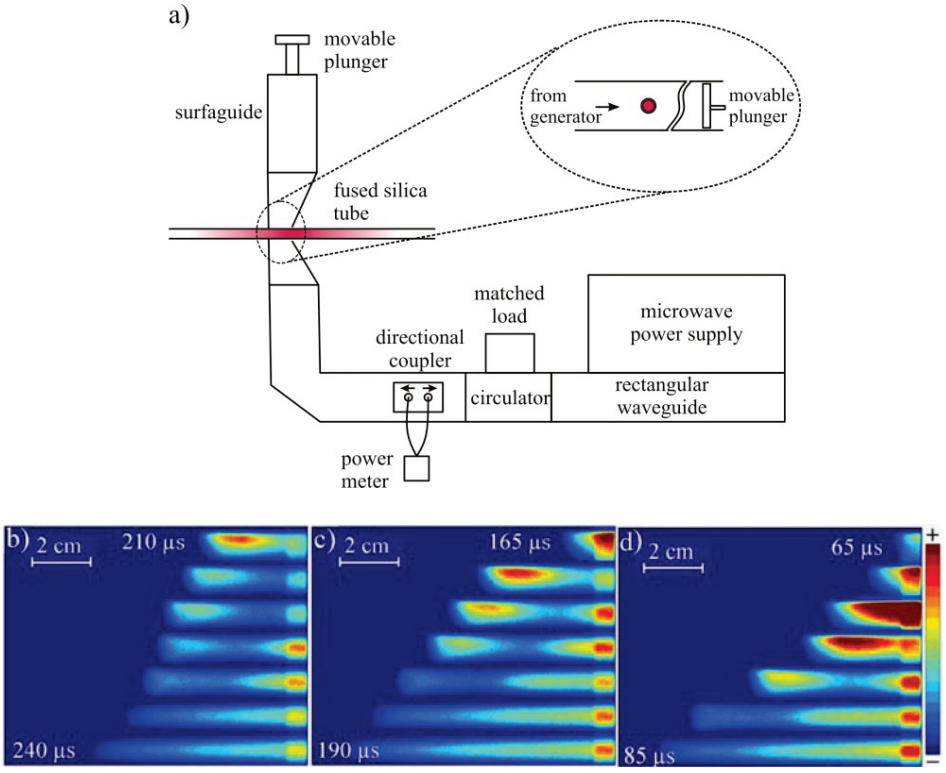

Figure 4. (a) Schematic diagram of the system utilized for achieving a SW plasma sustained with a surfaguide wave-launcher at 2450 MHz; (b), (c) and (d) are images taken with an iCCD under pulsed regime at a repetition rate of 50 Hz in helium gas at 5 Torrs (≈ 667 Pa) in a 8/10 id/od mm tube for 8, 16 and 23 W average absorbed powers, respectively, the plasma running from right (surfaguide interstice) to left on the pictures [10].

To investigate the space-wave radiation region of a SWD sustained with a surfaguide, it is enlightening to consider its operation under a pulsed regime, the mechanisms and properties of which are reported in [1]. Figures 4b, 4c and 4d display the variation of the total emitted-light intensity at successive elapsed times (from top to bottom), for a given average absorbed power. The plasma column runs from right (surfaguide interstice) to left on the pictures.

The maximum of light intensity observed in the initial moments of the discharge is gathered, on the photos, on the upper part of the discharge tube, i.e., on that sector of the tube wall facing the plunger (first upper row in (b), second upper row in (c) and third and fourth upper rows in (d)), which results, as already mentioned, from tuning for maximum absorbed power with the movable plunger. Consider more specifically, for example, 210 μs in Fig. 4b: the light intensity of the discharge not being distributed symmetrically with respect to the tube axis indicates that a higher ionisation rate is occurring close to the wall on the plunger side; however, as time goes on, the plasma becomes azimuthally symmetric. In addition, after some elapsed time (at 225 μs in Fig. 4b and earlier at higher average powers), a region of constant length and radial extent demarcates, in the end, as a small reddish rectangle (in the photo) in the immediate vicinity of the launching interstice (which we assign to the radiation region) while the plasma

[4] The gap of the launching interstice of the surfaguide is typically 15 mm for a WR-340 rectangular waveguide: it corresponds to the value of the tapering of the small wall of the waveguide such that the waveguide impedance matches that of the SW plasma column (seen as a transmission line). The thickness of the surfaguide plates forming the interstice is 0.9 mm [8].

column develops in length with time (as a result of the propagation of the ionisation front of the SW, making up a SWD). At the highest average power considered (Fig. 4d, 23 W), initially (≈ 68–75 μs) the plasma is non-azimuthally symmetric[5] over a longer plasma column length than at lower average powers. Nonetheless after some 75 μs in 4d and later on, the non-SWD plasma segment becomes constant in length (≈ 8 mm) and radial extent: we consider these two features as an attribute of the space-wave radiation region under continuous operation, although this zone has extended over a longer distance along the dielectric tube at earlier times. At long enough times after, the plasma column outside the space-wave radiation region becomes azimuthally symmetric, which we ascribe to a SW plasma column: it lends us to assume that the plasma column becomes azimuthally symmetric once the radiation region has itself become symmetric. At this point, we conclude that the SWD develops once the radiation region has become constant in length and radial extent, and azimuthally symmetric.

1.4. Space-wave radiation zone along the TIAGO plasma. Figure 5a is a schematic representation showing that part common to both the TIA and TIAGO devices. It is a hollow conducting rod, carrying the discharge gas within it, and ending in the form of a nozzle emerging from a surfaguide. The plasma flame achieved is composed of two regions (Fig. 5b): i) a bright, filament-like plasma, starting at the tip of the torch nozzle, corresponding to a non-SWD ionised segment, called the dart [1]; ii) the region beyond the dart, which increases in length (and then in volume) with power, called the plume, which we have demonstrated to be a SWD [1].

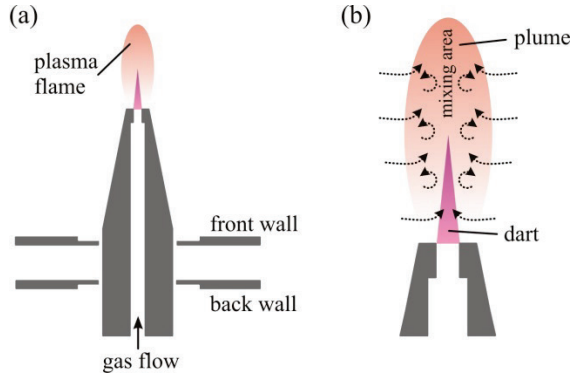

Figure 5. (a) The conducting rod ending in the form of a nozzle as it emerges from the surfaguide field-applicator (represented by its front and back (edgy) walls); the carrier gas flows through the inner part of the rod; (b) the plasma flame, starting at the nozzle tip, is constituted of the dart followed by the plume, the latter expanding both in length and volume with power. Reprinted from [12]. Copyright (2013), with (paid) permission from Elsevier.

Figure 6 is a photograph at a given flow rate of the plasma flame at the tip of the TIAGO as a function of microwave power. It shows that after reaching a given power level (≈ 250 W) and above it, the dart region does not vary in length. Beyond the dart, the plume starts to grow in length with power at 350 W and, in the present case, also in volume since plasma is confined within a (dielectric) tube: the extent of the plume is partially limited by the length of the surrounding tube, which furthermore induces reflection at its extremity. The fact that the dart region does not exceed a given length is a trait of the non-SWD region of tubular SWDs while, similarly, the fact that the plume region expands with microwave power is also a feature observed in tubular SWDs. These two characteristics are further examined in the next figures according, this time, to their electron density.

[5] Close observation of this non-SWD region suggests that the EM field initially progresses from the interstice along the upper wall of the dielectric tube, before it transforms into a SWD. In fact, a SW can propagate along a dielectric medium alone [11].

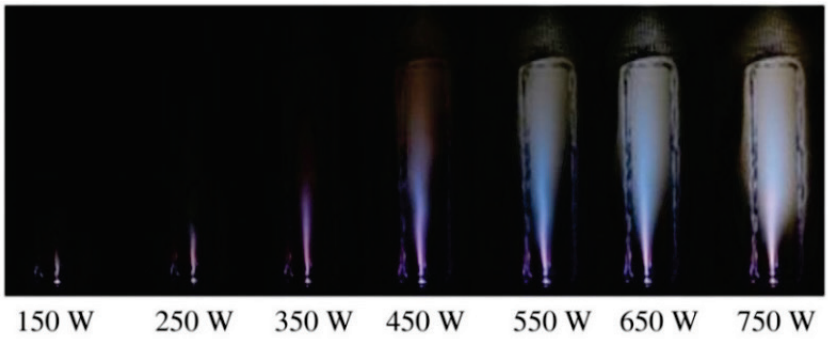

Figure 6. Several images taken (1/250 s exposure time) from the flame generated at 2450 MHz and atmospheric pressure at 0.5 standard litre per minute (slm) of argon for different microwave powers. Reprinted from [12]. Copyright (2013), with (paid) permission from Elsevier.

Figure 7 is a plot of the electron density (obtained from the Stark broadening of the H_β line, without accounting for the van der Waals broadening) as a function of distance from the tip of the TIA nozzle [13]. Plasma is sustained at 2450 MHz in a He/H_2 9/1 pre-mixed gas flow at a rate of 10 slm (a high enough flow rate for ensuring satisfactory confinement of the plasma flame) emerging at ambient atmospheric pressure. The $0 \leq z \leq 3$ mm region is a non-SWD plasma segment that we ascribe to the space-wave region. For $z > 3$ mm, the electron density decreases linearly with z and the plasma is thus sustained by a SWD, as we have previously demonstrated [1].

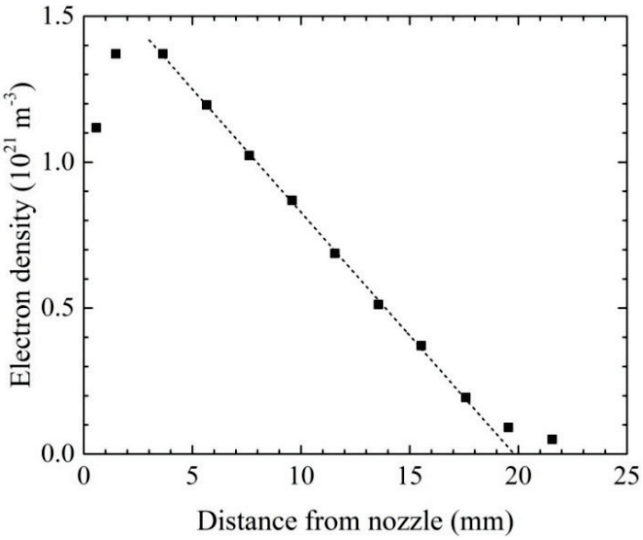

Figure 7. Measured electron density as a function of axial distance from the tip of the TIA nozzle. Plasma is sustained at 2450 MHz in a He/H_2 9/1 pre-mixed gas flow at a rate of 10 slm at atmospheric pressure [13]. The dotted line emphasizes that electron density depends linearly on axial position, as is the case with tubular SWDs [1]. Reproduced from [13] with permission.

From the various kinds of SWDs examined above, a general feature emerges: the extent in length of the space wave region decreases with frequency as reported in Table 1 (2450 MHz data for surfatron from [1], from [10] for surfaguide). The fact that the radiation segment extends on a distance much smaller than the wavelength, as reported in Table 1, is a characteristic of electromagnetically short antennas.

Table 1. Plasma column length of the space-wave radiation region L_{space} and ratio of L_{space} to corresponding EM wavelength in vacuum λ_0. Except otherwise indicated, there is no FC around the discharge tube

Frequency (MHz)	Wave launcher	L_{space} (cm)	L_{space} / λ_0
360	Surfatron	33 ± 1	0.40
915	Surfatron	4.3 ± 0.1*	0.13
2450	Surfatron	2.8 ± 0.2	0.23
2450	Surfaguide	0.7 ± 0.1	0.06
2450	Beenakker cavity	1.7	0.14
2450	TIAGO system	0.30 ± 0.05	0.025

*With R_{FC} = 67.5 mm where cut-off radius ≤ 96.1 mm

The space-wave region becoming smaller and smaller as the SW frequency is increased (in particular with the surfaguide as wave launcher), the existence of a radiation region might have escaped the attention of researchers at 2450 MHz.

1.5. The minimum length of a Faraday cage (FC) at cut-off that avoids perturbation to measurements due to space-wave radiation in the room. Determining the characteristics of the SWD sustained at 915 MHz led us to abandon probing a plasma column completely open to free space: the radiation emitted by the space wave into the room prevents making reliable and reproducible measurements. We therefore turned to implementing coaxially to the discharge tube a cylindrical FC at cut-off immediately at the surfatron exit (see Fig. 8), looking for the shortest such cage that would provide stable readings and recordings. A 3 cm long FC was found to do the job. This fact constitutes a further proof of the existence of a wave not guided along the plasma column (as a SW is), thus radiating into the room and that originates immediately past the launcher interstice showing, by the same token, that the SW, contrary to what was thought earlier, is not responsible for radiation in the room.

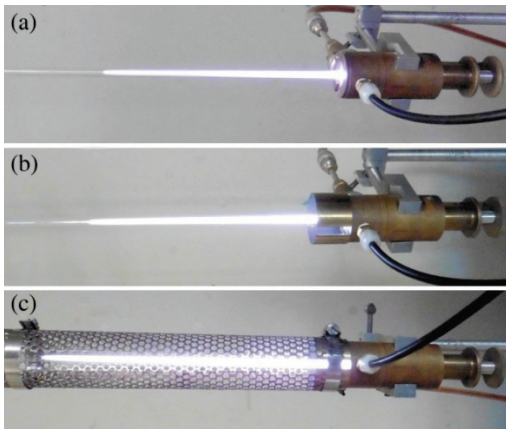

Figure 8. Photographs showing the plasma column obtained with a 915 MHz surfatron: a) no conducting cage at all; b) enclosed in a 22.5 mm radius FC corresponding to wave cut-off in a circular waveguide (see Footnote 1). The cage length is 3 cm, which was found to be the minimum FC length averting space-wave radiation from affecting our measurements; c) enclosed in a 22.5 mm radius FC, 30.5 cm long, which is beyond the plasma column length. Absorbed power is 300 W in each photo. The axial slot in the FC allows making field intensity and spectroscopic measurements along the plasma column.

1.6. The power lost from space-wave radiation reduces the total amount of electrons in the discharge. A possible way to cut down space-wave radiation losses is, as already mentioned, to enclose the discharge in a "circular waveguide" at cut-off. It prevents waves to propagate within this conducting (Faraday) cage (but not the SW, which uses the discharge tube and the plasma as its propagating medium) as well as it avoids wave power losses to the outside world due to *space-wave* (also possibly designated as volume or non-guided wave) radiation.

Figures 9a and 9b show that the plasma length is significantly longer when the discharge tube is entirely surrounded by a FC at cut-off. At 915 MHz (Fig. 9a, obtaining a 25 cm long column requires less

than 29% microwave power when inserted in the 30.5 cm long FC at cut-off compared to the 3 cm minimum length FC. At 2450 MHz, although the extent of the space-wave region is shorter than at 915 MHz (Table 1), Fig. 9b shows a similar power gain (or energy saving): a 17 cm long plasma column, surprisingly, also requires 29% less power (the error bar in both figures is nonetheless ± 10%). The longer plasma column length obtained under cut-off conditions is clearly the result of the space-wave power flow contributing to the SW power flow sustaining the SWD. This mechanism is further documented through Fig. 11 below and examined in Section 3.

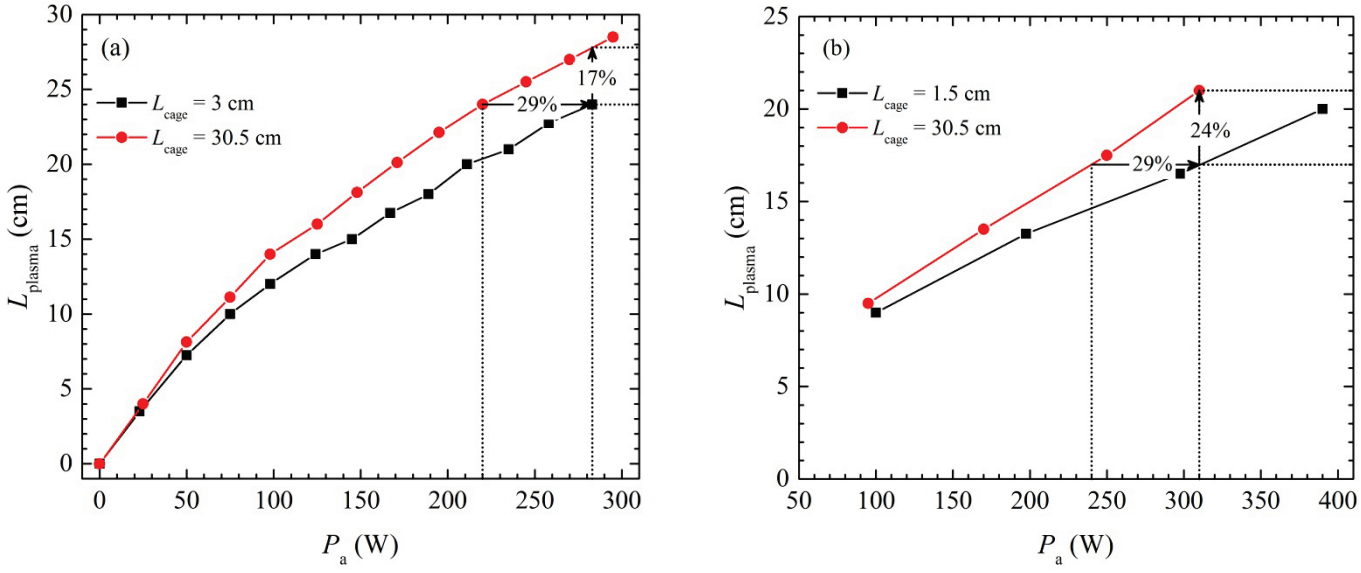

Figure 9. SWD column length as a function of microwave power when coaxially enclosed inside a cylindrical Faraday cage at cut-off (22.5 mm radius), one of minimum length (3 cm at 915 MHz in (a) and 1.5 cm at 2450 MHz in (b)) and the other being longer (30.5 cm) than the full length of the plasma column. At 915 MHz (a), 29% less power is required for a 24 cm long SWD fully surrounded by a FC at cut-off, while at 2450 MHz (b), also 29 % less power is needed for a 17 cm plasma length (the error bar is ± 10% in both cases!). The 915 MHz plasma column is sustained with a surfatron while at 2450 MHz the SWD is achieved with a surfaguide.

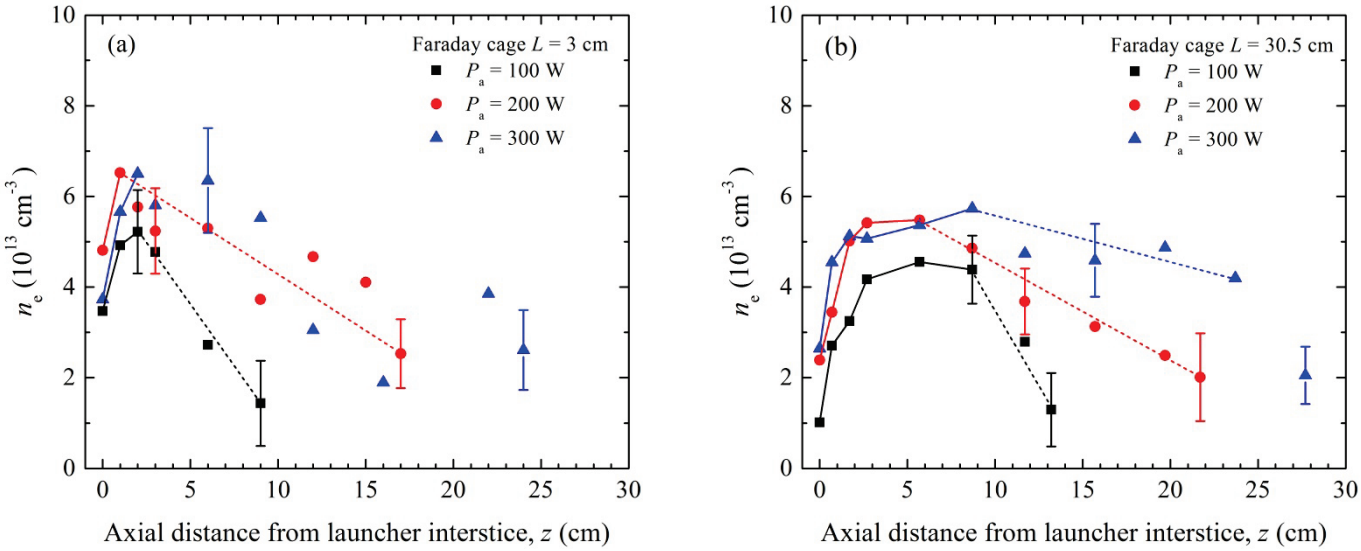

Figure 10. Axial distribution of electron density along a SWD sustained in argon at atmospheric pressure and at 915 MHz, enclosed in a Faraday cage under cut-off conditions (R_{FC} = 22.5 mm): (a) minimum length FC (3 cm); (b) longest FC (30.5 cm), longer than the plasma column length at 300 W.

Figures 10a and 10b display the axial distribution of electron density of the plasma column when enclosed inside a FC at cut-off: (a) with the FC of minimum length (3 cm); (b) with the longest FC (30.5 cm), longer than the plasma column at 915 MHz and 300 W. The data points are rather spread out in Fig. 10a, which could result from the remaining space-wave radiation since the FC is only 3 cm long, in contrast to Fig. 10b where the FC extends beyond the plasma column length.

In Fig. 10a, the electron density increases as z increases from 0 up to 1 or 2 cm and then decreases toward the end of the column. At 100 W, this decrease is somehow linear, as expected from a SWD plasma column; at 200 and 300 W, past the maximum of electron density it is only possible to observe that the electron density tends to decrease. In contrast, in Fig. 10b, the maximum of electron density is reached at a higher z value (5 or even 7 cm), furthermore the maximum of density is not as sharp as in 10a, but the axial distribution of electron density, at least at 100 and 200 W, decreases linearly when accounting for the uncertainty margins.

Figure 11 corresponds to the integration[6] of the electron density of the axial distributions in Figs. 10a and 10b obtained at 100, 200 and 300 W. Clearly, there are more electrons when the SWD is enclosed in a circular waveguide at cut-off; at 300 W, it means 30% more electrons.

Summarizing the findings of this Section: i) space-wave radiation is taking microwave power away from the SWD, in fact this power is lost in the room when there is no FC; ii) the maximum increase in plasma length is obtained with a FC at cut-off that exceeds the plasma column length; iii) the general shape of the axial distribution of electron density is similar with the plasma column surrounded or not by a FC at cut-off; iv) when the plasma column is completely enclosed in a FC, the microwave power absorbed per electron θ is clearly constant whatever the plasma column length (or microwave power). This comes out from the fact that the total average electron density (n_e total) increases linearly with microwave power, hence that the power absorbed per electron remains the same.

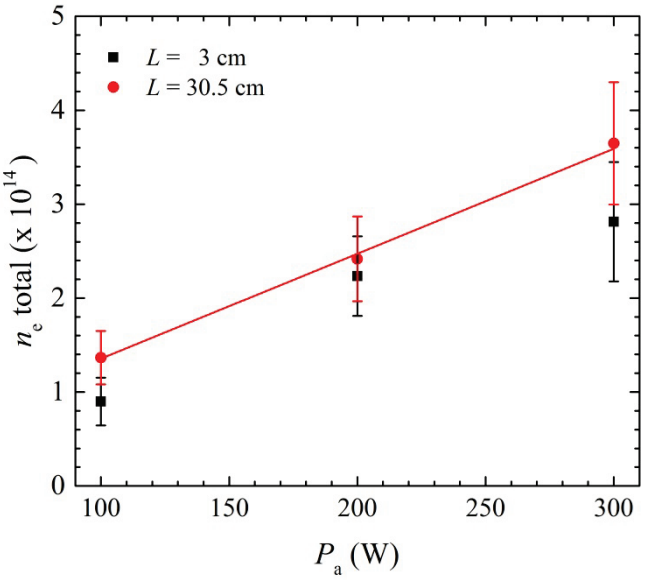

Figure 11. Average total electron density resulting from integration of the electron density of the axial distributions in Figs. 10a and 10b at 915 MHz in argon gas at atmospheric pressure in a 6/8 mm id/od fused silica tube. The radius of the FC is 22.5 mm.

[6] The total number of electrons resulting from the axial integration of their density is normalized to the corresponding discharge tube inner volume.

2. CALCULATED INFLUENCE OF THE RADIUS OF A CONDUCTING ENCLOSURE ON THE SW PLASMA COLUMN LENGTH WHEN NOT ACCOUNTING FOR SPACE-WAVE RADIATION

When the radius of the metallic enclosure coaxially surrounding the SWD is sufficiently small, calculations predict a shorter plasma column than that observed experimentally. This comes out from Fig. 12a, which shows that for a 915 MHz ***E***-field, the length of the SW plasma column, initially without any conducting enclosure (R_{FC} > 1000 mm), first slightly increases when decreasing the cage radius, showing a longer plasma column at R_{FC} = 96.1 mm, which is the minimum radius of a FC achieving cut-off conditions. However, for still smaller FC radii at cut-off, namely R_{FC} = 45 mm and 22.5 mm, the plasma column length becomes smaller and, in the latter case, much smaller (approximately half the length) than the plasma column with no FC. This outcome can be understood with Fig. 12b, which reveals (from right to left) that the attenuation coefficient α of the SW first decreases with decreasing R_{FC} values, reaching a minimum value at approximately 130 mm: a smaller attenuation coefficient yields a lower electron density, hence a longer plasma column; afterwards, as R_{FC} keeps on decreasing, α increases, thus the plasma column length decreases. The end result in Fig. 12a is in full opposition with experiments since, in reality, the SW plasma column becomes significantly longer when surrounded by a FC at cut-off (Figs. 9a and b).

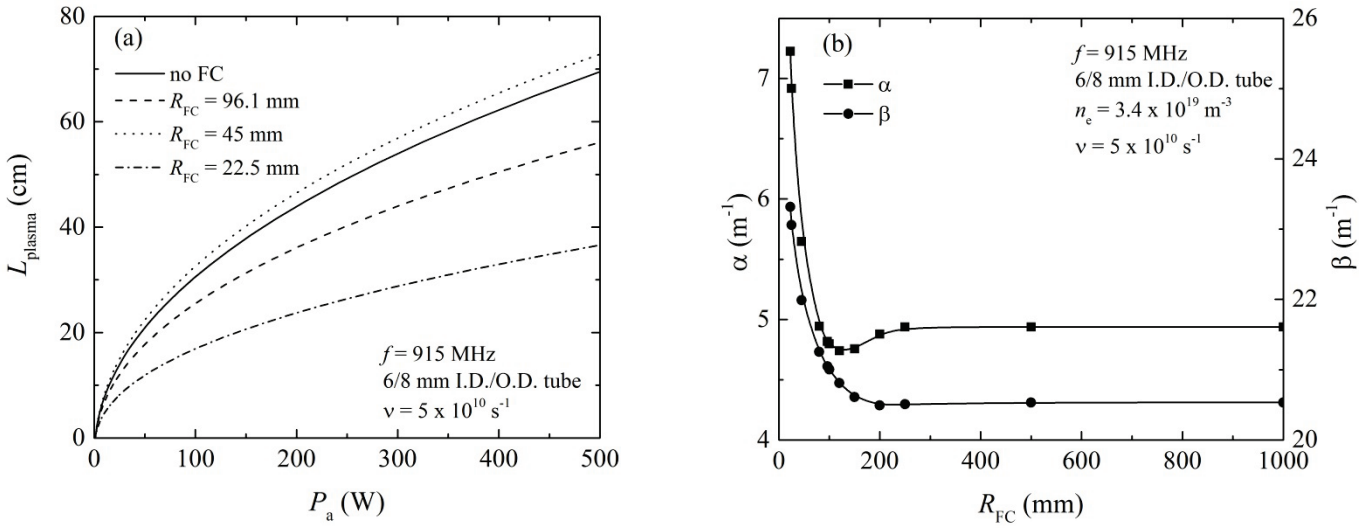

Figure 12. (a) Calculated plasma column length as a function of power in the following cases: open to free space (no FC), for the minimum R_{FC} ensuring cut-off (96.1 mm), and for R_{FC}= 45 mm and 22.5 mm (much below cut-off conditions), ignoring the space-wave radiation phenomenon; (b) calculated SW attenuation coefficient α showing that it decreases drastically as a function of the FC radius to reach a minimum value (130 ± 10 mm) and then slightly increases to set to a constant value.

3. CONTRIBUTION FROM THE SPACE-WAVE POWER FLOW TO THE SUSTAINING OF THE SWD WHENEVER THE PLASMA COLUMN IS SURROUNDED BY A FARADAY CAGE (FC) UNDER CUT-OFF CONDITIONS

EM fields are present all along the plasma column when generating a SWD. In the case where there is no FC at cut-off enclosing the discharge, there are two distinct and separate types of EM fields: i) that of the space wave due to the wave launcher, which gives rise to an EM radiation segment akin to the one encountered with (short) antennas in their near-field domain [14]; ii) that of the EM SW sustaining the plasma column as soon as the SWD starts developing. The transition from the (antenna) space wave to the surface wave is believed to occur whenever the electron density fills radially the discharge tube (in surfatron and surfaguide driven SWDs) such that its distribution is symmetric, which could be reached when the space wave is far enough from the antenna; then the space wave has become phase coherent (***E*** and ***H*** fields are now perpendicular to each other) and the ***E***-field intensity has attained a high enough value so as to generate, simultaneously, an average electron density allowing the SW to propagate and

thus sustain the discharge. In contrast, when a FC at cut-off extends all along the plasma column length, the space wave (which has become evanescent) and the SW powers flow, we believe independently, toward the end of the SWD as they attenuate, contributing both to the ionization of the SWD.

Figure 13 establishes through calculations (surfatron dimensions extended to 915 MHz from those of Hagelaar and Villeger at 2450 MHz [15]) and without any fitting that a little more than 30% of the power absorbed, in principle destined to sustain the SW plasma column, is lost through space-wave radiation in the case of a discharge tube open to free space (no FC). With increasing FC lengths up to 6 cm, radiation power loss is found to drop off rapidly while for longer FC lengths, the power decreases comparatively much slower to reach a zero value at L_{FC} = 22 cm, the assumed plasma column length.

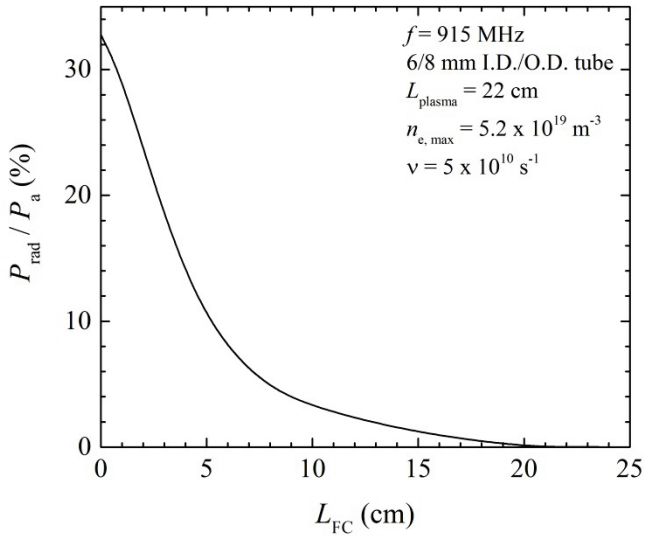

Figure 13. Calculated power radiated by the space wave as a function of the FC length at cut-off for a 2450 MHz surfatron wave launcher assuming it is operated at 915 MHz [15]. With no cage at all (L_{FC} = 0), approximately 30% of the absorbed power is lost in space-wave radiation. R_{FC} is assumed to be 22 mm and plasma column length 22 cm.

Figure 14 displays measured plasma column lengths as functions of microwave power at 915 MHz for different lengths of FC at cut-off (R_{FC}=22.5 mm). The shortest FC length examined is 3 cm, which is, as already mentioned, the minimum FC length under cut-off conditions to acquire stable and reliable measurements. Measured values obtained at 6.5 cm and up to 14.5 cm exhibit very similar plasma lengths, as can be inferred from the calculated curve in Fig. 13. The highest FC length considered, 30.5 cm, leads to a slightly higher plasma column length than the 6.5−14.5 cm set of curves. This might be due to the fact that the FC then totally encloses the plasma column length, avoiding wave reflection that can occur when part of the plasma column goes through the open end of a FC smaller than the plasma column length.

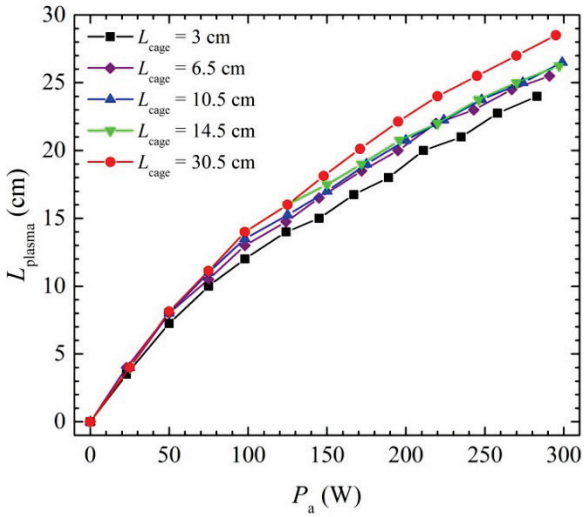

Figure 14. Measured plasma column lengths as functions of (absorbed) microwave power for different lengths of the FC at cut-off. Same conditions as in Figs. 10a and b.

Figure 15 is the calculated radiation pattern for the space wave generated from a surfatron (behaving as an antenna) at 915 MHz and for different lengths of the FC at cut-off (R_{FC} = 22 mm). It shows a polar angle close to 30° when the discharge is open to free space while there appear two lobes with respect to approximately 0^0 when the FC length is 75 mm or longer, these lobes then becoming of lower and lower intensities, as expected from Fig. 13.

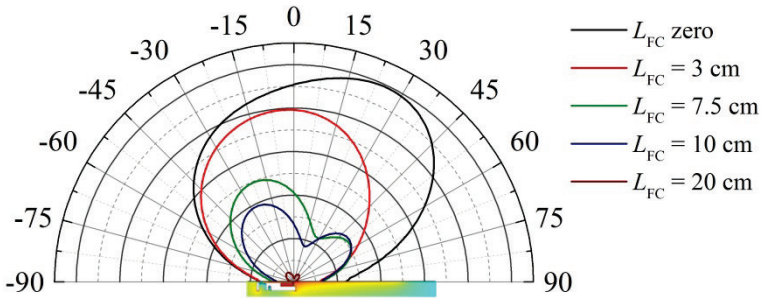

Figure 15. Calculated radiation pattern for the space wave in the case of a 915 MHz surfatron, as in figure 13. The plasma column axis is aligned along the -90° – 90° line, which makes that the elevation angle Θ, determined with respect to the SW propagation direction (discharge tube axis), is thus complementary of the polar angle relative to a right angle.

4. SPECIFIC FEATURES OF A PULSED OPERATED SWD DUE TO THE SPACE-WAVE RADIATION REGION PRECEDING THE DEVELOPMENT OF THE SW PLASMA COLUMN

In a previous paper [1], we have suggested that the maintenance ***E***-field intensity of a discharge is that applied by the operator at the very start of a pulse, provided the off-time of the previous pulse was long enough for the plasma particles to all vanish before. In some types of discharges, for example the positive column of a DC discharge, the beginning of the pulse should correspond to the maximum electron density attainable since afterwards the intensity of the maintenance ***E***-field decreases as the number of particles generated increases, increasing power losses. In the case of a SWD, the maximum electron density is reached only past the elapsed time required to span the space-wave radiation region. Thus, it is expected that maximum "efficiency" of the resulting SW discharge, i.e. reaching for instance the highest excitation and ionization rates, is obtained after a certain delay time, not at the very start of the pulse. To estimate the minimum delay time required before initiation of the SW plasma column, we turned to Figs. 4b, c and d, assuming that a SWD has begun to develop whenever the plasma column observed in the photos is symmetric and continuous (no break along it). The results are gathered in Table 2 for three different average powers.

Table 2. Minimum estimated time (or period) before a SWD develops after applying microwave power and corresponding pulse frequency

Average microwave power (W)	Beginning time of SWD (μs)	Corresponding minimum pulse frequency (kHz)
8	237	12.6
16	186	16
23	82	36.6

Clearly, the higher the applied average microwave power of the pulse, the shorter the time (period) needed for the SWD to start developing. This phenomenon could explain the observation of an optimum pulse repetition rate for a given plasma-related feature.

5. SUMMARY

To determine to what extent a space-wave radiation segment necessarily anticipates the formation of a SWD, four types of wave launcher, namely surfatron, surfaguide, Beenakker cavity and TIAGO system, were utilized to that effect. In all four cases, it was confirmed that the SWD starts to develop only after a space-wave radiation region has been established, the axial length of which (above a minimum microwave power) does not increase with increasing power level, but its electron density as a whole does. It was further found that the length of this non-SWD plasma segment decreases as frequency is increased. Recall that a SW plasma column is identified by the fact that the axial variation of its electron density, in contrast to the (initial) non-SWD segment, decreases linearly away from the launcher.

Such a non-guided radiating space wave had been first reported by Burykin *et al* [16] coming from a positive plasma column along which a (non-ionizing) SW had been launched. These authors attributed the generation of the radiation to a non-uniform portion of the cylindrical plasma column (a relatively abrupt change in the tube diameter) along which the SW propagated creating a space-wave. Under their operating conditions, they found experimentally a radiation pattern having its main lobe at an elevation angle $\Theta = 25°$. Later on, space-wave radiation forerunning a SWD was disclosed by Lebedev [6].

The space-wave segment generates EM emission in the lab to such an extent that it prevents making reliable measurements. A relatively short length FC under cut-off conditions (30 mm and 17 mm long at 915 and 2450 MHz, respectively) is, in this case, enough for preventing the non-guided wave to radiate in the lab. This is a further confirmation of the existence of space-wave radiation, and of the fact that the SW sustaining the discharge is, in contrast, well guided (and confined) along the plasma column.

Besides radiation in the environment, space-wave radiation is responsible for power losses, i.e. power not used to generate electrons in the SWD. For example, a FC under cut-off conditions with a length exceeding the SWD column length provides at 915 MHz in argon gas at atmospheric pressure 30% more electrons than with the 3 cm minimum length FC. In such a case, the space wave (which has become evanescent) and the SW powers are believed to flow independently, toward the end of the SWD as they attenuate, contributing both to the ionization of the SWD.

6. RESEARCH PERSPECTIVES

The power loss (and radiation in the environment) related to achieving SWD is a negative aspect that needs further examination as far as the operating conditions of SWDs are concerned (frequency, tube diameter, gas pressure). An important open question is how ionization is achieved in the non-SWD segment and how it "reconnects" with the SWD when it starts developing. In the case of the surfaguide SW plasma, photos clearly show that it is the dielectric material of the tube (specifically that part of its wall facing the plunger plane) that first carries the EM field into the tube at the same time that it generates some electrons in it (not enough to achieve SW propagation). The role of this non-SWD segment particularly needs to be clarified in the case of the TIAGO system, since there is no dielectric (except neutral gas) between the tip of the launcher and the atmospheric-pressure SWD plasma.

Acknowledgments

The authors wish to thank professors Ahmad Hamdan and John Michael Pearson together with Antoine Durocher-Jean, Ph.D. candidate, for commenting the manuscript and Dr. Danielle Kéroack for data processing, all at the Université de Montréal.

References

1. Moisan M., Nowakowska H., Plasma Sources Sci. Technol.**,** 2018, **27***,* 073001.
2. Glaude V.M.M., Moisan M., Pantel R., Leprince P., Marec J., J. Appl. Phys., 1980, **51***,* 5693.
3. Moisan M., Pantel R., Hubert J., Contributions to Plasma Physics**,** 1990, **30***,* 293.
4. Nowakowska H., Czylkowski D., Zakrzewski Z., J. of Optoelectronics and Advanced Materials, 2005, **7***,* 2427.
5. Zakrzewski Z., Moisan M., Sauvé G., Plasmas sustained within microwave circuits, in Microwave excited plasmas, M. Moisan and J. Pelletier, Editors. Elsevier: Amsterdam, 1992, p. 93.
6. Lebedev Yu.A., J. Moscow Phys. Soc., 1997, **7***,* 267.
7. Moisan M., Beaudry C., Leprince P., IEEE Transactions on Plasma Science, 1975, **3***,* 55.
8. Fleisch T., Kabouzi Y., Moisan M., Pollak J., Castaños-Martínez E., Nowakowska H., Zakrzewski Z., Plasma Sources Sci. Technol., 2007, **16***,* 173.
9. Nowakowska H., Jasiński M., Dębicki P.S., Mizeraczyk J., IEEE Transactions on Plasma Science**,** 2011, **39***,* 1935.
10. Hamdan A., Valade F., Margot J., Vidal F., Matte J.P., Plasma Sources Sci. Technol., 2017, **26***,* 015001.
11. Zucker F.J., Surface-wave antennas and surface-wave-excited arrays, in Antenna engineering handbook, R.C. Johnson and H. Jasik, Editors. McGraw-Hill, 1984, p. 12.1.
12. Rincón R., Muñoz J., Sáez M., Calzada M.D., Spectrochim. Acta B: Atomic Spectroscopy, 2013, **81***,* 26.
13. Ricard A., St-Onge L., Malvos H., Gicquel A., Hubert J., Moisan M., J. Phys. III France, 1995, **5***,* 1269.
14. Balanis C.A., Antenna Theory: Analysis and Design. New Jersey: John Wiley & Sons, 2005.
15. Hagelaar G.J.M., Villeger S., IEEE Transactions on Plasma Science, 2005, **33***,* 496.
16. Burykin Y.I., Levitskiy S.M., Martynenko V.G., Radio Engineering and Electronic Physics, 1975, **20***,* 86.

INTERACTION OF MICROWAVE PLASMA TORCH SUSTAINED BY TRAVELLING ELECTROMAGNETIC WAVE WITH LIQUIDS

E. Benova, P. Marinova[1], T. Bogdanov[2], I. Tsonev[3], F. Krčma[4], Y. Topalova[5], Y. Todorova[5], I. Yotinov[5]

DLTIS, Sofia University, 27 Kosta Loulchev street, 1111 Sofia, Bulgaria
[1] Faculty of Forest Industry, University of Forestry, 10 Kliment Ohridski Blvd., 1797 Sofia, Bulgaria
[2] Medical Faculty, Medical University – Sofia, 1 Georgi Sofiiski Blvd., 1431 Sofia, Bulgaria
[3] Faculty of Physics, Sofia University, 5 James Bourchier Blvd., 1164 Sofia, Bulgaria
[4] Faculty of Chemistry, Brno University of Technology, Purkyňova 118, 612 00 Brno, Czech Republic
[5] Faculty of Biology, Sofia University, 8 Dragan Tsankov Blvd., 1164 Sofia, Bulgaria

Abstract. Microwave Argon plasma torch is sustained by 2.45 GHz electromagnetic wave travelling along the plasma–dielectric boundary. When the plasma torch is in contact with a liquid both the plasma properties are changed during the interaction with the liquid and the liquid physical and chemical characteristics are modified as a result of the plasma treatment. This plasma is strongly non-equilibrium: the electron energy distribution function (EEDF) is non-Maxwellian and the gas temperature T_g is much lower than the electron temperature T_e ($T_g << T_e$). Usually for these plasmas $T_e \sim 1–2$ eV, and $T_g \sim 1000–4000$ K. In our case we have produced Argon plasma torch with T_g close to the room temperature. At these discharge conditions, as a result of plasma treatment, chemically active radicals are produced inside the liquid. In distilled water, even at short treatment time (30 to 60 s) and wave power up to 20 W a noticeable concentration of H_2O_2 is reached [1]. The pH and the liquid conductivity are also changed as a result of plasma treatment. The plasma properties also change at the interaction with liquids. These changes depend on the type of the liquid and the discharge conditions. Some aspects of the plasma torch interaction with water are studied in [2]. Other theoretical and experimental results are presented in this work.

1. INTRODUCTION

The low-temperature, non-equilibrium atmospheric pressure plasmas have attracted increasing interest as simple and less expensive plasma sources operating in open space for various applications in biology, medicine and environmental protection. One of the promising innovative technologies for removal of pollutants in wastewater is based on plasma generated by electrical discharges in liquids or gas discharges in contact with liquids [3–7]. This is the reason that the interaction of non-equilibrium plasmas with liquids is now a “hot topic” in plasma science and technology.

The plasma sources used in this interdisciplinary field are generally of three types: (i) gas discharge plasma jets produced above the liquid and interacting with it; in some cases the liquid plays the role of the second electrode; (ii) electrical discharge generated inside liquid; (iii) multiphase gas-liquid discharges such as gas discharges with sprays or foams and discharges in bubbles inside liquids. A detailed review and roadmap in the field of plasma–liquid interaction can be found in [8].

The most popular plasma jet sources are the DBD discharges created by radiofrequency (13.54 or 27.2 MHz) power supplies [9–11]. Typically, the plasma is produced in helium in order to provide a stable operation at low power at atmospheric pressure. In these plasma jets, the chemically active particles are produced in the active discharge zone and are flowing down-stream from it to the post-discharge region where the sample treatment takes place. These types of plasma jets were intensively studied in the frames of COST Action MP1101 [12–15].

We are investigating the interaction with liquids of another type of plasma source, a microwave Argon plasma torch. The plasma is sustained by travelling electromagnetic surface wave with frequency of 2.45 GHz excited by a surfatron type wave launcher [16], known as surface-wave-sustained discharge (SWD) (Fig. 1). Usually, SWDs operate at low and intermediate pressures and high wave power (> 100 W) in noble gases because filamentation occurs at atmospheric pressure [17]. We have produced stable and reproducible surface-wave plasma both inside the dielectric tube and outside it at low wave power (< 50 W) in Argon at atmospheric pressure. Electromagnetic surface wave excited by the surfatron propagates along the plasma–dielectric tube interface. If the discharge tube is short enough and the wave power is not completely spent at its end the wave continues its propagation after the end of the tube sustaining in this way plasma in the open air (plasma torch). The plasma torch is not afterglow as in the plasma jets but it is an active discharge region where the plasma is produced. Thus, all active plasma components, including short term living particles, are presented up to the end of the plasma torch: electrons, ions, radicals and excited atoms, electromagnetic field, UV radiation, heat. Therefore, all they are simultaneously involved in the treatment of the sample or liquid.

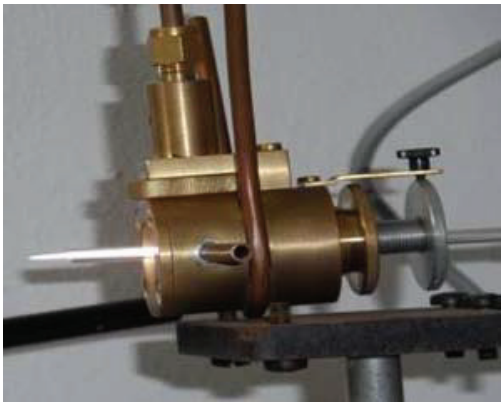

Figure 1. Argon plasma torch sustained by surfatron type electromagnetic wave launcher.

The surface-wave-sustained Argon plasma is non-equilibrium even at atmospheric pressure: the electron energy distribution function (EEDF) is non-Maxwellian and the translational temperature of the heavy particles (called gas temperature T_g) is much lower than the electron temperature T_e (defined as $T_e = 2/3 \langle u \rangle$, where $\langle u \rangle$ is the mean electron energy obtained from the EEDF), $T_g << T_e$. Usually $T_e \sim 1–2$ eV, and $T_g \sim 1000–4000$ K. In our experiments we have produced Argon plasma torch with $T_g < 100$°C and in some discharge conditions even close to the room temperature.

As it is shown in [1], the interaction of surface-wave-sustained Argon plasma torch with liquids leads to changes in both the liquid and the plasma properties. One of the plasma torch characteristics that changed due to the plasma–liquid interaction is the torch length. It depends on the wave power, working gas flow rate and the size and dielectric permittivity of the discharge tube. We are reproducing here in Fig. 2 the results presented in Fig. 5(b) in [1]. The torch length is measured from the end of the quartz discharge tube which is at 2 mm out of the surfatron. The wave power varies from 12 to 40 W at two Argon flow rates used. The results confirm the well-known almost linear dependence of the SWD length on the wave power. New and surprising result is that when the water is present below the plasma the torch length is higher and this is better noticed especially at higher power. This is also illustrated in Fig. 3 in the wave power range from 28 to 40 W.

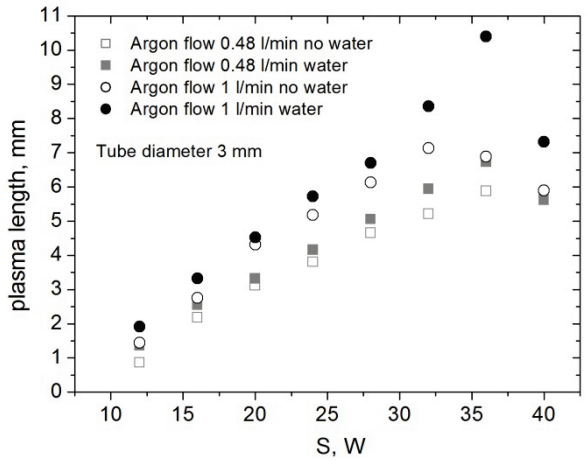

Figure 2. Plasma column length as a function of the wave power at different discharge conditions with and without water below the torch (reproduced from [1]).

One can see from the graphs in Fig. 2 and notice in Fig. 3 that the plasma torch length suddenly decreases at higher power deviating from the linear increase. Without water below the torch this happens at 36 W while with water below it is at 40 W at the fixed other discharge conditions. The reason is the appearance of a shorter second filament with wave power increasing which is noticeable in the last two photos in the first row and the last photo in the second row in Fig. 3.

From Fig. 2, it is also seen that the torch is longer when the Argon flow rate is higher at the same wave power. We should note that a stable plasma torch at a given wave power can be produced with a limited variation of the gas flow rate.

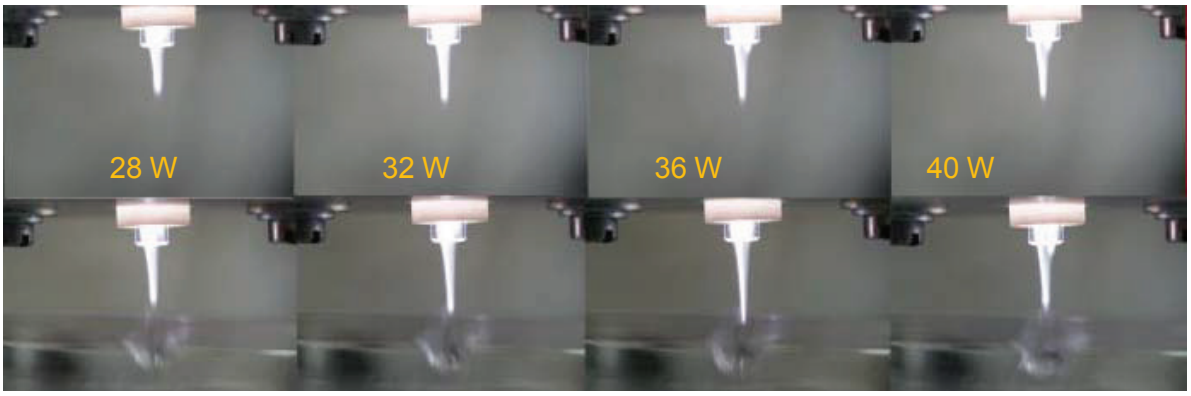

Figure 3. Plasma column length at internal tube diameter 3 mm and various input powers. Upper row – without water; lower row – with water below the torch.

It is also shown in [1] that as a result of plasma treatment of distilled water its properties change. Even at short treatment time (30 s), the characteristic concentration of hydrogen peroxide (generated by plasma–water interaction) inside the distilled water is noticeable and increases with increasing of the wave power. The H_2O_2 plays an important role in various biological, biomedical, environmental and wastewater treatments. It is one of the most powerful oxidizers, able to destroy organic contaminates which are ordinarily difficult to destroy, as well as inactivating cells of living organisms. This is the reason why its creation and concentration determination is important.

At low wave power used in our experiments, the plasma only can touch but not penetrate inside the liquid. In addition, because of the very high water relative dielectric permittivity (about 80 at 2.45 GHz) the electromagnetic wave with low power cannot propagate along a water–plasma boundary [2]. In order to understand the H_2O_2 production and the other effects inside the water we have investigated the processes at plasma–liquid interface and the concentration of active particles there.

2. EXPERIMENTAL

A part of the experimental set-up is shown in Fig. 4. For water treatment, we are using the surfatron in vertical position so that the produced plasma torch can touch the water surface.

The schematic drawing of the experimental set-up is similar to the one presented in [18]. We are using a solid state microwave power supply operating at 2.45 GHz frequency and power up to 200 W (Sairem, GMS 200 W) connected by a flexible coaxial cable to the electromagnetic surface wave launcher SURFATRON 80 (Sairem). The plasma is produced in a quartz tube (i.d. 3.0 mm, o.d. 8.0 mm) inside the surfatron but not appearing outside so that only the plasma torch exists at the surfatron and tube end. The wave power is fixed to 20 W and the Argon flow rate is 1.5 l/min. The FLAME-S-UV-VIS Spectrometer (Ocean Optics) was used for the spectra acquisition. The light emitted by the discharge was focused by quartz UV/VIS Collimating Lens, 200–2000 nm. Following the approach in [18], bands of NO-gamma, OH (A→X), N_2 second positive systems, as well as Argon and Oxygen atomic lines were determined in spectra at different conditions.

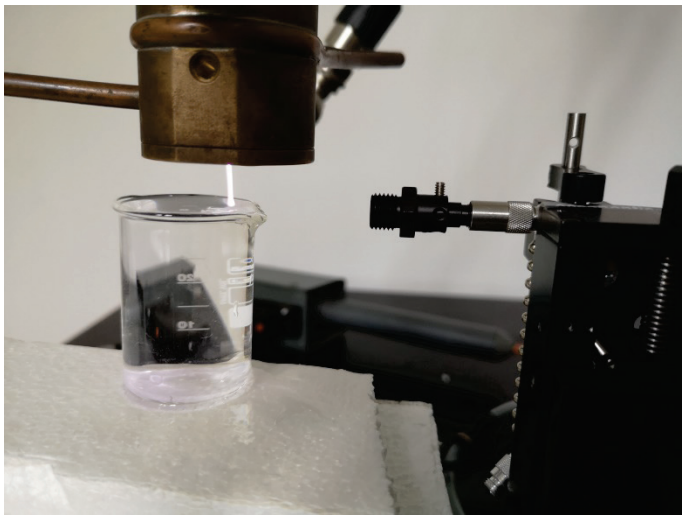

Figure 4. Part of experimental set-up showing the plasma torch position at the water surface.

Plasma torch at various discharge conditions is also used for water treatment. Samples were taken from two artificial lakes and they contain organic and inorganic natural pollutants. Generally, pollutants concentrations in these samples are lower than concentrations used in the model experiments.

3. RESULTS

3.1. Active particles at plasma–liquid interface. The spectra of the plasma torch emitted light are collected in three different cases: (i) pure Argon torch in the air without liquid below it; (ii) Argon plasma torch touching the distilled water below it; (iii) Argon plasma torch touching physiological saline solution (0.9% NaCl). It is presented in Fig. 5 for the wavelength range 200–850 nm. The following bands are shown in the spectrum: NO-gamma 0-2 band (244.5–248.0 nm), OH(A→X) 0-0 band (306.0–310.8 nm), N_2 second positive 0 sequence and argon and oxygen atomic lines. The comparison of the relative intensities in the three cases under investigation shows mostly significant increase when the liquid is below the plasma. It is better visible in Fig. 6 (a)–(d) for the different lines.

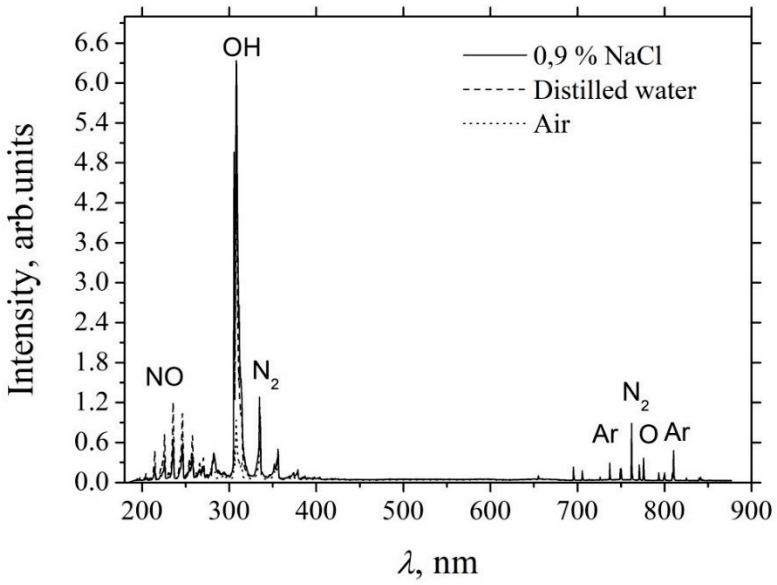

Figure 5. Emission spectra of Argon plasma torch in air (dot), at distilled water surface (dash) and at saline solution surface (solid).

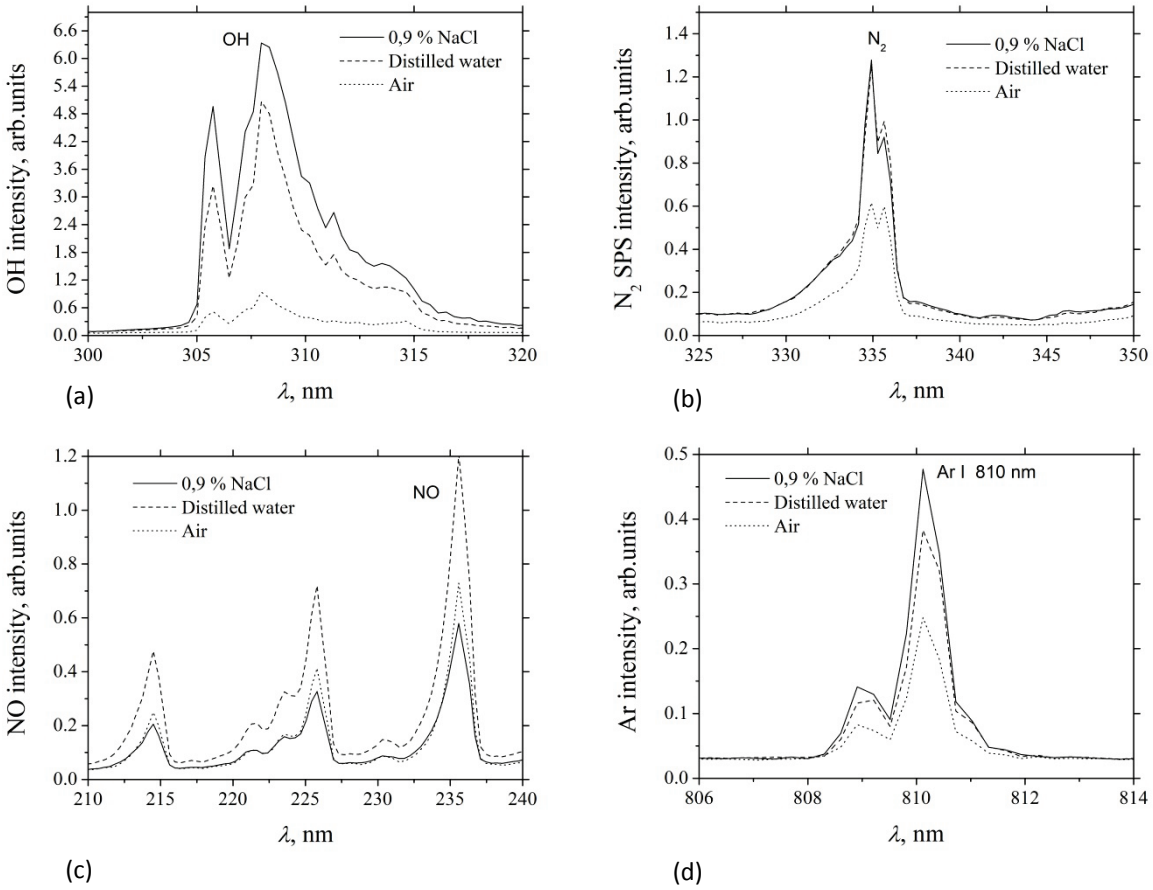

Figure 6. Magnified parts of emission spectra of Argon plasma torch presented in Fig.5 for: (a) OH; (b) N_2 second positive system; (c) NOγ system; (d) an Ar I lines.

As expected, the intensity of OH lines significantly increases (about 10 times) when the water (both distilled and with NaCl) is below the plasma torch and plasma interact with the liquid (Fig. 6a). With the liquid below the torch the N_2 intensity increases about 2 times and the intensity is almost the same for distilled water and saline solution (Fig. 6b). An interesting effect can be seen in Fig. 6c: the intensity of NO increases about two times when the plasma torch interact with the distilled water but slightly decreases when the torch is in contact with the saline solution in comparison to the NO intensity of torch in air. It is also interesting to notice that the Argon lines intensity increase with water below the torch which is shown in Fig. 6d. The atomic O lines have the same behavior as the Ar line in Fig. 6d (not shown here).

We assume that the plasma torch electrons react with the ambient air molecules to produce the above mentioned particles, e.g.

$$e^- + O_2 \rightarrow 2O\bullet + e^-,$$
$$e^- + N_2 \rightarrow 2N\bullet + e^-,$$
$$e^- + H_2O \rightarrow H\bullet + OH\bullet + e^-.$$

The OH concentration depends on the humidity at the given moment and cannot be well controlled. With water or water solution below the torch the region above the liquid surface is enriched with water molecules because of the evaporation which is one of the effects of plasma–water interaction. Thus, the OH intensity significantly increases.

The other observed effects in Fig. 6 need more complex chemistry to be taken into account. The increase of Ar line intensity with liquid below the plasma torch is just opposite to the behavior when small admixture of N_2 or O_2 is added to the Ar plasma torch in open space. As it is shown in [18] the Ar line intensity decreases in the latter case.

3.2. Effect of plasma treatment on nitrates and phosphates concentrations in water. Nitrogen and phosphorus are nutrients that are essential for life in aquatic ecosystems but both can cause environmental harm when present in excess. The nutrient pollution is one of major problems in water bodies having generally an agricultural origin via the use of the chemical manures, municipal wastewater inflows, and other human activities. The excess of these nutrients causes an eutrophication of water and algal blooms so it is necessary to develop and research alternative methods for the effective treatment of surplus amounts of nutrients. In the experiment described below, the microwave plasma potential to eliminate excess nitrogen and phosphorus in natural waters was evaluated. The water samples from two eutrophic reservoirs with serious algal bloom – Pchelina (marked with Pch) and Telish (marked with Tl) were treated with microwave plasma torch. The treated volume of samples was 125 ml, the wave power 20 or 30 W at the same Agon flow 2 l/min. The samples were treated without and with stirring (500 rpm). The nitrate and phosphate concentrations were analyzed before and after having been exposed to plasma torch treatment at exposure times of 1 and 5 min.

In natural waters, the nitrogen-based chemistry is very complicated. The nitrogen have a great variety of forms: dissolved inorganic forms – nitrates, nitrites, ammonium ions; gases (N_2, N_2O, NO); dissolved organic nitrogen – urea, uric acid, amino acids, proteins and others; particulate organic nitrogen. Nitrate is the most common, oxidized and stable form of inorganic nitrogen in environment. It can be produced by oxidation of reduced forms or degradation of organics. At plasma treatment, these forms are transformed into one another. Additionally, various reactive nitrogen species can be generated at contact of plasma with water. The study of phosphorus dynamics at plasma interaction with liquids attracts less interest until now, but it is likely to be affected significantly at plasma treatment. In Fig. 7 the concentrations of nitrates and phosphates are presented. As can be seen, the nitrate and phosphate concentrations increased at plasma treatment but the effect of mixing and change of wave power was not one-way.

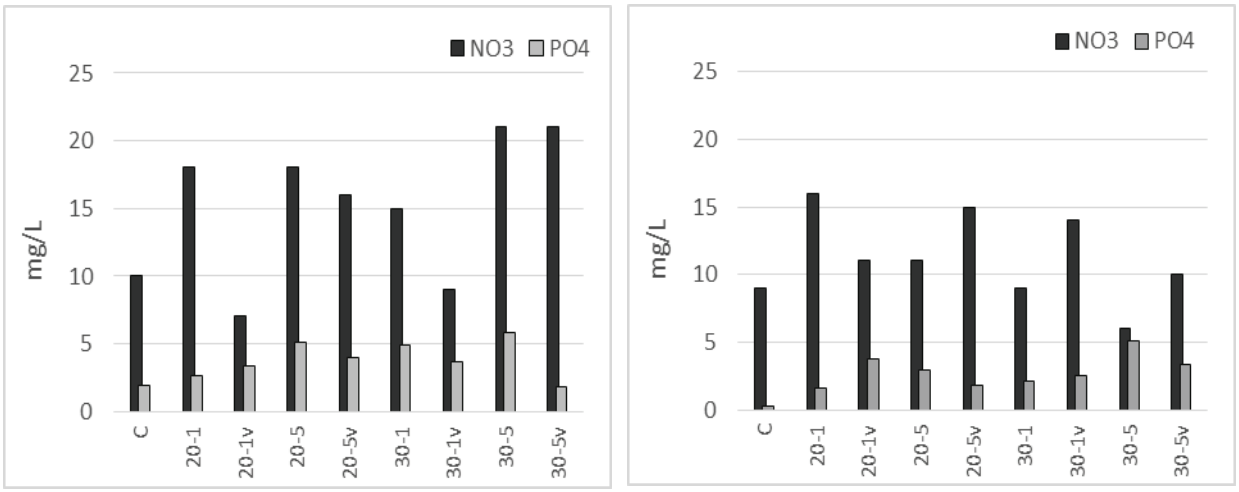

Figure 7. Dynamics of nitrates and phosphates at microwave plasma treatment of water from Pchelina reservoir (left) and Telish reservoir (right): C – control; 20-1 – 1 min treatment at 20 W; 20-1v – 1 min treatment at 20 W and stirring; 20-5 – 5 min treatment at 20 W; 20-5v – 5 min treatment at 20 W and stirring; 30-1 – 1 min treatment at 30 W; 30-1v – 1 min treatment at 30 W and stirring; 30-5 – 5 min treatment at 30 W; 30-5v – 5 min treatment at 30W and stirring.

3.3. Removal of hazardous organic pollutants from wastewater. A similar experiment was also performed to evaluate the effect of plasma on removal of high concentrations of hazardous organic pollutants – another serious threat, related to anthropogenic pollution of waters. The plasma characteristics and treatment conditions were the same with different exposure times – from 1 to 20 min. The organic pollutant was phenol (aromatic compound) in very high concentration – 500 mg/L. The results in Fig. 8 showed that the phenol was eliminated effectively by argon plasma torch, assessed by COD reduction in water (Chemical Oxygen Demand – test for easy measurement of organic oxidizable pollutants in water). More than 50% of the organic content is eliminated from the water in 5 minutes of treatment.

Initial results on the treatment of natural and heavily polluted waters with microwave plasma sources indicate that the oxidative potential of water systems is activated. This potential can be directed and applied to water treatment by accelerating various oxidation processes depending on the type and concentration of pollutants and technological modules and facilities.

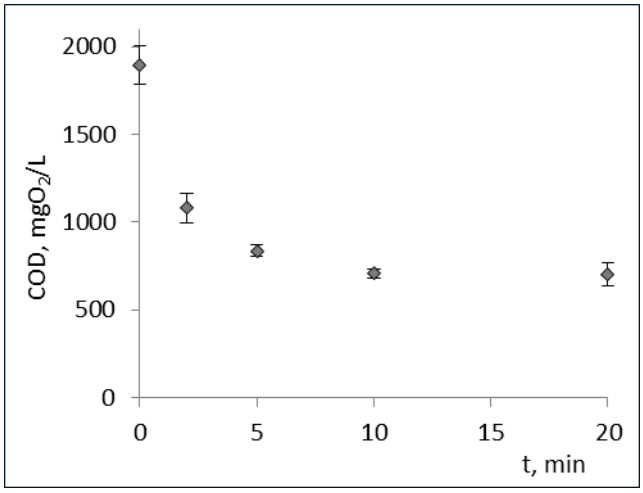

Figure 8. Removal of phenol, assessed by COD reduction at plasma treatment.

Acknowledgments

This work was financially supported by Bulgarian National Science Fund under Grant No. DN08/8, 2016 and partially by (i) the COST Action TD1208 "Electrical discharges with liquids for future applications", (ii) CEEPUS network AT0063, and (iii) the Operational programme "Science and Education for Smart Growth" 2014-2020, co-funded by the European union through the European structural and investment funds: Project BG05M2OP001-1.002-0019 „Clean technologies for sustainable environment – water, waste, energy for circular economy" (Clean&Circle CoC) by funding of the experts labor.

References

1. Marinova P., Benova E., Todorova Y., Topalova Y., Yotinov I., Atanasova M., Krčma F., Journal of Physics: Conf. Series, 2018, **982**, 012009.
2. Benova E., Atanasova M., Bogdanov T., Marinova P., Krčma F., Mazánková V., Dostál L., Plasma Medicine, 2016, **6**, N 1, 59.
3. Locke B.R., Sato M., Sunka P., Hoffmann M.R., Chang J.-S., Ind. Eng. Chem. Res., 2006, **45**, 882.
4. Cheng H.H., Chen S.S., Wu Y.C., et al., J. Environ. Eng. Manage., 2007, **17**, N 6, 427.
5. Zhang J., Chen J., Li X., J. Water Resource Prot., 2009, **2**, 99.
6. Magureanu M., Piroi D., Mandache N.B., et al., Water Res., 2010, **44**, 3445.
7. Thagard S.M., Stratton G.R., Dai F., Bellona C.L., Holsen T.M., Bohl D.G., Paek E., Dickenson E.R.V., J. Phys. D: Appl. Phys., 2017, **50**, 014003.
8. Bruggeman P.J., Kushner M.J., Locke B.R., et al., Plasma Sources Sci. Technol., 2016, **25**, 053002.
9. Yambe K., Konda K., Ogura K., Phys. Plasmas, 2015, **22**, 053513.
10. Xu Z., Shen J., Zhang Z., Ma J., Ma R., Zhao Y., Sun Q., Qian S., Zhang H., Ding L., Cheng C., Chu P.K., Xia W., Plasma Proces. Polym., 2015, **12**, 827.
11. Hensel K., Kučerová K., Tarabová B., Janda M., Machala Z., Sano K., Mihai C.T., Ciorpac M., Gorgan L.D., Jijie R., Pohoata V., Topala I., Biointerphases, 2015, **10**, 029515.
12. Wende K., Williams P., Dalluge J., Van Gaens W., Aboubakr H., Bischof J., von Woedtke T., Goyal S.M., Weltmann K.-D., Bogaerts A., Masur K., Bruggeman P.J., Biointerphases, 2015, **10**, 029518.
13. Schmidt-Bleker A., Reuter S., Weltmann K.-D., J. Phys.D: Appl. Phys., 2015, **48**, 175202.

14. Ellerweg D., Benedikt J., von Keudell A., Knake N., Schulz-von der Gathen V., New J. Phys., 2010, **12**, 013021.
15. Hefny M.M., Pattyn C., Lukeš P., Benedikt J., J. Phys.D: Appl. Phys., 2016, **49**, 404002.
16. Moisan M., Zakrzewski Z., Pantel R., J. Phys. D: Appl. Phys., 1979, **12**, 219.
17. Castaños-Martíınez E., Moisan M., Kabouzi Y., J. Phys. D: Appl. Phys., 2009, **42** 012003.
18. Krčma F., Tsonev I., Smejkalová K., Truchlá D., Kozáková Z., Zhekova M., Marinova P., Bogdanov T., Benova E., J. Phys. D: Appl. Phys., 2018, in press https://doi.org/10.1088/1361-6463/aad82b.

MULTIPACTOR DISCHARGE ON A DIELECTRIC AT DIFFERENT DIRECTIONS OF THE MICROWAVE ELECTRIC FIELD: THEORY AND EXPERIMENT

V. A. Ivanov[1,2], A. S. Sakharov[1], M. E. Konyzhev[1]

[1] A. M. Prokhorov General Physics Institute of the Russian Academy of Sciences, Vavilov Str., 38, Moscow, 119991, Russia
[2] National Research Nuclear University "MEPhI," Kashirskoe Shosse, 31, Moscow, 115409 Russia

Abstract. A brief review of theoretical and experimental studies of secondary electron emission microwave discharge (multipactor) on a dielectric, carried out at the Plasma Physics Department of the Prokhorov General Physics Institute, Russian Academy of Sciences, is presented. The coefficient of microwave power absorption by a single-surface multipactor on a dielectric is found as a function of the incident microwave power and secondary electron emission properties of the dielectric. The dependence of the microwave power absorbed by a single-surface multipactor on the angle between the microwave electric field and the dielectric surface is studied analytically and numerically. Results of experimental studies of a single-surface multipactor on a dielectric in a rectangular waveguide are presented and compared with theoretical results.

1. INTRODUCTION

Suppression of microwave discharges in vacuum transmission lines of high-power microwave devices is a very challenging problem in various fields of science and technology, such as space and ground-based microwave communication [1, 2] and systems for microwave plasma heating in magnetic confinement devices [3, 4]. Microwave discharges deteriorate the transmission properties of vacuum waveguides, lead to intermodulation and generation of microwave harmonics, and may cause damages of the elements of transmission lines, including destruction of the input and output dielectric windows [5–12]. On the other hand, microwave discharges are widely used in modern technologies for material processing [13, 14] and the knowledge of their properties and conditions for their excitation is of great practical significance.

An important stage of a microwave discharge on a dielectric or metal surface is the so-called electron multipactor − an electron avalanche caused by secondary electron emission (SEE) from the surface under bombardment by electrons accelerated in the microwave field. Two main types of multipactor discharge are traditionally considered in the scientific literature: single-surface multipactor on a dielectric and double-surface multipactor between two metal walls [15–19].

In the classical single-surface multipactor on a dielectric [16] (Fig. 1a), the external microwave electric field $\mathbf{E}_0 \sin\omega t$ is directed along the dielectric surface and the emitted electrons return back to the surface under the action of the restoring force caused by the positive charge accumulated on the dielectric due to SEE. For this type of discharge to develop, it is necessary that the electron oscillation energy in the microwave field $\varepsilon_{osc} = (eE_0/\omega)^2/2m_e$ be higher than the first crossover energy ε_1 (the energy of an incident electron above which the secondary emission yield (SEY) δ is larger than unity) [15, 16]. Here, e and m_e are the electron charge and mass, respectively; E_0 is the microwave electric field amplitude; and ω is the microwave field circular frequency.

In the simplest model of a double-surface multipactor [17, 18] (Fig. 1b), the external microwave field is directed perpendicular to the waveguide walls and the discharge develops if the electron transit time between the walls satisfies the resonance condition $t_{transit} \approx (2n+1)\pi/\omega$, where n is an integer.

The bombardment of the dielectric by the electrons generated in a single-surface multipactor leads to the heating of a thin (~1 μm) surface layer of the dielectric. High temperature gradients ($\geq 10^4$ K/cm)

arising in this layer result in the appearance of microcracks on the dielectric surface. The multipactor can also reduce the threshold for the development of a surface microwave breakdown due to either ionization of the residual gas near the dielectric surface [20] or a short-term increase in the conductivity of the dielectric surface caused by the accumulation and of point defects of the crystal lattice (color centers) under bombardment by electrons accelerated in the microwave field and relaxation of these color centers with a release of free electrons in the dielectric [7, 9, 21].

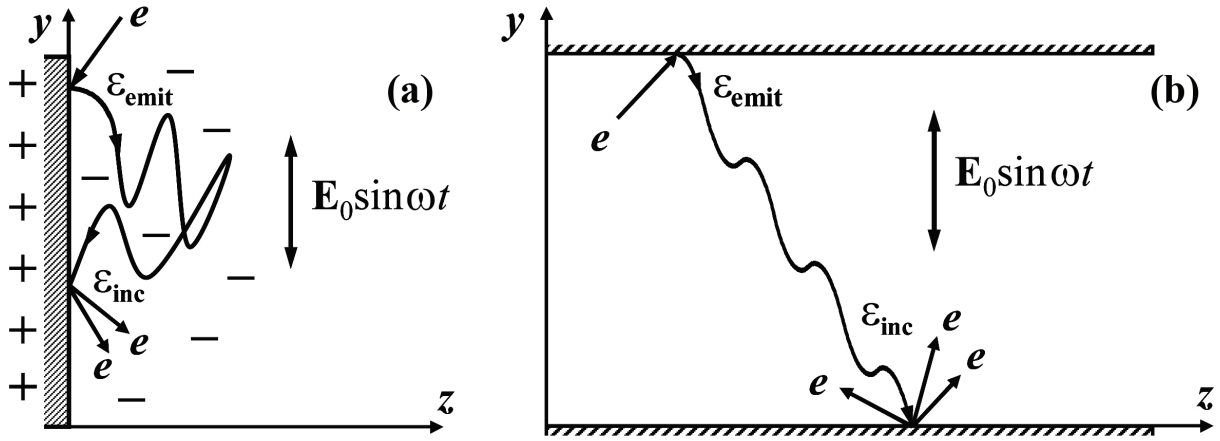

Figure 1. Two main types of multipactor discharge: (a) single-surface multipactor on a dielectric and (b) double-surface multipactor between two metal walls.

A typical scenario of a microwave discharge on a dielectric (LiF or NaCl single crystal) is illustrated in Fig. 2 [12]. The discharge develops through the multipactor, filamentary breakdown, and plasma flare stages. A feeble glow on the dielectric in the multipactor stage (Fig. 2a) is caused by the luminescence of color centers. The luminescence spectrum of short-lived (~1 μs) color centers produced under electron bombardment of an uncolored LiF crystal in a multipactor discharge is shown in Fig. 3a [21]. The growth of the luminescence intensity during the multipactor discharge (Fig. 3b) is related to the gradual accumulation of color centers in a narrow ($d \sim 0.05$ μm) surface layer of the dielectric. The surface density of color centers in the multipactor discharge can reach a value of $N^* \sim (1–3) \times 10^{14}$ cm^{-2}, which corresponds to their bulk density in the surface layer of $n^* \sim N^*/a \sim 10^{19}–10^{20}$ cm^{-3} [21]. Relaxation of short-lived centers results in the production of stable color centers with a density of ~10^{16} cm^{-3} for one multipactor discharge, i.e., the density required to form laser active medium in the crystal (~10^{20} cm^{-3}) can be achieved for 10^4 multipactor discharges.

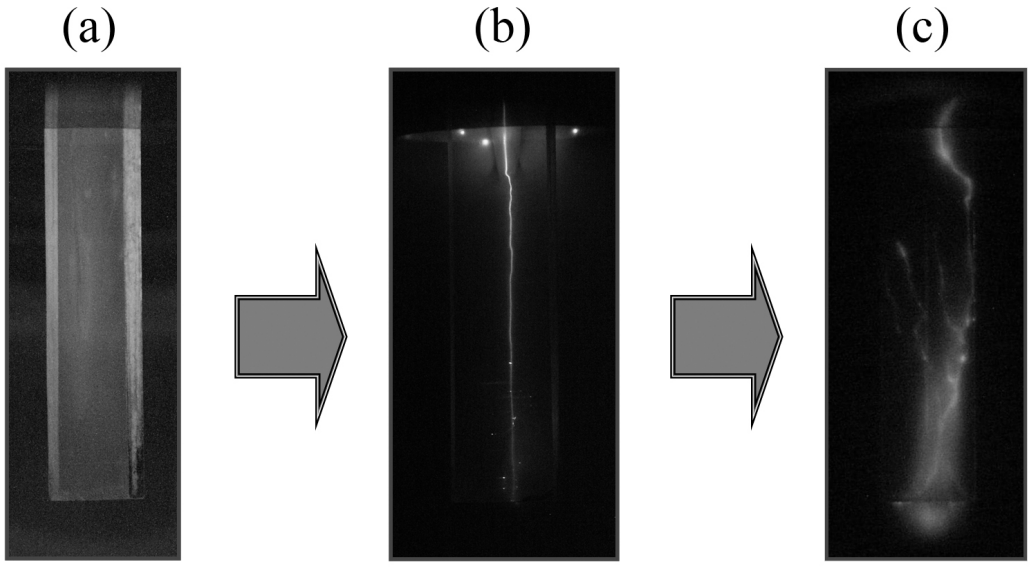

Figure 2. Three stages of an electrodeless microwave discharge excited by pulsed microwave radiation on a solid dielectric in vacuum [12]: (a) multipactor (1000-fold light amplification), (b) filamentary microwave breakdown (no light amplification), and (c) plasma-flare microwave discharge (fivefold light amplification).

Thus, depending on the conditions and purposes of a particular experiment, the multipactor discharge can have either a negative or a positive effect. The negative effects are damages of input/output microwave windows, initiation of microwave breakdowns, and intermodulation in far space transmission devices. The positive effect is the possibility of using multipactor discharges to modify the surface properties of crystal dielectrics by creating color centers with a number density of up to 10^{20} cm^{-3}, which can be used to form a surface layer of laser-active medium for the use in integrated circuits.

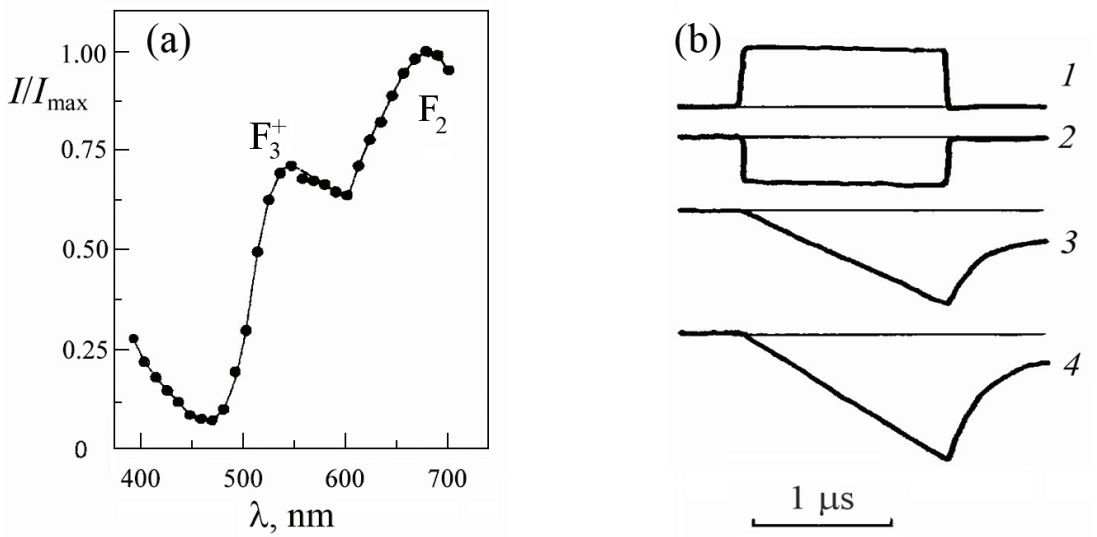

Figure 3. (a) Luminescence spectrum of an uncolored LiF crystal excited by a pulsed microwave discharge and (b) waveforms (in arb. units) of (*1*) microwave power, (*2*) electron current from the multipactor region, and (*3*, *4*) optical emission from the LiF crystal in the wavelength regions of 540 ± 2 and 670 ± 2 nm [21].

Single-surface multipactor on a dielectric can also develop when the microwave electric field is inclined with respect to the dielectric surface [22, 23]. Such conditions can occur on the surfaces of dielectric inserts on the waveguide walls and also when the microwave window is tilted relative to the axis of the microwave beam. Such a situation can also take place in the course of multipactor processing of dielectric crystals with the purpose of modifying their surface properties (coloring of jewelry crystals, creation of a surface layer of laser-active medium, etc.). In this case, the optimal regime of crystal processing can be determined not only by the power deposited in the discharge, but also the direction of the microwave electric field. In this context, it is of interest to examine how the coefficient of microwave power absorption in the multipactor depends on the inclination angle α of the microwave electric field relative to the dielectric surface.

In the two limiting cases, the multipactor is excited by the microwave field directed parallel ($\alpha = 0$) or perpendicular ($\alpha = \pi/2$) to the dielectric surface. Further, we will refer to these types of multipactor as "parallel" and "perpendicular" multipactors, respectively.

In this paper, we present a brief review of theoretical and experimental studies of multipactor discharges carried out at the Plasma Physics Department of the Prokhorov General Physics Institute, Russian Academy of Sciences. The focus is made on the coefficient of microwave power absorption in a single-surface multipactor discharge on a dielectric as a function of the angle α between the microwave electric field and the dielectric surface. In Section 2, parallel single-surface multipactor on a dielectric is analyzed theoretically and simulated numerically. Main attention is paid to the saturated multipactor at microwave intensities substantially exceeding the threshold intensity. The power absorbed by the saturated parallel multipactor is calculated. The influence of elastic and inelastic electron reflections from the dielectric surface on the multipactor parameters is examined in Section 3. It is shown the coefficient of microwave power absorption increases significantly in the presence of electron reflections. In Section 4, theoretical results are compared with results of experimental studies of parallel single-surface multipactor on a dielectric in a rectangular waveguide. In Section 5, microwave power absorption by a perpendicular single-surface multipactor is analyzed theoretically and numerically. Section 6 is devoted to calculating the coefficient of microwave power absorption by an "inclined" multipactor ($0 < \alpha < \pi/2$). It is

found that the power deposited per unit area of the dielectric surface has a minimum at a certain angle α_m, which depends of the SEE properties. In the Conclusions, the main results are summarized.

2. MICROWAVE POWER ABSORPTION BY A "PARALLEL" SINGLE-SURFACE MULTIPACTOR ON A DIELECTRIC

Previous estimates of the coefficient of microwave power absorption by a single-surface multipactor on a dielectric [24–26],

$$\kappa = W_{\text{abs}} / W_{\text{inc}}, \tag{1}$$

where W_{abs} is the power absorbed per unit area of the dielectric surface and $W_{\text{inc}} = cE_0^2/8\pi$ is the power flux density of the incident microwave radiation, have shown that this coefficient is rather low. In [24], the following estimate was obtained: $\kappa \approx 0.004T_e^{1/2}$, where T_e is the temperature (in eV) of secondary electrons emitted from the dielectric surface. According to this estimate, for typical T_e values at a level of 1–2 eV [27], the power absorbed by the multipactor discharge comprises about 1% of the incident microwave power. Nearly the same estimate of the absorption coefficient (~1%) was obtained in [25] when analyzing the effects related to the electron space charge in a single-surface multipactor. In spite of such a low absorption coefficient, the absolute value of the power surface density released on the surfaces of dielectric windows in modern high-power microwave sources ($W_0 \sim 1$ kW/cm^2) can be quite sufficient to cause inadmissible thermal and mechanical stresses in the surface layer of the dielectric, resulting in the appearance of microcracks on the window surfaces.

Particle-in-cell (PIC) simulations of a single-sided multipactor [26] showed that the absorption coefficient slowly increased with microwave intensity. Thus, as the electron oscillation energy was raised by two orders of magnitude (from ≈200 eV to ≈20 keV), the absorption coefficients increased only fourfold (from 0.5 to 2%). Note that, in [26], the reason for the gradual increase in the coefficient of microwave power absorption by a single-sided multipactor with increasing microwave power was not discussed and, accordingly, no analytical expression describing such an increase was derived.

When studying multipactor discharges analytically and numerically, the following empirical formula for the SEY, proposed by Vaughan [28], has received wide application (see Fig. 4, curve *1*):

$$\delta = \delta_m (Ve^{1-V})^k, \tag{2}$$

where $V = (\varepsilon_{\text{inc}} - \varepsilon_0)/(\varepsilon_{\text{max}} - \varepsilon_0)$. Here, ε_{inc} is the energy of an incident (primary) electron, ε_0 is the cutoff energy below which δ is zero, ε_m is the energy corresponding to the maximum SEY at a given incidence angle θ, $k = 0.62$ for $V < 1$, $k = 0.25$ for $V > 1$, $\delta_m = \delta_{m0}(1 + \theta^2/2\pi)$, and $\varepsilon_m = \varepsilon_{m0}(1 + \theta^2/\pi)$, with δ_{m0} and ε_{m0} being the peak value of the SEY at $\theta = 0$ and the incident energy corresponding to this peak, respectively. In theoretical works and numerical simulations, a simplified Vaughan's formula with $\varepsilon_0 = 0$ (Fig. 4, curve *2*) is widely used (see, e.g., [24–26, 29, 30]).

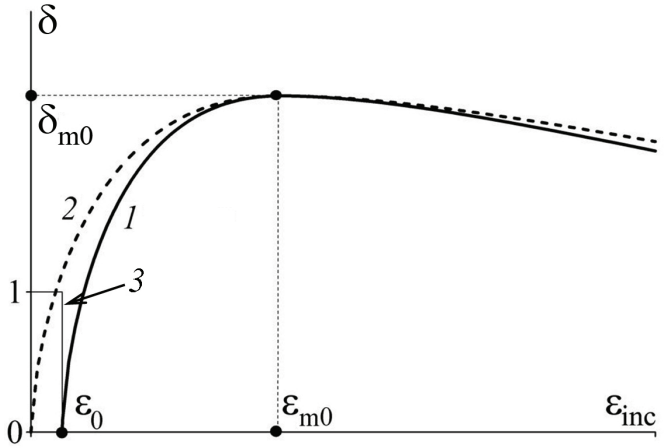

Figure 4. SEY as a function of the incident electron energy: (*1*) Vaughan's formula, (*2*) simplified Vaughan's formula with $\varepsilon_0 = 0$, and (*3*) unit step at $\varepsilon_{\text{inc}} < \varepsilon_0$ introduced by Vicente et al. [31] to take into account enhanced electron reflection at low energies (see Section 3).

In [32, 33], an analytical formula for κ as a function of the electron oscillation energy ε_{osc} was derived self-consistently with allowance for the finite temperature of secondary electrons and the space charge of the electron layer formed near the dielectric surface. Here, we only briefly describe the idea and scheme of deriving this formula, omitting algebraic manipulation.

Let us consider the classical single-surface multipactor on a dielectric (Fig 1a). When the electron oscillation energy ε_{osc} in the microwave field is higher than the first crossover energy ε_1, the emitted electrons return back to the surface with energies sufficient to knock out a larger number of secondary electrons, i.e., an electron avalanche develops, during which an electron layer forms near the dielectric surface, whereas the surface itself is charged positively. As the positive charge on the dielectric increases, the time during which the emitted electrons return back to the surface decreases, which leads to a decrease in the energy acquired by the electrons in the microwave field. Hence, as time elapses, the electron avalanche gradually decelerates and then reaches saturation.

In the saturated (quasi-steady) multipactor, the δ value averaged over the microwave oscillation period is equal to 1. If the oscillation energy is much higher than the first crossover energy ($\varepsilon_{osc} >> \varepsilon_1$), then the electron flight time Δt in the saturated multipactor must be much shorter than ω^{-1}; otherwise, the emitted electrons would acquire an energy larger than ε_1 and the number of secondary electrons would continue to grow. This means that, in such a highly overthreshold multipactor, the external microwave field varies only slightly during the flight time of secondary electrons and the multipactor characteristics have time to adjust to the instantaneous value of the microwave field. Hence, we can use the so-called "constant-field" approximation, in which the multipactor parameters are determined by the instantaneous value of the microwave electric field $E_y(t) = E_0 \sin\omega t$, i.e., depend on time parametrically.

In this approximation, assuming that emitted electrons have a Maxwellian distribution with a temperature $T_e << \varepsilon_1$ and that ε_1 is much smaller than ε_{m0}, the power deposited per unit area of the dielectric surface can be evaluated analytically [32]. Solving the equation of motion for emitted electrons in the normal electric field, which is the sum of the field produced by the electron space charge formed near the dielectric surface and the uncompensated positive charge accumulated on the dielectric, we find that the characteristic flight time of electrons from the surface and back is $\Delta t \sim 1/\omega_{pe} << 1/\omega$, where $\omega_{pe} = (4\pi e^2 n_0/m_e)^{1/2}$, with n_0 being the electron density just near the dielectric surface. The energy acquired by an emitted electron over the flight time Δt in the instantaneous microwave field $E_y(t)$ and transferred to the dielectric surface is $\varepsilon_{inc} \sim (eE_y\Delta t)^2/2m_e \sim (E_y)^2/8\pi n_0$. From the particle flux balance in the saturated multipactor, we find that $\varepsilon_{inc} \sim \varepsilon_1$, i.e., we have $n_0 \sim (E_y)^2/8\pi\varepsilon_1$. It follows from here that the energy flux density onto the dielectric surface is $W_{abs} \sim v_\perp n_0 \varepsilon_{inc} \sim v_T n_0 \varepsilon_1 \sim v_T (E_y)^2/8\pi$, where $v_T = (T_e/m_e)^{1/2}$. Averaging $W_{abs}(t)$ over time and dividing $\langle W_{abs} \rangle$ by $W_{inc} = cE_0^2/8\pi$, we find that the coefficient of power absorption is $\kappa \sim v_T/c$. Correct calculations performed with a simplified Vaughan's formula ($\varepsilon_0 = 0$) show that the tail of the Maxwellian distribution introduces an additional numerical factor on the order of $\ln(\varepsilon_{osc}/\varepsilon_1)$ (see [32] for details), so that finally we obtain

$$\kappa \approx \frac{v_T}{c}\sqrt{\frac{\pi}{2}}\ln(\varepsilon_{osc}/\varepsilon_1), \qquad (3)$$

i.e., the absorption coefficient grows slowly (logarithmically) with increasing microwave intensity.

We performed 1D3V (one-dimensional in coordinate space and three-dimensional in velocity space) particle-in-cell (PIC) simulations of a single-surface multipactor excited on the surfaces of various dielectrics: amorphous SiO_2 (quartz glass), LiF single crystal, and NaCl single crystal. These materials were chosen because there is a large database on their SEE properties in the literature (see, e.g., [27, 34]).

Figure 5 presents simulation results obtained for a LiF crystal ($\varepsilon_{m0} \approx 1000$ eV, $\delta_{m0} \approx 7.5$ [34]). The single-surface multipactor was excited by a microwave field with an intensity substantially exceeding the threshold value ($\varepsilon_{osc} = 450$ eV, $\varepsilon_1 = 14.5$ eV). The SEY was described by the simplified Vaughan's formula with $\varepsilon_0 = 0$, the frequency of the microwave field was $f = \omega/2\pi = 1.95$ GHz, and the temperature of secondary electrons was set at $T_e = 1$ eV. The multipactor was initiated by injecting seed electrons with an areal density of $S_{inj} = 0.05 n_{cr} v_T/\omega = 0.8 \times 10^7$ cm^2 from the dielectric (where $n_{cr} = m_e\omega^2/4\pi e^2$). The figure shows typical time dependences of the (a) effective thickness of the electron layer, $\delta z = S/n_0$ (where

$S(t) = \int_0^\infty n_e(z,t)dz$ is the areal density of emitted electrons), and (b) the electron density n_0 near the dielectric. Here, n_0 and δz are normalized to $n_{cr} = m_e\omega^2/4\pi e^2 = 4.7 \times 10^{10}$ cm^{-3} and $z_0 = v_T/\omega = 3.4 \times 10^{-3}$ cm, respectively.

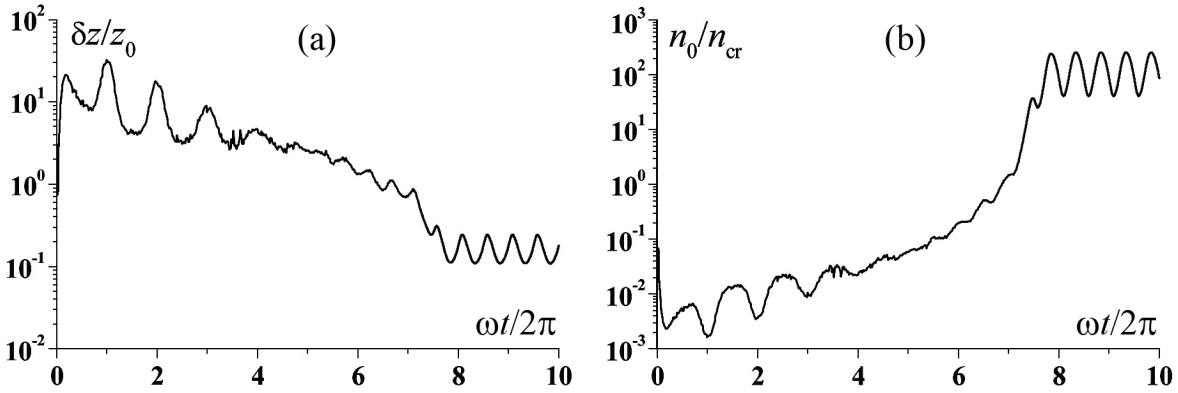

Figure 5. Time dependences of the parameters of a single-surface multipactor excited on the surface of a LiF single crystal for the electron oscillation energy substantially exceeding the first crossover energy (ε_{osc} = 450 eV, ε_1 = 14.5 eV): (a) effective thickness of the electron layer, $\delta z = S/n_0$, and (b) electron density n_0 just near the dielectric [32].

It is seen that, in the stage of electron avalanche, the number of electrons in the layer grows monotonically, while the layer thickness decreases to ~10^{-3} cm, after which the discharge saturates. In the saturated (quasi-steady) regime, the electron areal density, the electron density just near the dielectric, and the effective thickness of the electron sheath oscillate with the doubled frequency of the external field, 2ω, following oscillations of $E^2(t)$. It should be noted that, in the saturated multipactor, the electron density in the layer substantially exceeds the critical density. Nevertheless, the electron layer is almost fully transparent for microwave radiation, because, in this case, the skin depth $z_{skin} = c/\omega_{p0} \approx 0.25$ cm is much larger than the layer thickness.

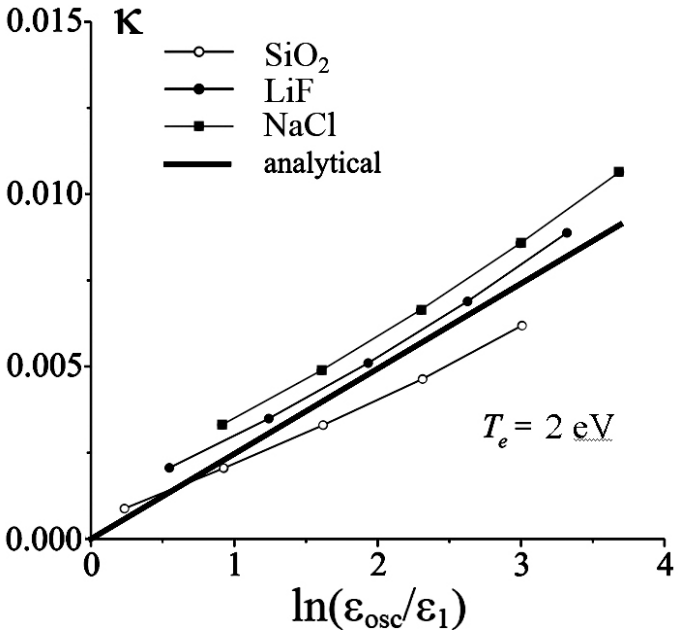

Figure 6. Calculated coefficient of microwave power absorption κ by a saturated multipactor discharge as a function of the electron oscillation energy ε_{osc} for different dielectric materials: SiO_2 (ε_{m0} = 400 eV, δ_{m0} = 2.4, ε_1 = 40 eV), LiF (ε_{m0} = 1000 eV, δ_{m0} = 7.5, ε_1 = 14.5 eV), and NaCl (ε_{m0} = 1200 eV, δ_{m0} = 10.5, ε_1 = 10.0 eV). The heavy solid line shows analytical dependence (3) [32].

Figure 6 shows the absorption coefficient κ calculated using 1D3V simulations as a function of the oscillation energy for SiO_2, LiF, and NaCl, assuming that T_e = 2 eV and the SEY is described by Vaughan's formula with $\varepsilon_0 = 0$. It can be seen that the simulation results agree satisfactorily with analytical formula: all curves group around dependence (3). It is worth noting that analytical formula (3) satisfactorily agrees with the simulation results not only at $\varepsilon_{osc} >> \varepsilon_1$ (i.e., when the constant-field

approximation is valid), but also near the threshold for the onset of a single-surface multipactor ($\varepsilon_{osc} \sim \varepsilon_1$). The larger deviation of the calculated curve for the NaCl single crystal from the analytical dependence compared to that for the LiF single crystal is probably related to the larger ratio T_e/ε_1 for the former (note that, in deriving formula (3), this ratio was assumed to be infinitely small). The deviation of the calculated curve from the analytical dependence for amorphous SiO_2 may be attributed to the first crossover energy ε_1 for SiO_2 being much closer to ε_{m0} than for LiF and NaCl crystals [34], because it was assumed that $\varepsilon_1 << \varepsilon_{m0}$ when deriving formula (3).

3. INFLUENCE OF ELECTRON REFLECTIONS ON THE MICROWAVE POWER ABSORPTION BY A PARALLEL MULTIPACTOR

The analytical expression for the SEY proposed by Vaughan [28] refers to the so-called "true" secondary electrons, which are emitted from a narrow surface layer of a dielectric or metal under bombardment by primary electrons. The energy spectrum of true secondaries is usually close to Maxwellian with a temperature of several eV [27]. The total energy spectrum of secondary electrons can also be significantly contributed by elastically reflected (scattered) and inelastically reflected (rediffused) primaries [27, 35]. A typical energy spectrum of secondary electrons for $\varepsilon_{inc} = 180$ eV is schematically shown in Fig. 7 [27].

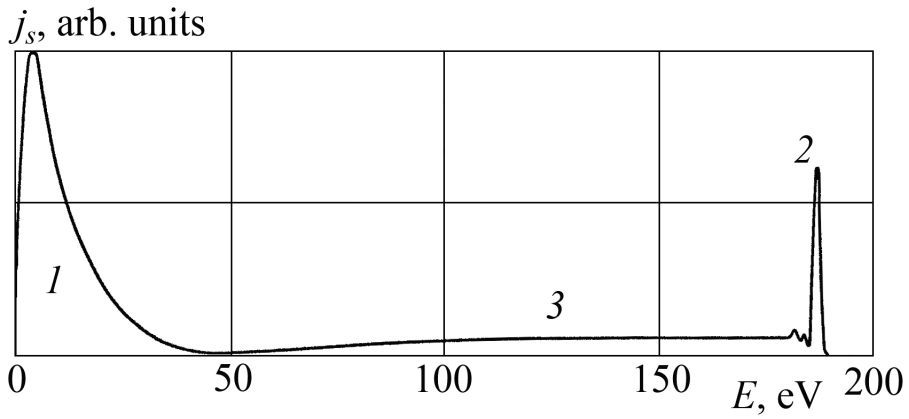

Figure 7. Typical energy spectrum of secondary electrons for $\varepsilon_{inc} = 180$ eV [27]: (*1*) true secondaries, (*2*) elastically reflected (scattered) electrons, and (*3*) inelastically reflected (rediffused) electrons.

The significant effect of electron reflections on the single-surface multipactor is illustrated in Fig. 8, which presents results of 1D3V simulations of a "parallel" ($\alpha = 0$) multipactor on a SiO_2 surface [32]. Upon elastic reflection, the energy of the reflected electron ε_{ref} was set equal to the energy of the incident electron ε_{inc}, whereas upon inelastic scattering, it could take any value between zero and ε_{inc} with equal probabilities. In both cases, the reflected electrons were distributed over velocity directions according to the law $dN/d\Omega \sim \cos\theta$ [27, 34].

The heavy line in Fig. 8 shows analytical dependence (3), curve *1* show the result of simulations by the simplified Vaughan's formula with $\varepsilon_0 = 0$, and curve *2* shows the result obtained using Vaughan's formula with a finite cutoff energy ($\varepsilon_0 = 30$ eV) without allowance for electron reflections. It is seen that the absorption coefficient somewhat decreases when the finite cutoff energy is taken into account.

Curve *3* in Fig. 8 shows the absorption coefficient calculated under the assumption that the coefficient of elastic electron reflections at $\varepsilon < \varepsilon_0$ is $R = 1$ (the unit step in δ in Fig. 4), as was proposed by Vicente et al. [31] in order to describe the experimentally observed high reflection coefficient of primary electrons at very low energies (see also [36]). According to experimental data [34], the coefficient of electron reflection from various dielectrics (including alkali halide crystals, such as NaCl or LiF) increases substantially at energies lower than the energy corresponding to the long-wavelength edge of crystal fundamental absorption. Moreover, this edge itself was in [37] associated with the boundary energy above which true SEE takes place (i.e., in fact, with ε_0). It is seen that reflections of low-energy electrons substantially increase the absorption coefficient.

Finally, curve *4* in Fig. 8 shows the absorption coefficient calculated with artificially introduced small elastic and inelastic electron reflections at $\varepsilon > \varepsilon_0$ with the coefficients $R = 0.1$ and $\eta = 0.1$, respectively. It is seen that even small reflections in this energy range additionally increase the absorption coefficient, especially at lower oscillation energies.

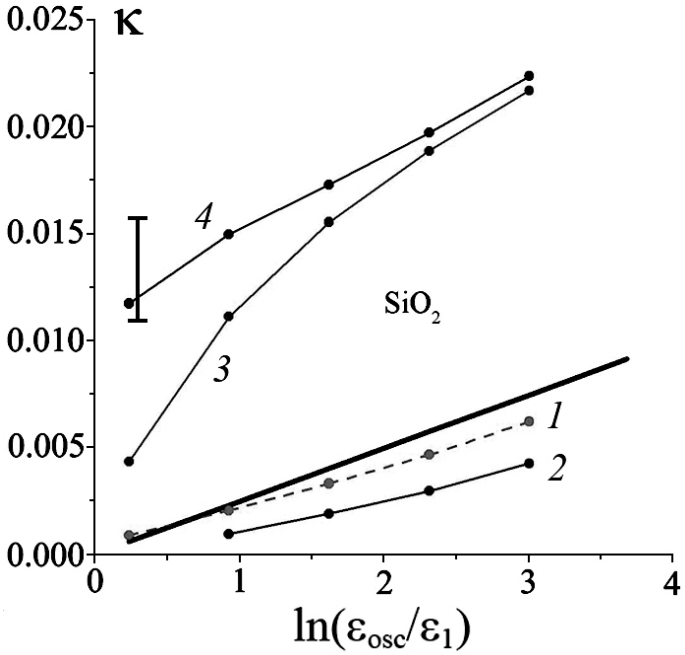

Figure 8. Influence of electron reflections on the coefficient of microwave absorption by a multipactor on SiO_2 for $T_e = 2$ eV: (*1*) simplified Vaughan's formula with $\varepsilon_0 = 0$, (*2*) Vaughan's formula with $\varepsilon_0 = 30$ eV without reflections, (*3*) Vaughan's formula supplemented with $R = 1$ at $\varepsilon_{inc} < \varepsilon_0$ (model [31]), and (*4*) Vaughan's formula supplemented with $R = 1$ at $\varepsilon_{inc} < \varepsilon_0$ and small elastic and inelastic reflections at $\varepsilon_{inc} > \varepsilon_0$ ($R = \eta = 0.1$). The heavy line shows analytical dependence (3). The vertical bar shows the range of κ values obtained experimentally at $P_{inp} = 85$ kW [32].

4. MEASUREMENTS OF THE MICROWAVE POWER ABSORBED BY A PARALLEL MULTIPACTOR

We performed experimental measurements of microwave power absorption by a multipactor discharge excited on a dielectric surface [32, 33]. The experiments were carried out at the BRUS device [7–9, 12, 21]. The scheme of the experiment is shown in Fig. 9. The dielectric target (LiF single crystal, NaCl single crystal, or SiO_2 plate) was placed in the antinode of the H_{10} standing mode of a 6 × 12-cm evacuated ($p \sim 10^{-6}$ Torr) rectangular waveguide. The input microwave power P_{inp} was from several tens of kilowatts to 2 MW, the duration of the microwave pulse being of up to 25 μs.

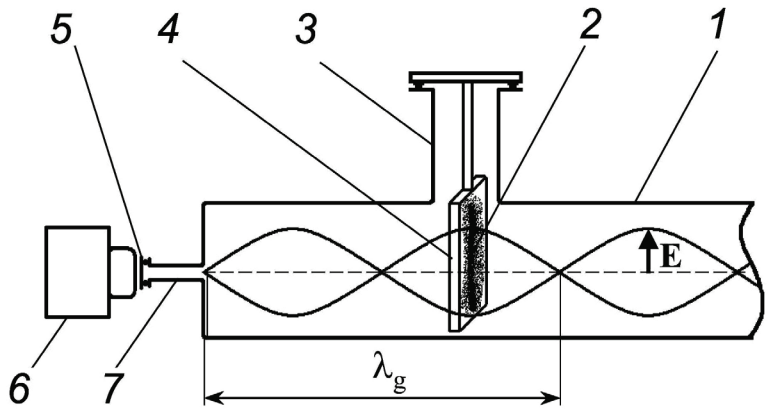

Figure 9. Arrangement of the experiment: (*1*) evacuated waveguide, (*2*) microwave discharge, (*3*) 24-mm-diameter below-cutoff circular waveguide, (*4*) dielectric plate, (*5*) diagnostic window, (*6*) photo camera, and (*7*) 10-mm-diameter below-cutoff circular waveguide. The free-space wavelength is $\lambda_0 = 15.4$ cm, and the waveguide wavelength is $\lambda_g \approx 20$ cm.

At high microwave powers ($P_{inp} \geq 1$ MW), three stages of the discharge on the dielectric target were observed: (i) multipactor discharge (which lasted for several microseconds), (ii) filamentary microwave breakdown (in which up to 70% of the microwave power was absorbed), and (iii) plasma-flare microwave discharge (in which the absorption coefficient dropped to 20–30%) [12]. At moderate microwave powers ($P_{inp} \leq 100$ kW), only the first stage was observed. The onset of a multipactor discharge was detected by the appearance of a feeble glow on the dielectric surface and the current onto the electron collector installed under the dielectric plate (Fig. 10) [21, 32, 33].

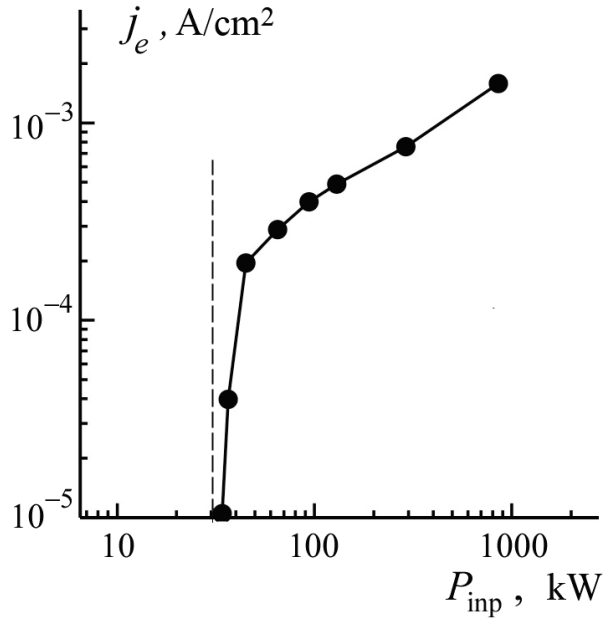

Figure 10. Current density measured by the electron collector installed under the LiF plate as a function of the input microwave power P_{inp}. The vertical dashed line shows the threshold power $P_{thr} \approx 32$ kW ($\varepsilon_{osc}^{thr} \approx 20$ eV) obtained from 1D3V PIC simulations for a LiF crystal ($\varepsilon_{m0} = 1000$ eV, $\delta_{m0} = 7.5$, $\varepsilon_1 = 14.5$ eV) by using Vaughan's formula with $\varepsilon_0 = 0$.

Figure 11 shows typical signals of the reflected microwave power and the current to the electron collector installed under the SiO_2 plate for a microwave power slightly exceeding the threshold power for the onset of multipactor discharge. It is seen that the appearance of the current at the collector, which indicates the onset of multipactor discharge, is accompanied by a decrease in the reflected microwave power. The height of the step in the reflected signal corresponds to the power absorbed by the multipactor.

Taking into account the geometry of the waveguide and dielectric plate, the ratio $\Delta P/P_{inp}$ can be recalculated into the absorption coefficient κ defined by expression (1). On one hand, the input microwave power P_{inp} is expressed through the amplitude of the input wave E_{inp} as $P_{inp} = 0.5c(E_{inp}^2/8\pi)ab\cos\chi$, where a and b are the width and height of the waveguide, $\cos\chi = (1-(\lambda_0/2a)^2)^{1/2}$, and λ_0 is the microwave wavelength in free space. On the other hand, according to (1), the absorbed power is equal to $P_{inp} = \kappa c(E_0^2/8\pi)S_{tot}$, where S_{tot} is the total area of the dielectric plate (note that the multipactor discharge develops on both sides of the dielectric plate). Then, taking into account that, in the antinode of the standing mode, $E_0 = 2E_{inp}$, we find that, for the parameters of our experiment, $\kappa \approx 0.58\Delta P/P_{inp}$.

Unfortunately, we could measure the ratio $\Delta P/P_{inp}$ only for input microwave powers of $P_{inp} \leq 85$ kW, slightly exceeding the threshold power for the onset of a multipactor discharge on a SiO_2 plate ($P_{thr} \approx 65$ kW), because, at higher powers, the multipactor discharge developed already at the front of the microwave pulse and no step was observed at the top of the reflected microwave signal. The range of κ values obtained from the experimental measurements of $\Delta P/P_{inp}$ at $P_{inp} = 85$ kW is shown in Fig. 8 by the vertical bar. It is seen that agreement between the theoretical results and the experimental data is achieved only if electron reflections from the dielectric surface are taken into account.

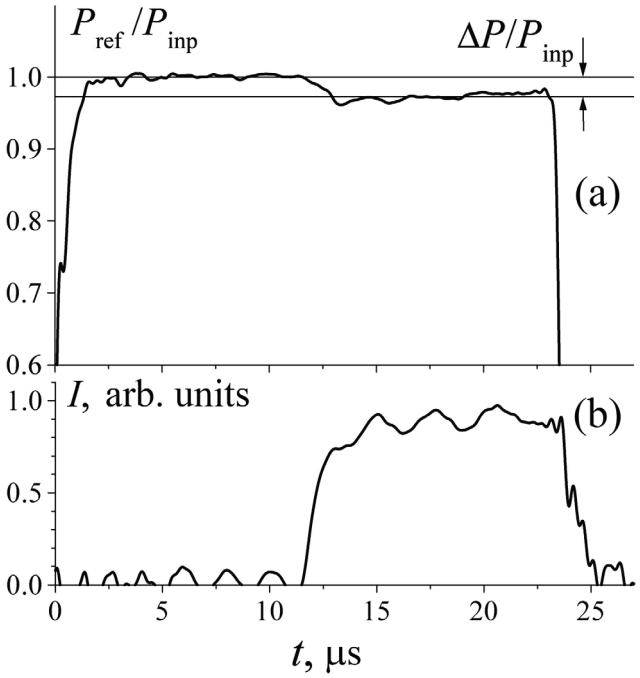

Figure 11. Typical signals of the (a) reflected microwave power and (b) current measured by the electron collector installed under the SiO_2 plate for the input microwave power P_{inp} = 85 kW, slightly exceeding the threshold power $P_{thr} \approx$ 65 kW for the onset of a multipactor discharge [32, 33].

5. "PERPENDICULAR" SINGLE-SURFACE MULTIPACTOR ON A DIELECTRIC

Let us now turn to the perpendicular multipactor, which develops when the microwave electric field is directed along the normal to the dielectric surface, $\mathbf{E}_0(t) = \{0, 0, E_0 \sin\omega t\}$ (Fig. 12a). In this case, in contrast to the parallel multipactor, secondary electrons can detach from the dielectric surface only in the microwave field phase in which the external field is negative ($E_{z0}(t) < 0$). Numerical simulations [38] show that the coefficient of microwave power absorption in the perpendicular multipactor increases somewhat faster with increasing electron oscillation energy, but differs insignificantly from the absorption coefficient in the parallel multipactor. However, in its structure, the perpendicular multipactor differs fundamentally from the parallel multipactor and is, in essence, quite a different type of discharge.

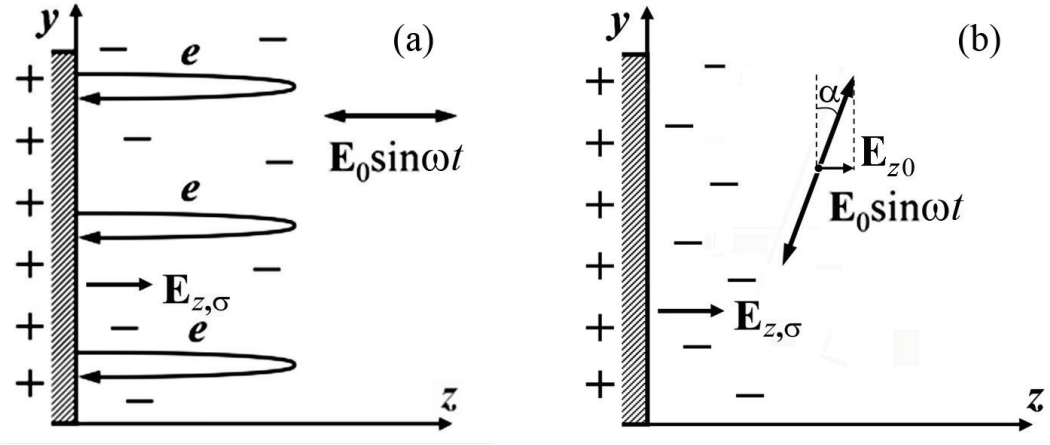

Figure 12. (a) Perpendicular and (b) inclined single-surface multipactors on a dielectric.

Figure 13 shows the electron phase portraits in the (z, v_z) plane in the perpendicular multipactor excited on the surface of a LiF crystal at f_0 = 1.95 GHz and ε_{osc} = 200 eV >> ε_1 for different instants of time during one microwave period ($-\pi \le \omega t < \pi$). It is seen from the figure that the electrons are periodically injected from the dielectric surface and further propagate in the form of jets in the phase plane. Most injected electrons return back to the surface during one oscillation period, whereas the

remaining electrons have time to execute several oscillations and move away from the dielectric surface over a distance of about several millimeters, which is several hundred times larger than the characteristic width of the electron layer in the parallel multipactor.

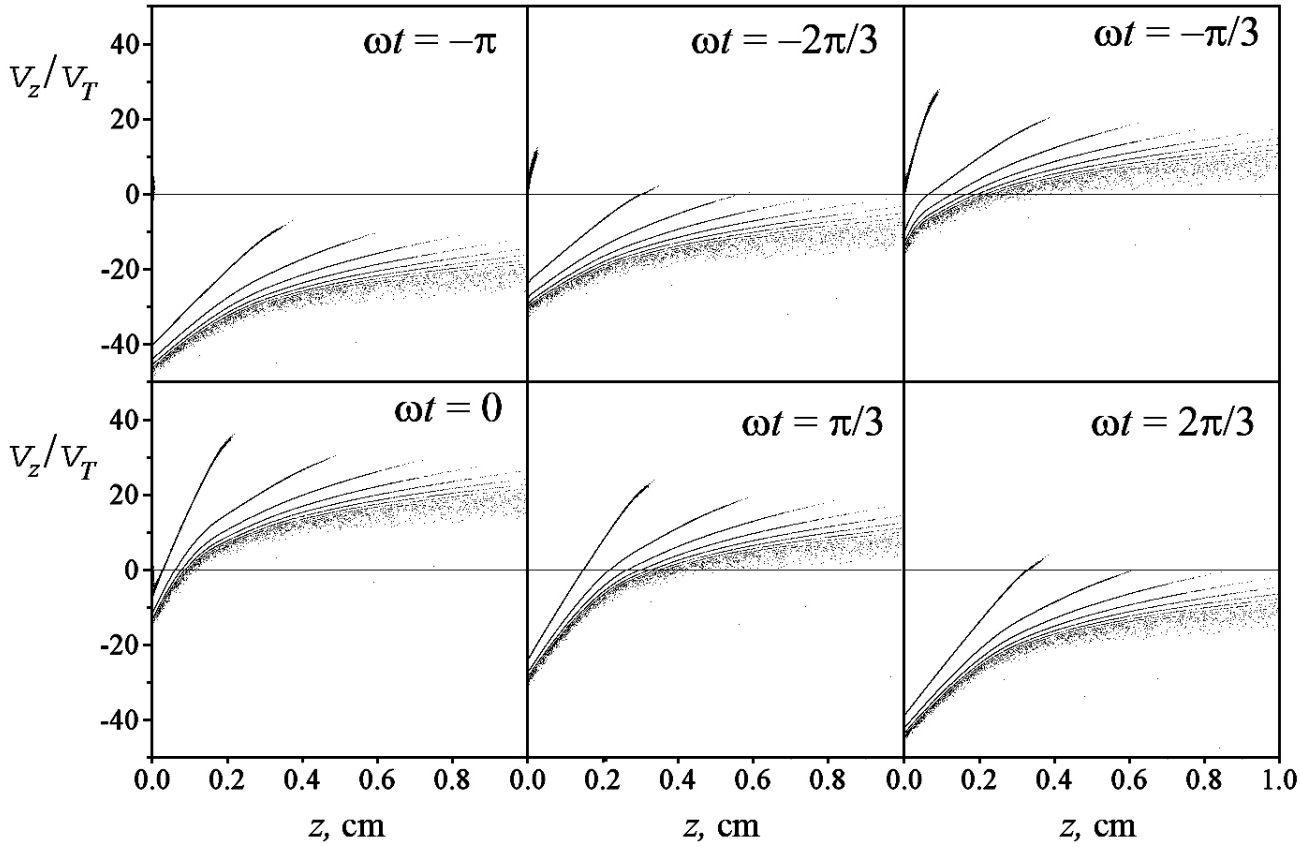

Figure 13. Electron phase portraits in the (z, v_z) plane in the perpendicular multipactor excited on the surface of a LiF crystal at f = 1.95 GHz and ε_{osc} = 200 eV >> ε_1 for different instants during one microwave period ($-\pi \le \omega t < \pi$). Here, $v_T = (T_e/m_e)^{1/2}$, where T_e = 1 eV is the effective temperature of secondary electrons [38].

The power absorbed by the perpendicular multipactor can be estimates as follows. Let the electrons be periodically injected in the discharge in the phase corresponding to the accelerating external field ($E_{z0}(t) = E_0 \sin\omega t < 0$) and further propagate in the form of a gradually expanding layer containing N electrons per unit area. Between the layer and the dielectric surface, the charge separation field $E_{z,\sigma}$ arises, which decelerates the electrons and returns them back to the dielectric surface, the average value of $E_{z,\sigma}$ within the layer being $E_{z,\sigma} = 2\pi eN$. In order for most electrons to return back to the surface over one microwave period $\tau = 2\pi/\omega$, it is necessary that $E_{z,\sigma} \sim E_0$. From here, we find that $N \sim E_0/2\pi e$. Then, the average (over the microwave period) density of the electron flux onto the surface is $\langle n_e v_z \rangle \sim N/\tau \sim \omega E_0/4\pi^2 e$. Since the electrons return back to the surface with an energy of about ε_{osc} (note that only some of them fall onto the surface in the phase favorable for the departure of secondary electrons), the mean density of the energy flux onto the surface is on the order of $\langle W_{abs} \rangle \sim \varepsilon_{osc} \langle n_e v_z \rangle \sim \varepsilon_{osc} \omega E_0 / 4\pi^2 e \sim v_{osc} E_0^2 / 8\pi^2$, where $v_{osc} = eE_0/m_e\omega$ is the electron oscillation velocity in the microwave field. Accordingly, the absorption coefficient defined as the ratio of the absorbed power per unit area of the dielectric surface to the microwave intensity $cE_0^2/8\pi$ (see (1)) is

$$\kappa = \beta (v_{osc}/c), \tag{4}$$

where β is a numerical factor on the order of unity. The 1D2V PIC simulations performed for a LiF crystal [38] confirm that κ in the perpendicular multipactor is nearly proportional to v_{osc}/c, the proportionality factor β being about 0.3.

The fundamental difference between the perpendicular and parallel multipactors is clearly demonstrated in Fig. 14. Figure 14a shows the mean flux density of secondary electrons $\langle n_e v_z \rangle$ as a

function of ε_{osc} for the parallel (curve *1*) and perpendicular (curve *2*) multipactors on the surface of a LiF single crystal obtained by means of 1D3V PIC simulations [38]. For the parallel multipactor, we have (see Section 2) $\langle n_e v_z \rangle \sim n_0 v_T \sim (E_0^2/\varepsilon_1) v_T$, i.e., the mean flux density of secondary electrons is proportional to ε_{osc}. In the perpendicular multipactor, the current density of secondary electrons is much lower and is proportional to v_{osc}. In contrast, it is seen from Fig. 14b that the mean energy of incident electrons in the perpendicular multipactor, defined as $\langle \varepsilon_{inc} \rangle = \langle W_{abs} \rangle / \langle n_e v_z \rangle$, is much higher than that in the parallel multipactor and increases linearly with increasing ε_{osc}, whereas in the parallel multipactor, $\langle \varepsilon_{inc} \rangle$ grows very slowly (logarithmically) with increasing ε_{osc}. It is noteworthy that the absolute values of the mean power $\langle W_{abs} \rangle \sim \langle n_e v_z \varepsilon_{inc} \rangle$ absorbed per unit area of the dielectric surface and, accordingly, absorption coefficients are close to one another for both types of multipactor (see Fig. 15).

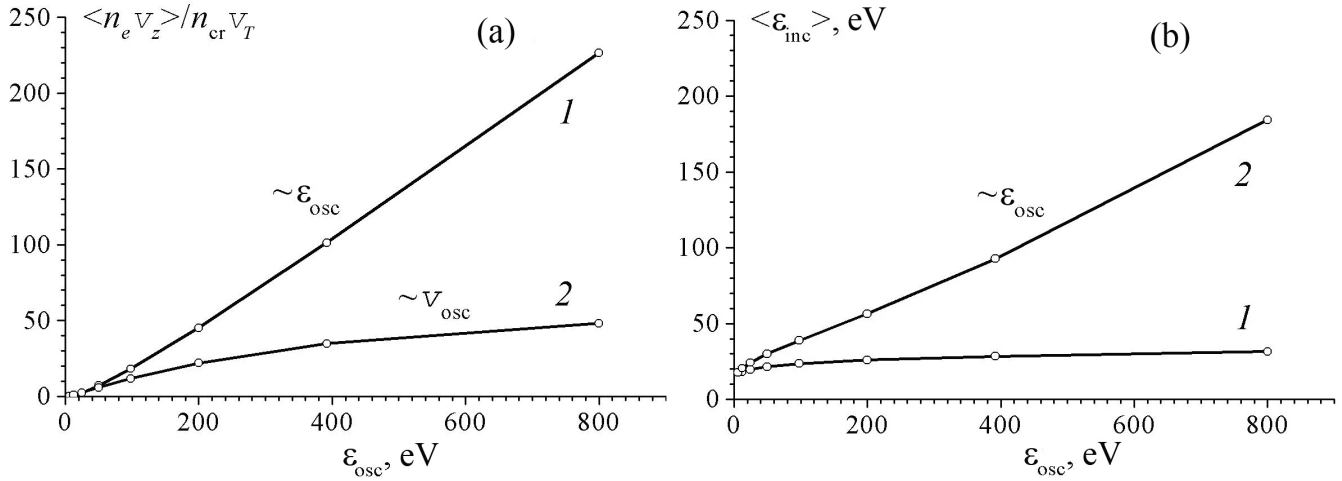

Figure 14. (a) Mean flux density $\langle n_e v_z \rangle$ of secondary electrons and (b) mean energy $\langle \varepsilon_{inc} \rangle$ of electrons incident on the dielectric surface as functions of ε_{osc} for the (*1*) parallel and (*2*) perpendicular multipactors on the surface of a LiF crystal. Here, $v_T = (T/m_e)^{1/2}$, where $T_e = 1$ eV is the effective temperature of secondary electrons [38].

Thus, the energy of incident electrons is larger for the perpendicular multipactor, whereas the flux density of incident electrons is larger for the parallel multipactor. These features of the perpendicular and parallel multipactors can be used when choosing modes of microwave processing of crystal dielectrics with the purpose of modifying their surface properties.

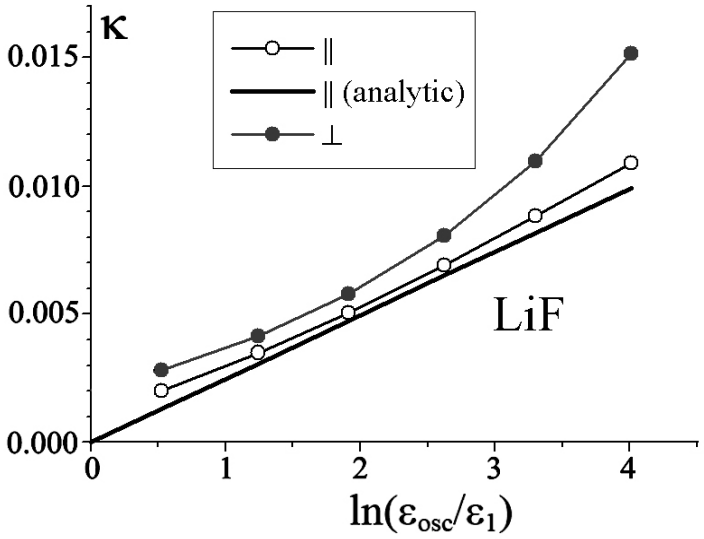

Figure 15. Coefficients of microwave power absorption $\kappa = W_{abs}/W_{inc}$ by the parallel (||) and perpendicular (⊥) multipactors on a LiF single crystal as functions of the electron oscillation energy in the microwave field [38].

6. "INCLINED" SINGLE-SURFACE MULTIPACTOR ON A DIELECTRIC

Let us now consider the "inclined" multipactor (Fig. 12b), which develops at intermediate inclination angles of the microwave electric field with respect to the dielectric surface, $0° < \alpha < 90°$. Such a situation

can take place when a *p*-polarized microwave beam (the microwave electric field vector lies in the incidence plane) passes through a tilted output window of a high-power microwave source. In this case, the amplitude of the normal component of the microwave electric field is $E_{z0} = E_0 \sin\alpha$.

At sufficiently small inclination angles, such that $\sin\alpha < (T_e/\varepsilon_1)^{1/2}$, the discharge structure remains close to that of the parallel multipactor, because, in this case, the normal component of the microwave electric field E_{z0} is smaller than the characteristic value of the electrostatic field in the parallel multipactor, $|\partial\varphi/\partial z| \sim 4\pi e n_0 \Delta z \sim (T_e/\varepsilon_1)^{1/2} E_0$. Accordingly, at small inclination angles, the absorption coefficient κ in the inclined multipactor is close to absorption coefficient (3) in the parallel multipactor.

At $\sin\alpha > (T_e/\varepsilon_1)^{1/2}$, the space charge layer near the dielectric surface is destroyed and the discharge structure becomes similar to that in the perpendicular multipactor. In this case, however, the electron motion along the z axis is determined by the field $E_{z0} = E_0 \sin\alpha$ (instead of $E_{z0} = E_0$ in the perpendicular multipactor). Estimating the number of secondary electrons emitted over one microwave period per unit area of the dielectric surface, as it was done above for the perpendicular multipactor, we obtain $N \sim E_0 \sin\alpha / 4\pi e$ and, accordingly,

$$\kappa = \beta \sin\alpha \left(v_{osc}/c \right), \tag{5}$$

where β is the proportionality factor on the order of unity ($\beta \approx 0.3$ for $\alpha = 90°$).

Figure 16a shows the absorption coefficient κ as a function of α for a multipactor on the surface of a LiF crystal for different values of ε_{osc}. It is seen that the absorption coefficient decreases with decreasing α in accordance with formula (5) and reaches its minimum value at $\alpha_m \approx \arcsin(T_e/\varepsilon_1)^{1/2} \approx 20°$ (for $T_e = 2$ eV), after which it increases to its value in the parallel multipactor (see (3)).

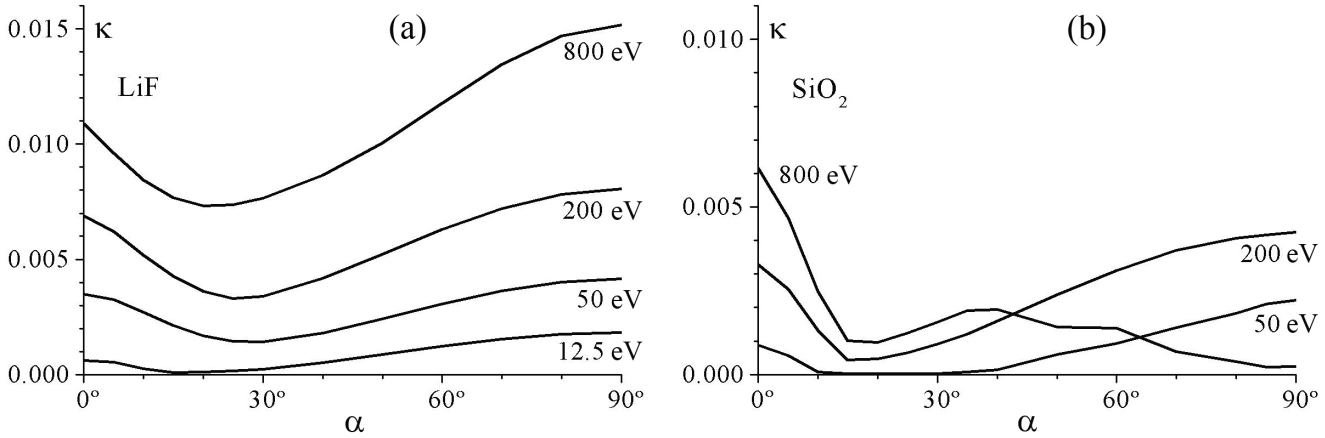

Figure 16. Absorption coefficient κ as a function of the angle α for multipactors on the (a) LiF ($\varepsilon_{m0} = 1000$ eV, $\delta_{m0} = 7.5$, $\varepsilon_1 = 14.5$ eV) and (b) SiO_2 ($\varepsilon_{m0} = 400$ eV, $\delta_{m0} = 2.4$, $\varepsilon_1 = 40$ eV) surfaces [38].

Figure 16b shows similar dependences for a multipactor on the SiO_2 surface. It is seen that the angular dependences of κ for SiO_2 also have minima at angles approximately corresponding to $\sin\alpha = (T_e/\varepsilon_1)^{1/2}$. Note that, at $\varepsilon_{osc} = 800$ eV, the absorption coefficient for the perpendicular multipactor on SiO_2 is reduced substantially, because, at such high oscillation energies, a considerable fraction of electrons return back to the dielectric surface with energies significantly exceeding the energy $\varepsilon_{m0} = 400$ eV, above which the SEY of SiO_2 decreases exponentially.

The presence of a minimum in the angular dependence of the absorption coefficient at $\alpha \sim 20°–30°$ indicates that the power released in the multipactor on the input/output microwave window can be reduced appreciably by tilting the window with respect to the axis of the microwave beam.

7. CONCLUSIONS

The results of these studies can be summarized as follows.

(i) An analytical expression for the coefficient of microwave power absorption by a parallel single-surface multipactor discharge on a dielectric surface has been derived under the assumption that the SEY

is described by the simplified Vaughan's formula with a zero cutoff energy, widely used in theoretical and numerical studies of multipactor discharges. The analytical expression satisfactorily agrees with the simulation results obtained under the same assumptions on the shape of the SEY. Although the obtained expression is of limited applicability, it can be used as a reference formula when analyzing the influence of various factors (such as electron reflections and the shape of the energy dependence $\delta(\varepsilon_{inc})$) on the coefficient of microwave power absorption by a multipactor discharge on a dielectric.

(ii) Multipactors developing on a dielectric surface inclined at an angle α with respect to the microwave electric field have been studied analytically and numerically. It is shown that the structure of the "parallel" multipactor (α =0) differs fundamentally from that of the "perpendicular" multipactor ($\alpha = \pi/2$). The parallel multipactor is concentrated in a narrow layer adjacent to the dielectric, the layer thickness being less than v_T/ω (<30 μm for $f \approx 2$ GHz), whereas the perpendicular multipactor extends from the solid surface to a distance of about several electron oscillation amplitudes in the microwave field ($a_0 = v_{osc}/\omega \geq 1$ mm for $f \approx 2$ GHz and $\varepsilon_{osc} \geq 100$ eV).

(iii) It is found that the relation between the average energy of electrons bombarding the dielectric surface and their average flux density in the perpendicular multipactor differs radically from that in the parallel multipactor, which should be taken into account when choosing modes for multipactor processing of crystal dielectrics.

(iv) It is shown that the dependence of the absorption coefficient on the inclination angle α of the dielectric surface relative to the microwave electric field has a minimum at $\alpha \sim 20–30°$. This effect can be used to minimize the microwave power released in multipactor discharges on the surfaces of input/output microwave windows, as well as to choose optimal regimes of processing of crystal dielectrics by electron fluxes generated in such discharges.

(v) The results of PIC simulations have shown that the coefficient of microwave power absorption increases substantially when electron reflections from the dielectric surface are taken into consideration.

(vi) The experiments on a multipactor discharge on a dielectric in a rectangular waveguide have shown that the coefficient of microwave power absorption by such a discharge can reach several percent, which should lead to various destructive processes on the dielectric and distortion of signals in microwave communication systems. Comparison of experimental data with results of theoretical studies and numerical simulations show that agreement between the calculated and measured values of the absorption coefficient is achieved only if the theoretical model takes into account the entire complex of SEE phenomena, such as emission of true secondaries and elastic and inelastic reflections of incident electrons in a wide energy range.

Acknowledgments

This work was supported by the Ministry of Science and Higher Education of the Russian Federation (state assignment no. 0024-2018-0046 "Fundamentals of Plasma, Microwave, and Beam Technologies").

References

1. Puech J., Anderson D., Buyanova M., et al., Proc. MULCOPIM-2005, 235.
2. Piro F., Brand Y., Proc. 8th Europ. Conf. Antennas and Propagation, 2014, 1643.
3. Goede A.P.H., Bongers W.A., Elzendoorn B.S.Q., et al., Fusion Eng. Des., 2010, **85**, 1117.
4. Giruzzi G., Lennholm M., Parkin A., et al., Nucl. Fusion, 2011, **51**, 063033.
5. Neuber A., Dickens J., Hemmert D., Krompholz H., et al., IEEE Trans. Plasma Sci., 1998, **26**, 296.
6. Ivanov V.A., Konyzhev M.E., Proc. XX Int. Symp. Discharges and Electrical Insulation in Vacuum, 2002, 499.
7. Ivanov V.A., Konyzhev M.E., Proc. V Int. Workshop Microwave Discharges: Fundamentals and Applications, 2003, 247.
8. Ivanov V.A., Konyzhev M.E., Gavrilenko V.P., Oks E., Proc. MULCOPIM-2005, 169.
9. Ivanov V.A., Sakharov A.S., Konyzhev M.E., Proc. VII Int. Workshop Microwave Discharges: Fundamentals and Applications, 2009, 34.

10. Hoff B.W., Mardahl P.J., Gilgenbach R.M., et al., Rev. Sci. Instrum., 2009, **80**, 094702.
11. Strong Microwaves: Sources and Applications. Ed. A.G. Litvak. Nizhny Novgorod: Institute of Applied Physics, Russian Academy of Sciences, 2009.
12. Ivanov V.A., Sakharov A.S., Konyzhev M.E., IEEE Trans. Plasma Sci., 2015, **43**, 1871.
13. Singh S., Gupta D., Jain V., Sharma A.K., Mater. Manuf. Process., 2015, **30**, 1.
14. Sun J., Wang W., Yue Q., Materials, 2016, **9**, 231.
15. Vaughan J.R.M., IEEE Trans. Electron Dev., 1988, **35**, 1172.
16. Kishek R.A., Lau Y.Y., Phys. Rev. Lett., 1988, **80**, 193.
17. Kishek R.A., Lau Y.Y., Ang L.K., et al., Phys. Plasmas, 1998, **5**, 2120.
18. Semenov V.E., Rakova E.I., Anderson D., et al., Phys. Plasmas, 2007, **14**, 033501.
19. Kossyi I.A., Lukyanchikov G.S., Semenov V.E., et al., J. Phys. D, 2008, **41**, 065203
20. Kim H.C., Verboncoeur J.P., Phys. Plasmas, 2006, **13**, 123506.
21. Batanov G.M., Ivanov V.A., Konyzhev M.E., Letunov A.A., JETP Lett., 1997, **66**, 170.
22. Grishin L.V., Dorofeyuk A.A., Kossyi I.A., et al., Tr. FIAN, 1977, **92**, 82.
23. Valfells A., Ang L.K., Lau Y.Y., Gilgenbach R.M., Phys. Plasmas, 2000, **7**, 750.
24. Ang L.K., Lau Y.Y., Kishek R.A., Gilgenbach R.M., IEEE Trans. Plasma Sci., 1998, **26**, 290.
25. Valfells A., Verboncoeur J.P., Lau Y.Y., IEEE Trans. Plasma Sci., 2000, **28**, 529.
26. Kim H.C., Verboncoeur J.P., Phys. Plasmas, 2005, **12**, 123504.
27. Hachenberg O., Brauer W., Adv. Electron. El. Phys., 1959, **11**, 413.
28. Vaughan J.R.M., IEEE Trans. Electron Devices, 1989, **36**, 1963.
29. Kishek R.A., Lau Y.Y., Phys. Rev. Lett., 1995, **75**, 1218.
30. Sazontov A., Semenov V., Buyanova M., et al., Phys. Plasmas, 2005, **12**, 093501.
31. Vicente C., Mattes M., Wolk D., et al., Proc. MILCOPIM-2005, 11.
32. Sakharov A.S., Ivanov V.A., Tarbeeva Yu.A., Konyzhev M.E., Plasma Phys. Rep., 2012, **38**, 1090.
33. Ivanov V.A., Sakharov A.S., Konyzhev M.E., Proc. VIII Int. Workshop Microwave Discharges: Fundamentals and Applications, 2012, 69.
34. Bronshtein I.M., Fraiman B.S., Secondary Electron Emission, Moscow: Nauka, 1969 [in Russian].
35. Dekker A.J., Solid State Physics, London: Macmillan, 1958, Chap. 17.
36. Cimino R., Nucl. Instrum. Meth. A, 2006, **561**, 272.
37. Fridrikhov S.A., Sov. Phys. Solid State, 1960, **2**, 157.
38. Sakharov A.S., Ivanov V.A., Konyzhev M.E., Plasma Phys. Rep., 2013, **39**, 1122.

ULTRATHIN METALLIC OXIDE NANOSTRUCTURES SYNTHESIZED BY MICROWAVE PLASMA AFTERGLOW FOR APPLICATIONS IN PHOTOCATALYSIS

T. Gries, C. Noël, T. Belmonte

Institut Jean Lamour, CNRS, Université de Lorraine, Nancy, F-54011, France

Abstract. Metallic oxide nanostructures are promising materials in photocatalytic applications, for example in water treatment and disinfection or for hydrogen production by water splitting. In this work, we report on two processes based on argon-oxygen microwave plasma afterglow oxidation to synthesize metallic oxide nanostructures: a micro-afterglow at atmospheric pressure and a flowing afterglow at low pressure. The morphology, shape and size distribution of nanostructures can be controlled with good reproducibility by adjusting the experimental parameters: amount of oxygen injected in the plasma, microwave power, treatment duration or composition of the substrate. For instance, the rapid growth of ultrathin ZnO nanoribbons and nanowires (~5 nm in diameter) is obtained from Cu/Zn stacks and these nanostructures exhibit significant improvement in photocatalytic activity. An enhancement of photocatalytic efficiency and photocurrent intensity under visible and UV light is observed for ultrathin nanowires, attributed to high separation efficiency of photoinduced electron-hole pairs and a reduction of charge carrier recombination.

1. INTRODUCTION

During the last decade, the quest for metallic oxide nanostructures with controlled shapes and size distribution have stimulated great interest in fundamental scientific research due to their morphology-dependent properties that offer potential wide-ranging applications. In this context, metallic oxide nanostructures are promising materials in photocatalytic applications, for example in water treatment and disinfection or for hydrogen production by water splitting. The surface area and thus the morphology are factors of paramount importance which affect directly the photocatalytic efficiency of metallic oxide semiconductors [1]. Growing metallic oxide nanostructures can be achieved by simple thermal oxidation of raw metallic materials. The use of direct plasma treatments increases the growth rate of nanostructures by several orders of magnitude [2−3] whereas remote plasma treatments improve the control of the design of nanostructures by moving the temperature window where nanostructures are formed by about 100 K downward. This shift enables the development of higher stress levels and offers the possibility to create dense areas of nanostructures [4−5]. For a given nanostructure, it is even possible to design them by driving growth instabilities using mixtures of metals [6−7]. We can thus expect to control the growth of ultrathin nanowires (with diameters typically below 5 nm) where quantum confinement is possible. In this work, we will compare different configurations to show the role of substrates on the morphology of as-grown oxide nanostructures: pure metallic thin films, alloys with different compositions and stacks, formerly deposited by magnetron sputtering. We report on two processes based on microwave plasma afterglow-assisted oxidation (at atmospheric pressure and at low pressure) to synthesize ultrathin metallic oxide nanostructures.

2. EXPERIMENTAL PART

The first plasma afterglow process operates at atmospheric pressure (Fig. 1). It consists in using a tubular fused silica tube, crossing a wave-guide connected to a microwave generator (2.45 GHz). The applied power is set equal to 100 W. Atmospheric pressure plasma (Ar – 9.1 vol. % O_2) is centered on the tube axis and active species exit the reactor through a tiny hole (500 µm in diameter). A total flow rate of 275 sccm (standard cubic centimeter per minute) is injected in the plasma, which produces a laminar afterglow containing oxygen atoms and other neutral excited oxygen molecules such as $O_2(a^1\Delta_g)$. These active species react with metallic thin films, alloys and stacks to perform the direct synthesis of oxide nanostructures without any template or surfactant (Fig. 1b). Figure 1c shows that active oxygen species oxidize thin films as concentric areas that extend radially up to several millimeters. Surface temperature is a key parameter in the growth of nanostructures. In the present experimental conditions, the gas temperature was estimated at about 1200 K in the afterglow with high thermal gradients near its edge (~ 1200 K / mm). A detailed thermal analysis by infrared camera measurements [6] showed that the maximum treatment temperature is about 733 K. This surface temperature decreases with the radial distance to reach about 473 K at 6 mm from the centre of treatment. These high thermal gradients lead to the production of different nanostructures as a function of the radial distance. This flexible procedure has been applied to synthesize CuO nanowire and nanowalls, Fe_2O_3 nanoblades or different RuO_2 nanostructures (Fig. 2). Larger surfaces can be treated by scanning the sample in front of the afterglow beam, thanks to a moving XY stage.

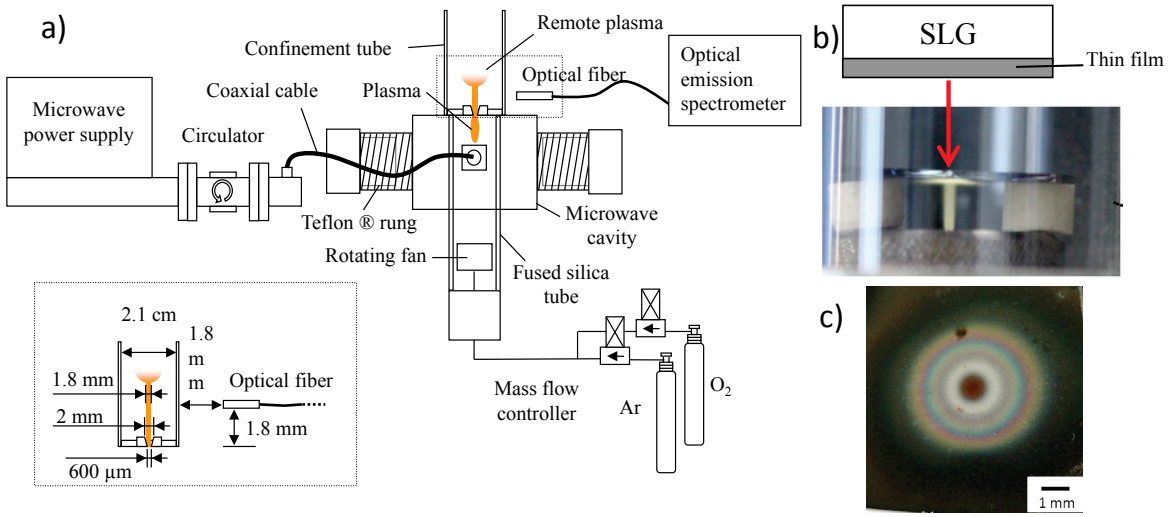

Figure 1. a) Experimental set-up of the micro-afterglow oxidation process. b) Picture of the atmospheric pressure afterglow, which hits directly the surface of thin films. c) Picture of a sample after afterglow treatment.

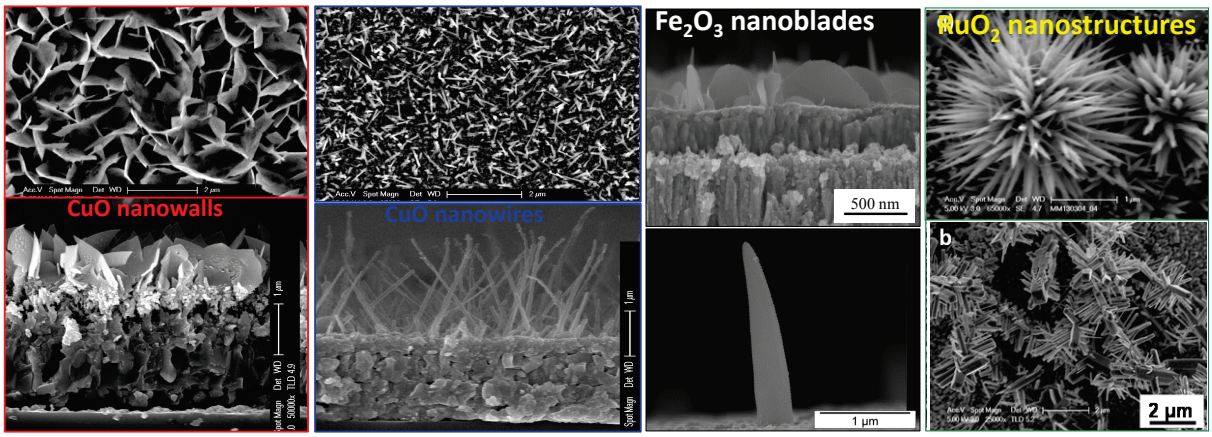

Figure 2. SEM micrographs of metallic oxide nanostructures grown respectively on copper, iron and ruthenium thin films by micro-afterglow oxidation at atmospheric pressure [4−7].

The shape of the afterglow evolves as a function of the total flow rate (Fig. 3). As the total flow rate increases from 0.5 to 5 slm, a straight beam of light progressively appears close to the nozzle and extends in length until it diverges into a cone shape.

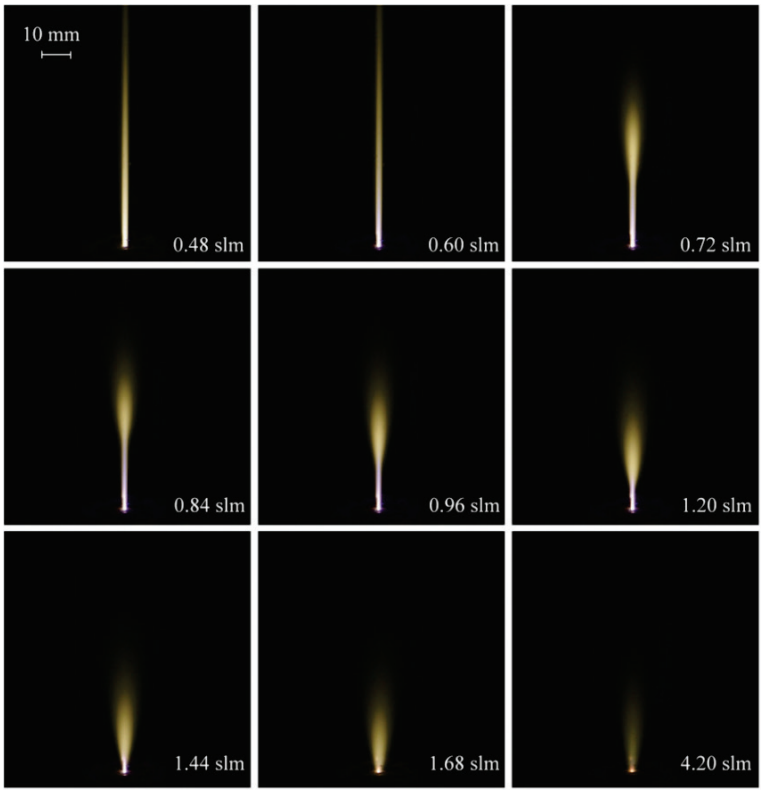

Figure 3. Photographs of the atmospheric pressure afterglow (Ar − 20 vol. % O_2) through a 600 µm hole for different total flow rates. Power: 70 W. From [8].

The second process consists in using a flowing microwave plasma process operating at low pressure (Fig. 4). The objective is to synthesize nanostructures with homogeneous morphology over larger surface (up to several tens of cm^2) in a single-step process. ZnO nanostructures are synthesized by oxidation of Cu/Zn stacks (50 nm Cu / 950 nm Zn films) formerly deposited by DC magnetron sputtering (80 W) on soda lime glass (SLG) substrates. These films are oxidized by using a microwave plasma produced in a quartz capillary from a surfaguide wave launcher. The samples are located in a quartz reactor tube downstream the plasma glow region, at a distance of 60 cm from the surfaguide. The temperature of the sample during oxidation is controlled by an additional furnace. As described in a previous work [9], copper thin film plays also a key role in the growth mechanism: this buffer layer prevents film evaporation and allows treatments at temperatures that are higher than the melting temperature of zinc (*m.p.* = 419.5°C) mainly due to the formation of $CuZn_5$ intermetallic by interdiffusion.

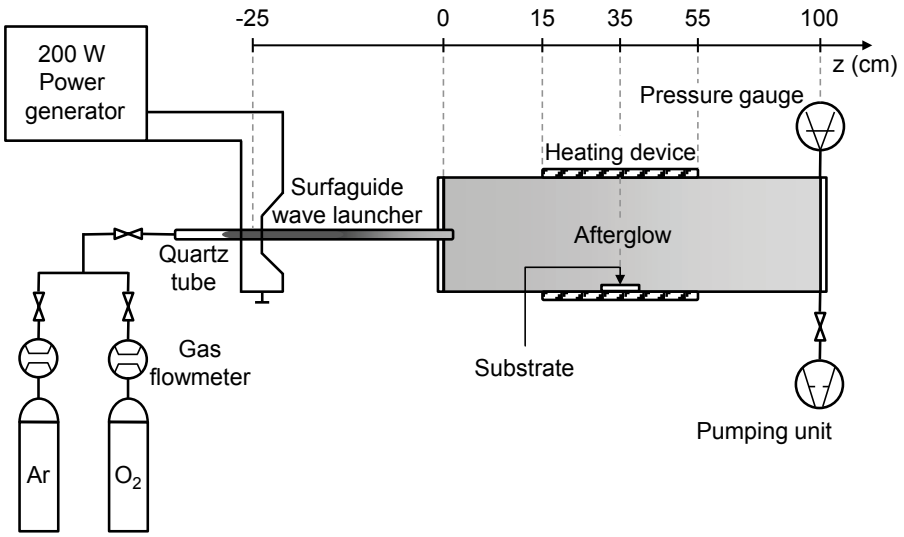

Figure 4. Schematic of the flowing afterglow oxidation process.

3. RESULTS

In Fig. 5a, the spectrum of emission of the O_2 ($b^1\Sigma_g^+ \rightarrow X^3\Sigma_g^-$) transition at 762 nm is depicted. An argon line appears at 763.5 nm that is removed to determine the rotational temperature of the gas according to data available in [10]. The rotational temperature of O_2(b) state is generally considered as a good approximation of the kinetic temperature of O_2 molecules in the ground state. A temperature of 330 ± 30 K was obtained, confirming the relatively low temperature of the afterglow. The concentration of oxygen atoms was determined by NO titration method along the flow tube. This two-step method, described in [11], leads to [O] = 3.2 ± 1.0 × 10^{15} cm^{-3}, which is consistent with the calculated value predicted by Kutasi *et al.* [12]. The electron density (Ne) of the microwave plasma was estimated by microwave interferometry in the small-diameter quartz tube. This technique which is based on the determination of the refraction index of plasmas is known to allow the measurement of Ne at moderate pressures like ours [13−14]. As expected, a large decrease of Ne is observed in the flow: an order of magnitude over 10 cm in the small-diameter quartz tube (Fig. 5b).

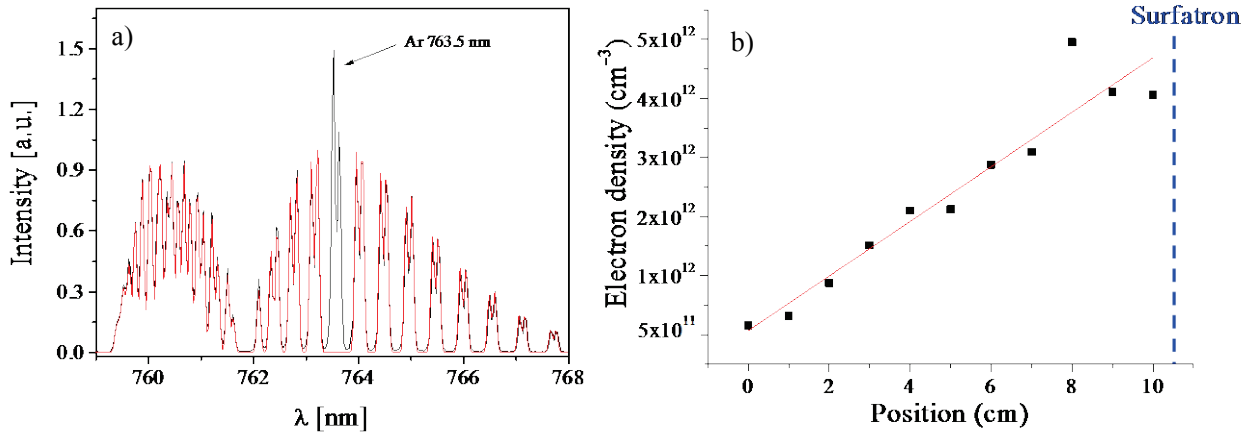

Figure 5. (a) Experimental (black) and simulated (red) rotational spectrum of the atmospheric band of O_2 corresponding to the O_2 ($b^1\Sigma_g^+ \rightarrow X^3\Sigma_g^-$) transition at 762 nm. To fit the spectrum, the Ar line that appears at 763.5 nm must be removed (560 sccm, Ar – 2 vol. % O_2, 200 Pa). (b) Variation of electron density as a function of the distance from the surfaguide wave launcher determined by microwave interferometry.

The morphology of synthesized nanostructures can be controlled by the experimental parameters: treatment duration, furnace temperature, oxygen concentration, pressure [9]. For instance, ultrathin zinc oxide nanowires, nanoribbons and nanocombs are successfully synthesized from Cu/Zn stacks (Fig. 6) for very short treatments, typically less than 1 min. The rapid growth of nanostructures is attributed to the non-equilibrium behaviour of the afterglow, which provides directly active species on the sample surface:

in the remote region, only neutral species, excited or not, can be found with the absence of electrons and ions. However, this afterglow is a very oxidizing medium since it contains high concentrations of oxygen atoms and excited oxygen molecules like $O_2(a^1\Delta g)$, $O_2(X^3\Sigma g^-)$ and to a lesser extent, $O_2(b^1\Sigma g^+)$ [15]. The surface morphology is clearly highly dependent on the pressure. Ultrathin nanowires with fairly high surface density are synthesized at 200 Pa, whereas ultrathin nanoribbons are obtained at 1000 Pa. The evolution of morphology with the working pressure could be mainly attributed to density profiles of active species which depend on experimental conditions including pressure. Kutasi *et al.* [12, 16] performed calculations at different pressures using self-consistent theoretical models developed to investigate the early and remote flowing afterglows of a surface-wave Ar-O_2 microwave discharge generated in a reactor with geometry close to that of this study. They especially observed a large increase in active oxygen species densities with pressure in the afterglow (Fig. 7).

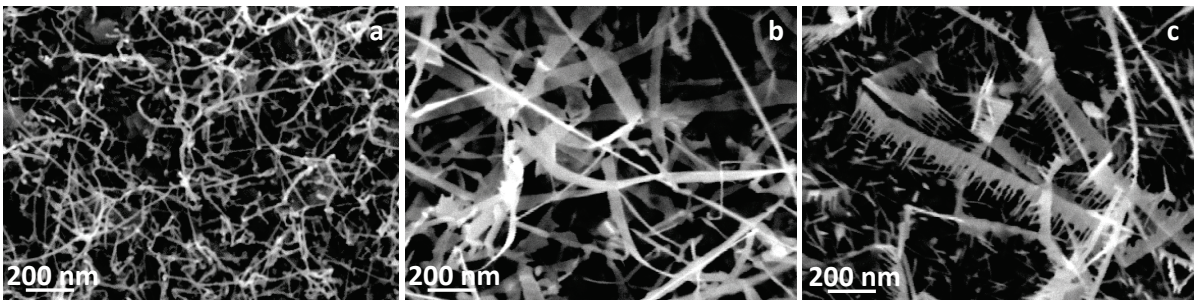

Figure 6. SEM micrographs of ZnO nanostructures synthesized in flowing afterglow as a function of working pressure: (a) nanowires at 200 Pa, (b) nanoribbons at 1000 Pa and (c) nanocombs at 2000 Pa. (Treatment duration = 40 s).

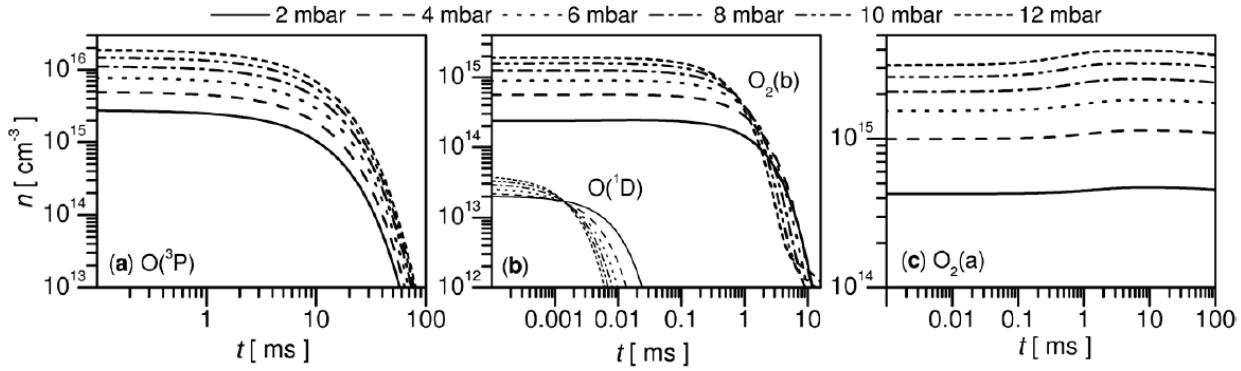

Figure 7. Calculated densities of (a) $O(^3P)$, (b) $O(^1D)$ and O_2(b), (c) O_2(a) along the afterglow for a 90% Ar – 10% O_2 mixture at different gas pressure. From [11].

The aspect ratio of the nanowires can also be controlled by the experimental parameters. Thus, by adjusting these treatment parameters, we succeed in decreasing the average diameter of nanowires down to 5 nm, with a fairly high surface number density. High-resolution transmission electron microscopy (HRTEM) analyses indicate that all the produced nanowires are single-crystalline ZnO with wurtzite structure and random axial crystallographic orientations. Furthermore, high-angle annular dark-field images (HAADF) show that the nanowires are well-crystallized up to the edges (Fig. 8). This observation was confirmed by photoluminescence (PL) measurements: PL spectra show a strong UV emission and a weak green peak. These results indicate that the defects in the samples are fairly weak with this synthesis method. The EDX mapping of these nanostructures show that nanowires are obviously mainly composed of zinc and oxygen. We observe that the copper signal is very weak, but not completely negligible (inferior to 1 at.% typically).

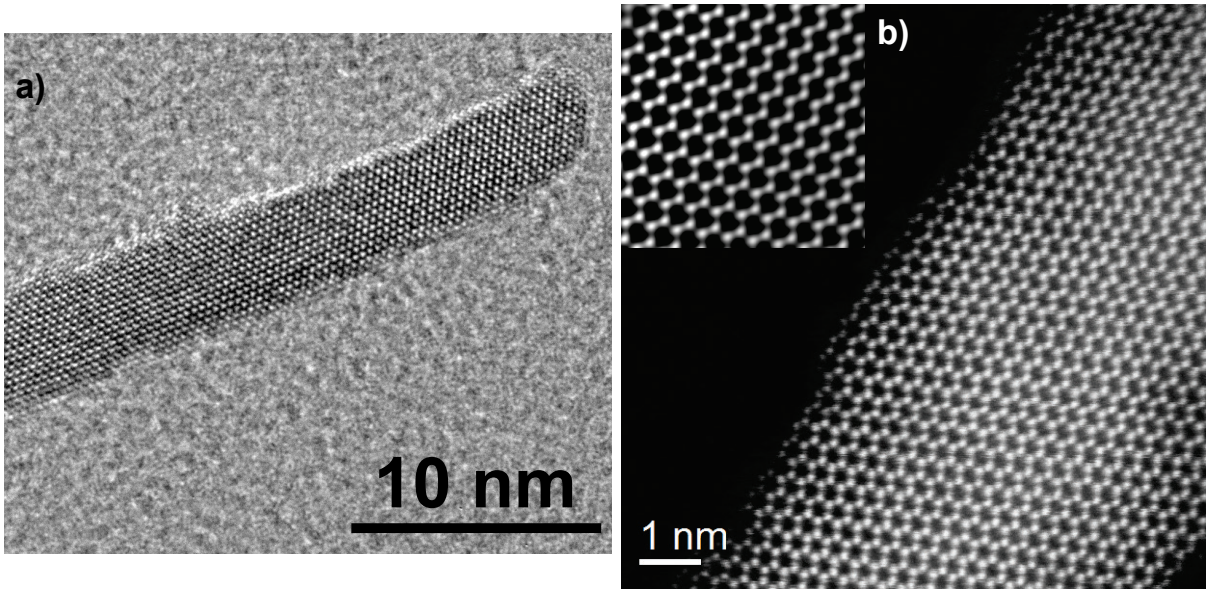

Figure 8. (a) HRTEM micrograph of a nanowire tip and (b) HAADF-STEM micrograph of an individual nanowire.

Photocatalytic activity of ZnO nanostructures is investigated from the photodecomposition of a model organic dye (methyl orange MO) under solar light irradiation. ZnO nanostructures exhibit higher photodegradation of MO than pure ZnO thin films without nanostructures or ZnO nanowires with larger diameter (~ 60 nm) synthesized by thermal annealing (Fig. 9). The enhancement in photocatalytic performance could be linked to higher surface area but also to higher transfer yield of photogenerated charge carriers to the surface of nanostructures: charge carriers need to diffuse only over a short distance (~5 nm) and then can reach active sites before their recombination. The limitation of charge carrier recombination is confirmed by photoelectrochemical measurements, the photocurrent response being related to the recombination efficiency of photogenerated carriers.

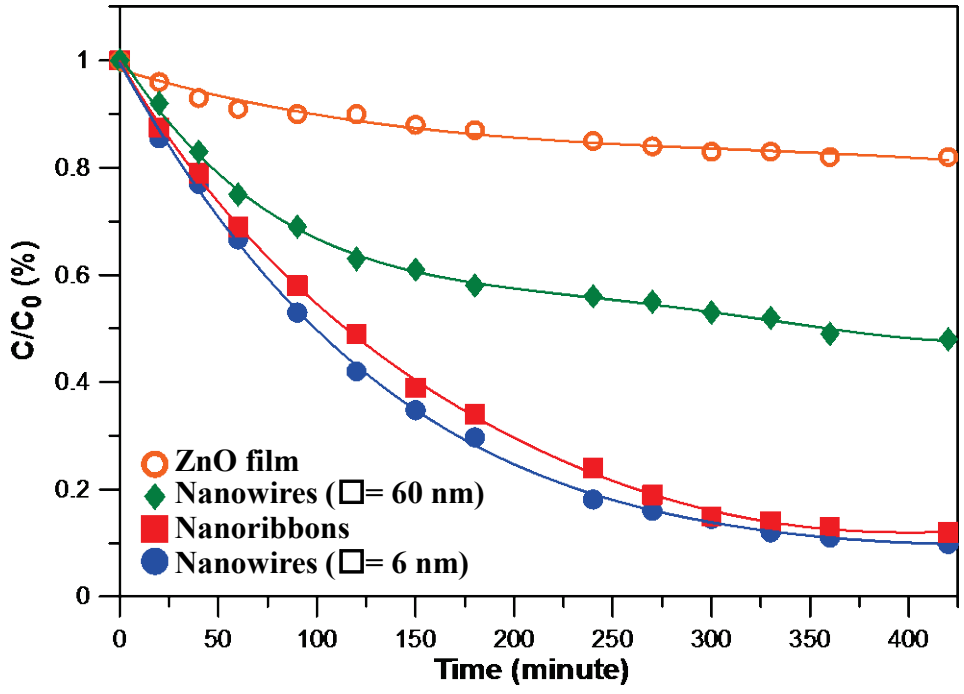

Figure 9. Methyl orange degradation rate under solar light irradiation, respectively without photocatalyst and in the presence of ZnO thin films and ZnO nanostructures.

Acknowledgments

The authors wish to thank S. Migot, J. Ghanbaja, P. Boulet, P. Miska and D. Mangin from Institut Jean Lamour (Nancy-France) for their contribution respectively on FIB, HRTEM, XRD, photoluminescence and SIMS measurements and for their interest in this work. The Réseau des Plasmas Froids of CNRS/MI (France) is acknowledged for providing the microwave interferometer.

References

1. Ahmed F., Arshi N., Anwar M.S., Danish R., Koo B.H., RSC Adv., 2014, **4**, 29249.
2. Cvelbar, U., J. Phys. D: Appl. Phys., 2011, **44**, 174014.
3. Mariotti D., Sankaran R.M., J. Phys. D: Appl. Phys., 2010, **43**, 323001.
4. Altaweel A., Gries T., Migot S., Boulet P., Mézin A., Belmonte T., Surf. & Coat. Technol., 2016, **305**, 254.
5. Kuete Saa D., Gries T., Migot-Choux S., Ghanbaja J., Mangin D., Boulet P., Laminsi S., Belmonte T., Surf. & Coat. Technol. 2016, **295**, 13.
6. Imam A., Boileau A., Gries T., Ghanbaja J., Mangin D., Hussein K., Sezen H., Amati M., Belmonte T., J. Cryst. Growth, 2016, **442**, 52.
7. Imam A., Gries T., Sezen H., Amati M., Mangin D., Belmonte T., Nano-structures & Nano-Objects, 2016, **7**, 41.
8. Arnoult G., Cardoso R.P., Belmonte T., Henrion G., Appl. Phys. Lett., 2008, **93**, 191507.
9. Altaweel A., Imam A., Ghanbaja J., Mangin D., Miska P., Gries T., Belmonte T., Nanotechnology, 2017, **28**, 085602.
10. Touzeau M., Vialle M., Zellagui A., Gousset G., Lefebvre M., Pealat M., J. Phys. D: Appl. Phys., 1991, **24**, 41.
11. Ricard A., Moisan M., Moreau S., J. Phys. D: Appl. Phys., 2001, **34**, 1203.
12. Kutasi K., Guerra V., Sa P.A., Plasma Sources Sci. Technol., 2011, **20**, 035006.
13. Grotjohn T.A., Asmussen J., Sivagnaname J., Story D., Vikharev A.L., Gorbachev A., Kolysko A., Diamond Relat. Mater., 2000, **9**, 32.
14. Gries T., Vandenbulcke L., de Persis S., Aubry O., Delfau J.L., J. Vac. Sci. Technol. B, 2009, **27**, 2309.
15. Belmonte T., Czerwiec T., Michel H., Surf. & Coat. Technol., 2001, **142**, 306.
16. Vesel A., Kolar M., Recek N., Kutasi K., Stana-Kleinschek K., Mozetic M., Plasma Process. Polym., 2014, **11**, 12.

PECULIARITIES OF CATALYST PREPARATION, PETROLEUM RESIDUES, POLLUTANTS AND LIGNIN CONVERSION UNDER MICROWAVE RADIATION

M. V. Tsodikov, O. V. Arapova, A. V. Chistyakov, G. I. Konstantinov

A.V.Topchiev Institute of Petrochemical Synthesis of the Russian Academy of Sciences, Leninsky prospect, 29, Moscow, 119991, Russia

Abstract. Action of MWI on carbon sorbent led to plasma generation. Conversion of phosphorous model compounds and tar adsorbed inner pores of carbon sorbents with microwave stimulation rearched up to ~ 99% for 10 min. H_2 was the main product in producing gas in case of microwave irradiation while the methane mainly formed by using convective heating. It was found that in case of MWI cracking of C−H bond dominated. This fact explains an increased hydrogen yield in comparison with convection heating where cracking C-C bond dominates. Dry reforming (DR) of lignin with supported different content of Ni and Fe nanoparticles under microwave irradiation (MWI) with plasma generation has been studied. It was found that Fe-containing nanoparticles provide for high-rate microwave-assisted dehydrogenation and dry reforming of lignin. Study of the microwave-assisted heating dynamics for a number of solid lignin samples with different Fe concentrations revealed the threshold concentration, 0.5 wt. % Fe, which ensures the highest heating rate up to the temperature of reforming and plasma ignition. After 10 min of DR at 700−750 °C recovery of H_2 from lignin reach up to 94 % and the H_2/CO ratio of ~1/1 at summary conversion of the lignin organic mass-65%. The maximum selectivity relates to syngas forming in DR process was achieved up to 94%. Enhanced contribution of metal components in the conversion of lignin to syngas comparison with its conversion without active components and results obtained at convective heating allows to classifying process as the plasma-catalytic

1. INTRODUCTION

The development of effective utilization methods of petroleum residues and pollutants is one of the most important ecological problems of considerable current interest. Petroleum and petrochemical industries have a strong ecological impact because of the release of harmful hydrocarbon pollutants into the natural environment. Crude oil, oil sludge, tars, and other harmful and toxic substances are environmental hazards [1−3].

In recent years, the use of microwave radiation (MWR) in the development of efficient pyrolysis processes for organic substrates has received considerable attention [4]. In this context methods based on microwave technologies are developed as effective approach for liquidation of petroleum contaminants and pollutants [5]. Another side MWR has been used in a number of studies for the catalytic cracking of lignin, in particular, in the presence of heterogeneous catalysts [6].

Our report presents the results on the effective use of microwave radiation to solve a number of environmental problems and development of green chemistry processes. Within the framework of these tasks, we report the results of studies on the high speed decomposition of harms such as petroleum residues and organophosphorus pollutants adsorbed in the pores of carbon sorbents under the action of microwave radiation. Another challenge for the future use of microwave radiation is the development of plasma-catalytic reforming of lignin into syngas in the presence of nanosized nickel- and iron-containing catalysts.

2. EXPERIMENTAL

Triethyl phosphate (TEP) and triphenyl phosphate (TPP) synthesized according to the known procedures [7] were used as model organophosphorus compounds OPC, which remain stable up to 110–130°C during convection heating. TEP and TPP were deposited onto the carbon sorbents by impregnation from a chloroform solution with a certain concentration of the complex to be applied. The sorbent with a deposited OPC was dried initially at room temperature and then in a vacuum oven at a reduced pressure and a temperature of 80°C and finally subjected to MW treatment at various temperatures and exposure times. The same procedure was using for deposition of tar separated from Siberia and bitumen oil onto the carbon sorbent. During MW irradiation, the carbon sorbent containing OPC and tar adsorbed in pores was purged with an inert gas (nitrogen, argon). The effluent purge gas from the reactor was passed through a microseparator cooled to -50°C and further to a collector from which it was sent to a mass spectrometer. The gas flow rate was 8–10 cm^3/min. Experiments were conducted at a constant radiation-induced temperature of 80 to 200°C for 5, 10, and 15 min. After completing an experimental run and cooling the system, the carbon sorbent was withdrawn and analyzed for the residual OPC.

The residual amount of TEP, TPP and tar in a CS sample was determined by solvent extraction followed by gas chromatographic analysis of the extracts. The extraction was carried out in a Dionex ASE 200 accelerated solvent extractor using isopropyl alcohol as the solvent, an extraction cell temperature of 70°C, a pressure of 200 atm., and an extraction time of 30 min.

Lignin (kraft lignin from Kirov Region, Russia). Composition, wt. %: C − 58.1, H − 5.4, Al − 1.2, Si − 3.1, Ca − 0.6, Fe − 0.8, Mg − 0.04, S − 1.2, N − 0.2, O − 28.9, other − 0.5 (the content of each component is less than 0.05%). GCS (gas coal sorbent): ash content − 14%, total pore volume − 1.52 cm^3/g, sorption pore volume − 0.52 cm^3/g, macropore volume − 1.00 cm^3/g. Reagents, solvents, and gases: $Ni(OAc)_2 \times 4H_2O$ (Aldrich, 98%); C_2H_5OH (Sigma-Aldrich, ≥99.8%); Ar and He (special purity grade, 99.99%).

Nickel-containing lignin was prepared using impregnation. Nickel was deposited from aqueous solutions of nickel acetate $Ni(OAc)_2 \times 4H_2O$. Lignin was preliminary processed under vacuum during 2 h at 1 Torr and 600°C. The wetness was determined using conventional method before the deposition. An aqueous solution of nickel acetate containing 0, 0.2, 0.6, 1.3, 1.6, or 2.2 wt. % nickel was slowly added to 4 g of lignin up to the moment the solution volume can be entirely absorbed by the dried volume of lignin. Then the lignin sample was kept for 2 h in a closed vessel, being stirred at intervals. The wet lignin was dried in air at room temperature for 24 h and in a drying oven at 110°C for 2 h. By the same procedure as iron system from an alcohol solution of iron acetylacetonate $Fe(AcAc)_3$ was applied to the surface of lignin and obtained samples containing 0.1% Fe. The nickel and iron content in dried lignin was determined by atomic absorption spectrometry. The procedure was reported in [8]. The chemical composition of the initial lignin was studied by atomic absorption and laser mass spectrometry on an EMAL-2 unit. The procedure was reported in [9].

The process flowchart and the unit for lignin conversion have been described in detail [10]. The carbon dioxide reforming was carried out in a 15 cm^3 flow type reactor. The reactor was mounted in a waveguide of the microwave unit fed from a 540 W M-140 magnetron generating the microwave radiation with a 2.45±0.05 GHz frequency and 100−150 mA current density. The temperature in the reactor was determined according to the previously described procedure using a tungsten-rhenium thermocouple placed into a thermowell [10]. The MWR-induced temperature at a specified current density was maintained using an automatic magnetron switch controller. The radiation powder was varied by the current density controller. At the reactor outlet, the residual radiation was absorbed by water. Carbon dioxide was fed to the reactor bottom at a 60cm^3/min flow rate and induced temperature of 750−800°C. For comparison, experiments on microwave irradiation of iron-containing lignin under Ar were carried out. Experiments on reforming induced by convective heating at 750−800°C and CO_2 flow rate of 60 cm^3/min were carried out for comparison with the results of microwave-assisted lignin conversion.

Gaseous reaction products were analyzed online by gas chromatography on a Kristallux-4000M chromatograph. The hydrocarbon fraction was analyzed using a 1.5 m packed column filled with α-Al_2O_3 grains (0.5 mm) with 15% of supported squalane phase using a flame ionization detector (FID) and He as the eluent. The contents of H_2, CH_4, CO and CO_2 were determined using thermal conductivity detector (TCD) and Ar as the eluent.

In order to determine the lignin absorption capacity for MWI lignin heating dynamics was measured. If absorption of MWI was insufficient to achieve the desired temperature (above 700°C), the reactor was charged with a mechanical mixture of lignin with the GCS carbon adsorbent having, according to [11], high dielectric loss tangent (12.72).

Lignin conversion based on hydrogen (%): $\alpha_{(H2)} = \frac{m_{H2in} - m_{H2res}}{m_{H2in}} \cdot 100\%$, where $m_{H_{2in}}$ and $m_{H_{2res}}$ are the H_2 weights in the initial lignin and in the solid residue after reforming, respectively.

The presented lignin conversion results are an average number of the three parallel experiments. The experimental error in each series varied from 5 up to 10%.

3. RESULTS

It was found that carbon sorbents exhibit different electrophysical properties depending on the pore structure and mineral composition (mainly, the presence of the magnetic iron oxide particles); because of this, the dynamics of formation of breakdown phenomena and associated heating of the material are essentially different [12]. Absorption of MWI by solid estimated as tangent of dielectric losses: tan $\delta = \varepsilon^{11}/\varepsilon^{1`}$, where ε^1 − dielectric permeability; ε^{11} − imaginary mean of dielectric permeability. In a number of publications, this effect was related to the phase transition of a ferromagnetic state of γ-Fe_2O_3 to a paramagnetic state (Curie point), which causes an increase in the contribution to the dielectric losses as the lost tangent tan $\delta_\mu = \mu''/\mu'$, where μ'' and μ' are the real and imaginary values of magnetic susceptibility, respectively [13].

The main characteristic of carbon sorbents (CS) is presented in the Table 1.

Table 1. Main characteristics of carbon sorbents

N/N	Sorbents	A^d, wt %	Pore volume, cm^3/g			ε	tg δ
			V_Σ	Ws	Vma		
1	WWS	2.5	1.19	0.27	1.02	2.1	8.6
2	FCS	13.4	2.52	0.23	2.29	2.07	8.2
3	GCS	25.1	0.97	0.48	0.49	3.31	12.7
4	BCS	24.0	1.00	0.47	0.53	3.24	9.4
5	OSS	6.8	0.75	0.37	0.38	3.03	0.43

Note: WWS is the wood waste sorbent; FCS is the flax chaff sorbent; GCS is the gas coal sorbent; BCS is the crushed brown coal sorbent; γ is the apparent density; A^d is the mineral matter content (ash content); V_Σ is the total pore volume; W_s is the volume of sorbing pores; V_{ma} is the volume of macropores; ε is the dielectric constant; and tan δ is the dielectric loss tangent.

We studied the influence of the concentration of the deposited organophosphorus compound, MW radiation conditions, and physicochemical characteristics of CS on the degree of degradation of OPC that had been adsorbed in CS pores. The conversion of TEP absorbing MW radiation takes place at abnormally low temperatures. The intense formation of gaseous and liquid products, which are condensed in the cooled collector, is observed at 100°C. An increase in radiation intensity to elevate the temperature to as low a value as 110–130°C allows for an almost compete degradation of TEP, although it is rather stable. The exhaustive destruction of TEP having this concentration is achieved by radiation at temperature of 200°C for 5 min. Convection heating to 200°C does not result in the degradation of TEP. The degradation of the substrate is evidently due to the action of microwave radiation on the OPC adsorbed in pores. At such low temperatures, plasma generation is visually undetected; however, the effects of repolarization processes in alternating electromagnetic field lead to severe degradation of the test substrate. The degree of decomposition of TPP linearly increases with an increase in the reactor temperature up to 300°C (and microwave power from 0.2 to 1.9 mW). At 300°C, which corresponded to the microwave power of 1.9 mW, TPP underwent almost complete degradation over 10 min of irradiation.

In the Table 2 presented balance of experiments of conversion phosphorous components 20% mass preliminary absorbed on sorbents at MW radiation. Conversion of phosphorous substrate was ~ 99%.

Table 2. Main results of OPC destruction (T=110−130°C for TEP; 300°C for TPP; τ − 15 min; conversion − 99%)

Sample	Impregnated compaund		Liquid product		Gas product		Adsorbed phosphorus		Losses	
	g	%	g	%	g	%	g	%	g	%
OSS+TEP	4.0	50	1.63	40.7	1.5	37.5	0.32	8.0	0.55	13.8
OSS+TPP	2.4	32	0.7	29.1	0.5	20.8	0.15	6.2	0.43	18.0
BCS+TPP	3.15	42	traces		2.5	79.4	0.2	6.3	0.45	14.0

A petroleum product was applied to each of the four carbon sorbent samples by impregnation from a solution in petroleum ether with a concentration of 10, 20, or 30 wt. % on a sorbent weight basis; then, the solvent was distilled off from the samples initially at room temperature and then in a vacuum oven at a reduced pressure and a temperature of 40°C. Two types of tar obtained from Western Siberian oil (I) and bituminous oil from the Moscow oil refinery (II) were used as petroleum products.

The degree of conversion of tar applied to the test sorbents in a concentration of 10 wt.% upon microwave radiation was higher than 99% regardless of the origin of tar, the temperature of treatment, and the physicochemical parameters of the test sorbents. In this case, in spite of the exhaustive conversion of adsorbed tar, a larger amount of carbon residue remained at 300°C, whereas more gaseous products were released at 600°C (Table 3).

An increase in the concentration of applied tar to 20 or 30 wt. % leads to a decrease in the degree of its conversion under the action of microwave radiation, but this conversion is no lower than 90%. Conversion of tar at 300 and 600°C in an electric furnace with convective heating was not exceeding 10 and 60% respectively.

The capacities for microwave absorption for the pristine and metal-containing lignin samples were determined by measuring the heating dynamics on exposure to MWR (Fig. 1).

Table 3. Results of the degradation of tar obtained from Western Siberian oil (I) and bituminous oil (II) adsorbed in the pores of carbon sorbents

N/N	Experimental conditions				Tar conversion, %
	Temperature, T°C	Tar	Tar content, wt. %	Sample	
1	300	I	10	BCS	>99
2	300	II	10	BCS	>99
3	600	I	10	BCS	>99
4	600	II	10	BCS	>99
6	600	II	10	GCS	>99
7	600	I	20	GCS	96
8	600	I	30	GCS	91
9	600	I	10	WWS	>99
10	600	I	10	FCS	>99

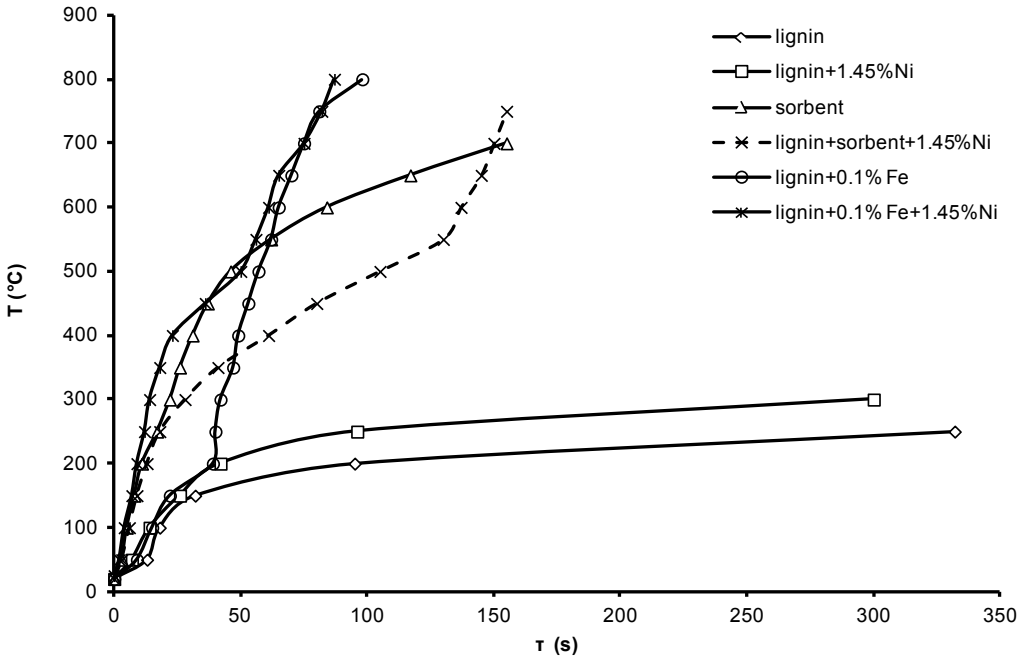

Figure 1. Microwave heating dynamics of lignin and sorbent samples.

As can be seen from the Fig. 1, curve 1, the pristine lignin does not possess a sufficient level of microwave absorption; therefore, it was subjected to conversion as a mixture with a carbon adsorbent. In a carbon dioxide atmosphere under MWI, the pristine lignin mixed with a carbon adsorbent is converted to the liquid hydrocarbon fraction, water, gas products, and a solid residue. The deposition of nickel acetate on lignin did not increase the microwave absorption capacity (Fig. 1); therefore, a carbon sorbent was also added to lignin for the experiments (entries 3 and 4, Table 4). The deposition of nickel increases the recovery of hydrogen up to 82–86%, which is accompanied by a sharp change in the process selectivity depending on the gas medium used. In an argon flow, the yields of liquid and gaseous products are identical to those obtained by the destruction of pristine lignin in Ar. When carbon dioxide is used as the medium, the yield of liquid products markedly decreases down to 8.3 wt. %, while the selectivity to syngas increases to 73%, with the H_2/CO molar ratio of ~1. The observed increase in the yield of hydrogen-containing gas is apparently attributable to the catalytic action of nickel, which intensifies the interaction of lignin with the liquid destruction products (guaiacyl, phenyl, and vanillin derivatives).

Unlike the deposition of nickel, deposition of a small amount of iron (0.1 wt. %) on lignin resulted in a sharp increase in the microwave absorption capacity, which was manifested as a rather fast generation of plasma and, correspondingly, enhanced heating dynamics of the system as a whole (Fig. 1) and as lignin conversion without a carbon material (Table 4). The introduction of iron compounds into lignin leads to decreasing yield of liquid products to 3 wt. % and increasing yield of gas products under the action of microwave radiation (Table 1). The yields of liquid and gas products formed upon destruction of iron-modified lignin in argon and carbon dioxide are identical, which attests to high process intensity with plasma being ignited directly in the lignin matrix. However, the selectivity to synthesis gas in carbon dioxide increases to 94% from 64% observed in argon, while the selectivity to light hydrocarbons proportionally decreases.

A comparison of the conversion of pristine lignin (entry 1, Table 4) and metal-modified lignin (entry 2-10, Table 4) under MWI with the results obtained upon convective heating (entries 11, 12, Table 4) indicates that the yield of solid residue is almost invariable in both cases, i.e., the degree of lignin conversion does not depend on the energy transfer mechanism. Meanwhile, the selectivity to liquid and gas products markedly changes. In the case of convective heating, the yield of liquid organic products increases to 40 wt. %; as in the case of MWI, these products include watered phenyl, guaiacyl, and vanillin derivatives. As has been shown in [10], C–H bond cleavage in organic substrates predominates in the case of microwave heating, while C–C bond cleavage is the major process in the case of convective heating. This accounts for increasing selectivity to hydrogen-containing gas upon lignin destruction in the

microwave field. The key difference between the MWI and convective heating modes is switching of the process selectivity, which can be directed towards either liquid organic substrates (by convective heating) or hydrogen-containing gas (by MWI).

Table 4. Main results of the lignin conversion process

№	M wt.%	Gas	oil, wt.%	gas, wt.%	char, wt.%	α(H_2), %	H_2 yield, wt %	CO yield, wt.%
Lignin+sorbent								
1	0	CO_2	22.1	23.5	54.4	75.5	6.2	10.9
2	0	Ar	41.7	13.3	45.0	75.1	5.9	3.2
Lignin+cat+sorbent								
3	0.1 Ni	CO_2	21.5	27.2	51.3	78.9	10.4	10.4
4	0.5 Ni	CO_2	19	31.9	48.4	80.5	12.9	12.0
5	1.05 Ni	CO_2	12.5	46.1	41.4	82.4	17.8	20.6
6	1.45 Ni	CO_2	8.3	48.5	43.1	85.6	21.0	21.8
7	2.09 Ni	CO_2	14.9	46.0	39.1	87.2	18.7	22.2
8	1.45 Ni	Ar	37.4	14.3	48.3	82.3	6.1	4.7
Lignin+cat								
9	0.1 Fe	CO_2	3.5	54.2	42.2	87.7	19.2	24.7
10	0.1 Fe+1.45Ni	CO_2	3.3	56.4	40.3	90.0	22.5	28.8
Convective heating								
11	0	CO_2	38.9	19.3	41.8	83.5	2.4	10.9
12	1.5 Ni	CO_2	39.8	16.3	43.9	86.6	4.2	8.0

In order to increase the selectivity to hydrogen and syngas, a combined technique was applied: 1.45 wt. % nickel was deposited onto lignin containing 0.1 wt. % iron. The catalytic tests showed that the deposition of nickel may increase the hydrogen recovery up to 90% and provide the maximum selectivity to syngas (84.5%), with the H_2/CO molar ratio of 0.8 (entry 10, Table 4). In all probability, in the carbon dioxide atmosphere, functional groups (methoxy, propyl, and propylphenyl) present in the polyaromatic lignin units are the first to be reformed on nickel and iron sites, which results in a noticeable decrease in the yield of liquid destruction products and increase in the yield of hydrogen. The remaining polyaromatic skeleton is dehydrogenated; probably, the nickel sites promote the Boudouard reaction, resulting in removal of surface carbon and in increasing yield of carbon monoxide. Modification of lignin with a minor amount of iron leads to ignition of plasma directly in the lignin matrix even at the radiation power of 0.5 kW, which substantially enhances the hydrogen recovery. In the presence of nickel sites in the CO_2 medium, the yield of syngas markedly increases, indicating a plasma catalytic type of the process.

The study of nickel and iron-contained particles structure and magnetic properties before and after the reforming provide the conclusion that different behavior of nanosized active components in the MW-assisted reforming are dictated by specific features of Ni- and Fe-contained particles stabilization on the lignin surface and by different electronic structures of active Ni sites.

4. CONCLUSIONS

MWI of carbon adsorbents is effective manner for destruction of preliminary adsorbed organic substrates. This approach is perspective for deep conversion of petroleum residues and phosphorous pollutants. Mechanism of destruction of adsorbed organic substrates undergoing by MWI distinguishes from one at convective heating. Iron-containing components show significantly high ability to absorb MWI in

comparison with nickel modified lignin. Addition of Fe-contained particles on the surface of lignin leads to plasma generation, and do not require using of carbon sorbents as microwave absorbents. Using lignin prepared by combined. MW-assisted dry reforming of lignin with surface-deposited nickel and iron particles results in high lignin-to-syngas conversions. The mechanism of MW-assisted reforming of Ni and Fe-containing lignin differs from the mechanism of the process induced by convective heating. It was shown that in case of MW treatment of organic compounds dominate C−H bond cracking, convective heating mainly induces lignin transformations with C-C bond cleavage, giving rise to liquid aromatics.

Analysis of the conditions for increasing the process efficiency identified a number of interesting trends concerning the formation of the nickel and iron catalysts on the surface. The yield of syngas increases for Ni and Fe containing lignin samples compared with the initial lignin both in a CO_2 and in a flow of Ar method in dry reforming under MWI can achieve high conversion of lignin to syngas. Molar ratio in gas product is $H_2/CO \sim 1$. Ni and Fe nanoparticles immobilized on the lignin surface contribute to catalytic activity of dry reforming and provide an opportunity for fast and selective dry reforming of lignin organic mass in plasma catalytic conditions.

This work financial supported by RFBR-ofi (grant N 16-29-10663).

References

1. Aleksandrov V.P., Emel'yanov V.P., Otravlyayushchie veshchestva (Chemical Warfare Agents), Moscow: Voenizdat, 1990.
2. Arens V.Zh., Gridin O.M., Yashin A.L., Ekol. Prom–st. Ross., 1999, **9**, 33.
3. Shimkovich V.V., Neftepererab. Neftekhim. Prom–st., Ser. Okhr. Okruzh. Sredy, 1996, **2**, 110.
4. Yunpu W., Leilei D., Liangliang F., Shaoqi S., Yuhuan L., Roger R., J. Anal. Appl. Pyrolysis, 2016, **119**, 104.
5. Hua V.J., Xu W., Fang L., Adv. Mater. Research. 2011, 356.
6. Fan L., Chen P., Zhang Y., Liu S., Liu Y., Wang Y., Dai L., Ruan R., Bioresource Technol., 2017, **225**, 199.
7. Kabachnik M.I., Mastryukova T.A., Mezhfazovyi kataliz v fosfororganicheskoi khimii (Phase-Transfer Catalysis in Organophosphorus Chemistry), Moscow: Editorial URSS, 2002.
8. Nikolaev S.A., Pichugina D.A., Mukhamedzyanova D.F., Gold Bull. 2012, **45**, 221.
9. Rodicheva G.V., Orlovskii V.P., Romanova N.M., Steblevskii A.V., Sukhanova G.E., Russ. J. Inorg. Chem. 1996, **41**, 728.
10. Tsodikov M.V., Konstantinov G.I., Chistyakov A.V., Arapova O.V., Perederii M.A., Chem. Eng. J., 2016, **292**, 315.
11. Tsodikov M.V., Perederii M.A., Chistyakov A.V., Konstantinov G.I., Kadiev Kh.M., Khadzhiev S.N., Solid Fuel Chem., 2012, **46**, 121.
12. Tsodikov M.V., Perederii M.A., Maksimov Yu.V., Gurko A.A., et al., Ross. Nanotekhnol., 2006, **1**, 153.
13. Hayes B.L., Microwave Synthesis: Chemistry at the Speed of Light, North Carolina: CEM Publ., 2002.

DUSTY FIRE-COLUMN-LIKE PLASMA EJECTED FROM BASALT BY LOCALIZED MICROWAVES

Y. Shoshani, E. Jerby

Faculty of Engineering, Tel Aviv University, Ramat Aviv 6997801, ISRAEL

Abstract. This paper presents a phenomenon of fire-column-like plasma ejected from minerals such as basalt. The experimental setup employs a microwave cavity including a *microwave-drill* device, which creates a molten hotspot from which the plasma column is ejected to the air atmosphere. This approach follows our previous studies on fireball- and fire-column-like plasma ejection from solids (glass, silicon, copper, titanium), and is related to the broader paradigm of localized-microwave heating (LMH), including the plasma generation and ejection from microwave-induced hotspots. Various *in-* and *ex-situ* diagnostics are used in order to characterize the dusty plasma and the nanoparticle products obtained from basalt. The experimental results are considered in various scientific and practical aspects, namely their potential relevance to natural ball-lightning and volcanic effects, as well as their significance for several applications, such as powder generation, microwave-induced breakdown spectroscopy (MIBS), and mineral extraction.

1. INTRODUCTION

Heating, cracking, braking and melting of basalt rocks by means of microwave irradiation have been studied in various aspects in the last years [1−6]. Basalt melting in a microwave cavity was reported by us in 2004 [1]. More recently, microwave-heating effects in basalts were investigated in several aspects, including the formation of cracks due to temperature gradients and thermal stresses [2, 3]; microwave-assisted rock breakage for space mining applications [4]; rock cracking and breakage for microwave-assisted underground excavation [5]; and feasibility studies of basalt melting by microwaves [6]. With respect to the latter, we showed that basalt melting by localized microwave heating (LMH) involves a thermal-runaway instability [7, 8], leading to a hotspot formation in the core of the basalt stone. The molten core erupts after a while as a *miniature volcano,* and flows as a stream of lava towards the surface outside.

The effect of fireball-like plasmoids ejected by localized microwaves from hotspots generated in other solid or liquid substrates was presented in [9, 10]. This effect resembles fireballs exited by microwaves in air atmosphere, as studied for instance in the context of their similarity to natural ball-lightning phenomena [11, 12]. The ejection of plasmoids by localized microwaves from solid substrates and its buoyancy in air [9, 13] has been demonstrated in several substrate materials, such as glass and silicates [14], germanium, salty water [10], titanium [15], and copper [16]. Some of these plasmoids were also examined by small-angle X-ray scattering (SAXS) at the European Synchrotron Radiation Facility (ESRF). The SAXS measurements revealed the presence of nanoparticles with diameters of ~50 nm within these plasmoids, in a number density of $n_d \sim 10^{16}$ m^{-3} [17]. The significant presence of dust grains, compared to electrons and ions, in these plasmoids leads to their classification as complex (dusty) plasma.

The present paper introduces our recent observations of similar fire-column and fireball-like plasmoids ejected by localized microwave from basalts. Various experimental techniques are applied in this study, as in the previous ones, in order to characterize the microwave heating, melting, and hotspot formation in the irradiated object, and the plasma ejected from it. These experimental means include microwave-scattering analyses, optical spectroscopy, and scanning electron microscopy (SEM). Each of these means, solely, is limited in certain aspects, but their ensemble may provide some more comprehensive insight of the phenomena observed, as presented in the next sections.

2. EXPERIMENTAL

The processes of basalt melting and plasmoid ejection therefrom are initiated in this study by directing localized microwave power into the basalt specimen. This localization effect is implemented by the *microwave-drill* mechanism [18], which creates the hotspot from which plasma is ejected in a form of a fire-column or a fireball, into the cavity.

The experimental setup shown in Figs. 1a, b includes a microwave cavity fed by a 2.45-GHz, 1-kW magnetron. The cavity is made of a 10×5 cm^2 cross-section waveguide, shorted at the end by a mirror made of metallic vanes under cutoff. This arrangement enables a direct view into the waveguide, with no disturbance to the various diagnostic means (e.g. the thermal camera which requires a direct line of sight). A similar array of vanes under cutoff is also installed as part of the side wall of the cavity, enabling a broader view (from both perpendicular directions) and more in-situ diagnostic means simultaneously.

The magnetron's switched-mode power supply (MagDrive-1000, Dipolar Ltd., Sweden) provides an adjustable input microwave power up to 1 kW. The microwave power is delivered to the cavity via an isolator and an impedance auto-tuner (Homer, S-Team Ltd., Bratislava, Slovak republic), as depicted in Fig.1a. The incident and reflected waves are recorded by the impedance-analyser mode of the auto-tuner, which also enables adaptive impedance matching and optimal transmission of the microwave power into the cavity. It also provides real-time measurements of the complex impedance of the load, in both actual and embedded modes.

The diagnostic means include video recording (at 200 fps) and thermal imaging by FLIR-SC300 camera, captured via the openings in the vanes along the waveguide. The optical spectral emission from the lava and plasma eruptions is captured by an optical spectrometer (Avaspec-3648) with 0.3-nm resolution in the range 200-1000 nm.

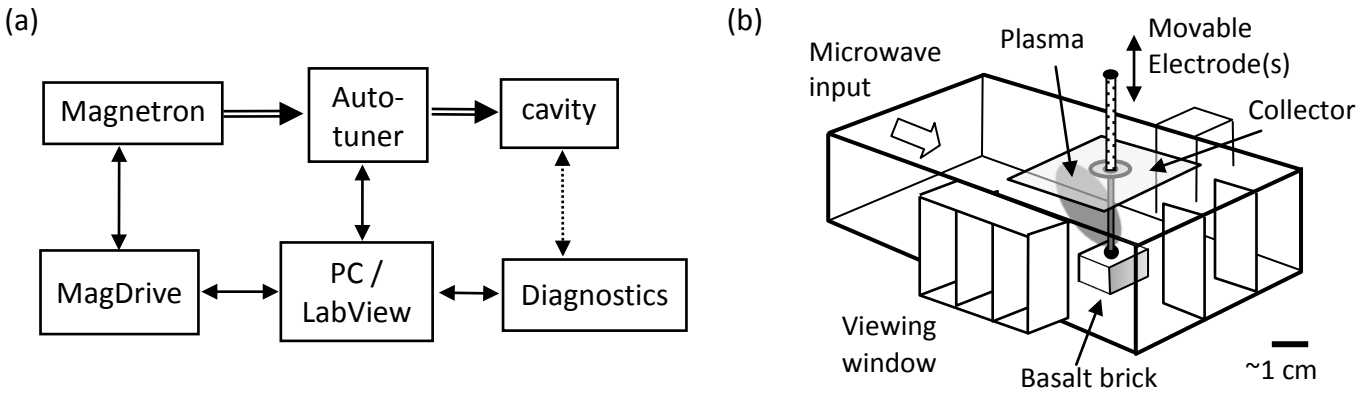

Figure 1. The experimental setup: (a) A block diagram of the experimental instrumentation, with the diagnostics including an optical spectrometer, thermal and video cameras, and an *I-V* probe. (b) The microwave cavity with a movable electrode (or optionally an electrode array) directing the microwaves into the basalt substrate hence creating a hotspot, from which the plasma-column is ejected to the air atmosphere within the microwave chamber, up to the aluminum-made collector.

In this experiment we use basalt stones (from the Golan heights) either in their original natural shapes or cut to (3-cm)^3 cubic bricks. This load is placed inside the cavity in an optimized position whereas the movable electrode directs the microwave energy locally into the substrate. Various level of focusing are optionally available in this setup, either by moving the single electrode shown in Fig. 1b, or by manipulating an array of nine moveable electrodes installed in the cavity ceiling, via the collector. The focusing possibilities include (a) a single-electrode focusing as in Fig. 1b, (b) no-electrode focusing, and (c) a multi-electrode array focusing. Each electrode in this array expedites the intentional excitation of the hotspot in its vicinity, when brought into contact with the basalt-stone surface, and hence enables the stimulation of the fire-column (and consequently of a fireball) in a more controlled fashion.

3. RESULTS

As visually observed (and confirmed by thermal-camera imaging), at the first stage in this experimental run the microwave irradiation heats up the basalt to its melting temperature, whereas the heat energy is being accumulated in its core, forming an inner hotspot (within the stone or the brick). After a while, effects like lava eruption, lava tunnelling and rock cracking are observed (as reported in [7]). In the present work we first observed, however, that by a further irradiation of the basalt the hotspot continues to evolve up to a point in which plasma is ejected from it, as shown in Figs. 2a-d. Staring from a molten hotspot (Fig. 2a), the plasma is first emitted (Fig. 2b) and evolves as a stable fire-column (Fig. 2c), which finally emits a fireball. The latter is buoyant in the air atmosphere within the cavity, and tends to move towards the magnetron (as in [9, 10, 13, 14]). Various modes of plasma ejection from basalts have been observed in this study, such as fire-column eruption from a dome made of a thin layer of obsidian (created by the lava eruption), and a simultaneous ejection of two plasma columns from two different hotspots.

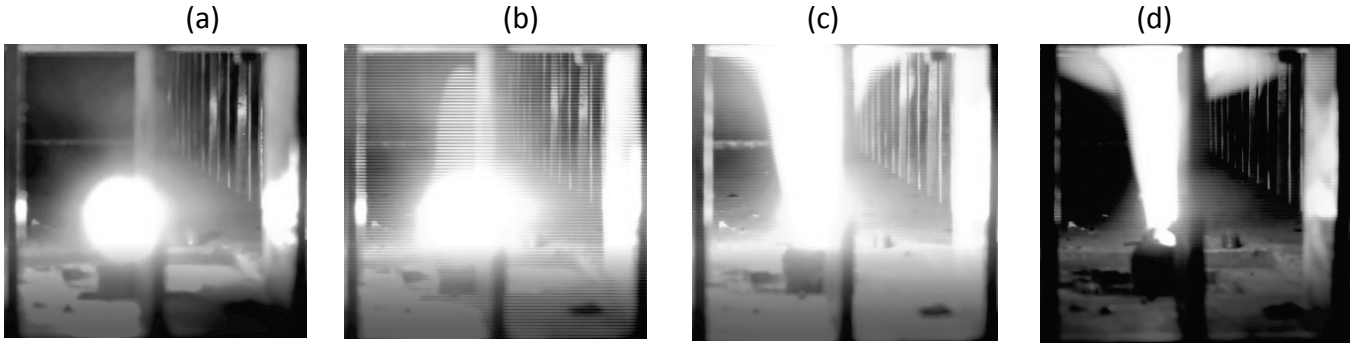

Figure 2. Plasmoid evolution from a molten hotspot in basalt: (a) The hotspot is formed and further evolved, (b) initial plasma plume is ejected from the hotspot, (c) a stable fire-column is fed by the hotspot, and (d) a fireball emitted from the fire-column is tending to fly towards the microwave-input port.

3.1. Microwave-scattering analyses. The microwave scattered from the plasmoid is analyzed in order to find its microwave impedance, and hence to estimate its dielectric and plasma properties. First, the reflections of the 2.45 GHz input power are measured during the various stages presented in Figs. 2a−d. The results for the complex reflection coefficient Γ are shown in Figs. 3a, b, in Smith-chart and time-dependent presentations, respectively.

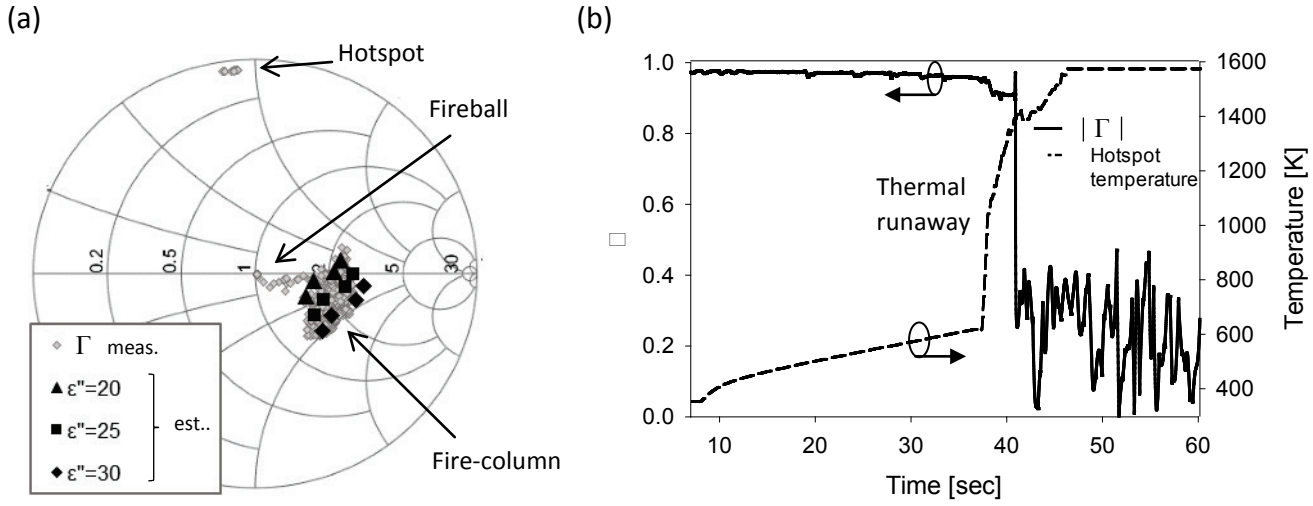

Figure 3. Microwave reflections during the various stages of the plasmoid evolution: (a) A Smith-chart presentation of the complex reflection coefficient Γ, starting from a mismatch (|Γ|~1) at the hotspot stage (Fig. 2a), reduced to |Γ|~0.4 at the fire-column stage (Fig. 2c), and matched (|Γ|~0) by the self-adapted fireball (Fig. 2d). Simulated dielectric-losses ($\varepsilon'' = 20,\ 25,\ 30$) for an equivalent column-shape load are marked for comparison. (b) The reflection coefficient ρ = | Γ| and the hotspot temperature measured vs. time, showing an abrupt drop of the microwave reflections during the thermal-runaway instability.

The results show that the microwave reflection tends to decrease after the plasma ejection (from |Γ|~1 to ~0.4), and to further decrease when a fireball emerges (to |Γ|~0). At the fire-column stage, the reflection coefficient is bouncing around ~0.4, while being attracted by the Smith-chart center. The corresponding power reflection is smaller than 20% at this stage, hence the plasmoid interacts with its microwave source as an adaptively matched load. At the fireball stage, this self-tuning mechanism tends to adaptively maximize the microwave power absorbed by the fireball, by optimizing its intensity, position and size. The reflection measurements enable us to find the impedance and dielectric properties of the fire-column by simulating an equivalent load, with the same shape, position and size, as presented in Fig. 3a.

Microwave scattering measurements are also performed at other frequency ranges, by irradiating the plasmoid by another probing signal. The latter is coupled via additional input and output ports (marked 1 and 2, respectively, in the inset of Fig. 4a). Scattering results for the microwave transmission coefficients (measured and simulated) at a lower frequency band (0.8–1.5 GHz) are shown in Fig. 4a, with and without the plasma. The results show that around the anti-node frequency of the coupling between Ports 1 and 2 (at ~1.25 GHz, which corresponds to $L \sim \lambda/2$ coupler arm length), the transmission coefficient S_{21} is increased by >20 dB in the presence of plasma. Indeed, below the plasma frequency, the fire-column behaves like a conductor, which short the coupler arm length by half ($\sim L/2 \sim \lambda/4$) and hence significantly increases the transmission. A numerical simulation of this coupler, with an equivalent column-shaped load inside, enables us to estimate the plasma dielectric permittivity, as above. The transmission increase follows the temperature rise, as shown in Fig. 4b for the anti-node frequency, in which the plasma actually switches between the decoupled and coupled states of Ports 1 and 2.

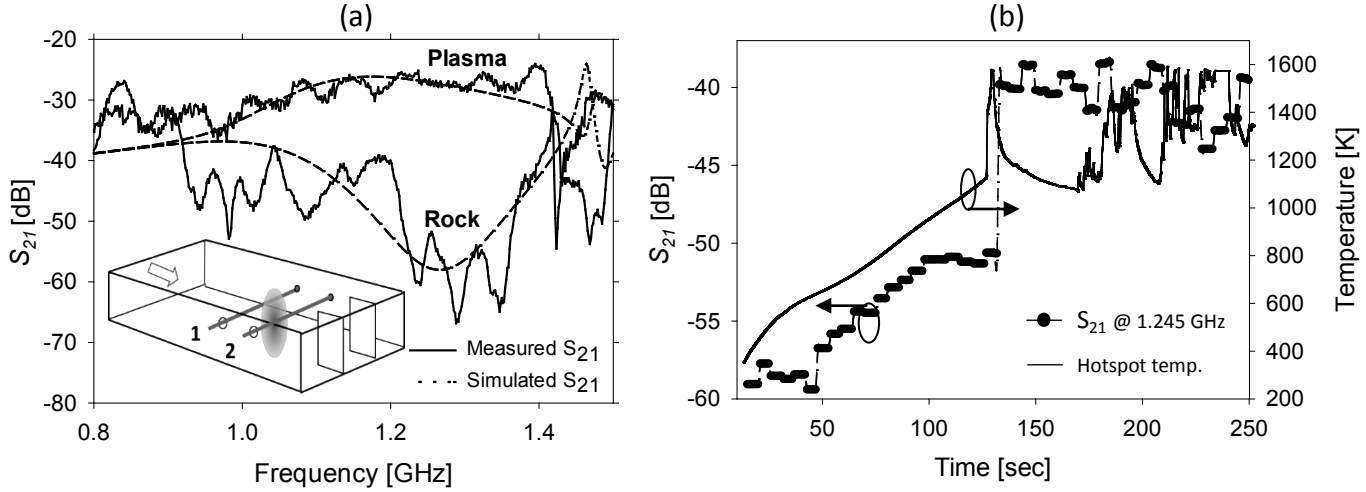

Figure 4. Scattering analyses of the plasma by an additional coupler at low frequencies: (a) The transmission coefficient S_{21}, measured with and without the plasma, shows a >20 dB increase in the coupling due to the plasma shortening of the coupler arms 1 and 2 (in the inset). An equivalent load simulation results in $\varepsilon_r \sim 0.3 - j50$. (b) A single-frequency measurement vs. time at the anti-node frequency (~1.245 GHz) with respect to the hotspot temperature. The abrupt change in the transmission coefficient associated with the decrease in the hotspot temperature occurs with the plasma ejection.

3.2. Optical spectroscopy. The optical spectrum of the light emitted by the basalt plasma-column presents spectral lines near 222, 328, 402, 567, 601 and 670 nm, identified as Fe, P, C, Si, Al and Ca lines [19], respectively, as shown in Fig. 5a. Due to the limited sampling resolution (0.3-nm), some of these lines are overlapping or weak (for instance, the continuum seen at the 750−800 nm range, may also indicate the presence of Mg). Nevertheless, all the elements detected by the plasma optical spectroscopy are known as components of basalt rocks.

The Boltzmann plot technique is implemented on the Fe and Ti lines, as shown in Fig. 5b, which results in excitation temperature T_{exc} estimates of ~ 0.3 and ~0.6 eV, respectively. The spectral emission of OH radicals is identified and compared by fitting to LifBase data [20]. As shown in Fig. 5c, the rotational temperature T_{rot} is also roughly estimated in the same range of ~ 0.3−0.6 eV.

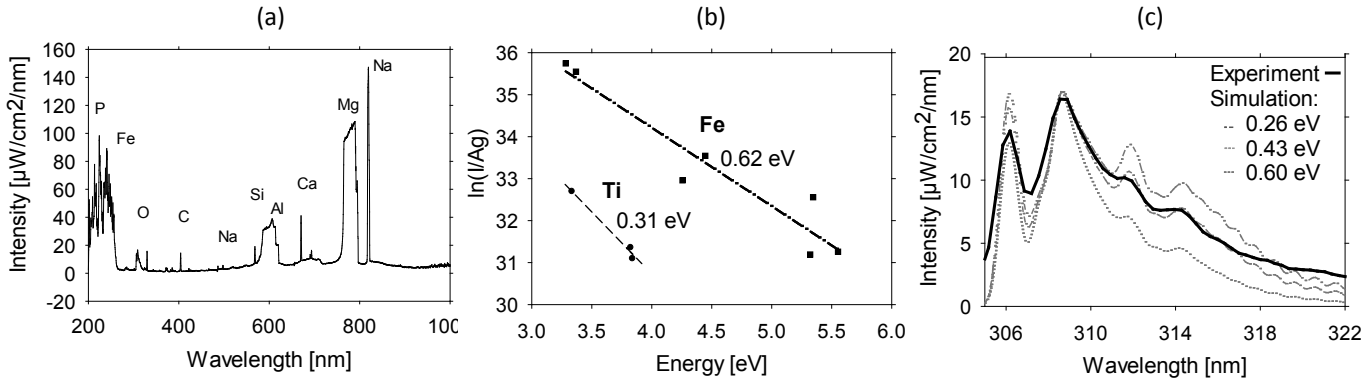

Figure 5. Optical spectroscopy measurements of basalt plasmoids (a); a Boltzmann plot of the Fe and Ti lines (b), and the OH-radical emission compared by fitting to LifBase simulation (c). Both estimates result in the range $T_{exc} \sim T_{rot} \sim 0.3$-$0.6$ eV.

3.3. *I-V* measurements. A Langmuir-like probe is inserted into the plasma in order to measure its I-V characteristics. As shown in Fig. 6a, the 1.6-mm diameter, 50-mm long probe is fed by a 50-Hz, ~100-V alternating voltage. Figure 6b shows the resulting current drawn by the plasma. Similar results are only observed when the melt exists as illustrated in Fig. 6a, and closes the electric circuits to enable the current flow (otherwise much smaller currents are erroneously measured). A presumable reason is the isolating powder oxide accumulated on the metal surfaces, which adds a significant resistant to the plasma current loop. The hysteresis observed in the *I-V* curve may also indicate a contamination of the electrode, which leads to a capacitive effect. The rough estimates of the electron temperature by the curves' slopes results in ~ 0.3 and ~ 0.6 eV for the voltage rise and fall, respectively, in Fig. 6b. This T_e range resembles the estimated optical results above.

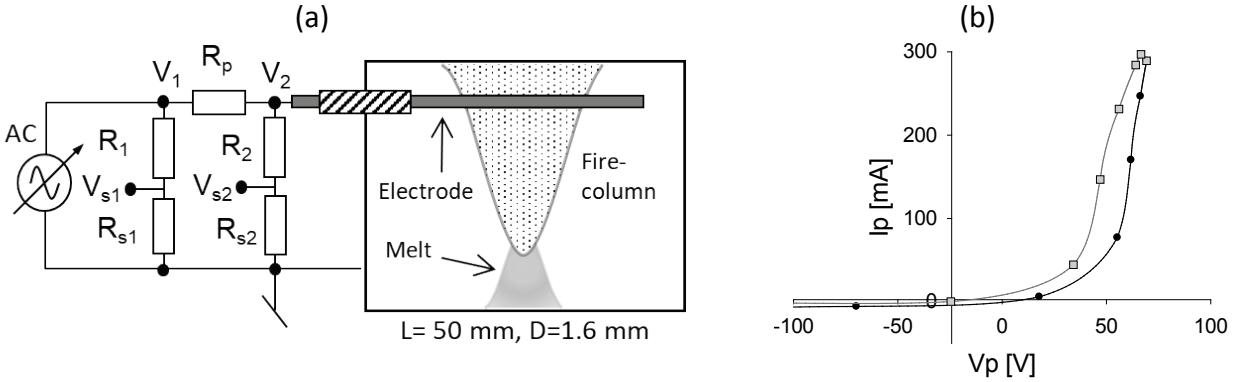

Figure 6. *I-V* curve measurements: (a) The electrical setup of the probe fed by a 50-Hz, 100-V alternating voltage. (b) A typical *I-V* curve measured with the probe. The different voltage rise and fall paths (possibly due to the powder deposition capacitance) are marked by round and square dots, respectively. The electron temperature estimate by the various slops is ~0.3−0.6 eV, similarly to the optical measurements above.

3.4. SEM observations. The basalt's plasma produces a significant amount of powder, deposited on the collector shown in Fig. 1b. The surface morphologies of the particles created by the plasma are characterized by a FEI Quanta 200FEG environmental SEM. The chemical element composition is analyzed using energy dispersive spectroscopy (EDS) with a Si(Li) liquid-nitrogen cooled Oxford INCA X-ray detector. The accumulated particles are observed in various shapes, mostly aggregates in few micro-meter sizes. Figure 7a shows aggregates of such particles on the collector surface as observed by SEM. The EDS analyses reveal that these aggregates are composed of elements typical to the basalt content, as listed in Table 1. The basalt's plasma also generates larger spherical particles, in sizes of tens of microns, as seen on the collector (Fig. 7b). Holes of similar sizes are also noticed on the collector surface (this finding may evident either particle bombardment or a plasma localization effect). Island-like regions are also observed upon the white powder deposition on the collector, as shown in Fig. 7c. EDS shows that they mostly consist of aluminum, as the collector itself.

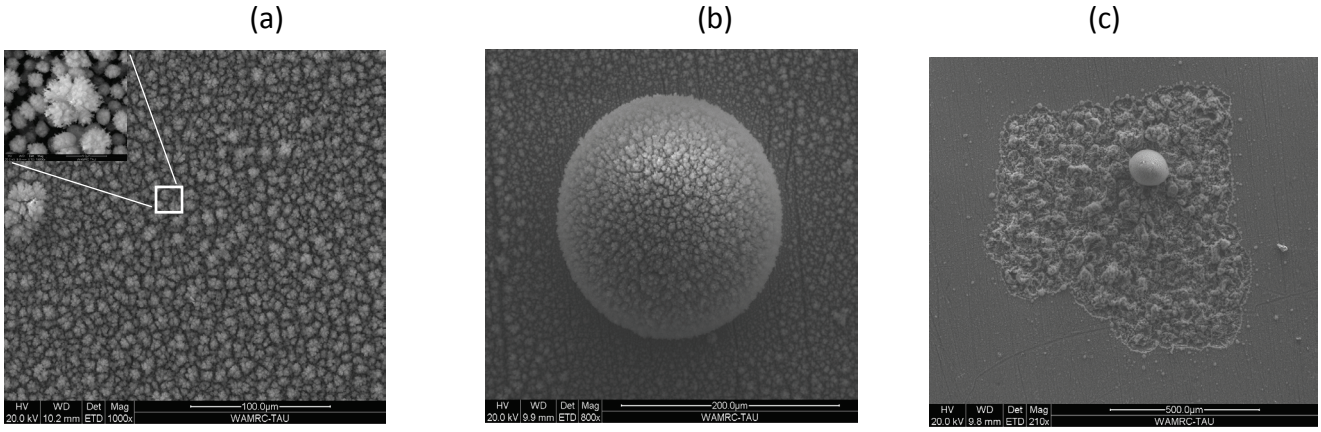

Figure 7. SEM observations of the collector: (a) Aggregates of flower-like shapes uniformly spread over the collector surface. The inset shows a typical particle of a ~ 5 μm diameter. (b) An example of a larger sphere observed, of a ~ 0.2 mm diameter. (c) Island-like region mostly consists of aluminum (possibly due to plasma etching of the collector).

EDS analyses were also conducted on the basalt stone surface, in its original and molten forms, in order to compare the compositions of the vitrified product (namely obsidian) and the natural stone. Table 1 shows the relative presence of the constitutive elements in the various phases of this process, namely the natural stone, the melt, and the deposited powder. The weight ratios differ between the various phases. However, it seems that the deposited powder consists of elements provided solely by the basalt (e.g. Si and Fe). These ingredients of the powder were most likely extracted from the basalt, evolved and transported by the plasma to the collector. Accordingly, these elements were also detected by optical spectrometry in the plasma.

Table 1. The elemental composition of the original basalt stone and the two solid phases produced, the vitrified melt (obsidian) and the powder accumulated on the collector (typical values in Wt. %)

	O	Si	Al	Fe	Ca	Na	Mg	K	Ti	P
Basalt	48	23	8	7	6	3	2	1	1	1
Obsidian	52	21	6	6	6	2	5	<1	1	<1
Powder	42	4	5	3	-	22	-	7	-	17

3. DISCUSSION

In this study we found that LMH of basalt may cause (in addition to hotspot formation, melting and cracking) also an ejection of intense plasma from the molten stone [21]. This plasma in a form of a fire-column (and possibly fireball), is found to be rich of nano- and micro-particles, and hence regarded as a dusty plasma. Using the simplified model of microwave excited dusty plasma assumed in [13−15], the main parameters of the basalt plasma are estimated as $n_e \sim 10^{17} - 10^{18}$ m^{-3}, $n_d \sim 10^{16}$ m^{-3}, and $T_e \sim 0.3 - 0.6$ eV, for the electron and dust densities, and for the electron temperature, respectively. This weakly-ionized, low-density plasma contains components of the original basalt stone (e.g. silicon and iron oxides), deposited in a powder form on the collector installed at the chamber ceiling. The remaining stone is cracked and partly melted to form a volcanic glass (obsidian).

Major challenges have remained for further research in the course of this ongoing study, including in-depth investigations and modeling of (a) the LMH interaction with basalt including phase transitions, (b) the plasma ejection mechanism, (c) effects of thermionic emission, (d) microwave interactions with dusty plasma and particle agglomeration therein, (e) plasma-surface interactions, and (f) plasma-chemical reactions which occur in this process.

In an interdisciplinary approach, the further progress in this LMH-plasma study is also oriented to volcanology and geosciences, in view of the basalt core-melting and lava-flow effects observed here in a miniature scale and their resemblance to giant natural volcanic phenomena. Also, the natural ball-lightning phenomena sometimes associated with volcanoes could be experimentally modeled to some extent by the LMH-generated fire-column and fireball-like plasmas [9]. Therefore, another major challenge in this study is to further develop this experimental setup as a small-scale laboratory simulator of volcanic phenomena.

In the more technological aspect, this study of LMH in basalts could be relevant to various potential applications, including for instance (a) microwave drilling in basalt [18], (b) cracking and crushing of basalts, for mining and construction operations [2-6], (c) basalt vitrification and glass production, (d) joining of basalt bricks, (e) direct extraction of minerals in a powder form from basalts, and (f) analyses of rock contents in the field, by portable microwave-induced breakdown spectroscopy (MIBS) systems [22].

Acknowledgement

This research is supported by The Israel Science Foundation (Grant No. 1896/16).

References

1. Jerby E., Dikhtyar V., Einat M., Proc. AIChE Annual Meeting, Nov. 7−12, 2004, Austin, Texas, Amer. Inst. Chem. Eng., 2004, 1673.
2. Peinsitt T., Kuchar F., Hartlieb P., Moser P., Hubert K., Restner U., Sifferlinger N.A., Int. J. Mining and Mineral Eng., 2010, **2**, 18.
3. Hartlieb P., Leind M., Kuchar F., Antretter T., Moser P., Minerals Eng., 2012, **31**, 82.
4. Satish H., Ouellet J., Raghavan V., Radziszewski P., Mining Technology IMM Trans., 2006, **115**, 34.
5. Hassani F., Nekoovaght P.M., Gharib N., J. Rock Mech. Geotechnical Eng., 2016, **8**, 1.
6. Mamontov A.V., Nefedov V.N., Tuv A.L. Yazykov D.A., Meas. Tech., 2012, **55**, 1068.
7. Jerby, E., Meir, Y., Faran, M., Proc. AMPERE 14th Int. Conf. Microwave High Freq. Heat., Sept. 16−19, 2013, Nottingham, UK, 2013, 255.
8. Jerby E., Chem. Eng. Proc., 2017, **122**, 331.
9. Dikhtyar V., Jerby E., Phys. Rev. Lett., 2006, **96**, 045002.
10. Jerby E., Dikhtyar V., Microwave discharges: Fundamentals and Applications, Lebedev Yu.A. (Ed.), Yanus-K, Moscow, 2006, 227.
11. Ofuruton H., Kondo N., Kamogawa M., Aoki M., Ohtsuki Y.H., J. Geophys. Res., 2001, **106**, 12367.
12. Egorov A.I., Stepanov S.I., Shbanov G.D., Physics-Uspekhi, 2004, **47**, 99.
13. Jerby E., Encyclop. Plasma Technology, Taylor and Francis, 2017, 819.
14. Meir Y., Jerby E., Barkay Z. Ashkenazi D., Mitchel J.B., Narayanan T., Eliaz N., LeGarrec J., Sztucki M., Meshcheryakov O., Materials, 2013, **6**, 4011.
15. Popescu S., Jerby E., Meir Y., Barkay Z., Ashkenazi D., J. Mitchel J.B., LeGarrec J, Narayanan T., J. Appl. Phys., 2015, **118**, 023302.
16. Jerby E., Golts A., Shamir Y., Wonde S., Mitchell J.B., LeGarrec J.L., Narayanan T., Sztucki M., Ashkenazi D., Barkay Z., Eliaz N., Appl. Phys. Lett., 2009, **95**, 191501.
17. Mitchell J.B., LeGarrec J.L., Sztucki M., Narayanan T., Dikhtyar V., Jerby E., Phys. Rev. Lett., 2008, **100**, 065001.
18. Jerby E., Dikhtyar V., Aktushev O., Grosglick U., Science, 2002, **298**, 587.
19. Kramida A., Ralchenko Yu., Reader J., NIST Atomic Spectra Database (Ver. 5.2), NIST ASD Team, 2014.
20. Luque J., Crosley D.R., SRI Int'l Report MP 99-009, 1999.
21. Jerby E., Shoshany Y., IEEE 45th ICOPS Conf. Plasma Sci., June 24−28, 2018, Denver, Colorado.
22. Meir Y., Jerby E., Microwave Opt. Tech. Lett., 2011, **53**, 2281.

MICROWAVE DISCHARGES IN LIQUIDS: CHARACTERISTICS AND AREAS OF APPLICATION

Yu. A. Lebedev

A.V. Topchiev Institute of Petrochemical Synthesis of the Russian Academy of Sciences (TIPS RAS), Leninsky Prospect, 29, Moscow, 119991, Russia

Abstract. The purpose of this review is to draw attention to the relatively new and poorly studied object of plasma physics, namely to the microwave discharges in liquids. **S**tudy of microwave discharges in liquids began only in early 2000-th and now they still remain one of the least studied plasma objects. Nevertheless, they are beginning to find application for solving various applied problems. The main types of experimental devices are described, and available information on the plasma parameters obtained by emission spectroscopy is presented. Results of studies on the use of such discharges in different applied areas are described: for water decontaminants, for generation of nanoparticles, for deposition of diamond coatings, for etching of photoresists, etc. Discharges can be created at pressure ranged from 0.1 kPa to atmospheric pressure at microwave powers from tens of watts to several kilowatts. Known data on the use of microwave discharges show their high efficiency in comparison with conventional discharges in the gas phase and in comparison with discharges of other types in liquids.

1. INTRODUCTION

Discharges in liquids have attracted the attention of researchers and are one of the priorities in the study of the physics of gas-discharge and low-temperature plasma [1−7]. This is explained, first of all, by promising applications of such discharges in solving environmental problems. In addition, such discharges can be used to produce various gas and solid products.

At present, different types of discharges are used to create plasma in liquids, but microwave discharges are the least investigated object. Publications on this item appeared in early 2000-th and counts in several tens papers in contrast to thousands of publications on other types of discharges. The current state of researches in this field is presented in recent review articles [8, 9]. Here we use the limited list of references and recommend readers to see these reviews containing large list of references. The present article can be considered as introduction to these reviews.

Why it is interesting to use microwaves for plasma generation in liquids?

1. Numerous microwave apparatus can de designed for plasma generation in liquids for a particular application.
2. Plasma can be created in any dielectric liquid.
3. As plasma ignited in gas bubbles but not due to breakdown of liquids, a well developed theory of microwave discharges in gases can be applied for description of microwave discharge in liquids.
4. Microwave discharges provide more soft conditions for plasma processing and do not require the extremely high electric field for breakdown. Excitation temperature in microwave plasma in liquid is less than that in RF plasma. Electron densities are close the same.
5. Microwaves require less energy to generate plasma in comparison with high voltage pulses and give possibility to produce more dense plasma with increased concentration of active particles (results of modeling).
6. Results on removal of methylene blue from water was compared with results in arc and RF plasma at the same power consumption showed that in microwave plasma the process is faster for a several times.
7. Concerning the plasma chemical processing, microwave discharges in liquids can unite attractive features of plasma processing and effectively developed now “microwave chemistry”
8. Lack of knowledge on microwave discharges in liquids (only several dozens of publications in

comparison hundreds publications for other types of discharges in liquids) cannot provide a comprehensive answer this question.

2. METHODS OF MICROWAVE PLASMA GENERATION IN LIQUIDS

First of all it should be noted that, although often talk about microwave discharges in liquids, in fact microwave plasma is created in a gas bubble (a few millimeters in diameter) inside the liquid. The bubbles can be created in different ways: (a) by evaporation of the liquid in the vicinity of the antenna heated by the microwave field, (b) by the transmission of additional gases (argon is most often used), (c) by action of ultrasonic waves The surface of the bubbles is located near the high-temperature plasma zone, which ensures a high rate input of evaporated molecules of fluids in the bubble This bubble can be considered as mini plasma chemical reactor. As a result of the intense flow of molecules into the bubble, high concentrations of active particles (atoms, radicals, charged particles) are created in the plasma. Therefore, the efficiency of physical and chemical processes in this reactor is high. Accordingly, the rate of formation of products is also high.

It should be also noted the initiation of physicochemical processes in the liquid by plasma active particles entering the liquid. This leads, for example, to the purification of water from pollutions.

Microwave plasma is an extremely interesting object for investigation, since it is often non-equilibrium, heterogeneous, with large spatial gradients of parameters. Plasma as a rule is unsteady and existing under conditions of permanent exchange by energy and particles with the surrounding liquid medium.

Various microwave-to-plasma applicators are used for generation of microwave discharges in different liquid dielectrics. Their task is to create the microwave field, having the strength sufficient to create a discharge, in the gas bubble. There are 4 main types of discharge devices [6]. This is the use of quarter-wavelength metal antennas (Fig. 1a), at the end of which a discharge is ignited in the gas bubble. This is the use of slot antennas (Fig. 1b) and creation of gas bubbles near their surfaces by the introduction of additional gas (multibubble system). Another method is the coaxial input of microwave energy into the liquid, in which the discharge is ignited at the end of the central conductor of the line (Fig. 1c). A more complex method is also used, in which both the microwave and ultrasonic radiation act simultaneously on the liquid.

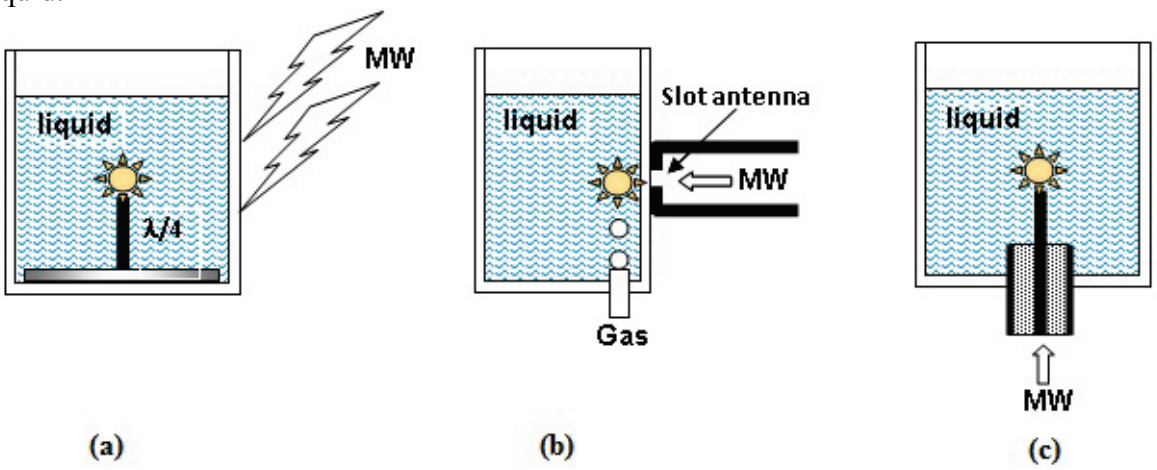

Figure 1. Schematics of different types of microwave discharges in liquids: (a) discharge on the base of quarter-wavelength antenna, (b) discharge on the base of the slot antenna, (c) discharge with energy input through the coaxial line.

In the case of creating plasma with the help of metal antennas, their erosion occurs. To reduce this process, various methods are proposed, in particular, the use of refractory metals, or coating of antennas with a heat-resistant dielectrics.

Discharges in liquids are generated both at reduced pressures (determined by the pressure over the surface of the liquid) and at atmospheric pressure. Water, water with admixtures and different liquid organics were processed in microwave discharges in liquids. Generally, microwave generators with a frequency of 2.45 GHz are used to create the plasma.

Note that if one do not take special measures, microwave discharges in carbon-containing liquids are nonstationary. This is due to the formation of solid carbon-containing particles, which are distributed in the volume of the liquid due to convective flows. This leads to the absorption of microwave radiation and to discharge failure. To eliminate this phenomenon, it is necessary to organize the circulation of the liquid with its purification from solid particles. This must be done when creating technological processes

Electrical discharges in liquids are extremely difficult for study. Using of contact diagnostic methods is difficult because the plasma is in a microwave field and the insertion of foreign objects in plasma distorts both the structure of the field and plasma. In addition, the microwave field can lead to the damage of diagnostic devices. Therefore, the only method for studying the plasma parameters is the optical methods. The most of papers cited in this review contain results of emission spectroscopy (mainly these results are related with measurements of excitation temperatures of plasma particles and gas temperatures).

Additional possibilities in study of discharge parameters are provided by modeling, which is rather complicated, since the discharge is non-stationary and constantly exchanges in energy and matter with the liquid wall. Most modeling papers are related with calculations of microwave fields in the discharge system. The results of zero-, one- and two-dimensional modeling of processes in plasma are referred, in [8, 9].

Known information on the properties of microwave plasma in liquids can be summarized as follows:

- The conditions for ignition of the discharge (incident microwave power and pressure above the surface of the liquid) depend on the liquid. In liquids with a large loss tangent, ignition of the discharge is hampered by the absorption of microwave energy, which leads to its heating and boiling. It should be noted that it is not the microwave power important for the ignition of a discharge, but the microwave field strength that is achievable in this experimental device. Thus the ignition conditions depend on the design of the device.
- The pressure above the surface of the liquid lies in the range between 0.1 kPa and atmospheric pressure (for example, a discharge in water is usually maintained at a pressure of the order of vapor saturation pressure).
- The incident microwave power lies in the range from tens of watts to several kilowatts
- Plasma is often in nonequilibrium state (the gas, rotational, vibrational, and electron temperatures are different)
- Plasma is nonstationary.
- The gas temperature lies between 300 K and 5000 K, depending in the conditions.
- The electron density exceeds the critical density n_{ec} ($n_{ec}[см^{-3}] \approx 1{,}24\times10^{10} f^2[\text{GHz}]$, where f is the field frequency in GHz).

3. AREAS OF APPLICATIONS OF MICROWAVE PLASMA IN LIQUIDS

This paragraph only lists possible areas applications microwave discharges in liquids. Detailed description of areas of applications and references are given in [8, 9].

3.1. Decomposition of substances in liquids by microwave discharge. The main goal of publications in this field is the purification of water from hazardous impurities in microwave discharges in water under the action of active particles formed in a microwave discharge in a gas bubbles. All of them showed the effectiveness of the proposed method of water purification. Special are related with application of such plasma in miro- and nanoelectronics (ething, photoresist removal, etc).

3.2. Gas phase products of microwave discharges in liquids. One of the important tasks that can be solved with the help of microwave discharges in organic liquids is the production of hydrogen. Since the efficiency of such discharges is high, they can compete with traditional gas-phase processes. Hydrogen production was tested from *n*-dodecane ($C_{12}H_{26}$), benzene (C_6H_6), commercially available cooking oil, engine oil, and waste cooking oil, waste engine, aqueous solutions of methanol (CH_3OH) and ethanol (C_2H_5OH), methane hydrate. Methane, acetylene and ethylene also produced in microwave discharges in carbonaceous liquids.

3.3. Solid products of microwave discharges in liquids. Publications in this topic are related with production of micro and nanoparticles, chemical vapor deposition in plasma (diamond and diamond-like films), and with surface treatment in various technologies, mainly in micro- and nanoelectronics.

New field in application of microwave discharges in liquids was demonstrated in [10, 11]. The method was proposed for extraction of valuable metals (Al, Co, Cu, Fe, Mo, Ni, V, Zn) contained in heavy petroleum and in the products of it processing by use of microwave discharge in the volume of these liquid heavy hydrocarbons. It was shown that the content of valuable metals in the carbonaceous material deposited on the antenna is much larger than in the initial hydrocarbons and the degrees of enrichment for different metals are in the range of 10−20 times.

3.4. Synthesis of new compounds in liquid hydrocarbons. Active particles formed in a microwave discharge in a gas bubble can penetrate into the surrounding liquid and can initiate chemical transformations in it. Publications in which these phenomena are investigated are few. For example these products change the color of liquid hydrocarbons after processing, but concentration of these products are very small.

4. CONCLUSIONS

Microwave discharges in liquids are extremely interesting object for fundamental study as they unite phenomena of electrodynamics, plasma physics, plasma chemistry in non-equilibrium/quasi-equilibrium and non-homogeneous (in general) conditions.

The field of plasma physics considered in this review is relatively new, and publications on this subject are mainly devoted to methods of microwave plasma generation in different liquids, phenomenological description of such plasma, and its applications.

These new plasma objects produce a vast field of activity, because information on the parameters of plasma in liquids (unlike to plasma of other types of gas discharges in liquids) are almost absent.

Further development of this promising field of plasma physics and application requires solution of diagnostic problems and simulation of microwave plasma in liquids.

Acknowledgements. This study was supported in part by RFBR grant # 18-08-00146.

References

1. Gaisin F.M., Son E.E., Electrophysical processes in discharges with solid and liquid electrodes. Sverdlovsk, Publ. Company of Ural University, 1989 (in Russian).
2. Samukawa S. et al., J. Phys. D: Appl. Phys. 2012, **45,** 253001.
3. Bruggeman P., Leys C. J. Phys. D: Appl. Phys., 2009, **42**, 053001.
4. Yang Y., Cho Y. I., Fridman A., Plasma discharge in liquid: Water Treatment and Application CRC Press, 2012 ISBN 9781439866238.
5. Bruggeman P. J., et al., Plasma Sources Sci. & Technol., 2016, **25**, 053002.
6. Foster J., Plasma-Based Water Purification: Challenges and Prospects for the Future. Phys. Plasmas, 2017, **24,** 055501.
7. S. Horikoshi, N. Serpone. RSC Adv., 2017, 7, 47196.
8. Lebedev Yu.A., Plasma Phys. Reports, 2017, **43**, 676.
9. Lebedev Yu.A. High Temperature, 2018, **56**, 811.
10. Averin K.A., Lebedev Yu.A. High Energy Chem. 2018, **52**, 263.
11. Lebedev Yu.A., Averin K.A. J. Phys. D: Appl. Phys. 2018, **51**, 214005.

MICROWAVE-DISCHARGE PLASMA LIGHT SOURCES AND APPLICATONS

Jin Joong Kim,[1] Kyoung Shin Kim, Dong Ho Won, Hyun Sung Yoon, and Jin Soo Baek

Maltani Corporation R&D Center for Lighting Technology, Hansin IT Tower (Rom 411), 272 Digital-ro Guro-gu, Seoul 08389, Republic of Korea

Abstract. We review the status of the microwave discharge plasma lights in the kW range that are in practical use. We show examples of the applications, including grow lighting, entertainment lighting, sports lighting, etc. The unique features of plasma lights are explained. The prospects of further advancing the technology are discussed.

1. INTRODUCTION

Since the times of Nikola Tesla [1] and John Townsend [2] in the late 1890's, electrodeless light sources using RF/microwaves have been the subject of much investigations to develop long lasting lamps with *no electrodes*. The main line efforts in the early periods were in the development of low power RF/microwave discharge light sources in the range of a few tens of watts mainly by industrial investigators [3−13]. The advent of "microwave discharge electrodeless sulfur lamps" in the early 1990's was a landmark of developing high power electrodeless light sources in the kW range [10, 12]. Since then, there have been limited but steady efforts mainly in the industrial laboratories for the commercialization of RF/microwave discharge plasma lights in the hundred watt range [14] and in the kW range [15, 18, 19]. Owing to the freedom from electrode corrosions in *electroded* discharge lamps, the advantage of electrodeless lamps is attractive and many di-atomic molecular radiators were studied, including S_2, Se_2, Te_2, GeS, GeSe, etc. [13].

The majority of the R&D efforts in the industry were reported in the patent literature and little has been published in the scientific and technical literature. There were some efforts conducted in other places including Russian research organizations but no serious commercial products were introduced. In the early part of the 2000's, there were some intense research activities in the academia to study the physical mechanisms of the sulfur lamps for a brief period [20−23]. To our knowledge, there is no serious research activity in progress in the academia at the present time.

Although the light emitting diodes (LEDs) have become the main line lamps in the low power general lighting industry in recent years, the microwave discharge high power plasma lights in the kW range cover a parameter regime that is not easily accessable by LEDs for several technical and practical reasons. In the agricultural grow light industry, high pressure sodium (HPS) lamps based on *electroded* discharges have been dominating, but it has its own shortcomings, including the deficiency of blue light that is important for chlorophyll photosynthesis in plants, the short lifetimes of the bulbs, and the containment of environmentally hazardous materials like mercury. LEDs are also used in the horticultural applications but their limited spectral contents have resulted in questionable results in crops, despite their high efficiency.

In this paper, we will first briefly review the technology of generating white light using microwave discharges of diatomic molecular vapors, and will describe what we have developed using non-rotating bulbs in the kW range that show attributes that are best suited for grow and entertainment lighting. The basic techniques were reported in previous publications elsewhere [16, 17]. The specifications of the lights include the high color rendering index of up to 99 Ra, near perfect natural light close to the sun light, a wide range of correlated color temperatures (CCTs) possible in the range of 4500 K to 7000 K, the lack of environmentally hazardous materials like mercury, semi-permanent bulb lifetimes beyond 50000 hours owing to the lack of electrodes in the bulb, and small size bulbs that make it convenient to design

reflectors for appropriate light distributions, the use of *non-rotating* bulbs in circularly polarized microwaves, to name just a few. Partial enhancement in a particular part of the color will be shown, which is particularly useful for agricultural lighting. We will focus on the *applications* of the microwave discharge plasma lights for agri- and horti-culture, entertainment and fast photography, and large scale speedy sports. We will conclude with a brief discussion of the prospects, including recent progress made in using solid state power amplifiers (SSPAs) to generate plasma light, which may replace the magnetron to generate RF/microwaves in the kW range in the near future.

2. TECHNICAL

Figure 1 shows a schematic diagram of the microwave-discharge plasma light system that we have developed. Basically, a magnetron working at 2.45 GHz is inserted into the launcher of a WR340 waveguide in which a TE_{10} mode is excited. At the other end of the waveguide, a specially designed *circular polarizer* converts the microwaves into circularly polarized waves in a circular resonant cavity that excites a TE_{11} mode rotating in the cavity [16, 17, 23]. In other words, the electric fields are rotating in the TE_{11} mode.

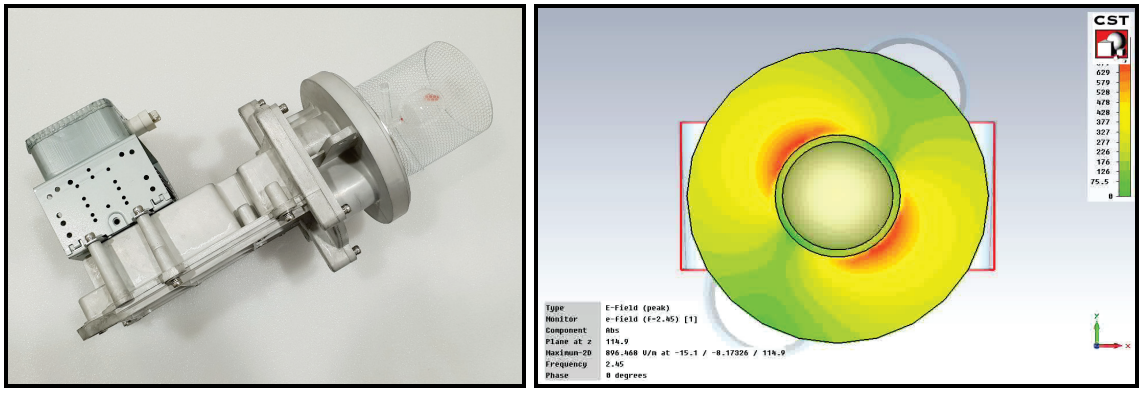

Figure 1. The E-fields are circularly polarized by a specially designed circular polarizer in TE_{11} mode (L) and the field itself rotates within the cavity (R). The bulb is stationary. No motor is necessary to rotate the bulb.

A *stationary* bulb, about 30 mm in diameter, for example, which is filled with a buffer gas of a few Torr and a radiator material in powder form, is placed within the cavity and the buffer gas is discharged by the rotating microwaves. After a few seconds, the radiator material is completely evaporated by the buffer gas plasma and the radiator vapor starts emitting white light in a plasma state. It is estimated the vapor pressure of the radiator vapor in the bulb is of the order an atmosphere. The output spectrum is a convolution of hundreds of transition lines of the diatomic molecules of the radiator material and appears as a continuum in the whole range of the visible. The spectra vary but in general their color rendering indices (CRIs) are high in the range of 80 Ra to 98 Ra, depending on the radiating materials.

Conventional methods require *rotating* the bulb since the TE_{11} mode sets up electric fields linearly polarized within the cavity and hot spots are formed on the bulb, causing punctures in a few seconds. In order to circumvent the problem, the bulb is *rotated* by an external motor at a high rotating rate, a feature that is not desirable for practical lamps. Fig. 2 shows a schematic diagram of a conventional system with a simulation of the TE_{11} fields in the resonant cavity.

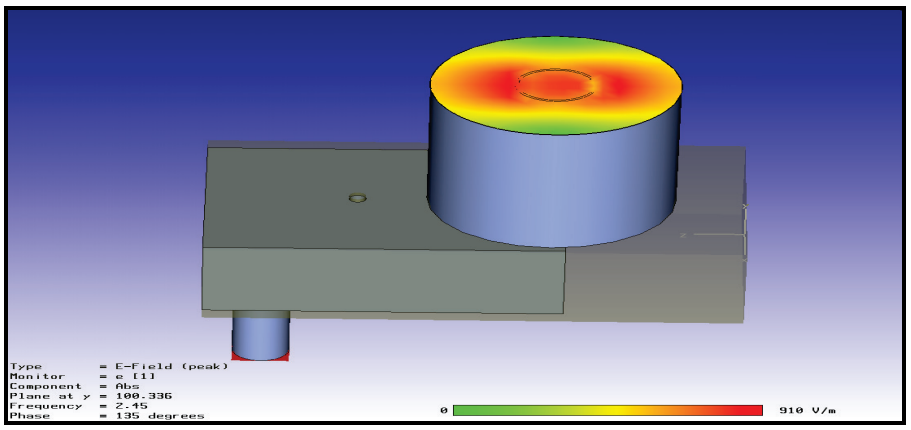

Figure 2. Conventional microwave discharge plasma lights use a rotating bulb in TE_{11} mode of electric fields within the cavity. The bulb has to be *rotated* using an external motor to avoid punctures in the bulb owing to hot spots formed by the linearly polarized electric fields.

3. RESULTS

Figure 3 shows an example of the spectrum that shows color contents particularly suitable for grow lighting. It is enhanced in the red color for high yields of crops in the flowering stage. Fig. 4 shows the extended spectrum covering the visible (blue and red for chlorophyll absorptions) and the abundant green light also helps photosynthesis for carotenoid. Infrared radiation is important for general photomorphogenesis of plants and for helping replenish nutrition to the plants by proper evaporation of moist from the leaves.

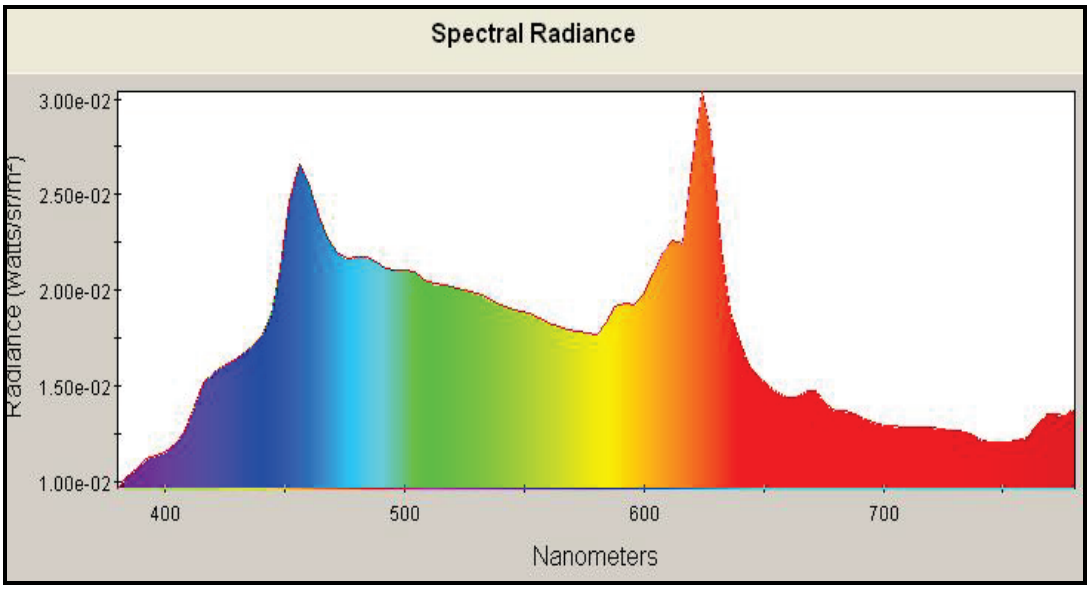

Figure 3. Spectrum of SolaRay plasma light enhanced in the red in the PAR region. This is ideal light for plant photomorphogenesis. The enhanced peaks at the blue and the red are the most effective photosynthesis for chlorophyll A and B. The green light helps photosynthesis for carotenoid inside the leaves.

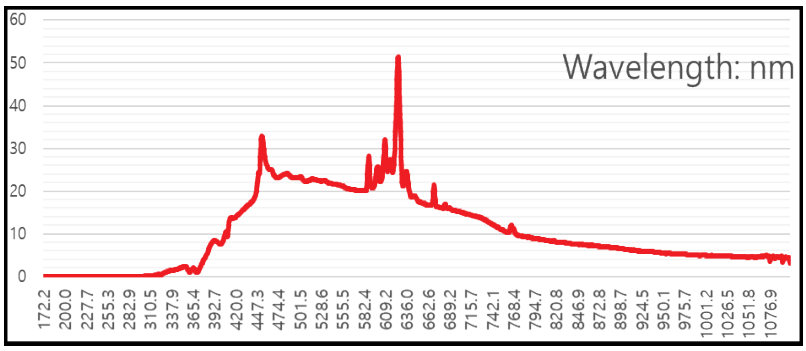

Figure 4. SolaRay plasma light emits radiation in a wide range, including UV, visible, and IR that are all essential for morphogenesis. The spectrum is enhanced in the red color in grow lights for better photosynthesis during the flowering stages.

Some examples of grow lighting are shown for roses and cannabis grown under plasma lights in Figs. 5 and 6, respectively.

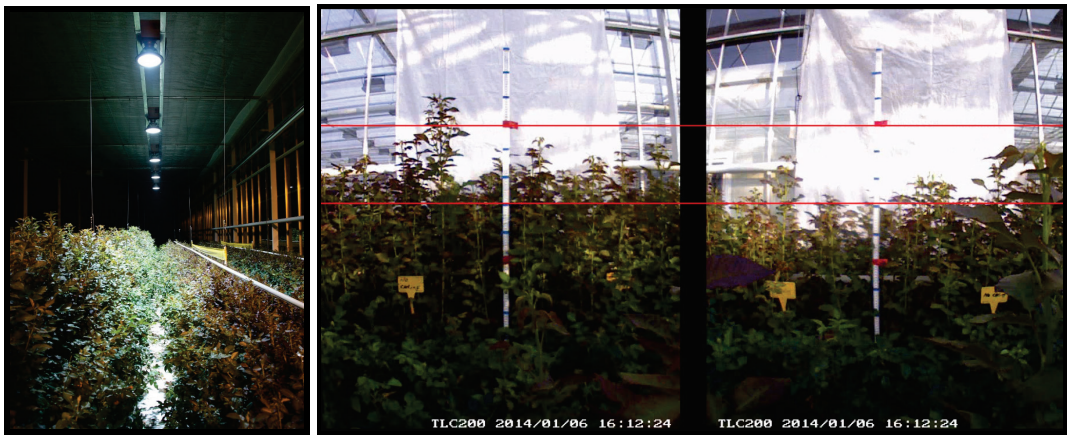

Figure 5. Roses grow about 20% faster and yield more rose buds under SolaRay plasma lights (L) than under other supplemental lights (R). Studies were made over a period of two years in a rose farm in Jonju, S. Korea.

Figure 6 shows cannabis grown under SolaRay plasma lights. It was demonstrated that the plants grow faster than under other lights by more than 20% with stronger stems and petioles grown. The enhanced red color helps increase the yields in the flowering stage.

Figure 6. Cannabis under SolaRay plasma light grow with strong and healthy stalks and bushy leaves in the vegetative stage and produce high yields of crops in the flowering stage. (Private correspondence with a grower in the U.S.).

Photosynthetic photon flux density of several hundred micromoles/sec-m^2 can readily achieved by appropriate reflectors. In particular, for large scale greenhouse applications, it is very benefitial to have

high power light sources for “large scale plant manufacturing” in the regions where sun light is deficient, or in greenhouses that are completely shielded from external light and entirely rely on artificial lights.

Growing plants under artificial lights have many advantages, including the ability to maintain a constant illumination intensity over the growth period with a controlled level of photosynthetically active radiation (PAR) and the control of the day length a year around for an optimal growth for plants of various kinds.

Figure 7 shows a typical spectrum of SolaRay plasma light that is used for entertainment and fast photography lighting. It shows a color rendering index of 98 Ra, near perfect natural light. The high CRI at a high power level is best suited for movie and video lighting and for fast photography in automobile or other vehicle crash experiments, for example.

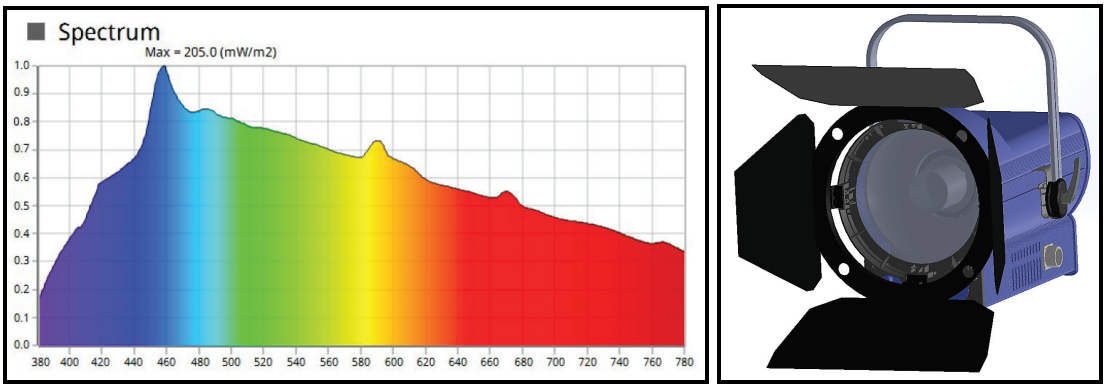

Figure 7. Spectrum used for entertainment and fast photography lighting that requires high CRI with no flickering. SolaRay produces white light of CRI of 98 Ra. The CCT may be chosen in the range of 5000K and 6500K for high quality photographies. (Units of wavelengh in nm).

Figure 8 shows a solar simulator that uses 16 sets of SolaRay lights with the total power of 16 kW. It is used to inspect the quality of large solar cell modules that are used for solar power generation.

Figure 8. A solar simulator using 16 units of SolaRay plasma lights with the total power of 16 kW. It is used to inspect a large solar panel for its performance quality. SolaRay is the best light source for such an application owing to its near perfect spectrum close to the sun light. SolaRay lights were classfied as a Class AAA light source for solar simulations. [Courtesy Woowon Tech in Seoul].

Figure 9 shows two examples of sports lighting. On the left is shown a golf driving range illuminated b SolaRay plasma lights, and on the right is shown a climbing wall lighted by a plasma light.

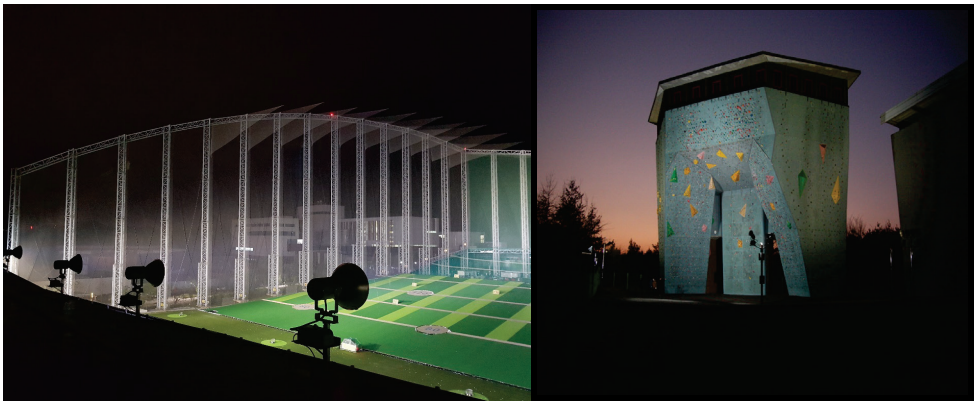

Figure 9. Plasma lights are used for sports lighting. A golf driving range is well illuminated by plasma lights. The flying ball can be clearly visible at a distance of over 200 m away (L). A rock climbing wall is illumiated at night (R).

4. SUMMARY AND PROSPECTS

Electrodeless microwave-discharge plasma lights have come a long way for real world applications in many areas after periods of great expectations and setbacks and despite the challenges and competitions from other light source technologies. In the high power regime, microwave discharge plasma lights have a number of features and specifications that cannot be easily matched by LEDs or other conventional light sources. Stable and high quality white light can be generated by use of a variety of radiator materials with long lifetimes of the bulbs and with no environmentally hazardous materials. Its applications include lighting for agri- and horti-culture, entertainment and fast photography, fast sports, solar simulation for solar cell inspections, and many other applications that require high-quality light.

The prospects are very good for RF/microwave-discharge plasma lights. The emerging technology in the high power solid state power amplifiers (SSPAs) in the kW range is opening up the possibility of developing a new class of microwave discharge plasma lights. It is expected SSPAs will replace the legacy magnetrons and will enable the development of the next generation plasma lights. Industrial innovations in high power RF/microwave plasma light technology using SSPAs like GaN and LDMOS in the kW range will be dependent on the availability of *efficient* and *cost-effective* SSPAs.

Further work is necessary in both the academia and the industry to advance this important and useful technology for a wide range of applications.

References

1. Nikola Tesla and David H. Childress, The Fantastic Inventions of Nikola Tesla, (Adventures Unlimited Press, IL, USA, 1993).
2. John S.E. Townsend, Phil. Mag. 1928, **5**, 178 and Phil. Mag. 1929, **5**, 600.
3. Spero D.M., B.J. Eastlund, R.S. Braden, C.H. Wood, Apparatus and method of generating radiation, US Patent 3,872,349 (1975).
4. Haugsjaa P.O., McNeill W.H., Rean R.J., Lech J.M., Electrodeless light source with a termination fixture having an improvd center conductor for arc shaping capability, U.S. Patent 3,942,068 (1976).
5. Haugsjaa P.O., Regan R.J., McNeill W.H., U.S. Patent 3,993,927 (1976).
6. Haugsjaa P.O., McNeill W.H., Regan R.J., Lech J.M., US Patent 3,943,402 (1976).
7. Ury M.G., Eastlund B.J., Braden R.S., Wood C.H., Microwave generated radiation apparatus, US Patent 4,042,850 (1977).
8. Offermanns S., J. Appl. Phys., 1990, **67**, 115.
9. Niemann U., Offermanns S., Weber B., High pressure gas discharge lamps, European Patent 0420335 A2 (1991).

10. Dolan J.T., Ury M.G., Wood C.H., A novel high efficacy microwave powered light source, Proc. 6th Int. Symp. on the Science and Technology, pp. 301-312 (1992), Ed. L. Bartha and F.J. Kedves (1992), Technical University of Budapest, Hungary; US Pat 5,404,076 (1995).
11. Waymouth J.F., Application of Microwave Discharges to High Power Light Sources, in *Microwave Discharges: Fundamentals and Applications*, edited by C. M. Ferreira and M. Moisan (Plenum, New York, 1993); and references therein.
12. Turner B.P., Ury M.G., Leng Y., Love W.G., J. Illum. Eng. Soc. 1995, **26**, 10.
13. Hilbig R., Koerber A., Baier J., Scholl R., Molecular Discharges as Light Sources, Proc. The 10th Int. Symposium on the Science and Technology of Light Sources, Toulouse, France, 18-22 July 2004, 75.
14. Luxim, Topanga, and Ceravision websites.
15. Websites of LG Electronics, Maltani Lighting (formerly Taewon Lighting), Plasma International, and Solaronix.
16. Kim J.J., Kim K.S., Kyoung S. Oh, Dong H. Won, Hyun Sung Yoon, The 11th Int. Symp. on the Science and Technology of Light Sources, Shanghai, China, May 20-24, 2007, 301.
17. Kim J.J., *et al*., US Patent 6,873,119 B2.
18. Babykumar V., Neate A., Odell E., Preston B, Sadiq A., Devonshire R., The 11th Int. Symp. on the Science and Technology of Light Sources, Shanghai, China, 20-24 May 2007, p. 109.
19. Meyer A., Courret G., Croci M., European Patent EP 1 876 633 A1 (2007).
20. Johnston C.W., Transport and Equilibrium in Molecular Plasmas: the Sulfur Lamp, PhD Thesis, Eindhoven University of Technology, the Netherlands, ISBN 90-386-1635-X (2001).
21. Johnston C.W., van der Heijden H.W.P., Janssen G.M., van Dijk J., van der Mullen J.J.A.M., J. Phys. D: Appl. Phys. 2002, **35**, 342.
22. Johnston C.W., van der Mullen J.J.A.M., J. Phys. D: Appl. Phys. 2004, **37**, 573.
23. Kim J.J., Ko J.T., Won D.H., Kim S.S., Chang H.-Y., Appl. Phys. Lett. 2004, **84**, 2769.

SUBTHRESHOLD DISCHARGE IN MICROWAVE BEAM AS A SYSTEM OF MICROEXPLOSIONS. PLASMACHEMICAL PROPERTIES

I. A. Kossyi, K. V.Artem'ev, G. M.Batanov, N. K.Berezhetskaya, K. A.Sarksyan, N.K.Kharchev

Prokhorov General Physics Institute of the Russian Academy of Sciences, Vavilov Str., 38, Moscow, 119991, Russia

Abstract. Physical and plasmachemical applications of a peculiar form of gas discharge excited by means of microwave beams under high –pressure gas (atmospheric pressure or more than it and subthreshold microwave beam power conditions are under discussion. Discharge form being studied has some features discriminating it from all known discharges including described in literature microwave ones. Physical model of investigated discharge (with given such a name as self-nonself sustained (SNSS) discharge) has been elaborated in the GPI. Model which accounts for the fact that discharge is excited at a such high pressure that electron-neutral collisions frequency is much higher than the cyclic microwave frequency and power of microwave beam is much less than threshold for self-sustained discharge excitation. Results of experiments on the action of SNSS discharge on the gas environment of modern megalopolis (Moscow) are presented. They are pointed to some kind peculiarities which make this discharge application very attractive for ecological problems solution. Schematic variants of cleaning of town environment are presented.

1. INTRODUCTION

Studies on the fundamental physics problems of microwave-driven discharges in a gas, which were carried out at General Physics Institute of RAS (GPI), have provided the basis for the development of a series of original plasma sources intended for use in physical laboratories and for solving current technological problems of interest. The most promising discharge for future technology is a plasmatron based on the subthreshold generation of a discharge initiated by a pulse microwave beam. This new type of microwave discharge, which is named a SNSS discharge, is realized when the following conditions are initially fulfilled:

(a) The microwave beam propagates in a gas where the pressure is so high that a strong inequality holds:

$$\nu_{eff} >> \omega \qquad (1)$$

(Here, ν_{eff} is the effective electron-neutral collision frequency, and ω is the microwave cyclic frequency);

(b) The reduced microwave electric field is so low that it is initially much less than the beam volume that is required for excitation of a self-sustained discharge:

$$\gamma \equiv E_0/n_m << [E_0/n_m]_{thr} \qquad (2)$$

(Here, E_0 is the microwave electric field amplitude, n_m is the neutrals density, and $[E_0/n_m]_{thr}$ is the reduced microwave electric field required for excitation of a self-sustained discharge);

(c) Finally, the local pulsed initiator of the discharge in a certain volume, Σ_d, is much smaller than the volume occupied by the microwave beam, Σ_{MW}, such that

$$\Sigma_d << \Sigma_{MW} \qquad (3)$$

This initiator acts during time τ_i, which is shorter (much less) than the duration of the microwave pulse, τ_{MW}:

$$\tau_i << \tau_{MW} \qquad (4)$$

In all of the initiation methods used in experiments conducted at the GPI, it has been shown that the local excitation of the self-sustained discharge in a volume that is much less than the volume occupied by the microwave beam is accompanied by an ionization wave. This wave propagates toward the microwave generator and builds an axial plasma column. In this case, the greater the beam pulse duration, the greater the plasma column length. Thus, unexpectedly, a new phenomenon was demonstrated, i.e., the formation of an extended gas discharge plasma column in microwave fields that are less (and even substantially less) than the threshold fields required for exciting a self-sustained discharge in a gas in free space. Characteristic photograph of SNSS discharge, which was initiated with the help of metal–dielectric target, is presented in Fig. 1.

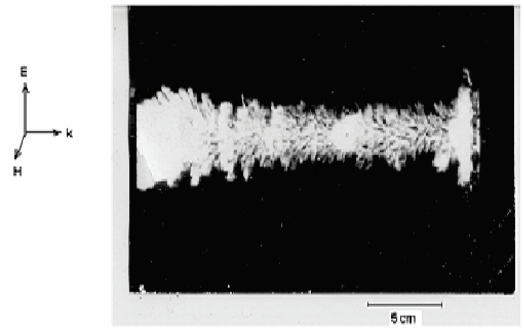

Figure 1. Typical photograph of SNSS discharge.

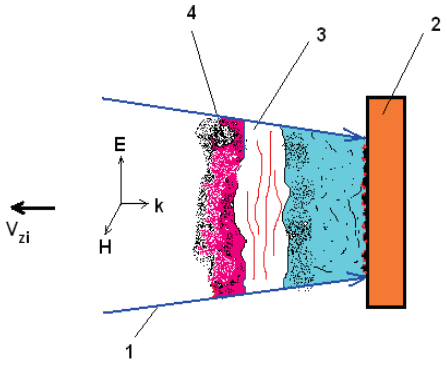

Figure 2. Scheme explaining the SNSS discharge formation. 1 – microwave beam; 2 – metal-dielectric initiator of local discharge; non-self sustained discharge.

2. PHYSICAL PROCESSES UNDERLYING THE GENERATION OF SNSS DISCHARGE

It is generally accepted that the gas discharges known and described in the literature are in one of two categories: self-sustained and non-self-sustained discharges [1, 2]. However, research carried out at the GPI [3−5] allows us to amend this idea and to describe a third discharge category. This involves plasma formation via the SNSS discharge, which represents an unusual transition sequence from self-sustained to a non-self-sustained stage through a strongly nonlinear phase of ionization-overheating instability.

The physical analysis carried out in Refs. [3−5] explains the mechanisms of formation of an ionization wave in an initially extremely subthreshold microwave beam in high-pressure gases. The model presented in Refs. [3−5] proceeds via the assumption that ultraviolet radiation has a decisive role in both the initiation stage and in later stages, and specifically, in its front. The model is shown in Fig. 2 of the schematic boundaries of the microwave beam and ionization wave at a particular time. Also shown are the discharge channels (filaments) that arise near the initiator and in the formed propagating axial ionization wave, specifically at its front due to the transformation of the non-self-sustained discharge into the self-sustained discharge via the strong nonlinear stage of ionization-overheating instability. Discharge channels in the front of the ionization wave play a part in the UV radiation source ahead of the ionization wave front at a distance of $l \le l_f$ (l_f is the average free path of the ionization radiation). The microwave beam interacts with this plasma, becomes partially absorbed, and heats the gaseous medium through the electron component.

As described in Ref. [3], the velocity of the SNSS discharge propagation toward the microwave beam in air at a high pressure ($\nu_{eff} >> \omega, \nu_{eff}^*$) can be estimated using the following relation:

$$V_{яi} \approx 10\, n_e\, E_0^3 / p_0^4 \approx 3.2\, 10^5\, n_e\, I_f^{3/2} / p_0^4 \qquad (5)$$

Here, ν_{eff}^* is the electron-neutral collision rate that corresponds to the gas molecular density n_m^* such that $\gamma = \gamma_{thr}$, where n_e is the electron density of photo-ionized plasma ahead of the SNSS discharge front, p_0 is the initial pressure of the gas in Torr, E_0 is expressed in kV/cm, and I_f is the microwave intensity in W/cm^2.

The nonlinear stage of the ionization-overheating instability growth in the non-self-sustained microwave discharge was theoretically studied [6]. In that paper, the plasma parameters in the arising filaments were estimated. The final electron temperature in the filaments can be calculated by the formula

$$T_e \approx (\nu_{eff}^0/\omega)^2 \, T_{e0} \tag{6}$$

and the electron density has the form

$$n_e \approx (\nu_{eff}^0/\omega)^{\beta i+1} \, \nu_a/\nu_T \;\; n_{e0} \tag{7}$$

Here, $\beta_i \approx 5 - 6$; ν_{eff}^0 is the electron-neutral effective elastic collision rate; n_{e0} and T_{e0} are the initial density and temperature of the electrons, respectively, in the uniform plasma of the non-self-sustained discharge. $\nu_a = 1/\tau_a$, where τ_a is the electron loss time (due to attachment, recombination, or diffusion).

$$\nu_T \approx 10^{-9} \, \sigma_0 \, E_0^2/p_0 \tag{8}$$

where σ_0 is the initial plasma conductivity in electrostatic units, and E_0 is in units of V/cm.

Upon substituting values for ν_{eff}^0, T_{e0}, σ_0, and ν_a that are characteristic of the experiments described in Refs. [3−5], we found that the final plasma state in the channels corresponds to almost total ionization at an electron temperature of several hundreds of electron-volts. However, the real values of the electron density and temperature can be limited by a number of unknown processes in Ref. [6], e.g., the reflection of microwaves from filaments, etc. Nevertheless, the results of the estimation and experimental results show that the discharge filaments are indeed the regions of dense and high-temperature plasma that fit the measurements conducted in Ref. [7] that provide values of $n_e \approx 10^{16}$–10^{17} cm^{-3} and reveal the presence of a photo-ionized plasma 'aureole' around the discharge channels. The gas temperature in the filaments was measured in several studies [8] and found to be on the order of $T_g^* \approx 5000$–7000 K.

3. SNSS DISCHARGE AS A NEW (UNIQUE) TYPE OF IONIZATION WAVE

There is reason to believe that SNSS-type discharges that possess regions of fast and high heating of the gas with subsequent fast cooling of the gas may be a very efficient method for processing gaseous media.

The achievement of microwave plasma generation that is unusual in its physical properties but is also promising for some technological applications, namely the SNSS discharge in large gas volumes at pressures above or on the order of atmospheric pressure, led us to construct the TORCH installation at the GPI. This installation is assembled around the MIG-3 GYROTRON complex, generating a microwave beam with the following parameters: a microwave pulse power of $P_i \leq 600$kW, a pulse duration of $\tau_{MW} \leq$ 20 ms, and a wavelength of $\lambda \approx 0.4$ cm.

In experiments carried out in the TORCH installation, SNSS discharges have been excited with diverse microwave beam cross sections generated by the MIG-3 GYROTRON complex via help by special initiators. Even at maximum powers in a microwave pulse, the reduced electric field values in the beam do not exceed 10^{-16} V cm^2. This value is more than one order lower than the threshold to generate a self-sustained discharge in free space [1]: $\gamma_{thr} \approx 10^{-15}$ V cm^2.

In the TORCH installation, we studied the SNSS discharge excitation in free space in atmospheric air and in a closed chamber filled with various gases or gas mixtures at pressures that are also close to atmospheric pressure. The schemes of microwave subthreshold discharge experiments in atmospheric air and in the closed chamber are shown in Figs. 3 and 4, respectively.

The experiments conducted on the TORCH bench shown in the schemes in Figs. 3 and 4 demonstrated the excitation of the SNSS discharge (in free space and in a closed chamber) at atmospheric pressure in single microwave pulses beginning with a peak power on the order of $P_i \approx$ 200 kW and up to 600 kW with a pulse duration of $\tau_{MW} \approx 200$ μs and up to 20 ms. The discharge was excited with the help of a special-purpose initiator and occupied an extended volume. The greater the power or the longer the microwave pulse, the larger the axial length of the discharge.

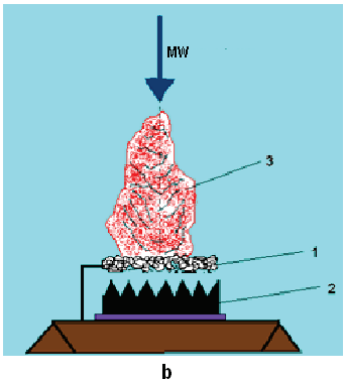

Figure 3. Experimental scheme of SNSS discharge excitation in free space in atmospheric air. 1 – initiator; 2 – microwave absorber; 3 – SNSS discharge.

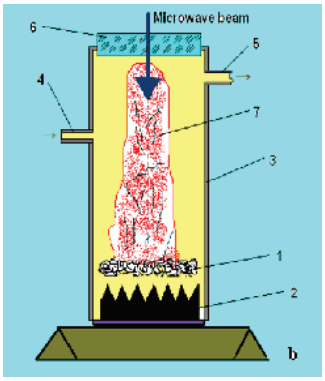

Figure 4. Experimental scheme of SNSS discharge excitation in a closed cylindrical chamber. 1 – initiator; 2 – microwave absorber; 3 – cylindrical chamber; 4 – working gas intake fitting; 5 – working gas withdrawal fitting; 6 – MW transparent window; 7 – SNSS discharge.

Based on (5), the power dependence of velocity V_{zi} on the microwave power level P_i with a power index of 3/2 predicts that $V_{zi} \sim P_i^{3/2}$. Additionally, the predicted dependence of the specific energy distribution in the discharge, ε, on the power of the microwave beam is inversely proportional to the latter with the power dependence at an exponent of ½: $\varepsilon \sim 1/P_i^{1/2}$. Unfortunately, until recently, no experimental study has been carried out that confirmed or refuted the predicted dependences (and consequently, the nature of the unusual wave).

Recently, experiments have been conducted with subthreshold beams of microwaves in search of an answer to the question regarding the main physical processes that are responsible for this new type of microwave discharge. The aim of the experiments was to obtain similar dependences for the axial velocity of the SNSS discharge and its parameters that were on the level of the electric fields (specific microwave power) in a microwave beam.

The gyrotron radiation pulse and its magnitude were recorded using a quasi-optical reverse coupler located in the quasi-optical path. Using the same coupler, the radiation pulse that reflected from the head of the discharge was recorded. In the registration channel of the reflected radiation, a reference signal was introduced that branched from the signal of the gyrotron radiation pulse. Thus, as a result of mixing and detecting the reference and reflected signals, the change in the phase of the reflected radiation was measured, and the average speed of the head of the discharge was measured. The signal from the detector was received by an amplifier with a 20 MHz band and a digitized ADC with a frequency of 10 MHz.

As a second tool for measuring the axial speed of the head of the discharge, a line of five collimated C-UVA512SD photodiodes with a sensitivity band from 240–360 nm was used. The distance between the photodiode slits was 5 cm, and they were located along the axis of the microwave beam at a radius of ~10 cm from the axis.

A summary of the dependence of the mean velocity of the discharge front on the microwave beam power as measured in several experiments is shown in Fig. 5. As shown in the figure, certain axial velocities of the front of the discharge propagation (ionization wave) fall well enough within the dependence of $V_{zi}(P_i) \sim P_i^{3/2}$ predicted by the model from Ref. [3].

The direct determination of the specific heat input, ε, in the study of microwave discharges is a task with extreme complexity when there are strong spatial inhomogeneities in magnitude, and it causes sufficiently fast temporal changes, an inability to use contact methods of measurement, etc. In the described experiment, a set of indirect measurements (based on the optical spectroscopic method for determining the maximum temperature, Tg) is achievable in the region of the discharge. As an approximation that requires further studies of special cases, there is an assumption of the proportionality of this temperature to the level of specific energy distribution: $T_g \sim \varepsilon$. The temperature in this experiment was determined by the discharge emission continuum using the method from Ref. [9]. The measurement results are shown in Fig. 6. The solid curve in the figure was calculated and corresponds to the inverse proportional dependence: $T_g \sim 1/P_i^{1/2}$. As shown in the figure, the experimentally measured values for the

maximum gas temperature are sufficiently close to the calculated curve. This allows us to assume that the specific energy release is $\varepsilon \sim 1/P_i^{1/2}$, which corresponds to the dependence predicted in Ref. [3].

Thus, the dependence of the axial velocity of the SNSS discharge propagation in the subthreshold Gaussian microwave beam on the power level, P_i, of the beam was determined. According to the results presented in Fig. 5, the experimentally determined dependence of the axial velocity of propagation of the ionization wave, which is essentially a SNSS discharge, on the power level in the Gaussian beam falls well within the predicted [3] dependence.

The inversely proportional dependence of the measured gas temperature that was achieved in the discharge on the power level for the Gaussian beam was very close to the predicted dependence (see Fig. 6).

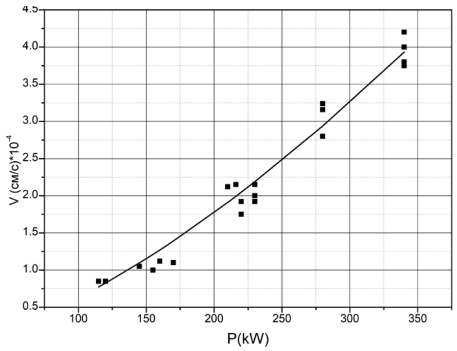

Figure 5. Dependence of the axial velocity of the SNSS discharge propagation on the microwave beam power. Solid curve was calculated for $V_{zi} \sim P_i^{3/2}$. Points were experimentally determined.

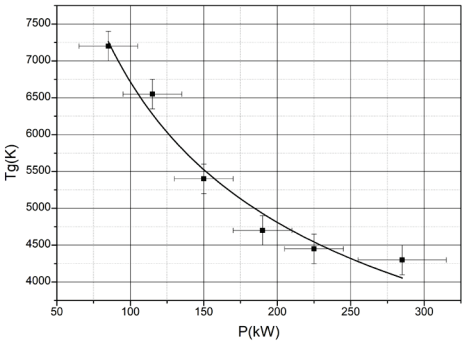

Figure 6. Gas temperature in the SNSS discharge as a function of the microwave beam power. Solid curve was calculated for $Tg \sim 1/P_i^{1/2}$. Points were experimentally determined.

The obvious similarities between the dependences of $V_{zi}(P_i)$ and $T_{g(}P_i)$ obtained in the experiment compared with those in the physical model [3] allow us to consider the mechanism of alternating excitation of the non-self-sustaining and self-sustaining discharges in a strongly subthreshold microwave beam as an adequate physical phenomenon of the observed ionizing wave. This wave that was first observed at the GPI has no analogues among those described in the literature, either in the microwave range or when working with laser beams.

Analysis of the problem of forming ionization waves in electromagnetic wave beams was performed, in particular, in monographs (see Refs. [1, 2]). Of note, the discharge tended to spread. There are always mechanisms of energy transfer from the discharge plasma to the neighboring non-ionized gas layers that contribute to their ionization and that bring them to a state that is capable of absorbing an electromagnetic wave. If these layers are in a strong enough field, they form a self-sustaining discharge that acts on the net layer. The spread of discharges in pre-trial intensity fields should be associated with any transfer mechanism for the ionizing agent. Among these agents are the thermal conductivity, the diffusion of electrons, the diffusion of resonance optical radiation, etc., which are unknown for the analogue discovered in the GPI wave based on the SNSS discharge. By incorporating a new discharge based on the excitation of a SNSS discharge, the results presented in this paper provide the foundation to expand the set of ionizing waves and breakdown waves that are typical for interacting with electromagnetic waves beams in a gas medium.

According to the schemes shown Figs. 3 and 4, a series of experiments were conducted at the GPI to study the cleaning effect of the SNSS discharge on model and real gas mixtures that are typical in ecological problematic areas in a modern metropolis. The appeal of the SNSS is due to the peculiarities of this type of microwave discharge as a means of plasma chemical action on a gas medium. According to the physical model presented in Ref. [3], this discharge develops via an ionization wave propagating towards microwave radiation as a sequence of "micro explosions" in thin channel ("filamentous") structures. The physics of the formation of the ionization wave involves alternating between a non-self-sustained discharge supported by "frontal" UV radiation and a self-sustaining discharge resulting from the development of ionization-overheating instability that reaches a highly nonlinear stage in microwave fields. The plasma-chemical effects are based on the rapid heating processes of the gaseous medium with

the formation of "thread" structures (the speed, which reaches values of $dTg/dt \geq 10^6$ kK/s) and fast-cooling areas of contraction before the temperature of the surrounding gas environment changes (with a speed of $-dTg/dt \approx 10^4$ kK/s). In accordance with these type of thermodynamic features, the SNSS discharge can be represented as a plasma chemical object with locally arising reactors – a fast gas heating reactor and a fast cooling reactor – that provides effective decomposition of molecules and effective "hardening" of decomposition products with the possibility of a very complicated reverse reactions.

In prior experiments [10], the energy price for cleaning SNSS discharge air samples from the Lefortovo auto-tunnel in Moscow and from the premises of a Paint production facility in the Moscow region was determined. The energy price to reduce the level of MPC of environmentally hazardous impurities was on the order of:

$$\eta \geq 5\ 10^{-3}\ \text{kW h / liter} \tag{9}$$

In this paper, for the first time, we investigated the impact of SNSS discharge on gas samples simulating emissions from urban landfills or taken directly from landfills that are smearing sites. One of the first experiments was to study the effectiveness of the impact of the SNSS discharge on air mixtures with mercaptan (thiol) and a mixture of air with mercaptan and methane. Mercaptan is one of the most harmful components from gas emissions in urban landfills because it a strong nerve poison with a narcotic effect. In low concentrations, it is characterized by an extremely unpleasant odor. Measurement of the composition of a mercaptan/air mixture before and after treatment with SNSS discharge showed that the specific concentration of the mercaptan before the experiment was 68 mg/m^3, which decrease to 0.62 mg/m^3 after treatment with the discharge. The specific cost of microwave energy per 1 liter of the mixture was approximately:

$$\eta \approx 7\ \text{kW h / liter} \tag{10}$$

The features of the SNSS that make its application very promising include the following:

- The possibility of excitation at atmospheric (and higher) pressure without the involvement of vacuum systems or requiring energy costs of the initiators;
- Its ionization wave propagating towards the microwave radiation and capturing significant amounts of the processed gas medium;
- The possibility of simultaneous output (purification) of the treated gas for a wide range of environmentally harmful impurities;
- The possibility of excitation of the SNSS discharge both in closed volumes and in free air space at the surface of the Earth and at relatively large distances from it.

4. CONCLUSIONS

Potential applications of the sub-threshold microwave discharge are shown in Figs. 7–9. In Fig. 7, a scheme for exciting the SNSS in a surface atmosphere using a system of chaotically intertwined thin stainless steel wires, as developed and used at the GPI as an initiator, is shown. Moving the initiator with its input into the microwave beam formed by the ground generator was performed with the help of an unmanned aerial vehicle. This option is applicable, in particular, for the purification of an urban atmosphere with localized Freon emissions (see Ref. [11]). In Fig. 8, the SNSS discharge is used for purification of industrial gas emissions directly in the pipes of the enterprise. In Fig. 9, the investigated category is considered as the basis of the system, which performed cleaning and disinfection of air directly in production facilities.

Experiments to clarify the energy price of microwave beam exposure in a polluted urban atmosphere and a technical and physical analysis of using plasma-chemical electric-discharge for the restoration of environmental safety in an urban environment are the main objectives of subsequent studies at the GPI

Due to the experiments performed at the GPI, a new type of subthreshold self/non-self-sustained (SNSS) discharge has been realized. For the first time, the excitation of this discharge at atmospheric gas

pressures (and higher) have been demonstrated in free space in ambient air and in a closed cylindrical chamber filled with different gases.

Research on SNSS discharge for plasma-chemical applications has led to a new direction: **"plasma chemistry of microexplosive plasma formations".** A wide range of urban problems that can be solved using this field of plasma chemistry are described in this paper. We describe the peculiarities that make the application of this discharge very attractive for solving ecological problems.

For the first time, the SNSS discharge was created using millimeter wavelength microwave beams at a high pulse power of ≈600 kW. Additionally, the discharge was initiated in any beam cross section using a specially made construction composed of metallic thin threads. In this case, discharge initiation and its maintenance in the form of an axially propagating ionization wave was carried out using only one microwave energy.

The discharge parameters are compatible with those predicted by the physical model, which considered the SNSS discharge as a progression of sequential transitions of non-self-sustained and self-sustained discharges through the excitation and development of ionization-overheating instability.

The gyrotron was applied, which is capable of generating a microwave radiation with an average power of several hundred kW (at the peak pulse power of ≈600 kW) in a pulse-periodical regime. Due to its relative simplicity, this microwave radiation, which is interfaced with a cylindrical reactor chamber and has a highly efficient microwave energy contribution to the subthreshold discharge in a gas medium, allows us to draw conclusions about the feasibility of plasma–chemical reactor creation based on the gyrotron and SNSS discharge. It can satisfy the modern industrial requirements of various chemical technologies, such as methane conversion in syngas, CO_2 utilization, and industrial gaseous waste cleaning.

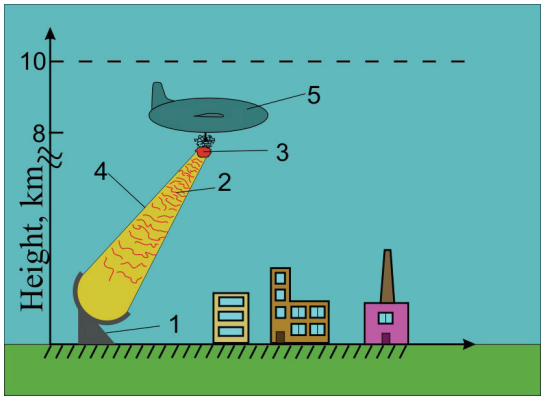

Figure 7. Schematic of atmospheric cleaning system. 1 – gyrotron and MW antenna; 2 – SNSS discharge; 3 – initiator; 4 – MW beam; 5 – pilotless vehicle.

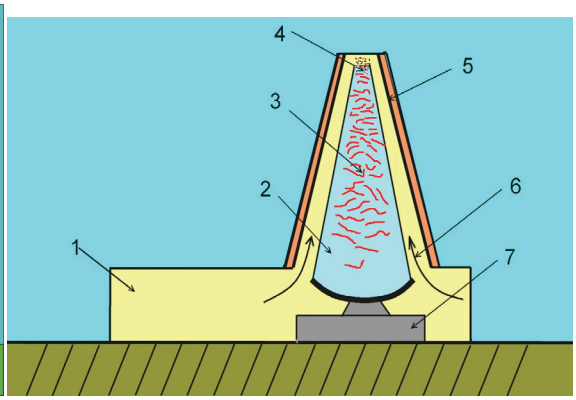

Figure 8. Industrial gs ejection cleaning. 1 – plant building; 2 – MW beam; 3 – SNSS discharge; 4 – initiator; 5 – plant chimney; 7 – gyrotron and MW antenna.

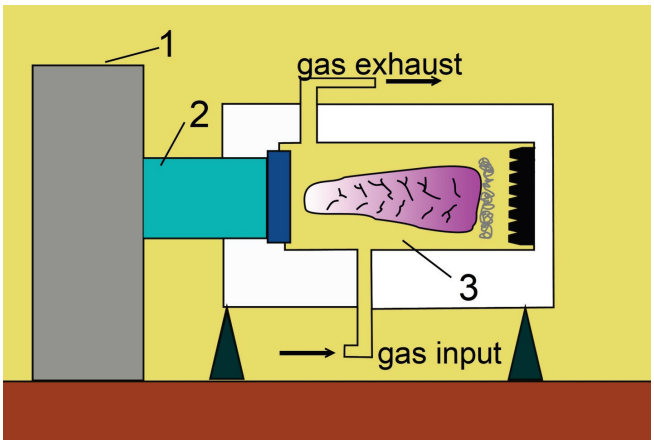

Figure 9. Cleaning of the gas environment in the workshop. 1 – gyrotron; 2 – MW beam; 3 – plasmachemical reactor.

The work is supported by the Russian Science Foundation (Project 17-12-01352) and the Program of Basic Research of the Russian Academy of Sciences, 2017, III.2.

References

1. Raizer Yu. P. Gas Discharge Physics. Springer, Berlin, 1991.
2. MacDonald A.D. Microwave Breakdown in Gases. Ed. By Palo Alt. New York–London–Sydney: John Wiley & Sons INC, 1966.
3. Batanov G.V., Gritsinin S.I., Kossyi I.A., Magunov A.N., Silakov V.P., Tarasova N.M., High-Pressure Microwave Discharge. Plasma Physics and Plasma Electronics. Ed. by L. Kovrizhnykh, Commack: Nova Science Publishers, 1985.
4. Kossyi I.A. New microwave plasma sources based on the latest advances of fundamental gas-discharge physics, Proc. of 8th Int. Workshop "Strong Microwaves and Terahertz Waves Sources and Applications, 2011, N. Novgorod – St. Petersburg, Institute of Applied Physics RAS, Russia, p. 25.
5. Kossyi I.A. Self-non-self-sustained microwave discharge as a new type of large-size plasma source, 44th AIAA Aerospace Sciences Meeting and Exhibit (Reno, Nevada), Report AIAA-1457, 2006.
6 Kim A.V., Fraiman G.M., Fizika Plazmy, 1983, **9,** 613 (in Russian).
7. Avetisov V.G., Gritsinin S.I., Kim A.V., et al., JETP Letters, 1990, **51**, 348.
8. Kossyi I.A., Batanov G.M., Berezhetskaya N.K., Davydov A.M., Sarksjan K., Harchev N.K., Physical basis and topical applications of a new type gas discharge excited by powerful pulse microwave beam in the high-pressure gases, Proc. 43rd Conference on Plasma Physics EPS-2016, Leuven, Belgium, 2016, p. 1.
9. Batanov G.M., Berezhetskaya N.K., Kop'ev V.A., Kossyi I.A., Magunov A.N., High Tempetature, 2008, **46,** N 1, 124.
10. Batanov G.M., Berezhetskaya N.K., Davydov A.M., Konchekov E.M., Katorgin I.N., Kossyi I.A., Sarksyan K.A., Stepakhin V.D., Temchin S.M., Plasma-chemical cleansing of urban atmosphere in the reactor based on the deeply subthreshold discharge excited by microwave beam, 7th Central European Symposium on Plasma Chemistry, Book of Abstracts, Sveti Martin na Muri, Croatia, 2017, p 43.
11. Askar'yan G.A., Batanov G.M., Barkhudarov A.E., Gritsinin S.I., Korchagina E.G., Kossyi I.A., Silakov V.P., Tarasova N.M., Sov. J. Plasma Phys., 1992, **18**, 625.

3. Topical papers

DISSOCIATION OF MOLECULAR HYDROGEN AND MECHANISMS OF POPULATION OF ATOMIC HYDROGEN ELECTRONIC EXCITED STATES IN MICROWAVE DISCHARGE

V. A. Shakhatov, Yu. A. Lebedev

A.V. Topchiev Institute of Petrochemical Synthesis of the Russian Academy of Sciences (TIPS RAS), Leninsky Prospect, 29, Moscow, 119991, Russia

Abstract. Interest in the study of kinetic processes in microwave discharge at low and moderate pressures in hydrogen is due to the various applications of hydrogen-containing low-temperature plasma in technologies. The internal logic of the development of plasma chemistry dictates the development of a rapid, affordable price and least time-consuming experimental − computational techniques based on combination of methods of emission spectroscopy and level-to-level collisional-radiative models of atomic-molecular plasma. This combination significantly expands the diagnostic capabilities of emission spectroscopy. The application of these methods allows: 1) for obtaining data on mechanisms of physical-chemical processes responsible for the formation of non-equilibrium distribution of populations of particles in excited radiating states; 2) for optimizing the input of reagents and catalytic additives in the discharge zone and output that of the reaction products; 3) for performing the selection of the atomic lines and molecular bands in the emission spectrum for the diagnostics of plasma parameters. Insufficient degree of completeness of the kinetic schemes of the formation and destruction of excited states of molecules and atoms of hydrogen of models of the atomic-molecular plasma reported in the literature limits their use for spectroscopic plasma diagnostics. This paper is devoted to development of the level-to-level semiempirical collisional-radiative model of molecular hydrogen plasma to investigate the processes of dissociation of molecular hydrogen and populations of electronically excited states of the hydrogen atom in microwave discharges at low and moderate pressures.

1. INTRODUCTION

An investigation of a sources of the neutral and charged atoms based on microwave discharges in hydrogen (deuterium) is given special attention. A necessary stage of the investigation is the development of spectral methods (emission spectroscopy and optical actinometry) for diagnostics the degree of the hydrogen molecule dissociation in discharge systems. An important component of the spectral methods is a collisional – radiative model of low temperature plasma for processing and interpreting the experimental data by emission spectroscopy and optical actinometry.

A critical analysis of experimental and theoretical results of the investigation of the hydrogen low-temperature plasma is presented in the review [1]. No systematic studies of the molecular hydrogen dissociation are carried out in the microwave discharges. The microscopic and macroscopic models of the non-equilibrium and thermal hydrogen molecule dissociation are numerous. When comparing the results of theory and experiment, authors note the difficulties of the theoretical reproducing of the hydrogen molecule dissociation measurements in microwave discharges.

It is generally accepted that:

1. The description of hydrogen dissociation close to the experiment is given to the microscopic models (in the approximation of the basic level kinetics).
2. Dissociation of molecular hydrogen in low temperature plasma is markedly due to electron impact through the formation of the triplet states of the hydrogen molecule.
3. The discrepancy between theory and experiment seems to be due to the difficult to control processes of interaction of atoms with the surface of reactors.

From the above survey of the hydrogen low temperature plasma models, it follows that the description of the kinetics of processes proceeding in hydrogen plasma becomes ever more detailed, but processes involving hydrogen molecules in triplet and singlet electron states have not yet received adequate study.

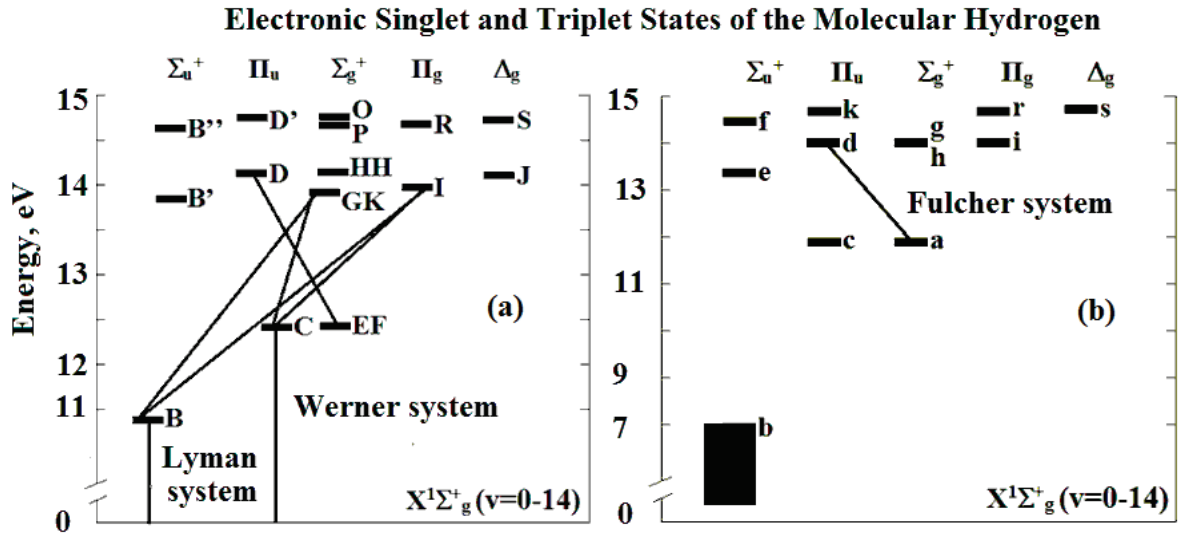

Figure 1. Diagrams of the singlet (a) and triplet (b) states levels.

The next part of this paper is devoted to the development of the level-to-level zero-dimensional semiempirical collisional-radiative model (CRM) that takes into account in detail the kinetics of singlet and triplet excited states of hydrogen molecules. Databases are created:

- collision-radiative characteristics of processes involving hydrogen molecules in triplet and singlet states;
- spectra emitted by the plasma;
- macro- and micro-parameters of microwave discharges.

This will make it possible to work out experimental-computational procedures for a spectral diagnostics of the hydrogen low-temperature plasma.

2. THEORY

In relation to models known from the literature [1−7], the zero-dimensional level-to-level semiempirical collisional-radiative model formulated in this section employs an extended kinetic scheme of processes and incorporates a greater number of excited atomic levels and molecular states of interest for emission spectroscopy and optical actinometry [8−10]. The diagrams of triplet and singlet states levels are shown in Fig. 1. The allowed electric dipole transitions $H_2\left(2C^1\Pi_u \to X^1\Sigma_g^+, v\right)$, $H_2\left(2B^1\Sigma_u^+ \to X^1\Sigma_g^+, v\right)$ and $H_2\left(3d^3\Pi_u \to 2a^3\Sigma_g^+\right)$ are used for the optical diagnostics of the degree of dissociation and vibrational excitation of hydrogen molecules. The allowed electric dipole transitions $H_2\left(3I^1\Pi_g \to 2C^1\Pi_u\right)$, $H_2\left(3I^1\Pi_g \to 2B^1\Sigma_u^+\right)$, $H_2\left(3D^1\Pi_u \to 2EF^1\Sigma_g^+\right)$, $H_2\left(2EF^1\Sigma_g^+ \to 2C^1\Pi_u\right)$ and $H_2\left(2EF^1\Sigma_g^+ \to 2B^1\Sigma_u^+\right)$ are used for measurements of the translational temperature by emission spectroscopy in ultra violet and visually wavelength range. The allowed dipole transitions between electronic states of atomic hydrogen are also interesting for practical optical actinometry and high resolution spectroscopy for determination the translational temperature and the degree of dissociation of hydrogen molecules. The study of the population mechanisms of the upper electronic states of the hydrogen molecules and atoms is practical interest for the diagnostics of hydrogen low-temperature plasma.

In model, one considers simultaneously kinetic processes involving hydrogen molecules in singlet ($N^1\Lambda_\sigma$=$2B^1\Sigma_u^+$, $2C^1\Pi_u$, $3B'^1\Sigma_u^+$, $3D^1\Pi_u$, $4B''^1\Sigma_u^+$, $4D'^1\Pi_u$, $2EF^1\Sigma_g^+$, $3I^1\Pi_g$, $3HH^1\Sigma_g^+$, $3GK^1\Sigma_g^+$, $3J^1\Delta_g$, $4P^1\Sigma_g^+$, $4O^1\Sigma_g^+$, $4R^1\Pi_g$, and $4S^1\Delta_g$) and triplet ($N^3\Lambda_\sigma$=$2b^3\Sigma_u^+$, $2c^3\Pi_u$, $2a^3\Sigma_g^+$, $3e^3\Sigma_u^+$, $3d^3\Pi_u$, $3h^3\Sigma_g^+$, $3g^3\Sigma_g^+$, $3i^3\Pi_g$, $4f^3\Sigma_u^+$, $4k^3\Pi_u$, $4r^3\Pi_g$, and $4s^3\Delta_g$) electronic states and hydrogen atoms in the ground $\left(1s\text{-}^2S_{1/2}\right)$ and

metastable $\left(2s\text{-}^2S_{1/2}\right)$ states and in $nl\text{-}^2L_J\left(l=s,p,d....\right)$ electron-excited levels under the assumption of resolved electron principal quantum numbers n = 2−6, total orbital angular momenta $L=S,P,D,F,G$, and angular momenta J=1/2−2/9.

Semi-empirical collisional radiative model of low-temperature hydrogen plasma includes computational modules to determine electron energy distribution function (EEDF) and concentrations of particles in excited states. The following processes are taken into account at the solving equations for the isotropic part of the EEDF and for concentrations of the excited particles:

momentum transfer in the elastic scattering of electrons by H_2 and H

$$H_2+e\rightarrow H_2+e,\quad H+e\rightarrow H+e; \tag{1}$$

electron – impact rotational excitation of the H_2

$$H_2\left(X^1\Sigma_g^+,v,J'\right)+e\leftrightarrow H_2\left(X^1\Sigma_g^+,v,J''\right)+e,\quad v=0,J'<J'',J'=0\text{-}12,J''=1\text{-}13; \tag{2}$$

resonant electron-impact vibrational excitation of the H_2

$$H_2\left(X^1\Sigma_g^+,v\right)+e\leftrightarrow H_2\left(X^1\Sigma_g^+,v'\right)+e,\quad v<v',v=0\text{-}13,v'=1\text{-}14; \tag{3}$$

electron – impact excitation of the triplet and singlet states of H_2

$$H_2\left(X^1\Sigma_g^+,v\right)+e\rightarrow H_2\left(N^1\Lambda_\sigma\right)+e, \tag{4}$$

$N^1\Lambda_\sigma=2B^1\Sigma_u^+, 2C^1\Pi_u, 3D^1\Pi_u, 4B''^1\Sigma_u^+, 4D'^1\Pi_u, 3I^1\Pi_g, 3HH^1\Sigma_g^+, 3GK^1\Sigma_g^+, 3J^1\Delta_g, 4P^1\Sigma_g^+, 4O^1\Sigma_g^+, 4R^1\Pi_g, 4S^1\Delta_g$,

$$H_2\left(X^1\Sigma_g^+,v\right)+e\rightarrow H_2\left(N^3\Lambda_\sigma\right)+e, \tag{5}$$

$N^3\Lambda_\sigma=2b^3\Sigma_u^+, 2c^3\Pi_u, 2a^3\Sigma_g^+, 3e^3\Sigma_u^+, 3d^3\Pi_u, 3h^3\Sigma_g^+, 3g^3\Sigma_g^+, 3i^3\Pi_g, 4f^3\Sigma_u^+, 4k^3\Pi_u, 4r^3\Pi_g, 4s^3\Delta_g$;

electron – impact excitation of H and electron capture by H

$$H\left(1s\text{-}^2S_{1/2}\right)+e\leftrightarrow H(Y)+e, \tag{6}$$

$Y=nl\text{-}^2L_J$, $n=2\text{-}6$, $l=s, p, d, f, g$, $L=S, P, D, F, G$,

$$H\left(1s\text{-}^2S_{1/2}\right)+e\rightarrow H^-+h\nu; \tag{7}$$

dissociative electron capture by vibrationally – excited molecules $H_2\left(X^1\Sigma_g^+,v\right)$

$$H_2\left(X^1\Sigma_g^+,v=0\text{-}14\right)+e\leftrightarrow H^-+H\left(1s\text{-}^2S_{1/2}\right); \tag{8}$$

dissociative ionization of the vibrationally – excited molecules by electron impact

$$H_2\left(X^1\Sigma_g^+,v=0\text{-}14\right)+e\rightarrow H_2^+\left(X^2\Sigma_g^+\right)+e+e\rightarrow H^++H\left(1s\text{-}^2S_{1/2}\right)+e+e, \tag{9}$$

$$H_2\left(X^1\Sigma_g^+,v=0\text{-}14\right)+e\rightarrow H_2^+\left(B^2\Sigma_u^+\right)+e+e\rightarrow H^++H\left(1s\text{-}^2S_{1/2}\right)+e+e; \tag{10}$$

dissociative excitation of electronic states of H_2 by electron impact

$$H_2\left(X^1\Sigma_g^+,v\right)+e\rightarrow H_2\left(N^1\Lambda_\sigma\right)+e\rightarrow e+H(Y)+H\left(1s\text{-}^2S_{1/2}\right), \tag{11}$$

$v=0\text{-}14$, $Y=2p\text{-}^2P_{1/2}, 2p\text{-}^2P_{3/2}, 3d\text{-}^2D_{3/2}, 3d\text{-}^2D_{5/2}, 3s\text{-}^2S_{1/2}, 3p\text{-}^2P_{1/2}, 3p\text{-}^2P_{3/2}, 4p\text{-}^2P_{1/2}, 4p\text{-}^2P_{3/2}, 4f\text{-}^2F_{5/2}, 4f\text{-}^2F_{7/2}$, $N^1\Lambda_\sigma=2B^1\Sigma_u^+, 2C^1\Pi_u, 3D^1\Pi_u, 4B''^1\Sigma_u^+, 4D'^1\Pi_u, 3I^1\Pi_g, 3HH^1\Sigma_g^+, 3GK^1\Sigma_g^+, 3J^1\Delta_g, 4P^1\Sigma_g^+, 4O^1\Sigma_g^+, 4R^1\Pi_g, 4S^1\Delta_g$,

$$H_2\left(X^1\Sigma_g^+,v\right)+e\rightarrow H_2\left(N^1\Lambda_\sigma\right)+e\rightarrow e+H\left(2s\text{-}^2S_{1/2}\right)+H\left(1s\text{-}^2S_{1/2}\right), \tag{12}$$

$v=0\text{-}14$, $N^1\Lambda_\sigma=3B'^1\Sigma_u^+, 2EF^1\Sigma_g^+$,

$$H_2\left(X^1\Sigma_g^+,v=0\text{-}14\right)+e\rightarrow H_2\left(3e^3\Sigma_u^+\right)+e\rightarrow e+H\left(2s\text{-}^2S_{1/2}\right)+H\left(1s\text{-}^2S_{1/2}\right), \tag{13}$$

$$H_2\left(X^1\Sigma_g^+,v=0\text{-}7\right)+e\rightarrow H_2\left(2b^3\Sigma_u^+\right)+e\rightarrow e+H\left(1s\text{-}^2S_{1/2}\right)+H\left(1s\text{-}^2S_{1/2}\right); \tag{14}$$

single-quantum VT – and VV – energy exchange between H_2

$$H_2\left(X^1\Sigma_g^+,v+1\right)+H_2\leftrightarrow H_2\left(X^1\Sigma_g^+,v\right)+H_2, \tag{15}$$

$$H_2\left(X^1\Sigma_g^+,v\right)+H_2\left(X^1\Sigma_g^+,w+1\right)\leftrightarrow H_2\left(X^1\Sigma_g^+,v+1\right)+H_2\left(X^1\Sigma_g^+,w\right); \quad (16)$$

multi-quantum VT energy exchange between $H_2\left(X^1\Sigma_g^+,v\right)$ and H

$$H_2\left(X^1\Sigma_g^+,v\right)+H\leftrightarrow H_2\left(X^1\Sigma_g^+,v'=v+i\right)+H, \quad (17)$$

i=1−9;

radiative decay of the singlet molecular $N^1\Lambda_\sigma$ and atomic Y states into the ground states

$$H_2\left(N^1\Lambda_\sigma\right)\rightarrow H_2\left(X^1\Sigma_g^+,v=0\text{-}14\right)+h\nu, \quad H(Y)\rightarrow H\left(1s\text{-}^2S_{1/2}\right)+h\nu; \quad (18)$$

radiative decay of the singlet molecular $N'^{1,3}\Lambda_\sigma$ and atomic Y′ states in the electronic states below $N''^{1,3}\Lambda_\sigma$ and Y″ (the cascade radiation processes)

$$H_2\left(N'^{1,3}\Lambda_\sigma\right)\rightarrow H_2\left(N''^{1,3}\Lambda_\sigma\right)+h\nu, \quad H(Y')\rightarrow H(Y'')+h\nu; \quad (19)$$

stepwise excitation and de-excitation of molecular $N^{1,3}\Lambda_\sigma$ and atomic Y states by electron impact

$$H_2\left(N''^{1,3}\Lambda_\sigma\right)+e\leftrightarrow H_2\left(N'^{1,3}\Lambda_\sigma\right)+e, \quad H(Y'')+e\leftrightarrow H(Y')+e; \quad (20)$$

dissociation of H_2 through the vibrational continuum (unstable state $2b^3\Sigma_u^+$) due to VT energy exchange between atoms and molecules and between molecules

$$H_2\left(X^1\Sigma_g^+,v_{max}\right)+H_2\rightarrow H_2+H\left(1s\text{-}^2S_{1/2}\right)+H\left(1s\text{-}^2S_{1/2}\right), \quad (21)$$

$$H_2\left(X^1\Sigma_g^+,v\right)+H_2\rightarrow H_2+H\left(1s\text{-}^2S_{1/2}\right)+H\left(1s\text{-}^2S_{1/2}\right), \quad (22)$$

$$H_2\left(X^1\Sigma_g^+,v_{max}\right)+H\rightarrow H+H\left(1s\text{-}^2S_{1/2}\right)+H\left(1s\text{-}^2S_{1/2}\right), \quad (23)$$

$$H_2\left(X^1\Sigma_g^+,v\right)+H\rightarrow H+H\left(1s\text{-}^2S_{1/2}\right)+H\left(1s\text{-}^2S_{1/2}\right); \quad (24)$$

dissociation of H_2 through the vibrational continuum (unstable state $2b^3\Sigma_u^+$) due to VV energy exchange between molecules

$$H_2\left(X^1\Sigma_g^+,v_{max}\right)+H_2\left(X^1\Sigma_g^+,v\right)\rightarrow H_2\left(X^1\Sigma_g^+,v\text{-}1\right)+H\left(1s\text{-}^2S_{1/2}\right)+H\left(1s\text{-}^2S_{1/2}\right); \quad (25)$$

dissociation of H_2 as a result of cascade radiation transitions into an unstable state $2b^3\Sigma_u^+$

$$H_2\left(N^3\Lambda_\sigma\right)\rightarrow H_2\left(2b^3\Sigma_u^+\right)+h\nu\rightarrow H\left(1s\text{-}^2S_{1/2}\right)+H\left(1s\text{-}^2S_{1/2}\right)+h\nu, \quad (26)$$

$N^3\Lambda_\sigma$=$3a^3\Sigma_g^+$, $3h^3\Sigma_g^+$, $3g^3\Sigma_g^+$, $3i^3\Pi_g$, $4r^3\Pi_g$.

An approach is proposed to take into account the processes of particle energy deactivation

$$H_2\left(X^1\Sigma_g^+,v\right)+Wall\rightarrow products, \quad (27)$$

$$H_2\left(N^{1,3}\Lambda_\sigma\right)+Wall\rightarrow products, \quad (28)$$

atom recombination

$$H\left(1s\text{-}^2S_{1/2}\right)+H\left(1s\text{-}^2S_{1/2}\right)+Wall\rightarrow products, \quad (29)$$

on the surface of reactors. It is a further development of the equally accessible surface method [11−13].

Database collisional-radiative characteristics of the processes are given in [1, 3–5, 14]. The initial data in the model for microwave and ECR discharges are taken from [7, 15−18].

3. RESULTS

Figures 2a and 2b illustrate the results of calculations of the concentration time dependence of the atomic hydrogen in the ground and metastable states.

It is established that the processes of dissociation of hydrogen molecules through triplet states by electron impact (13) and (14) make a significant contribution to the formation of atomic hydrogen. It is important to note that a commensurate contribution is also made by chemical reaction (26) of the decay of H_2 through the unstable state $2b^3\Sigma_u^+$. It is populated by cascade radiation transitions from a number of triplet states $N^3\Lambda_\sigma$=$3a^3\Sigma_g^+$, $3h^3\Sigma_g^+$, $3g^3\Sigma_g^+$, $3i^3\Pi_g$ and $4r^3\Pi_g$.

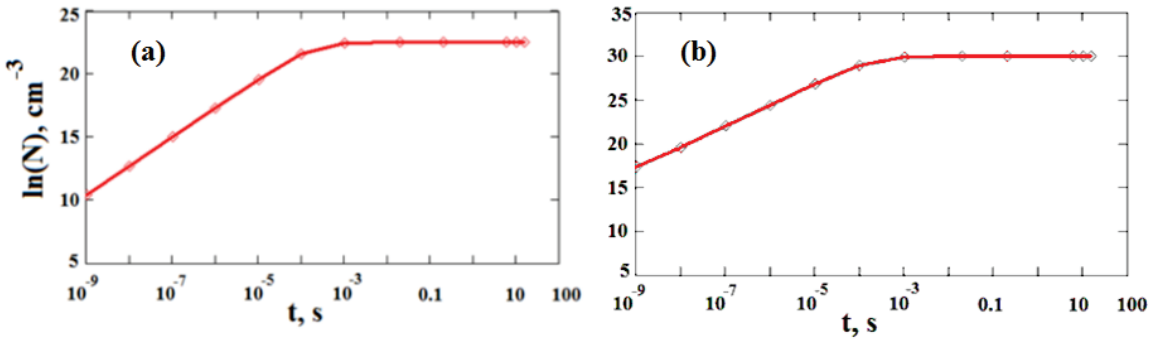

Figure 2. Concentration time dependence of the atomic hydrogen: (a) in the metastable ($2s\text{-}^2S_{1/2}$) state; (b) in the ground ($1s\text{-}^2S_{1/2}$) state. The calculations are made for the test conditions given [7, 15−18].

Figure 3 shows the results of calculations of the concentration time dependence of the atomic hydrogen in the electronic excited states. Distribution of atomic hydrogen population among electronic levels is different from the Boltzmann distribution. It is due to the competition of dissociative excitation of singlet states of the molecule by electron impact (11), direct electron impact from the basic electronic state of the hydrogen atom (6) and processes of the radiative decay (18)−(20).

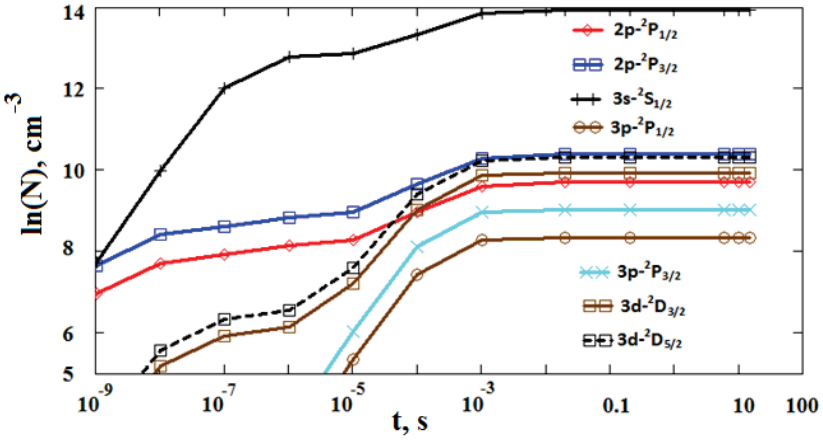

Figure 3. Concentration time dependence of the atomic hydrogen in the electronic excited states. The calculations are made for the test conditions given [7, 15−18].

Acknowledgments

This work was carried out within the State Program of TIPS RAS

References

1. Shakhatov V.A., Lebedev Yu.A., J. Phys. D: Appl. Phys., 2018, **51**, 213001.
2. Shakhatov V.A., Lebedev Yu.A., Lacoste A., Bechu S., J. Phys. Conf. Ser. 2017, **927**, 012052.
3. Shakhatov V.A., Lebedev Yu.A., Lacoste A., Bechu S., High Temp., 2016, **54**, 123.
4. Shakhatov V.A., Lebedev Yu.A., Lacoste A., Bechu S., High Temp., 2015, **53**, 569.
5. Shakhatov V.A., Lebedev Yu.A., High Temp., 2011, **49**, 257.
6. Shakhatov V.A., Lebedev Yu.A., Plasma Physics Reports, 2017, **43**, 1016.
7. Shakhatov V.A., Lebedev Yu.A., High Temp., 2017, **55**, 496.

8. Bentounes J., Béchu S., Jean L., Biggins F., Michau A., Gavilan L., Menu J., Bonny L., Fombaron D., Bès A., Lebedev Yu. A.; Shakhatov V. A., Svarnas P., Hassaine T., Lemaire J. L., Lacoste A., Plasma Sources Sci. Technol., 2018, **27**, 055015
9. Béchu S., Aleiferis S., Bentounes J., Gavilan L., Shakhatov V. A., Bès A., Svarnas P., Mazouffre S., De Oliviera N., Engeln R., Lemaire J. L., Appl. Phys. Lett., 2017, **111**, 074103.
10. Shakhatov V.A., Lebedev Yu.A., Lacoste A., Bechu S., High Temp., 2016, **54**, 467.
11. Berkut V.D., Dorochenko V.M., Kovtun V.V., Kudryavtsev N.N. Non-Equilibrium Physical and Chemical Processes in Hypersonic Aerodynamics, Moscow: Energoatomizdat, 1994 (in Russian).
12. Shakhatov V.A., Gordeev O.A., Technical Physics, 2005, **50**, 1592.
13. Frank-Kamenetskii D.A. Diffusion and Heat Transfer in Chemical Kinetics, Moscow: Nauka, 1987 (in Russian).
14. Shakhatov V.A., Lebedev Yu.A., Plasma Physics Reports, 2018, **44**, 126.
15. Lacoste A., Lagarde T., Bechu S., Arnal Y., Pelletier J., Plasma Sources Sci. Technol., 2002, **11**, 407.
16. Svarnas P, Annaratone B. M., Bechu S., Pelletie J., Bacal M., Plasma Sources Sci. Technol., 2009, **18**, 045010.
17. Lacoste A., Bechu S., Maulat O., Pelletier J., Arnal Y., Plasma Sources Sci. Technol., 2009, **18**, 015017.
18. Bechu S., Soum-Glaude A., Bes A., Lacoste A., Svarnas P., Aleiferis S., Ivanov A.A., Bacal Jr. M., Phys. Plasmas, 2013, **20**, 101601.

THE GENERAL THEORY OF IONIZATION INSTABILITY IN INFINITE AND BOUNDED PLASMA

S. Dvinin[1], V. Dovzhenko[2] , O. Sinkevich[3]

[1] Lomonosov Moscow State University, Leninskie Gory, 1–2, Moscow, 119991, Russia
[2] A.M.Obukhov Institute of Atmospheric Physics RAS, Pyzhyovskiy pereulok, 3, Moscow, 119017, Russia
[3] National Research University Moscow Power Engineering Institute, Krasnokazarmennaya, 14, Moscow, 111250, Russia

Abstract. Development of ionization instability in an infinite and bounded plasma slab with a high electron density n_e (which can be either above or below the critical one n_c) supported by a microwave is considered. In the first case, the excited electromagnetic field is represented as a sum of surface and leaking waves, in the second, a sum of surface and evanescent waves. Separately, field perturbations associated with the continuity of the total current flowing through the plasma are identified. The equations, describing the development of instability, are obtained. Instability areas are determined and its increments are found. For a bounded plasma, the nonlinear stage of instability development is described using a model equation.

1. INTRODUCTION

The paper deals with the ionization instability in radio frequency (RF) and microwave gas discharges with a high electron density in infinite and spatially bounded plasma slabs. Experimentally the spatial structures formation associated with this type of instability was discovered many years ago [1, 2]. Their formation in dc discharges [3] and in semiconductor plasma [4] was studying for many years, and a number of interesting results in this field were obtained. However, theoretical description of the development and stabilization of instability in HF and microwave plasma was absent until last years. In the article [5], the continuity condition of the total current was used to calculate the electromagnetic field, which does not allow to evaluate the role of the plasma's eigen waves in the development of instability; in [6] the field related to the continuity of the total current was not explicitly identified. Thus, the transition from resonant mode, taking into account Eigen mode excitation, to nonresonant mode of instability was not studied.

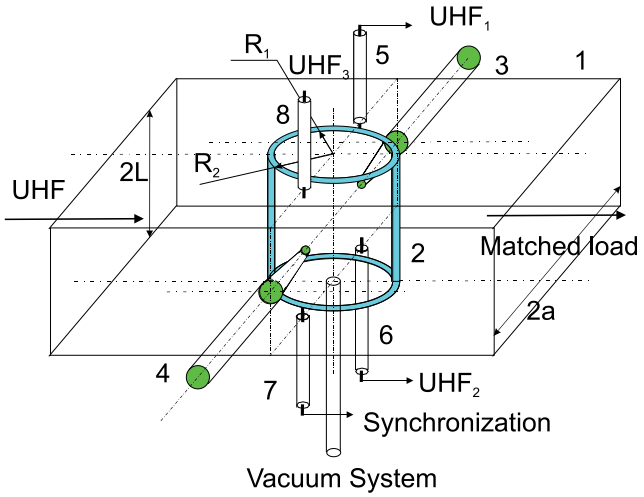

Figure 1. Discharge geometry. Plasma filled glass discharge tube, placed into rectangular waveguide. 2a – 72 mm, 2L – 34 mm. The incident microwave, supported the discharge, guided to the tube from the left.

In this paper, disturbances associated with the continuity of the total current (generally used in the theoretical description) and with the excitation of electromagnetic waves (surface and evanescent waves for bounded plasma column and surface and leaking waves for an infinite) are separated in the field excited during the instability development. The calculations, made in the theoretical model, were verified in experimental setup, which is shown in Fig. 1. The discharge was created in dielectric tube, placed in a rectangular waveguide 72×34 mm^2. The setup made it possible to measure the incident on the discharge, reflected from the discharge and transmitted power, the electron density, using an 8 mm interferometer, and the field near the discharge, using microwave probes introduced into the waveguide.

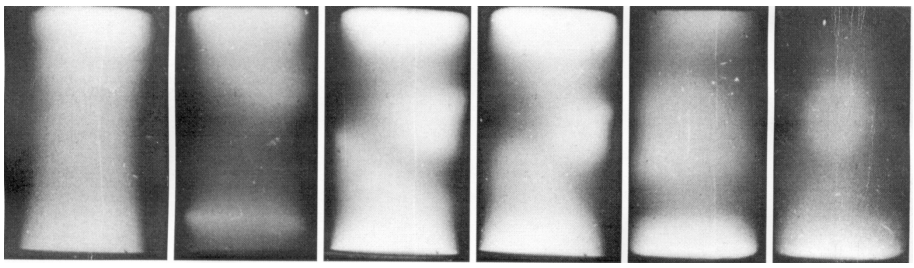

Figure 2. An example of structures realized in microwave when the instability takes place. Xenon, pressure is 0.1 Torr, tube radius – 1 cm, microwave frequency 3.2 GHz. Incident wave power is: A) – 140 W, B) – 9 W (discharges in state I), C) – 17 W, D) – 9 W, E) – 6.5 W, F) – 4.5 W (discharges in state II, Figs. 4–5).

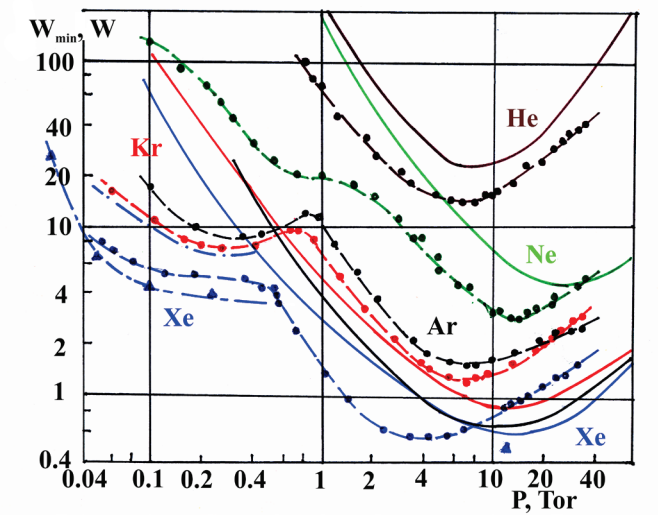

Figure 3. Minimum power needed to maintain the discharge W_{min} as a function on the gas pressure in helium, neon, argon, krypton and xenon for a microwave discharge in a waveguide. Points – experiment in a tube with a radius of 0.6 cm, solid curves – calculation in the homogeneous column model (V. Dovzhenko), dashed dotted curve – calculation taking into account ionization instability [7], triangles – experiment [8].

Calculations have shown that, in bounded plasma, in addition to a violation of the plasma homogeneity, observed in the experiment (Fig. 2), the development of instability leads to a partial transfer of energy from a plane wave to the surface wave. The total electric field in the discharge exceeds the field of the incident wave, ensuring that the integral balance of the number of particles is satisfied, and a hysteresis is observed in the dependence of the plasma parameters on the microwave power [7, 8]. This effect also causes an increase in electromagnetic field absorption. Thus, a significant decrease in the power, which is necessary to maintain the discharge (Fig. 3), take place. In an infinite plasma column, the instability will be convective, and the instability increment will depend on the correlation of ionization rate and the group velocity of the electromagnetic wave, as well as on the attenuation coefficient of the excited wave.

2. SYSTEM OF EQUATIONS

Discharge will be described by the system of balance equations for electron density n_e and their temperature T_e, averaged over the tube cross section

$$\frac{\partial n_e}{\partial t} - D_a \frac{\partial^2 n_e}{\partial z^2} = \left(\nu_i(T_e, n_e) - \frac{D_a}{\Lambda^2}\right) n_e ,$$
$$\frac{3}{2} n_e k_B \frac{\partial T_e}{\partial t} - \frac{\partial}{\partial z}\left(\kappa \frac{\partial T_e}{\partial z}\right) = \frac{1}{2}\left\langle \frac{n_e e^2 \nu}{m(\omega^2 + \nu^2)} \mathbf{E}\mathbf{E}^* \right\rangle - n_e w_1 \qquad (1)$$

and Maxwell equations

$$\left[\nabla \times \mathbf{H}(t,\mathbf{r})\right] + \varepsilon_0 \left(i\omega\varepsilon(\omega,r) + \frac{\partial \omega\varepsilon(\omega,r)}{\partial \omega} \frac{\partial}{\partial t} \right) \mathbf{E}(t,\mathbf{r}) = 0 , \quad \left[\nabla \times \mathbf{E}(t,\mathbf{r})\right] - \mu_0 \left(i\omega + \frac{\partial}{\partial t} \right) \mathbf{H}(t,\mathbf{r}) = 0 . \qquad (2), (3)$$

Here, $D_\alpha = \mu_i k_B T_e / e$ is an ambipolar diffusion coefficient, μ_i is ionic mobility; κ is an electronic heat diffusion coefficient, $\Lambda = R/2{,}405$ is the transverse diffusion length; ν is the effective frequency of electron-atom collision, $w_1 = \frac{3}{2}\sum_k \delta_{ek} \nu_{ek} k_B (T_e - T_k)$ is average energy, lost by electrons per one second, k_B is Boltzmann's constant, ν_{ek} and δ_{ek} are the frequency of electrons collision and average part of energy, lost by electrons at one collision with heavy particles of the type k; e, m are charge and mass of electron, T_k is temperature of particles of sort k; $k_0 = \omega/c$, ω are field frequency, c is the light velocity. Sign < > denotes

averaging over the tube cross section. Since the focus of our investigation is on the electrodynamic characteristics of discharge, here we will use the most simple kinetics model. For a bounded plasma column at the points $z=-L$, L, the conditions for the zero tangential component of the electric field, and for $r\to\infty$, nonreflecting Sommerfeld boundary condition were set. For the electron density at $z=-L$, L, Neumann model boundary conditions were used.

3. MATHEMATICAL MODEL FOR FINITE SYSTEM

The solution of the system of equations (1) – (3) is assumed to be

$$\begin{pmatrix} n_e \\ T_e \\ \mathbf{E}_z \\ \mathbf{H}_\varphi \end{pmatrix} = \begin{pmatrix} n_{e0}(t) \\ T_{e0}(t) \\ \mathbf{E}_{0z}(t,r) \\ \mathbf{H}_{0\varphi}(t,r) \end{pmatrix} + \begin{pmatrix} \delta n_e(t)\cos(hz) \\ \delta T_e(t)\cos(hz) \\ \delta\mathbf{E}_z(t,r)\cos(hz)\exp(-i\omega t) \\ \delta\mathbf{H}_{z\varphi}(t,r)\sin(hz)\exp(-i\omega t) \end{pmatrix}, \tag{4}$$

where the homogeneous along the 0Z axis components and periodic perturbations arising due to instability are clearly marked. In accordance with equation (2), components related to the excitation of an electromagnetic wave $\delta\mathbf{E}_1 = \left(i\omega\varepsilon_0\varepsilon(\omega)\right)^{-1}\left[\nabla\times\delta\mathbf{H}\right]$ and the conservation of the total current $\delta\mathbf{E}_1 = -\left(\varepsilon(\omega)\right)^{-1}\delta\varepsilon\mathbf{E}_0$ were distinguished in the electric field for disturbances. The solution satisfies the equations for the volume-average density and temperature of electrons

$$\frac{\partial n_0}{\partial t} = \left(\nu_i(T_{e0},n_0) - \frac{D_a}{\Lambda^2}\right)n_0, \tag{5}$$

$$\frac{3}{2}n_0 k_B\frac{\partial T_{e0}}{\partial t} = \frac{1}{2}\frac{n_0 e^2\nu}{m\left(\omega^2+\nu^2\right)}\left(\left\langle\mathbf{E}_0\mathbf{E}_0^*\right\rangle + \frac{1}{2}\sum_S\left\langle\mathbf{E}_S\mathbf{E}_S{}^*\right\rangle\right) - n_e w_1, \tag{6}$$

and field perturbations

$$\delta\mathbf{E} = \mathbf{E}_S\cos(h_S z) = \frac{\delta n_{eS}(t)E_0}{n_C\left(1+i\nu/\omega\right)}\frac{1}{\varepsilon_{pl}}\left[\frac{\varepsilon_{resS}\left(\delta n_{eS}/n_{e0},h_S\right)C_S}{\varepsilon_{pl}-\varepsilon_{resS}\left(\delta n_{eS}/n_{e0},h_S\right)}\mathbf{e_S}+\mathbf{e_0}\right]\cos(hz), \tag{7}$$

as well as the equation for the instability increment

$$\frac{\Gamma\left(n_0,n_{eS},h_S\right)}{\nu_{i0}}n_{eS} = \left\{-h_S^2\Lambda^2 + \frac{\partial\nu_i(T_e,n_e)}{\partial n_e}\left(n_{e0}/\nu_{i0}\right) + \left(\frac{1}{\nu_{i0}}\frac{\partial\nu_i(T_e,n_e)}{\partial T_e}-1\right)\frac{w_1}{(\kappa h^2+\partial w_1/\partial T_e)\nu_{i0}}\times\right.$$
$$\left.\frac{\left\langle\mathbf{E}_0\mathbf{E}_0^*\right\rangle}{\left\langle\mathbf{E}_0\mathbf{E}_0^*\right\rangle+\frac{1}{2}\sum_S\left\langle\mathbf{E}_S\mathbf{E}_S^*\right\rangle}\frac{n_{e0}}{n_C}\left(1-\Delta\left(\frac{\delta n_{eS}}{n_{e0}}\right)^2\right)\mathrm{Re}\,2\varepsilon_{pl}^{-1}\left(1+i\frac{\nu}{\omega}\right)^{-1}\left[1+\frac{\varepsilon_{resS}C_S}{\left(\varepsilon_{pl}-\varepsilon_{resS}\right)}\right]\right\}n_{eS} \tag{8}$$

Here Δ is a phenomenological parameter, closed to unity, reflecting the fact that the amplitude of density perturbation cannot exceed the average density. n_{eS} is the amplitude of the electron density perturbation with the wave number h_S. In the absence of surface wave excitation, the last equation allows calculating the instability increment for a uniform plasma density distribution, and together with (5) – (7), determine plasma parameters in the absence of instability, as well as in the plasma state, established after instability stabilization.

4. STATIONARY SOLUTION AND COMPARISON WITH EXPERIMENT

The calculation shows that possibility of instability development is determined by the phase shift between the surface wave field and waveguide H_{10} field, supporting the plasma (see (7)). If this shift is less than $\pi/2$ in the space where the electron density disturbances are positive, the instability will take place. The strongest influence of this type of instability on the power characteristics of the discharge will be observed at relatively low pressures $\nu/\omega<<1$, but the instability cannot be suppressed by transfer processes.

The parameters of the plasma calculated in the steady state using the system of equations (5) – (8) are shown in Fig. 4. The theory correctly describes the regions of electron density, at which instability is observed, and gives values close to experiment for the power, supporting the discharge. Direct measurement of the phase shift between z-component of electric field at the ends of the discharge tube, using electric probes, shows that the amplitude of the surface wave can exceed the amplitude of the pump wave, since for a surface wave the discharge is a high-Q resonator. This process leads to a hysteresis of the power characteristics and a decrease in the power range at which the discharge can be maintained in the low pressure region (Fig. 3).

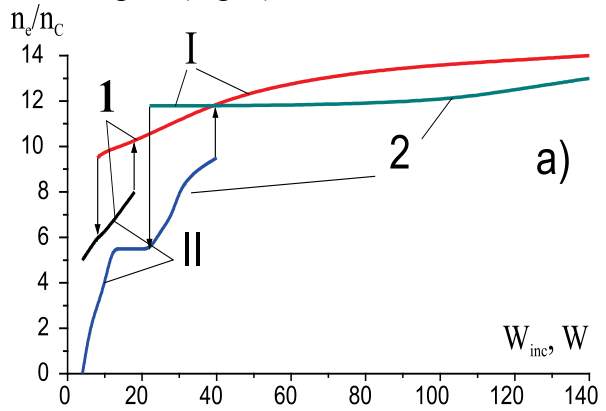

Figure 4. Dependence of electron density n_e/n_c on incident power (1 is experiment, 2 is theory).

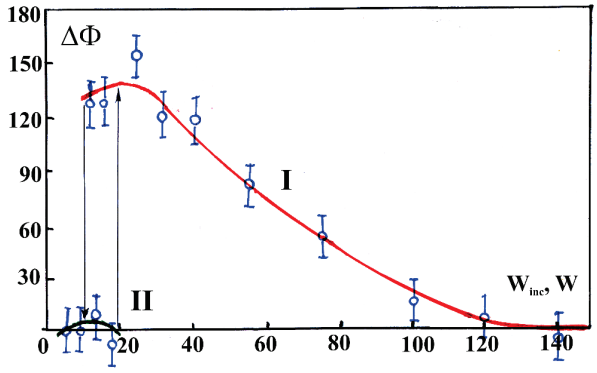

Figure 5. Phase shift between the signals (ΔΦ) from UHF capacitive probes, placed at the upper and lower ends of the discharge tube as a function of the incident power.

5. IONIZATION INSTABILITY IN INFINITE PLASMA SLAB

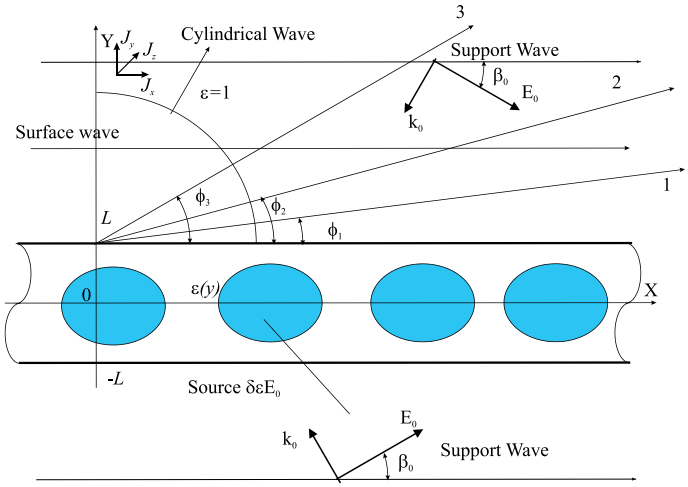

Figure 6. Scattering of the pump wave on the plasma slab.

As was shown in the previous paragraphs, the ionization instability, associated with appearing of a surface wave, is easily excited in limited systems. This process can disrupt the uniform density distribution of the charged particles and qualitatively changes the electron density dependencies on the power of the wave, supporting plasma. Therefore, the studying of similar instabilities appearance in infinite plasma column is actual. We suppose that the plasma slab is maintained by an electromagnetic wave incident on it at angle β_0 (Fig. 6). The plasma was described by the same system of equations (1) – (3). The conditions of non-reflection for the electromagnetic wave from infinity were set. Consider the behavior of an arbitrary perturbation of the plasma density that occurred at time t=0. Using Laplace transform in time and the Fourier transform in space [9] means that perturbations of the density and temperature of the electrons and the electromagnetic field can be written as

$$\begin{pmatrix} E_+^{(1)}(x,y,t) \\ E_-^{(2)*}(x,y,t) \\ \delta n(x,t) \\ \delta T(x,t) \end{pmatrix} = \begin{pmatrix} E_+^{(1)} \exp(-i\omega t)\exp\left(-i\Omega t + i\left(h + k_0 \sin\beta_0\right)x\right) \\ E_-^{(2)*} \exp(i\omega t)\exp\left(-i\Omega t + i\left(h - k_0 \sin\beta_0\right)x\right) \\ \delta n \exp(-i\Omega t + ihx) \\ \delta T \exp(-i\Omega t + ihx) \end{pmatrix}. \quad (9)$$

Here $E_+^{(1)}$ and $E_-^{(1)}$ are amplitudes of anti-Stokes (with a total frequency ω+Ω) wave and Stokes (with a differential frequency ω–Ω) waves. Long calculations lead to a dispersion equation that takes into account surface and leaking wave excitation. Leaving in the resulting expression only surface waves, we get

$$\left\{\left(-i\left(\frac{\Omega}{\nu_{i0}}\right)+h^2\Lambda^2-\gamma_N\right)\left(-\frac{3k_BT_0}{2w_{10}}i\left(\frac{\Omega}{\nu_{i0}}\right)+\frac{K}{n_{e0}w_{10}}h^2\Lambda^2+\gamma_W\right)-\gamma_T\mathbf{E}_0^*\mathbf{E}_0\frac{1}{4}\left[\left(1+\frac{\left(1+V^2\right)}{\left(\left(1+\Omega/\omega\right)^2+V^2\right)}\right)\frac{1}{\varepsilon_+}\frac{n_0}{n_+\left(1+i\nu/\omega\right)}C_{2+}\right.\right.$$

$$\left.\left.+\left(1+\frac{\left(1+V^2\right)}{\left(\left(1-\Omega/\omega\right)^2+V^2\right)}\right)\frac{1}{\varepsilon_-^*}\frac{n_0}{n_-\left(1-i\nu/\omega\right)}C_{2-}^*\right]\right\}\frac{\delta n_e}{n_0}=\gamma_T\mathbf{E}_0^*\mathbf{E}_0\frac{1}{4}\left\{\left(1+\frac{\left(1+V^2\right)}{\left(\left(1+\Omega/\omega\right)^2+V^2\right)}\right)\frac{1}{\varepsilon_+}\frac{n_0}{n_+\left(1+i\nu/\omega\right)}\frac{C_{1+}F_+\left(h\right)}{\left(h-h_+\right)}\right.$$

$$\left.+\left(1+\frac{\left(1+V^2\right)}{\left(\left(1-\Omega/\omega\right)^2+V^2\right)}\right)\frac{1}{\varepsilon_-^*}\frac{n_0}{n_-\left(1-i\nu/\omega\right)}\frac{C_{1-}^*F_-^*\left(h\right)}{\left(h-h_-^*\right)}\right\}\frac{\delta n_e}{n_0}+I\left(\Omega,h\right),$$

where

$$F_\pm\left(\omega,\Omega,\omega_{Pe},\nu\right)=\frac{\left(\frac{\left(\omega\pm\Omega\right)^2}{c^2}\varepsilon_\pm-h^2\right)}{h^2\mp\frac{\Omega\left(2\omega\pm\Omega\right)}{c^2}\left(1\mp\frac{i\nu\omega_{Pe}^2}{\left(\omega\pm\Omega+i\nu\right)\left(2\omega\pm\Omega\right)\left(\omega+i\nu\right)}\right)}$$

and C_{1+}, C_{1-}, C_{2+}. C_{2-} – normalization coefficients:

$$C_{1\pm}=\frac{1}{2L}\int_{-L}^{L}dy\frac{\cos\left(\tilde{\kappa}_+\left(h\right)y\right)}{\cos\left(\tilde{\kappa}_+\left(h\right)L\right)}\frac{\cos\left(\sqrt{\omega^2\varepsilon^*/c^2}\,y\right)}{\cos\left(\sqrt{\omega^2\varepsilon^*/c^2}\,L\right)},\ C_{2\pm}=\frac{1}{2L}\int_{-L}^{L}dy\frac{\cos\left(\sqrt{\omega^2\varepsilon/c^2}\,y\right)}{\cos\left(\sqrt{\omega^2\varepsilon/c^2}\,L\right)}\frac{\cos\left(\sqrt{\omega^2\varepsilon^*/c^2}\,y\right)}{\cos\left(\sqrt{\omega^2\varepsilon^*/c^2}\,L\right)}.$$

The dispersion expression describes negative feedback related to the conservation of the total current (the corresponding term is in square brackets in the left side of the equation), as well as resonant terms in right side, containing the terms in the denominator responsible for excitation of Stokes or anti-Stokes waves. The analysis shows, that one of the excited waves under certain conditions may be amplified due to ionization instability. Due to the fact that the ionization frequency is much less than the frequency of the wave, the spatial amplification factor turns out to be very small. However, when the plasma slab is placed in a resonator, the system may become unstable, as it was obtained above. One can qualitatively investigate the behavior of instability by using model equations. We can write such a system of equations, for example, as

$$\frac{\partial n_1}{\partial t}-D\frac{\partial^2 n_1}{\partial x^2}=\mu\left(\mathbf{E}_0^*\delta\mathbf{E}_1\right),\ -i\mathrm{M}_2\left(n_1E_0\right)+\left(\frac{\partial}{\partial t}+V\frac{\partial}{\partial x}+\left(-i\omega+iVk+\Gamma\right)\right)E_1=0. \qquad (10)$$

The first equation describes the change in plasma density due to diffusion and additional ionization in the region of space, where the field of the pump wave and the scattered wave are in phase. The second equation can also be written as

$$\left(\frac{\partial}{\partial t}+V\frac{\partial}{\partial x}+i\left(k-h_0\right)+\Gamma\right)E_+=i\mathrm{M}_2\left(n_1E_0\right)$$

and describes the excitation of a scattered wave with a wavenumber $h_0=\omega/V-k$ (ω is the frequency of the pump wave, k is the projection of its wave number onto the plane of the plasma slab, V is the group velocity of the scattered wave) due to the resulting electron density perturbations. μ and M_2 are constants that describe ionization interaction. Dispersion equation corresponding to the system (10) has the form

$$\left(-i\Omega n_1+Dh^2+\Gamma_n\right)\left(-i\Omega+iV_{G+}H+k_0\sin\beta_0+\Gamma\right)-i\mathrm{M}_2\mu\left(\mathbf{E}_0\mathbf{E}_0^*\right)=0.$$

It can be analyzed using the technique given in [9]. The analysis shows that under certain conditions the ionization interaction can lead to convective instability.

6. CONCLUSIONS

The development of ionization instability in infinite and bounded plasma slabs with a high electron density n_e is considered.

In a spatially bounded plasma, instability develops, when the excited eigenmode of the plasma is in phase with the pump wave at points, where the electron density disturbances are positive.

In infinite plasma slab, when propagation direction of microwave, supporting discharge, is perpendicular to the plasma, the Stokes and anti-Stokes waves are excited simultaneously. In case of oblique fall in, the electron density fluctuations with a wavelength $\Lambda=2\pi/K$, can lead to excitation of the Stokes wave or to excitation of anti-Stokes one only.

In the approximate interaction model, the distribution of electron density and temperature over the width of the plasma slab is assumed to be homogeneous. In the absence of ionization nonlinearity, the solution of the diffusion and heat transfer equations for an isotropic plasma and Maxwell's equations for an electromagnetic field gives us two diffusion-heat-conduction modes describing the damping of perturbations in space and electrodynamic modes involving a surface wave (for $n_e > 2n_c$) and the leaking waves. When ionization nonlinearity is taken into account, the transfer of pump wave energy to the Stokes and anti-Stokes waves changes the effective coefficient of wave attenuation, and under certain conditions, leads to their amplification (convective instability).

The proposed calculation method also makes it possible to consider the instability in a plasma slab limited in longitudinal direction, with allowance for the reflection of waves from the ends of the plasma. In this case, the range of parameters, under which absolute instability is observed, expands, since feedback is activated due to the backward wave, reflected from plasma boundary.

Resonant ionization field instabilities can be observed in a low-pressure plasma in all cases when at least two types of electromagnetic waves supporting discharge exist under given conditions, for example, a plane wave incident from outside and a surface wave. Therefore, the appearance of instability in RF discharges in technological installations containing a large-sized plasma is possible due to the interaction of even and odd surface waves propagating along the plasma-metal boundary [10].

The calculations performed are consistent with experiments carried out in a discharge in a microwave discharge in a waveguide, in which the characteristics of the plasma and the structure of the electromagnetic field were measured. The results obtained are important in explaining the characteristics of low-frequency RF and microwave discharges, including discharges in a magnetic field, and for the development of technological installations containing large-sized plasma supported by a radio frequency and microwave field.

References

1. Jerpetov Kh., Zaitsev A.A., Sov. Phys.: Doklady, 1953, **89,** 825.
2. Zaitsev A.A., Jerpetov Kh., Sov Phys.: JETP 1953, **24,** 516.
3. Landa P.S. Oscillations in distributed systems Moscow: URSS Book House "Librokom", 2010, 183 (In Russian).
4. Kerner B.S., Osipov V.V., Autosolitons: A New Approach to Problems of Self-Organization and Turbulence Fundamental Theories of Physics. Dordrecht, Boston, London: Kluwer Academic Publisher, 1994.
5. Mackey D., Plantie L., Turner M.M., Applied Mathematical Letters, 2005, **18**, 865.
6. Dvinin S.A., Dovzhenko V.A., Solntzev G.S., Sov. Physics: Fizika plasmy, 1982, **8,** 1228.
7. Dvinin S.A., Dovzhenko V.A., Solntzev G.S., Sov. Physics: Fizika plasmy, 1983, **9,** 1058.
8. Dvinin S.A., Postnikov S.A., Solntzev G.S., Tsvetkova L.I., Sov. Physics: Fizika plasmy, 1983, **9,** 1297.
9. Bers A., Handbook of Plasma Physics. Vol. 1. Ed. A.A. Galeev and R.N. Sudan, North-Holland Publishing Company, 1983, 451.
10. Dvinin S.A., Vologirov A.G., Mikheev V.V., Sviridkina V.S., Plasma Physics Reports, 2008, **34**, 688.

MODELING OF CARBONACEOUS PARTICLES PRODUCTION IN MICROWAVE DISCHARGE IN LIQUID *N*-HEPTANE

I. L. Epstein, Yu. A. Lebedev, A. V. Tatarinov, I. V. Bilera

A.V. Topchiev Institute of Petrochemical Synthesis of the Russian Academy of Sciences (TIPS RAS), Leninsky Prospect, 29, Moscow, 119991, Russia

Abstract. Three different models of the microwave discharge in liquid *n*-heptane and results of correspondent simulations are presented. A simplified 2D model describes the dynamic processes of boiling of the liquid *n*-heptane, heat transfer mechanisms and forming of the near-electrode gas bubbles filled with plasma. Main accent of the work is made on a 0D model of time dependent processes, occurring inside the plasma bubble. The model includes both the description of gas phase processes and formation of solid carbon-containing particles at atmospheric pressure. The linear and planar PAH growth mechanisms of generation of solid particles are considered. Both of them describe simultaneous processes of the initial *n*-heptane pyrolysis and nucleation, surface growth and coagulation of soot particles. A 1D model with shortened set of gas phase reactions describes the evolution processes of ionization, heat transfer and formation of gas and solid products inside the plasma bubble. The results of calculations are compared with known experimental results.

1. INTRODUCTION

Plasmas inside liquids are one of the perspective objects for study and application. Currently the discharges are created in various dielectric fluids, including hydrocarbons, and the aim is to obtain various useful products (hydrogen, nanoparticles, nanotubes), coatings, removal of the photo resist, etc. When the plasma is located inside the liquid, the efficiency of physical and chemical processes under the action of its active particles and radiation is large. The appropriate rates of formation and decomposition of products are quite high. Different types of discharges are used to create plasma. The interest in microwave discharges is caused primarily by the fact that the microwave technique allows to provide localization of areas of high field strength by simple methods and, therefore, obtaining discharges of low input power. For this purpose metal electromagnetic antennas (vibrators) of various shapes are used.

Microwave discharges in liquid hydrocarbons are described in *n*-dodecane [1], in benzene, commercially available cooking oil, engine oil, waste cooking oil and waste engine oil [2], in silicone oil [3] and in alcohol [4].

The experiments in liquid *n*-heptane are carried out on the installation described in detail in [5, 6] and schematically depicted in Fig. 1. It includes the microwave generator, waveguide-coaxial junction and a movable short-circuiting piston, used for matching. The central conductor serves as an antenna for entering microwave energy into the discharge section. The central electrode of the coaxial line is made of

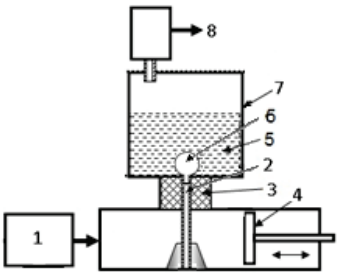

Figure 1. Sketch of the experimental set up. 1 - microwave generator, 2 – antenna, 3 - dielectric, 4 – shorting plunger, 5 – liquid hydrocarbon, 6 – discharge region, 7 – quartz reactor, 8 – exit to chromatograph.

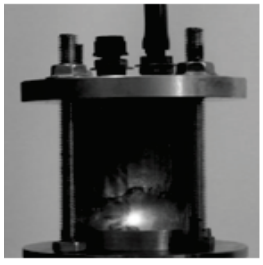

Figure 2. Photo of a discharge in *n*-heptane.

copper tube with an outer diameter of 3 mm. A discharge is sustained at 100 watts of input power. The discharge burns at the tip of antenna inside a quartz glass (diameter 55 mm) (Fig. 2). The volume of liquid in the cuvette is about 40 ml. The pressure above the liquid surface is atmospheric. The content of gas

products, originated due to pyrolysis of *n*-heptane in the microwave discharge, is determined by the gas chromatography.

Solid carbonaceous particles are one of the main products of microwave discharges in liquid hydrocarbons and consist principally of amorphous carbon (soot). In the analysis of electronic microphotographs of the soot samples obtained under different conditions, it was found that it consists mainly of spherical or almost spherical particles of 20–40 nm size containing about 10^6 carbon atoms. These 'elementary soot particles' are combined into chains of various shapes and other complex structures. The minimum soot particle size is about 1.5–2 nm and contains 30-100 carbon atoms.

The main contribution to the increase in soot particle mass is made by surface growth with the participation of gas phase molecules, among which acetylene has determining influence [7, 8]. Participation of the polyaromatic hydrocarbons (PAHs) in this process, including PAH radicals, remains a subject of discussion [7, 8]. The surface growth of the soot particle is a heterogeneous process, in which adsorption and desorption processes of molecules from the gas phase on the surface of the particles should be considered,

Our 2D model [9, 10] has been developed on the base of a simplified brutto mechanism for the dissociation of *n*-heptane. We have studied the dynamics of the gas plasma bubbles originated in the vicinity of the antenna inside liquid *n*-heptane. It is shown that the gas temperature inside plasma bubble is about 1500K. In our 0D model we have developed a mechanism that allows to associate the gas-phase kinetics with the kinetics of the formation of solid particles. Finally in our 1D model we combine electro dynamic and heat conducting processes with simplified kinetics of gas phase and solid *n*-heptane dissociation products.

2. 2D MODEL. PROBLEM FORMULATION AND MAIN RESULTS

In 2D model we make the following assumptions:

- Gas bubbles are created by evaporation of liquid into the bubble.
- In plasma formed inside the bubble, the main ion is $C_7H_{16}^+$.
- Heating of the bubble is due to Joule heating of plasma electrons.
- Cooling of the bubble is due to energy transfer to ambient liquid for evaporation and endothermic pyrolysis of *n*-heptane.
- The size and shape of the bubbles is determined by the surface tension and the sum of the pressure forces.
- Lifting of the bubble is determined by the Archimedean force and viscosity.
- The initial temperature of the liquid and gas phase is equal to the boiling point.
- A small bubble of evaporated gas of atmospheric pressure is set inside the near-electrode cavity.

Here we note that the model contains only a simplified brutto mechanism for the dissociation of *n*-heptane, though detailed kinetics of gas products and solid soot particles is absent.

The code is based on joint solution of the Maxwell equations, Navier–Stokes equation, heat equation, continuity equations for electrons (written in the ambipolar diffusion approximation) and the *n*-heptane concentration (including its thermal decomposition and dissociation by electron impact) and the Boltzmann equation for free electrons of the plasma.

The results of the simulations allowed to found out the following:

- Boiling process depends on the input power. There is a certain range of input power, when there is a regime of periodic formation of bubbles and their further rise (Fig. 3).
- The plasma burns only inside the cavity, in close proximity to the central electrode. When a bubble floats up, plasma disappears inside it. This is due to the fact that the microwave field is concentrated near the end of the central electrode and falls very sharply outside it (Fig. 4). At a power > 500 W, the microwave field at the electrode end reaches 10 kV/cm. The temperature in this area is about 1500 - 1700 K, which is in good agreement with our experimental data.
- As the bubble rises, it cools very quickly due to energy transfer to ambient boiling liquid needed for its evaporation. So temperature of the rising bubble very soon becomes approximately equal to the boiling point.

- For times less than 10^{-3} with the dissociation of *n*-heptane occurs under the action of electron impact, and then is dominated by thermal dissociation.

Figure 3. Bubble formation at times: 0.01, 0.03, 0.06, 0.09, 0.11, 0.12 sec. 2D simulation. P=110W.

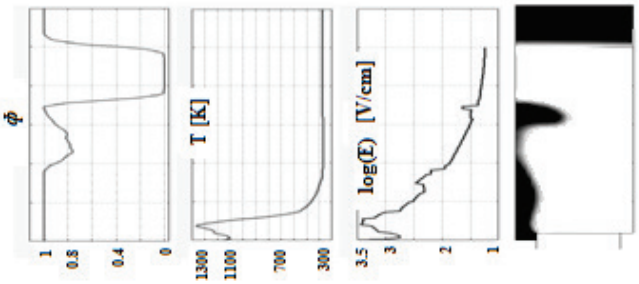

Figure 4. Axial profiles of gas phase, gas temperature and microwave field at t = 0.01 sec. 2D simulation. P = 500W.

3. 0D MODEL

It was shown in 2D simulations that the electron impact affects the dissociation of *n*-heptane only during a short time period (<10^{-3} sec), when the gas temperature is below 1000 K. Over the longer time periods *n*-heptane is dissociated thermally. According to modern views, the soot formation includes the stages: decomposition of the starting hydrocarbon into a variety of radicals and stable molecules, the formation of molecular precursors of the soot from these fragments, surface growth and coagulation of precursors.

The mechanism for *n*-heptane pyrolysis is published previously in [11, 12]. Acetylene is the most important in the formation of soot particles. For the description of pyrolysis of acetylene, we used a mechanism published by Wang and Frenklach in [13].

It is currently believed that the formation of precursors of soot particles (nuclei) comes from polyaromatic hydrocarbons (PAH) in reactions with acetylene and other hydrocarbons. According to the well-known HACA mechanism (an acronym for "H-abstraction-C_2H_2-addition"), the growth of molecules occurs when the sequence of two stages is repeated: detachment of the H-atom from the molecule of PAH due to collision with other H-atom and addition of the molecule C_2H_2 from the gas phase to the vacant site.

3.1. Nucleation. The linear and planar mechanisms of the molecular precursor size growth are shown in Figs. 5 and 6. In our linear model, we followed the growth mechanism of precursors (Fig. 5) offered in [14]. In this mechanism, two molecules of acetylene compose a new ring in two stages (R1-R2), described by the overall reaction (R3). Here we denote the line-structured molecule consisted of i PAH rings by A_i symbol. Reaction (R3) is used further in the surface growth mechanism of solid particles.

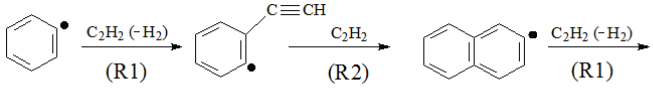

$$\begin{cases} A_1\bullet + C_2H_2 \rightarrow A_1C_2H\bullet + H_2 & (R1) \\ A_1C_2H\bullet + C_2H_2 \rightarrow A_2\bullet & (R2) \end{cases}$$

$$A_i + 2C_2H_2 \rightarrow A_{i+1} + H_2 \qquad (R3)$$

Figure 5. Two-stage linear mechanism (R1)-(R2) for molecular precursor size growth [14]

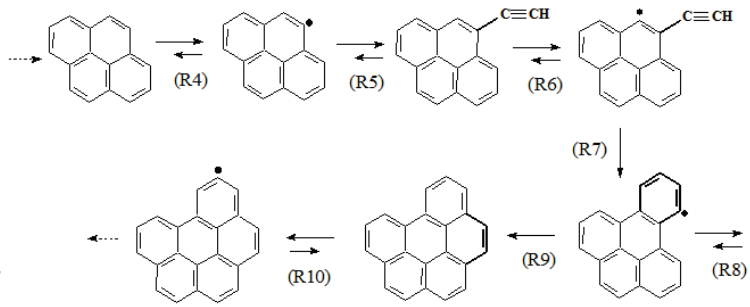

$$\begin{cases} P_4 + H \rightleftharpoons P_4\bullet + H_2 & (R4) \\ P_4\bullet + C_2H_2 \rightleftharpoons P_4C_2H + H & (R5) \\ P_4C_2H + H_2 \rightleftharpoons P_4C_2H\bullet + H_2 & (R6) \\ P_4C_2H\bullet + C_2H_2 \rightarrow P_5\bullet & (R7) \\ P_5\bullet + H_2 \rightleftharpoons P_5 + H & (R8) \\ P_5\bullet + C_2H_2 \rightarrow P_6 + H & (R9) \\ P_6\bullet + H_2 \rightarrow P_6 + H & (R10) \end{cases}$$

$$P_i + 3C_2H_2 \rightarrow P_{i+2} + 2H_2 \qquad (R11)$$

Figure 6. Planar mechanism for molecular precursor size growth via the HACA reaction sequence. Reactions (R4)–(R7) represent a two-stage composing of the first aromatic ring affiliated to pyrene and reaction (R9) represents a one-stage ring-closure of an armchair bay.

For our planar PAH growth model we developed the following chemical growth of soot precursors (Fig. 6) via the HACA reaction sequence (R4-R10) with an appropriate brutto reaction (R11). We denote the plane-structured molecule consisted of *i* PAH rings by P_i symbol.

The kinetic scheme for the *n*-heptane and acetylene pyrolysis is supplemented by appropriate gas phase reactions of the two-stage mechanism (R1) and (R2) for each of A_2–A_8 molecules in the linear model. For the planar model the appropriate gas phase reactions of the three-stage mechanism (R4)–(R10) for each of P_2–P_8 molecules are added.

The mechanism of the molecular precursor size growth is shown in Fig. 7.We assume that A_8 and P_8 are no longer gas molecules, but solid precursors, which from now enlarge their sizes by participating in the surface growth and coagulation processes.

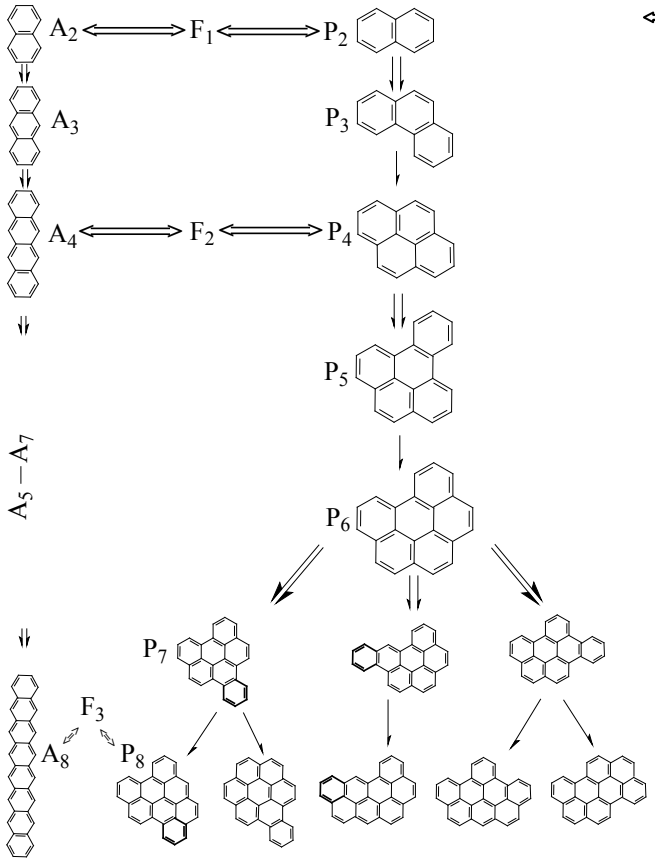

⇐ **Figure 7.** Linear (A2–A8) and planar (P2–P8) mechanisms for molecular precursor size growth of soot precursors. The symbol F*i* is used in both models, where index *i* gives a number *N* of benzene rings in the molecule: $N = 2^i$. Single and double arrows correspond to one-stage and two-stage processes.

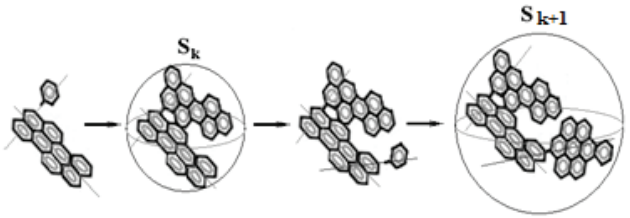

Figure 8. Planar mechanism for the surface growth of a solid soot particle. Two 8-ring plates are growing at different angles to the initial plane precursor via the HACA reaction sequence, forming a 3D solid molecule. S_k and S_{k+1} are the surface areas of a molecule with one and two attached 8-ring plates.

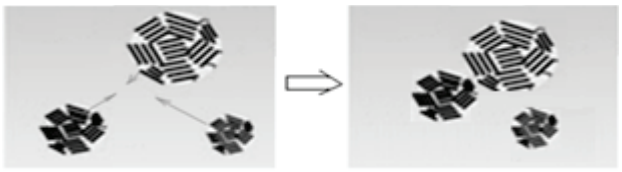

Figure 9. Coagulation scheme of solid molecules of different number PAH rings and plates.

3.2. Surface growth and coagulation of new-phase particles. The surface of the soot particle is considered as the edge of a large PAH molecule covered with C–H bonds. This assumption determines the nature of the active centers, which interact with acetylene molecules from the gas phase, and makes it possible to calculate the growth rate of the particle surface (Fig. 8).

We describe [14, 15] the size growth of molecules, which consist of large number of aromatic rings by a partial differential equation $\frac{\partial f(x,t)}{\partial t} = -\frac{\partial}{\partial x}\left[K''(x)\, n_A(t)\, f(x,t)\right]$, where x is the number of aromatic rings in a particle; $f(x,t)$ is the nonstationary size distribution function of soot particles; $n_A(t)$ is the concentration of acetylene; $K''(x) = K_{het}(x) \cdot S(x)$ is rate constant for heterogeneous regime; $K_{het}(x)$ is the rate constant for acetylene decay on the nucleus surface $S(x)$. Since the soot size range is wide enough, we choose the average size x of groups to be equal to 2^m and hence have: $f(x,t) \to F(m,t)$, m = 4, 5, …, N, where N is the number of the group with the largest size. Choosing N = 20 we can describe the change in particle concentration for systems containing up to 2^{20} aromatic rings, or about 4×10^6 carbon atoms, i.e. to account for practically the whole size range of soot particles. A single rate expression for the planar growth process is: $K_{het}(x) = \frac{K_2 K_1 \cdot [H]}{K_{-1} \cdot [H_2] + K_2 \cdot [C_2H_2]}$, where K_1, K_{-1} correspond to direct and inverse rate coefficients of reaction (R4), K_2 is a recalculated direct rate coefficient of reaction (R5).

The coagulation process describes the coalescence of two soot particles with different number of rings (Fig. 9). The coagulation terms in the mass balance equation for groups F_i of particle sizes 2^i are: $\left(V_r \frac{dF_i}{dt}\right)_{co} = V_r \cdot 0.5 \cdot K_{i-1,i-1} \cdot F_{i-1}^2 + V_r \cdot 0.75 \cdot K_{i-1,i-2} \cdot F_{i-1} \cdot F_{i-2} + V_r \cdot F_i \cdot \sum_{m=N'}^{i-2} A_{mi} \cdot K_{mi} \cdot F_m - V_r \cdot F_i \cdot \sum_{m=i-1}^{20} \psi \cdot K_{mi} \cdot F_m$. The first generation term is due to the coalescence of two soot particles with i-1 rings: $F_{i-1} + F_{i-1} \rightarrow F_i$, the second term corresponds to the process: $F_{i-1} + F_{i-2} \rightarrow F_i$, the third term describes the coalescence of all soot particles with numbers of rings in range $m = N', \cdots, i\text{-}2$: $F_{N'} + \cdots + F_{i-2} \rightarrow F_i$, the forth term is the loss of F_i particle in all coalescence processes. Details can be found in [15].

3.3. System of equations. A full set of balance equations for each component of the gas phase and solid products has been solved numerically. The kinetic simulations have been implemented using COMSOL Multiphysics - Reaction Engineering Laboratory [16]. The processes take place inside a spherical bubble, which is regarded as a continuous stirred tank reactor (CSTR) of constant pressure and volume with continuous input of gaseous *n*-heptane, which evaporates into the bubble from the external liquid.

3.4. Results of 0D model. The simulation results (Figs. 10, 11) are compared with known experimental data (Tab.1).

Table 1. Contents of main gas products generated in microwave plasma in liquid n-heptane. Chromatography data.

H_2 [vol.%]	C_2H_2 [vol.%]	C_2H_4 [vol.%]	CH_4 [vol.%]
71	18	8	3

It is concluded that the planar PAH growth model is better in describing the experimental results.

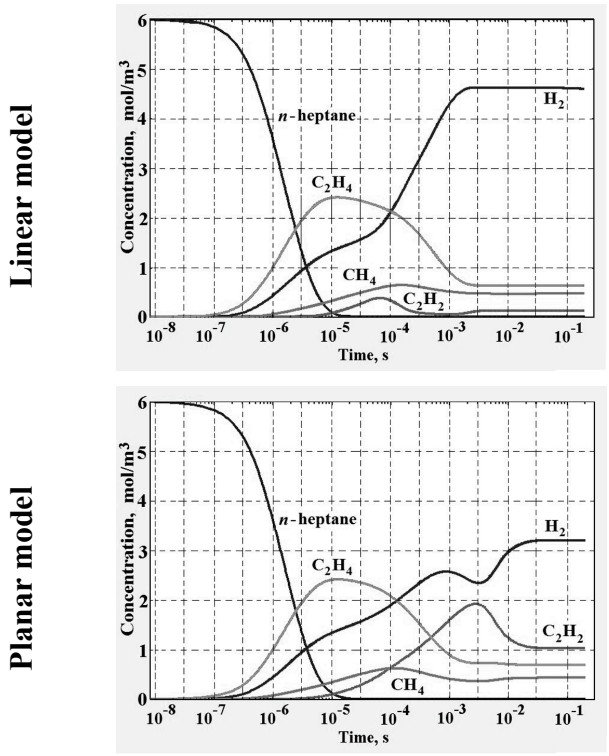

Figure 10. Evolution of gas phase products for the linear and planar models. Pyrolysis of *n*-heptane at T = 1500 K, p = 1 atm. 0D simulation.

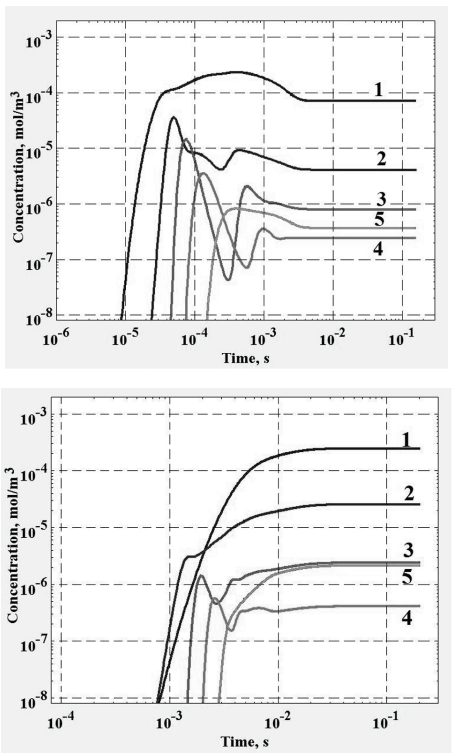

Figure 11. Evolution of solid products for the linear and planar models. Concentrations of soot particles F_i: 1—F_4; 2—F_8; 3—F_{12}; 4—F_{16}; 5—F_{20}. The same 0D simulation.

4. 1D MODEL: PROBLEM FORMULATION AND MAIN RESULTS

The code is based on joint solution of the heat conduction equation, the balance equation for the electron density in a singly ionized plasma, the Boltzmann equation for free electrons of the plasma, the balance equations for the weight fraction for all gas and solid products of *n*-heptane pyrolysis (with shortened

kinetics for gas particles and the planar PAH growth mechanism for solids) and a simplified equation for the microwave field (i.e. a field in a spherical capacitor filled with plasma). In Fig. 12 the radial profiles of physical parameters inside the plasma bubble are shown for two typical times.

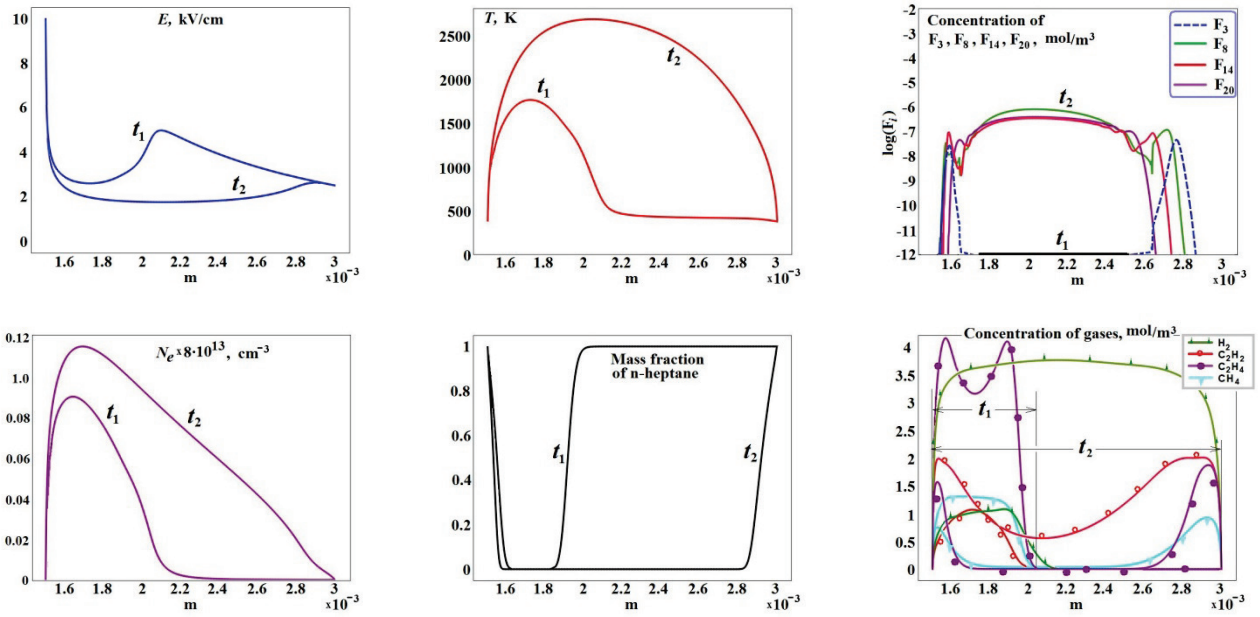

Figure 12. 1D simulation. Intermediate (t_1=0.001 sec) and stationary (t_2=0.006 sec) radial profiles of physical parameters inside the plasma bubble. From left to right top to bottom: E – microwave field; T – gas temperature; F_3, F_8, F_{14}, F_{20} – soot particles with different number of aromatic rings; N_e – electron density; mass fraction of n-heptane; mole fractions of gas products H_2, C_2H_2, C_2H_4, CH_4.

The results of the simulations are the following:

- Shortened kinetic scheme gives a good match with the full scheme.
- The average temperature inside the bubble is about 2100 K, and is close to the measured value.
- The one-dimensional model made it possible to combine hydrodynamic calculations of the two-dimensional model and detailed kinetics of the zero-dimensional model taking into account the solid phase. This allowed us to obtain a good agreement on the experimental values of T, E and the relative content of the decomposition products.

References

1. Nomura S., Toyota H., Appl. Phys. Lett., 2003, **83**, 4503.
2. Nomura S., Toyota H., Tawara M., Yamashota H., Appl. Phys. Lett., 2006, **88**, 231502.
3. Nomura S., Toyota H., Mukasa S., Yamashita H., Maehara T., Appl. Phys. Lett., 2006, **88**, 211503.
4. Toyota H., Nomura S., Takahashi Y., Mukasa S., Diamond & Related Materials, 2008, **17**, 1902.
5. Lebedev Yu.A., Konstantinov V.S., et al., High Energy Chem.. 2014, **48**, 385.
6. Buravtsev N.N., Konstantinov V.S., et al., Microwave Discharges: Fund. & Appl. (Proc. VII Int. Workshop, 10-14 September 2012, Zvenigorod, Russia), Ed. by Lebedev Yu.A., Moscow: Yanus K.
7. Richter H, Howard J.B., Prog. Energy Combus. Sci., 2000, **26**, 565.
8. Frenklach M., Phys. Chem. Chem. Phys., 2002, **4**, 2028.
9. Lebedev Yu.A., Tatarinov A.V., Epstein I.L., Plas. Chem. Plas. Processes, 2016, **36**, 535.
10. Lebedev Yu.A., Tatarinov A.V., Epstein I.L., Plasma Phys. Reports, 2017, **43**, 510.
11. https://combustion.llnl.gov/mechanisms/alkanes/n-heptane-detailed-mechanism-version-3
12. Curran H.J., Gaffuri P., Pitz W.J., Westbrook C.K., Combust. Flame, 1998, **114,** 149.
13. Wang H., Frenklach M., Combust. Flame, 1997, **110**, 173.
14. Merkulov A.A., Ovsyannikov A.A., Polak L.S. et al., Plas. Chem. Plas. Processes, 1989, **9**, 95.
15. Epstein I.L., Lebedev Yu.A., Tatarinov A.V., Bilera I.V., J. Phys. D: Appl. Phys., 2018, **51**, 214007.
16. COMSOL Multiphysics www.comsol.com/chemical-reactionengineering-module

APPLICABILITY OF TRIPLET-STATE EMISSION OF MOLECULAR HYDROGEN FOR SPECTRAL DIAGNOSTICS OF THE GAS DISCHARGES

V. A. Shakhatov, Yu. A. Lebedev, S. Béchu[1], A. Lacoste[1]

A. V. Topchiev Institute of Petrochemical Synthesis of the Russian Academy of Sciences (TIPS RAS), Leninsky Prospect, 29, Moscow, 119991, Russia
[1]Centre de Recherché, Plasma-Materiaux-Nanostructures (CRPMN), Grenoble, France

Abstract. Study of kinetics of the singlet and triplet states population of hydrogen molecule is directly connected with the justification of diagnostics of nonequilibrium plasma by the method of optical emission spectroscopy and optical actinometry. We briefly consider the approach to development of the zero-dimension hydrogen collision-radiative model, which in addition to kinetic models of vibrational states population kinetics of hydrogen molecule takes into account singlet and triplet excited states, and electron states of hydrogen atom. The model is based on the analysis of a large number of known experimental data which, among other things, are used to verify the model. The model is used for investigating the possibility of using emission of triplet hydrogen states for diagnostics of nonequilibrium DC discharges, microwave discharges, and ECR discharge. In particular, the limitations are shown on the applicability of the simplified coronal plasma model for the diagnostics of these discharges by the frequently used emission of the Fulcher system bands.

1. INTRODUCTION

The study of molecular spectra in nonequilibrium hydrogen plasma allows obtaining information on the plasma parameters (degree of the molecule dissociation, the gas (translational) temperature T_g, the electric (reduced) field amplitude E (E/N), the vibrational distribution function (VDF) of molecules in the ground electronic state, the electron number density N_e and temperature T_e et. al.) using known collisionally-radiative characteristics of molecules (factors of the Franck-Condon, cross sections et. al.) in simplified coronal model [1−4].

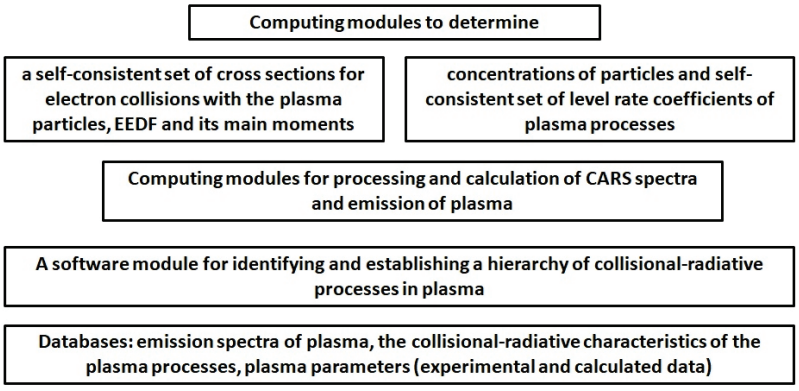

Figure 1. Schematic diagram of the zero-dimensional level-to-level semi-empirical collisional-radiative model.

It is based on the assumption that the radiating state is excited by electron impact from the ground state, and that is deactivated by radiation. The presence of additional collisional-radiative secondary processes that determine the excitation and deactivation of the emitting states of the molecule leads to the failure of this assumption renders impossible the use of a simplified coronal model. In general, problem of identification and analysis of the secondary processes in the mechanisms of the electronic state molecule excitation remains poorly understood.

Table. Comparison of the calculated $T_v^{th}\left(X^1\Sigma_g^+\right)$ and measured $T_v^e\left(X^1\Sigma_g^+\right)$ values of the vibrational temperature. DCGD is the direct-current glow discharge, RFD is a radio-frequency discharge, TECMFD is a thermal-emission cathode in a magnetic field, MD is a microwave discharge, HCD is a hollow-cathode discharge, PGD is a pulsed glow discharge, ECRD is a electron cyclotron resonance discharge.

Discharge;	p (Torr);	N_e (cm^{-3});	T_g (K);	$T_v^e\left(X^1\Sigma_g^+\right)$ (K)	$T_v^{th}\left(X^1\Sigma_g^+\right)$ (K)	References
DCGD	15	1.5×10^{10}	600(±50)	1800-2300 (±50)	1800 - 2600	[5]
DCGD	0.9	3.7×10^{9}	530		1100	[6]
DCGD	0.3	5.3×10^{9}	410		1600	[7]
DCGD	0.3	1.2×10^{10}	360		1500	[8]
DCGD	2.5	6.5×10^{10}	550		3000	[9]
RFD	2.0	$10^{10} – 10^{12}$	330(±20)		<2000	[10, 11]
RFD	1.5	$10^{10} – 10^{12}$	540(±120)	3400 (±540)	3100	[12, 11]
RFD	8.0	$10^{10} – 10^{12}$	750(±50)	2700 (±420)	2700	[12, 11]
TECMFD	2×10^{-2}	10^{11}	370(±50)	1600 (±100)	1700	[13−15]
TECMFD	3×10^{-2}	5.7×10^{11}	470(±50)	1780 (±100)	1800	[16−18]
MD	19	9.3×10^{11}	2150	2350 (±400)	2700	[19, 20]
MD	1.0	10^{11}	550		3000	[1, 2]
MD	8.0	10^{11}	800		3400	[1, 2]
HCD	0.1	5.4×10^{10}	410(±50)	2400 (±100)	2400	[21]
PGD	760	10^{14}	310		3580	[22]
ECRD	2×10^{-3}	1.6×10^{10}	550(±100)	3050 (±550)	2600	[3, 23−26]
ECRD	9.6×10^{-3}	3.1×10^{10}	400		3000	[23−26]
ECRD	2×10^{-3}	5.9×10^{10}	400		1750	[23−26]

A detailed discussion on the self-consistent collisional-radiative models nonequilibrium hydrogen plasma in the zero approximation is presented in [4]. In the majority of the studies devoted to the development of the zero-dimensional plasma models, the analysis is restricted to considering collisional-radiative processes involving $H_2\left(X^1\Sigma_g^+,v=0\text{-}14\right)$, hydrogen atoms in the $1s\text{-}^2S_{1/2}$ ground state and in excited states, electrons, and negatively and positively charged atomic ions and molecular compounds. For a number of the electron-excited states, the kinetics of processes involving them is taken into account only in solving the kinetic transport equation for electrons. They are not considered in solving the balance equations for the concentrations of the excited particles. From the above survey of models, it follows that the description of the kinetics of processes proceeding in the hydrogen plasma becomes ever more detailed, but these processes involving hydrogen molecules in triplet and singlet electron states have not yet received adequate study.

The paper is dedicated to the development of the semi-empirical collisional-radiative model of hydrogen low temperature plasma for processing and interpreting the results of absorption and emission spectroscopy, and optical actinometry. This problem is solved by modeling the processes of excitation and deactivation of the singlet and triplet states of hydrogen molecules in DC glow, microwave and an electron cyclotron resonance (ECR) discharges. The limitations are investigated on the applicability of the simplified coronal plasma model for the diagnostics of these discharges by the frequently used emission of the Fulcher system bands.

2. THEORY

In relation to models known from the literature [4], the zero-dimensional level-to-level semi-empirical collisional-radiative model formulated in this section employs an extended kinetic scheme of processes and incorporates a greater number of excited atomic levels and molecular states of interest for emission spectroscopy.

In model, one considers simultaneously kinetic processes involving hydrogen molecules in singlet ($N^1\Lambda_\sigma$=$2B^1\Sigma_u^+$, $2C^1\Pi_u$, $3B'^1\Sigma_u^+$, $3D^1\Pi_u$, $4B''^1\Sigma_u^+$, $4D'^1\Pi_u$, $2EF^1\Sigma_g^+$, $3I^1\Pi_g$, $3HH^1\Sigma_g^+$, $3GK^1\Sigma_g^+$, $3J^1\Delta_g$, $4P^1\Sigma_g^+$,

$4O^1\Sigma_g^+$, $4R^1\Pi_g$, and $4S^1\Delta_g$) and triplet ($N^3\Lambda_\sigma$=$2b^3\Sigma_u^+$, $2c^3\Pi_u$, $2a^3\Sigma_g^+$, $3e^3\Sigma_u^+$, $3d^3\Pi_u$, $3h^3\Sigma_g^+$, $3g^3\Sigma_g^+$, $3i^3\Pi_g$, $4f^3\Sigma_u^+$, $4k^3\Pi_u$, $4r^3\Pi_g$, and $4s^3\Delta_g$) electronic states and hydrogen atoms in the ground $\left(1s\text{-}^2S_{1/2}\right)$ and metastable $\left(2s\text{-}^2S_{1/2}\right)$ states and in $nl\text{-}^2L_J$ (l=s,p,d....) electron-excited levels under the assumption of resolved electron principal quantum numbers n=2−6, total orbital angular momenta L=S,P,D,F,G, and angular momenta J=1/2-2/9.

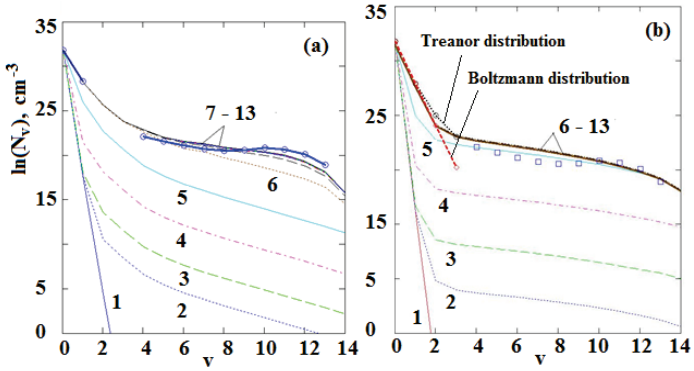

Figure 2. Results of calculating (curves) and measuring (symbols) the VDF of the hydrogen molecule in the ground state at different instants (1−4 from 10^{-19} to 10^{-9} s, 5 – 10^{-7}, 6 – 10^{-6}, 7 – 10^{-5}, 8 – 3×10^{-5}, 9 – 6×10^{-5} s, 10−13 for $\tau_D = 9\times10^{-5} - 2\times10^{-4}$ s) for the experimental conditions [13−15] (see Table): (a) − conventional kinetic scheme of the hydrogen molecule vibrational excitation through singlet states; (b) – this study.

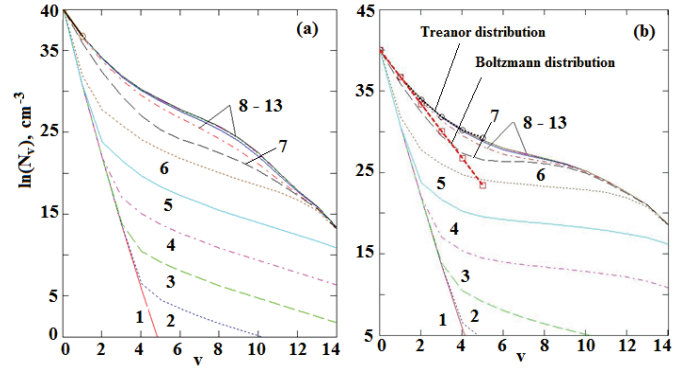

Figure 3. Results of calculating (curves) and measuring (symbols) the VDF of the hydrogen molecule in the ground state at different instants (1 – 10^{-19} s, 2 – 10^{-13}, 3 – 10^{-11}, 4 – 10^{-9}, 5 – 10^{-7}, 6 – 10^{-6}, 7 – 3×10^{-3} s, 8−13 for $\tau_D = 5\times10^{-3} - 0.4$ s) for the experimental conditions [5] (see Table): (a) − conventional kinetic scheme of the hydrogen molecule vibrational excitation through singlet states; (b) – this study.

The schematic diagram of the model is illustrated in Fig. 1. This model is semi-empirical, and its implementation requires knowing experimental data on plasma parameters (gas pressure p and temperature T_g, electric-field strength, electron concentration, and electron energy distribution function (EEDF) in a number of cases). The experimental databases are used to test and to develop the model. In particular, the calculation and processing of coherent anti-Stokes scattering spectra and spectra of radiation from hydrogen plasma are used to determine the translational and rotational temperatures, the distributions with respect to rotational and vibrational levels of hydrogen molecules both in the $X^1\Sigma_g^+$ ground state and in excited states, and the distribution of atoms with respect to energy levels.

The rate constant for relevant processes and their cross sections were set to values chosen based on an analysis of a vast amount of data from computations and experimental data. In model, the approaches that are discussed in [4] are used to determine EEDF and its basic moments, concentrations of particles in excited states, and a self-consistent set of level cross sections and rate constants for the processes being considered.

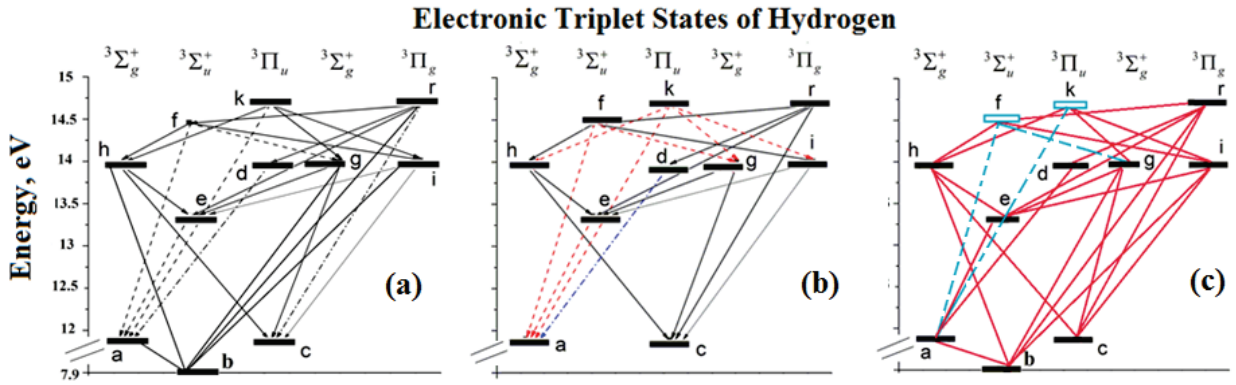

Figure 4. The schemes of the dipole-allowed transitions between the hydrogen molecule triplet states in the different discharges (see table): (a) – DCGD; (b) – MD; (c) – ECRD.

The importance of processes that lead to the population of emitting atomic levels and molecular states was analyzed based on comparing their characteristic times. This made it possible to establish the hierarchy of collisional-radiative processes.

The kinetic equations for electrons and the balance for particle concentrations are integrated by the gas residence time τ_D in the discharge zone.

3. RESULTS

The Table illustrates the model input data (the gas pressure p, the electron number density N_e, the gas temperature T_g et. al.) in the study of the hydrogen molecule excitation kinetics in discharges. It presents the results of the model testing: comparison of the values of the vibrational temperature of the hydrogen molecule in the ground electronic state calculated $T_v^{th}\left(X^1\Sigma_g^+\right)$ by the model and measured $T_v^e\left(X^1\Sigma_g^+\right)$ in these discharges.

The determined self-consistent set of level rate coefficients of the processes satisfactorily reproduces the measured values of the vibrational temperature and the vibrational distribution functions of the hydrogen molecule in the ground electronic state (see Figs. 2 and 3).

The populations of the hydrogen molecule in the $X^1\Sigma_g^+$ state that are calculated for the discharge conditions from [5−26] decrease monotonically as the vibrational-level number v increases from 4 to 14. We note that the VDF calculated for the hydrogen molecule in the ground state describes satisfactorily its counterpart measured in [13−15] for all values of the vibrational-level number in the range of v=0-14 (Fig. 2). The extended kinetic scheme of model with allowance for processes involving a hydrogen molecule in the $N^1\Lambda_\sigma$ singlet states made it possible to find out how these processes form VDF for a hydrogen molecule in the $X^1\Sigma_g^+$ state, depending on gas-discharge conditions and the time of gas residence in the discharge zone [27, 28]. The inclusion of processes involving hydrogen molecules in excited singlet states in the model can lead to a decrease in the vibrational relaxation time in comparison with that obtained using the usual approach:

$$H_2\left(X^1\Sigma_g^+,v\right)+e\rightarrow H_2\left(B^1\Sigma_u^+,C^1\Pi_u\right)+e\rightarrow H_2\left(X^1\Sigma_g^+,v'\right)+e+h\nu\,.$$

The calculations reveal that the effect of these processes on the population of $X^1\Sigma_g^+,v>3$ states is especially pronounced in a pulsed glow discharge [22], a discharge at a thermal-emission cathode in a magnetic field [13−18] (see Fig. 2), a hollow-cathode discharge [21], a microwave [1, 2, 19, 20] and ECRD [23–26]. In PC of DCGD [5], this effect is minimal (see Fig. 3). This is due to the difference in the degree of vibrational-translational disequilibrium (distinction between the vibrational and gas temperatures), the electron concentration, and EEDF in gas discharges. It has already been indicated that, under the conditions described in [13−26], EEDFs have a bi-Maxwellian form enriched in electrons at

energies in the range where the thresholds for the electron-impact-induced excitation of singlet states of the hydrogen molecules lie (≈ 11 – 15 eV). As for a microwave discharge [1, 2, 19, 20] and a pulsed glow discharge [22], the difference here stems from a high electron concentration in it.

Figure 4 illustrates the schemes of the dipole-allowed transitions between the hydrogen molecule triplet states. It explains applicability of the simplified coronal model for processing spectral data obtained in the PC of the DCGD, the MD and the ECRD (see Table).

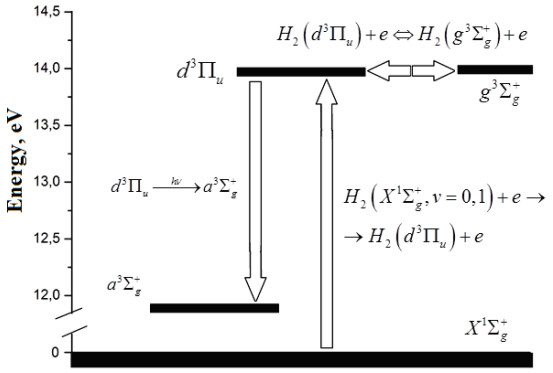

Figure 5. Processes of the excitation and deactivation of the $d^3\Pi_u$ triplet state of the hydrogen molecule in discharges.

The black solid lines indicate transitions that the simplified coronal model cannot be used for spectral data processing in a wide range of changing parameters of the discharges. It is due to the high role of the secondary processes in the kinetics of the excitation and deactivation of the upper radiating triplet states $2c^3\Pi_u$, $2a^3\Sigma_g^+$, $3h^3\Sigma_g^+$, $3g^3\Sigma_g^+$, $3i^3\Pi_g$. The secondary processes at times $\tau_D > 10^{-9}-10^{-8}$ s play an important role in the mechanisms of the excitation and deactivation of the singlet and triplet states of hydrogen molecule. As a consequence stationary distributions of populations of the hydrogen molecules in the singlet and triplet states are markedly different from Boltzmann distribution.

Composition, number and hierarchy of the secondary processes depend on the test conditions and time residence of gas τ_D in the discharge zone. They differ from one state to another and require analysis for each state separately.

The secondary processes give the least contribution to the excitation and deactivation of triplet states: $3e^3\Sigma_u^+$, $4k^3\Pi_u$, $3d^3\Pi_u$, $4r^3\Pi_g$ and $4f^3\Sigma_u^+$ in the PC of the DCGD; $3e^3\Sigma_u^+$, $4k^3\Pi_u$, $3d^3\Pi_u$, $4r^3\Pi_g$ and $4f^3\Sigma_u^+$ in the MD; $4k^3\Pi_u$ and $4f^3\Sigma_u^+$ in the ECRD. The dotted lines indicate transitions that the simplified coronal model is recommended for spectral data processing in the wide range of the discharge parameters. The dash-dotted lines indicate transitions that the simplified coronal model can also be used for spectral data processing in a limited range of the discharge parameters.

The results of the analysis of the mechanism of the excitation and deactivation of the $3d^3\Pi_u$ triplet state are particular interest.

The Fulcher system is often used in the spectral diagnostics of the discharges in hydrogen. Figure 5 gives the block diagram of the processes of excitation and deactivation of the $3d^3\Pi_u$ triplet state in the discharges. The simplified coronal model application is true for the spectral diagnostics: PC of the DCGD at p = 0.3–2.5 Torr, E/N = 65–130 Td and $N_e = 1.2\times10^{10} - 6.5\times10^{10}$ cm^{-3}; MD at p <1 Torr, E = 60–200 V/cm and $N_e = 10^8–10^{11}$ cm^{-3}. The simplified coronal approximation is not valid: PC of the DCGD at p=2.5–15 Torr, E/N = 30–65 Td, $N_e = 4.0\times10^9–1.2\times10^{10}$ cm^{-3}; MD at p > 8 Torr, E = 60–200 V/cm, $N_e = 10^8–10^{11}$ cm^{-3}. It is due to that the intensive energy exchange between triplet state $3d^3\Pi_u$ and $3g^3\Sigma_g^+$ caused by collisions of electrons with these excited hydrogen molecules

$$H_2\left(3d^3\Pi_u\right)+e \Leftrightarrow H_2\left(3g^3\Sigma_g^+\right)+e$$

limits the use of the simplified coronal model for spectral diagnostics of the stationary discharges in the hydrogen.

Acknowledgments

This work was carried out within the State Program of TIPS RAS.

References

1. Lebedev Yu.A., Mokeev M.V., Plasma Phys. Rep., 2000, **26**, 272.
2. Lebedev Yu.A., Mokeev M.V. Plasma Phys. Rep., 2001, **27**, 418.
3. Shakhatov V.A., Lebedev Yu.A., Lacoste A., Bechu S., High Temp., 2016, **54**, 467.
4. Shakhatov V.A., Lebedev Yu.A., J. Phys. D: Appl. Phys., 2018, **51**, 213001.
5. Shirley J.A., Hall R.J., J. Chem. Phys., 1977, **67**, 2419.
6. Slovetskii D.I. Mechanisms of Chemical Reactions in Non-Equilibrium Plasmas, Moscow: Nauka, 1980 (in Russian).
7. Amorin J., Loureiro J., Baravian G., Touzeau M., J. Appl. Phys., 1997, **82**, 2795.
8. Berdichevskii M.G., Marusin V.V. Izv. Sib. Otd. Akad. Nauk SSSR, 1982, **1**, 28 (in Russian).
9. Brovikova I.N., Galiaskarov E.G., Rybkin V.V., Bessarab A.B. High Temperature, 1998, **36**, 842.
10. Shakhatov V.A., de Pascale O., Capitelli M., European Physical Journal D: The Atoms, Molecules, Clusters and Optical Physics, 2004, **29**, 230.
11. Shakhatov V.A., Gordeev O.A., Optics and Spectroscopy, 2007, **103**, 468.
12. Shakhatov V.A., de Pascale O., Capitelli M., Hassouni K., Lombardi G., Gicquel A., Physics of Plasmas, 2005, **12**, 5436.
13. Wagner D., Dikmen B., Dobele H.F., Plasma Sources Sci. Technol., 1998, **7**, 462.
14. Mosbach T., Katsch H.M., Dobele H.F., Phys. Review Letters, 2000, **85**, 3420.
15. Mosbach T., Plasma Sources Sci. Technol., 2005, **14**, 610.
16. Pealat M., Taran J.-P.E., Bacal M., Hillion F., J. Chem. Phys., 1985, **82**, 4943.
17. Pealat M., Taran J.-P.E., Bacal M., Proc. 16th Int. Conf. on Phenomena in Ionized Gases (ICPIG), Düsseldorf, 1983, 297.
18. Lefebvre M., Pealat M., Taran J.-P.E., Pure Appl. Chem., 1992, **64**, 685.
19. Scott C.D., A Technical Memorandum, 1993, 104765 (NASA).
20. Carl D.S., Farhat S., Gicquel A., Hassouni K., Lefebvre M., J. Thermophys. Heat Tran., 1996, **10**, 426.
21. Shikama T., Kado S., Kuwahara Y., Kurihara K., Scotti F., Tanaka S., Plasma Fusion Res., 2007, **2**, 1045.
22. Amirov R.Kh., Asinovskii E.I., Markovets V.V., Teplofiz. Vys. Temp., 1984, **22**, 1002 (in Russian).
23. Bechu S., Soum-Glaude A., Bes A., Lacoste A., Svarnas P., Aleiferis S., Ivanov A.A., Bacal M. Jr., Phys. Plasmas, 2013, **20**, 101601.
24. Svarnas P., Annaratone B.M., Bechu S., Pelletie J., Bacal M., Plasma Sources Sci. Technol., 2009, **18**, 045010.
25. Lacoste A., Lagarde T., Bechu S., Arnal Y., Pelletier J., Plasma Sources Sci. Technol., 2002, **11**, 407.
26. Lacoste A., Bechu S., Maulat O., Pelletier J., Arnal Y., Plasma Sources Sci. Technol., 2009, **18**, 015017.
27. Shakhatov V.A., Lebedev Yu.A., Lacoste A., Bechu S., High Temp., 2016, **54**, 123.
28. Shakhatov V.A., Lebedev Yu.A., Lacoste A., Bechu S., High Temp., 2015, **53**, 569.

A PORTABLE COLD MICROWAVE PLASMA TORCH: THE LARGE-AREA SURFACE TREATMENT DESIGN AND PROBE MEASUREMENTS

S. Antipov, A. Chistolinov, V. Chepelev, M. Gadzhiev

Joint Institute for High Temperatures of the Russian Academy of Sciences, Izhorskaya Str., 13, Bld. 2, Moscow, 125412, Russia

Abstract. We present a new atmospheric-pressure non-thermal microvawe plasma generator (plasmatron) that intended for large-area surface treatment of delicate organic and non-organic materials such as textiles, polymers, biological objects, etc. The prototype of the generator was produced on the base-type low-power microwave plasma source by SPE "AgroEcoTech" LLC (Obninsk, Russia) and was assembled and launched this year in JIHT RAS laboratory. The plasmatron combines many advantages such as small size and weight, easy handling and low cost. It has flexible open architecture design friendly for maintenance and further modernization. The probe measurements were made in the cold afterglow plasma generated in Ar plasma jet by electrode torch device. The probe floating potentials and I-V probe characteristics were obtained and plasma density was estimated.

1. INTRODUCTION

At the present time the possibility of using atmospheric cold plasma jets is actively investigated in applications for plasma-chemical treatment of surfaces of various materials in such industries as practical medicine, microbiology, agriculture and food industry [1–3]. The interest is due to the fact that in such jets non-equilibrium "streaming-afterglow" plasma is generated and excited particles and radicals with high reactivity are produced. At that, the temperature of the gas flow in the jet can be reduced to almost room temperature, which does not have a destructive effect on a material during processing. This combination of low temperatures and a high reactivity of plasma particles makes cold plasma jets technologically advantageous and effective tool in the above-mentioned industries. And of course, the convenience of using such jets is now seemed obvious, since plasma jets allow to treat a surface of objects of various shapes and sizes outside a closed discharge chamber.

The effect of the plasma jet on a surface is complex and includes the following main factors: UV radiation, chemically active particles, and charged-particle impact. By selecting an appropriate set of processing parameters, it is possible to carry out technological processes such as plasma cleaning, plasma surface activation, plasma deposition and plasma etching.

A special place among the sources of non-equilibrium atmospheric pressure plasma is occupied by microwave discharges of both electrode and electrode-free types. Cold plasma jets based on microwave discharges has a much higher charge density and, as a consequence, greater reactivity compared to other types of discharges at the same energy input. A microwave discharge initiated in molecular gases lead to effective dissociation of molecules and generation of active radicals.

Despite the fact that the use of plasma jets of atmospheric pressure microwave discharges is constantly broadened out and new opportunities for plasma processing are opened up, methods for diagnostics and properties of "streaming-afterglow" plasma are still insufficiently studied and remain uncertain. This makes it difficult to study the mechanisms of modification of the surface properties of materials being processed and, in general, hinders the development of plasma processing technologies. It should also be noted that for many plasma technologies, an important characteristic of a plasma source device (plasmatron) is the area of the surface that can be processed by the plasma jet. The size of the outlets of most existing plasmatron burners (torches) is less than 1 cm in diameter. For surface treatment of a large area, various "tricks" are used: processing with "matrix" (or module) consisting of several burners (micro-plasmas arrays [3]), or surface "scanning" by one burner. However, such approaches are

inconvenient, and can hardly be attributed to technological advantages. The prototype of the multi-purpose microwave plasmatron, assembled and launched at present, has a discharge chamber with an outlet of 2.5 cm in diameter with the possibility of increasing the size of the torch outlet by using nozzles of various configurations. This work is devoted to study of characteristics of the plasmatron.

2. EXPERIMENTAL INSTALLATION

The developed microwave plasmatron allows initiating microwave discharges of atmospheric pressure with a frequency of 2.45 GHz both in the rectangular metal waveguide with a power range from 0 to 2.5 kW (electrodeless discharge) and in the remote portable torch with electrode discharge of a power of up to 200 W (Fig. 1). The prototype was produced on the base-type low-power microwave plasma source by SPE “AgroEcoTech” LLC (Obninsk, Russia) [9, 10]. One of the main differences of the produced plasmatron from the base model is a sectional waveguide design (three sections), with the possibility of replacing the middle section for connecting discharge devices of various designs. So, the microwave plasmatron includes the following components (Fig. 2):

- high-voltage three-phase power supply,
- microwave unit, including water-cooled magnetron,
- sectional waveguide system with two sets of flanges with gaskets and with splitter and load,
- 50 ohm coaxial cable with a length of 2 m and two N-connectors,
- burner (plasma torch) with 6 electrodes in common chamber (Fig. 2).

As already mentioned above, the design of the waveguide system provides the possibility of choosing between two types of microwave discharges. According to the classical scheme, plasma is generated in a discharge tube crossing the resonator (waveguide), and the plasma jet is formed by the flow of gas through the tube. At that temperature of a plasma jet can reach several thousand degrees of K. In our case, it is possible to use discharge tubes with a diameter of up to 4 cm, that, along with mw power, gas composition and gas flow rate, will allow changing the discharge regimes and, as a result, plasma jet parameters. In addition to the classical scheme the portable electrode burner is used, developed to study the plasma of non-destructive ("soft") action at about room temperature on the distance of several centimeters from the outlet of the burner. The microwave power to the burner is withdrawn from the waveguide via a coaxial cable connected to the splitter section. Gas is flown through the burner, and the discharge channels arise between the cylindrical discharge chamber and the six rod-like electrodes inside it (Fig. 3). The burner outlet diameter is 2.5 cm. Air, inert gases, as well as nitrogen and mixtures of argon with nitrogen can be used for plasma generation. Gas flow rate can vary from units to several tens of liters per minute.

Figure 1. Atmospheric pressure microwave plasmatron installation.

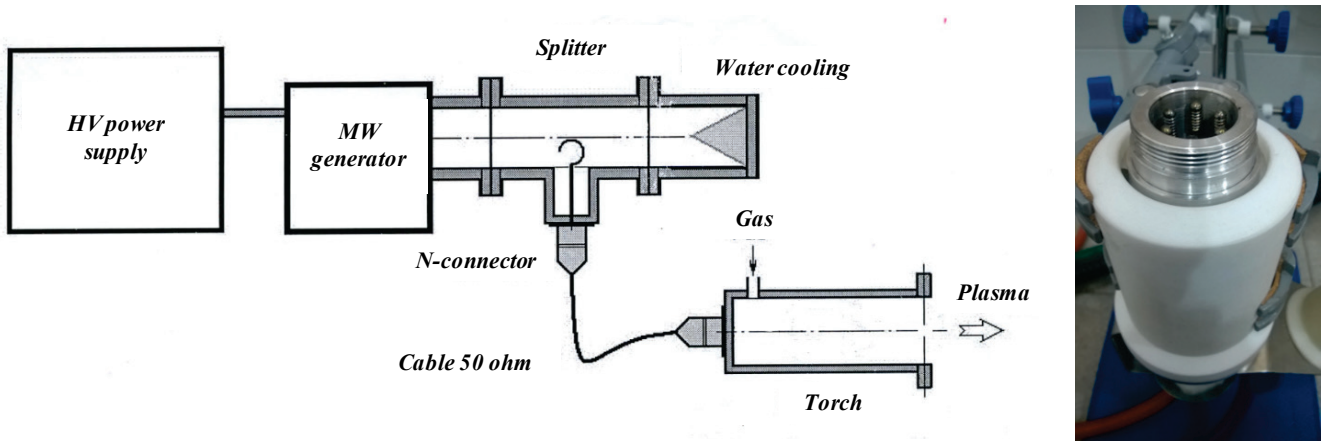

Figure 2. Schematic diagram of the microwave plasmatron with portable discharge torch (left) and view of the torch discharge chamber without a nozzle (right).

The design of the plasma torch provides the possibility of fast replacement of a nozzle after turning off generation of the magnetron. The use of nozzles of various sizes and geometry of metal and non-conducting materials (PTFE, quartz, etc.) allows stabilizing the mw discharge and optimizing plasma jet parameters.

In Fig. 3 an example of burning of the atmospheric pressure microwave discharge in argon in the discharge burner with the straight cylindrical nozzle of 2 cm in height is shown.

It should be noted that the closest analogue of the developed cold mw plasma torch is the low-temperature argon plasma generator MicroPlaSter β by ADTEC Plasma Technology Co. Ltd. [6, 7]. However, the latter is a highly specialized device designed for biomedical applications. As to plasmatron investigated in this work, it is suitable for laboratory investigations and combines many advantages: small size and weight, easy handling and very low cost. But most importantly, our plasmatron has flexible open architecture design friendly for maintenance and modernization.

Further, for the purpose of studying parameters of the cold plasma jet, a planar electrical probe in the form of a disk with a diameter of 1.6 cm was used mounting on an adjustable holder and orienting perpendicular to gas flow direction in the flow center.

3. MEASUREMENTS AND DISCUSSION

To investigate temporal characteristics of plasma generated, oscillograms of floating potential of the probe were obtained (Fig. 3). As can be seen, the generation of plasma in the gas flow is periodic with a frequency of 50 Hz. We believe that such periodicity is due to the power supply and magnetron operation features. Next, let us consider a simplified scheme of operation of a magnetron in order to explain the periodicity detected.

The magnetron power supply unit is designed to generate the necessary voltages driving a magnetron, namely anode voltage and filament voltage. Its main high-voltage elements are: a transformer, a booster capacitor and a diode. The last two elements double the voltage of a high-voltage transformer. Such a high voltage is necessary on the anode of a magnetron for its normal operation. Let us briefly describe the process of voltage doubling. In the first half-cycle a high voltage from the transformer charges the capacitor through the open diode. At that, the voltage on the magnetron is zero since the open diode shunts it. In the second half-period the diode is closed, the capacitor voltage is applied to the magnetron and the voltage of the negative half-period of the high-voltage winding of the transformer is added as well. These two voltages are summed and create a high operating voltage on the magnetron. When a sufficient voltage is reached on the magnetron anode, the magnetron starts operating at a frequency of 2.45 GHz.

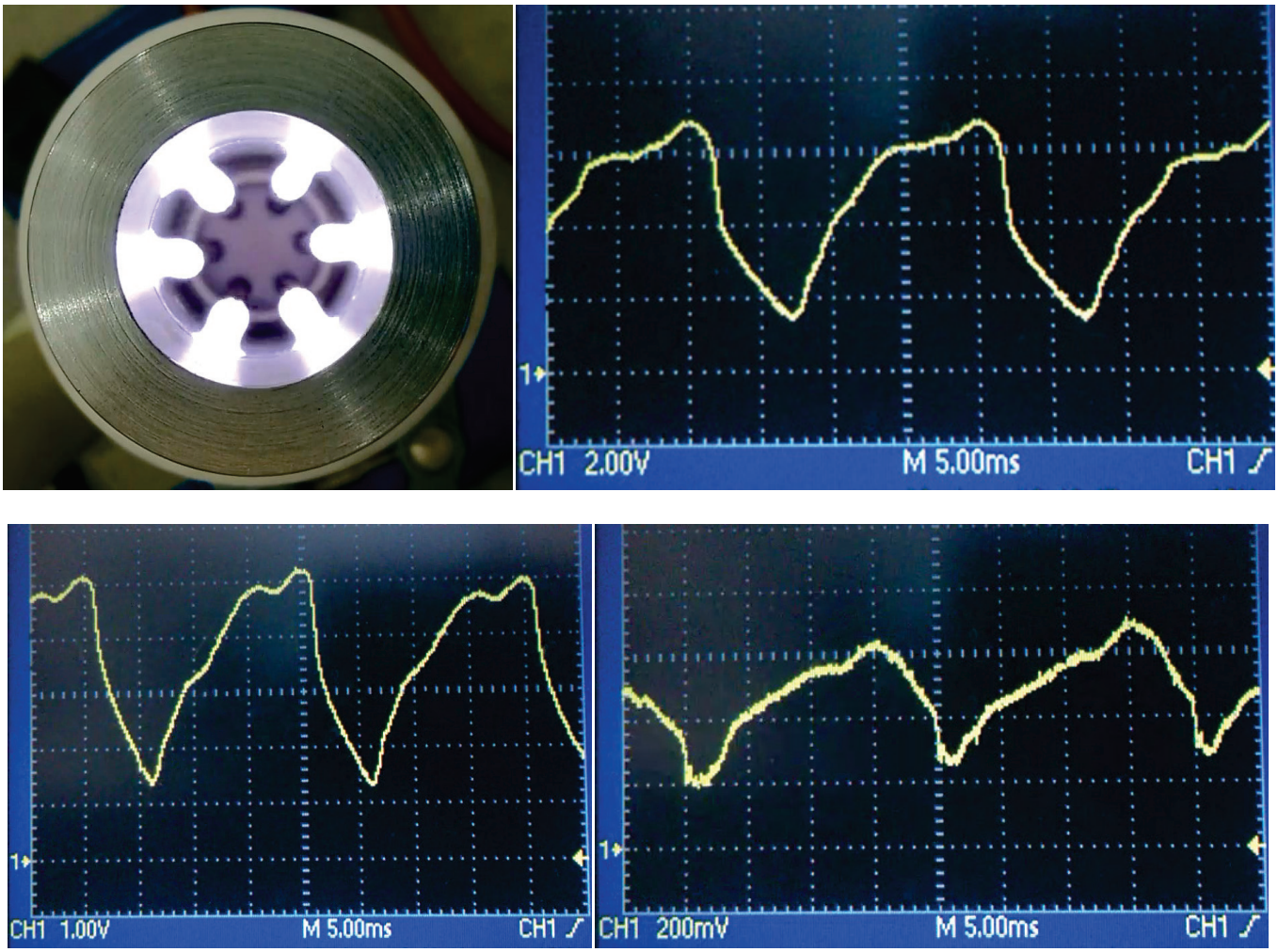

Figure 3. Atmospheric microwave discharge in Ar flow in the torch with straight nozzle of 2 cm height (top left). Oscillogrames of probe floating potential on the distances from the torch outlet 0 (top right), 0.7 (bottom left) and 2.5 cm (bottom right).

When the voltage on the magnetron drops below the threshold value, the magnetron stops generating. Then, at the end of the half-wave, voltage drops to zero due to a decrease in the voltage amplitude of the high-voltage transformer winding and discharge of the booster capacitor. Thus, the magnetron operates (generates) in a pulse mode (50 pulses per second) and only in one half-cycle of high-voltage transformer. In each pulse magnetron outputs a 2.45 GHz wave packet (50-Hz modulated 2.45-GHz microwaves).

We also used the planar probe to estimate plasma density in a plasma jet. Such a probe plays the role of a charged particles collector in afterglow plasma. Examples of the distribution of the RMS value of the floating potential along the plasma jet in Ar and the current-voltage characteristic of the probe in the region near the torch outlet are shown in Fig.4. It is clearly seen that the afterglow plasma exists at distances up to 3.5 cm from the torch nozzle. At atmospheric pressure the mean free paths of charged particles are much smaller than a probe size and the disturbed region near a probe. Therefore, it is necessary to take into account the diffusive character of the movement of these particles [11–13]. Taking into account that the determination of plasma parameters when using a probe of such large size is not always possible and justified, we will nevertheless try to estimate the plasma density at least in order of magnitude. For this purpose, we use the ion part of the characteristic and consider the current of positive ions to the negative probe in the atmospheric plasma. In many cases the mean free path of an ion at high gas pressure is determined by charge-exchange process.

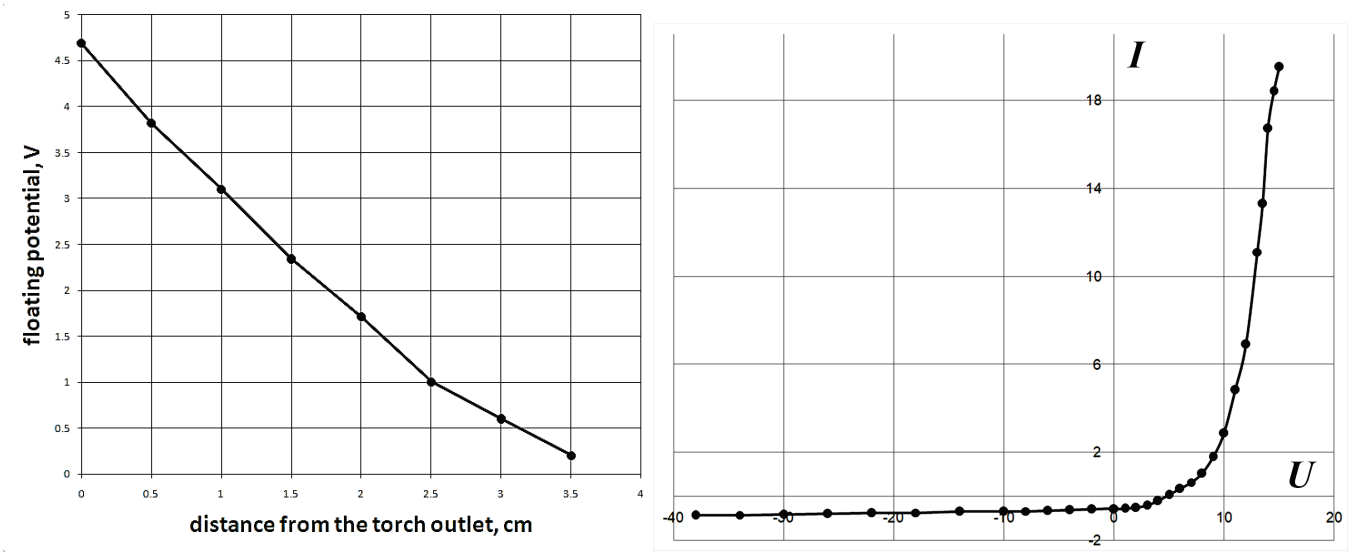

Figure 3. Probe floating potential and I-V probe characteristic in Ar plasma jet (RMS values). MV power about 100 W. gas flow rate 7.5 slm.

Then, to calculate the drift velocity of ions in electric field E, one can use the expression [11, 13]

$$v_d = 0.24 \frac{eE}{p\sigma_r} \left(\frac{2kT_n}{M_i}\right)^{1/2},$$

where σ_r – resonant charge-exchange cross-section, p – gas pressure, T_n – gas temperature. Neglecting the gas flow, for the current density of the ions on the probe we take $j_i = en_i v_d$. Then, taking from the experimental results I_0 = 0.6 μA, $T_n \approx 200$ ^{0}C, $E \approx 1.5$ V/cm and $\sigma_r = 6.5\times10^{-15}$ cm^2 [13], we obtain $n_i = 5\times10^5$ cm^{-3}.

Acknowledgements

This work is supported by the Russian Foundation for Basic Research (Project no. 18-08-01312).

References

1. Prokopenko A.V., Smirnov K.D., Appl. Phys., 2011, **5**, 64.
2. Levshenko M.T., Filippovich V.P., Prokopenko A.V., Smirnov K.D., Storage and Process. of Farm Products, 2011, **10**, 13.
3. Weltmann K.-D., Brandenburg R., von Woedtke T., Ehlbeck J., Foest R., Stieber M., Kindel E. J., Phys. D: Appl. Phys., 2008, 41, 194008.
4. von Woedtke T., Reuter S., Masur K., Weltmann K.-D., Phys. Rep., 2013, **530**, 291.
5. Kazak A.V., Kirillov A.A., Simonchik L.V., Nezhvinskaya O.E., Dudchik N.V., Plasma Medicine, 2017, **7**, 109.
6. Shimizu T. et al., Plasma Process. Polym., 2008, **5**, 577.
7. Shimizu T. et al., Plasma Process. Polym., 2010, **7**, 288.
8. Ermolaeva S., Petrov O., Zigangirova N., Vasiliev M., Sysolyatina E., Antipov S., et al., In Plasma for Bio-Decontamination, Medicine and Food Security. NATO Science for Peace and Security Series A: Chemistry and Biology. Ed. Z. Machala, K. Hensel and Y. Akishev. Dordrecht: Springer, 2012, 163.
9. Tikhonov V.N., Ivanov I.A., Kryukov A.E., Tikhonov A.V., J. Prikl. Fiz., 2015, **5**, 102 (in Russian).
10. Tikhonov V.N., Aleshin S.N, Ivanov I.A., Kryukov A.E., Tikhonov A.V., J. Phys.: Conf. Ser., 2017, **927**, 012067

11. Kozlov O.V., Elektricheskii Zond v Plazme. Electric Probe in Plasma (in Russian). Moscow: Atomizdat, 1969.
12. Boyd R., Proc. Phys. Soc., 1951, **B64**, 795.
13. Zakharova V.M., Kagan Y.M., Mustafin K.S., Perel' V.I., Sov. Phys. Tech. Phys., 1960, **5**, 411.

CALCULATION OF CAPACITIVE DISCHARGE IMPEDANCE AT THE ACCOUNT OF SURFACE WAVES EXCITATION ON PLASMA-METAL INTERFACE

S. Dvinin, Z. Kodirzoda[1], D. Solikhov[1]

Lomonosov Moscow State University, Leninskiye Gory 1–2, Moscow, 119991, Russia
[1] Tajik National University, Faculty of Physics, Rudaki Avenue, 17, Dushanbe, 734025, Tajikistan

Abstract. A capacitive High-Frequency (HF) low-pressure discharge ($\nu \ll \omega$) with large-area electrodes (radius greater than 20 cm) when excited by an electromagnetic field with frequency 13.56 – 500 MHz in a metal discharge chamber is considered. An analytical model for calculating the field distribution and an equivalent discharge circuit are proposed. The specific feature of this work is the allowance for the asymmetry of the discharge, leading to an additional RF current on the side wall and additional ionization in this region. Analytical calculations of discharge properties were supplemented by numerical modeling using Comsol Multiphysics. The possibility of controlling plasma homogeneity and the amplitudes of a symmetric and anti-symmetric surface waves due to a change in the properties of the lateral surface is studied.

1. INTRODUCTION

High-frequency capacitive discharges are widely used in scientific research and technological installations for the past 50 years [1, 2]. In the early stages of studies, it was shown that at low gas pressures, when the frequency of collisions between electrons and neutral particles much smaller than the frequency of electromagnetic field, which supports the ionization, capacitive discharges have resonant properties.

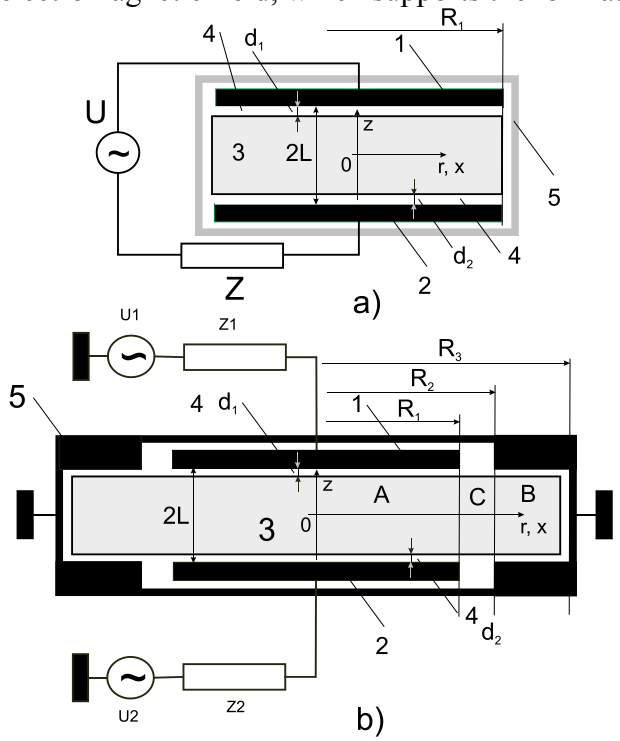

Figure 1. Typical schemes of experimental installations: simple research discharge camera a) and industrial plasma reactor b). 1, 2 – electrodes, 3 – plasma, 4 – sheathes, 2L – interelectrode distance, d_1, d_2, d_3 – sheathes thicknesses.

This resonance is associated with compensation of the capacitive impedance of the space-charge sheath and inductive impedance of the plasma [3]. The resonance was observed in the condition $\omega_{Pe}^2/\omega^2 = L/2\Delta$, where ω_{Pe} – the plasma frequency corresponding to the electron density n in the discharge, L – electrode spacing, Δ – sheath thickness. Later it was shown [4], that the resonant character of the impedance of the discharge gives rise to a hysteresis in the current-voltage characteristics of the discharge. These calculations have been confirmed experimentally [5] at a time, when the size of the discharge was less than the depth of penetration of the field into the plasma, so the quasi-static approximation, which was used in the model [3], gave the correct results. This work is devoted to investigation of resonances in discharge with large electrodes. New resonances can be connected with excitation of odd and even surface waves. The typical example of discharge excitation in the experimental setup is shown in Fig. 1a. The discharge is maintained between the two cylindrical

electrodes 1 and 2. RF voltage U is applied to electrodes through a matching circuit Z. Electrodes placed in a dielectric vacuum chamber 5. Plasma 3 is separated from the electrodes by sheath, which is formed at its boundary. In the more complex technological installations (Fig. 1b) the HF current between electrodes and metallic vacuum chamber is used for making electron density spatial distribution homogeneous. A side result of this current may be excitation of odd surface wave, which length is shorter. In a simple system (Fig. 1a), this wave is not excited.

In this work, in an analytical study, we restrict ourselves to an analysis of the electrodynamic properties of the discharge, assuming the electron density in the plasma and their collision frequency to be given (the cold plasma approximation was used). Maxwell's equations are conveniently written in such a way as to distinguish explicitly the wave impedance of the vacuum. $\rho_0 = \sqrt{\varepsilon_0/\mu_0}$:

$$[\nabla\times\mathbf{H}] + ik\sqrt{\frac{\varepsilon_0}{\mu_0}}\varepsilon\mathbf{E} = 0,\ [\nabla\times\mathbf{E}] - ik\sqrt{\frac{\mu_0}{\varepsilon_0}}\mathbf{H} = 0 \qquad (1)$$

Here $k=\omega/c$, ω – is the field frequency, c – is the speed of light; ε_0, μ_0 are the dielectric and magnetic permeabilities of vacuum, $\mathbf{E}(\mathbf{r})$, $\mathbf{H}(\mathbf{r})$ are complex electric and magnetic field strengths, the time dependence is chosen in the form of $\exp(-i\omega t)$; ε is the dielectric constant of the medium. In the sheath we will assume $\varepsilon = 1$, in the plasma $\varepsilon = \varepsilon_P = 1 - n_e/n_C(1 - i\nu/\omega)$.

2. SURFACE WAVE CHARACTERISTICKS

We will solve Maxwell equation in vacuum chamber (fig.1) with zero tangential electric field boundary condition, using matrix sheath model [3]. Plasma density distribution is assumed to be a homogeneous. As it was mentioned in [6, 7], electric field between electrodes can be expressed as a sum of surface (index S) and evanescent waves (h>0 in plasma without absorption)

$$\begin{Bmatrix}\mathbf{E}\\ \mathbf{B}\end{Bmatrix} = \left(\begin{Bmatrix}\mathbf{E}_{S+}\\ \mathbf{B}_{S+}\end{Bmatrix}J_0(h_{S+}r) + \begin{Bmatrix}\mathbf{E}_{S-}\\ \mathbf{B}_{S-}\end{Bmatrix}J_0(h_{S-}r) + \sum_{m=1}^{\infty}\begin{Bmatrix}\mathbf{E}_{m+}\\ \mathbf{B}_{m+}\end{Bmatrix}I_0(h_{m+}r) + \sum_{m=1}^{\infty}\begin{Bmatrix}\mathbf{E}_{m+}\\ \mathbf{B}_{m+}\end{Bmatrix}I_0(h_{m-}r)\right)\exp(-i\omega t)\cdot \qquad (2)$$

To find propagation constant $h_{S\pm}$ and $h_{m\pm}$ it's better to use plane wave conception, which allows represent the field in the upper and lower sheathes as (index $_m$ below corresponds evanescent waves and $_S$ one to surface waves, $h_{m\pm}$ have ascending ordering, $\varepsilon_1 = \varepsilon_2 = 1$),

$$\begin{Bmatrix}e_z(z)\\ e_x(z)\\ b_y(z)\end{Bmatrix} = A_1\begin{pmatrix}-ih\cosh\left(\sqrt{k^2\varepsilon_1 - h^2}\,(L-z)\right)\Big/\sqrt{h^2-k^2\varepsilon_1}\\ -\sinh\left(\sqrt{h^2-k^2\varepsilon_1}\,(L-z)\right)\\ \sqrt{\frac{\varepsilon_0}{\mu_0}}ik\varepsilon_1\cosh\left(\sqrt{h^2-k^2\varepsilon_1}\,(L-z)\right)\Big/\sqrt{h^2-k^2\varepsilon_1}\end{pmatrix}\frac{\exp(-i\omega t+ihx)}{\cosh\left(\sqrt{k^2\varepsilon_1-h^2}\,d_1\right)},\quad \begin{Bmatrix}e_z(z)\\ e_x(z)\\ b_y(z)\end{Bmatrix} = A_3\begin{pmatrix}-ih\cdot\cosh\left(\sqrt{k^2\varepsilon_2-h^2}\,(z-L)\right)\Big/\sqrt{h^2-k^2\varepsilon_2}\\ \sinh\left(\sqrt{h^2-k^2\varepsilon_2}\,(z-L)\right)\\ \sqrt{\frac{\varepsilon_0}{\mu_0}}\cdot ik\varepsilon_3\cosh\left(\sqrt{h^2-k^2\varepsilon_2}\,(z-L)\right)\Big/\sqrt{h^2-k^2\varepsilon_2}\end{pmatrix}\frac{\exp(-i\omega t+ihx)}{\cosh\left(\sqrt{k^2\varepsilon_2-h^2}\,d_2\right)}$$

and in the plasma as ($L' = L - (d_1+d_2)/2$, $d = (d_1-d_2)/2$

$$\begin{Bmatrix}e_z(z)\\ e_x(z)\\ b_y(z)\end{Bmatrix} = \frac{\exp(-i\omega t+ihx)}{\cosh\left(\sqrt{k^2\varepsilon_P-h^2}\,L'/2\right)}\left\{A_2\begin{pmatrix}-ih\cosh\left(\sqrt{k^2\varepsilon_P-h^2}\,(z-L'/2-d)\right)\Big/\sqrt{h^2-k^2\varepsilon_P}\\ \sinh\left(\sqrt{h^2-k^2\varepsilon_P}\,(z-L'/2-d)\right)\\ \sqrt{\frac{\varepsilon_0}{\mu_0}}ik\varepsilon_P\cosh\left(\sqrt{h^2-k^2\varepsilon_P}\,(z-L'/2-d)\right)\Big/\sqrt{h^2-k^2\varepsilon_P}\end{pmatrix} + B_2\begin{pmatrix}-\frac{ih}{\sqrt{h^2-k^2\varepsilon_P}}sh\left(\sqrt{k^2\varepsilon_P-h^2}\,(z-L'/2-d)\right)\Big/\sqrt{k^2\varepsilon_P-h^2}\\ \cosh\left(\sqrt{h^2-k^2\varepsilon_P}\,(z-L'/2-d)\right)\\ \sqrt{\frac{\varepsilon_0}{\mu_0}}ik\varepsilon_P\sinh\left(\sqrt{h^2-k^2\varepsilon_P}\,(z-L'/2-d)\right)\Big/\sqrt{h^2-k^2\varepsilon_P}\end{pmatrix}\right\}.$$

The field distribution leads to the dispersion equation for *E*-waves

$$D = \frac{\sqrt{h^2-k^2\varepsilon_1}}{\varepsilon_1}th\left(\sqrt{h^2-k^2\varepsilon_1}\,d_1\right) + \frac{\sqrt{h^2-k^2\varepsilon_2}}{\varepsilon_2}th\left(\sqrt{h^2-k^2\varepsilon_2}\,d_2\right) + \frac{\sqrt{h^2-k^2\varepsilon_P}}{\varepsilon_P}th\left(\sqrt{h^2-k^2\varepsilon_P}\,L'\right) -$$
$$-\frac{\varepsilon_P\sqrt{h^2-k^2\varepsilon_1}\sqrt{h^2-k^2\varepsilon_2}}{\varepsilon_1\varepsilon_2\sqrt{h^2-k^2\varepsilon_P}}th\left(\sqrt{h^2-k^2\varepsilon_3}\,d_3\right)th\left(\sqrt{h^2-k^2\varepsilon_1}\,d_1\right)th\left(\sqrt{h^2-k^2\varepsilon_P}\,L'\right) = 0 \qquad (3)$$

An example of the calculated characteristics of the surface wave is shown in Fig. 2. Field frequency is equal to 27.12 MHz and sheathes thickness is 3 mm for symmetric discharge and 2 and 5 mm for non-symmetric one. According to the calculation, in wide range of plasma densities the surface waves have different propagation constants. We will call the shorter wave antisymmetric, since the z-component of

the electric field has different signs at the electrodes, and the second wave we call symmetric, although the fields of these waves have the required symmetry only when the thicknesses of both sheathes are the same. In all cases engineers try to use second wave to support plasma. At large sizes of the vacuum chamber, resonances associated with the excitation of both the first and second waves are possible.

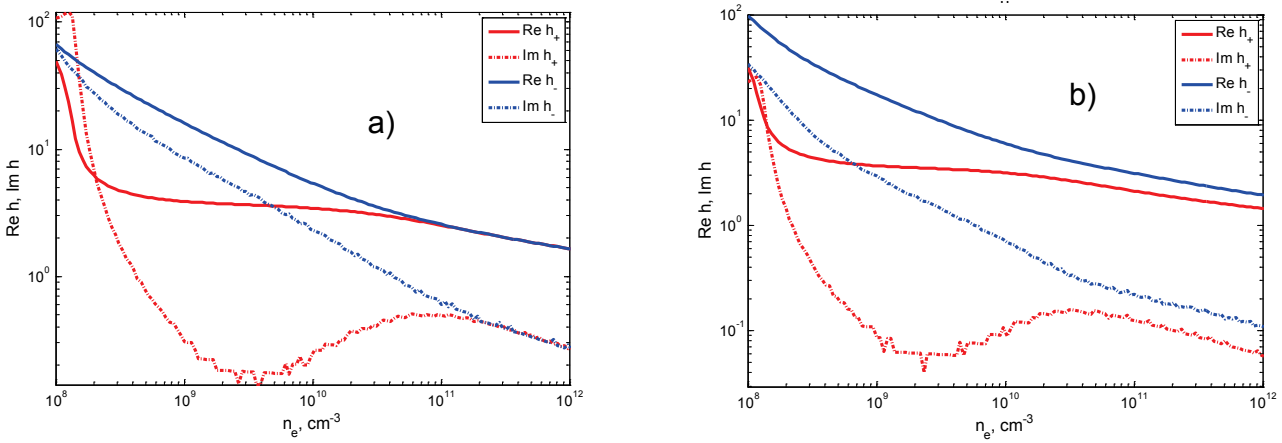

Figure 2. Propagation constant of surface waves as a function of electron density. The wave frequency is 27.12 MHz, the sheathes lengths are a) d_1, d_2 – 0.3 cm both ones, b) d_1 – 0.5 мм, d_2 – 0.2; ν/ω= 0.3

3. ANALYTICAL CALCULATION OF DISCHARGE IMPEDANCE

Suppose now that sheathes lengths are the same, and the distance between the plasma boundary and side wall of the discharge chamber is large. Since the antisymmetric surface wave in this case is not excited, the discharge impedance can be calculated using the simple formula

$$Z=\frac{J_0(h_+R_1)}{2\pi R_1 J_1(h_+R_1)}\frac{h_+}{ik\varepsilon_2}\sqrt{\frac{\mu_0}{\varepsilon_0}}\left\{\frac{2th\left(\sqrt{h_+^2-k^2\varepsilon_2}\,(L-d_1)\right)}{\sqrt{h_+^2-k^2\varepsilon_2}}+\frac{\varepsilon_2}{\varepsilon_1}2d_1\right\}, \tag{4}$$

The last formula shows that with a small absorption in the discharge, both a current resonance and a voltage resonance $\mathrm{Re}\,J_0(h_+R)\approx 0$ can be observed. In the case of strong absorption, we can use the representation for the Bessel function through the Hankel function of the first and second kind

$$Z=\frac{H_0^{(1)}(h_+R_1)}{2\pi R_1 H_1^{(1)}(h_+R_1)}\frac{h_+}{ik\varepsilon_2}\sqrt{\frac{\mu_0}{\varepsilon_0}}\left(\frac{1+H_0^{(2)}(h_+R_1)/H_0^{(1)}(h_+R_1)}{1+H_1^{(2)}(h_+R_1)/H_1^{(1)}(h_+R_1)}\right)\left\{\frac{th\left(\sqrt{h_+^2-k^2\varepsilon_2}\,(L-d_1)\right)}{\sqrt{h_+^2-k^2\varepsilon_2}}+\frac{\varepsilon_2}{\varepsilon_1}2d_1\right\} \tag{5}$$

In this case, the discharge impedance is determined by the wave impedance of the line, on which small resonances associated with the reflection of the traveling wave from the center of the discharge chamber are imposed. The presence of these resonances is due to the peculiarities of the distribution of the electromagnetic field along the radius.

In addition to these resonances, it is necessary to separately distinguish the geometric resonance plasma – space charge sheath [3], which exists independently of the previous ones and is associated with the features electromagnetic field spatial distribution along the 0Z axis.

$$\frac{\varepsilon_P L_1}{L_2}+\frac{\tanh\left(\sqrt{h_+^2-k^2\varepsilon_P}\,L_2\right)}{\sqrt{h_+^2-k^2\varepsilon_P}\,L_2}=0, \tag{6}$$

In the approximation $\sqrt{h_+^2-k^2\varepsilon_P}\,L_2<<1$ (6) yields standard expression $\varepsilon_P(d_1+d_2)/\varepsilon_1(2L-d_1+d_2)+1=0$ for resonance [3]. In a discharge at low frequencies, when surface waves length turns out to be larger than the system size, this resonance causes a sharp change in the discharge impedance with electron density. The expression for the discharge impedance with nonsymmetrical discharges ($d_1 \neq d_2$) is very cumbersome, therefore, below we give the expression for the impedance in the limiting case, when the interaction of surface waves at opposite plasma boundaries are negligible.

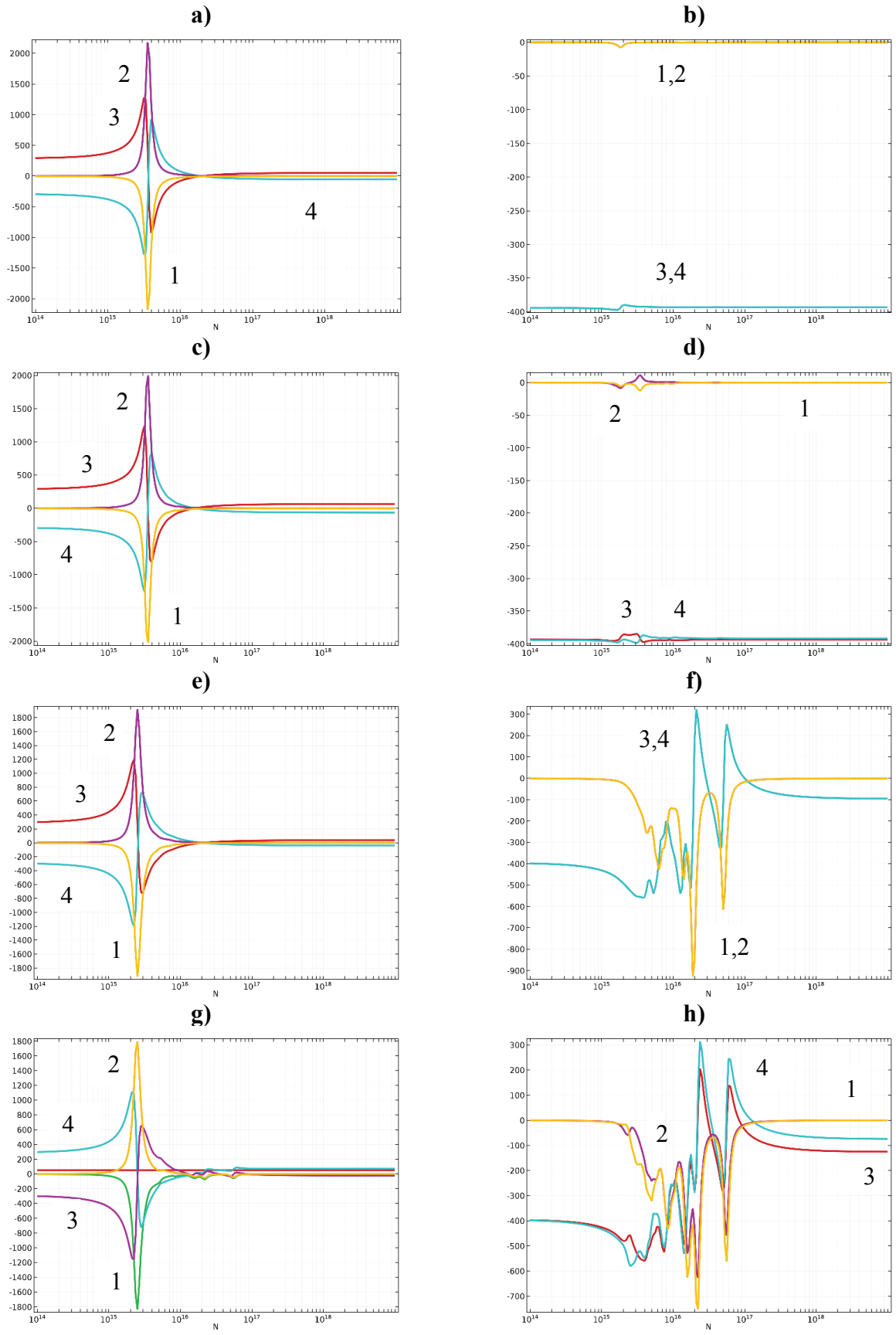

Figure 3. The dependence of electrodes voltages (V) as a function of the electron density (in m^{-3}). The field frequency is 27.12 MHz. a), c), e), g) – antiphase excitation (the current to the side wall is zero), b), d), f), h) – in-phase excitation (all current goes to the side wall), a), b), c), d) – is a discharge not contacting with the side wall, e), f), g), h) is a discharge occupying the entire volume of metal chamber (sheath thickness near side surface is 3 mm). a), b), e), f) – symmetrical discharge with sheathes thickness d_1,d_2 equal to 3 mm, c), d), g), h) – asymmetric discharge (sheath thickness at the top electrode is 5 mm, at the bottom one is 2 mm). (1) and (2) curves correspond to the real part of the voltage, (3) and (4) – to imaginary ones. Curves 1, 2 and 3, 4 in fig. 3b) and 3h) coincide due to the discharge symmetry.

$$Z=\frac{J_0(h_+R_1)}{2\pi R_1 J_1(h_+R_1)}\frac{h_+}{ik\varepsilon_P}\sqrt{\frac{\mu_0}{\varepsilon_0}}\left\{\frac{\varepsilon_P}{\varepsilon_1}d_2+\frac{th\left(\sqrt{h_+^2-k^2\varepsilon_P}L'\right)}{\sqrt{h_+^2-k^2\varepsilon_P}}\right\}+\frac{J_0(h_-R_1)}{2\pi R_1 J_1(h_-R_1)}\frac{h_-}{ik\varepsilon_P}\sqrt{\frac{\mu_0}{\varepsilon_0}}\left\{\frac{\varepsilon_P}{\varepsilon_2}d_2+\frac{th\left(\sqrt{h_-^2-k^2\varepsilon_P}L'\right)}{\sqrt{h_-^2-k^2\varepsilon_P}}\right\}$$

The task becomes even more complicated if the plasma is in contact with the side wall, and the excitation of the short wave mode occurs not only due to the asymmetry of sheathes, but due to the currents to the side wall.

4. CALCULATION OF DISCHARGE IMPEDANCE AND FIELD DISTRIBUTION

To test the reasoning carried out in the preceding paragraphs, a numerical calculation of the discharge impedance and the distribution of the electromagnetic field in the discharge chamber shown in Fig. 1b was carried out. The results of the calculations are shown in Fig. 3. The radii of R_1, R_2, and R_3 in the calculations were 24, 26 and 35 cm, respectively. The plasma radius was 22 cm (Fig. 3a – d), and the sidewall current can be neglected in the case. In other calculations (Fig. 3e – h) plasma filled the entire discharge chamber. Figure 3 shows the voltage on the electrodes with antiphase (Fig. 3a, c, e, g) and in-phase (Fig. 3b, d, f, g) excitation. In first case the HF current flows into the electrode is equal to the current flowing through second one (the voltages on the electrodes have different signs). In second case the flowing current is closed on the side wall of the chamber (Fig. 3b, d, f, g). In all cases, the electrode current was equal to 1 A. When the plasma boundary is far from the side wall and the sheathes are the same, resonance is observed only in a symmetric mode (Fig 3a), the antisymmetric wave is suppressed due to the small capacitance C_L between the plasma and side wall, which limits discharge current (Fig 3b). The weak asymmetry associated with the difference in sheathes thickness does not lead to a significant increa-

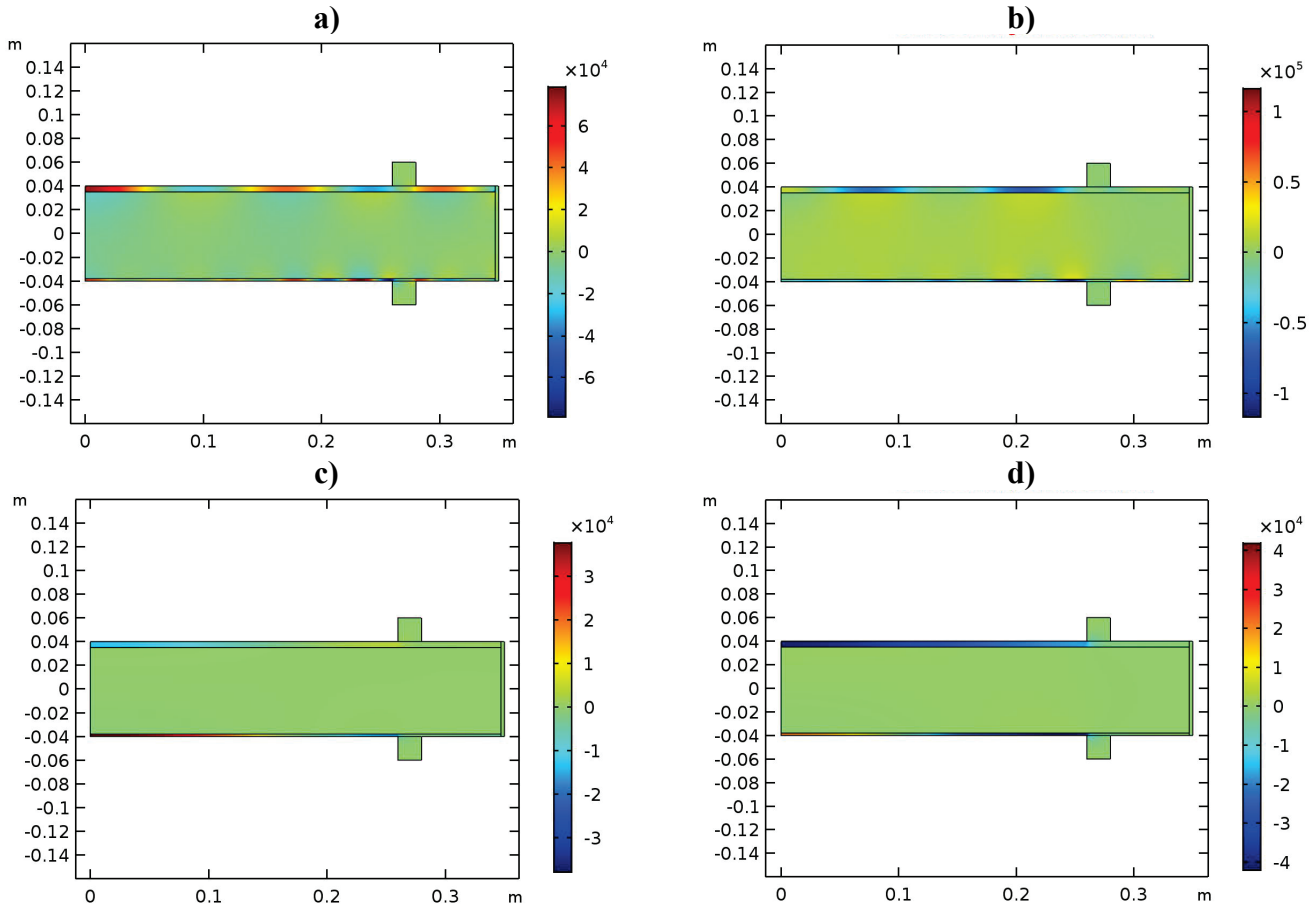

Figure 4. Spatial distribution of the high-frequency field in the discharge. Excitation conditions correspond to fig. 3g. Fig. 4a, s – Re E_z, 4b, d – Im E_z. The electron density in the plasma is 4a, b is the electron density of $5\cdot10^9$ cm^{-3}, 4c, d is the electron density of $5\cdot10^{10}$ cm^{-3}.

se in the amplitude of the asymmetric wave, and its contribution is not practically noticeable in Fig 3c, due to the same smallness of C_L. At antisymmetric excitation, the amplitudes of both waves are small, and the resonance for each wave is observed at various electron densities (Fig 3d). If the symmetric discharge fills the entire discharge chamber (Fig. 3e, f) and the in-phase and anti-phase surface waves can be excited equally effectively, and the number of resonances for the anti-phase wave is much larger due to the smaller wavelength. In an asymmetric discharge, the presence of resonances associated with the excitation of both waves can be seen on both in-phase and antiphase excitation (Fig. 3g, h).

Examples of calculated space distribution of z-component of electric field in discharge chamber are shown in Fig. 4. The most interesting pictures showing the case with different sheathes thicknesses and plasma filling the entire discharge chamber are shown. At a low electron density ($5 \cdot 10^9$ cm^{-3}), the excitation of waves with different wavelengths is well noticeable. With a higher density of $5 \cdot 10^{10}$ cm^{-3}, the electric field near the electrodes have a different sign, that is, the discharge is supported mainly by an antiphase surface wave.

5. CONCLUSIONS

Low-pressure capacitive RF discharge ($\nu \ll \omega$) with large area electrodes with frequency 13.56 – 500 MHz in a metal discharge chamber is considered. It is shown that under these conditions the discharge is supported by surface waves propagating along the plasma – sheath – metal interface.

1. Analytical expressions for CCP HF discharge impedance, including excitation of these surface waves, propagating are obtained. Influence of even and odd surface take into account. Numerical calculation of the impedances and the spatial distribution of the electromagnetic field qualitatively confirmed the analytical calculations.
2. The main observed resonance is similar in nature to the geometric plasma - sheath, other resonances are the resonances of currents and voltages in the long line associated with the excitation of symmetric surface waves.
3. When the discharge is asymmetric, is excited asymmetrically, additional resonances associated with the excitation of antisymmetric surface waves appear. It is found, that the role of symmetric and antisymmetric waves is defined by geometry of discharge and properties of matching device.
4. Specified approach allows to calculate discharge impedance and explains possible ambiguity of plasma impedance, connected with these resonances and chemical processes in plasma.

References

1. Lieberman M.A., Lichtenberg A.J., Principles of Plasma Discharges and Material Processing. N.-Y.: Wiley, 2005.
2. Ivanovski G.,F., Petrov V.I., Ion-plasma materials processing. M.: Radio i Svyaz. 1986. 232 p. (In Russian).
3. Taillet J., American Journal of Physics, 1969, **37**, 423.
4. Leprince P., Mattieussent G., Allis W.P., J. Appl. Phys., 1971, **42**, 4.
5. Godyak V.A., Sov. Physics: Fizika plasmy, 1976, **2**, 141.
6. Dvinin S., Park W.-T., Kalinin A., Kashaba A., Nikishin N., Microwave Discharges: Fundamentals and Applications. Ed. Yu.A. Lebedev, Moscow, Yanus-K, 2012, p. 53.
7. Vologirov A., Dvinin S., Mikheev V., Sviridkina V., Plasma Phys. Reports, 2008, **34**, 746.

MICROWAVE PLASMA-CHEMICAL REACTOR BASED ON PLASMA JET INTERACTION WITH WATER

E. M. Barkhudarov[1], I. A. Kossyi[1], N. Christofi[2], M. A. Misakyan[3]

[1]A. M. Prokhorov General Physics Institute of the Russian Academy of Sciences, Vavilov Str., 38, Moscow, 119991, Russia
[2]Edinburgh Napier University, Edinburgh, United Kingdom
[3]National Research University "Higher School of Economics", Myasnitskaya Str., 20, Moscow, 101000, Russia

Abstract. The design of the reactor for steam conversion of gases and its testing.CO_2 gas is given as an example in this paper. The principle of operation of the reactor is based on the interaction of the plasma jet created by the microwave with water. The system works steadily when using CO_2 and with mixtures of nitrogen and argon. The process of conversion of CO_2, which is accompanied by the formation of carbon nanoparticles of different structures, is demonstrated qualitatively. The reactor can be used in solving a number of applied problems, including cleaning water and gases from chemical and microbiological contamination.

1. INTODUCTION

Plasma-fluid interaction is a growing interdisciplinary research area embracing plasma physics, hydrodynamics, heat and mass transfer, photolysis, multiphase chemistry, and so on [1]. A separate area consists of studies using microwave sources of plasma of various designs [2−4]. Physical, plasma chemical processes of interaction of microwave plasma jet with water are quite complex and depend on jet power, water temperature, geometry, etc. [2, 4]. The attractiveness of the problem lies in the possibility of an efficient, relatively simple solution of a number of important applied problems, one of which is steam conversion of gases.

2. EXPERIMENTAL SETUP

The design of the reactor for the conversion of gases and its validation using the example of CO_2 is given in the paper. The scheme of the reactor is shown in Fig. 1.

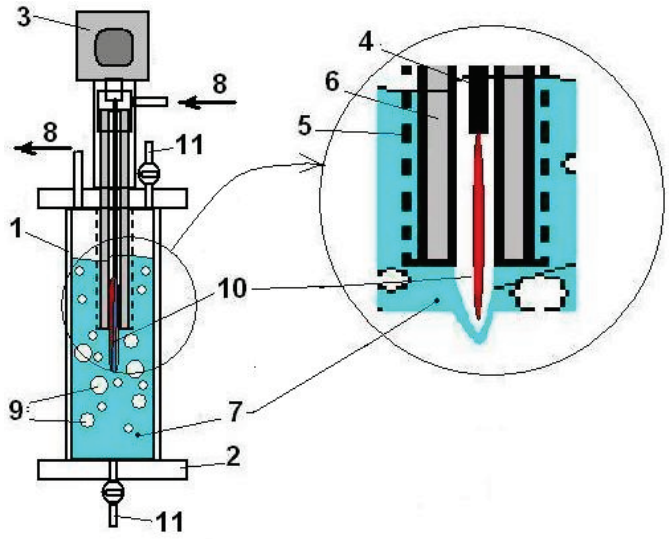

Figure 1. Reactor layout. 1 − cylindrical tube of Plexiglas; 2 − flange; 3 − magnetron (N = 850 W, f = 2.45 GHz), 4 − internal electrode of the coaxial waveguide; 5 − external electrode of a coaxial waveguide; 6 − quartz tube; 7 − water; 8 − holes for pumping gas; 9 − gas bubbles; 10 − plasma jet; 11 - holes for pumping water.

The magnetron (3) is connected to a coaxial waveguide with a shortened internal electrode (4) (rod diameter 2.5−3 mm). The pointed end of the inner electrode was made of titanium and tantalum. The outer electrode (5) is a cylindrical tube, with a diameter of 35−40 mm, made of a metal mesh,

almost opaque for microwave radiation. Between the electrodes and coaxial with them, is a quartz tube (6) with a diameter of 25 mm, into which gas is injected. The gas flow rate was regulated in the range up to 20 L/min. The device is placed in a tube of transparent plastic (1), which is filled with water to the desired level.

The design of the plasma torch is based on the results of [5−7], in which it is shown that the plasma generated by the torch (jet) is thermodynamically in nonequilibrium, has a complex spatial structure: a small "core" region near the end of the inner electrode with a concentration $n = 10^{16}$ cm^{-3} and the gas temperature $T = (4−5) \cdot 10^3$ K and the adjacent main region with $n = (1−3) \cdot 10^{14}$ cm^{-3} and $T = 2 \cdot 10^3$ K.

A magnetron with a power N = 850 W, (λ = 12.24 cm), pulse repetition frequency f = 50 Hz, pulse duration τ = 8 ms was used with a pause of τ = 12 ms.

The injected gas displaces water from the tube. In the formed gas region, a plasma jet is generated which is a continuation of the internal electrode of the coaxial waveguide. This contributes to the further propagation of the electromagnetic wave. The interaction of the plasma jet with the water surface leads to the entry of vapours into the reactor volume and the formation of a vapour-gas mixture. Due to the kinetic energy, the plasma jet penetrates into the water, decaying into many small bubbles, which contribute to the rapid cooling of the products of the plasma chemical reactions occurring in the hot zone of the reactor. Depending on the gas flow rate, the size of the gas cavity, the power of the magnetron, the shape of the quartz tube (end in the form of a nozzle) etc., different modes of reactor operation are possible.

The picture of the interaction of a plasma jet with water was demonstrated in [2]. The reactor works steadily on various gases: air, argon, N_2, CH_4, CO and CO_2. To test the device, experiments were performed using CO_2. Research methods involved IR spectrophotometry, integrated emission spectra ($400 \leq \lambda \leq 750$ nm), microphotography and elemental composition of the powder formed as a result of the conversion of CO_2.

3. RESULTS

Some preliminary results are given below.

Testing of titanium and tantalum as the sharpened tips of the electrode 4 (Fig. 1) showed high stability of tantalum. Under the same conditions, titanium is markedly destroyed. At an energy cost of 100 kJ titanium consumption was 0.028 cm^3.

Figure 2 shows IR absorption spectra of reaction products in the absence of water vapour (a) and in their presence (b). Titanium was used as the electrode. In the case of (a) the bands of CO_2 and CO stand out against the background of a wide absorption region. Perhaps this is due to the presence of products from the interaction of gas with titanium vapour.

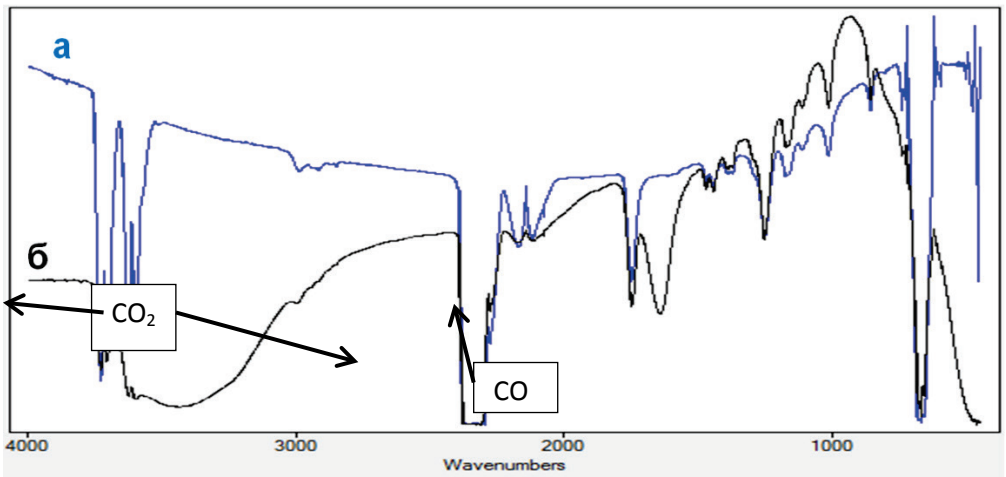

Figure 2. IR absorption spectrum, a − electrode from titanium, CO_2 (in the absence of water vapour) and b − electrode titanium, CO_2 (in the vapour-gas mixture).

Figure 3 shows the integrated spectrum of radiation using a titanium electrode in a mixture of a water vapour and CO_2. On the continuous part of the spectrum, the bands CO_2, CO, C_2 and the lines Ti II and Ti I are singled out.

In the process of steam-gas transformation of CO_2, carbon nanoparticles of different structures are formed that precipitate on the walls of the quartz tube and, in part, get into the water (Fig. 4).

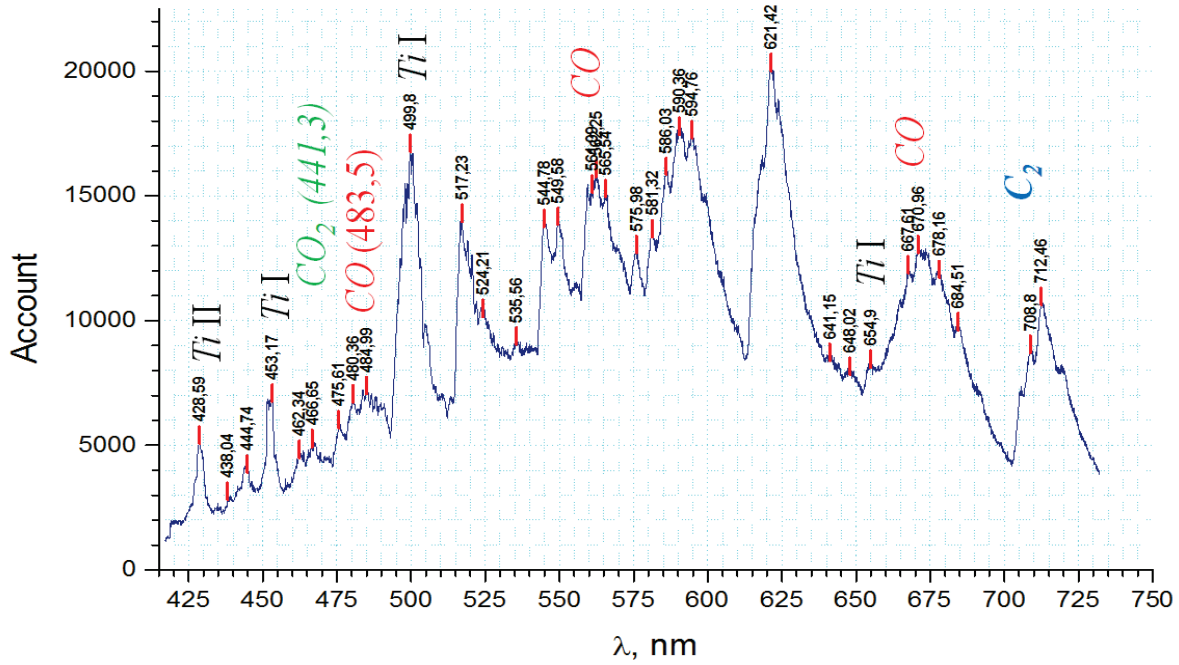

Figure 3. Radiation spectrum, titanium electrode (CO_2 − water vapour).

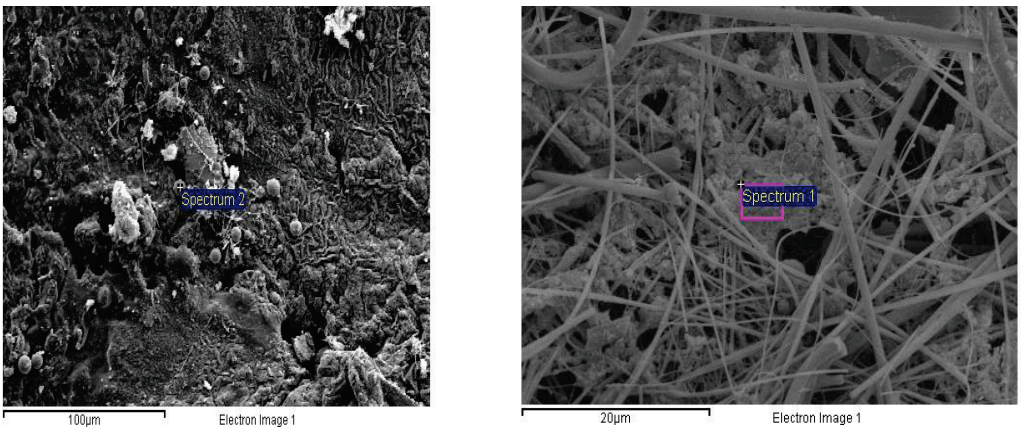

Figure 4. A micrograph of a powder deposited on the walls of a quartz tube of a plasmatron and a powder obtained following water filtration of plasmatron treated samples.

4. CONCLUSIONS

A prototype of the reactor based on the interaction of a microwave plasma jet with water is developed, which makes it possible to realize plasma-chemical reactions in a complex three-phase system-gas, water, vapour. A number of preliminary experiments have been performed. The device can be used for steam-gas transformation of gases, purification of gases, water from chemical and microbiological contamination, production of nanoparticles, etc.

References

1. Bruggeman P.J., Kushner M.J., Locke B.R. et al., Plasma Sources Sci. Technol., 2016, **25**, 053002.
2. Lebedev Yu.A., Plasma Physics Reports, 2017, **43**, N 6, June, 685.
3. Barkhudarov E.M., Kossyi I.A., Misakyan M.A., New microwave plasma source in water. In: Lebedev Y.A., Ed., Microwave discharges: fundamentals and applications. Moscow: Yanus-K, 2012, p.159.
4. Benova E., Atanasova M., Bogdanov T., Marinova P., Krema F., Mazankova V., Dostal L., Plasma Medicine, 2016, **6**, N 1, 59.
5. Berezhetskaya N.K., Kop'ev V., Kossyi I.A. et al., Eur. Phys. J. Appl. Phys., 2008, **42**, 327.
6. Barkhudarov E.M., Grtitsinin S.I., Dreiden G.V. et al., Plasma Physics Report, 2004, **30**, N 6, 531.
7. Gritsinin S.I., Knyazev V. Yu., Kossyi I.A. et.al., Plasma Physic Reports, 2004, **30**, N 3, 255.

TRANSMISSION SPECTRUM SWITCHING SPEED OF PLASMA ELECTROMAGNETIC BAND GAP STRUCTURE

V. S. Babitski, Th. Callegari*, L. V. Simonchik, J. Sokoloff*, M. S. Usachonak

Institute of Physics NAS of Belarus, Ave. Nezalezhnastsi 68-2, 220072 Minsk, Belarus
*LAPLACE CNRS, 118 route de Narbonne, 31062 Toulouse, France

Abstract. The switching speed of transmission spectrum of the plasma electromagnetic band gap (EBG) structure formed by pulse discharges at atmospheric pressure was under investigation. The ability to obtain a nanosecond transmission spectrum switching time of plasma EBG structures was demonstrated. It has been shown that switching frequency could be about 100 kHz. The switching properties of 1D and 2D EBG structures with plasma control elements were tested at high microwave power of about 50 kW. Obtained results can be used for a high–speed microwave devises development that are able to work at high power levels and can be used as a part of automated systems for receiving and transmitting microwave signals.

1. INTRODUCTION

During the last decade, there has been a sharp increasing interest in high-speed tunable microwave devices based on EBG structures for use in telecommunication systems that are capable of operating at high power levels. Devices with variable parameters can be created based on a waveguide, coaxial or microstrip lines and use magnetostatic waves [1], p-i-n diodes, mechanical or electromechanical devices for switching [2, 3]. Their switching times can reach tens of nanoseconds at the maximum power up to watt [2], or milliseconds at kilowatt power of microwave radiation [3]. Gas discharge plasma as a control element of such devices has high potential for switching purpose due to its variability in size, density and geometry [4]. Also plasma can be used as an element of power limiter [5]. One-dimensional plasma EBG structures in the X-band waveguide formed by discharges at low and atmospheric pressure were presented in [6, 7]. The main purpose of these studies was the establishing of the EBG structure transmission spectrum dependence on plasma parameters (electron density, collision frequency, diameter, etc.). Also in [7, 8] the possibility of controlling a high power microwaves propagation by one- and two-dimensional EBG structures with plasma elements was demonstrated. At the same time, the switching speed of the transmission spectrum was not sufficiently investigated.

In this work, the switching speed of transmission spectrum of the plasma EBG structure formed by pulse discharges at atmospheric pressure was under investigation.

2. THE 1D PERIODIC STRUCTURE

One-dimensional electromagnetic band gap structure [7] is a 3 plasma columns placed on axis of a standard waveguide of rectangular cross-section 23×10 mm^2 in perpendicular to the wide walls of it with distance between plasma columns of l = 30 mm (Fig. 1a). The chosen distance corresponds to $l = \Lambda_0$, where Λ_0 is a wavelength in the waveguide for frequency f_0 = 11.9 GHz, which is expressed by relation

$$\Lambda_0 = \lambda_m (1 - (\lambda_m / 2a)^2)^{-1/2}. \quad (2)$$

where λ_m is the wavelength corresponding to the middle of the pass band; a = 23 mm is the waveguide wide wall dimension. The transmission spectrum of the structure is shown in Fig. 1*b*. Experimental transmission spectrum is in good agreement with modeling results obtained in the Ansoft HFSS program [9].

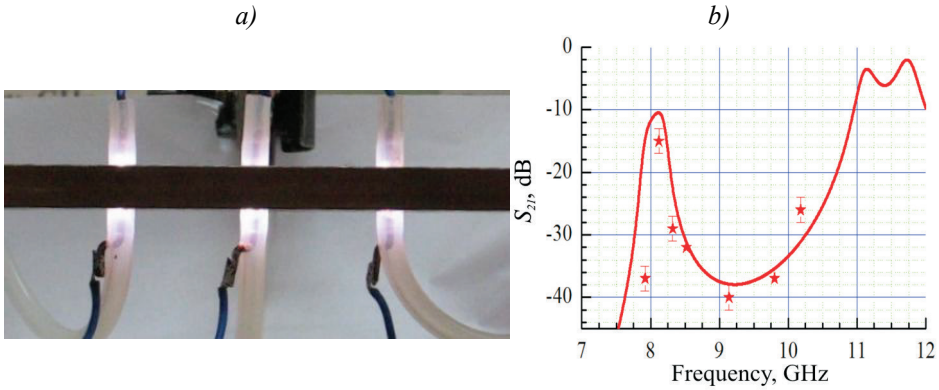

Figure 1. Photo of the waveguide section with electromagnetic band gap structure formed by gas discharges and (*b*) it's transmission spectrum at current maximum (stars – experiment, continues curve – modeling in HFSS).

Gas discharges were formed in quartz tubes with an external diameter of 4.8 mm and an internal diameter of 2.5 mm between rod copper electrodes (diameter - 2 mm) with interelectrode distance 10 mm. Working gas (helium, argon or air) flow per tube was about 1 l/min. A pulse voltage source was used for discharges generation (Fig. 2a).

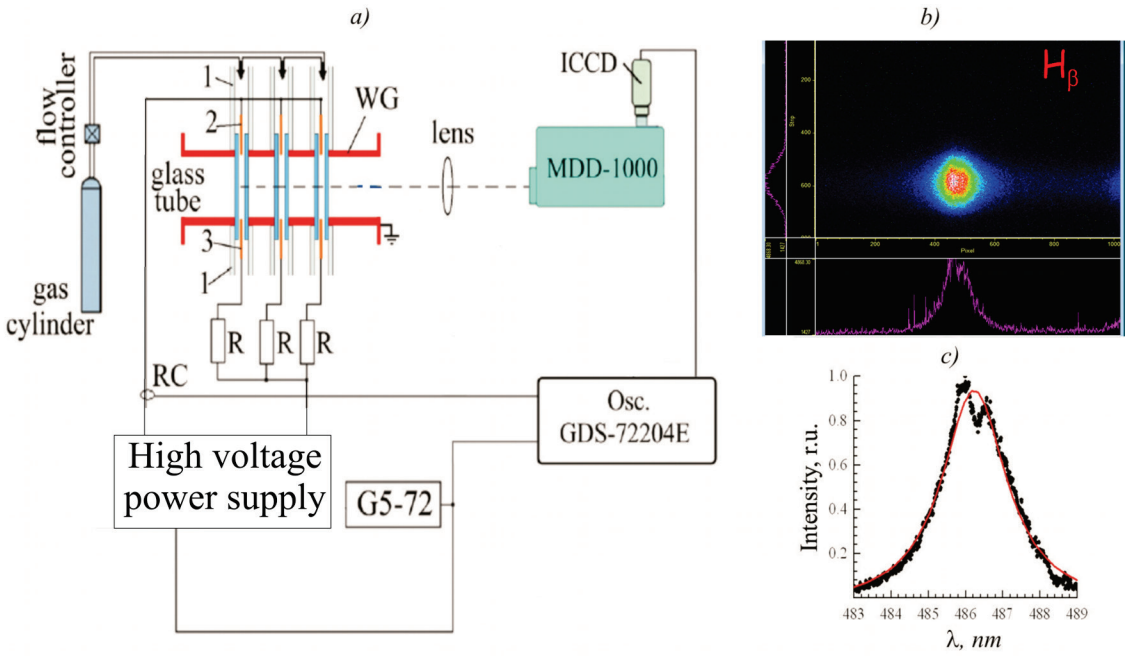

Figure 2. (a) Electrical scheme of the 1D plasma EBG structure and (b) the emission spectrum of the discharge in the vicinity of the H_β line and (c) its contour at the maximum of the discharge current.

Each discharge gap is connected to the output of the high voltage pulse power supply through a resistor R (1 kΩ). The discharge current is registered using Rogowski coil (time constant of 0.2 μs) and digital oscilloscope GDS-72204E (200 MHz, 1 GS/s). The ignition of the discharge is synchronized by the pulse generator G5-72.

The electron density in the discharge plasma was estimated from the FWHM contour of the H_β or H_α lines [10]. An example of the emission spectrum of the discharge registered in the maximum discharge current in helium in the vicinity of the H_β line is shown in Fig. 2b. The discharge plasma emission was focused with a lens with a focal length of 150 mm on the entrance slit of the double 1-meter high-resolution diffraction monochromator MSDD-1000 (2 gratings at 1200 strokes/mm) and recorded using a ICCD camera PI-MAX-2. The exposure time of the camera was set to 5-10 μs. For abscissa axis the resolution is 0.011 nm/pixel. The camera was synchronized with the discharge current pulse, and averaging over several discharge pulses was performed, if necessary. The ordinate axis represents the distance along the entrance slit of the monochromator, which was oriented perpendicular to the axis of the

discharge. Color gradations (gray) reflect the intensity at a given wavelength at a given point across the discharge. The contour of the H_β line on the discharge axis in the middle of the discharge gap is shown in Fig. 2c. It can be seen that the H_β line is strongly broadened and splits into two peaks. The contour was normalized, approximated by the Lorentz contour (Fig. 2c, a thin line) and the width of the contour was determined at half-height $\Delta\lambda$. The electron density was determined from the relation: $\Delta\lambda = 2.5\cdot10^{-9}\cdot\alpha_{H\alpha}\cdot n_e^{2/3}$, where $\alpha_{H\alpha}$ is the Stark broadening parameter [11]. The instrumental broadening was 0.045 nm, the Doppler and van der Waals broadenings did not exceed 0.05 nm, and under experimental conditions, when the spectral line was broadened to more than 0.5 nm, they were not taken into account.

The time dependences of the structure transmission were recorded using a microwave diode and a digital oscilloscope GDS-72204E (Fig. 3). The source of the continuous microwave signal G3-14A generator had an output power of about 5 mW and with a frequency of about 9.15 GHz, which corresponded to the middle of the forbidden band (Fig. 1*b*). Discharge current pulses for different gases are shown in Fig. 3, *a*–*c*. Maximum electron density in all cases was about 10^{16} cm^{-3}. It can be seen that one's consist of a limited number of damped oscillations, which total duration is 5 μs (helium, argon) and about 8 μs in air.

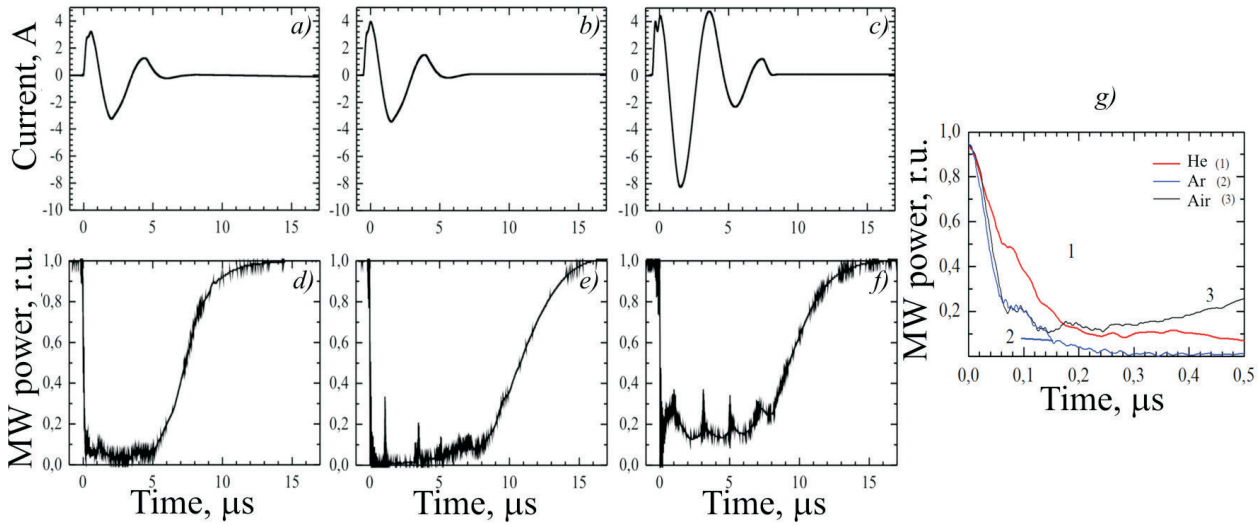

Figure 3. Current pulses in helium (*a*), argon *(b)* and (*c*) air, and envelopes of the1D plasma EBG structure transmission in helium (*d*), argon (*e*) and air (*f*) and their initial stages (*g*).

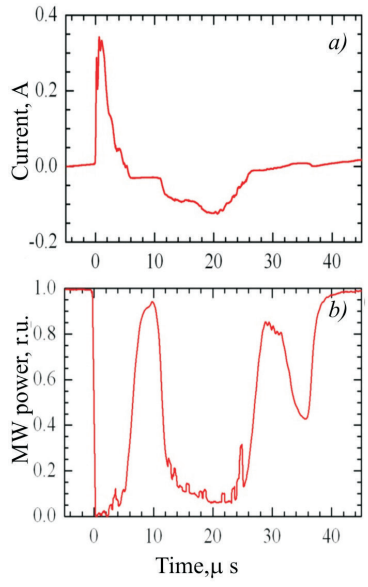

Fiure 4. Discharge current pulse (*a*) and envelop of the 1D plasma EBG structure transmission (*b*).

It can be seen (Fig. 3, *d*–*f*) that the duration of the signal suppression is determined by the time of the current flow and depends on the type of gas: about 8 μs for discharges in helium and about 13 μs in argon and air. The maximum level of suppression in discharges in different gases is also different. The transmission is restored in about 5 μs.

The switch on time was estimated from the initial stages of the microwave signal envelops, which are presented in Fig. 3*g*. It can be seen that the change in the transmission level from 0.9 to 0.1 in argon and air occurs in a time of less than 100 ns, and in helium in about 200 ns.

It should be noted that at the moment of the current direction change there is an increase of transmitted microwave power (Fig. 3), which is apparently connected with a decrease in the electron concentration at these moments. With an increase of the capacitance C to 4 μF, the time between the peak values of the discharge current oscillations can be increased. As it follows from the envelops in Fig. 4, a significant suppression of the passing microwave signal at

current peaks and almost full transmission at currents close to zero were observed in this case. The shortest peak current period was about 10−20 μs, which corresponds to a maximum switching frequency of about 50−100 kHz.

3. THE 2D PERIODICAL STRUCTURE

Possibility to control the propagation of an electromagnetic wave at 18 GHz in a 2D EBG structure has been demonstrated experimentally by Lo et al. [12]. For our work, the EBG structure has been modified for operation at frequency of 9.15 GHz [8]. Investigated structure is formed by copper rods of 5 mm diameter distributed uniformly with a lattice constant of 22 mm (Fig. 5*a*). This arrangement allows diagonal wave propagating mode (around ~ ±45°) for frequencies in the 9.15 GHz range and the principal propagating mode (0° direction) being forbidden. In order to excite the diagonal mode, it is necessary to put a defect in the front rod row of the EBG structure by removing one or two rods (Fig. 5, inset II) or by adding a rod (or plasma column) (Fig. 5, inset III). The structure is irradiated by continuous MW radiation at frequencies in the range of 8.5−10.0 GHz and power of 5 mW using a horn antenna (directivity 55). Microwave radiation transmitted through the 2D EBG structure is received by another horn antenna (directivity 5.5). Receiving antenna with a waveguide-to-radio adapter is moved along a circular arc of 0.5 m radius, centered in the middle of the triangular periodic structure base. This movement is realized within an angle range of ± 60° relative to the axis of the radiating horn antenna (Fig. 5). The transmitted signal was controlled and registered by spectrum analyzer S4-27 or microwave diode with digital oscilloscope GDS-72204E, respectively.

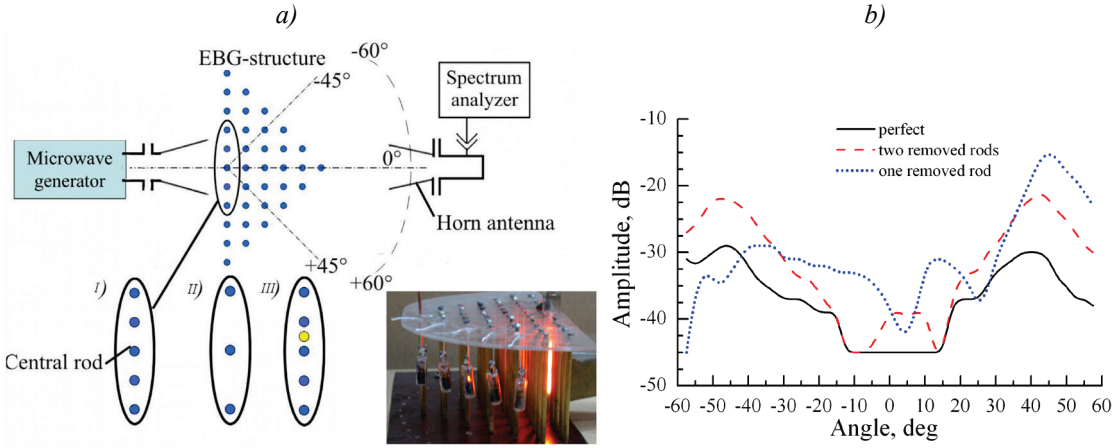

Figure 5. *a*) Schematic of the experimental setup (I – perfect EBG structure, II – structure with two vacations, III – structure with additional defect). The inset (bottom-right) –photo of the 2D EBG structure with plasma as additional rod. *b)* Radiation patterns of the 2D EBG structure.

When the structure has no defect (Fig. 5, solid), there is only weak microwave radiation reaching the receiving antenna, where the signal level is less than the microwave radiation signal from the radiating horn antenna without 2D EBG structure by 3−4 orders of magnitude. If the two nearest rods to the central one in the first row are removed, then microwave radiation begins to propagate in directions ±45° and signal level grows up by 7 dB (dashed curve). If there is only one rod removed, a microwave signal increases by 15 dB (dotted) at the removed rod side. The same behavior takes place for radiation pattern in case of additional defect as well.

After that we replaced a defect in EBG structure (vacancy or additional rod) by plasma inhomogeneities and tested the structure transmission properties at high-power microwaves (pulse regime, about 50 kW at a frequency f_0=9.15 GHz, pulse repetition frequency is 2 kHz and pulse duration is about 150 ns). Discharge lamp GSh-2 (inner diameter 6 mm, external one – 8 mm, gas - neon at low pressure about 30 Torr) was used as a plasma inhomogeneity. The envelopes of high-power microwave pulses transmitted in 45° direction are presented in Fig. 6. The initial microwave power leads to the gas breakdown in the lamp and appearing plasma modifies the 2D EBG structure radiation pattern. For

example, when plasma is placed as additional rod, the microwaves are transmitted in 45° direction, that can be seen from small glowing lamps on the edge of the structure (inset on Fig. 5). Disappearing (plasma replaced vacancy) or appearing (plasma replaced additional rod) of a microwave signal in 45° direction occurs with the delay of about 30-40 ns which probably corresponds to the time of electron density growth. When the lamp GSh-2 is ignited at current of 150 mA (about 6×10^{12} cm^{-3}), a switching appeared slightly faster (curve 3 in Fig. 6) in result of a faster increase of electron density.

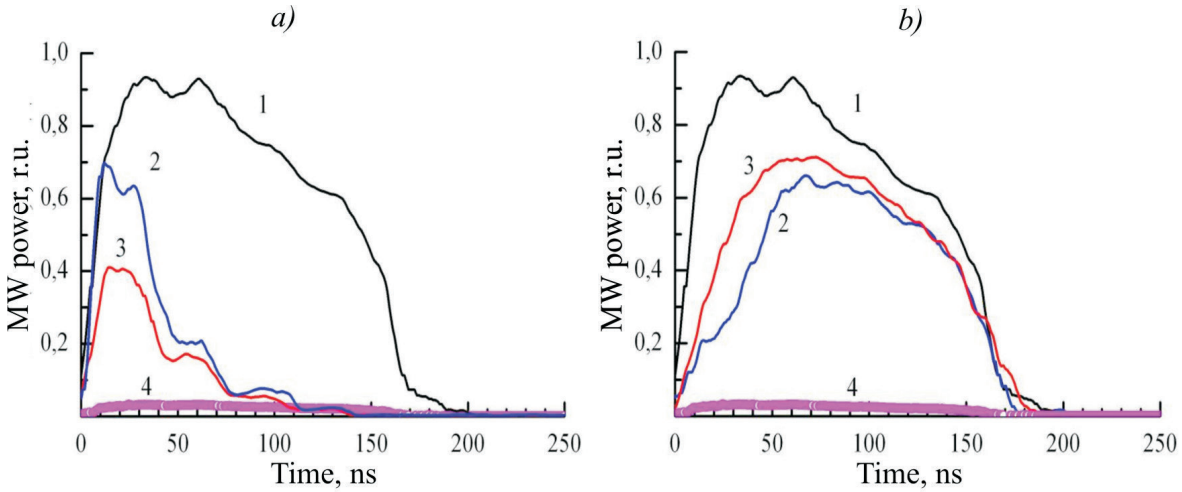

Figure 6. Envelops of transmitted pulses for 2D EBG structure with plasma as defect compensator (*a*) and as additional defect (*b*). 1 – defect exists; 2 – plasma initiated in GSh-2 by microwave power; 3 – direct current in GSh-2 (150 mA); 4 – perfect structure.

4. CONCLUSIONS

One and two-dimensional EBG structures with plasma control elements have been studied in terms of transmission spectrum and its switching speed. Specially designed discharges were created and placed in EBG structures. The time resolved H_α and H_β lines profiles were registered using ICCD camera PI-MAX 2 and a time behavior of electron density was determined during the discharge. Maximum electron density in helium, argon and air was about 10^{16} cm^{-3}. It was shown, that the switching speed is higher in case of using argon discharges as EBG structure inhomogeneities in comparison with discharges in helium and air with the same electrical characteristics, and a nanosecond switching time of a transmission spectrum could be reached. Switching frequency could be about 100 kHz. The switching properties of 2D EBG structure with plasma control elements were tested at high microwave power of about 50 kW. Tens nanoseconds switching time was obtained.

Obtained results can be used for a high–speed microwave devises development that are able to work at high power levels and can be used as a part of automated systems for receiving and transmitting microwave signals.

This work was supported by the CNRS (grant No. 7423).

REFERENCES

1. Coaxial band YIG-tuned filters, Magnetron. - http://www.magneton.ru/cat.php?id=109#main_top .
2. Diode Switches, IEM Kvarz. – http://www.kvarz.com/general/perekluchatel2E.html
3. Waveguide Switches, Dow-Key Microwave. – http://www.dowkey.com/product-category/waveguide-switches/.
4. Sakai O., Tachibana K., Plasma Sources Science and Technology, 2012, **21**, N 1, 013001.
5. Simon A. et al., IEEE Transactions on Plasma Science, 2018, **46**, 2512.
6. Arkhipenko V.I. et al., J. Appl. Phys., 2014, **116**, 123302.

7. Babitski V.S. et al., J. Appl. Phys., 2017, **122**, 083302.
8. Simonchik L.V., Usachonak M.S., 41st EPS Conf. on Plasma Physics, P2.126. http://ocs.ciemat.es/EPS2014PAP/pdf/P2.126.pdf .
9. Ansoft HFSS, http://www.ansys.com .
10. Ivković M., Konjević N., Pavlović Z., J. Quantitative Spectroscopy & Radiative Transfer, 2015. **154**, 1.
11. Griem H.R., Plasma spectroscopy, M.: Atomizdat, 1969, 452.
12. Lo J., Sokoloff J.et al., Appl. Phys. Lett., 2010, **96**, 251501.

4. Poster papers

SOME PROPERTIES OF MICROWAVE DISCHARGE IN LIQUID *N*-HEPTANE WITH AND WITHOUT BUBBLE FLOW OF ARGON

K. A. Averin, I. V. Bilera, I. L. Epstein, Yu. A. Lebedev, V. A. Shakhatov

A.V. Topchiev Institute of Petrochemical Synthesis of the Russian Academy of Sciences (TIPS RAS), Leninsky Prospect, 29, Moscow, 119991, Russia

Abstract. Emission spectra and gas products of a microwave discharge in liquid *n*-heptane with and without argon bubbling (6−40 l / h) are investigated. The discharge was excited in a system with a coaxial input of energy. The pressure above the surface of the liquid was equal to atmospheric pressure. It is shown that the addition of argon changes the spectral composition of the plasma radiation, in which the emission of atomic lines of hydrogen and argon appears. The addition of argon does not affect the rotational temperature of the state $C_2\left(d^3\Pi_g\right)$, the composition and the ratio of the main gas products (H_2, CH_4, C_2H_2, C_2H_4).

1. INTRODUCTION

Discharges in liquids have attracted the attention of researchers and are one of the priorities in the study of the physics of gas-discharge and low-temperature plasma [1−5]. This is explained, first of all, by promising applications of such discharges in solving environmental problems. In addition, such discharges can be used to produce various gas and solid products.

At present, different types of discharges are used to create plasma in liquids, but microwave discharges are the least investigated object. Publications on this item appeared in early 2000-th and counts in several tens papers (in liquid organic compounds the quantity of papers is even less) in contrast to hundreds of publications on other types of discharges. Introduction to current state of researches in this field is presented in recent review articles [6, 7].

This paper presents results on optical emission spectra and gaseous products of microwave discharge in liquid *n*-heptane (*n*-C_7H_{16}) with and without bubble flow of argon.

2. EXPERIMENTAL SETUP

The experiments were carried out at a facility, described in detail in Refs. [8−10] and schematically depicted in Fig. 1. The attenuator allows receiving smoothly varying incident power in a range from 100 W to 2.5 kW. The discharge section is a waveguide-to-coaxial junction, the central conductor of which serves as an antenna for introducing microwave energy into the discharge section. For matching, a movable short-circuiting piston was used. The central electrode of the coaxial line is made of a copper tube. Tubes with external diameters of 1.5 and 6 mm were used. Reducing the diameter of the antenna made it possible to organize a discharge at powers of the order of 100 W. The discharge was created at the end of the antenna in a quartz cuvette (diameter 55 mm) placed in a protective screen (Fig. 1). The volume of the liquid in the cuvette is of the order of 40 ml, which ensures that the end of the inner electrode of the coaxial line lies below the surface of the liquid. Argon was fed into the chamber (flow rate 0−40 l / h) through the internal channel in the electrode. The pressure above the surface of the liquid was equal to atmospheric pressure.

The discharge was focused by optics on the input aperture of the optical fiber directing the radiation to the entrance slit of the AvaSpec 2048 spectrograph. The time averaged emission spectra of the discharge in the wavelength range 200−700 nm were recorded. Relative calibration of the spectrograph was carried

out using a tungsten band-lamp (SI-8-200). The technique for processing the spectrum is described in detail in [11]. The discharge was visualized by a digital camera with a frame rate of up to 240 frames per second.

The gas composition of microwave discharge products in liquid *n*-heptane was determined by gas chromatography.

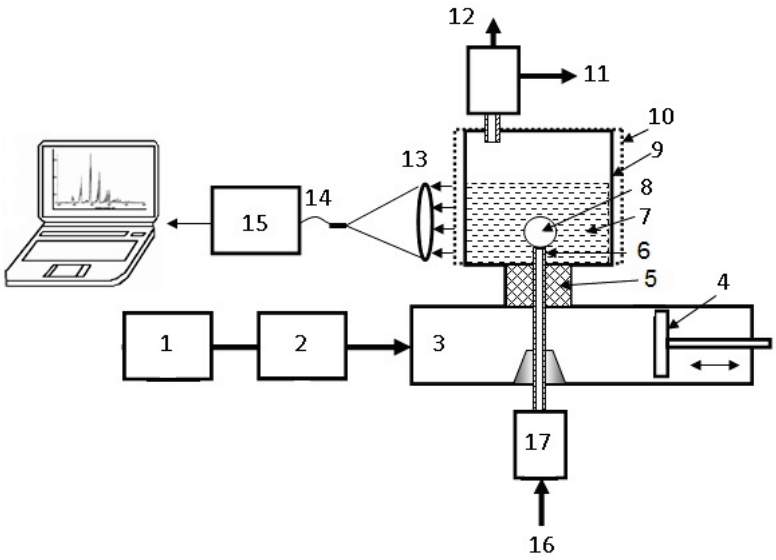

Figure. 1. Schema of experimental setup 1− microwave generator, 2 – reflectometer, 3− waveguide-to coaxial junction, 4 – shorting plunger, 5 – dielectric, 6 – antenna, 7– liquid hydrocarbon, 8 – discharge region, 9 – quartz reactor, 10 – metal screen, 11 − to chromatograph, 12 – gas exhaust, 13 – optical system, 14 − optical fiber, 15 – spectrograph AvaSpec- 2048, 16 – additional plasma gas, 17 − flowmeter.

3. RESULTS AND DISCUSSION

Emission spectra of microwave discharge in *n*-heptane includes the Swan bands (transition $C_2\left(d^3\Pi_g - a^3\Pi_u\right)$) of sequences $\Delta\upsilon = 0$ (maximum at 516.5 nm), $\Delta\upsilon = 1$ (maximum at 563.5 nm), $\Delta\upsilon$ =-1 (maximum at 473.75 nm), and the band at 436.5 нм ($\Delta\upsilon$ = -2) is superimposed with the band 0-0 of *CH* emission at 431.2 nm (transition $CH(A^2\Delta - X^2\Pi)$). The wide band spectrum of hard carbonaceous particles is also observed (Fig. 2). Spectrum 2 was obtained after ignition of discharge in the *n*-heptane previously processed with microwave discharge.

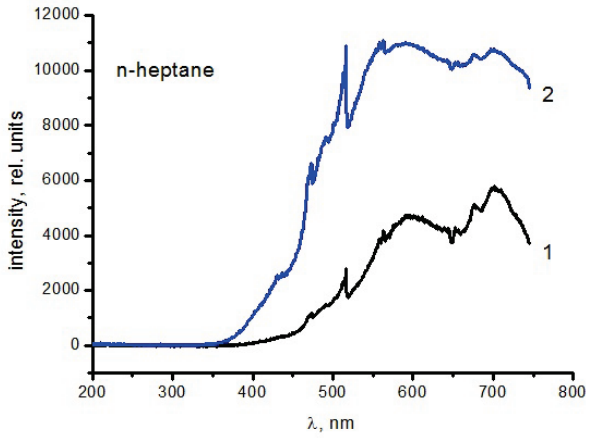

Figure 2. Emission spectra of microwave discharge in liquid *n*-heptane. 1 − in pure *n*-heptane, 2 − in *n*-heptane with carbonaceous particles (after previous processing).

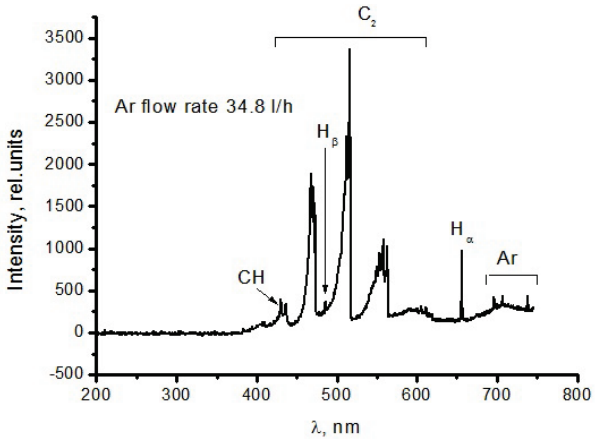

Figure 3. Emission spectra of microwave discharge in liquid *n*-heptane with addition of Ar (34.8 l/h).

Difference of curves 1 and 2 in Fig. 2 is unclear as content of liquid hydrocarbon before and after processing practically was unchanged [15]. The only difference was the presence of carbonaceous particles. It seems that the medium inside the plasma bubble is enriched in carbon due to these particles in the evaporated boundary. This causes the increase of intensity of broadband continuum.

At high argon consumption the structure of the spectrum changes qualitatively (Fig. 4). It produces the emission of the H line (threshold 12.09 eV), and with increasing argon flow, also H_β (threshold 12.75 eV) and lines of argon radiation with thresholds of the order of 13.3 eV (Fig.3.)

When analyzing the results, the results of calculations of the electron energy distribution function (EEDF) in a mixture of argon and a hydrocarbon were used. The Boltzmann equation for a stationary, isotropic part of the EEDF, recorded in the two-term approximation of the expansion of the EEDF into spherical harmonics [13] has been used. Calculations indicate that EEDF and coefficients electron impact initiated processes are strongly depend on the dilution of hydrocarbons by argon (Figs. 4, 5). Calculation of ratios of intensities of H_α и H_β emission and comparison with the measured value gives information on the microwave field in plasma (Fig. 4).

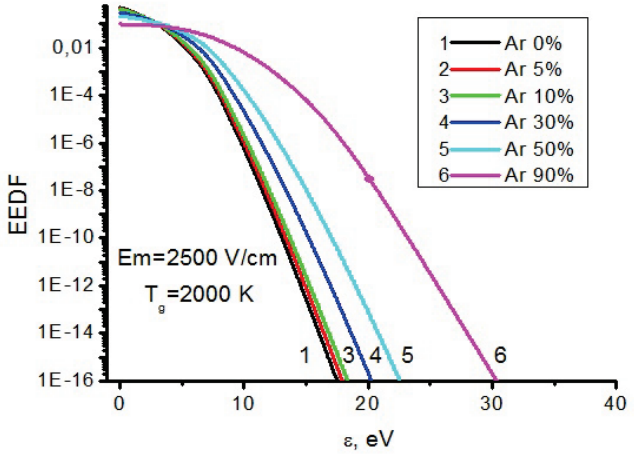

Figure 4. Electron energy distribution functions in hydrocarbon diluted with argon at atmospheric pressure at gas temperature 2000 K.

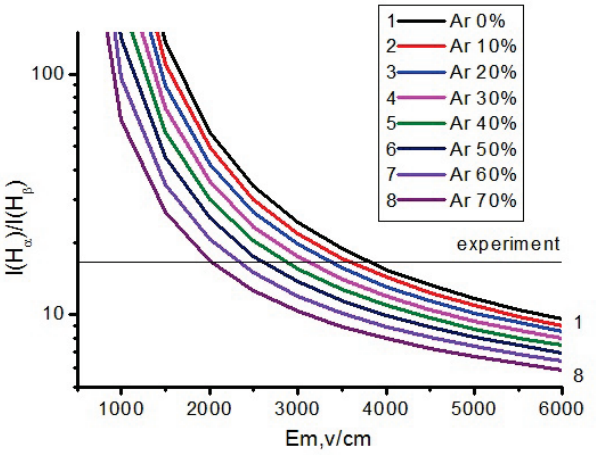

Figure 5. Ratios of electron impact excitation coefficients of H_α and H_β emission at different content of argon in hydrocarbon and microwave field strength.

Detailed analysis of gaseous products showed that the main products are H_2, CH_4, C_2H_4, and C_2H_2. Table 1 shows the ration of the main products at different additions of argon (respectively to H_2 volume concentration).

Table 1. Distributions of main products of microwave discharge in liquid *n*-heptane with and without bubble flow of argon

Ar, l/h	H_2	CH_4	C_2H_4	C_2H_2
0	1	0,059	0,184	0,269
6.8	1	0,049	0,233	0,306
17.3	1	0,037	0,264	0,340
36.8	1	0,040	0,184	0,281

4. CONCLUSIONS

The emission spectra of microwave plasma in liquid *n*-heptane with and without bubble flow of argon at atmospheric pressure above the surface of a liquid are studied. Without the addition of argon and with its small expenditure in the emission spectra there is no emission of atomic lines. An analysis of the emission

of Swan bands showed that the addition of argon at a flow rate of 6-40 l / h does not change the rotational temperature of the state $C_2(d^3\Pi_u)$, which is ~ 2000 K. At atmospheric pressure this temperature can be identified with the gas temperature. When the flow of argon is high, the plasma emission spectrum becomes more complicated, and the emission of the H_α line appears in it, and with an increase in the addition of argon, as well as lines H_β and lines of argon radiation. The range of the microwave field strength in the plasma (2000-4000 V / cm) is determined from the ratio of the emission intensities of the H_α and H_β lines. Since the gas composition in the plasma bubble is not known, this range cannot be narrowed.

Difference in the spectra obtained in the pure *n*-heptane and in the *n*-heptane after processing is related with difference in the content of evaporated liquid boundary followed by the difference in the gas composition of plasma. Thus the nonstationarity of the discharge in addition to other factors is related with time changing of the boundary conditions.

It is shown that the main gaseous products of the discharge are hydrogen, methane, ethylene, and acetylene. Hydrogen has highest volume concentration and methane have the minimal concentration. Ethylene and acetylene have close concentration with predominance of acetylene. Addition of argon does not change the distribution of main products.

Acknowledgements

Study of the microwave discharge in *n*-heptane without argon was fulfilled in the frame of TIPS RAS State Plan. Study of the microwave discharge in *n*-heptane with argon was fulfilled in the frame RFBR grant № 18-08-00146.

References

1. Samukawa S. et al., J. Phys. D: Appl. Phys. 2012, **45,** 253001.
2. Bruggeman P., Leys C., J. Phys. D: Appl. Phys., 2009, **42**, 053001.
3. Yang Y., Cho Y.I., Fridman A., Plasma discharge in liquid: Water Treatment and Application CRC Press, 2012 ISBN 9781439866238.
4. Bruggeman P.J., et al, Plasma Sources Sci. & Technol., 2016, **25**, 053002.
5. Foster J., Phys. Plasmas, 2017, **24,** 055501.
6. Lebedev Yu.A., Plasma Phys Reports, 2017, **43**, 676.
7. Lebedev Yu.A. High Temperature, 2018, **56**, 811.
8. Averin K.A., Lebedev Yu.A., Shakhatov V.A., Plasma Phys.Reports, 2018, **44**, 110.
9. Lebedev Yu.A., Averin K.A. J. Phys. D: Appl. Phys., 2018, **51**, 214005.
10. Averin K.A., Lebedev Yu.A., High Energy Chem., 2018, **52**, 263.
11. Lebedev Yu.A., Epstein I. L., Shakhatov V.A., Yusupova E.V., Konstantinov V.S. High Temperature, 2014, **52**, 319.
12. Lebedev Yu.A., Averin K.A., Borisov R.S., Garifullin A.R., Bobkova E.S., Kurkin T. S. High Energy Chemistry, 2018, **52**, 324.
13. Hagelaar G.J.M., Pitchford L.C. Plasma Sources Sci. Technol., 2005, **14**, 722.

.

.

OBTAINING OF RELATIVISTIC PLASMA BUNCHES UNDER GYROMAGNETIC AUTORESONANCE IN A MAGNETIC MIRROR

V. V. Andreev, A. A. Novitsky, A. M. Umnov, D. V. Chuprov

RUDN University, Miklukho-Maklay Str., 6, Moscow, 117198, Russia

Abstract. Relativistic plasma bunches obtained under gyromagnetic autoresonance in a magnetic mirror are investigated by radiometrical and radiographical analysis of bremsstrahlung radiation. It is shown that the obtaining plasma bunches with relativistic electron component have average energy of few hundred keV and density range of $2–7\cdot10^{10}$ cm^{-3}. The parameters of the bunches depend on parameters of initial plasma, microwave electric field strength, and the rate of the pulse magnetic field increase and can be controlled by varying of such working parameters.

1. INTRODUCTION

Gyromagnetic autoresonance (GA) ensures the phase stability of the motion of a relativistic electron under cyclotron resonance conditions in a slow increasing magnetic field. It leads to the automatic maintenance of resonance conditions, and an increase in the average electron energy according to the law of magnetic field increase [1−3].

In case of magnetic field growing in time a consequence the resonant condition

$$\omega_{ce} = \frac{eB(t)}{m_0 \gamma c} = \omega ,$$

(ω – HF frequency, $B(t)$ − induction of the magnetic field, m_0, e – the rest mass and the charge of the electron, respectively, c – speed of light in vacuum, γ – relativistic factor) can be maintained automatically. Under GA the electron's phase - φ (the angle between the vector of the electric field strength and the vector of the electron's momentum**)** is being trapped into the interval that average time energy of the electron growth in accordance with the law of the magnetic field growth. In this case the magnetic field can be approximately presents as linear function of time

$$B(t) = B_0 + B_{pulsed} = B_0(1 + \alpha\omega t) ,$$

where α − dimensionless parameter determines the rate of increase of the pulsed magnetic field B_{pulsed},

where $B_0 = m_0 c\omega / e$.

In simplified case of uniform electric and magnetic fields and $\gamma \approx 1$, trapping condition of electron under GA regime is [2]

$$\alpha < \alpha_{cr} = 1.19 g_0^{4/3}, \; g_0 = \frac{E_{HF}}{B_0} ,$$

where g_0 is a dimensionless amplitude of the microwave electric field strength - E_{HF}.

The achieved average energy of trapped electrons under GA is determined by the strength of the pulsed magnetic field and doesn't depend on the microwave field strength.

This work is aimed to the radiographic imaging of a plasma bunch and the subsequent evaluation of the concentration of a high-energy electron component and its spatial distribution.

2. EXPERIMENTAL

The experimental set-up described in detail in [2]. It is an axially symmetrical system with microwave cavity (1 in Fig. 1a), disposed in the interpolar space of the electromagnets that create the static magnetic field of mirror configuration. The Helmholtz coils of pulsed magnetic field combined in a single unit with the cavity. The cavity parameters are: height − 11 cm, diameter − 9.4 cm, Q=750, SWR=2.5. TE_{111} mode is excited by the pin feeder at the frequency 2.4 GHz. Internal pulsed microwave power can vary up to P_{HF}=2500 W. Static magnetic mirror field with mirror ratio of 1.6 satisfies the ECR condition within the volume of the cavity.

The X-ray images were obtained by combination of the KODAK MXG X-ray film and intensifying luminescent screen both housed in a light-tight container (2 in Fig. 1a) placed in front of the view port. The film darkness is a quasi linear function of the amount of radiation reaching the film and was calibrated upon source ^{133}Ba of known activity. The view port for radiographical diagnostic is situated in the midplane of the cavity and covered by Be-foil of 0.5 mm thick. The absorption of this foil is negligible at photon energies above 10 keV.

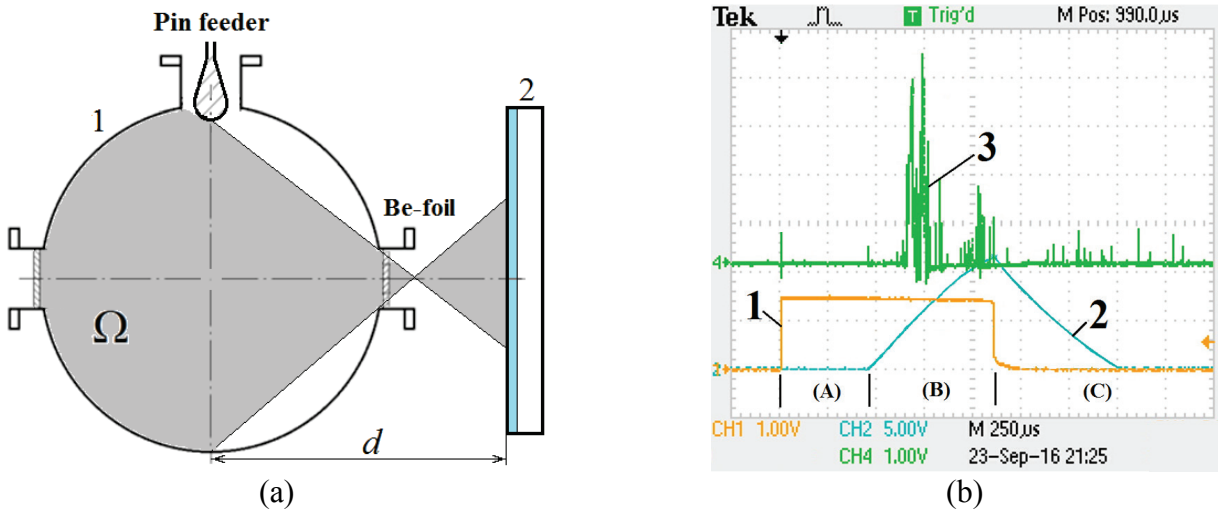

Figure 1. Experimental set-up – (a), typical time diagrams − (b): waveforms of microwave (1), pulsed magnetic field (2) and NaI(Tl) detector signal (3).

In Fig. 1b typical time diagrams with three significant phases of the experiment are presented. In stage (A) microwave pulse (1) leads to the breakdown of gas in the cavity producing initial ECR-plasma. At the moment when all transition processes are finished, pulse current through coils produce a pulse magnetic field of quasi triangular form (2). Increase of the magnetic field accompanied by HF corresponds to GA process producing of the relativistic plasma bunch – stage (B). In stage (C) decompression and confinement of plasma bunch occurs. Waveform 3 in figure 1b is typical signal of a standard X-ray detector with 2.5”x2.5” NaI(Tl) crystal used in foregoing experiments [2, 3] for spectrometry and radiometry.

Typically, the system of synchronization tunes microwave pulse to turn off at the same time as increase of the magnetic field ends. The parameter α can be varied in a wide range by varying of increasing time and the amplitude of the pulsed magnetic field within the intervals of 200 ÷ 800 µs and 200 ÷ 1000 G, respectively. The cavity’s stainless wall thickness allows penetration of the pulse magnetic field with a small decrease in its strength and slight phase delay. The experimental set-up operates in the pulse-periodic mode with the frequency 35 Hz. The design of the experimental set-up, the operating parameters and the principle of its operation are described in detail in [2]. Experiments were performed with Ar plasma ($1\cdot10^{-4}\div 1\cdot10^{-5}$ Torr).

3. RESULTS

Registered X-ray image of bremsstrahlung from the cavity is represented in Fig. 2. The equivalent exposure time with respect to the duty factor was 1 min. For comparison the image of the testing point source with 60 min exposition is placed in the lower right corner. The source ^{133}Ba with activity of 100.9 kBq was located close to the container with the X-ray film.

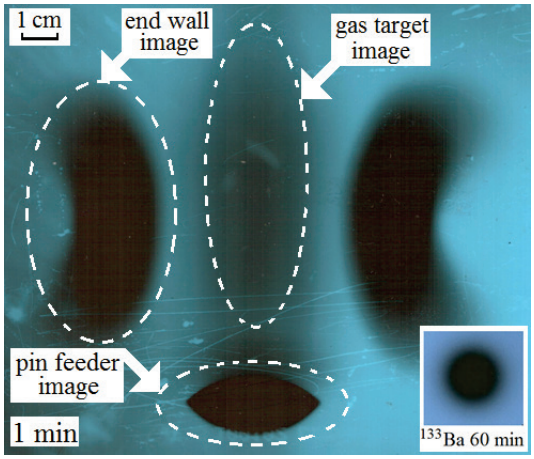

Figure 2. X-ray image of bremsstrahlung from the cavity. In the lower right corner there is the image of the testing point source.

There are three characteristic areas in the image which corresponds to different sources of bremsstrahlung radiation from the cavity. The bottom image with sharp boundary we can determine as an image of a point source of X-ray radiation located in the upper part of the chamber. It is obvious that the only point source of radiation in the chamber can be a microwave feeder which immersed in a cavity by 3 mm.

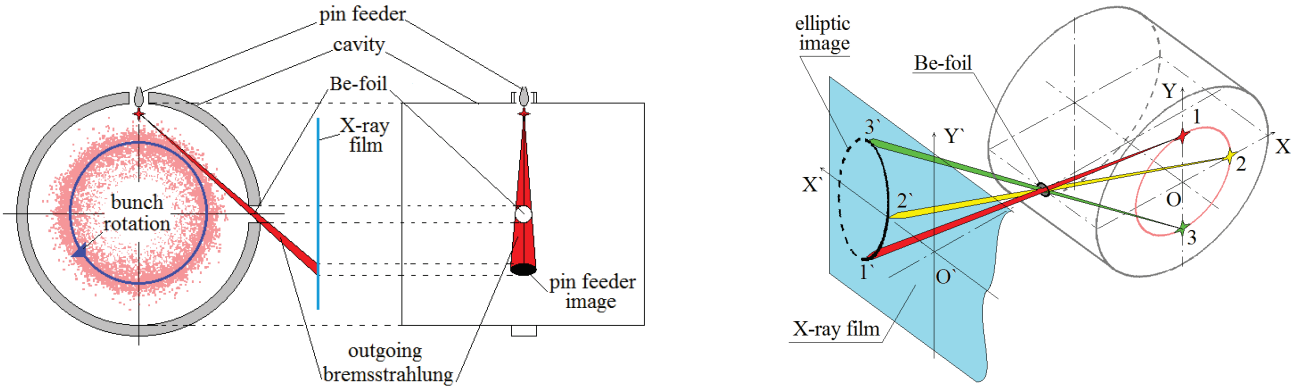

Figure 3. Mechanism of production of pin feeder – (a) and end walls – (b) images.

Figure 3a shows the mechanism of production of pin feeder image. The particles of the relativistic plasma bunch obtained under GA conditions and confined in mirror magnetic trap have a significant azimuth component of momentum. They are rotates in the midplane of the cavity, some particles on outer radius of the bunch hits the microwave feeder and produce bremsstrahlung. View port of the cavity acts here as a diaphragm that limits the outgoing radiation. It results in the formation of an image with sharp boundary.

Moreover this is the reason why particles of the bunch cannot reach the side wall of the chamber. The same conclusion follows from the results of modeling [3], which say that the main losses of particles accelerated in the process of GA are due to their landing on the feeder.

Two symmetrical arc-shaped images are formed by the emission of particles that hits the end walls of the chamber due to bounce oscillations. Figure 3b shows the idea of this image production. Let us

suppose that hot electrons landing the end wall in plane XY within a thin annular region and choose three characteristic points on this ring (1, 2 and 3 in Fig. 3b) which will be point sources of bremsstrahlung radiation. The diaphragm of the view-port gives the images 1`, 2` and 3` of this points in the X`Y` plain of X-ray film. So the image of the above-mentioned annular region is an ellipse. Radiation of annular regions of different radii limited by extended channel of view port forms the arc image of end wall. It is clear that by the minimum distance between two arcs of image, one can judge the maximum radius of the landing of particles. Taking into account the dimensions of the chamber and the diaphragm, this radius is of the order of 3.5 sm.

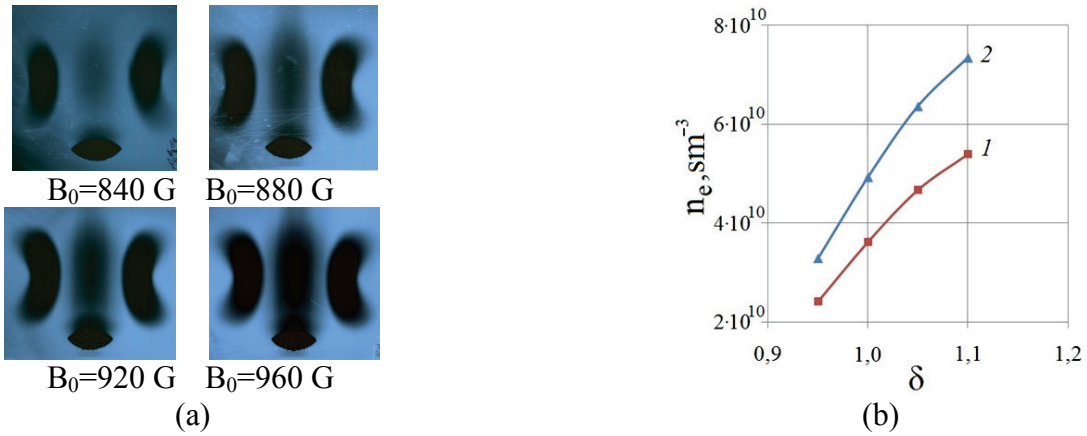

Figure 4. X-ray images for different B_0 – (a), the dependence of the bunch density n_e on parameter δ – (b).

The central part of the X-ray image (Fig. 2) is a result of bremsstrahlung of distributed gas target. Variation of initial magnetic field of the mirror trap gives images presented in Fig. 4a. It's easy to see that darkening of the gas target image strongly depends on induction of the magnetic field at the center of the system B_0. The point is that with increasing of B_0, the area of the ECR surface increases and the number of trapped particles increases too and hence the radiation intensity becomes larger.

Density of hot electrons of the bunch can be calculated from [4]:

$$n_e = \sqrt{\frac{I_{BR}}{\overline{E}_0 \bar{v} V \varphi_{BR}}},$$

were I_{BR} − intensity of bremsstrahlung, $\overline{E}_0$ − average energy of hot electrons, $\bar{v}$ − corresponding average speed, and bremsstrahlung cross section $\varphi_{BR} = Z^2 \cdot 3{,}1 \cdot 10^{-27}$ sm^2 (Z–nucleus charge).

Density n_e was calculated for average energies of hot electrons of 0.5 MeV and 0.3 MeV (curve 1 and 2 in Fig. 4b, respectively).

ACKNOWLEDGEMENTS

The publication was prepared with the support of the Russian Science Foundation (Project No. 17-12-01470).

References

1. Andreev V.V., Umnov A.M., Phys. Scripta, 1991, **43**, N 5, 490.
2. Andreev V.V., Novitsky A.A., Umnov A.M., Chuprov D.V., Instruments and Experimental Techniques, 2012, **55**, 301.
3. Andreev V.V., Chuprov D.V., Ilgisonis V.I. et al., Physics of Plasmas, 2017, **24**, 093518.
4. Ivanov B.I., Butenko V.I, Prischepov V.P., Problems of atomic science and technology, 2010, N 3, Ser.: Nuclear Physics Investigations (54), 18.

EXCITATION OF AN ION-SOUND WAVE IN AXIALLY SYMMETRIC PLASMA

A.A. Balmashnov, N. B. Butko, A. V. Kalashnikov, S. P. Stepina, A. M. Umnov

RUDN University, Mikluho-Maklay Str., 6, Moscow, 117198, Russia

Abstract. The article provides the results of an experimental study of the conditions for the occurrence of low-frequency oscillations in a plasma ring formed by an ECR discharge in a narrow coaxial resonator; establishes the region of discharge parameters, for which these oscillations are stable and the possibility of forming an axially symmetric plasma ring with increasing particle concentration outside the ECR region, as well as the determining influence of spatial inhomogeneity in the resonator's region on the formation of phased oscillations of charged particles and the fact that the recorded oscillations are a consequence of the occurrence of an ion-acoustic wave propagating in the azimuth direction.

1. INTRODUCTION

The study of oscillations of charged particles in axially symmetric plasma objects is not only important from the scientific point of view, but is also of practical interest, as they can significantly influence the operating modes of various experimental devices and devices used in various fields of technology. In particular, research [1–5] has shown that plasma potential oscillations propagating as azimuthal waves are observed in the channels of stationary plasma engines (SPE), and their presence significantly affects the efficiency of the engines' operation.

The CERA-RI-2 plasma injector that we are currently developing differs significantly from SPE and is a version of ECR injectors based on coaxial resonators [6, 7], which research efforts have focused on recently due to the possibility of creating microwave plasma systems with small weight and dimensions. CERA-RI-2 uses an ECR discharge to generate plasma ($\omega_c \approx \omega_0 = 2\pi f_0 = 1.5 \cdot 10^{10}$ rad/s, where ω_c is the cyclotron frequency of the electrons, ω_0 is the frequency of the HF field), and unlike known systems with coaxial resonators, the ECR discharge is realized in the azimuthally symmetric region, thus generating a plasma ring detached from the walls of the discharge chamber [8]. It was found [9] that in the plasma in the ECR region, CERA-RI-2, like SPE, records oscillations of particles, the frequency and amplitude of which depend on the working gas (*Ar*) pressure and the level of the HF power supplied into the resonator. In this case, the oscillations of ions and electrons are always in antiphase, and the oscillations of ions recorded in regions located at an angle of $\pi/2$ relative to each other at the same distance from the center of the plasma ring also occur in antiphase. An analysis of the results obtained gave us reasons to suggest that the presence of low-frequency oscillations in the plasma ring can result from the excitation of an electrostatic (ion-acoustic) wave propagating in the azimuth direction, while the existence of a phase pattern of the oscillations can be due to the geometric dimensions of the plasma ring and the temperature of the electronic plasma component. To confirm this assumption, we studied the plasma generation conditions in region $\omega_c < \omega_0$, in which, as had been established earlier [10, 11], the formation of high-concentration plasma can be a consequence of the following processes: linear transformation of the electromagnetic wave into an oblique Langmuir wave takes place in the region of the upper hybrid resonance ($\omega_c = (0.5-0.7)\omega_o$), and this wave splits into a new oblique Langmuir wave and an ion-acoustic wave. The processes of decay and coalescence of waves lead to the occurrence of an electromagnetic wave of blue and red satellites of its fundamental frequency in the spectrum of oscillations, where the frequency difference between those waves is equal to the frequency of the ion-acoustic wave. In this case, the length of the ion-acoustic wave is determined by the geometric dimensions of plasma. The aim of the study was also to determine the cause of the phase pattern of oscillations, which in [10, 11] was determined by boundary conditions.

2. EXPERIMENTAL DEVICE AND DIAGNOSTIC METHODS

The possibility of forming a plasma ring outside the ECR interaction region was studied by changing the magnetic field profile in CERA-RI-2: the ECR region was shifted to the resonator axis and the diagnostic system was modified to use two single electrical probes that could move in the radial and azimuth directions. Earlier measurements [9] had been carried out with single fixed electric probes.

The plasma source diagram is shown in Fig. 1 [12]. It consists of a narrow cylindrical coaxial resonator (7.0 cm in diameter, 1.0 cm in height) with one of its walls (2) being a replaceable electrode. The working gas was fed directly into the resonator region. The HF power ($\omega_0 = 1.5 \cdot 10^{10}$ rad/s) was supplied to the axial electrode of the resonator. The supplied and reflected HF power was measured using a directional coupler. The azimuthally symmetric stationary magnetic field was generated by annular magnets containing a branch pipe made of a soft magnetic material. The ECR region is at distance $z = 0.5$ cm from the end wall of the resonator and at distance $R_c = (1.2 \pm 0.2)$ cm from its axis.

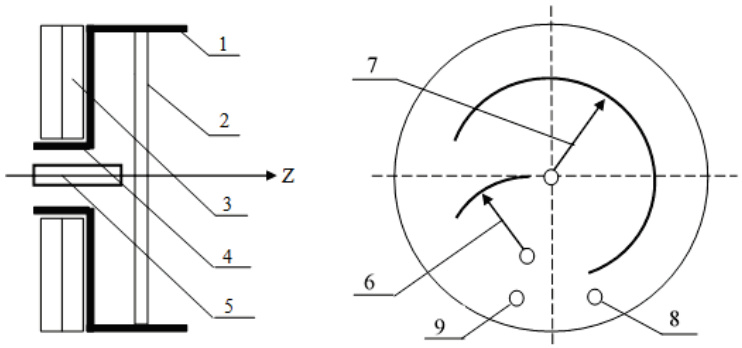

Figure 1. Diagram of the plasma source. 1 − cylindrical resonator casing, 2 − end wall of the resonator, 3 − annular magnets, 4 − branch pipe made of a soft magnetic metal, 5 − central electrode of the coaxial resonator, 6 − location of the probe moving in the radial direction, 7 − position of the probe moving in the azimuth direction, 8 − working gas feed, 9 − location of the HF diagnostic antenna.

In this study, we used single longitudinally oriented electric probes capable of moving in the radial and azimuth directions. The active parts of the radially and azimuthally moving probes were located at a distance of 0.5 cm and 0.1 cm from the end wall of the resonator, accordingly. The radial location of the probe moving in the azimuth direction was determined based on the results of preliminary studies, consisting in determining the operating mode of the plasma injector (working pressure and supplied HF power), in which a plasma ring with an increased particle concentration is detected in the region remote from the ECR interaction zone. The phase correlations of the oscillations of the plasma particles in the remote plasma ring were determined by the displacement of the signals recorded by the probes moving in the radial and azimuth directions.

The current-voltage characteristics of a single electrical probe were recorded and processed automatically with a software. A turbomolecular pump (TMN 500) was used for the study. The below values of the working gas pressure in the vacuum system of the device were measured by a conventional method.

3. EXPERIMENTAL RESULTS

Figure 2 shows the radial distributions of ionic saturation currents and amplitudes of LF oscillations for the HF discharge in Ar ($P_{HF} = 20$ W). It was established that the floating potential in the region of the plasma ring formation (R = (1.8−2.2) cm) was minus (15±5) V, the electron temperature was T_e = (17±4) eV, and the concentration exceeded the critical value for the used HF field frequency. At the same time, plasma near the ECR region of the interaction was a two-temperature one with T_e = (17±4) eV and (35±7) eV.

In the ECR region, the frequency of stable particle oscillations was 72 kHz for $P_{Ar} = 0.84 \cdot 10^{-4}$ Torr and 60 kHz for $P_{Ar} = 0.98 \cdot 10^{-4}$ Torr, and in the region of the remote plasma ring was 89 kHz and 77 kHz for $P_{Ar} = 0.84 \cdot 10^{-4}$ Torr and $P_{Ar} = 0.98 \cdot 10^{-4}$ Torr, accordingly.

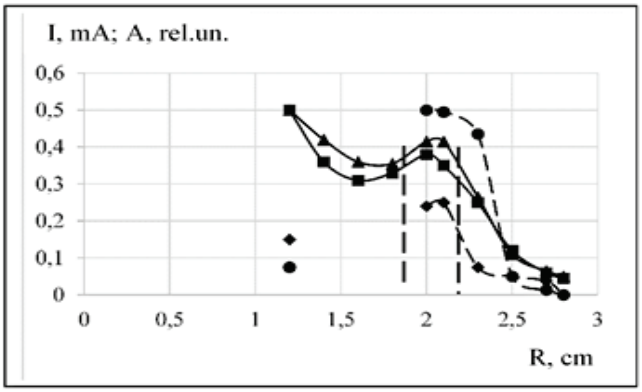

Figure 2. Radial distribution of the ion saturation current (I, solid lines) and amplitudes of LF oscillations (A, dotted lines) for different working gas pressures in the system (P_{Ar}). ▲, ♦ – $P_{Ar} = 0.84 \cdot 10^{-4}$ Torr; ■, ● – $P_{Ar} = 0.98 \cdot 10^{-4}$ Torr.

The obtained results of the remote plasma ring localization allowed identifying the region location, moving in the azimuthal direction of the electric probe ($R_\varphi = (2.0 \pm 0.1)$ cm), used to measure the LF oscillation phase shifts with respect to the reference probe, previously used to measure the radial distribution of the plasma parameters. The reference probe was located at distance R_φ from the resonator axis. Figure 3 shows the measurement results (ECR discharge at pressure $P_{Ar} = 0.98 \cdot 10^{-4}$ Torr); Figure 4 shows the spectrum of high-frequency oscillations, recorded in the HF wave reflected from the resonator.

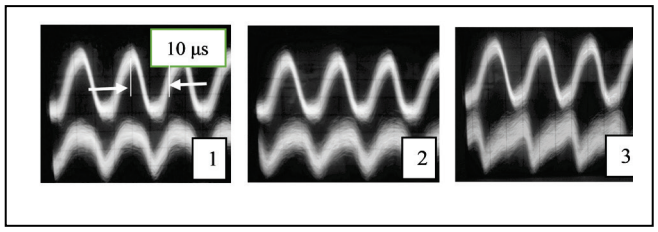

Figure 3. Dependence of the phase of LF oscillations from the angle of rotation of the moving probe (Δφ) with respect to the reference probe. The upper beam in the oscilloscope record is the signal from the reference probe, and the lower one is from the probe moving along φ. The azimuthal position of the moving probe relatively to the reference probe was: 1 – $\Delta\varphi = \pi$, 2 – $\Delta\varphi = 3\pi/4$, 3 – $\Delta\varphi = \pi/2$.

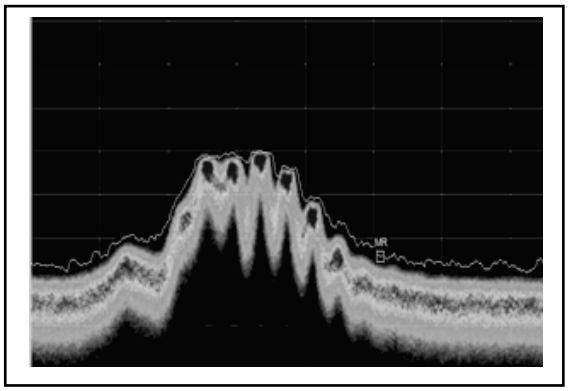

Figure 4. Spectrum of high-frequency oscillations. The scan scale is 200 kHz/div.

Studies aimed at determining the cause of the phase pattern of oscillations showed [13] that it is a local inhomogeneity in the resonator region. The experiments were performed with a blind end wall of the resonator (Fig. 1) and with holes in the wall at an angle of $\pi/2$ at distance R_φ from its axis, one of which holes was used to insert the electrical probe and the other for recording oscillations with a photoelectric detector. It was found that with a blind wall, oscillations are recorded but do not have a phase pattern, which appears when the probe is inserted into the resonator to a depth of more than 0.3 cm.

In order to identify the type of the wave forming oscillations in plasma, we performed experiments to record their frequency for HF discharges in *Xe*, *Ar*, and N_2. It was found that, other conditions being equal (electron temperature (20 ± 5) eV, $R_\varphi \approx 2.1$ cm), phased oscillations are recorded in the region where plasma with an increased concentration of particles occurs, and the frequency of such oscillation was $f \sim (1 / M)^{1/2}$, where M is the atomic mass of the ion (see Table). The spectra of the recorded oscillations are shown in Fig. 5. Based on the results obtained, we assume that it is an ion-acoustic wave.

Table

(f_{Ar} / f_{Xe})	$(M_{Xe} / M_{Ar})^{1/2}$	(f_{Ar} / f_N)	$(M_N / M_{Ar})^{1/2}$	(f_{Xe} / f_N)	$(M_N / M_{Xe})^{1/2}$
1.65	1.81	0.54	0.59	0.32	0.33

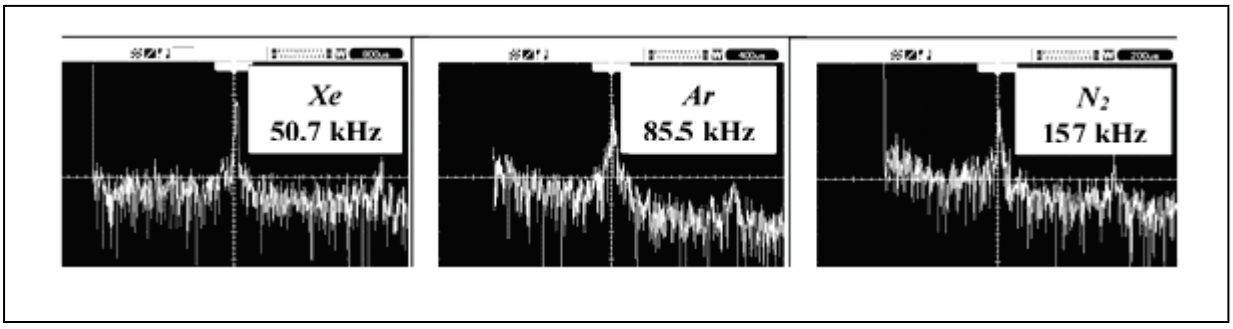

Figure 5. Spectra of low-frequency oscillations of ECR discharges in xenon, argon, and nitrogen.

4. CONCLUSIONS

It was experimentally established that the wave forming phased oscillations in axially symmetric plasma with an increased particle concentration is an ion-acoustic wave excited in the region with local inhomogeneity of the electric HF field intensity.

The publication was prepared with the support of the Russian Science Foundation (project No. 17-12-01470).

References

1. Morozov A.I., Esipchuk Yu.V., Kapulkin A.M., Nevrovsky V.A., Smirnov V.A., ZhTF, 1973, **XLIII**, N 5, 972.
2. Smirnov V.A., Proc. 3rd All-Union Conference on Plasma Accelerators. Minsk, 1976, 12.
3. Veselovzorov A.N., Dlougach E.D., Pogorelov A.A., Svirsky E.B., Smirnov V.A., Proc. IEPC-2011-060. Wiesbaden, Germany, 2011.
4. Veselovzorov A.N., Dlougach E.D., Pogorelov A.A., Svirsky E.B., Smirnov V.A., Proc. IEPC-2013-080. Washington, USA, 2013.
5. Veselovzorov A.N., Dlugach E.D., Pogorelov A.A., Svirsky E.B., Smirnov V.A., ZhTF, 2013, **83,** N 7, 38.
6. Cannat F., Jarrige J., Elias P-Q., Packan D., Space Propulsion - 2014 - 2980728. Cologne, Germany, 2014.
7. Cannat F., Jarrige J., Lafleur T., Elias P-Q., Packan D., Proc. IEPC-2015-90492 / ISTS-2015-b-90492. Hyogo-Kobe, Japan, 2015.
8. Balmashnov A.A., Stepina S.P., Umnov A.M., U.P.F., 2014, **2**, N 3, 224.
9. Balmashnov A.A., Kalashnikov A.V., Kalashnikov V.V., Stepina S.P., Umnov A.M., Plasma Physics Reports, 2018, **44**, N 6, 626.
10. Balmashnov A.A., Golovanivsky K.S., Kamps E., Proc. Intern. Conf. on Plasma Physics. Kiev, 1987, **2**, 239.
11. Balmashnov A.A., Kalashnikov A.V., Kalashnikov V.V., Stepina S.P., Umnov A.M., Prikladnaya Fizika, 2016, N 2, 57.
12. Balmashnov A.A., Kalashnikov A.V., Umnov A.M., Plasma Physics Reports, 2018, **44**, N 6, 594.
13. Balmashnov A.A., Butko N.B., Kalashnikov A.V., Stepina S.P., Umnov A.M., Plasma Physics Reports, 2018, submitted for publication.

OPTICAL EMISSION MEASUREMENTS ON INERT GASES OF MICROWAVE RESONANT PLASMA DISCHARGE

V. V. Andreev, M. A. Korneeva

RUDN University, Miklukho-Maklay Str., 6, Moscow, Russia

Abstract. This reports the results of experimental studies of the spectral and photometric characteristics of radiation generated by a pulse-periodic microwave (2.45 GHz, time-duration – 2 ms, repetition rate – 10 ms, pulsed input power up to 400 W) ECR plasma of initial vacuum. Quite often in gas–plasma physics the phenomenon of nonlinear and turbulent behavior of parameters is observed. In our experiments was found change abruptly and hysteresis of radiation intensity as well as absorbed UHF power occur only as pressure of plasma-forming gas (Ar, He) was varied. At certain pressures (~$5\cdot10^{-3}$ and ~0.9(for argon)/0.3(for helium) Torr), secondary ignition of discharge is observed, accompanied by the upward jumps in radiation intensity. It is found that at pressure between $5\cdot10^{-3}$ and 0.1 Torr hysteresis is observed in the illumination and absorbed power which precedes the transition from a low-density mode plasma to a high-density mode. It is determined that when the pressure is increased in above range, the radiation intensity is twice as high as when the pressure is reduced. The obtained experimental data also showed the efficiency of converting UHF energy into radiation at a pressure above 0.3 Torr. The maximum intensity of radiation obtained at a power of 270 W. These values were 450 lx for argon at a pressure of 9 Torr and 270 lx for helium at a pressure 0.8 Torr. Probe measurements show that the electron concentration in this mode is significantly higher than the critical value for the operating frequency of UHF. The observed hysteresis is probably due to nonlinear processes associated with the balance of ionization.

1. INTRODUCTION

Resonant generation of the microwave plasma confined by an external magnetic field of a mirror trap eliminates need for application of the strong microwave electric fields and has significant effect on the level of a energy consumption necessary for achievement of a high degree of ionization. Discharges under electron cyclotron resonance (ECR) conditions are of particular interest because of their attractive features: wide range of operating pressures, high degree of ionization and generation plasma with a density above the critical value. In addition, discharges of this type have the ability to easily control of plasma parameters.

The advantage of the pulsed mode of the discharge is that with the same, in comparison with the stationary discharge, the average input power in the pulsed mode, it is possible to create a plasma with higher values of temperature and density. Moreover, in this type of the discharge significantly increased radiation fluxes from the plasma, improving the luminous characteristics of the radiation increases, its energy efficiency as the light source.

2. EXPERIMENTAL SETUP

The resonance microwave discharge was formed in the cylindrical quartz flask located in the TE_{111} resonator placed in a magnetic field of the mirror trap (R= 2, L=10 cm) created by permanent magnets with the system of closed magnetic circuit made of permalloy. Changing the position of the magnets with adjusting screws have provided reorganization of a magnetic field of the trap. Thus, an induction of a magnetic field in a minimum of a magnetic trap could change from 750 to 950 Gs. To working frequency of the generator there corresponded an induction of a magnetic field 875 G. The working range of pressure of plasma-forming gas changed in the range from $1\cdot10^{-5}$ to 100 Torr. The residual pressure in the

flask was no higher than 10^{-5} Torr. The pulsed operation of the magnetron generator was provided with the modulator. The modulator scheme allows one to vary the duration and repetition rate of pulses.
In the described experiments the pulse duration was 2.0 ms, while the pause of 8 ms. Earlier [1] it was shown that in the range of working parameters the low-temperature (T_e = 3÷5 eV) with a high degree of ionization ($1\cdot10^{-3}$÷$5\cdot10^{-5}$) plasma up to the over dense ($n_e = 1\cdot10^{10}$÷$4\cdot10^{11}$ cm^{-3}) is created.

The experimental setup was equipped with several diagnostic systems. Optical spectroscopy was carried out using a monochromator-spectrograph MS3504i. The behavior of the integral light intensity in time was recorded by a high-speed photodetector (SD3421/5421, 500–1100 nm, time constant 15 ns) with a linear dependence of the output voltage on the radiation intensity in the spectral sensitivity region. The detector was attached to a vacuum-tight window with UV-glass and detected radiation in a direction perpendicular to the side surface of the resonator. The solid angle of the detector covered almost the entire volume of the quartz flask. The signal from the detector was fed to the digital oscilloscope. Illumination was recorded using a certified photometers ТКА-ПКМ С051 (380—760 nm) with a range from 10 to 200000 Lux (error of ± 8,0%). Optical detectors of the photometers were installed in the process of measurements similar to the photodetector. The input and reflected microwave power were controlled during the experiments. The percentage of power absorbed by the discharge was determined as the ratio of the difference of the input and reflected power (P_{in}-P_{out}) to the input power of the P_{in}.

3. RESULTS AND DISCUSSION

The study of the discharge behavior from the plasma-forming gas pressure was carried out at different values of the invested power (up to 600W). A typical type of light dependence on pressure is shown in Fig.1. When the first threshold pressure P~$5\cdot10^{-3}$ Torr passes, the illumination produced by the discharge increases by an order of magnitude. Changing the mode of discharge generation with increasing pressure is accompanied by a significant decrease in the breakdown time. If at pressures below the threshold for the breakdown of the discharge requires ~12 μs, then after switching to the efficient generation mode, the discharge is punched for a time of ~1.5 μs (Fig. 1). For breakdown at pressures below the threshold, 12 μs is required, and changeover to the efficient generation mode the break-down time of the discharge is about ~1.5 μs (Fig. 1).

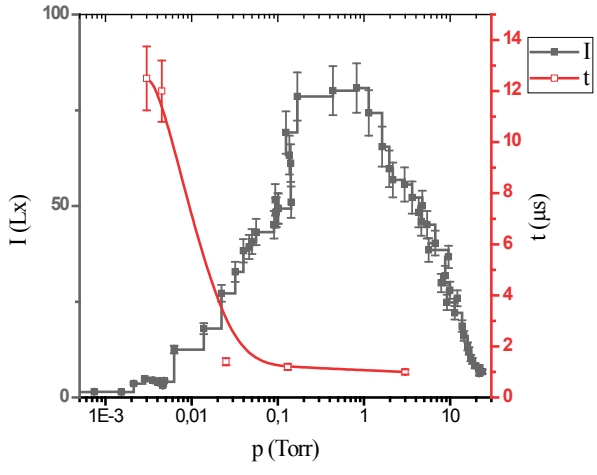

Figure 1. Dependence of illumination (I) and breakdown time (t) on pressure (250 W, 875 Gs, argon).

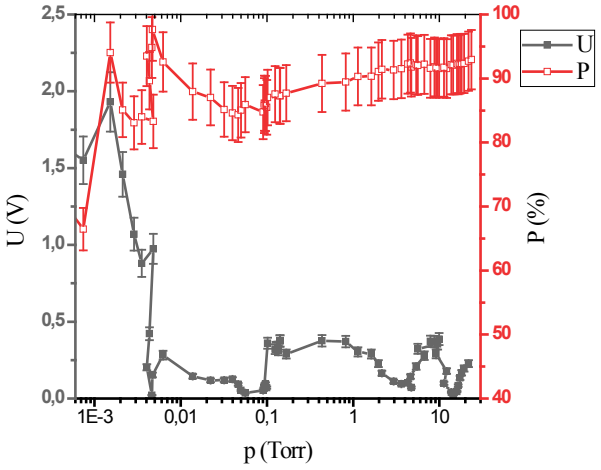

Figure 2. The dependence of the signal from the loop antenna (U) and the absorbed power (P) on the pressure (250 W, 875 Gs, argon).

When used as a working gas of helium, the increase in illumination begins at a higher pressure than on argon, but the General form of the dependences remains. In the same mode of operation of the magnetron, the maximum achieved illumination on helium is twice lower than for argon.

The breakdown time for helium at low pressures is no different from the breakdown time in argon. At high pressures, the breakdown time in helium is almost twice the breakdown time in argon. Obviously,

this is due to the fact that under high pressures for the breakdown of helium electrons need more time to achieve the energy required for ionization, in addition, the cross-section of argon ionization at optimal ionization energy is an order of magnitude greater than the cross-section of helium ionization. Changes in the discharge generation mode are also well traced by the level of power absorbed by the discharge: an increase from 70% to 90-95% occurs (Fig.2).

Ignition of discharge re-starts under pressure P_2~0.9 Torr (argon) or P_2~0.3 Torr (helium). This mode corresponds to the maximum light output level of the discharge. The experimentally recorded maximum illumination for argon was 1000 lux and 500 lux for helium. Despite significant changes in the illumination level at a pressure above P_2, the amount of power absorbed by the discharge remains practically unchanged and remains at the level ~90%.

Probe measurements show an increase in the electron concentration upon transition to regimes with an effective light output. At a pressure above P1, the concentration is above the critical value for the working frequency of the magnetron (>$7{,}5 \cdot 10^{10}$ cm^{-3}). This is possible because of the small thickness of the plasma, comparable to the depth of penetration of the microwave wave.

4. CONCLUSIONS

The obtained experimental results indicate the effective transfer of microwave energy to the plasma. The change in the pressure of the plasma-forming gas over a wide range made it possible to study the features of the discharge formation under various conditions. The effect of "secondary" ignition was detected, accompanied by a threshold, sudden increase in the intensity of the light flux. It is shown that at a pressure of 1 Torr, for argon, the light output of the discharge is maximal.

Acknowledgements

The publication was prepared with the support of the Ministry of Education and Science of the Russian Federation (agreement 3.2223.2017.4.6) and partially by the Russian Foundation for Basic Research (project no. 16-02-00640\16).

References

1. Andreev V.V., Plasma Physics Reports, 2017, **43**, N 11, 1119.

EFFECT OF A DC EXTERNAL ELECTRIC FIELD ON THE PROPERTIES OF A NONUNIFORM MICROWAVE DISCHARGE IN NITROGEN AT REDUCED PRESSURES

Yu. A. Lebedev[1], G. V. Krashevskaya[1,2], A. Yu. Titov[1], I. L. Epstein[1]

[1] A.V. Topchiev Institute of Petrochemical Synthesis of the Russian Academy of Sciences (TIPS RAS), Leninsky Prospect, 29, Moscow, 119991, Russia
[2] National Nuclear Research University "MEPhI", Moscow, Russia, Kashirskoe Shosse, 31, Moscow, 115409, Russia

Abstract. Electrode microwave discharge in nitrogen at pressure 1-9 Torr was studied by the method optical emission spectroscopy with spatial resolution. It is shown that the emission intensities of the nitrogen molecules and ion emission bands decrease with distance from the antenna. The ratio of the intensities of the nitrogen band at 337 nm and the emission of the ion band at 391 nm is used to determine the microwave field strength. When a DC voltage is applied to antenna, the intensities of the emission bands after the fall begin to increase in the vicinity of the plane grounded electrode placed at the distance of 3 cm from antenna. Emission of the first negative nitrogen ion system has the highest intensity. The vibrational distributions of nitrogen molecules and their dependence on direct current and position between antenna and grounded electrode are determined.

1. INTRODUCTION

One of the tasks of physics of gas discharges is to find ways to control plasma parameters. This is important both for studying the fundamental properties of discharges, and for determining the possible directions of their use. One of the promising directions is the generation of plasma by using electric fields of different frequency ranges.

The present work continues the study of an electrode microwave discharge (EMD) at reduced pressure in nitrogen [1−14] and series of studies of the effect of DC field on its parameters [4, 12, 13]. Previously, the influence of DC field on the plasma parameters was investigated [12] in the layer near the surface of antenna. In the present work, by means of emission spectroscopy, the discharge region between a cylindrical antenna and a plane grounded electrode located 2.5 cm away from it was investigated.

2. EXPERIMENTAL SETUP AND METHODS OF DIAGNOSTICS

Experiments were carried out on an installation described in detail in [15] (Fig. 1). The discharge chamber is a stainless steel cylinder with a diameter of 15 cm, with four windows for discharge observation, located in a cylindrical wall. An electromagnetic wave with a power of up to 200 W and a frequency of 2.45 GHz was fed into the discharge chamber through a waveguide-to-coaxial junction, the central conductor of which is an electrode/antenna (5 mm diameter copper cylindrical tube with an internal diameter of 3 mm). It is introduced into the chamber through the upper end of cylindrical chamber along the axis (discharge axis) through the vacuum seal. The microwave power was varied within the limits of 60-100 W. The antenna is isolated by a direct current from the grounded chamber that allows to change independently its potential. The DC voltage between the antenna and the camera varied from -200 to +350 V (the ballast resistor was of 8 kΩ). This paper presents results with positively biased antenna. Negative potential of antenna practically did not influenced the discharge. A grounded plane electrode with a diameter of 2.5 cm was placed at a distance of 3 cm from the end of the antenna.

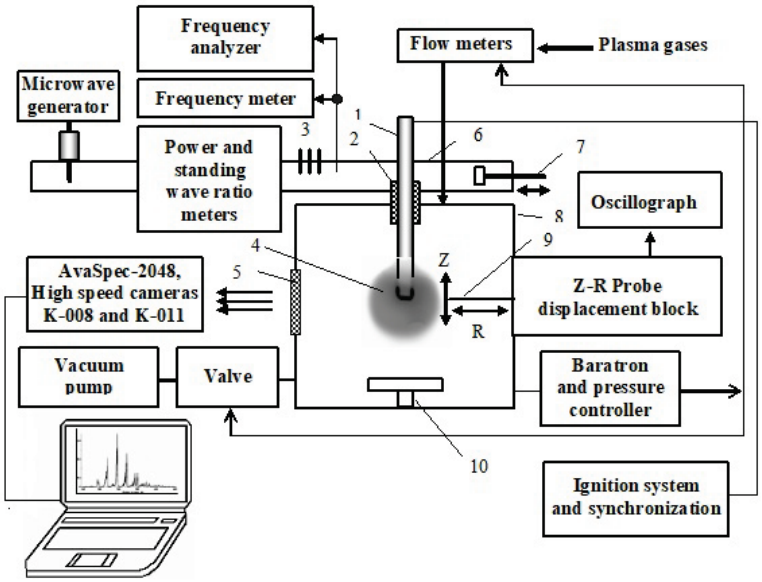

Figure 1. Schema of experimental set-up.1 – electrode/antenna, 2 – isolator, 3 – 3-slab impedance transformer, 4 – plasma, 5 – optical windows, 6 – waveguide-to-coaxial transformer, 7 – shorting plunger, 8 – discharge chamber, 9 movable double probe, 10 – grounded electrode.

The discharge camera is equipped with quartz windows to observe the discharge. The EMD is ignited near the end of the electrode/antenna. The luminous region of the discharge have a radially symmetric structure with a bright near-electrode region (region of self-sustained discharge) and a spherical outer region with a sharp boundary (region of a non-self-sustaining discharge). The region occupied by the luminous plasma is much smaller than the volume of the chamber. For visualization of the discharge (spatial distributions of the spectral radiation intensity of the discharge and along the line of sight) and the investigation of emission spectra in the 200−700 nm range, the unit is equipped with a nanosecond electron-optical video camera K-008, operating in a continuous recording mode and with AvaSpec-2048 spectrometer (spectral resolution was of 1 nm). A quartz condenser projected a plasma image to the plane of the input aperture of the movable optical fiber. The fiber could move in the axial direction from the end of antenna to the grounded electrode (the spatial resolution of the system was not worse than 0.1 mm) giving the spatial distribution of plasma emission.

Experiments were carried out in nitrogen at pressures of 1−9 Torr, incident microwave power of 80 W and flow rate of 60 cm^3/min under normal conditions. The gas was fed through a channel in the top chamber cover. The MKS system, consisting of a controlled flowmeter, a throttling tap and a capacitive pressure meter (Baratron), was used for independent control of pressure and flow.

3. RESULTS AND DISCUSSION

Results of measurements are presented in Fig. 2, a−h. They can be summarized as follows.

1. In the absence of direct current, the luminous area at the antenna is surrounded by dark space. When a DC voltage is applied, a glow appears in the area of a grounded flat electrode.
2. The spectral composition of the discharge radiation near the antenna is represented by bands of the first and second positive systems of nitrogen and weakly depends on the direct current (Fig. 2a, b, g). This confirms the earlier conclusion that, due to the high concentration of electrons at the antenna region, the applied DC voltage is concentrated in the peripheral regions of the microwave electrode discharge [4] and the discharge at the grounded electrode is a DC discharge, and in the experiments under consideration, this electrode is a cathode.

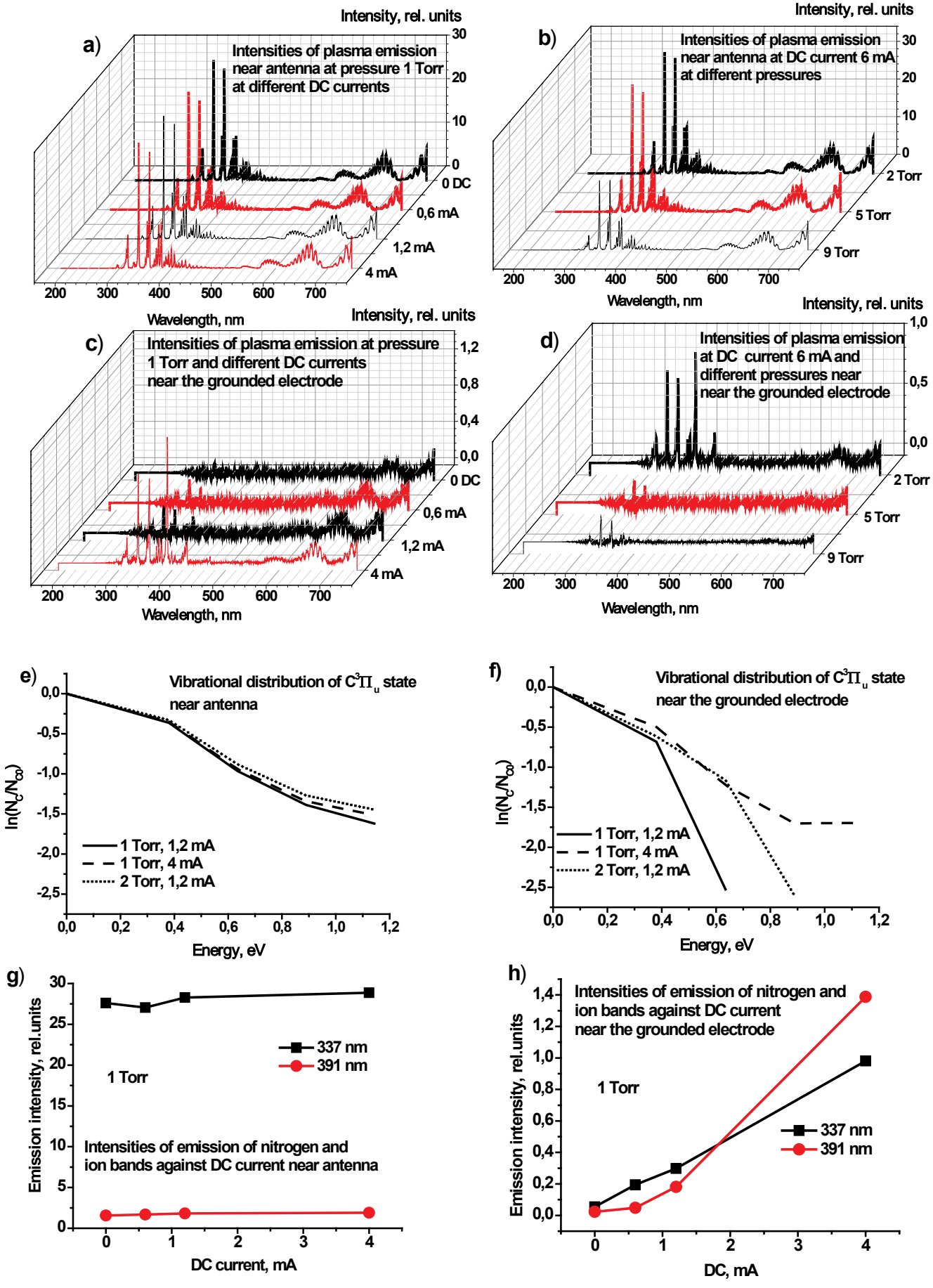

Figure 2. Results of OES measurements.

3. The spectral composition of radiation in the region of a grounded electrode at low currents is represented by bands of the first positive nitrogen system, The radiation of the second positive and first negative nitrogen systems appears with increasing current. The intensity of the latter prevails over the intensity of the second positive system with increasing DC current (Fig. 2c, d, h).
4. The vibrational distribution of nitrogen molecules in the $C^3\Pi_u$ state near the antenna is not Boltzmann and weakly dependent on the direct current (Fig. 2e).
5. The vibrational distribution of nitrogen molecules in the $C^3\Pi_u$ state near the grounded electrode is not Boltzmann, the excitation temperature of the first level is lower than that in the antenna region and increases with increasing DC current (Fig. 2f).
6. The microwave field near the antenna was determined at pressures 1−9 Torr from comparison of measured and calculated ratios of intensities of the second positive and first negative bands of nitrogen. The Boltzmann equation was used in calculations ration of intensities assuming the direct electron impact excitation and results are shown in Fig. 3. It was shown that the value of microwave field does not depend on the DC current. Peak values of the field increase with pressure and lay in the interval 410–880 V/cm at pressures 1 –9 Torr.

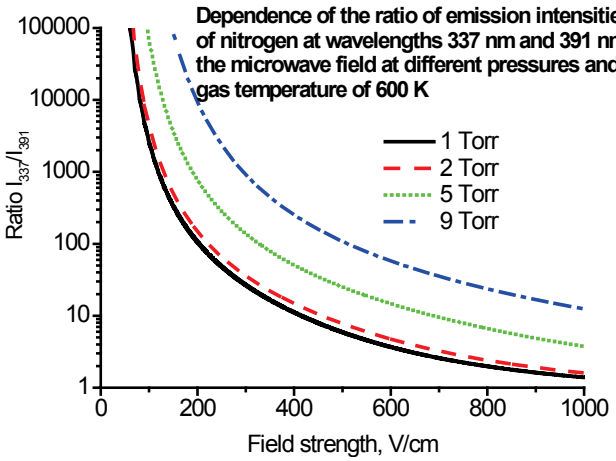

Figure 3. Calculated ratio of intensities of 2^+ and 1^- bands.

References

1. Bardos L., Lebedev Yu.A., High Temperature, 2000, **38**, 528.
2. Lebedev Yu.A., Mokeev M.V., High Temperature, 2000, **38**, 358.
3. Lebedev Yu.A., Shakhatov V.A., Plasma Phys. Rep., 2006, **32**, pp. 56.
4. Lebedev Yu. A., Epstein I. L., Plasma Phys. Rep., 2007, **33**, 63.
5. Lebedev Yu.A., Tatarinov A.V. Epstein I.L., Plasma Sources Sci. Technol., 2007, **16**, 726.
6. Lebedev Yu.A., Tatarinov A.V., Epshtein I.L., High Temperature, 2007, **45**, 283.
7. Lebedev Yu.A., Solomakhin P.V., Shakhatov V.A., Plasma Phys. Rep., 2007, **33**, 157.
8. Lebedev Yu.A., Mokeev M.V., Tatarinov A.V., Shakhatov V.A., Epstein I.L., J. Phys. D: Appl. Phys., 2008, **41**, 194001.
9. Lebedev Yu.A., Mavlyudov T. B., Shakhatov V.A., Epstein I.L., Karpov M.A., Plasma Phys. Rep., 2010, **36**, 182.
10. Lebedev Yu.A., Mavlyudov T.B., Shakhatov V.A., Epstein I.L., High Temperature, 2010, **48**, 315.
11. Lebedev Yu.A., Mavludov T.B., Epstein I.L., Chvyreva A.V. Tatarinov A.V., Plasma Sources Sci. Technol., 2012, **21**, 015015.
12. Lebedev Yu.A., Yusupova E.V., Plasma Phys. Rep., 2012, **38**, 620.
13. Lebedev Yu.A., Epshtein I.L., Yusupova E.V., Plasma Phys. Rep., 2013, **39**, 183.
14. Lebedev Yu.A., Krashevskaya G.V., Gogoleva M.A., Plasma Phys. Rep., 2016, **42**, 100.
15. Lebedev Yu.A., Krashevskaya G.V., Tatarinov A.V., et al., Plasma Phys. Rep., 2017, **43**, 99.

X-RAY RADIATION OF GA-PLASMA BUNCHES GENERATED IN A LONG MIRROR AND ITS SPECTRAL CHANGIES

V. V. Andreev, A. A. Novitsky, A. M. Umnov

RUDN University, Miklukho-Maklay Str., 6, Moscow, Russian Federation

Abstract. In this paper, implemented version of the scenario process gyromagnetic autoresonance (GA) in the reverse magnetic field of the mirror system. A detailed study of the spectral-angular distribution of bremsstrahlung in different operating modes was carried out. The experimentally observed pattern of changes in time of bremsstrahlung intensity corresponds to the dynamics of the generated plasma bunches with an energetic electronic component obtained by numerical simulation, both in the GA phase and in the confinement mode.

1. INTRODUCTION

The well-known and traditionally used methods for obtaining plasma bunches with an energetic electronic component in the combination of electromagnetic and magnetostatic fields or with the help of adiabatic magnetic compression, although they are widely used, require the use of powerful power sources. In addition to these methods of obtaining such plasmas, it is possible to obtain it under electron cyclotron resonance conditions (ECR) in an adiabatically increasing in time [1, 2] or in space [3] magnetic field, the gyromagnetic autoresonance (GA) effect. During this process the relativistic change of the electron mass is automatically compensated by change of the magnetic field and resonant conditions are fulfilled. This leads to the formation of a long-lived relativistic plasma bunch, which has the form of an ion-filled cloud of energetic electrons with an average energy on the order of several hundred keV confined by the external magnetic field. Thus, the GA-effect belongs both to plasma physics and charged particle accelerator physics, and the sphere of its applications may be very wide such as, collective ion acceleration, obtaining high-charge ions, creating pulsed sources of hard bremsstrahlung.

2. EXPERIMENTAL SETUP AND NUMERICAL MODEL

The experimental setup is a cylindrical microwave resonator (mode TE_{118}, resonance frequency 2.45 GHz) placed in an axisymmetric magnetic field of the extended mirror configuration (mirror ratio R = 1.2, L = 80 sm) with induction of the magnetic field at the minimum of the 1200 G trap. A stationary magnetic field is created by three pairs of coaxial coils fed by three DC sources.

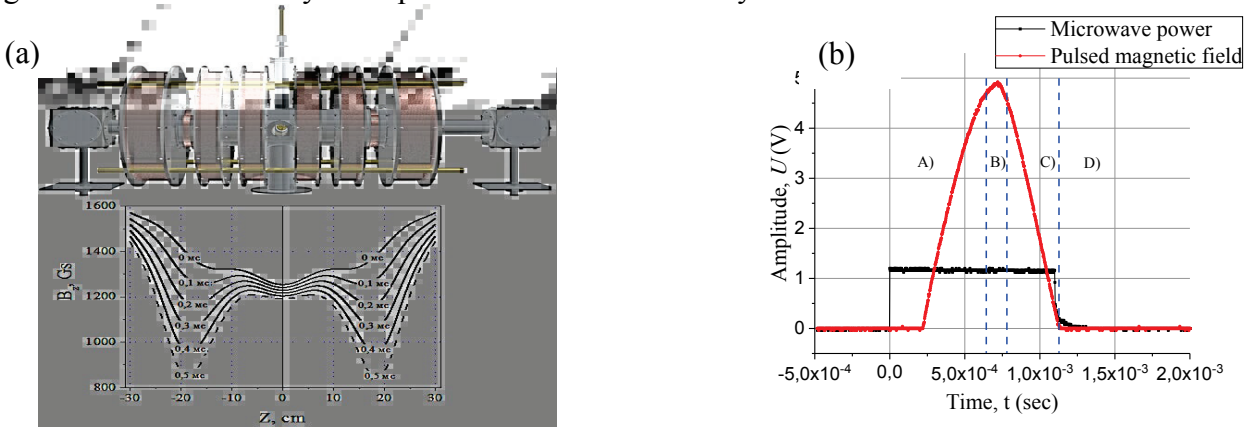

Figure 1. The 3D-design of the experimental setup (a), the duty cycle of the setup (b).

The pulsed magnetic field required for the implementation of the GA regime is generated by the pulsed current flowing through a pair of coils axisymmetric with the cavity and the coils of the stationary magnetic field. The coils of the pulsed magnetic field are placed symmetrically with respect to the position of the minimum of the magnetic field in the trap in antinodes of the electric field of a standing wave TE_{118}-mode. The 3D-design of the experimental setup, together with the axial distribution of the induction of the resulting magnetic field at different times of the current rise time in the reversing coils of the pulsed field is presented in Fig. 1a. The direction of the current in the pulsed coils provides the creation of a pulsed magnetic field with direction of the induction opposite to the induction of the stationary field, thus reduce locally the stationary magnetic field to a level corresponding to the ECR value for the operating frequency. The reduction of the current in the pulse coils and the restoration of the initial profile of the stationary magnetic field in the presence of the microwave field ensure the trapping and acceleration of the initial plasma electrons into the GA regime and the generation of plasma bunches in two symmetrical zones of the setup. The operating cycle of the setup is a current pulse in pulsed magnetic coils with a duration of 900 μs, synchronized with the forward front of the microwave pulse with a duration of 1.1 ms. The duty cycle of the setup is shown in Fig. 1b: phase A – reduction of the resulting magnetic field to values of the ECR within of two zone of the trap, the phase B − formation of initial plasma under ECR in two local zone of the trap, phase C – mode of GA-effect, stage D – confinement mode of the produced plasma bunch in a stationary field of the mirror trap. Power supply systems allow to realize pulse periodic operation of the unit with a duty cycle of 35. The oscillograms of the microwave and magnetic field pulses (working cycle) characterizing the script of the experiment are presented in Fig. 1b. The restoration of the initial profile of a stationary magnetic field with small gradients leads to the movement of produced bunches to the region of the minimum of the trap and their accumulation. The unit operates in a pulse-periodic mode with a variable duty of GA-cycle.

The evolution of plasma parameters has been also studied through 3D modeling. The numerical model built based on the PIC method of particles in a cell with allowance for electrostatic interactions, described in detail in [4], was adapted to the study of the processes of plasma bunches creation in a long magnetic mirror.

3. RESULTS AND DISCUSSION

The experimental setup was tested under the following conditions: the pressure of the plasma-forming gas varied from $P = 1 \cdot 10^{-5}$ Torr to $P = 5 \cdot 10^{-5}$ Torr, the microwave power of heating varied from 800 W to 5000 W, the microwave duration τ = 1.1 ms, T = 35 ms, the magnitude of the reverse magnetic field varied from 375 to 500 G, and the value of the static magnetic field strength at the locations of the reverse field coils was 1250 G.

The simulation was carried out for the following main parameters: the microwave field intensity E=0.25...3.00 kV/cm, the initial plasma density $n=10^{10}$ cm^{-3}, the rise (decrease) time of the pulsed magnetic field 5 μs, the minimum value of the magnetic field in local magnetic traps B=870 G, the microwave field is turned off after the magnetic field's profile recovery.

X-ray radiation was detected by two identical detectors based on the NaI (Tl) scintillator, 40x40, with magnetic shielding elements in the direction both orthogonal with respect to the magnetic field vector in the central part and along the end of the installation. Radiation from the interaction region was registered by detectors through aluminum windows, 1 mm thick. Both detectors were located in lead shields 1 cm thick, to reduce the influence of background radiation.

The experimental study of the spectral characteristics of the bremsstrahlung radiation allowed to obtain the dependences of the maximum achievable energy of the plasma injection electrons accelerated in the reverse GA mode on the amplitude of the pulsed magnetic field presented in Fig. 2.

The distinctive features of the recorded bremsstrahlung spectra are that the maximum energy detected in the transverse direction is clearly determined by the amplitude of the pulsed magnetic field and reaches its maximum value (300 keV) at B_{pulse} = 500 G (Fig. 2a). It should also be noted that the bremsstrahlung spectrum in the longitudinal direction is recorded mainly in the ECR phase of duty cycle at the phase of

primary plasma creation. Registered maximum energy of these spectra didn't exceed 55−70 keV and does not depend to the magnitude of the amplitude of the reverse magnetic field (Fig. 1b).

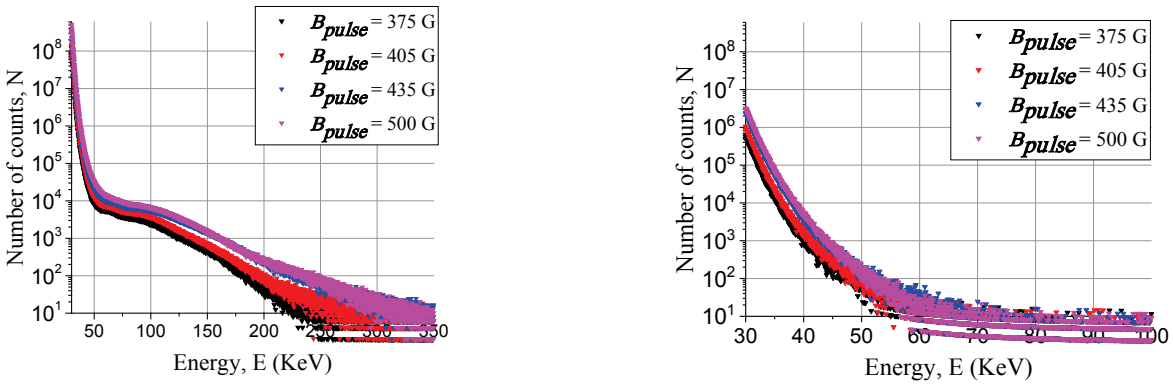

Figure 2. The spectral characteristics of the bremsstrahlung: a − transverse field component Bz, b − Bz along the field component magnitude of the pulsed magnetic field.

Of great interest from the point of view of particles trapping in GA is the time of implementation of phase creation of primary plasma under ECR within time duration of duty cycle 1.1 mS. Figure 3 shows the bremsstrahlung spectra of primary plasma under ECR at different instants within the microwave pulse. As can be seen from Fig. 3a, the maximum trapping is observed at 700 μs after the start of the microwave pulse.

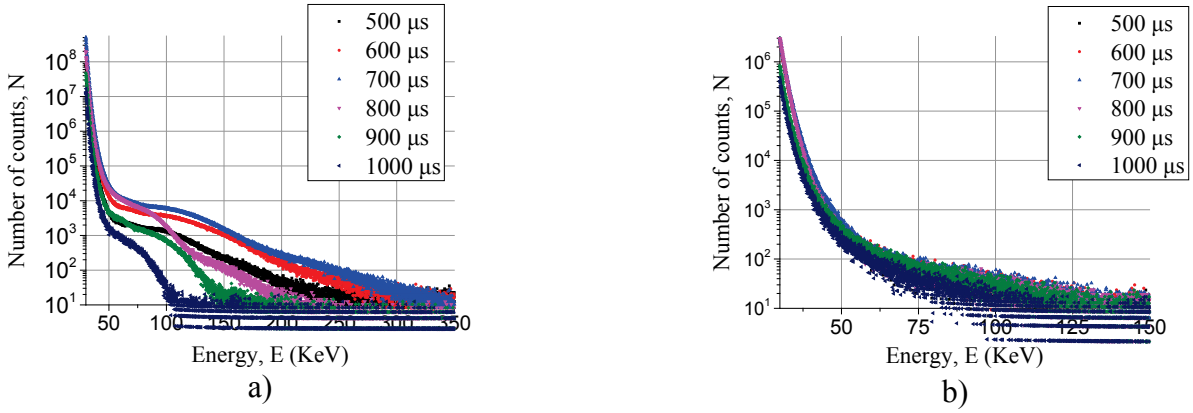

Figure 3. Bremsstrahlung spectra at various time points starting plasma in GA injection mode a − transverse field component Bz, b − the components of Bz along the field.

The steady-state existence of a spatially isolated region of X-ray radiation due to the interaction of fast electrons with atoms of the plasma-forming gas indicates that as a result of the cycle of GA acceleration. A stable plasma bunch with energetic electron of several hundred keV scale is formed in the working volume and is retained for a long time in the magnetic trap of a classical mirror trap. This is confirmed by experiments on X-ray imaging (Kodak MXG film) when a flat target-probe immersed along the radius of the resonator's midplane (Ta-target, 8x5 mm). The film was located at a distance of about 1 m from the central part of the resonator where the target was located. To obtain a clearer image of the plasma formation, a pinhole camera with a lead diaphragm (5 mm thick) and a 1.5 mm diameter hole was used.

Figure 4. Radiographs immersion flat target into the plasma volume.

In Fig. 4, where in addition to the target image there are two ring formations, the first one − of larger diameter due to the background radiation from the cavity's walls, the second formation of smaller diameter is a consequence of the interaction of the electrons of plasma bunch with gas. Figure 3 clearly shows an area with higher contrast, which is most likely due to thermal spray of the target metal and gas desorption from the target surface due to its thermal heating and subsequent interaction of metal and gas particles with the electron of the bunch. The processing of the X-ray patterns made it possible to accurately determine the radius of the plasma bunch, which is on the order of 2.5−3 cm.

Detection of bremsstrahlung when a flat target was immersed in the central part of the resonator, perpendicular to the direction of the magnetic field, made it possible to determine the distribution profile of the hot electronic component. Figure 5 shows the integral characteristics of bremsstrahlung from the target, where it is seen that there is a pronounced intensity maximum corresponding to the radius of the bunch, estimated using the X-ray imaging presented in Fig. 4.

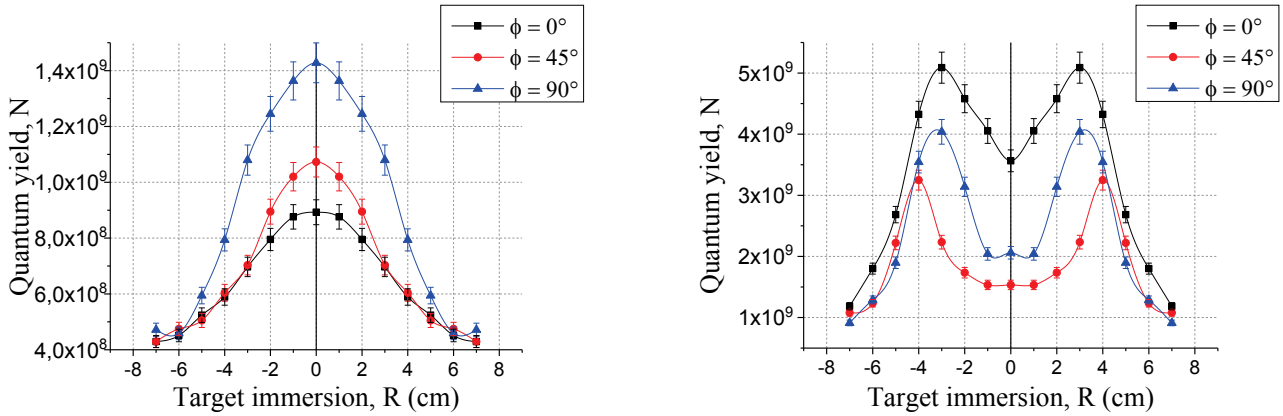

Figure 5. Spectral characteristics and integral bremsstrahlung in immersion flat target, a − along the field component B_z, b − transverse field components B_z.

Measurements showed that the intensity of bremsstrahlung radiation depends on the orientation of the target, and the maximum is observed at angles close to 90º, which indicates the directional movement of electrons in the bunch. From the results obtained, when the target is immersed, one can obtain a simplified representation of the nature of the motion of a bunch of relativistic electrons and describe its motion in the form of rotation around the leading center, relative to the axis of symmetry.

Acknowledgements

The study was supported by a grant from the Russian Science Foundation (Project No. 17-12-01470).

References

1. Andreev V.V., Chuprov D.V., Ilgisonis V.I., Novitsky A.A., Umnov A.M., Physics of Plasmas, 2017, **24**, 093518, doi: 10.1063/1.4986009.
2. Andreev V.V., Novitsky A.A., Korneeva M.A., Umnov A.M., Plasma Physics Reports, 2017, **11**, 1114, doi: 10.1134/S1063780X17110010.
3. Friedland L., Phys. Plasmas, 1994, **1**, N 2, 421, https://doi.org/10.1063/1.870843.
4. Andreev V.V., Umnov A. M., Plasma Sources Sci. Technol., 1999, **8**, 479, doi.org/10.1088/0963-0252/8/3/318.

ECR DISCHARGE AS A SOURCE OF INTENSE PLASMA FLUXES WITH HIGH IONIZATION DEGREE

R. A. Shaposhnikov, S. V. Golubev, I. V. Izotov, R. L. Lapin, S. V. Razin, A. V. Sidorov, V. A. Skalyga, A. F. Bokhanov, M. Yu. Kazakov

Federal Research Center “Institute of Applied Physics of the Russian Academy of Sciences", Ul`yanova Str., 46, Nizhny Novgorod, 603950, Russia

Abstract. Nowadays one of the widespread types of ion sources is systems with plasma heating by microwave radiation in a magnetic field under conditions of the electron cyclotron resonance (ECR) – ECR ion sources. The main direction of the ECR ion sources development is an increase of the extracted ion beams current. The use of gyrotrons as a source of millimeter wave radiation in an ECR discharge makes it possible to obtain plasma with high electron density ($> 10^{13}\ cm^{-3}$), electron temperature at the level of 50−300 eV, low ion temperature at the level of 1 eV, and high ionization degree close to 100%. There are various configurations of the magnetic field, which can be used for plasma confinement: a simple mirror magnetic trap, a cusp or even a single solenoid field. In the framework of recent research it was demonstrated that using of the gyrotron radiation with frequencies of 37.5 and 75 GHz allows to obtain plasma fluxes with densities up to $10\ A/cm^2$. The low temperature of plasma ionic component makes it possible to use such plasma fluxes for formation of ion beams with high current density and low emittance, which opens the possibility for using of these systems in many applications. Recent research in this direction in the Institute of Applied Physics is aimed at development of a point-like neutron source using a sharp focusing of the high-current deuteron beams on a deuterium saturated target and also at the formation of high-current ion beams with large apertures (about 10 cm). The latest results in these fields will be presented in this report.

1. INTRODUCTION

Electron-cyclotron resonance (ECR) ion sources are one of the most widespread types of systems for producing ion beams. Previous experiments in IAP RAS were aimed at creating sources of multiply charged ions with a high plasma density in such magnetic field configurations as open magnetic trap and cusp. It was demonstrated that in such systems the electron concentration can reach values $10^{13}\ cm^{-3}$, electron temperature at the level of $100\ eV$, and the ion beam current has record values up to 500 mA [1−3]. System which is based on the ECR discharge in one solenoid magnetic fields has prospects for producing sources of singly charged ions and formation of plasma fluxes with large apertures as an alternative to existing magnetic plasma confinement systems. This paper is concerned with an experimental investigation the transversal plasma fluxes distribution and measurements of plasma parameters obtained in the ECR discharge in a single magnetic coil sustained by a powerful millimeter-wave gyrotron radiation.

2. EXPERIMENTAL RESULTS

The experiments were carried out at the IAP RAS on facility SMIS 37 (see Fig.1), partly modified the single coil studies. Gyrotron radiation at the frequency of 37.5 GHz with the power up to 100 kW and pulse duration up to 1.5 ms was used for electron heating and discharge ignition. The microwave radiation is launched through a quasioptical system into the discharge chamber with diameter of 68 mm and 250 mm long placed inside pulsed magnetic coil. Magnetic field in the centre of the coil varies from 1 to 4 T. ECR value of magnetic field for the frequency of external electromagnetic radiation 37.5 GHz is

1.34 T. The operating gas (hydrogen) was inlet into the discharge chamber in pulsed mode along the axis of the magnetic system through a gas-entry system integrated into the electrodynamic system for microwave radiation injection. To control neutral gas inlet the pressure in the gas buffer chamber above the gas valve was varied from 0.25 atm. up to 0.92 atm.

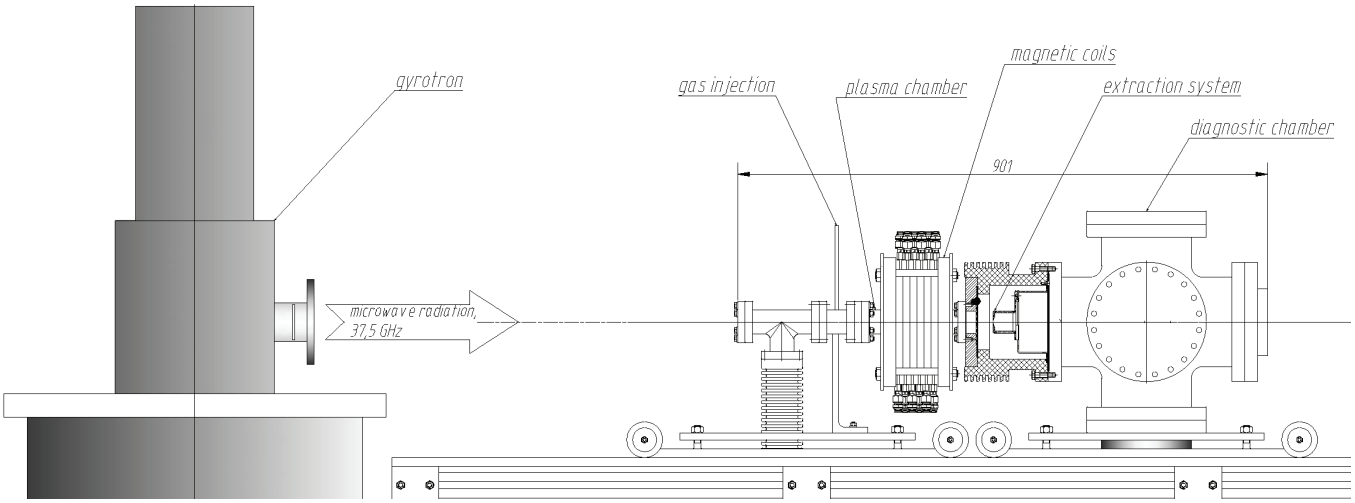

Figure 1. The scheme of experimental facility SMIS 37.

The first experiments were aimed to determine breakdown conditions in this system. At the first step experiments with a constant neutral gas injection were performed to study the possibility of the discharge ignition and to determine a threshold microwave power for it at various pressures. Breakdown curve plotted according to the experimental data is shown in Fig. 2. Also it was demonstrated that discharge could be realized only if maximum magnetic field in the chamber is above ECR value.

The second part of the experiments was aimed to measurements of transverse profile of the plasma flux outgoing along the axis of magnetic system. During the experiments, the parameters of the system were optimized in such a way as to achieve the most homogeneous plasma flux radial distribution. The measurements were carried out using a Langmuir probe moved both in the radial and in the axial directions. As a result of experiments, the plasma flux profiles were measured at various distances from the center of the magnetic coil.

Example of the radial plasma flux distribution at the distances from the center of the magnetic coil of 31, 21, 12, 10 and 8 cm at gyrotron power $Q = 100\ kW$ and at the value of magnetic field at the center of the probe $B_c = 2.16\ T$ is shown in Fig. 3. The vertical axis represents the density of the plasma flux, the horizontal axis represents the radial coordinate.

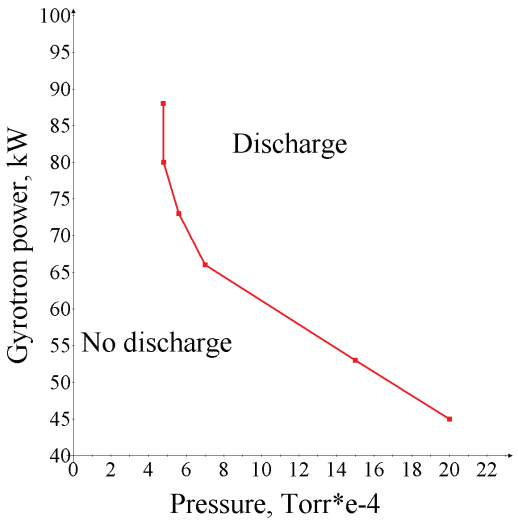

Figure 2. Breakdown threshold curve for hydrogen.

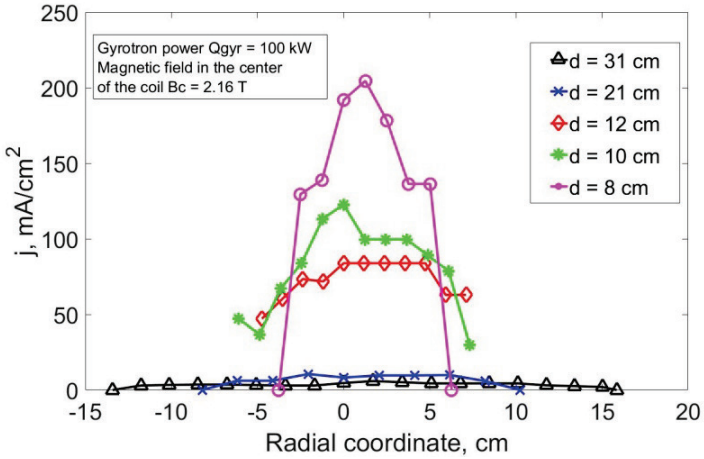

Figure 3. Plasma flux distribution in a cross section, d − distance between the probe and the centre of the coil.

The third part of the experiments was devoted to measuring the plasma parameters obtained as a result of the ECR discharge in the magnetic field of a single solenoid. During the experiments, the plasma density was measured at a distance of 31 cm from the center of the magnetic coil at different gyrotron powers, result is presented in Fig. 4. It is clearly seen from the dependence that the plasma density in the discharge increases with the microwave power and reach values $10^{10} cm^{-3}$. Measurements of the plasma density at various magnetic fields were also done. It is clear from the Fig. 5 that plasma density increases with the growth of the magnetic field.

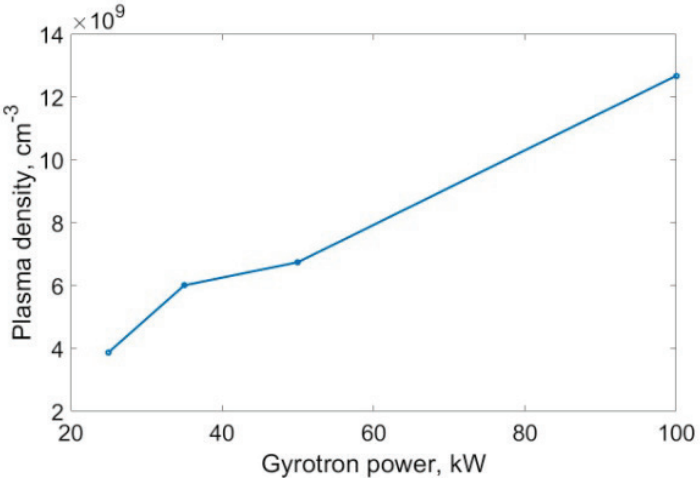

Figure 4. Dependence of plasma density on the gyrotron power, d = 31 cm.

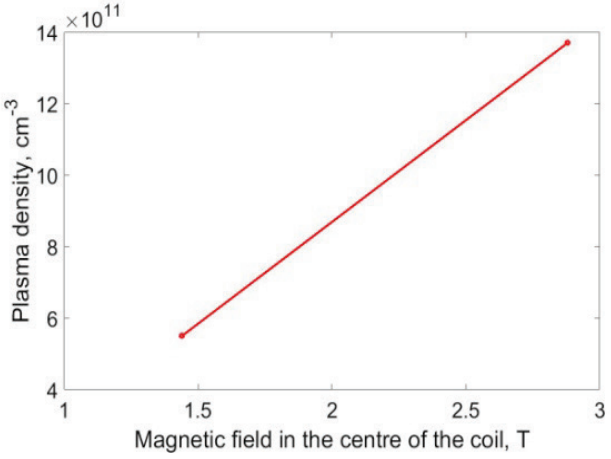

Figure 5. Dependence of plasma density on magnetic field.

The final part of the experiments was concerned with optimization of system parameters on purpose to obtain the maximum electron density in the discharge and to measure the current density of the ion beam. The maximum electron density in the center of the magnetic coil obtained in the experiments was $Ne_{max} = 2 \cdot 10^{13} cm^{-3}$, and the electron temperature was in the range $10 - 30\ eV$. The ion beam current reached 15 mA through a hole with a diameter of 1 mm, which corresponds to the ion current density of $j_{max} \approx 1.5\ A/cm^2$.

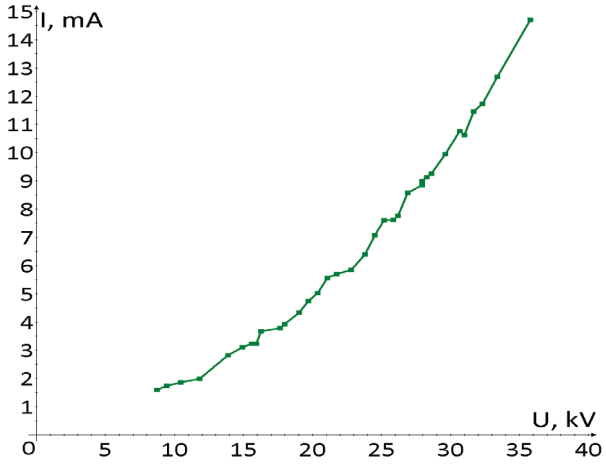

Figure 6. Ion beam current dependence on the extraction voltage.

3. CONCLUSIONS

Experimental results obtained during the investigation of ECR discharge in one solenoid magnetic field demonstrated the possibility of producing wide-aperture plasma fluxes with a homogeneous radial distribution at different distances from the magnetic coil. It was also demonstrated that the plasma density increases with gyrotron power and magnetic field. As a result of the experiment parameters optimization plasma density of $Ne_{max} = 10^{13} cm^{-3}$ and the electron temperature at the level of $Te \approx 10 - 30\ eV$ were obtained. Density of ion current extracted through the 1mm hole reached record values $j_{max} \approx 1.5\ A/cm^2$. Thus, these experimental results demonstrate that such system has clear prospects for producing of a wide-aperture plasma fluxes with high current density.

Acknowledgments

Presented work was supported by the grant of Russian Science Foundation # 16-19-10501.

References

1. Golubev S., Izotov I., Razin S., Sidorov A., Skalyga V., Vodopyanov A., Zorin V., Bokhanov A., Nuclear Instruments and Methods in Physics Research B, 2007, **256**, 537.
2. Sidorov A., Dorf M., Bokhanov A., Izotov I., Razin S., Skalyga V., Zorin V., Balabaev A., Spädtke P., Roßbach J., Review of Scientific Instruments, 2008, **79**, 02A317.
3. Skalyga V., Izotov I., Razin S., Sidorov A., Golubev S., Kalvas T., Koivisto H., Tarvainen O., Review of Scientific Instruments, 2014, **85**, N 2, 02A702-1.

APPARATUS COMPLEX FOR OBTAINING LOW-TEMPERATURE MICROWAVE PLASMA AT ATMOSPHERIC PRESSURE

V. Tikhonov, I. Ivanov, A. Tikhonov

Russian Institute of Radiology and Agroecology,
Kievskoe Shosse, 109th km, Obninsk, Kaluga Region, 249032, Russia

Abstract. Over the past two decades, the scientific and technological community has made significant efforts to develop, maintain and use atmospheric non-thermal plasma (ANTP) because of its numerous scientific and industrial applications. A hardware complex was designed and manufactured to produce low-temperature microwave plasma at atmospheric pressure. ANTPs are generated by a diversity of microwave electrical discharges such as dielectric barrier discharges (DBD), atmospheric pressure plasma jet (APPJ) and atmospheric pressure Argon streamer plasma. A feature of the developed complex of equipment is the presence of a powerful (up to 3 kW) and inexpensive magnetron microwave generator with its power source. In addition, the equipment includes three types of applicators, splitter, cable assembly and water load. The splitter allows an adjustable sampling of microwave power from the waveguide path to the payload by 50 Ohm coaxial cable in the range from 0 to 400 W.

1. INTRODUCTION

At present, there is an urgent need for economical, simple and reliable sources of low-temperature plasma for use in promising areas of science, medicine, industry and agriculture. Low-temperature plasma, unlike the high-temperature, "hot" plasma, used in works on thermonuclear fusion, where the temperature is measured in millions of degrees, is non-equilibrium, that is, the temperatures of ions, neutrals and free electrons in it may differ by several orders of magnitude. This is because most of the electrical energy is embedded in the electronic component, while plasma ions and neutral components remain at a relatively low temperature. Traditional plasma generators, such as electric arc, high-frequency and microwave plasma torches produce plasma with operating temperatures from several thousand to tens of thousands of degrees, but according to the classification of physicists, such plasma also refers to low-temperature plasma. This subdivision is due to the importance of high-temperature plasma in the problem of controlled thermonuclear fusion [1].

Over the past two decades, the scientific and technical community has made significant efforts to develop, maintain and use atmospheric non-thermal plasma (ANTP) in which ions and neutral components remain at or near room temperature [2]. This allows the use of such ANT plasma for low-temperature plasma chemistry and for the processing of heat-sensitive materials, including polymers and biological tissues. The unique properties of ANTP, which include a strong thermodynamic non-equilibrium nature, low gas temperature, the presence of chemically active radicals and high selectivity, provide a huge potential for the use of "cold" plasma sources in a wide range of applications. The growth and importance of the ANTP technology and its application has spread to a large number of areas, such as environmental engineering, aerospace engineering, biomedicine, textiles, food and agricultural technologies, analytical chemistry and several others [3]. The unique capabilities and diverse applications of the ANTP technology are associated with its enormous potential for ensuring environmental friendliness and energy saving, technological flexibility and the ability to create new products and technologies.

The purpose of this work is to present a universal hardware complex, designed to generate both traditional low-temperature plasma and two types of ANTP in the R&D works on new materials and technologies, and also to intensify existing technological processes.

2. DESIGN DEVELOPMENT

The hardware complex in the basic configuration consists of a microwave generator with HV power supply, a set of replaceable elements of the waveguide system, a water load, a 50 Ω cable assembly with N-connectors and one or several ANTP applicators (Fig. 1).

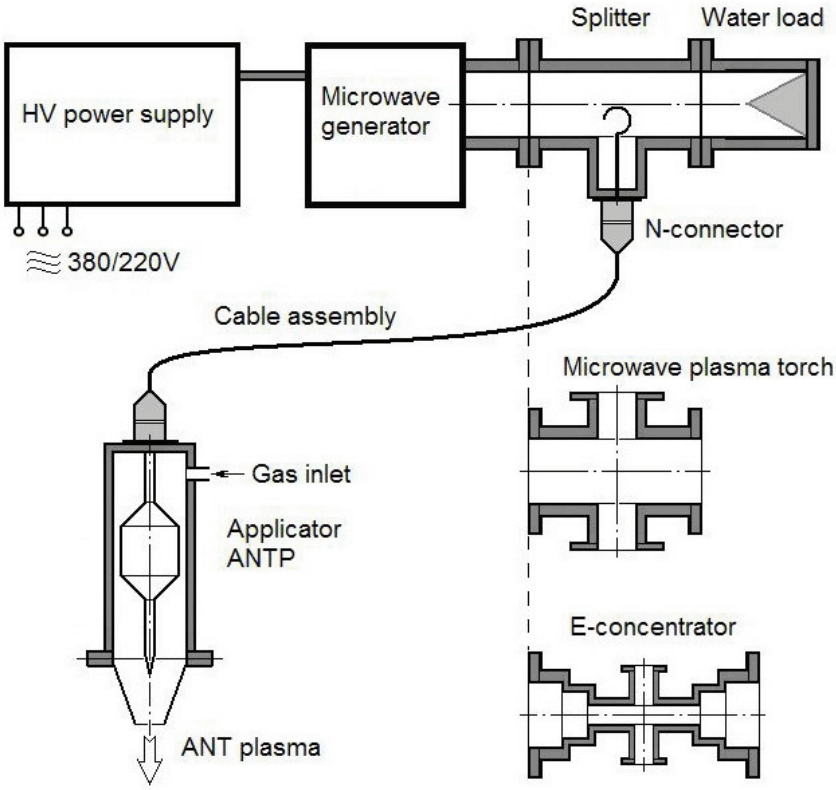

Figure 1. Schematic diagram of components and blocks of the hardware complex.

The basis of the presented hardware complex is a low-budget the 2.45 GHz magnetron microwave oscillator with a high-voltage power unit built on the magnetrons, transformers and capacitors used in microwave ovens for domestic and industrial use [4]. The output power of the microwave generator can be changed discretely, in the range from 0.5 to 3 kW, the number of stages (three or more) and a specific set of power levels can be established in agreement with the customer. If the maximum required microwave power level does not exceed 1.5 kW, an air-cooled magnetron, such as LG-246, can be used. In the case of higher power, liquid cooling of the magnetron is necessary.

The main elements of the waveguide system are made of stainless steel on the basis of a standard rectangular profile of 100×50×2 mm^3, with WR-340 flanges size. In the basic configuration, the waveguide path is loaded onto the final resonant water load. Between the output of the microwave generator and the load, the waveguide path elements from the next set can be placed.

1. The microwave plasma torch on the main type H_{01} oscillations in the waveguide. Continuing our traditional principle of maximum use of the ready-made components, now we supply our microwave plasma systems with plasma torches, built on the basis of standard threaded stainless steel and brass fittings for metal pipes [5]. Availability of fittings, at an affordable price and the huge assortment allows quickly select the configuration of the plasma burner for a specific task (Fig. 2, left). As the plasma temperature can reach several thousand degrees, water cooling of the support tube or the entire waveguide section creates opportunities for the implementation of long-term technological processes (Fig. 2, right).

2. E-field concentrator of a step-by-step design or with a smooth change in the height of the waveguide serves to increase the electric field strength in the microwave plasma torch placement zone. The narrowing of the waveguide can be symmetrical or one-sided.

3. An inductive-type splitter is a coupling loop located on a narrow wall of the waveguide. The design of the coupler allows you to change the communication value by rotating the loop plane, which is loaded

on the N-type coaxial connector. At the maximum coupling value, of about 14% of the microwave generator power branches off into the coaxial, while in the main waveguide the introduced reflections do not exceed 4%.

Figure 2. Plasma jet on standard fittings (left) and additional water cooling.

The payload (ANTP applicator) is connected to the splitter using a cable assembly that is a 50 Ω section of a flexible coaxial cable with N-type connectors at the ends. It is possible to combine a splitter and a microwave plasma torch in one node.

One of the variants of the ANTP applicator design is shown in Fig. 3 on the left. The plasma reactor vessel and air cooling radiator are made of aluminum alloy, the protective body of the applicator is made of Teflon. The N-type cable connector is located on the applicator cover, here there is also a supply pipe for working gas (argon) and two chutes of the reactor forced air cooling system.

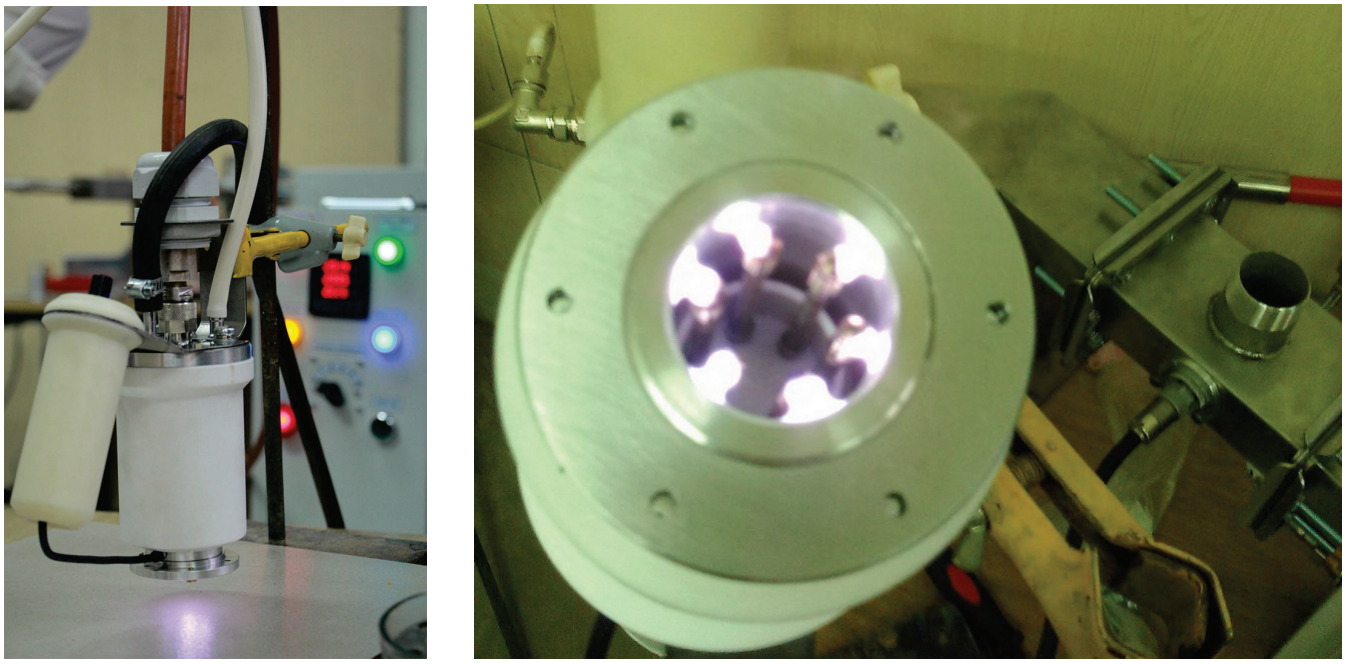

Figure 3. ANTP applicator (left) and image of an Argon streamer discharge.

The combustion region of the discharges at the ends of the applicator electrodes is as close as possible to the tip of the reactor flange, which allows to expand the temperature limits of the impact modes on the

treated objects. Initiation of the plasma discharge is carried out using a piezo ignition system located in the handle of the applicator, the ignition button is located directly on the end of the handle. A typical form of a streamer microwave discharge in Argon is shown in Fig. 3 on the right, here we can see a splitter combined with a microwave plasmatron section of waveguide system too.

3. RESULTS

Thus, a universal hardware complex of variable configuration for generation low-temperature microwave plasma at atmospheric pressure has been developed. It is designed for both laboratory and industrial applications. The general view of the complex is shown in Fig. 4.

Figure 4. The general view of universal hardware complex for obtaining of low-temperature and ANT plasma.

The development of new elements for the hardware complex continues. In particular, experimental studies are being conducted on the development of sources of an ANTP based on a dielectric barrier microwave discharge in a coaxial and waveguide structure, as well as on applicators for studying the interaction of microwave plasma with various liquids. To expand the technical and technological capabilities, the hardware complex can be additionally equipped with a microwave circulator, a contactless mobile waveguide short-circuiting plunger and strip directional couplers to measure the incident and reflected waves.

References

1. Encyclopaedia of Low-Temperature Plasma. Entrance Volume, Book 2. Ed. by V. E. Fortov. Moscow: MAIK Nauka/Interperiodika, 2000 [in Russian].
2. Vijay Nehra, Ashok Kumar, H.K. Dwivedi, Int. J. Eng., 2008, **2**, N 1, 53.
3. Misra N.N., Schlüter O., Cullen P.J., Cold Plasma in Food and Agriculture: Fundamentals and Applications. London, United Kingdom: Academic Press, 2016.
4. Tikhonov V.N, Ivanov I.A, Kryukov A.E., Tikhonov A.V, Prikladnaya Fizika (Appl. Phys.), 2015, N 5, 102 [in Russian].
5. Tikhonov V.N., Aleshin S.N., Ivanov I.A., Tikhonov A.V., Journal of Physics: Conf. Series 927, 2017, 012067 doi:10.1088/1742-6596/927/1/012067.

X INTERNATIONAL WORKSHOP ON MICROWAVE DISCHARGES: FUNDAMENTALS AND APPLICATIONS

LIST OF PARTICIPANTS

ANTIPOV Sergey: Joint Institute for High Temperatures Russian Academy of Sciences, Izhorskaya Str., 13, Building 2, Moscow, 125412, Russia,
E-mail: antipov@ihed.ras.ru

ANTONOVA Irina: A. M. Prokhorov General Physics Institute Russian Academy of Sciences, Vavilov Str., 38, 119991, Moscow, Russia,
Tel.: +7 926 366 6982, Fax: +7 926 366 6982
E-mail: vil2276@gmail.com

ARTEM'EV Konstantin: A. M. Prokhorov General Physics Institute, Russian Academy of Sciences, Vavilov Str., 38, Moscow, 119991, Russia,
Tel.: +7 499 503 8237,
E-mail: artemevkv@gmail.com

AVERIN Konstantin: A. V. Topchiev Institute of Petrochemical Synthesis of the Russian Academy of Sciences, Leninsky prospect, 29, Moscow, 119991, Russia,
Tel.: +7 968 598 7549, Fax: +7 495 633 8520
E-mail: averin@ips.ac.ru

BALMASHNOV Alexander: RUDN University, Miklukho-Maklay Str., 6, Moscow, 117198, Russia,
Tel.: 7 495 955 0923,
E-mail: abalmashnov@rambler.ru

BENOVA Evgenia: Sofia University "St. Kliment Ohridski", Kosta Loulchev Str., 27, Sofia, 1111, Bulgaria,
Tel.: 359 878748837, Fax: 359 2 9460255,
E-mail: geni_benova@abv.bg

BOGDANOV Sergey: Institute of Applied Physics of the Russian Academy of Sciences, Ul'yanov Str., 46, Nizhny Novgorod, 603950, Russia,
Tel.: +7 831 416 4960, Fax: +7 831 416 4960,
E-mail: bogser@appl.sci-nnov.ru

BRITUN Nikolay: Chimie des Interactions Plasma Surface (ChIPS) University of Mons, Place du Parc, 23, Mons, Hainaut, 7000, Belgium
Tel.: +32 065 55 49 56, Fax: +32 065 55 49 41
E-mail: nikolay.britun@umons.ac.be

CHUPROV Denis: RUDN University, Miklukho-Maklay Str., 6, Moscow, 117198, Russia,
Tel.: +7 495 955 0759, Fax: +7 495 955 0827,
E-mail: chu_d@mail.ru

DAVYDOV Alexey: A. M. Prokhorov General Physics Institute of the Russian Academy of Sciences, Vavilov Str., 38, 119991, Moscow, Russia,
Tel.: +7 499 503 8344, Fax: +7 926 366 6982
E-mail: freaman@mail.ru

DIAS Francisco: Instituto de Plasmas e Fusão Nuclear, Instituto Superior Tecnico, Universidade de Lisboa, Av. Rovisco Pais, Lisbon, 1049-001, Portugal,
Tel.: 352 218419326, Fax: 352-218464455,
E-mail: francisco.dias@ist.utl.pt

DVININ Sergey: Moscow State University, Physics department, Leninskiye Gory, Moscow, 119991, Russia,
Tel.: +7 910 458 3055, Fax. +7 495 939 1787,
E-mail: sadvinin@gmail.com

EPSTEIN Irene: A. V. Topchiev Institute of Petrochemical Synthesis of the Russian Academy of Sciences, Leninsky prospect, 29, Moscow, 119991, Russia,
Tel.: +7 495 647 5927, extens. 314, Fax.: +7 495 633 8520,
E-mail: epstein@ips.ac.ru

GORBACHEV Alexey: Institute of Applied Physics of the Russian Academy of Sciences, Ul'yanov Str., 46, Nizhny Novgorod, 603950, Russia,
Tel.: +7 831 416 4960, Fax: +7 831 416 4960
E-mail: gorb@appl.sci-nnov.ru

GRIES Thomas: Institut Jean Lamour − CNRS, Campus ARTEM - 2 allée André Guinier - B.P. 50840, Nancy, Grand-Est, 54011, France
Tel.: +33.372.742.497, Fax: No
E-mail: thomas.gries@univ-lorraine.fr

IVANOV Igor: Russian Institute of Radiology and Agroecology, Kievskoe Shosse, 109th km, Obninsk, Kaluga reg., 249032, Russia
Tel.: +7 (48439) 9-69-36, Fax: +7(48439) 6-80-66,
E-mail: ivanov.i.an@mail.ru

IVANOV Vyatcheslav: A. M. Prokhorov General Physics Institute of the Russian Academy of Sciences, Vavilov Str., 38, Moscow, 119991, Russia,
Tel. +7 499 503 8344, Fax. +7 499 135 8011,
E-mail: ivanov@fpl.gpi.ru

JERBY Eli: Tel Aviv University, Faculty of Engineering, Ramat Aviv, 6997801, Israel,
Tel.: +972 3 640 8408, Fax: +972 3 640 7860,
E-mail: jerby@eng.tau.ac.il

KIM Jin Joong: Maltani Corporation, Hansin IT Tower (Room 411), 272 Digital-ro Guro-gu, Seoul, N/A, 08389, Republic of Korea
Tel.: +82-(0)10-4949-9896, Fax: +82-(0)2-837-9107
E-mail: kimjj@maltani.co.kr

KLUTE Michael: Institute of Theoretical Electrical Engineering, Ruhr University Bochum, Universitaetsstrasse,150, Bochum, NRW, 44780, Germany,
Tel.: +49(0)234/32–29909, Fax: +49(0)234/32–14479,
E-mail: Michael.Klute@tet.ruhr-uni-bochum.de

KORNEEVA Maria: RUDN University, Miklukho-Maklay Str., 6, Moscow, 117198, Russia,
Tel.: +7 926 499 7840, Fax: No,
E-mail: korneevama@mail.ru

KOSSYI Igor: A. M. Prokhorov General Physics Institute of the Russian Academy of Sciences, Vavilov Str., 38, Moscow, 119991, Russia
Tel.: +7 499 135 41 65, Fax: No,
E-mail: kossyi@fpl.gpi.ru

KRASHEVSKAYA Galina: National Research Nuclear University MEPhI, Kashirskoe Shosse, 31, Moscow, 115409, Russia,
Tel.: +7 495 788 5699, extens.9674, Fax: +7 499 324 2111,
E-mail: krashevskaya-gv@mail.ru

KUDRLE Vit: Masaryk University, Dept. of Physical Electronics, Kotlarska, 2, Brno, CZ-61137, Czech Republic,
Tel.: +420549495433, Fax: 000,
E-mail: kudrle@sci.muni.cz

LACOSTE Ana: University Joseph Fourier – LPSC, 53 rue des Martyrs 38026 Grenoble Cedex, Grenoble, France,
Tel.: +33 4 76 28 40 14, Fax: +33 4 76 28 40 11
E-mail: ana.lacoste@ujf-grenoble.fr

LEBEDEV Yuri: A. V. Topchiev Institute of Petrochemical Synthesis of the Russian Academy of Sciences, Leninsky prospect, 29, Moscow, 119991, Russia,
Tel. +7 495 647 5927, ext. 322, Fax. +7 495 633 8520,
E-mail: lebedev@ips.ac.ru

MISAKYAN Mamikon: Higher School of Economics National Research University, Myasnitskaya Str., 20, Moscow, 101000, Russia,
Tel.: +7 903 561 0067, Fax: No
E-mail: misakyan@hse.ru

MOISAN Michel: Université de Montréal, Département de Physique, Pavillon Roger-Gaudry, Montréal, Québec, H3C 3J7, Canada,
Tel.: (1)5143436671, Fax: (1)5143432071,
E-mail: michel.moisan@umontreal.ca

van der MULLEN Joost: Université Libre de Bruxelles, Avenue F.D. Roosevelt 50, B-1050, Brussels, CP115/1, Belgium,
Tel.: +32 2 6502357,
E-mail: jjamvandermullen@gmail.com

NOVITSKY Andrey: RUDN University, Miklukho-Maklay Str., 6, Moscow, 117198, Russia,
E-mail: temple18@mail.ru

van ROOIJ Gerard: Dutch Institute for Fundamental Energy Research (DIFFER), Eindhoven, the Netherlands,
Tel.: +31 (0)40 3334 744
E-mail: G.J.vanRooij@differ.nl

SANCHEZ-VALENCIA Juan Ramon: Materials Science Institute of Seville (CSIC-US), C/Americo Vespucio, 49, Seville, 41092, Spain,
Tel.: 0034 954489500 +ext. 909249, Fax: 0034 954460165,
E-mail: jrsanchez@icmse.csic.es

SATUNIN Sergey: A. M. Prokhorov General Physics Institute of the Russian Academy of Sciences, Vavilov Srt., 38, Moscow, 119991, Russia,
Tel. +7 495 132 8344, Fax. +7 495 135 8011,
E-mail: sato@fpl.gpi.ru

SHAKHATOV Viacheslav: A. V. Topchiev Institute of Petrochemical Synthesis of the Russian Academy of Sciences, Leninsky prospect, 29, Moscow, 119991, Russia,
Tel.: +7 495 647 5927, ext. 324, Fax: +7 495 633 8520,
E-mail: shakhatov@ips.ac.ru

SHAPOSHNIKOV Roman: Institute of Applied Physics of the Russian Academy of Sciences, Ul'yanov Str., 46, Nizhny Novgorod, 603950, Russia, Tel.: +7 915 949 2711,
E-mail: shaposhnikov-roma@mail.ru

SKALYGA Vadim: Institute of Applied Physics of the Russian Academy of Sciences, Maxim Gorkii Str., 140-43, Nizhny Novgorod, 603000, Russia,
Tel.: +7 915 949 2711, Fax: +7 831 416 0616,
E-mail: skalyga.vadim@gmail.com

SVARNAS Panagiotis: University of Patras, Electrical and Computer Engineering Department, Patras, Rion, 26500, Greece,
Tel.: 00306977767301, Fax: 00302610997358,
E-mail: svarnas@ece.upatras.gr

TATARINOV Alexey: A. V. Topchiev Institute of Petrochemical Synthesis of the Russian Academy of Sciences, Leninsky prospect, 29, Moscow, 119991, Russia,
Tel.: +7 495 647 5927, ext. 314, Fax: +7 495 633 8520,
E-mail: atat@ips.ac.ru

TIKHONOV Viktor: Russian Institute of Radiology and Agroecology, Kievskoe Shosse, 109th km, Obninsk, Kaluga reg., 249032, Russia,
Tel.: +7(48439) 9-69-36, Fax: +7(48439) 6-80-66,
E-mail: v.n.tihonov@yandex.ru

TITOV Alexander: A. V. Topchiev Institute of Petrochemical Synthesis of the Russian Academy of Sciences, Leninsky prospect, 29, Moscow, 119991, Russia,
Tel. +7 495 647 5927, ext. 241, Fax: +7 495 633 8520,
E-mail: 0131shaokhan@mail.ru

TOYODA Hirotaka: Nagoya University, Furo-cho, Chikusa-ku, Nagoya, Aichi, 464-8603, Japan,
Tel.: +81 52 789 4698, Fax: +81 52 789 3152,
E-mail: toyoda@nuee.nagoya-u.ac.jp

TSODIKOV Mark: A. V. Topchiev Institute of Petrochemical Synthesis of the Russian Academy of Sciences, Leninsky prospect, 29, Moscow, 119991, Russia,
Tel. +7 495 647 5927, ext. 304, Fax: +7 495 633 8520,
E-mail: tsodikov@ips.ac.ru

USACHONAK Maxim: Institute of Physics of NAS of Belarus, Nezalezhnasci Ave., 68, Minsk, 220072, Belarus
Tel.: +375 17 284 1431, Fax: +375 17 284 0879
E-mail: m.usachonak@dragon.bas-net.by

VASIL'KOV Dmitry: A. M. Prokhorov General Physics Institute of the Russian Academy of Sciences, Vavilov Str., 38, Moscow, 119991, Russia,
Tel. +7 495 132 8344, Fax: +7 495 135 8011,
E-mail: ivanov@fpl.gpi.ru

VODOPYANOV Alexander: Institute of Applied Physics of the Russian Academy of Sciences, Ul'yanov Str., 46, Nizhny Novgorod, 603950, Russia,
Tel.: 7 831 416 4652, Fax: (831)4164960
E-mail: avod@yandex.ru

VORONOVA Elena: A. M. Prokhorov General Physics Institute of the Russian Academy of Sciences, Vavilov Str., 38, Moscow, 119991, Russia,
Tel. +7 495 132 8344, +Fax: +7 495 135 8011,
E-mail: ivanov@fpl.gpi.ru

YUROV Vladimir: A. M. Prokhorov General Physics Institute of the Russian Academy of Sciences, Vavilov Str., 38, Moscow, 119991, Russia,
Tel.: +7 905 571 1244, Fax: +7 499 135-0270,
E-mail: yurov6591@gmail.com

3-7 September, 2018, Zvenigorod, Russia

REPORT

on the business meeting of the International Scientific Committee on "Microwave Discharges: Fundamentals and Applications"
(September 5, 2018, Zvenigorod, Russia)

The agenda of the meeting was:

1. Regular changes (rotation) in the ISC.
2. On the place of the XI-th Int. Workshop on " Microwave Discharges: Fundamentals and Applications".
3. Election of the Chairman of the ISC for the period of 2018-2021.
4. On the Honorary members of the ISC.

Decisions:

1. Regular changes (rotation) in the ISC:
   a) Prof. H. Toyoda was elected as representative of Japan in the ISC;
   b) Members of the International Scientific Committee are:
      J. Asmussen (USA)
      P. Awakowicz (Germany)
      E. Benova (Bulgaria)
      F. Dias (Portugal)
      A. Gamero (Spain)
      E. Jerby (Israel)
      Yu. Lebedev (Russia, Chairman)
      A. Lacoste (France)
      M. Moisan (Canada)
      J.J.A.M. van der Mullen (Belgium)
      H. Toyoda (Japan)
2. The XI-th Int. Workshop on Microwave Discharges: Fundamentals and Applications will take place in 2021 in Bulgaria.

3. Professor E. Benova was elected the Chairman of the International Scientific Committee for the period 2018-2021.

4. On the Honorary members of the ISC:
   a) Professor M. Nagatsu was elected the Honorary Member of ISC for his invaluable contribution to the development and success of the Workshop.
   b) Honorary members of the ISC:
      Prof. J. Marec (France)
      Prof. M. Kando (Japan)
      Prof. M. Nagatsu (Japan)

Prof. Yuri A. Lebedev
Chairman of ISC (2015-2018)

AUTHOR INDEX

MICROWAVE DISCHARGES:
FUNDAMENTALS AND APPLICATIONS

Сдано в набор 01.11.2018. Подписано в печать 20.11.2018.
Формат 70x 100/16. Бумага офсетная №1. Печать офсетная.
Уч.-изд. л. 18,0. Физ. пл. 17,0. Тираж 150 экз.

ООО «Издательство «Янус-К»,
127411, Москва, Учинская ул., д.1

Отпечатано в ООО «БИЗНЕСГАРАНТ»
107031, Москва, ул. Рождественка, д.6/9/20, стр.1

ISBN 5-9903264-9-1

ISBN 5-8037-0746-5